

On pole position: new approaches to quantifying polar wander and relative paleomagnetic displacements

Bram Vaes

Utrecht Studies in Earth Sciences No. 283

Members of the dissertation committee:

Prof. dr. Andrew J. Biggin
University of Liverpool - Liverpool, United Kingdom

Prof. dr. David A. D. Evans
Yale University - New Haven, USA

Prof. dr. Richard G. Gordon
Rice University - Houston, USA

Prof. dr. Wentao Huang
Chinese Academy of Sciences - Beijing, China

Dr. Johanna Salminen
University of Helsinki - Helsinki, Finland

ISBN: 978-90-6266-653-9

Author contact: vaes.bram@gmail.com

Cover image: Elen11 (iStock by Getty Images). Design: Margot Stoete

Copyright © 2023 B. Vaes. All rights reserved. No part of this publication may be reproduced in any form, by print or photo print, microfilm or any other means, without written permission by the author.

Printed in The Netherlands by Ipskamp

On pole position: new approaches to quantifying polar wander and relative paleomagnetic displacements

Over poolpositie: nieuwe benadering van het kwantificeren van poolzwerfing en relative paleomagnetische verplaatsingen
(met een samenvatting in het Nederlands)

Proefschrift

ter verkrijging van de graad van doctor aan de Universiteit Utrecht op gezag van de rector magnificus, prof. dr. H.R.B.M. Kummeling, ingevolge het besluit van het college voor promoties in het openbaar te verdedigen

op dinsdag 27 juni 2023 des middags te 12:15 uur

door

Bram Vaes

geboren op 13 september 1993 te Eindhoven

Promotor: Prof. dr. D. J. J. van Hinsbergen

This thesis was accomplished with financial support from NWO Vici grant 865.17.001.

Contents

- 8 **Summary**
- 10 **Introduction**
- 19 **Chapter 1** **Reconstruction of subduction and back-arc spreading in the NW Pacific and Aleutian Basin: clues to causes of Cretaceous and Eocene plate reorganizations**
*B. Vaes, D. J. J. van Hinsbergen & L. M. Boschman (2019). *Tectonics*, 38(4), 1367-1413.*
- 73 **Chapter 2** **On pole position: causes of dispersion of the paleomagnetic poles behind apparent polar wander paths**
*B. Vaes, L. C. Gallo & D. J. J. van Hinsbergen (2022). *Journal of Geophysical Research: Solid Earth*, 127(4), e2022JB023953.*
- 101 **Chapter 3** **Reliability of paleomagnetic poles from sedimentary rocks**
*B. Vaes, S. Li, C. G. Langereis & D. J. J. van Hinsbergen (2021). *Geophysical Journal International*, 225(2), 1281-1303.*
- 135 **Chapter 4** **Influence of data filters on the position and precision of paleomagnetic poles: what is the optimal sampling strategy?**
*D. Gerritsen, B. Vaes & D. J. J. van Hinsbergen (2022). *Geochemistry, Geophysics, Geosystems*, 23(4), e2021GC010269.*
- 155 **Chapter 5** **A global apparent polar wander path for the last 320 Ma calculated from site-level paleomagnetic data**
*B. Vaes, D. J. J. van Hinsbergen, S. H. A. van de Lagemaat, E. van der Wiel, N. Lom, E. L. Advokaat, L. M. Boschman, L. C. Gallo, A. Greve, C. Guilmette, S. Li, P. C. Lippert, L. Montheil, A. Qayyum, & C. G. Langereis. *Earth-Science Reviews*, in review.*
- 197 **Chapter 6** **APWP-online.org: a global reference database and open-source tools for calculating apparent polar wander paths and relative paleomagnetic displacements**
*B. Vaes, D. J. J. van Hinsbergen & J. Paridaens. *Tektonika*, in review.*
- 215 **Chapter 7** **The wandering pole: improved paleomagnetic constraints on true polar wander during the last 320 Ma**
B. Vaes & D. J. J. van Hinsbergen

228	Supplementary information to chapters
229	References
264	Summary in Dutch (Samenvatting in het Nederlands)
266	Acknowledgements (Dankwoord)
268	Curriculum vitae
269	Bibliography

Summary

Paleomagnetism provides the only quantitative tool to reconstruct the position and motion of tectonic plates and continents in deep geological time. These reconstructions often rely on apparent polar wander paths (APWPs), which describe the past position and motion of plates relative to the Earth's spin axis. In addition to providing a paleomagnetic reference frame for paleogeography, these paths serve to quantify relative tectonic displacements with other lithospheric blocks. A long-discussed problem is that conventional approaches to computing polar wander do not propagate key sources of uncertainty in the underlying data, such as data scatter or age uncertainty, but proposed solutions remained mostly qualitative. Recently, this problem became more urgent: Rowley (2019) showed that as much as 50% of the data that underlie the currently most widely used global APWP are statistically significantly displaced relative to that APWP. This implies that the resolution at which a geologically meaningful statistical difference between a paleomagnetic dataset and an APWP may be determined, is strongly limited, which undermines the current tectonic and paleogeographic applications of paleomagnetism.

This thesis aims to examine the causes of dispersion of paleomagnetic data behind APWPs and to build a global APWP in which key data uncertainties are propagated, such that it may be used to determine geologically meaningful relative displacements. We show that the uncertainty of APWPs computed from paleomagnetic poles, which is the current standard, is mostly determined by the arbitrary choice of how many datapoints are used per pole. This thesis then develops a novel approach in which apparent polar wander paths are computed from site-level paleomagnetic data instead of paleomagnetic poles. In this approach, larger weight is assigned to larger datasets and temporal and spatial uncertainties in the paleomagnetic data are incorporated. We introduce a set of reliability criteria for the inclusion of sediment-derived datasets in the computation of the APWP and show that they may provide high-quality paleomagnetic records if they are corrected for inclination shallowing and adequately represent paleosecular variation. We demonstrate that the application of within-site data filters and cutoffs do not significantly improve the position or precision of paleomagnetic poles and that the most effective way to determine the time-averaged pole position is by collecting as many independent spot readings of the past geomagnetic field as possible. We used these criteria to compile a new global paleomagnetic database, which includes only the ~32% most reliable data from previous compilations.

We present a global apparent polar wander path for the last 320 Ma using the new statistical approach proposed in this thesis. We find that the first-order geometry of this path is similar to previous models but with smaller uncertainties. Moreover, we show that correcting for temporal bias in the paleomagnetic data allows improved quantification of

polar wander rates, and that previously observed peaks in polar wander likely resulted from such bias. We introduce the open-source web application APWP-online.org that provides user-friendly tools to compute apparent polar wander paths using our new methodology as well as the computation of relative paleomagnetic displacements. The website also hosts the global paleomagnetic reference database that underlies the new global apparent polar wander path and is aimed to serve as a community platform for the continuous improvement of the path in the future through the addition of new high-quality paleomagnetic data.

Finally, we provide new quantitative estimates of true polar wander during the last 320 Ma by comparing our new global apparent polar wander path with existing mantle reference frames. The computed true polar wander paths suggest that the true polar wander rotations occurred about two roughly orthogonal axes in the equatorial plane. We discuss the geodynamic implications of these findings and highlight future opportunities for the identification and quantification of true polar wander on geological timescales.

Introduction

Paleomagnetic data, obtained from measurements of the past geomagnetic field recorded in rocks, provide quantitative constraints on the position and motion of tectonic plates and continents relative to the geomagnetic pole. Paleomagnetism serves as one of the principal tools for deciphering paleogeography, thereby providing essential input for many disciplines in the Earth sciences that rely on the configuration of continents and plate boundaries through time, such as geodynamics, paleoclimatology, paleoceanography, and paleobiology. The tectonic and paleogeographic applications of paleomagnetism strongly rely on the reliability of the underlying paleomagnetic data and an adequate description of the associated uncertainties. During the past few decades, researchers have focused on solving tectonic problems that require paleomagnetic constraints with increasingly higher spatial and temporal resolution and better control on the uncertainties. However, conventional paleomagnetic approaches do not incorporate important sources of uncertainties in the underlying paleomagnetic data, and it was recently shown that current approaches to determine relative tectonic displacements strongly overestimate paleomagnetic resolution. In this thesis, I aim to overcome these problems, and attempt to develop a methodology to reliably determine geologically meaningful relative paleomagnetic displacements, taking into account the uncertainties and limitations of paleomagnetic data, and explore the implications of such a methodology for apparent and true polar wander behavior.

Scientific background

Reconstructing paleogeography using paleomagnetism

Paleomagnetism played a fundamental role in the confirmation of relative motion between continents ('continental drift', *sensu* Wegener, 1912) and the subsequent development of the theory of plate tectonics. In the 1950s and 1960s, several groundbreaking paleomagnetic studies provided the first independent geophysical evidence for the movement of continents (see overview by Creer & Irving, 2012). Creer et al. (1954) showed that the estimated positions of the past geomagnetic pole for different geological time periods were notably different from the position of the present-day pole, suggesting that either the geomagnetic pole itself had moved or that the continent from which the data were derived (Great Britain/Europe) had moved relative to the pole through geological time. Although these authors preferred the former interpretation at that time, Runcorn (1956) interpreted observed differences between paleomagnetic pole positions of North America and Europe as quantitative evidence for the relative 'drift' of these continents due to opening of the Atlantic Ocean.

This interpretation was further supported by the work of Vine and Matthews (1963),

who recognized that marine magnetic anomalies preserved in oceanic crust reflect the recording of reversals of the geomagnetic field during seafloor spreading at mid-ocean ridges, a process that was described by Hess (1962) the year before. This process of seafloor spreading provided a mechanism that allowed continents - or tectonic plates - to 'drift' apart, for instance during the opening of an oceanic basin like the Atlantic Ocean. These studies provided key building blocks for the development of the paradigm of plate tectonics in the following years. Records of seafloor spreading, consisting of marine magnetic anomaly, transform fault, and fracture zone data provide direct quantitative constraints on the relative motions of tectonic plates and have been widely used as input for detailed regional and global plate motion reconstructions (e.g., Engebretson et al., 1985; Seton et al., 2012; Müller et al., 2016, Torsvik & Cocks, 2016; DeMets & Merkouriev, 2021). However, these records cannot be used to quantitatively reconstruct relative plate motions prior to the break-up of Pangea, because the marine magnetic anomaly records derived from oceanic lithosphere are rarely older than Jurassic in age (~175 Ma, Torsvik et al., 2008a).

Prior to the Jurassic, paleomagnetism provides the main quantitative tool to reconstruct paleogeography and to estimate 'absolute' plate tectonic motions (Torsvik et al., 2008a; Domeier & Torsvik, 2014). Paleomagnetic data has played a key role in deciphering paleogeography in deep geological time and forms the foundation of most Precambrian plate reconstructions (Piper, 1974; Merdith et al., 2017, 2021; Li et al., 2023), providing quantitative constraints on the past existence and configuration of supercontinents, such as Rodinia, Nuna and other - more speculative - continents like Kenorland (Evans, 2013), as well as on the onset of plate tectonics in deep geological time (e.g., Evans & Pisarevsky, 2008; Brenner et al., 2020; 2022). In addition to these deep-time applications, paleomagnetic data also has many applications for the reconstruction of relative motions of tectonic terranes through time (Beck, 1976; Demarest, 1983; Butler, 1992): allowing the estimation of vertical-axis rotations, relative convergence, and the paleolatitudinal evolution of intra-oceanic terranes.

The geocentric axial dipole hypothesis

The paleogeographic and tectonic applications of paleomagnetism rely on the key assumption that the Earth's time-averaged magnetic field closely resembles that of a geocentric axial dipole (GAD) field, such that the position of the geomagnetic pole coincides with the Earth's rotation axis (e.g., Runcorn, 1959; Butler, 1992; Johnson & McFadden, 2007). The GAD hypothesis was already applied by Hospers (1954) and Creer et al. (1954) to infer paleomagnetic pole positions for different age intervals. One of the advantages of a dipolar field structure is that it provides a simple relationship between the paleomagnetic inclination and the paleolatitude of the location from which the paleomagnetic samples are derived: the so-called dipole formula (e.g., Irving, 1964). To test the validity of the GAD hypothesis, paleolatitude estimates derived from paleomagnetic data have often been compared with independent constraints on the paleolatitude provided by paleoclimatic indicators, such as evaporites, carbonate rocks and fossil assemblages (Irving, 1956, 1964; Blackett, 1961; McElhinny & McFadden, 2000, Evans, 2006). In addition, the dipolar field structure has been intensely studied and tested by high-quality paleomagnetic data obtained from relatively recent (last few million years) volcanic rocks (e.g., Johnson et al., 2008; Cromwell et al., 2018; Bono et

al., 2020). For deeper geological time, the dipolar nature of the geomagnetic field may be evaluated by looking at the agreement between coeval paleomagnetic poles from different locations of the same stable plate, continent, or craton. In principle, coeval paleopoles – after correcting for relative plate motions - should be reasonably-well clustered if the time-averaged geomagnetic field was indeed dipolar (e.g., Butler, 1992). On short time-scales (<10 ka), the geomagnetic field cannot be approximated as a geocentric axial dipole, as the secular variations in the Earth's magnetic field cause the geomagnetic pole to be deflected from the spin axis up to tens of degrees (e.g., McElhinny & McFadden, 1997). Obtaining a time-average paleomagnetic pole position thus requires the averaging of the paleosecular variation (PSV) for a sufficiently long period of time: paleomagnetists therefore carefully collect dozens of samples that record independent readings of the past geomagnetic field (van der Voo, 1990; Deenen et al., 2011; Meert et al., 2020).

Whether the time-averaged axial dipole field has been persistently present throughout Earth's history remains unclear and is actively investigated, particularly for pre-Cambrian times (Evans, 2006; Biggin et al., 2020; Veikkolainen & Pesonen, 2021; Sears, 2022). More complex geomagnetic field morphologies with significant non-dipole contributions have often been invoked to explain unexpected paleomagnetic observations, such as discrepancies between paleomagnetic pole positions from different continents included in Pangea or the large dispersion of coeval poles in the Devonian (van der Boon et al., 2022) and Ediacaran (Abrajevitch & Van der Voo, 2010). The observed dispersion of paleopoles may be – at least partly – attributed to partial averaging of the shorter time-scale variations of the field like PSV (e.g., Harrison & Lindh, 1982a) or regional geomagnetic field anomalies that may have existed for several million years (e.g., Engbers et al., 2020). Most studies that investigated the nature of the past geomagnetic field find that the Earth's magnetic field is not a perfect geocentric axial dipole, and non-dipolar contributions to the past geomagnetic field have been estimated to be as large as 5% (e.g., Butler, 1992; Besse & Courtillot, 2002, Johnson et al., 2008; Bono et al., 2020). However, the axial dipole contribution to the field is considered to be dominant, and it has now been widely accepted that the time-averaged geomagnetic field is well-approximated by a GAD field, at least since mid-Carboniferous times (e.g., Butler, 1992; McElhinny & McFadden, 2000; Johnson & McFadden, 2007, Biggin et al., 2020).

The paleomagnetic reference frame: uses and limitations

The application of the GAD assumption allows the determination of the position of the geographic pole relative to a fixed plate or continent. When the position of the time-averaged paleomagnetic pole, as a proxy for the geographic pole, is plotted for different moments in the geological past, it appears that the poles 'wander' away from the present-day geographic pole position, as first observed by Creer et al. (1954). This 'apparent' polar wander path reflects the motion of the plate or continent relative to the geographic pole (that is, the Earth's spin axis). The construction of an APWP thus enables the description of the motion of a tectonic plate or continent in a 'absolute' frame of reference, that is relative to an assumed fixed reference point. By transferring paleomagnetic data from the major tectonic plates/continents to a single reference plate using a model of relative plate motions, a 'global' paleomagnetic reference frame may be constructed that constrains the motion relative to a fixed rotation axis of all plates and geological terranes that are linked by the relative plate motion reconstruction (e.g., Phillips &

Forsyth, 1972; Besse & Courtillot, 1991; 2002; Torsvik et al., 2008a; 2012). This reference frame may serve as a global paleolatitude framework, allowing the determination of the paleolatitude or paleolatitudinal evolution of a chosen location (van Hinsbergen et al., 2015), providing essential input for studies of paleoclimate, paleoenvironment and paleobiology. In addition, a paleomagnetic reference frame provides the reference against which independent paleomagnetic datasets may be compared to determine relative paleolatitudinal displacements or vertical-axis rotations (Demarest, 1983; Butler, 1992), as well as a geochronological tool to date, for instance, remagnetization, ore deposits or fault rocks (e.g., Torsvik et al., 2014a).

The motion of a tectonic plate relative to the geographic pole is the result of two processes: plate tectonic motion and true polar wander (TPW), defined as the rotation of the entire crust-mantle system relative to the rotation axis (e.g., Goldreich & Toomre, 1969; Gordon & Livermore, 1987). Paleomagnetic data allow the determination of the azimuthal orientation and paleolatitudinal motion of tectonic plates and crustal blocks through time, which may be caused either by plate tectonic motions or by TPW. Distinguishing TPW and plate motion-induced polar wander based on only paleomagnetic data is not always straightforward (Evans, 2013; Mitchell & Jing, 2023; Brenner et al., 2023), but TPW may be quantified by determining a common rotation of all continents around an axis in the equatorial plane (Steinberger & Torsvik, 2008; Torsvik et al., 2012, 2014b). However, because of the symmetry of the geocentric axial dipole field, paleomagnetism does not provide constraints on the longitudinal position or motion of relative to the geomagnetic pole.

To derive ‘absolute’ paleolongitudes, constraints may be derived from the surface expressions of mantle upwellings such as hotspot tracks and kimberlites (e.g., Torsvik et al., 2008b; 2014b), the centers of past supercontinents (Mitchell et al., 2012) or the fitting of past locations of subduction to interpreted subducted slabs in the mantle imaged by seismic tomography (Van der Meer et al., 2010, 2018). The use of such data requires certain assumptions, such as the vertical rise of mantle upwellings from the edges of basal mantle structures (e.g., Burke & Torsvik, 2004; Torsvik et al., 2014b), the formation of a supercontinent at 90 degrees from its predecessor (‘orthoversion’, Mitchell et al., 2012) or the vertical sinking of detached slab remnants through the mantle (Van der Meer et al., 2010; 2018; Domeier et al., 2016). Models that describe the motion – both in a latitudinal and longitudinal sense – of tectonic plates at the Earth’s surface relative to the deep mantle are commonly referred to as ‘mantle’ reference frames. Examples of such reference frames include those based on hotspot tracks (e.g., Müller et al., 1993; O’Neill et al., 2005; Torsvik et al., 2008a; Doubrovine et al., 2012), the locations of subducted slab remnants (van der Meer et al., 2010) or on a set of tectonics-based ‘rules’ (Müller et al., 2022). Combined or ‘hybrid’ reference frames are used to express plate motions for the Paleozoic (Torsvik et al., 2008a; 2014b).

The comparison of mantle and paleomagnetic reference frames may be used to identify and quantify phases of TPW (Morgan, 1981; Harrison & Lindh, 1982b; Courtillot & Besse, 1987). By placing an APWP for a given tectonic plate, describing the motion of the spin axis relative to that plate, in a mantle reference frame provides a direct estimate of the motion of the spin axis relative to the ‘mean’ mantle, i.e., TPW. The rate and magnitude of TPW depends on the properties and dynamics of the Earth’s mantle, such as viscosity, slab sinking rates and the stability of basal mantle structures, and may provide insights into the

workings of the Earth's interior through geological time (e.g., Fu et al., 2022). Although being driven by processes in the Earth's interior, the reorientation of the solid earth relative to the spin axis may have profound impact on regional paleoclimate, paleoenvironment and extinction events (Evans, 2003; Yi et al., 2019; Jing et al., 2022).

One of the main aims of this thesis is to construct a new global apparent polar wander path that provides a paleomagnetic reference frame for the reconstruction of paleogeography and the determination of absolute plate motions. Comparing this new frame with existing mantle reference frames will be used to derive new estimates of true polar wander since 320 Ma. To enable the robust quantification of apparent and true polar wander, the first part of this thesis is mainly devoted to the reliability and uncertainties of the paleomagnetic input data. The new insights into key sources of uncertainty in paleomagnetic data will then be used to develop a novel statistical approach to the application of paleomagnetism to plate tectonics and paleogeography.

Outline of this thesis

Chapter 1 develops a plate-kinematic reconstruction of the northwest Pacific region for the last 85 Ma. This chapter shows the 'classical' application of paleomagnetic data as a tool to test and improve plate-kinematic reconstructions, following conventional paleomagnetic approaches. The chapter first reviews plate-kinematic constraints on the convergence history between the Pacific and eastern Eurasian plates, and then documents structural geological and stratigraphic constraints on the evolution of a deformed active margin, and rocks that were accreted to that margin from now-subducted plates. From this, a kinematic restoration of these subducted plates is proposed, which is then tested against paleomagnetic data following conventional statistical approaches. Paleomagnetic data were used to reconstruct the Neogene rotation of the northeast and southwest Japan and the intra-oceanic motion history of two Late Cretaceous to Eocene intra-oceanic arcs that are now preserved onto the continental margin at the Kamchatka Peninsula. The publication of Rowley (2019) that questioned the validity of such paleomagnetic procedures was published around the same time as this chapter. The paleomagnetic analyses performed in this chapter are revisited in **Chapter 6**, where we use the methods developed in **Chapters 2** and **5** to evaluate the benefits and improvements of the methodology presented in this thesis. In this Chapter 1, we also highlight and discuss the potential role of the plate boundary evolution in the northwest Pacific region in proposed plate tectonic reorganizations around ~85 and ~50 Ma that we will return to in **Chapter 7**.

Chapter 2 zooms in on the problem of the unexpected large dispersion of coeval paleomagnetic poles that was identified by Rowley (2019), which causes half of the poles behind global apparent polar wander paths are statistically significantly displaced relative to those paths. In this chapter, we attempt to identify the underlying causes for the dispersion of poles, such as inclination shallowing or undersampling of paleosecular variation. We highlight the problems of using arbitrarily-defined paleopoles poses as a basis for calculating apparent polar wander paths. This paper focuses on the nature and causes dispersion of paleopoles, and its implications for the robust use and error propagation of paleomagnetic data when calculating reference frames. The absence of uncertainty incorporation in conventional approaches is also highlighted, and ways forward are discussed and presented.

Chapter 3 investigates the reliability of paleomagnetic poles obtained from sedimentary rocks, which provide a significant part of the paleomagnetic data used in paleogeographic reconstructions and for calculating apparent polar wander paths. We analyze the use of the widely-applied elongation-inclination correction for inclination shallowing (Tauxe & Kent, 2004); a common and notorious problem for obtaining reliable estimates of the paleomagnetic pole using sedimentary rocks. In this chapter, a set of reliability criteria and recommendations for obtaining and using sediment-derived paleomagnetic poles are presented.

Chapter 4 provides an analysis of how the accuracy and precision of paleomagnetic poles may be influenced by how paleomagnetic samples are distributed over paleomagnetic sites as well as by the application of filters and cutoffs to the paleomagnetic datasets from which they are computed. In particular, it tests whether the reproduction of paleomagnetic directions at the site level that is often used as a requirement for a reliable paleopole is effectively improving the accuracy and precision of those poles. This chapter highlights the trade-off between the collection of paleomagnetic sites versus multiple samples per site and recommendations for collecting paleomagnetic samples in the field for the purpose of obtaining a robust estimate of the time-averaged paleomagnetic pole position.

Chapter 5 presents a new global apparent polar wander path for the last 320 Ma calculated from (simulated) site-level data. This novel approach is based on the philosophy presented in **Chapter 2** and involves the parametric re-sampling of site-level data from a collection of paleomagnetic poles to propagate spatial and temporal uncertainties into the computation of the apparent polar wander path. We present a fully updated global plate circuit and paleomagnetic database including the most recent high-quality paleomagnetic and marine geophysical data. Compared to previous apparent polar wander paths, we apply more stringent selection criteria, including those presented in **Chapters 3** and **4** for sedimentary and igneous rock-derived datasets, respectively. We show that the new path has a similar first-order geometry to previous models but has smaller uncertainties and provides improved constraints on rates of apparent polar wander, particularly because true reference pole age can be computed.

Chapter 6 presents the freely-available online portal *APWP-online.org* to allow paleomagnetists to apply the new paleomagnetic approach of **Chapter 2** and the global apparent polar wander path of **Chapter 5**. This web application includes three tools that aim to stimulate and facilitate the application of the new global apparent polar wander path and the site-level comparison approach to tectonic and paleogeographic problems. The first tool allows the computation of custom apparent polar wander paths using the method developed in **Chapter 5**. The second tool enables users to apply the site-level comparison approach outlined in **Chapter 2** to quantify relative paleomagnetic displacements that may be interpreted as tectonic displacements, which we illustrate using the datasets compiled in **Chapter 1**. Finally, we present a portal that hosts the global reference database that underlies the computation of the global apparent polar wander path of **Chapter 5** and where new datasets may be submitted for inclusion in future updates.

Finally, **Chapter 7** presents new quantitative estimates on true polar wander during the last 320 Ma. We determine the magnitude, rate, and direction of true polar wander by placing the global apparent polar wander path of **Chapter 5** in four different mantle reference frames. We show that true polar wander rotations during this time interval have occurred mainly along two equatorial axes that are approximately orthogonal. We discuss the implications of the observed rates and trends in the true polar wander paths for mantle dynamics and provide preliminary links to subduction history and plate reorganizations (as discussed in **Chapter 1**). Finally, we outline future avenues for improving our understanding of true polar wander, its causes, and its links to Earth's dynamics.

1

Reconstruction of subduction and back-arc spreading in the NW Pacific and Aleutian Basin: clues to causes of Cretaceous and Eocene plate reorganizations

This chapter has been published as:

Vaes, B., Van Hinsbergen, D. J., & Boschman, L. M. (2019). Reconstruction of subduction and back-arc spreading in the NW Pacific and Aleutian Basin: Clues to causes of Cretaceous and Eocene plate reorganizations. *Tectonics*, 38(4), 1367-1413.

Abstract

The Eocene (~50–45 Ma) major absolute plate motion change of the Pacific plate forming the Hawaii-Emperor bend is thought to result from inception of Pacific plate subduction along one of its modern western trenches. Subduction is suggested to have started either spontaneously, or result from subduction of the Izanagi-Pacific mid-ocean ridge, or from subduction polarity reversal after collision of the Olyutorsky arc that was built on the Pacific plate with NE Asia. Here we provide a detailed plate-kinematic reconstruction of back-arc basins and accreted terranes in the northwest Pacific region, from Japan to the Bering Sea, since the Late Cretaceous. We present a new tectonic reconstruction of the intraoceanic Olyutorsky and Kronotsky arcs, which formed above two adjacent, oppositely dipping subduction zones at ~85 Ma within the north Pacific region, during another Pacific-wide plate reorganization. We use our reconstruction to explain the formation of the submarine Shirshov and Bowers Ridges and show that if marine magnetic anomalies reported from the Aleutian Basin represent magnetic polarity reversals, its crust most likely formed in an ~85- to 60-Ma back-arc basin behind the Olyutorsky arc. The Olyutorsky arc was then separated from the Pacific plate by a spreading ridge, so that the ~55- to 50-Ma subduction polarity reversal that followed upon Olyutorsky-NE Asia collision initiated subduction of a plate that was not the Pacific. Hence, this polarity reversal may not be a straightforward driver of the Eocene Pacific plate motion change, whose causes remain enigmatic.

Key points

- At 85-80 Ma, a plate reorganization occurred in the northern Pacific that included the formation of two subduction zones and the Kula plate
- Our reconstruction predicts that the Aleutian Basin crust formed between 85 and 60 Ma in a back-arc basin behind the Olyutorsky arc
- Subduction polarity reversal from Kamchatka to Sakhalin at ~50 Ma is not a straightforward driver of the Eocene Pacific plate motion change

1. Introduction

A major event in the tectonic history of the Pacific region is a plate reorganization that occurred ~50 Ma (Müller et al., 2016; O'Connor et al., 2013; Seton et al., 2015; Torsvik et al., 2017; Whittaker et al., 2007). This reorganization is part of a wider, global plate motion change event which included changes in absolute plate motion of, for example, the Australian (Whittaker et al., 2007), South American (Oncken et al., 2006; Schepers et al., 2017), Caribbean (Boschman et al., 2014), and Indian plates (Copley et al., 2010; van Hinsbergen et al., 2011). For the Pacific plate, the sharp bend in the Hawaii-Emperor seamount chain dates the absolute plate motion change at ~47 Ma (Sharp & Clague, 2006; Torsvik et al., 2017; Whittaker et al., 2007). Recent studies based on numerical models suggested, however, that the bend may have resulted from a change in absolute plume motion relative to a continuously moving Pacific plate (e.g., Hassan et al., 2016; Tarduno et al., 2009). Although paleomagnetic data from the Emperor Seamounts indicate a southward drift of the Hawaiian hotspot from ~80 to 47 Ma (e.g., Tarduno et al., 2003), Torsvik et al. (2017) recently demonstrated that the formation of the Hawaii-Emperor bend cannot be explained without a significant change in absolute plate motion of the Pacific plate around 47 Ma.

The Eocene plate reorganization event holds key lessons on the driving mechanisms behind plate tectonics and is therefore widely studied. Current models invoke that the absolute plate motion change affecting the Pacific plate is the result of its first subduction along its modern western plate boundaries, including the Izu-Bonin-Marianas (Arculus et al., 2015; Ishizuka et al., 2011; Seton et al., 2015), and Aleutian and Kuril-Kamchatka Trenches (Domeier et al., 2017). Faccenna et al. (2012) postulated that the main driving force for the Pacific absolute plate motion change was the onset of slab pull acting on the Pacific plate following the inception of subduction of its western parts along the East Asia margin. This subduction has been postulated to have initiated (i) spontaneously at a transform plate boundary with an ill-defined plate whose relics are now preserved in the Philippine Sea plate (Arculus et al., 2015; Stern, 2004; Stern et al., 2012; Stern & Bloomer, 1992), (ii) after complete consumption of the conceptual Izanagi plate that contained the conjugate set of the marine magnetic anomalies preserved on the northwesternmost part of the Pacific plate (Seton et al., 2015; Whittaker et al., 2007), or (iii) after subduction polarity reversal following the collision of the Olyutorsky-East Sakhalin-Nemuro arc with NE Asia (Domeier et al., 2017). Domeier et al. (2017) proposed that this arc formed on the Pacific plate upon ~85–80 Ma intraoceanic subduction initiation at the Izanagi-Pacific ridge. This 85–80 Ma event itself is intriguing, since it is part of another Pacific-wide plate reorganization, including the formation of the Kula-Pacific and Pacific-Antarctica mid-ocean ridges (e.g., Mortimer et al., 2019; Wright et al., 2016).

The youngest marine magnetic anomalies preserved on the Pacific plate interpreted as conjugate to the Izanagi plate are Early Cretaceous in age, and all younger NW Pacific plate lithosphere has subducted (Seton et al., 2012). Timing of subduction of the Izanagi-Pacific ridge must thus be circumstantially inferred. Seton et al. (2015), for instance, inferred subduction of the Izanagi-Pacific ridge and the formation of a slab window below the east Asian margin from a disruption of arc magmatism in Korea and SW Japan from 55–50 to 43–42, and a gap in accretion in the Shimanto Belt of SW Japan between ~55 and 43 Ma, and extrapolated the thus inferred ridge subduction episode synchronously along the east Asian margin toward Kamchatka.

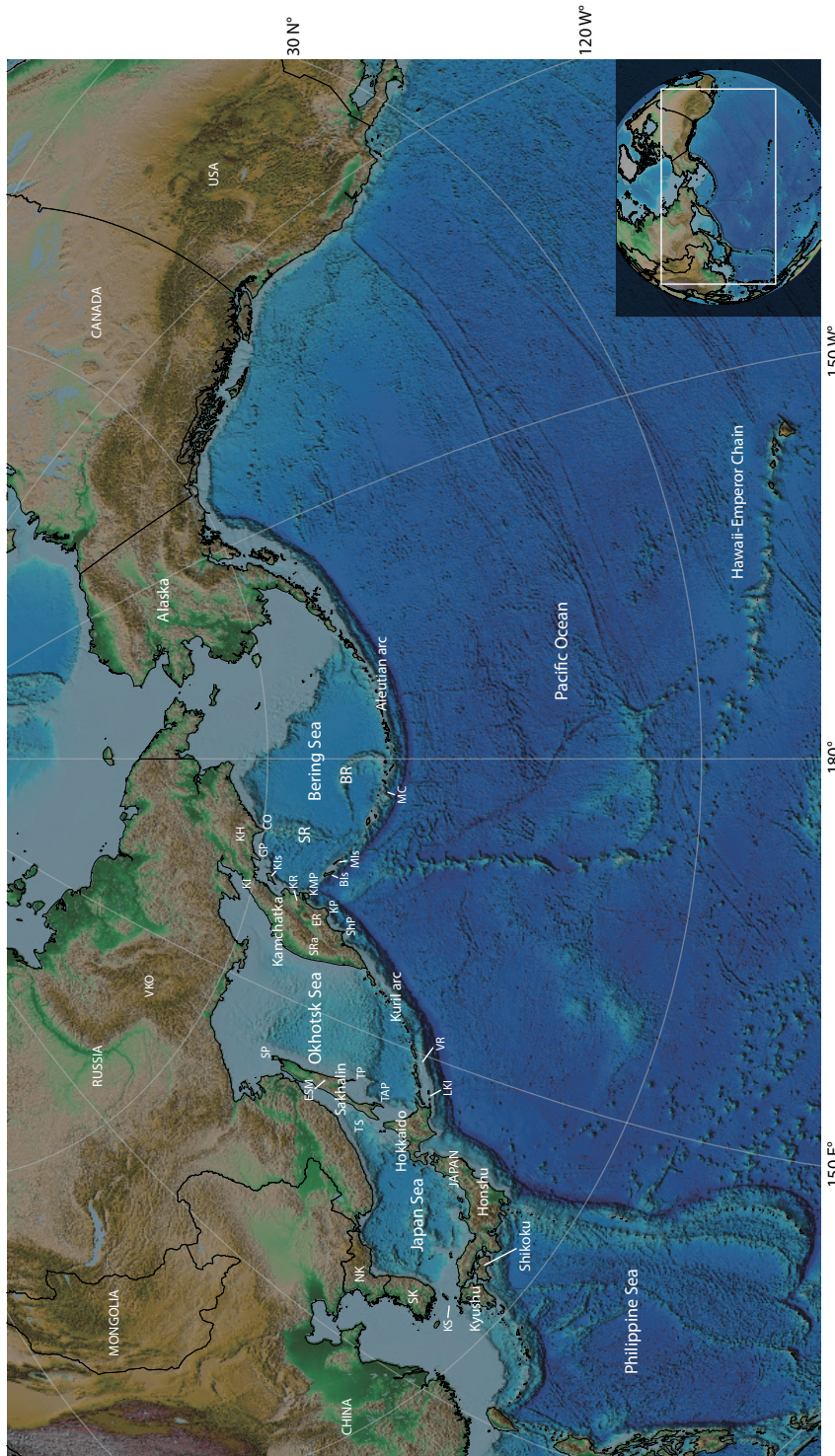


Fig. 1. Geographic map of the northwest Pacific region. Country names are shown in capital letters. Key to abbreviations: BIs = Bering Island; BR = Bowers Ridge; CO = Cape Olyutorsky; ER = Eastern Ranges; ESM = East Sakhalin Mountains; GP = Govena peninsula; KH = Koryak Highlands; KI = Kamchatka isthmus; KIs = Karaginsky Island; KP = Kronotsky peninsula; KMP = Kamchatka Mys peninsula; KR = Kumroch Range; KS = Korea Strait; LKI = Lesser Kuril islands; MC = Murray Canyon; MIs = Medny Island; NK = North Korea; ShP = Shipunsky peninsula; SK = South Korea; SP = Schmidt peninsula; SR = Shirshov Ridge; SRA = Sredinny Range; TAP = Tonin-Aniva peninsula; TP = Terpeniya peninsula; TS = Tartary Strait; VKO = Verkhoyansk-Kolyma Orogen; VR = Vityaz Ridge.

While continuous westward subduction below most of Japan throughout the Phanerozoic is well established from the Japanese accretionary prisms (Isozaki et al., 1990, 2010), the geology of the northwestern Pacific active margin hosts remnants of the long-recognized Late Cretaceous to Eocene Olyutorsky-East Sakhalin-Nemuro intraoceanic arc and ophiolites that are found on Kamchatka, Sakhalin, and East Hokkaido (Konstantinovskaya, 2001; Nokleberg et al., 2000; Parfenov et al., 2011; Shapiro & Solov'ev, 2009; Zharov, 2005; Figs. 1 and 2). Paleomagnetic data indicate that formation of the island-arc rocks occurred at much lower paleolatitudes than expected for Eurasia and North America, suggesting that they must be exotic (e.g., Bazhenov et al., 1992; Konstantinovskaya, 2001; Shapiro & Solov'ev, 2009). These arcs are generally interpreted to have formed above southeastward-dipping, intraoceanic subduction within the northwest Pacific region, followed by a subduction polarity reversal in the Eocene (Domeier et al., 2017; Konstantinovskaya, 2001; Shapiro & Solov'ev, 2009). Domeier et al. (2017) recently noted that this intraoceanic subduction is not incorporated in the plate models that are used to investigate the cause of the Pacific plate motion change (e.g., Faccenna et al., 2012; Müller et al., 2016; Seton et al., 2012; 2015; Torsvik et al., 2017). Because geological data show that the Olyutorsky arc obducted onto the east Asian continental margin of Kamchatka from 55 to 45 Ma (Hourigan et al., 2009; Konstantinovskaya, 2001, 2011; Nokleberg et al., 2000; Shapiro et al., 2008; Shapiro & Solov'ev, 2009), and in the Middle Eocene on southern Sakhalin (Bazhenov et al., 2001; Zharov, 2005), conspicuously close to the timing of the Hawaii-Emperor bend, this subsequent subduction polarity reversal and inception of westward subduction at the modern Kuril-Kamchatka subduction zone at 50–45 Ma (Konstantinovskaya, 2001, 2011; Shapiro & Solov'ev, 2009) was therefore recently identified by Domeier et al. (2017) as a potential trigger of the Eocene plate reorganization and the formation of the Hawaii-Emperor bend.

Carefully restoring the Late Cretaceous-Eocene kinematic history of the plate that contained the Olyutorsky-East Sakhalin-Nemuro arc is thus key to assess whether the Pacific plate may have started subducting westward in the Eocene. However, several first-order observations have not been taken into account in kinematic reconstructions so far. First, the remnants of the Olyutorsky arc continue to north Kamchatka, well to the north of the Aleutian subduction zone (Fig. 2). Interestingly, subduction at the Aleutian subduction zone also started ~50 Ma, based on the oldest arc volcanic rocks in the Aleutians (Jicha et al., 2006; Layer et al., 2007). Initiation of this subduction is suggested to have trapped a fragment of oceanic crust, below the Aleutian Basin, that still lies east of the Olyutorsky arc below the Bering Sea (Fig. 2), and may have been part of the same plate as the crust underlying the Olyutorsky arc (Scholl, 2007; Worrall, 1991) and thus hold clues to the NW Pacific plate motion history. Within the Bering Sea, the kinematic history of the Bowers and Shirshov Ridges, thought to be intraoceanic arc remnants, and the Komandorsky and Bowers Basins remain enigmatic (Chekhovich et al., 2012; Scholl, 2007; Shapiro & Solov'ev, 2009; Fig. 2). Finally, a second, Kronotsky, intraoceanic island arc that formed ~85 Ma within the northwestern paleo-Pacific realm went extinct ~40 Ma, collided with Kamchatka ~10–5 Ma and is currently found structurally below the Olyutorsky arc (e.g., Konstantinovskaya, 2011; Shapiro & Solov'ev, 2009).

Between Kamchatka and Japan, the Sea of Okhotsk-Kuril back-arc basin opened after the Eocene arc-continent collision and disrupted the accreted Olyutorsky-East Sakhalin-Nemuro arc (Parfenov et al., 2011; Schellart et al., 2003). For the Sea of Japan back-arc

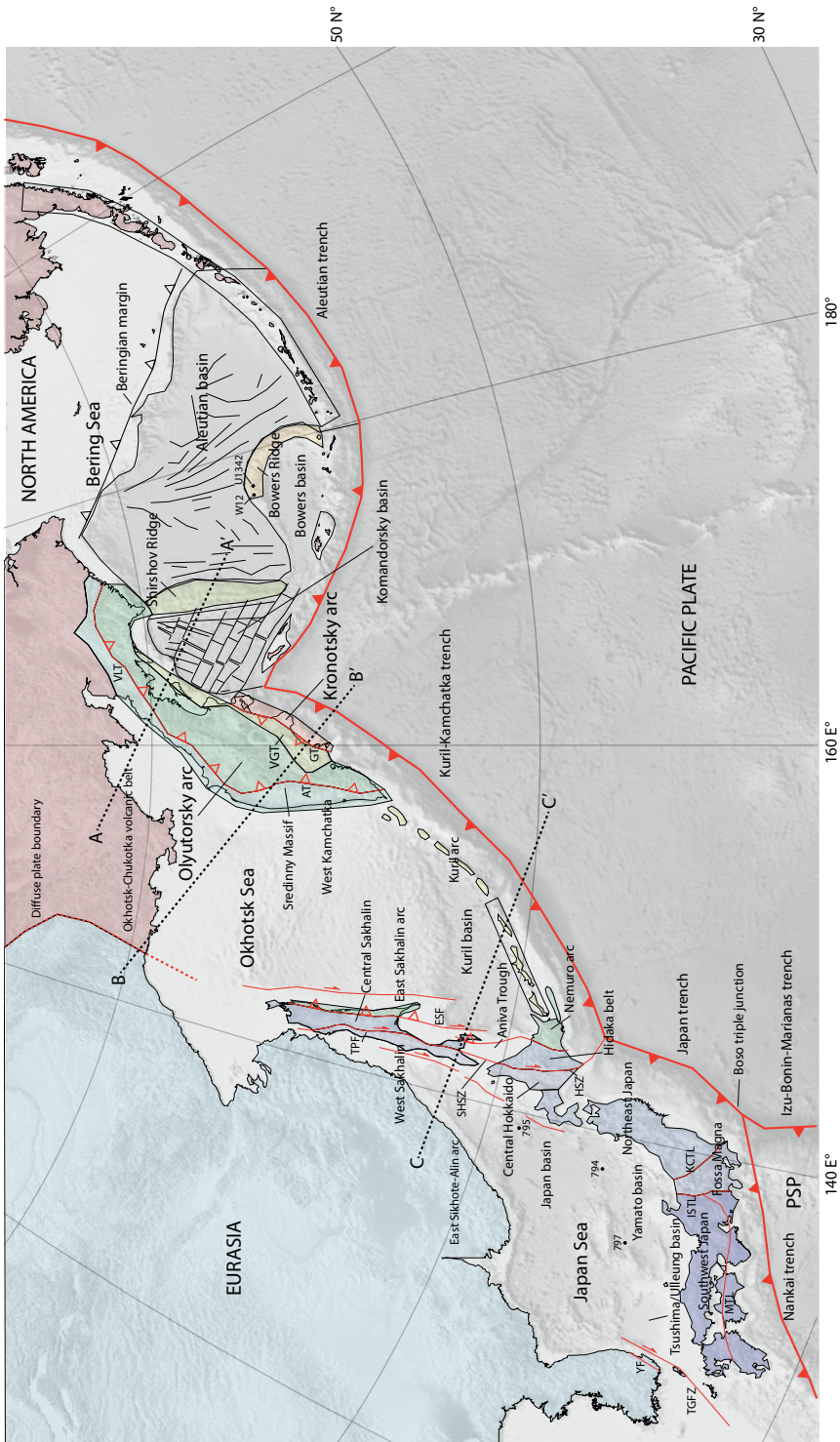


Fig. 2. Simplified tectonic map of the northwest Pacific region. Major tectonic plates are given in capital letters. Colored polygons represent the tectonic blocks used in the reconstruction (see section 7 and Figs. 9 and 10). Thick red lines with filled triangles indicate present-day subduction zones. Major faults are shown as thin red lines (after, e.g., Bogdanov & Khain, 2000; Fournier et al., 1994; Schellart et al., 2003). Key collisional sutures and extinct subduction zones are indicated with open triangles in red and black, respectively. Marine magnetic anomalies of the Komandorsky and Aleutian Basins used in this study are from the tectonostratigraphic terrane map of Nokleberg et al. (1996) and shown as thin black lines. These represent the magnetic anomaly patterns from Valyashko et al. (1993) for the Komandorsky Basin and Cooper et al. (1992) for the Aleutian Basin, respectively. Locations of drill sites are shown by black dots with a reference to the drill site number/code (see section 4; W12 = Wanke et al., 2012). Locations of cross-sections of Fig. 3 are shown as dashed black lines. Abbreviations: AT = Andrianovka thrust; ESF = East Sakhalin fault; GT = Grechishkin thrust; HSZ = Hidaka Shear Zone; ISTL = Itoigawa-Shizuoka Tectonic Line; KCTL = Kashiwazaki–Choshi Tectonic Line; MTL = Median Tectonic Line; PSP = Philippine Sea plate; SHSZ = Sakhalin-Hokkaido Shear Zone; TGFZ = Tsushima-Goto fault zone; TPF = Tym-Poronaysk fault; VGT = Vetlovsky-Govena terrane; VLT = Vatyn-Lesnaya fault; YT = Yangsan fault.

basin, two competing models were proposed, either invoking trench-normal extension with oroclinal bending of the Japan arc (e.g., Martin, 2011; Otofujii et al., 1985), or transtensional opening with southward motion of Japan relative to Eurasia (e.g., Jolivet et al., 1994; Jolivet & Tamaki, 1992). The latter model would, if correct, significantly influence the restoration of the Nemuro arc.

To allow for quantitative analysis of NW Pacific plate motions, we first provide a detailed kinematic restoration of the post-accretionary deformation of the Olyutorsky-East Sakhalin-Nemuro arc due to back-arc basin formation and restore its links with the crust underlying the Bering Sea. We then use paleomagnetic data from the arc to further test whether the arc may have been part of the Pacific plate, as recently inferred (Domeier et al., 2017), or of a plate adjacent to the Pacific (e.g., Konstantinovskaya, 2011; Shapiro & Solov'ev, 2009). In addition, we restore the evolution of the Kronotsky arc and provide a new reconstruction of the kinematic evolution of the Bering Sea region, including the history of the Shirshov and Bowers Ridges and the spreading history of the oceanic crust of the Komandorsky and Bowers Basins. Our model covers the NW Pacific region from Japan to western Alaska (Fig. 1). Finally, we compare the subduction evolution inferred by our reconstruction against the locations of subducted slabs in the mantle (e.g., van der Meer et al., 2018). We use our model to discuss the implications for the large-scale tectonic evolution of the Pacific realm, with an emphasis on the fate of the Izanagi-Pacific ridge and the possibility that the ~50 Ma NW Pacific arc-continent collision and polarity reversal drove the Pacific plate reorganization.

2. Approach

The present-day geological architecture of the NW Pacific region followed from the interplay between continent-hosting Eurasian and North American plates and several oceanic plates that originated in the Panthalassa Ocean. The relative motions between these large tectonic plates provide the boundary conditions for our plate-kinematic reconstruction of the region. Marine magnetic anomaly and fracture zone data from the Pacific plate were used to reconstruct major conceptual oceanic plates that contained the

conjugate anomalies, including the Izanagi plate in the west and Farallon and Kula plates in the north and east (e.g., Engebretson, 1985; Müller et al., 2016; Seton et al., 2012; Woods & Davies, 1982; Wright et al., 2016). We develop our reconstruction in the GPlates plate reconstruction software (www.gplates.org; Boyden et al., 2011) and use the plate circuit of Seton et al. (2012), updated with Pacific reconstructions of Wright et al. (2016), as a basis. Our shape and rotation files are provided in the supporting information (Data Set S1).

As data input, we rely on available quantitative kinematic data, that is, data that provide information on the direction, magnitude, and/or timing of relative motion between geological units. We apply the following reconstruction hierarchy, adapted from Boschman et al. (2014). We first restore extensional records, as these provide the most complete geological record at the end of the deformation event. If available, we use marine magnetic anomaly-derived isochrons to constrain the direction and rate of seafloor spreading in an oceanic basin. Second, we use estimates of the amount and direction of continental extension. Third, we use transform and strike-slip fault displacements. Although the exact amount of displacement may not be determined, strike-slip and transform faults provide clear constraints on the orientation and direction of relative motion between adjacent units. Next, we use records of contractional deformation. At the end of a collisional event, the minimum geological record is preserved, therefore only providing an estimate of the minimum amount of shortening. In the case of oceanic subduction, these records may be very incomplete, as shown by Isozaki et al. (1990) for the accretionary belts of the Japanese islands. We use stratigraphical or geochronological constraints to determine the timing of accretion of a geological unit from one tectonic plate onto another, and subsequently use the plate circuit to estimate the location of the unit in the period prior to the accretion event.

We fine-tune the reconstruction in such a way that for areas where limited kinematic data are available, geometrical consistency is ensured, that is, no overlaps or “gaps” between geological units should be present without geological evidence for extension or shortening. Any modifications to the reconstruction to make sure that it remains geometrically consistent are regarded as model predictions and will be clearly indicated in the reconstruction section. Also, our reconstruction should be in accordance with the basic rules of plate tectonics, stating that all tectonic plates are surrounded by plate boundaries that end in triple junctions (Cox & Hart, 2009). If relative motion between geological units is inferred, then there is a discrete fault or plate boundary between them.

After obtaining a tectonic model of the NW Pacific region based on quantitative geological data, we test our reconstruction twice with independent data sets. First, we test it against available paleomagnetic data. We use the thereto developed APWP tool by Li et al. (2017) that is integrated into the statistics portal of the *n* platform of Paleomagnetism.org (Koymans et al., 2016). This tool allows calculating a Global Apparent Polar Wander Path (whereby we used the version of Torsvik et al., 2012) in the coordinates for any element in the reconstruction. To this end, we calculate total reconstruction Euler poles of a tested element (e.g., polygon) in 10 Myr intervals relative to South Africa, using the global plate circuit of Seton et al. (2012), including the updates of Wright et al. (2016) for the Pacific region. This procedure allows for testing the paleomagnetic declinations and inclinations predicted by our reconstruction against published paleomagnetic data for key reconstructed elements, and iteratively adjusting our kinematic restorations where needed provided these remain consistent with available structural constraints.

Second, we test our updated kinematic reconstruction, consistent with paleomagnetism, against seismic tomography. Our tectonic model contains several (extinct) subduction zones, which can be compared with tomographic images of the upper and lower mantle (e.g., Domeier et al., 2017; van der Meer et al., 2018; www.atlas-of-the-underworld.org). Positive wave speed anomalies in the mantle may be linked to (detached) subducted plates, and therefore, to the locations of (former) subduction. To compare the locations of inferred slab remnants in the mantle with our reconstruction, we place the reconstruction in a global moving hotspot reference frame (Dobrovine et al., 2012) and we gain insight into the geodynamical assumptions of trench advance, retreat, or stationarity that are required to make our reconstruction consistent with the present-day mantle structure.

3. Plate circuit and marine magnetic anomaly-based isochrons

The tectonic framework for our reconstruction is provided by the relative motions of the Eurasian, North American, and Pacific plates, which are linked by a global plate circuit. The Euler rotation poles that quantitatively describe the motion between these and other major tectonic plates are calculated from records of past seafloor spreading, which are constrained by marine magnetic anomalies and transform fault/fracture zone data. The motion of the Pacific plate relative to Eurasia and North America is constrained by the plate circuit through Antarctica and Africa. We use the rotation poles of Wright et al. (2016), which include poles from Wright et al. (2015) and Croon et al. (2008), for the motion of the Pacific plate relative to West Antarctica, and the poles of Granot et al. (2013) for West Antarctica relative to East Antarctica. The motion of East Antarctica relative to Africa is constrained by combining the poles of Royer and Chang (1991), Bernard et al. (2005), and Cande et al. (2010), with minor motion between Somalia and South Africa restored according to Horner-Johnson et al. (2007) and Lemaux et al. (2002). We apply the reconstruction poles of Müller et al. (1999) for the relative motion of North America with respect to Africa. For Eurasia relative to North America we use recent reconstructions of the opening of the northern Atlantic based on the high-resolution rotation poles of DeMets et al. (2015) for the Neogene and the poles of Gaina et al. (2002) for older times. The motions of the oceanic Farallon, Kula, and Izanagi plates relative to the Pacific plate are determined from the magnetic anomalies that are preserved on the Pacific plate. For our reconstruction we use the poles of Seton et al. (2012) for the Izanagi plate and the recent compilation of Wright et al. (2016) for the Kula and Farallon plates.

The northwest Pacific region includes a number of marginal basins that are (partly) underlain by oceanic crust. Following the reconstruction hierarchy outlined in the previous section, we would ideally base our reconstruction of these basins on available marine magnetic anomaly data. However, the marine magnetic anomalies in this region are often poorly constrained or poorly dated. We summarize the available observations for each basin below.

In the Japan Sea (Fig. 1), several NW-SE oriented marine magnetic anomalies were identified in the eastern part of the Japan Basin (Isezaki, 1986; Seama & Isezaki, 1990), but no conclusive age correlation was made (Fukuma et al., 1998; Isezaki, 1986; Jolivet & Tamaki, 1992). No magnetic anomalies indicative of seafloor spreading have been observed in other basins in the Japan Sea despite their possible oceanic nature, perhaps owing to the formation of sill-sediment complexes (Fukuma et al., 1998). Marine magnetic

lineations are also absent in the oceanic Kuril Basin (Fig. 2). The Komandorsky Basin, located between Kamchatka and the Shirshov Ridge, contains NE-SW fossil spreading centers and magnetic anomalies and NW-SE striking fracture zones (Baranov et al., 1991; Cooper et al., 1976), with estimated age of formation between 10 and 20 Ma (Valyashko et al., 1993; Fig. 2). We use these as input for our Komandorsky basin reconstruction.

Marine magnetic data of the Aleutian Basin (Fig. 2) shows a set of roughly north-south-trending magnetic anomalies (see, e.g., Fig. 4 in Cooper et al., 1992, or Fig. DR1 in the supporting information of Steinberger & Gaina, 2007). These anomalies were initially correlated with the Early Cretaceous M1-M13 sequence (Cooper et al., 1976), that is, ~128–138 Ma (Ogg et al., 2016). Later, Cooper et al. (1992) cautioned that this age determination remains uncertain. Steinberger and Gaina (2007) tentatively suggested that the most prominent north-south-oriented magnetic lineations in the eastern part of the basin may correspond to chron 34 (~84 Ma) to chron 32 (~71 Ma). Although no definitive correlation with the magnetic polarity timescale has been made, the north-south-trending anomalies are generally interpreted as being formed by seafloor spreading (Cooper et al., 1976, 1992; Scheirer et al., 2016; Scholl, 2007; Steinberger & Gaina, 2007). In addition to the main set of N-S-trending anomalies, several enigmatic NE-SW oriented magnetic anomalies were traced on the northwest of the Aleutian Basin, interpreted by Cooper et al. (1992) to have formed in a Cenozoic back-arc spreading center. This structure, named the “Vitus arch,” was instead interpreted by Chekhovich et al. (2012) as a large push-up structure formed along a large strike-slip fault during the Middle Eocene. However, a recent seismic study of the crustal structure of the Aleutian Basin across the Vitus Arch by Christeson and Barth (2015) found no evidence for Cenozoic spreading or push-up structures and we do not reconstruct significant Cenozoic deformation in this region.

Several north-south-oriented magnetic lineations have been observed in the eastern part of the Bowers Basin, separated from the Aleutian Basin by the Bowers Ridge (Cooper et al., 1976). No reliable match with published reversal time scales has been made so far. Cooper et al. (1976) initially suggested that the anomalies may correlate with the anomalies in the Aleutian Basin. In a later paper, however, Cooper et al. (1992) considered this correlation unlikely and suggested that the Bowers Basin formed in Eocene to Oligocene times by back-arc spreading behind the Bowers Ridge, due to eastward rollback of the Bowers subduction zone.

4. Review

4.1. General outline

The northwest Pacific region, from Japan to Alaska, hosts a system of linked subduction zones located at the Japan, Kuril-Kamchatka, and Aleutian Trenches (Fig. 2). These trenches form a continuous convergent plate boundary between the subducting oceanic Pacific plate and continental and oceanic lithosphere of the Eurasian and North American plates, which share a diffuse plate boundary through the Verkhoyansk-Kolyma orogen of NE Siberia (Figs. 1 and 2). This present-day plate configuration is thought to have been established during Eocene times (~50–40 Ma, e.g., Domeier et al., 2017; Seton et al., 2012; Wright et al., 2016). Prior to this time, during the Early to mid-Cretaceous, the northern half of the proto-Pacific Ocean was floored by the major Izanagi, Farallon, and Pacific plates, which were separated by mid-ocean ridges (Engebretson, 1985; Wright et al., 2016; see Fig. S1). Magnetic anomalies preserved on the Pacific plate suggest that at or before

~83 Ma a new oceanic plate, the Kula plate, formed out of lithosphere that previously belonged to the Pacific, Izanagi, and Farallon plates (Wright et al., 2016). Magnetic anomalies indicate that spreading between the Kula and Pacific plates continued until ~40 Ma (Wright et al., 2016). The Izanagi, Farallon, and Kula plates have now been almost completely lost to subduction.

The present-day trenches of the northwest Pacific region are separated from the stable Eurasian or North American plates by zones of intense deformation including marginal, partly oceanic basins, accretionary orogens, and ophiolite belts, as well as active and inactive volcanic arcs. Fig. 3 shows schematic cross-sections of the geological structure of the northwest Pacific region, from the stable continent toward the oceanic basins. The region includes three major marginal basins: the Japan Sea, Okhotsk Sea, and Bering Sea (Fig. 1). The Japanese islands, located between the Japan Sea back-arc basin and the Nankai and Japan Trenches (Fig. 2), consist of the Japan accretionary prisms that hosts a discontinuous record of ocean-derived sedimentary and volcanic rocks as well as foreland basin sediments (Isozaki et al., 1990, 2010). On top of the accretionary prism is the active Japan volcanic arc, associated with the subduction below its two trenches. The northernmost large island of Japan, Hokkaido, consists mainly of accretionary prism units. Its geological structure includes Mesozoic accretionary prism units including ophiolites, HP-LT metamorphic rocks, and thick forearc basin deposits (Ueda, 2016). The N-S-trending subduction-related terranes that form the basement of central Hokkaido continue northward on the island of Sakhalin. The Cretaceous-Paleocene East Sikhote-Alin arc forms the volcanic arc associated with the subduction below Hokkaido and Sakhalin (Kemkin et al., 2016; Martynov et al., 2017; Nokleberg et al., 2000; Parfenov et al., 2009; Tang et al., 2016; Figs. 2 and 4). Structurally above the units interpreted to belong to Eurasia, or on Hokkaido separated from Eurasia by a strike-slip fault, are the Late Cretaceous to early Paleogene East Sakhalin-Nemuro island-arc units found on east Hokkaido and east Sakhalin (e.g., Nokleberg et al., 1996, 2000; Ueda, 2016; Zharov, 2005; Figs. 2-4). The Kuril volcanic arc, associated with the subduction of the Pacific plate below the Kuril Trench, extends from eastern Hokkaido to the Kamchatka peninsula (Figs. 1 and 2), with the oldest magmatic rocks dated as Early Oligocene (De Grave et al., 2016). Behind the Kuril arc is the wedge-shaped oceanic Kuril Basin (Fig. 2). North of the Kuril Basin is the extensional Okhotsk Basin, underlying the marginal Okhotsk Sea. The Okhotsk Sea is separated from the East Sakhalin-Nemuro island-arc units on top of the eastern part of Sakhalin Island by a major dextral strike-slip system (Fournier et al., 1994; Schellart et al., 2003; Worrall et al., 1996; Fig. 3). To the east, the Kamchatka peninsula consists of an accretionary prism and an active volcanic arc, associated with the subduction of the Pacific plate below the Kamchatka Trench. The basement of Kamchatka largely consists of Cretaceous ophiolites and Upper Cretaceous-lower Paleogene island-arc rocks of the Olyutorsky arc that are structurally above the basement rocks of NE Siberia to the west (e.g., Konstantinovskaya, 2011; Shapiro & Solov'ev, 2009). To the east, the Olyutorsky arc terrane structurally overlies the Paleogene accretionary prism units of the Vetlovsky-Govena terrane (Fig. 3). Remnants of a second intraoceanic island-arc, the Late Cretaceous-Eocene Kronotsky arc, are found structurally below the Vetlovsky-Govena terrane on the eastern peninsulas of Kamchatka (e.g., Alexeiev et al., 2006; Konstantinovskaya, 2011). East of Kamchatka lies the Bering Sea region, which is separated from the Pacific Ocean Basin by the Aleutian arc (Fig. 1). The Aleutian

arc extends from the Kamchatka Strait in the west—approximately 200 km east of the Kamchatka Mys Peninsula—to Alaska in the east. The Bering Sea comprises three oceanic basins: the Neogene Komandorsky Basin, and the Aleutian and Bowers Basins (Fig. 2). Importantly, the precise age of the oceanic crust below the Aleutian and Bowers Basins is still unknown. The basins are bounded in the (north)east by the submarine Bowers and Shirshov Ridges. In the following, we review the geological records summarized above in detail, focused on kinematic constraints that allow reconstructing the Late Cretaceous to present tectonic history of this region, from south to north (east).

4.2. Japan Sea region

4.2.1. Japan fold-thrust belt

Japan lies in an overriding plate position relative to both the subducting Philippine Sea plate at the Nankai Trench and the Pacific plate at the Japan Trench (Fig. 2). These trenches meet in the Boso trench-trench-trench triple junction, just southeast of Central Honshu, together with the intraoceanic Izu-Bonin-Marianas Trench where the Pacific plate subducts below the Philippine Sea plate (Fig. 2). Japan is characterized by an accretionary fold-thrust belt composed of rocks derived from subducted oceanic lithosphere as well as trench-fill deposits derived from the overriding plate (e.g., Isozaki et al., 1990). The Japan fold-thrust belt is generally subdivided into a southwestern (including western Honshu, Shikoku, and Kyushu) and a northeastern (including northern Honshu and Hokkaido) segment. The boundary region between these is the structurally complex Fossa Magna region (Fig. 2).

The Japan fold-thrust belt consists of an overall eastward and structurally downward younging series of accretionary complexes intruded by arc-related intrusives and was constructed over a ca. 600 Myr subduction history (Isozaki et al., 2010). During this period of successive accretion of crustal units from subducting oceanic lithosphere, the fold-thrust belt has grown for several hundreds of kilometers in the direction of the present-day Pacific Ocean.

In the southwestern segment, a large Mesozoic ENE-WSW-trending dextral strike-slip fault known as the Median Tectonic Line separates an older Inner Zone with lower Paleozoic granites and gneisses to the north from a younger Outer Zone with anchimetamorphic Upper Cretaceous to Paleogene trench-fill sediments to the south (Isozaki et al., 2010; Van Horne et al., 2017; Fig. 2). No such distinction in the pre-Neogene bedrock was made in NE Japan, where the Median Tectonic Line and the Inner and Outer Zones are absent. In NE Japan, the bedrock is mainly composed of Paleozoic shallow marine sediments, unmetamorphosed Mesozoic accretionary sediments, and Mesozoic granitic intrusive rocks (Van Horne et al., 2017; and references therein).

The tectonic boundary between the NE and SW Japan is the Fossa Magna region (Martin, 2011): a diffuse zone of deformation bounded by the NNW-SSW-trending Itoigawa-Shizuoka Tectonic Line in the west and the NW-SE-trending Kashiwazaki-Choshi Tectonic Line in the east (Kato, 1992; Martin, 2011; Fig. 2). The Fossa Magna region underwent Early to Middle Miocene subsidence and extension (Kato, 1992; Martin, 2011; Takeuchi, 2004). Extensional structures strike perpendicular to the fold-thrust belt and trench, and accommodated trench-parallel stretching (Martin, 2011; H. Sato et al., 2004; Takeuchi, 2004) of at least 25 km and perhaps up to 60 km of extension in the north and at least 40 km and perhaps up to 200 km in the south (Elouai et al., 2004; Martin,

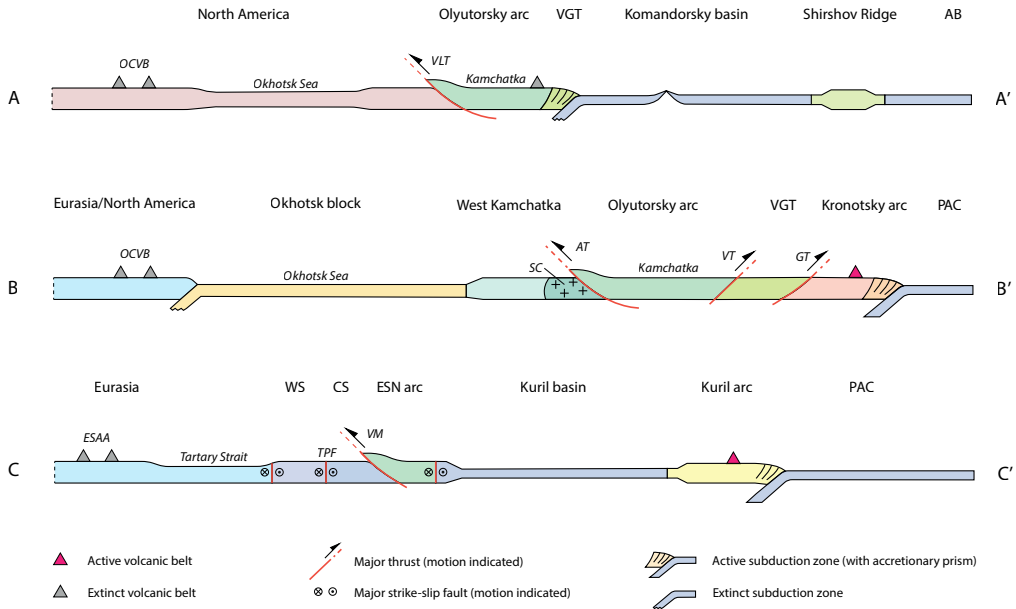


Fig. 3. Schematic cross-sections of the geological structure of the northwest Pacific region. Locations are shown in Fig. 2. See legend for an explanation of the different symbols. Abbreviations: AB = Aleutian Basin; AT = Andrianovka thrust; CS = Central Sakhalin; ESAA = East Sikhote-Alin arc; ESN arc = east Sakhalin-Nemuro arc; GT = Grechishkin thrust; OCVB = Okhotsk-Chukotka volcanic belt; PAC = Pacific plate; SC = Sredinny Complex; TPF = Tym-Poronaysk fault; VGT = Vetlovsky-Govena terrane; VLT = Vatyn-Lesnaya thrust; VM = Vavai mélangé zone; VT = Vetlovsky thrust; WS = West Sakhalin.

2011; H. Sato et al., 2004), opening basins with 5–10 km of sediments (Kato, 1992).

After the early Middle Miocene, inversion led to the separation of north and south Fossa Magna (Kato, 1992; H. Sato et al., 2004; Takeuchi, 2004). The amount of shortening in the northern Fossa Magna Basin since the late Neogene varies from 11 km since the Late Miocene in the north to 23 km since the Middle Miocene in the south (Elouai et al., 2004; H. Sato et al., 2004). This along-strike diachroneity may relate to the (north) eastward migration of the Bono triple junction and the subducting Izu-Bonin arc relative to the Japan fold-thrust belt (Kato, 1992; Martin, 2011).

4.2.2. Japan Sea

The Japan fold-thrust belt and overlying arc became separated from the continental crust of the Eurasian plate in Late Oligocene to Middle Miocene times by the opening of the Sea of Japan back-arc basin (e.g., Jolivet et al., 1994; Jolivet & Tamaki, 1992; Martin, 2011; Otofui et al., 1985; Sato, 1994; Van Horne et al., 2017). The Japan Sea consists of three main basins: the Japan Basin, the Yamato Basin, and the Tsushima or Ulleung Basin (Fig. 2). Only the Japan Basin is underlain by typical oceanic crust, based on its structure and crustal thickness of ~8 km (Hirata et al., 1992; T. Sato et al., 2014). The Yamato and Tsushima/Ulleung Basins are underlain by crust with a thickness of 12–16 km (Hirata et al., 1989; Kim et al., 1998, 2003; Nakahigashi et al., 2013; Nishisaka et al., 2001; Sato et al., 2006, 2014; T. Sato et al., 2014; Yoon et al., 2014), interpreted as either thickened oceanic

crust (Cho et al., 2004; Kim et al., 1998, 2003; T. Sato et al., 2014; Van Horne et al., 2017) or strongly attenuated island-arc crust (Jolivet & Tamaki, 1992; Nakahigashi et al., 2013; Sato et al., 2006; Tamaki et al., 1992; Yoon et al., 2014). The deep major basins are separated by basement highs with a continental (or arc) crustal thickness of about 18–22 km (Martin, 2011; Sato et al., 2006). Stretched continental crust also borders the eastern Russian margin and northeastern Honshu (Nakahigashi et al., 2013; Nishisaka et al., 2001), where it forms a transition zone between the Japan Sea Basin and the ~35 km thick crust of the Japan fold-thrust belt and arc (Iwasaki et al., 2013). A narrow, 50-km-wide zone of ~10 km thick (excluding sediments), thinned continental crust separates the Tsushima/Ulleung Basin from the Korean peninsula, which has a ~30 km crustal thickness (Kim et al., 1998, 2003; Sato et al., 2006).

The oceanic crust of the Japan Sea Basin has been dated by $^{40}\text{Ar}/^{39}\text{Ar}$ dating of basalts recovered by the Oceanic Drilling Program Leg 127/128 at Site 795 (Fig. 2), providing an age range of 23.7 ± 1.2 to 17.1 ± 0.6 Ma (Kaneoka, 1992), although the reliability of these plateau ages has been questioned (Nohda, 2009). Basalt samples from Sites 794 and 797 (Fig. 2) in the Yamato Basin showed ages from 21.2 ± 0.8 to 17.7 ± 0.5 Ma (Kaneoka, 1992) and tuffs overlying the basalts at Site 794 (east Yamato Basin) are dated as 14.9 ± 0.2 Ma (Barnes, 1992), suggesting that mafic magmatism ceased between 17.7 and 14.9 Ma (Nohda, 2009). Sediments directly overlying the basaltic basement at the different ODP sites were biostratigraphically dated at 13 to 18.5 Ma (Tamaki et al., 1992).

Estimates for the age of onset of extension between the Asian mainland and NE Japan prior to the ~20 Ma onset of oceanic crust formation in the Japan and Yamato Basins (Kaneoka, 1992; Nohda, 2009) range from the Oligocene to the earliest Miocene (e.g., Jolivet & Tamaki, 1992; Martin, 2011; Van Horne et al., 2017). Kano et al. (2007) argued that slow initial extension and subsidence may have occurred as early as 35 Ma, indicated by thin deposits of shallow marine sediments, but most authors assume that major extension started around 23 Ma (Ingle, 1992; Jolivet & Tamaki, 1992; Nakajima, 2013; Sato, 1994; van der Werff, 2000; Van Horne et al., 2017; Yoshida et al., 2014). Detailed seismic reflection studies between Korea and Japan (e.g., Cukur et al., 2015; Kim et al., 1998, 2007, 2015; Lee & Kim, 2002; Yoon et al., 2014) also suggested that the separation of SW Japan from the Korean peninsula started around 23 Ma (G-B Kim et al., 2011; Kim et al., 2007, 2015; Lee & Kim, 2002).

Van Horne et al. (2017) estimated that a total of ~500 km of extension occurred in the northeastern Japan Sea. Structural and seismic investigations suggest that the eastern Japan Sea margin experienced ESE-directed, that is, trench-perpendicular, extension from ~17 to 18 Ma, following the main phase of spreading in the Japan Sea (Sato, 1994; van der Werff, 2000). Rifting affected a ~100- to 150-km-wide zone of the western margin of present-day NE Honshu, leading to extensional basin formation and rapid subsidence (Martin, 2011; Nakajima, 2013; Yoshida et al., 2014). Hisada et al. (2008) and S. Kojima et al. (2008) suggested that prior to rifting, southwest Japan was located adjacent to the Korean peninsula based on geological correlation. Sillitoe (1977) suggested that SE Korea and SW Japan shared a single metallogenic belt that appears to have been of offset by 200–250 km after its pre-42 Ma formation and inferred that the belt was displaced along two major dextral strike-slip faults, the Yangsan and Tsushima-Goto faults (Fig. 2). A recent study by Cheon et al. (2019) shows that the Yangsan fault did not accommodate any significant dextral motion during the opening of the Japan Sea, but earlier. Structural and

stratigraphic data from the Korea Strait islands suggest 22–16 Ma dextral displacement on the Tsushima-Goto fault system (Fabbri et al., 1996), followed by a minor sinistral reactivation upon Middle Miocene basin inversion (Fabbri et al., 1996; Son et al., 2015). The amount of displacement along this fault remains poorly constrained, however.

The cessation of back-arc opening of the Japan Sea is considered to be at ~15 Ma (e.g., Jolivet et al., 1994; Martin, 2011; Van Horne et al., 2017). In the southwestern Japan Sea, this is marked by basin inversion at ~15.5 Ma that resulted from NW-SE compression, indicated by broad anticlines and thrust faults along the southern margin of the Tsushima/Ulleung Basin (Kim et al., 2011; Lee et al., 2001, 2011; Lee & Kim, 2002). Tectonic inversion in the eastern part of the Japan Sea commenced in Pliocene times (~3.5 Ma), after a ~10 Myr transitional phase with a nearly neutral stress regime (Sato, 1994). The magnitude of shortening associated with inversion is limited, especially on the scale of the basin (Jolivet & Tamaki, 1992).

4.3. Okhotsk Sea region

4.3.1. Hokkaido

Hokkaido, between Honshu, Sakhalin, and the Kuril island arc (Fig. 1), is located at the triple junction between the subducting Pacific plate and the diffuse plate boundary between the Eurasian and the North American plate. The pre-Neogene basement of Hokkaido is divided into, from west to east, the N-S aligned Oshima, Sorachi-Yezo, Hidaka, Tokoro, and Nemuro tectonostratigraphic belts that are part of the Hokkaido-Sakhalin fold system (Nokleberg et al., 2000; Ueda, 2016; Ueda & Miyashita, 2005; Fig. 4). The Oshima belt consists mainly of Jurassic accretionary complexes, with cherts and limestones dating back to the upper Carboniferous, which are intruded by Early Cretaceous granitoids and overlain by volcanic rocks of the Rebun-Kabato belt along its eastern margin (Ueda, 2016; and references therein; Fig. 4). The belt is considered to be contiguous with the Japan fold-thrust belt and arc of NE Honshu (Ueda, 2016; Zharov, 2005). The Sorachi-Yezo belt consists of Middle Jurassic to Cretaceous accretionary complexes, ophiolites, and metamorphic rocks unconformably overlain by Cretaceous to Paleocene marine clastic sediments interpreted as forearc deposits (Ueda, 2016). HP-LT metamorphic rocks and serpentinites of the Kamuikotan Zone are locally exposed in the cores of anticlines within the forearc basin. These are thought to be the metamorphosed and exhumed equivalents of the ophiolites and arc-bearing accretionary complex of the Idonnappu suture zone that forms the eastern margin of the Sorachi-Yezo belt (Ueda, 2016; Fig. 4).

The Hidaka belt lies structurally below the Sorachi-Yezo zone and is characterized by Paleocene-Eocene accretionary complexes containing mudstones and turbiditic sandstones (Nokleberg et al., 2000; Ueda, 2016). MORB-basalts and dolerites erupted and intruded into the unconsolidated trench-fill sediments, interpreted as seafloor spreading in the downgoing plate adjacent to the continental margin, that is, ridge subduction (Ueda, 2016; and references therein). The western boundary of the Hidaka Belt is formed by the Sakhalin-Hokkaido dextral shear zone, which was active from the Oligocene-Miocene (Fournier et al., 1994; Jolivet & Miyashita, 1985; Worrall et al., 1996; Fig. 2). The westernmost fault branches of this shear zone continue south across the Tartary Strait along west Sakhalin and west Hokkaido (Fournier et al., 1994; Jolivet & Tamaki, 1992; Schellart et al., 2003; Figs. 1 and 2).

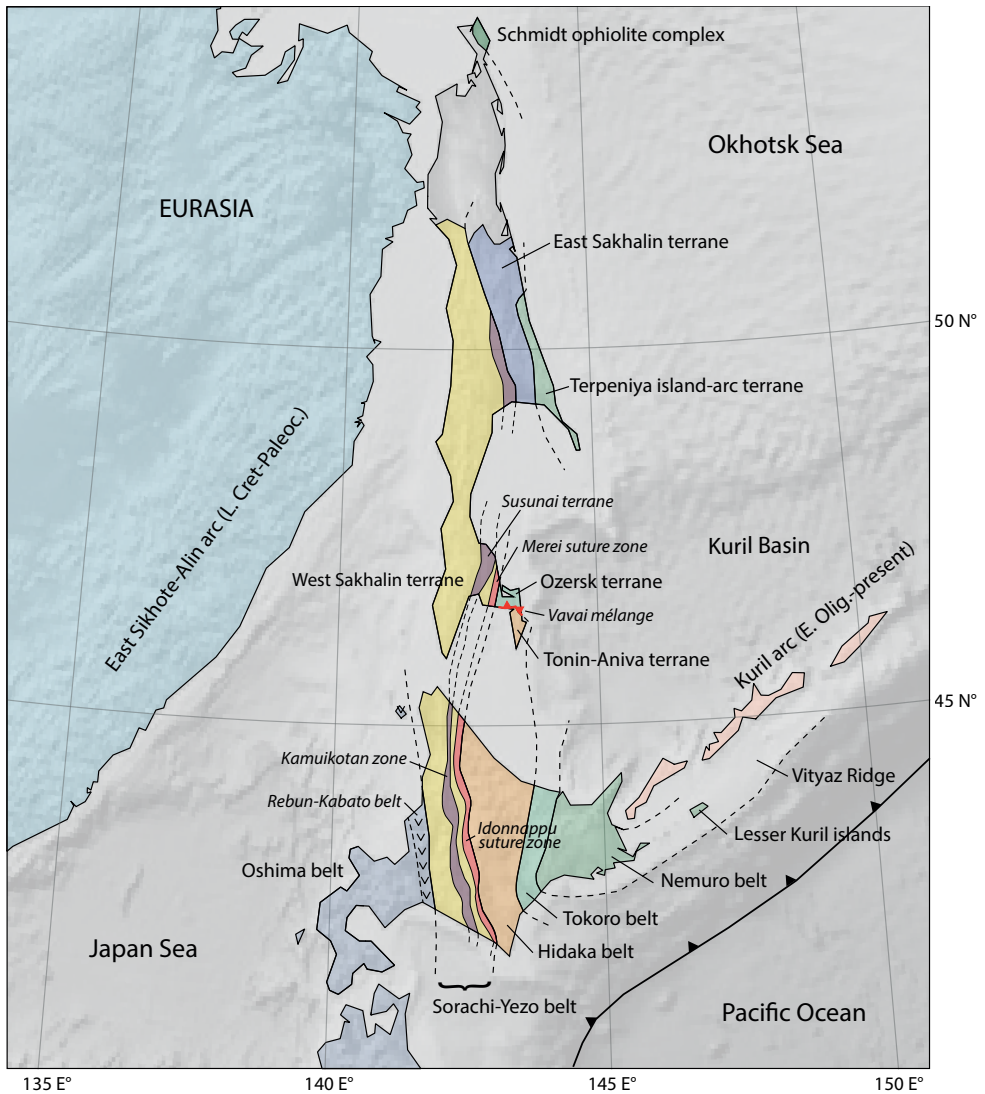


Fig. 4. Schematic map of the basement terranes and belts of Hokkaido and Sakhalin. Sub-belts are denoted in italics. Dashed lines indicate the inferred location of the terrane/belt boundaries. Note that the (Mesozoic) terranes of the east Asian continent are not shown. Based on figures by, for example, Zharov (2005), Ueda (2016), and Liao et al. (2018).

The Hidaka belt is bounded to the east by the Tokoro belt that consists of Cretaceous to Paleogene accretionary complexes comprising Campanian to Lower Eocene volcanoclastic sediments, turbidites, and conglomerates, as well as Middle Jurassic to mid-Cretaceous oceanic rocks (Ueda, 2016; Zharov, 2005; Fig. 4). The conglomerates contain clasts of alkali plutonic rocks that were interpreted to derive from the easternmost, Nemuro belt of Hokkaido (Ueda, 2016; Figs. 2 and 4). In contrast with the characteristic north-south trend observed on Hokkaido, the Nemuro belt follows an approximately east-west

structural trend (Maeda, 1990; Ueda, 2016) and continues in the forearc of the Lesser Kuril islands where it is exposed on several islands (Ueda, 2016), and may continue eastward to the submarine Vityaz Ridge (Lelikov & Emelyanova, 2011; Figs. 1 and 4). The belt is composed of Campanian to Eocene volcanogenic sediments and volcanic rocks, mainly consisting of basalt and andesites (Ueda, 2016; Zharov, 2005). The oldest volcanic sequences are dated by K-Ar geochronology and radiolarians as Campanian-Maastrichtian (Nokleberg et al., 2000).

The zones of Hokkaido are interpreted to have formed in at least three different subduction zones. The Oshima, Sorachi-Yezo, Hidaka belts together with the East Sikhote-Alin arc are collectively interpreted to represent a foreland propagating accretionary prism, arc, and forearc system that formed on the Eurasian upper plate, equivalent to the Japan fold-thrust belt (Kemkin et al., 2016; Nokleberg et al., 2000; Ueda, 2016). Upper Jurassic-Lower Cretaceous island-arc rocks and andesite-chert sequences within the Idonnappu Zone are interpreted as remnants of a distant intraoceanic arc (the Oku-Niikappu arc) that went extinct tens of Myr prior to accretion in the accretionary prism below Eurasia in the mid-Cretaceous (Ueda & Miyashita, 2005; van der Meer et al., 2012). The rocks of the Nemuro belt are commonly interpreted as remnants of an intraoceanic island arc that formed above an east or southeast dipping intraoceanic subduction zone (Bazhenov & Burtman, 1994; Domeier et al., 2017; Konstantinovskaya, 2001; Maeda, 1990; Nokleberg et al., 2000; Parfenov et al., 2011; Ueda & Miyashita, 2005). The Tokoro belt is suggested to have formed the forearc and accretionary wedge terrane associated with this intraoceanic subduction zone (Kanamatsu et al., 1992; Zharov, 2005). The Tokoro belt is thought to also thrust over the Hidaka belt (Kimura, 1994; Ueda, 2016), but how the juxtaposition of these belts may be influenced by the opening of the Sea of Okhotsk and Kuril Basins will be studied in the reconstruction part of this paper.

4.3.2. Sakhalin

The belts of central Hokkaido associated with subduction below the Asian margin continue northward on the 1,000 km-long, 25–170 km-wide island of Sakhalin (e.g., Nokleberg et al., 2000; Parfenov et al., 2009; Ueda, 2016; Zharov, 2005; Figs. 1, 2, and 4), although different names are used for the Sakhalin terranes. Aptian-Paleocene turbidite units of the West Sakhalin terrane are correlated with the forearc deposits of the Sorachi-Yezo belt (Ando, 2003; Zharov, 2005; Fig. 4). In southernmost Sakhalin, the metamorphic Susunai terrane lies to the east of this terrane, forming the continuation of the Kamuikotan zone with a similar Cretaceous age and structure (Kimura et al., 1992; Ueda, 2016; Zharov, 2005). The Merei suture zone is the northward continuation of the Idonnappu suture zone (Zharov, 2005). The Tonin-Aniva terrane, composed of Aptian-Cenomanian turbidites and olistostromes with lenses of Middle Triassic to Lower Cretaceous oceanic tholeiites and (sub)alkaline basalts, forms a subduction-related trench-fill terrane similar to the Hidaka belt (Nokleberg et al., 2000; Parfenov et al., 2009; Zharov, 2005). To the north, the East Sakhalin terrane forms a middle Cretaceous to Paleocene accretionary complex, hosting Upper Cretaceous-Paleocene metamorphic rocks and an ophiolitic mélangé with tectonic slices of Permian-Late Cretaceous rocks (Khanchuk, 2006; Liao et al., 2018; Zhao et al., 2018; Zharov, 2005; Zhabrev, 2011; Fig. 4).

Remnants of an Upper Cretaceous-Paleogene intraoceanic island arc and accretionary complex equivalent to the Nemuro and Tokoro belts are found on the eastern parts of the

Tonin-Aniva and Terpeniya peninsulas and along east Sakhalin (Figs. 1, 2, and 4; e.g., Grannik, 2012; Nokleberg et al., 2000; Parfenov et al., 2009; Zharov, 2005). Santonian-Campanian and Maastrichtian-Danian volcanic and volcanosedimentary rocks of the Terpeniya terrane are found on the Terpeniya peninsula, east of the East Sakhalin terrane (Khanchuk, 2006; Nokleberg et al., 2000; Terekhov et al., 2010; Zhabrev, 2011; Fig. 4), and likely continue offshore (Terekhov et al., 2010). These sequences are straightforwardly correlated with the Nemuro belt of eastern Hokkaido, suggesting that they formed part of a contiguous intraoceanic island-arc now preserved in an area extending from eastern Sakhalin to eastern Hokkaido (Bazhenov et al., 2001; Grannik, 2012; Nokleberg et al., 2000; Parfenov et al., 2009; Ueda, 2016). Consequently, many authors infer that east Hokkaido was located next to southeastern Sakhalin prior to the Neogene opening of the Kuril back-arc basin (e.g., Kimura, 1994; Maeda, 1990; Ueda, 2016). The contrasting E-W trend of the Nemuro belt in the Kuril forearc (Fig. 4) further suggests that the island-arc terrane was disrupted by post-accretion deformation of the Okhotsk Sea and Kuril Basin.

Ophiolite complexes that may be associated with the East Sakhalin arc are preserved on the Schmidt peninsula in northernmost Sakhalin (Nokleberg et al., 2000; Piip & Rodnikov, 2004; Raznitsin, 2012; Rodnikov et al., 2013; Figs. 1 and 4), and are thought to continue offshore eastern Sakhalin based on gravity and magnetic anomalies (Raznitsin, 2012; Rodnikov et al., 2013), and deep seismic profiles (Piip & Rodnikov, 2004). The lowest structural unit of the Schmidt ophiolite complex consists of a serpentinite mélangé with Upper Jurassic-Early Cretaceous radiolarian cherts (Nokleberg et al., 2000). Radiolarian cherts found within a pillow lava sequence structurally above the mélangé have been dated as Albian-Cenomanian (Nokleberg et al., 2000; Raznitsin, 2012).

The accretionary prism below the East Sakhalin arc is preserved in the northern parts of the Tonin-Aniva peninsula and is known as the Ozersk terrane, correlated with the Tokoro belt on Hokkaido (Bazhenov et al., 2001; Zharov, 2005). The terrane was formed from the Campanian to Early Eocene based on tuffs, turbidites, flysch, and island arc basalts of that age. The Ozersk accretionary prism contains thrust slices of different ages and lithologies, the oldest being tholeiitic basalts and jaspers with late Permian to Middle Triassic ages (Bazhenov et al., 2001; Zharov, 2005). The Ozersk terrane is separated from the Tonin-Aniva terrane by the 5- to 8-km-wide, 70-km-long Vavai mélangé zone including serpentinites, gabbroic lenses, fragments of Mesozoic oceanic crust, mid-Cretaceous accretionary units, and Campanian-Paleocene island-arc rocks (Zharov, 2005; Fig. 4). It is interpreted as the suture zone between the Ozersk and Tonin-Aniva terranes that formed upon westward obduction of the East Sakhalin island arc (Bazhenov et al., 2001; Zharov, 2005).

On the Tonin-Aniva peninsula, the timing of obduction is marked by Early Eocene sediments and tuffs in the Ozersk terrane, the occurrence of mid-Eocene (44–38) Ma granitoid intrusions that cut the suture zone (Glorie et al., 2017; Liao et al., 2018; Zharov, 2005) and an unconformable cover of Upper Eocene-Lower Oligocene terrigenous sediments (Zharov, 2005; and references therein). These observations constrain the obduction in southern Sakhalin to the Middle Eocene (Bazhenov et al., 2001; Parfenov et al., 2011; Zharov, 2005). Zharov (2005) argued for early Paleogene obduction in east Sakhalin, most probably limited to the latest stages of the Paleocene. Recently, the collision of the East Sakhalin terrane and an exotic terrane, referred to by the authors as the Okhotsk Sea Plate, was constrained between 49 and 38 Ma, based on the maximum

depositional age in the East Sakhalin accretionary complex and the Late Eocene age of both the undeformed sedimentary cover and the emplacement of granitic plutons (Zhao et al., 2018). Collectively, the constraints on the arc-continent collision in Sakhalin indicate that it occurred sometime between ~50 and 38 Ma.

4.3.3 Okhotsk Sea and Kuril Arc

The Okhotsk Sea forms an approximately 1,500-km-long and 800-km-wide marginal sea bounded by the Kamchatka peninsula to the east and separated from the Pacific Ocean to the south by the Kuril island arc and trench (Fig. 1). The Okhotsk Sea is underlain by continental crust that varies in thickness from >25 km below the submarine rises to 20–25 km below the troughs (Gnibidenko & Khvedchuk, 1982; Piip & Rodnikov, 2004; Piskarev et al., 2012; Rodnikov et al., 2013; Savostin et al., 1983). Magmatic rocks recovered from the basement highs are dominated by Lower to Upper Cretaceous granitoids and felsic volcanics (Gnibidenko & Khvedchuk, 1982; Lelikov & Pugachev, 2016). Pre-Cretaceous rocks of Paleozoic age or even older have been suggested to occur in the Sea of Okhotsk basement (Gnibidenko & Khvedchuk, 1982; Piskarev et al., 2012; Worrall et al., 1996), but there are no reliable isotope ages to confirm these.

The intermediate crust beneath the Okhotsk Sea is generally considered to be a former microcontinental “Okhotsk” block (Parfenov & Natal’in, 1986; Worrall et al., 1996; Yang, 2013; Zhao et al., 2018; Zonenshain, 1990). Alternatively, Ueda and Miyashita (2005) suggested that the Sea of Okhotsk may instead be underlain by an amalgamation of far-traveled intra-Panthalassa island-arcs. The collision of the Okhotsk Block with the Siberian margin is correlated to cessation of continental arc magmatism in the 3,000-km-long Andean type Okhotsk-Chukotka volcanic belt in NE Siberia (Bindeman et al., 2002; Parfenov & Natal’in, 1986; Yang, 2013; Fig. 2) around 81–77 Ma (Akinin & Miller, 2011; Hourigan & Akinin, 2004; Tikhomirov et al., 2012). In the easternmost part of the volcanic belt, ~2,000 km away from the Okhotsk Sea, subduction-related volcanism ended around the same time, at ~85 Ma (Pease et al., 2018).

The Okhotsk Sea accommodated major N-S-directed extension, first during the (mid-) Eocene to Early Miocene, as inferred from seismic subsurface data (Gnibidenko & Khvedchuk, 1982; Worrall et al., 1996). Progressively thinner crust toward the south suggests that the majority of extensional deformation took place in the central and southern parts of the Okhotsk Sea (Schellart et al., 2003). The southernmost part of the Okhotsk Sea is underlain by the oceanic Kuril Basin (Baranov et al., 2002; Gnibidenko & Khvedchuk, 1982; Savostin et al., 1983; Figs. 2 and 4). This wedge-shaped oceanic basin is approximately 750 km long and has a maximum width of ~300 km (Fig. 2). Although no distinct spreading ridge is observed, the geometry of the basin and orientation of faults implies a NW-SE opening (Maeda, 1990; Schellart et al., 2003; Takeuchi et al., 1999). The timing of opening remains poorly constrained due to the absence of marine magnetic anomalies or directly dated samples of the oceanic basement. Southward shifting volcanic activity from southern Sakhalin (23–21 Ma) to central and eastern Hokkaido (15–9 Ma) led Takeuchi et al. (1999) to constrain the opening of the basin from 23 to 9 Ma. This is consistent with the findings of Ikeda et al. (2000), who argued that spreading in the Kuril Basin continued to 7–9 Ma, based on the occurrence of basaltic rocks with back-arc affinity in northeast Hokkaido.

The N-S extension in both the Okhotsk Sea and the Kuril Basin is bounded in the west

by the ~2,000-km-long, dextral, N-S-trending strike-slip faults of the eastern Sakhalin-Hokkaido dextral shear zone (Fournier et al., 1994; Schellart et al., 2003; Worrall et al., 1996). Formation of this shear zone followed upon the obduction of the East Sakhalin-Nemuro arc and started in the Late Eocene (Liao et al., 2016; Maeda, 1990; Schellart et al., 2003; Weaver et al., 2003; Worrall et al., 1996). Major faults include the Tym-Poronaysk fault, which runs from north to south through the central part of Sakhalin, the East Sakhalin fault, and offshore faults running through the Gulf of Tartary and the western Okhotsk Sea (Figs. 2 and 3). Movements along the strike-slip faults displaced the preexisting accretionary and subduction-related terranes of the basement of Hokkaido and Sakhalin. Most of the motion along the shear zone is suggested to have occurred since ~25 Ma, bounding the opening of the Okhotsk-Kuril Basins to the east (Fournier et al., 1994; Jolivet & Tamaki, 1992). Displacements are thought to be equal to the amount of extension in the Okhotsk-Kuril Basin. Schellart et al. (2003) estimate the amount of extension in the western Kuril Basin at ~300 km for the western part of the basin, that is, roughly equal to the width of the oceanic crust. Assuming a crustal thickness of 40 km prior to deformation, the total amount of extension in the western Okhotsk Sea would comprise an additional 500–700 km (Schellart et al., 2003). However, observed dextral displacements of the faults on Sakhalin show much lower values of displacement. Fournier et al. (1994) obtain a minimum of 50 km of dextral displacement since the Miocene along the strike-slip faults in the East Sakhalin Mountains, based on a summation of observed offsets of several en echelon faults. Fournier et al. (1994) and Schellart et al. (2003) suggested that the bulk of the motion must have been accommodated along offshore strike-slip faults.

The continuation of the Sakhalin-Hokkaido dextral shear zone through central Hokkaido is often named the Hidaka Shear Zone, which connects to the Japan Trench to the south (Jolivet & Miyashita, 1985; Jolivet & Tamaki, 1992; Fig. 2). The displacement along the Hidaka Shear Zone is poorly constrained, but is expected to be somewhat higher than in Sakhalin as a result of extension in the Aniva Trough between Hokkaido and Sakhalin (Takeuchi et al., 1999; Fig. 2). Existing models incorporate a total displacement of about 200 km (Itoh & Tsuru, 2006; Jolivet & Tamaki, 1992). This would place Sakhalin far to the north at ~23 Ma, very close to the Siberian margin, which implies high amounts of Neogene extension and crustal thinning north of Sakhalin that is not supported by observed crustal thicknesses (Bogdanov & Khain, 2000). Instead, we estimate 50 km of extension in the Aniva Trough between 23 and 9 Ma, based on the average crustal thickness of 25–27 km and assuming a preextensional thickness of 35 km (Bogdanov & Khain, 2000), giving a total of ~100 km of dextral displacement in the Hidaka Shear Zone between 23 and 9 Ma.

The Okhotsk Sea is separated from the Pacific Ocean by the >1,000-km-long Kuril island arc, forming a segment of the active Kuril-Kamchatka volcanic arc that formed above the subducting Pacific plate (Figs. 1 and 2). The active part of the Kuril arc is thought to have developed in the Late Oligocene to Early Miocene (Avdeiko et al., 2007; Martynov et al., 2010). Recently, De Grave et al. (2016) obtained a U-Pb zircon age of 31.3 ± 1.1 Ma from a granodiorite intrusion derived from the basement of Kunashir Island, indicating that the Kuril arc started activity in or prior to the Early Oligocene. Dredged rocks of the submarine Vityaz Ridge similar to those of the onshore Nemuro belt (Lelikov & Emelyanova, 2011) imply that the modern Kuril arc was built upon crust of the East Sakhalin-Nemuro paleo-arc.

The most recent stage of deformation in Sakhalin and Hokkaido that followed upon dextral strike-slip-dominated tectonics was E-W compression compatible with the present-day motions. These led to shortening and uplift on both islands from the Middle-Late Miocene to present times (e.g., Fournier et al., 1994; Jolivet & Huchon, 1989). The amount of shortening and deformation is highest in the southern central parts of Hokkaido, estimated to be 60–100 km, where the Kuril and Japan arcs are actively converging since the Middle Miocene (~13 Ma), induced by westward motion of the Kuril forearc sliver by oblique subduction (Ito, 2002; Iwasaki et al., 2004; Kato et al., 2004).

4.4. Kamchatka

The Kamchatka peninsula forms an assemblage of subduction-related terranes, including remnants of intraoceanic island arcs, accretionary wedges, and ophiolites, which progressively accreted from northwest to southeast since Cretaceous times (Geist et al., 1994; Harbert et al., 1998; Nokleberg et al., 2000; Zinkevich & Tsukanov, 1993; Zonenshain, 1990). The basement of Kamchatka can be divided into four terranes: the West Kamchatka terrane, the Olyutorsky (or Achaivayam-Valaginsky) arc terrane, the Vetlovsky-Govena terrane, and the Kronotsky arc terrane (Figs. 2 and 3). The West Kamchatka terrane consists mainly of Upper Cretaceous to Eocene continental-derived turbiditic sandstones and shales (Harbert et al., 1998; Shapiro & Solov'ev, 2009), for which many different names are used depending on the location (e.g., the Ukelayat, Lesnaya, Khozgon Groups). The oldest rocks of the West Kamchatka terrane are formed by Upper Mesozoic high-grade metamorphic rocks of the Sredinny Complex consisting of granulites, amphibolites, migmatites, and granites. These are exposed in a north-south-oriented 200-km-long and 30- to 40km-wide zone in the southern part of the Sredinny Range (Fig. 1). The Sredinny Complex is either part of the Okhotsk block (e.g., Bindeman et al., 2002; Konstantinovskaya, 2011; Parfenov & Natal'in, 1986), or a separate West Kamchatka microcontinental block (Bogdanov & Chekhovich, 2002; Chekhovich et al., 2009; Filatova, 2014; Zonenshain, 1990), or represents the metamorphosed equivalent of the terrigenous sediments of the Asian continental margin (e.g., Hourigan et al., 2009; Kirmasov et al., 2004; Shapiro & Solov'ev, 2009). The structurally lowest and highest-grade unit, the Kolpakova Group, consists of Lower to Upper Cretaceous granulite- and amphibolite-facies gneisses and migmatites (Hourigan et al., 2009; Tararin, 2008; Vinogradov et al., 1988; Fig. 5). These are cut by Campanian (78–80 Ma) gneissic granites (Krutogorov Complex; Hourigan et al., 2009; Luchitskaya et al., 2008), which are coeval with an inferred phase of regional metamorphism around 77 Ma (Bindeman et al., 2002). Both units are unconformably overlain by amphibolite- to greenschist-facies metasedimentary schists and gneisses of the Kamchatka Group (Rikhtyer, 1995; Fig. 5), suggested to be of Paleocene age (~60 Ma; Hourigan et al., 2009). The youngest phase of metamorphism and felsic magmatism of the Sredinny Complex occurred during the Early Eocene (Bindeman et al., 2002; Hourigan et al., 2009; Luchitskaya & Soloviev, 2012). U-Pb (SHRIMP) zircon age data of metamorphic and magmatic rocks constrain peak metamorphism, migmatization, and granitic magmatism at 47–55 Ma (Bindeman et al., 2002; Hourigan et al., 2009; Luchitskaya et al., 2008; Luchitskaya & Soloviev, 2012). These events are correlated to the obduction of the Olyutorsky island-arc complex and underlying ophiolite onto the Sredinny complex (Bindeman et al., 2002; Hourigan et al., 2009; Luchitskaya & Soloviev, 2012).

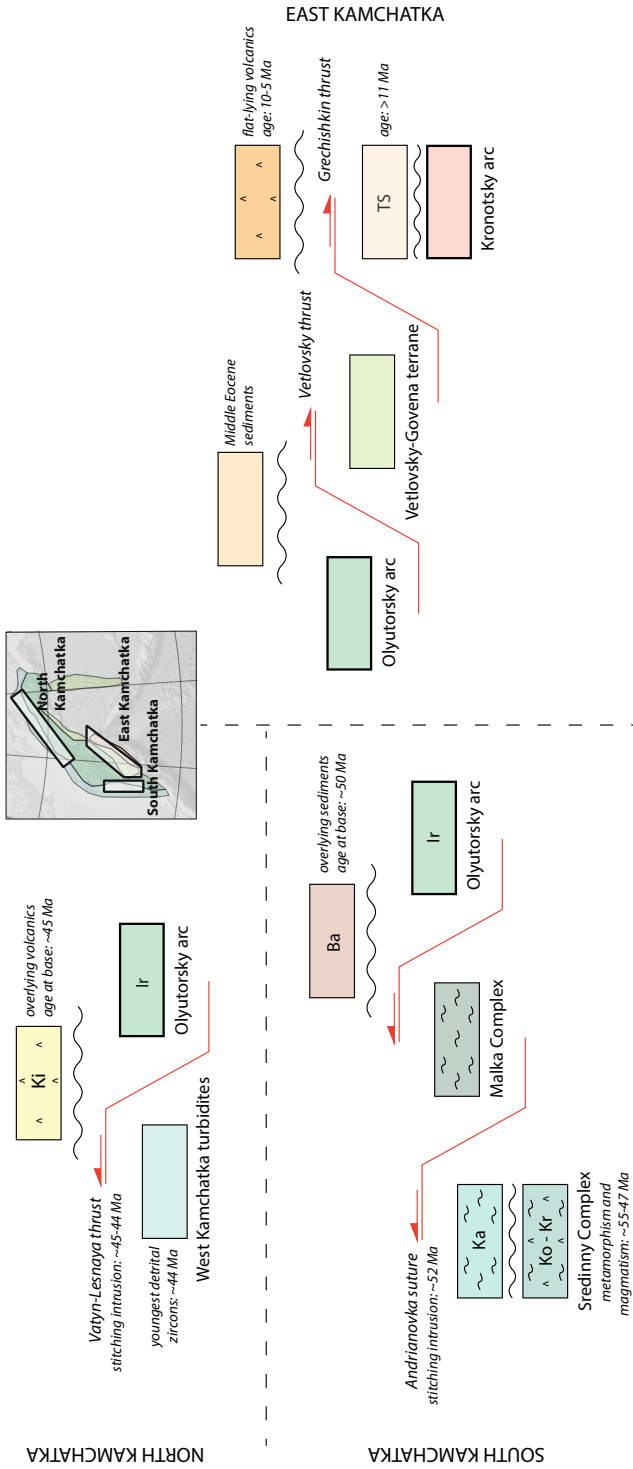


Fig. 5. Schematic overview of the geological structure of Kamchatka. Each box represents a terrane/formation that is described in the text (section 4.4). Island-arc terranes are shown with thick boundaries. Key structural/spatial relationships and age constraints are indicated for north, east, and south Kamchatka (see inset map). See text for details. Major thrust faults are shown in red. Unconformities are shown by black wavy lines. Key to abbreviations: Ba = Baraba Formation; Ir = Iruney Formation; Ka = Kamchatka Group; Ki = Kimkil Group; Ko = Kolpakova Group; Kr = Krutogorov Complex; TS = Tyushev Series.

The West Kamchatka terrane is overthrust by the Olyutorsky island-arc terrane along a thrust front that extends along the entire length of Kamchatka (Figs. 2, 3, and 5). The geological structure of the collision zone and the timing of collision/obduction are notably different in the southern part of Kamchatka (in the Sredinny Range) compared to the northern part (Kamchatka isthmus and Koryak Highlands; e.g., Shapiro et al., 2008). In the south, the Sredinny Complex is overthrust by greenschist to amphibolite-facies metamorphic rocks of the Malka Complex along the Andrianovka thrust or suture (Figs. 3 and 5), which is characterized by lenses of mafic and ultramafic rocks in a serpentinite mélangé (Kirmasov et al., 2004; Rikhtyer, 1995). The Malka Complex consists of metamorphosed mafic volcanics, cherts, and siliceous sediments, interpreted to be derived from the Olyutorsky island-arc terrane (Hourigan et al., 2009; Kirmasov et al., 2004; Konstantinovskaya, 2011; Shapiro et al., 2008; Solov'ev & Palechek, 2004). The Malka Complex is structurally overlain by its nonmetamorphic equivalent, the Irunev Formation (Fig. 5), which consists of Santonian or Campanian to Maastrichtian volcanoclastics and cherts with locally occurring massive tuffs and pillow basalts (Hourigan et al., 2009; Konstantinovskaya, 2011; Luchitskaya et al., 2008).

The timing of arc-continent collision/obduction of the southern segment of the Olyutorsky arc over the West Kamchatka terrane in south Kamchatka is confined to a narrow time interval. The upper age limit is marked by continental conglomerates and sandstones that unconformably overlie both the Malka Complex and the Upper Cretaceous Olyutorsky island-arc rocks (Irunev Formation; Shapiro et al., 2008; Solov'ev, Hourigan, et al., 2004; Solov'ev et al., 2007; Fig. 5). The sediments at the base of the succession, belonging to the Baraba Formation, contain pebbles from most of the basement rocks of the Sredinny Range, including the volcanics and Santonian-Campanian cherts from the Irunev Formation and the metamorphics of the Sredinny and Malka Complexes (Konstantinovskaya, 2011; Solov'ev, Hourigan, et al., 2004; Solov'ev et al., 2007; Zinkevich et al., 1994). A tuff layer from the lower part of the Baraba Formation provided an U-Pb (SHRIMP) zircon age of 50.5 ± 1.2 Ma (Solov'ev, Hourigan, et al., 2004). The lower age limit is provided by a detailed analysis of the age of detrital zircon grains that indicate that deposition of sediments between the margin and the Olyutorsky island-arc continued to ~ 55 Ma (Hourigan et al., 2009). In addition, granite intrusions cutting through the metamorphics of the Sredinny Complex yielded U-Pb (SHRIMP) ages of 50.1 ± 1.7 to 54.9 ± 0.5 Ma with one intrusion stitching the Andrianovka suture yielding an age of 51.5 ± 0.7 Ma (Hourigan et al., 2009; Luchitskaya et al., 2008), coeval with the timing of peak metamorphism of the Sredinny Complex at ~ 52 Ma (Hourigan et al., 2009; Konstantinovskaya, 2011). Collectively, obduction of the Olyutorsky arc over the southern part of Kamchatka is thus constrained to 55–50 Ma (Kirmasov et al., 2004; Shapiro et al., 2008).

The crystalline basement rocks of the Sredinny Massif that are structurally positioned below the remnants of the Olyutorsky arc are restricted to southern Kamchatka. In northern Kamchatka, in the Kamchatka isthmus and the Koryak Highlands, the Upper Cretaceous-Paleogene turbidite sediments of the West Kamchatka terrane directly underlie (unmetamorphosed) rocks of the Olyutorsky arc terrane, along the more than 800-km-long Vayn-Lesnaya thrust fault (Filatova, 2013; Solov'ev et al., 2001, 2011; Figs. 2, 3, and 5). The suture zone consists of a tectonic mélangé of chert (dated by radiolarians as Santonian-Maastrichtian), tuff, pillow basalt, and volcanic sandstone blocks, with a matrix

of highly deformed sediments derived from the West Kamchatka terrane (Solov'ev et al., 2001, 2011; Solov'ev, Shapiro, & Garver, 2002).

The timing of collision of the northern segment of the Olyutorsky island-arc can be tightly bracketed by the age of the youngest sediments below the suture and the age of the undeformed overlap sequence. Detrital zircon fission-track data from the upper part of the West Kamchatka sediments suggest that sedimentation continued up to the Middle Eocene, with the youngest dated detrital zircons yielding ages of ~44 Ma (Garver et al., 2000; Solov'ev, Shapiro, Garver, Shcherbinina, et al., 2002). In the Kamchatka isthmus, the Vatyn-Lesnaya Fault is unconformably overlain by volcanics of the Kinkil Group (Fig. 5), which contain Lutetian microfossils and from which basal rhyolites yielded U-Pb zircon, K-Ar biotite, and zircon and apatite fission-track ages between ~46 and 44 Ma (Solov'ev et al., 2011; Solov'ev, Shapiro, & Garver, 2002). These ages are consistent with a granodiorite massif that cuts through the fault zone and is dated at 45–44 Ma by a U-Pb and Rb-Sr geochronology (Solov'ev et al., 2011; Solov'ev, Shapiro, & Garver, 2002). The formation of the Vatyn-Lesnaya suture during obduction of the Olyutorsky arc in northern Kamchatka is thus tightly constrained at 45–44 Ma. The total displacement of the Olyutorsky arc over the continental margin is estimated to be at least 50–100 km (Solov'ev et al., 2011; Solov'ev, Shapiro, & Garver, 2002). From the above data, it follows that the obduction of the Olyutorsky arc onto NE Siberia occurred at different times in the north and south of Kamchatka: 55–50 Ma in the south and until ~45 Ma in the north (Kirmasov et al., 2004; Konstantinovskaya, 2001; Shapiro et al., 2008; Shapiro & Solov'ev, 2009; Solov'ev et al., 2011). Therefore, it was hypothesized that the arc may have been segmented by a transform fault, causing the northern segment to collide with the continental margin 5–10 Myr later (Shapiro et al., 2008; Shapiro & Solov'ev, 2009).

Apart from the Sredinny mountain range and the Koryak Highlands, the Olyutorsky arc rocks are also widely exposed in the Eastern Ranges and on Karaginsky Island (e.g., Hourigan et al., 2009; Konstantinovskaya, 2011; Figs. 1 and 2). There, island-arc units mostly consist of basalts and andesites, as well as tuffs, volcanoclastic sandstones and siltstones, cherts, and jaspers (Konstantinovskaya, 2011). Radiolarians of the chert and mudstone layers in the Eastern Ranges have been dated as Campanian-Danian (Zinkevich et al., 1994). Ophiolites associated with the Olyutorsky arc are found in different localities in eastern Kamchatka. Upper Cretaceous peridotites, gabbros, and diabases belonging to a coherent ophiolite complex are exposed within a serpentite mélangé in the Kumroch Range (Tsukanov et al., 2009). A well-preserved ophiolite sequence from Karaginsky Island yielded U-Pb (SHRIMP) zircon ages of ~76–72 Ma (Campanian; Tararin et al., 2012). A Late Cretaceous age of formation of ~100–70 Ma was also obtained for the ophiolitic gabbros and peridotites in eastern Kamchatka (Tararin et al., 2012). Based on their geochemical signature, the ophiolites of the Kumroch Range and Karaginsky Island are interpreted to have formed in a suprasubduction zone setting (Kravchenko-Berezhnoy & Nazimova, 1991; Skolotnev et al., 2018; Tsukanov et al., 2009).

The Vetlovsky-Govena terrane comprises the highest structural unit of an accretionary prism that underlies the Olyutorsky arc to the east (Figs. 2, 3, and 5), thought to have formed in a northwest-dipping subduction zone that existed from the Middle Eocene to the Pliocene to the east of the Olyutorsky arc (Bakhteev et al., 1994; Shapiro et al., 2004; Solov'ev, Shapiro, et al., 2004). The boundary between the Olyutorsky arc terranes and the Vetlovsky-Govena terrane is marked by the northwest-dipping Vetlovsky thrust

zone that comprises a serpentinite-hosted tectonic *mélange* containing ultramafic rocks, gabbros, and sediments (Figs. 3 and 5), running from the Shipunsky peninsula in the south through eastern Kamchatka and Karaginsky Island to the Govena peninsula in northern Kamchatka (Figs. 1 and 2; Konstantinovskaya, 2011; Zinkevich & Tsukanov, 1993). The Vetlovsky thrust is unconformably overlain by a Middle Eocene mudstone and sandstone (Fig. 5), limiting the age of the fault, and thereby the onset of westward subduction below the Olyutorsky arc terrane, to the latest Early Eocene (Bakhteev et al., 1994; Konstantinovskaya, 2011).

The oldest unit of the Vetlovsky-Govena terrane consists of Upper Paleocene to Lower Eocene volcanoclastic sediments, tuffs, cherts with lenses of basalts, jasper, and micritic limestone (Bakhteev et al., 1994; Gladenkov, 2016; Zinkevich & Tsukanov, 1993). Mafic volcanic rocks as well as pillow lavas and tuffs found in tectonic slices of the terrane, characterized by a tholeiitic MORB geochemical signature (Tsukanov et al., 2018; Zinkevich & Tsukanov, 1993). These MORB-like basalts are dated as Paleocene-Lower Eocene and may have formed by back-arc spreading behind the Olyutorsky arc (Bakhteev et al., 1994; Konstantinovskaya, 2001; Solov'ev, Shapiro, et al., 2004; Tsukanov et al., 2018). Middle-Upper Eocene terrigenous units of the East Kamchatka accretionary prism unconformably overlie this unit (Bakhteev et al., 1994; Gladenkov, 2016; Solov'ev, Shapiro, et al., 2004). The youngest sediments of the accretionary prism consist of Oligocene-Miocene flysch, which is separated from the Vetlovsky-Govena terrane by the steeply, top to the southeast, northwest-dipping, ophiolite-free Grechishkin thrust (Bakhteev et al., 1997; Solov'ev, Shapiro, et al., 2004; Figs. 2, 3, and 5). To the east and in the footwall of this thrust lies the Kronotsky arc terrane, which incorporates accreted thrust units derived from the Kronotsky island-arc. Exotic Miocene pelagic cherts and the Early-Middle Miocene (24–11 Ma) age of the youngest deformed sandstones of the Tyushev Series below the Grechishkin thrust (Bakhteev et al., 1997; Solov'ev, Shapiro, et al., 2004). indicate that Kronotsky arc accretion probably occurred during the Late Miocene (Levashova et al., 2000; Solov'ev, Shapiro, et al., 2004). The upper age limit of the arc-continent collision is estimated from an angular unconformity between the deformed Lower to Middle Miocene marine sediments and flat-lying Upper Miocene-Pliocene (10–5 Ma) volcanics (Levashova et al., 2000; Shapiro et al., 1996; Fig. 5).

The Kronotsky arc is interpreted as a second island-arc that accreted to the Asian margin of Kamchatka. Remnants of the arc are exposed on the Shipunsky, Kronotsky, and Kamchatka Mys peninsulas in eastern Kamchatka (e.g., Alexeiev et al., 2006; Bazhenov et al., 1992; Nokleberg et al., 2000; Zinkevich & Tsukanov, 1993; Figs. 1 and 2). The intraoceanic volcanic arc was active from the Late Cretaceous (~85 Ma) to the Middle Eocene (e.g., Bazhenov et al., 1992; Levashova et al., 2000; Nokleberg et al., 2000; Shapiro & Solov'ev, 2009; Tsukanov et al., 2014). The youngest island-arc basalts are ~40 Ma (Beniamovsky et al., 1992; Gladenkov, 2016; Levashova et al., 2000). The Kronotsky arc was suggested to have formed above a northward dipping subduction zone (Alexeiev et al., 2006; Domeier et al., 2017; Konstantinovskaya, 2001; Shapiro & Solov'ev, 2009), evidenced by the relative position of the remnants of the volcanic belt, the fore-arc and the accretionary wedge, and the dip-direction of thrust planes in the accretionary wedge (Alexeiev et al., 2006). The Kronotsky arc overlies an ophiolite sequence exposed on the eastern peninsulas of Kamchatka. Three ophiolite complexes of the Kamchatka Mys peninsula are distinguished by Tsukanov et al. (2007): (i) an Aptian-Cenomanian complex

of ancient oceanic crust, forming the basement of the Kronotsky arc, occurring mainly as thin tectonic slices in Campanian-Maastrichtian island-arc rocks on the Kamchatka Mys peninsula; (ii) an Upper Cretaceous ophiolite complex with suprasubduction zone geochemistry; and (iii) a Paleocene-Lower Eocene complex of island-arc or back-arc origin, consisting of gabbros, diabase, and basalts.

Portnyagin et al. (2008) showed that enriched tholeiites from the Kamchatka Mys ophiolite, dated by microfauna as Albian-Cenomanian (~113–93 Ma; Khotin & Shapiro, 2006; and references therein), share similar geochemical characteristics with the northernmost, Detroit, and Meiji seamounts of the Hawaii-Emperor seamount chain. It was suggested that these Upper Cretaceous Hawaiian hotspot-related volcanics were accreted below the Kronotsky arc sometime during its intraoceanic activity (Khotin & Shapiro, 2006; Lander & Shapiro, 2007; Portnyagin et al., 2008). A subsequent geochemical study of ultradepleted melts in MORB-like basalts obtained from a serpentinite mélange in the Kamchatka Mys ophiolite complex suggested that the mid-ocean ridge at which the ophiolite formed may have had interaction with the Hawaiian hotspot during the middle-Cretaceous, that is, before subduction started below the Kronotsky arc (Batanova et al., 2014; Portnyagin et al., 2009). This suggests that the mid-Cretaceous oceanic crust on which Kronotsky arc formed, originated from a spreading center near the Hawaiian mantle plume. Following the arrest of intraoceanic subduction at ~40 Ma, the Kronotsky arc and its underlying accretionary prism welded to the Pacific plate and was transported toward Kamchatka where it arrived and accreted in the Late Miocene (Domeier et al., 2017; Konstantinovskaya, 2001; Shapiro & Solov'ev, 2009; van der Meer et al., 2018).

4.5. Bering Sea

The Bering Sea is the largest marginal sea basin of the Northern Pacific realm. It is separated from the Pacific Ocean by the Aleutian island arc, which extends over 2,000 km from the southwestern tip of Alaska to the southern Kamchatka peninsula (Fig. 1). The Pacific plate is actively subducting below the North American plate at the Aleutian Trench, whereby the curved shape of the Aleutian Trench leads to an increasing subduction obliquity from east to west (e.g., Boyd & Creager, 1991). The oldest reliably dated rocks from the Aleutian Arc have $^{40}\text{Ar}/^{39}\text{Ar}$ isochron ages of 46.3 ± 0.9 Ma for an andesite of the deep submarine Murray Canyon west of Kiska Island and 46.2 ± 1.5 Ma for a tholeiitic basalt of Medny Island, in the western Aleutians (Jicha et al., 2006; Layer et al., 2007; Fig. 1). The Bering and Medny islands (Fig. 1), together referred to as the Komandorsky Islands, form the westernmost islands of the Aleutian arc, and were suggested to contain remnants of the Kronotsky island arc and fore-arc basin (Alexeiev et al., 2006; Bazhenov et al., 1992; Rostovtseva & Shapiro, 1998). Fore-arc deposits exposed on the Komandorsky Islands were dated as Late Paleocene to Early Eocene using bio-magnetostratigraphy (Bazhenov et al., 1992; Minyuk & Stone, 2009; Rostovtseva & Shapiro, 1998), although the interpretation of the biostratigraphy is debated (Scholl, 2007). The oldest radiometric ages from rocks interpreted to belong to the Aleutian arc of ~46 Ma are only a few million years younger than the youngest arc volcanics found on the Beringian margin (Fig. 2), where K-Ar and U-Pb zircon ages from dredged arc volcanics are 54.4 to 50.2 Ma (Davis et al., 1989). Therefore, conventional tectonic models of the Bering Sea region suggest that subduction initiation below the Aleutian Trench was related to a jump of the subduction zone from the Beringian margin in the north toward the Aleutian Trench in the south

around 50–46 Ma, likely related to the obduction of the Olyutorsky arc on Kamchatka (Scholl, 2007; Worrall, 1991).

The oceanic lithosphere of the Aleutian Basin underlies the largest deepwater basin of the Bering Sea. It has been suggested that the Aleutian Basin lithosphere was captured by the North American plate upon formation of the Aleutian subduction zone around 50 Ma (e.g., Cooper et al., 1976, 1992; Scholl et al., 1975). Since the age interpretation of observed marine magnetic anomalies remains uncertain (see section 3) and no dredge samples from the acoustic basement are available for direct age determination, the exact age and the origin of the Aleutian Basin is still unknown. Presently, any conceptual model of its formation must rely on indirect constraints. If the observed magnetic anomalies indeed represent magnetic reversals indicative of seafloor spreading (section 3), the orientation of the anomalies would provide an independent constraint for the orientation of the ridge at which the Aleutian Basin crust accreted. We use this constraint to test the predicted orientation of that ridge in our reconstruction.

Two major submarine highs are located below the Bering Sea: the Bowers and Shirshov Ridges (Figs. 1 and 2). These separate the Aleutian Basin from the smaller Komandorsky and Bowers Basins. The Bowers Ridge forms an arcuate ridge extending from the Aleutian arc to the north. The ridge seems to be structurally connected to the Aleutian arc and has a asymmetric structure with a deep trench filled with about 8–10 km of mainly Miocene sediments along its steep northern and eastern slopes (Cooper et al., 1981, 1987; Scholl, 2007). Recent new data on the composition and age of dredged rocks of the Bowers Ridge (Wanke et al., 2011, 2012) showed island-arc rocks on the northern slopes of the ridge (Fig. 2) with a moderate adakitic chemical signature interpreted as indicator of the generation of melt above an obliquely subducting slab (Wanke et al., 2012). Those authors obtained $^{40}\text{Ar}/^{39}\text{Ar}$ ages ranging from 32.3 ± 2.0 to 26.0 ± 0.7 Ma for the volcanic rocks of the ridge. Two basement samples of trachybasalts from a seamount located on the western extension of the arcuate ridge were dated at 22.2 ± 2.7 and 24.4 ± 0.8 Ma. Two volcanic episodes were distinguished by Sato et al. (2016) based on $^{40}\text{Ar}/^{39}\text{Ar}$ dating of volcanic rocks collected at International Ocean Discovery Program Site U1342 (Expedition 323) from the northern part of the ridge (Fig. 2): 34–32 and 28–26 Ma. All the above ages are considerably younger than the initiation of the Aleutian arc, suggesting that the Bowers Ridge formed within the Bering Sea during northward subduction at the Aleutian Trench. The age and origin of the back-arc basin west of the Bowers Ridge, the Bowers Basin, is still largely unknown (see section 3). The oldest sediments found on the basin floor of the Bowers Basin are Oligocene in age (Scholl, 2007). Cooper et al. (1992) and Chekhovich and Sukhov (2015) associated the formation of the Bowers Basin with relative motion of the Bowers Ridge and Trench to the NE relative to the Aleutian Trench.

The Shirshov Ridge forms an approximately 550 km-long N-S striking submarine ridge in the western part of the Bering Sea (Fig. 2). The ridge is morphologically connected to the Asian mainland at Cape Olyutorsky in the north (Fig. 1). No deformation structures indicative of a collisional contact between the Shirshov Ridge and the exposed rocks on Cape Olyutorsky are observed (Scholl, 2007; and references therein). The Shirshov Ridge is connected with the Bowers Ridge by a roughly E-W-trending fracture zone (Hoernle et al., 2016). According to Baranov et al. (1991), two different rock complexes form the main structure of the Shirshov Ridge: an oceanic complex consisting of amphibolites and gabbros, as well as deep-sea cherts and massive basaltic lavas. Microfauna obtained

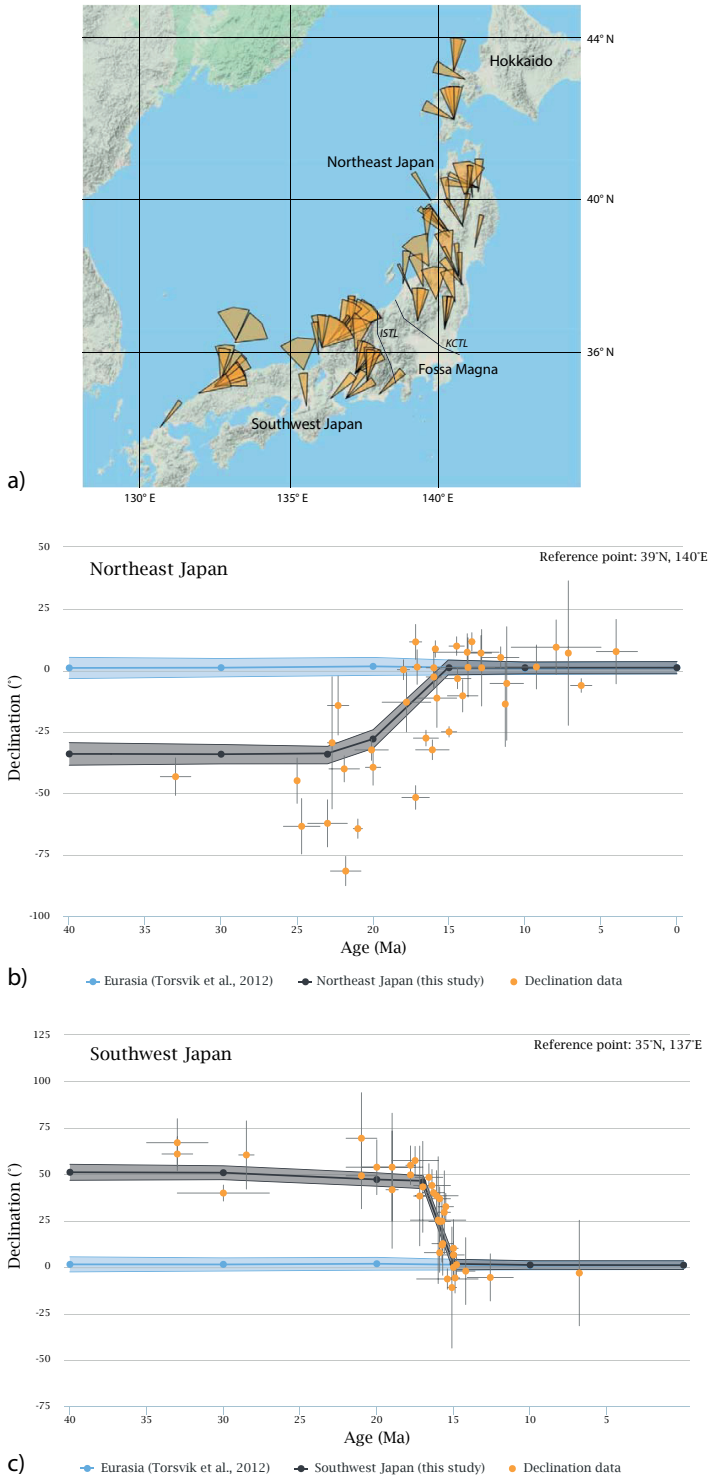


Fig. 6. (a) Map showing the locations and declinations (and their uncertainties) of the paleomagnetic sites compiled for the Japanese islands. Black lines indicate the tectonic boundaries of southwest and northeast Japan: the Itoigawa-Shizuoka Tectonic Line (ISTL) and Kashiwazaki-Choshi Tectonic Line (KCTL). Data files and references are provided in the supporting information (Data Set S2). (b) Paleomagnetic declination curves predicted for a reference point on northeast Honshu (39°N, 140°E) using the Global Apparent Polar Wander Path of Torsvik et al. (2012), in the case that the reference point was rigidly attached to Eurasia (blue), and as reconstructed in this study (black). See section 2 for more details. The colored envelopes indicate the uncertainty range. Yellow dots (with errors) represent the compiled paleomagnetic declinations for northeast Japan (northeast Honshu and west Hokkaido). (c) Same as (b), but now for a reference point (35°N, 137°E) on southwest Honshu. The black curve shows the predicted declination through time for southwest Japan as reconstructed in this study. Yellow dots show the declinations for southwest Japan (southwest Honshu, Kyushu and the Oki islands).

from the cherts constrain its age at Late Cretaceous (Campanian-Maastrichtian) to Early Paleogene (Baranov et al., 1991; and references therein), that is, contemporaneous with the Olyutorsky arc. Recent $^{40}\text{Ar}/^{39}\text{Ar}$ dating of dredged island-arc rocks from the central Shirshov Ridge gave ages of 65–69 Ma (Hauff et al., 2016). Island-arc rocks from the southern end of the ridge consisting of andesites and volcanoclastics provided a much younger age of 27.8 ± 1.1 Ma (Cooper et al., 1987). This young material may represent a fragment of the Aleutian Arc (Scholl, 2007), or the Bowers Ridge that rifted away in the Neogene, based on the occurrence of the rocks in a NW-SE-oriented sector of the ridge, which is parallel to the fracture zones in the Komandorsky Basin to the west of the Shirshov Ridge, and strike-slip faults in the western part of the Aleutian Arc. Amphiboles within the amphibolites from the oceanic complex were K-Ar dated as 47 ± 5 Ma and zircons gave a 72 ± 1.4 Ma age (Sukhov et al., 2011). The amphibolites, metagabbro, and Upper Cretaceous to Paleocene volcanic and sedimentary rocks all underwent intense deformation (Chekhovich et al., 2012).

The Komandorsky Basin, located west of the Shirshov Ridge has an estimated age of 10 and 20 Ma, based on interpreted marine magnetic anomalies (see section 3; Valyashko et al., 1993; Fig. 2). The only dated sample from the basin floor is a basaltic rock that was dated at 9.3 ± 0.8 Ma (Rubenstone, 1984). The Komandorsky Basin is bounded in the west by a sediment-filled trench along the eastern margin of North Kamchatka (Avdeiko et al., 2007; Baranov et al., 1991; Fig. 3), west of which is a Miocene-Pliocene calc-alkaline volcanic arc in the Kamchatka isthmus (Hochstaedter et al., 1994; Shapiro & Solov'ev, 2011).

5. Paleomagnetic constraints

5.1. Compilation of paleomagnetic data

We compiled published paleomagnetic data from the NW Pacific region based on 112 paleomagnetic sites from >50 studies. The database was built using the online paleomagnetic analysis tool www.paleomagnetism.org (Koymans et al., 2016). We included data derived from Upper Cretaceous and younger island-arc rocks of the Aleutians, Kamchatka, Sakhalin, and Hokkaido (see Table S1). For the Japanese Islands, only data from Oligocene and younger rocks were compiled to test opening scenarios for the Japan Basin. We used selection criteria formulated by Lippert et al. (2014) and Li et al. (2017) excluding sites that (1) were not used by the authors of the original publication

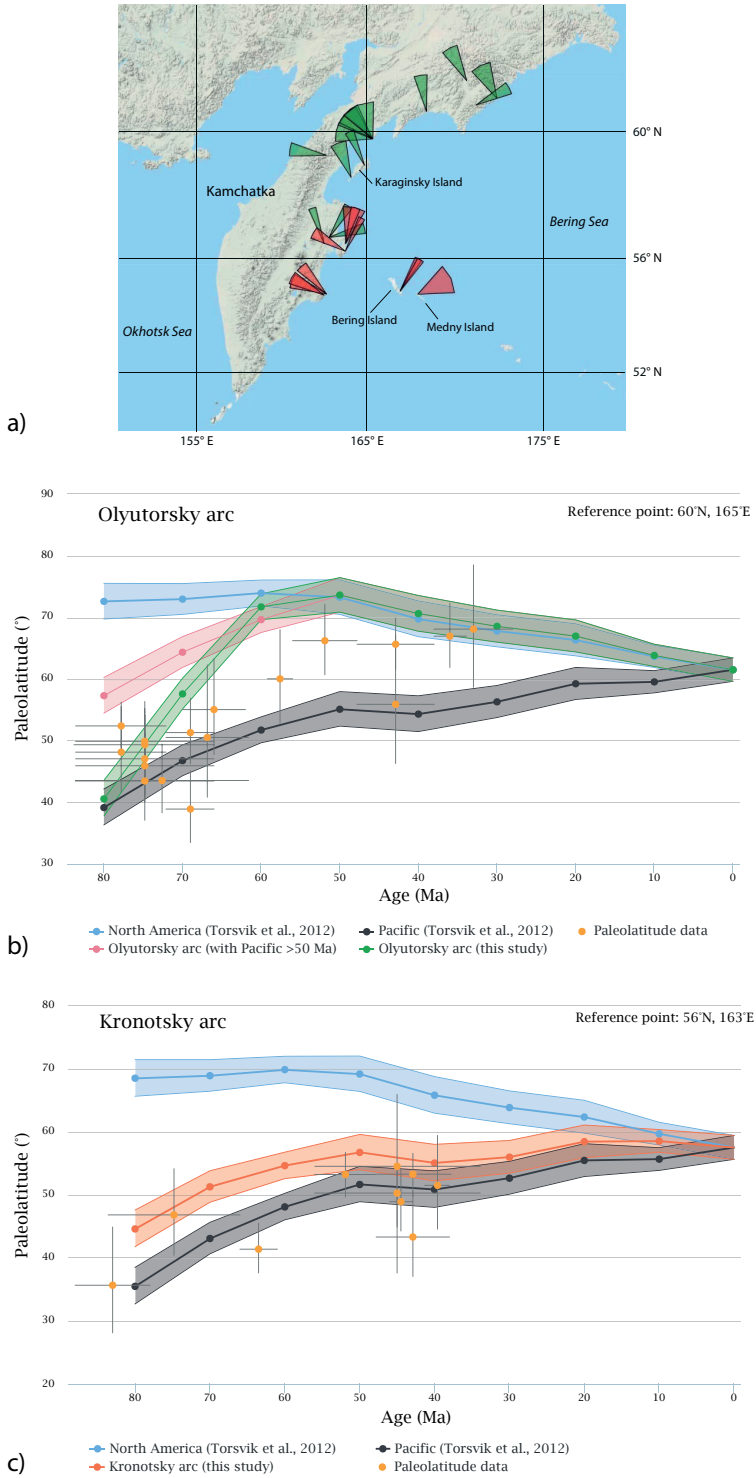
if reason for exclusion was provided; (2) were not analyzed using principle component analysis (Kirschvink, 1980); (3) were (most likely) remagnetized according to the original authors; (4) include less than four samples for sedimentary or igneous sites, or less than four lava sites for volcanic localities; (5) have k -values (precision parameter of Fisher, 1953) below 50 for volcanic sites, or an $A95$ value exceeding $A95_{max}$, or below $A95_{min}$ sensu (Deenen et al., 2011) for igneous or sedimentary sites. We excluded paleomagnetic localities that were based on an average of multiple sedimentary site averages if statistical details on a per-site level were not reported.

The paleomagnetic analyses on paleomagnetism.org uses individual paleomagnetic directions as basis, facilitating compiling site averages weighed by the number of observations within such sites. For sediment-derived sites, the paleomagnetic direction of each sample can be approximated as a spot reading of the paleomagnetic field (Deenen et al., 2011). We therefore included paleomagnetic directions that together defined sedimentary sites where reported by the original authors. Unfortunately, original individual sample directions are rarely published in the paleomagnetic literature, and only statistical descriptions of the data sets are provided on a per site level. In such cases, we parametrically sampled sites (see Koymans et al., 2016). For lava sites, site averages do represent spot readings of the paleomagnetic field (provided $k < 50$ as reliability cut-off, following, e.g., Johnson et al., 2008, and Biggin et al., 2008) and these are normally published on a per-lava site level. In such cases, we compiled sites by including multiple nearby lava site directions in a locality (provided $n > 3$) without parametric sampling. The resulting paleomagnetic database (see supporting information) is used to test our reconstruction based on the kinematic constraints outlined in the previous section.

5.2. Paleomagnetic constraints on the opening of the Japan Sea

Paleomagnetic data from Japan show opposite rotations of southwest and northeast Japan during the Neogene (e.g., Kawai et al., 1961; Martin, 2011; Otofujii, 1996; Otofujii et al., 1985; Fig. 4). Across southwest Honshu, that is, west of the Itoigawa-Shizuoka Tectonic Line, and northern Kyushu, paleomagnetic declinations consistently show a $\sim 50^\circ$ clockwise rotation between ~ 18 and 15 Ma (Fig. 6c). Paleomagnetic data from northeast Honshu indicate ~ 30 – 40° counterclockwise rotations of northeast Japan between ~ 20 and 15 Ma (Fig. 6b). A similar counterclockwise rotation history was recorded from West Hokkaido (Fujiwara & Sugiyama, 1986; Otofujii et al., 1994; Tanaka et al., 1991).

Fig. 7. (a) Map showing the locations and declinations (and their uncertainties) of the paleomagnetic sites compiled for the Olyutorsky (green) and Kronotsky (red) island-arc terranes. Data files and references are provided in the supporting information (Data Set S2). (b) Paleolatitude paths predicted for a reference point (60°N , 165°E) on the Olyutorsky arc terrane using the Global Apparent Polar Wander Path of Torsvik et al. (2012), in the case that the reference point was rigidly attached to North America (blue), to the Pacific plate (black), to the Pacific plate prior to 50 Ma and North America < 50 Ma (pink), and as reconstructed in this study (green). Yellow dots (with errors) represent the (uncorrected) paleomagnetic data for the Olyutorsky arc terrane. (c) Paleolatitude paths predicted for a reference point (56°N , 163°E) on the Kronotsky arc terrane using the Global Apparent Polar Wander Path of Torsvik et al. (2012), in the case that the reference point was rigidly attached to North America (blue), to the Pacific plate (black), and as reconstructed in this study (orange). Yellow dots (with errors) represent the (uncorrected) paleomagnetic data for the Kronotsky arc terrane.



Declinations of Upper Oligocene to Lower Miocene sediments of Central Hokkaido indicate a $\sim 30\text{--}35^\circ$ clockwise rotation since the Early Miocene and 20° since Middle Miocene, ascribed to right-lateral displacements along the Sakhalin-Hokkaido Shear Zone (Kodama et al., 1993; Tamaki et al., 2010). Clockwise rotations similar to Central Hokkaido were found on Sakhalin, thought to be associated with deformation along the Sakhalin-Hokkaido Shear Zone (Takeuchi et al., 1999; Weaver et al., 2003). Following these authors, we do not consider these declinations as representative for regional block rotations, but interpret them as local, strike-slip-related rotations. These data do suggest, however, that East and West Hokkaido were not juxtaposed until after the Middle Miocene opening of the Japan Sea.

5.3. Paleomagnetic constraints From accreted intraoceanic island arcs

The paleolatitudes obtained from paleomagnetic inclination data provide an independent means of constraining the plate motion history of the intraoceanic island arc terranes in the NW Pacific region since the Late Cretaceous. We compiled 32 paleomagnetic sites from 19 studies of island arc rocks from the East Sakhalin-Nemuro, Olyutorsky, and Kronotsky arcs (Fig. 7). Most paleomagnetic sites consist of tuffs and volcanogenic sediments and were dated by radiolarians. Paleolatitudes for the Olyutorsky-East Sakhalin-Nemuro arc show a $25\text{--}30^\circ$ northward paleolatitude shift between ~ 80 and ~ 50 Ma, after which time the inclination data generally correspond with the expected inclination of the North American plate (Fig. 7b). When compared to the paleolatitude evolution of the reference location of $60^\circ\text{N}/165^\circ\text{E}$ tied to the Pacific plate, the data indicate that the Olyutorsky-East Sakhalin-Nemuro arc migrated faster northward between ~ 80 and 50 Ma than the Pacific plate, after which there was paleolatitudinal convergence between the two until today. In addition, the plot suggests that the Olyutorski-East Sakhalin-Nemuro arc was initially not far, that is, within $\sim 5^\circ$, of the lithosphere that currently subducts below Kamchatka, which is estimated to be ~ 100 Ma (Müller et al., 2016; Wright et al., 2016). The majority of paleomagnetic declinations indicate that the Olyutorsky arc underwent a counterclockwise rotation of about $40\text{--}50^\circ$ since the Late Cretaceous (Fig. 7a). Data from upper Paleogene rocks also indicate counterclockwise rotations, possibly related to extension in the Okhotsk Sea west of Kamchatka. Taking into account the present-day NNE-SSW orientation of the Olyutorsky arc terrane, the paleomagnetic declination data suggests that the Olyutorsky arc-trench system was probably oriented ENE-WSW during the Late Cretaceous-early Paleogene.

Data published for the East Sakhalin-Nemuro arc that is thought to be equivalent to the Olyutorsky arc (Domeier et al., 2017; Grannik, 2012; Konstantinovskaya, 2001; Nokleberg et al., 2000) come from the Nemuro and Tokoro belts of Hokkaido and the Ozersk terrane of southeasternmost Sakhalin (see Fig. S2). These show much shallower inclinations, indicating much lower paleolatitudes than expected if these terranes were part of the Eurasian continent, suggesting an allochthonous, intra-Panthalassa origin. The declinations from the Nemuro belt show that it experienced a $\sim 15\text{--}25^\circ$ counterclockwise rotation since the Late Cretaceous (Bazhenov & Burtman, 1994; Fujiwara & Ohtake, 1974; Fig. S2). The site from the NNE-SSW-trending Tokoro belt shows a $\sim 130^\circ$ clockwise rotation (Kanamatsu et al., 1992). The above data suggests that paleo-strike of the East Sakhalin-Nemuro arc was approximately ENE-WSW-trending, similar to the Olyutorsky paleo-arc.

The data set of the Kronotsky arc of Kamchatka was mainly derived from Eocene tuffs and (volcanogenic) siltstones and sandstones. Inclinations from sediments are somewhat lower than expected for the Pacific APWP, whereas inclinations from lava localities of the Kronotsky peninsula provided a similar paleolatitude to the Pacific reference, suggesting that the Kronotsky arc moved together with the Pacific plate since the Eocene (Fig. 7c).

6. Seismic tomographic constraints

The geological record predicts that several intraoceanic and continental margin subduction zones have been active in the North Pacific region since the Late Cretaceous, remnants of which are found in the upper and lower mantle below the North Pacific region. A comprehensive overview of slab-like anomalies in the mantle was recently provided on www.atlas-of-the-underworld.org (van der Meer et al., 2018), and two of these anomalies were recently used by Domeier et al. (2017) as a constraint on their kinematic model for NW Pacific evolution.

Below, we summarize the mantle anomalies from the global compilation of slabs of van der Meer et al. (2018) that are relevant for our reconstruction (Fig. 8), as well as the correlations between anomalies and geological records of the NW Pacific region as proposed by van der Meer et al. (2018). We test our reconstruction against the presence of slabs in the mantle at locations predicted, although we may in places provide different interpretations than van der Meer et al. (2018), in the light of our new reconstruction. We assume that, after breakoff from surface plates, slabs sink vertically (Domeier et al., 2016; van der Meer et al., 2010), but that during their subduction they may roll back, or be dragged forward or sideways through the mantle (e.g., Chertova et al., 2014; Funicello et al., 2008; Schellart et al., 2008; Spakman et al., 2018; van de Lagemaat et al., 2018). We therefore test whether slabs are present in the mantle at locations where our model predicts their break-off, at depths consistent with globally determined sinking rates of $\sim 1\text{--}2$ cm/year (Butterworth et al., 2014; van der Meer et al., 2010, 2018). When comparing our model to mantle structure, we place our reconstruction in the global moving hotspot reference frame of Doubrovine et al. (2012).

Active subduction zones in the northern Pacific region are associated with well-imaged slabs in the upper mantle, and in places also the top of the lower mantle. The Aleutian subduction zone is associated with the north-dipping Aleutian slab that is located in the upper mantle and transition zone (Gorbatov et al., 2000; Koulakov et al., 2011; Martin-Short et al., 2016; Qi et al., 2007; van der Meer et al., 2018; Figs. 8a and 8b). At the Kuril-Kamchatka subduction zone, a northwest-dipping slab appears to penetrate into the lower mantle, where it connects to a subhorizontal slab segment at 800–1,000 km depth (Gorbatov et al., 2000; Jiang et al., 2009; Koulakov et al., 2011; Spakman et al., 1989; van der Hilst et al., 1991; van der Meer et al., 2018; Figs. 8a and 8b). Van der Meer et al. (2018) interpreted this whole body as a single slab that subducted along the Kuril-Kamchatka Trench after polarity reversal upon Olyutorsky-Kamchatka collision, following (Shapiro & Solov'ev, 2009). Below Japan, the peculiar west-dipping Manchuria slab is over 2,500 km long, flat-lying and almost entirely contained in the upper mantle, disconnected from deeper anomalies in the lower mantle (Figs. 8a and 8b). Van der Meer et al. (2018) followed the interpretation of Seton et al. (2015) that this slab represents Pacific plate lithosphere that subducted after the $\sim 60\text{--}50$ Ma arrival of the Izanagi-Pacific ridge at the Japan Trench.

In addition to these actively subducting slabs, a series of detached anomalies were identified (e.g., Domeier et al., 2017; van der Meer et al., 2018). In the upper-lower mantle transition zone below the central Bering Sea lies the Bering slab (Fig. 8b), which was correlated by van der Meer et al. (2018) to Oligocene subduction at the Bowers Ridge. Also in the transition zone, but below Kamchatka, lies the Mayn slab (Fig. 8b). Van der Meer et al. (2018) followed the interpretation of Chekhovich et al. (2012) that there was ~30–15 Ma subduction below the Shirshov Ridge, and proposed that this would have produced the Mayn slab. To the west, between ~1,600 and 800 km depth in the lower mantle below the northern Sea of Okhotsk lies the Ushky slab (Fig. 8c). This slab was correlated by van der Meer et al. (2018) to Cretaceous subduction along the NE Asian margin producing the Okhotsk-Chukotka arc that ended around 80 Ma upon collision with the Okhotsk block (Akinin & Miller, 2011; Hourigan & Akinin, 2004; Pease et al., 2018; Tikhomirov et al., 2012; Yang, 2013). The Sakhalin slab toward the southwest, between ~1,000 and 700 km depth was interpreted by van der Meer et al. (2018) to be closely related to the Ushky slab, reflecting Cretaceous subduction prior to Okhotsk Block accretion below the Sakhalin margin producing the East Sikhote-Alin arc. South of the Komandorsky Islands, between 1,400 and 600 km depth lies the Agattu slab (Fig. 8c). This slab is clearly south to southerly dipping, and even flat-lying around 1,200–1,400 km depth and was correlated by van der Meer et al. (2018) as well as Domeier et al. (2017) to the Olyutorsky arc. Toward the east, from southern Alaska toward the southwest, at a depth of 1,400–800 km, lies the North Pacific anomaly, which was correlated by (Domeier et al., 2017) and van der Meer et al. (2018) to intraoceanic subduction below the Kronotsky arc (Fig. 8c). Finally, to the north of the North Pacific slab, between 1,100 and 800 km depth below Alaska lies the Yukon slab (Fig. 8c), correlated by van der Meer et al. (2018) to the Late Cretaceous Kluane arc that is contained in the complex Alaskan orogen.

7. Reconstruction of NW Pacific active margins

We used the global plate circuit and the geological, kinematic, and paleomagnetic data reviewed above for a plate kinematic restoration of the NW Pacific region as illustrated in Figs. 9 and 10. We present this history from today's configuration back in time to the Late Cretaceous (to 85 Ma) and explain below which interpretations are used in this reconstruction. 7.1 25 to 0 Ma: Opening of Japan Sea, Kuril, and Komandorsky Basins.

The Neogene history of the NW Pacific region includes the opening of the Japan Sea, Kuril, and Komandorsky back-arc basins, the main phase of dextral strike-slip motion along the Sakhalin-Hokkaido Shear Zone and the accretion of the extinct Kronotsky island-arc. To reconstruct these, we have divided the Japanese islands and Sakhalin into rigid blocks (see Fig. 2) based on their Eocene-present (~40–0 Ma) tectonic history. A detailed reconstruction of the Late Cretaceous to Early Paleogene history of the (mostly Mesozoic) subduction-related terranes of the Asian margin, preserved on the Japanese Islands and Sakhalin (see Fig. 4), is beyond the scope of this paper. In our reconstruction, we infer that also the undated Bowers Basin, between the Bowers Ridge and the Aleutian Trench, is of Miocene age, but because this follows from the Paleogene reconstruction of the Bowers Ridge subduction, we will explain this line of reasoning in section 7.2.2.

7.1.1. Opening of the Japan Sea Basin

The opening mechanism of the Japan Sea and its underlying basins is debated and two

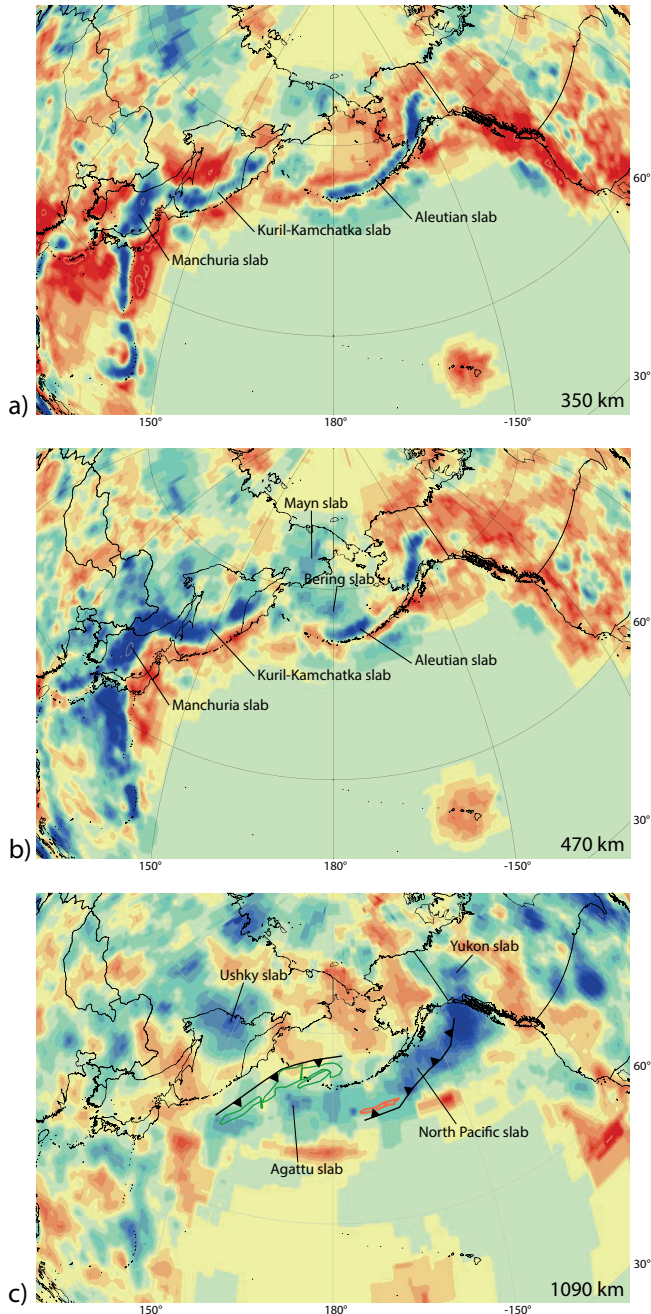


Fig. 8. Horizontal depth slices through the UU-P07 P-wave velocity model (Amaru, 2007) of the present-day mantle structure at depths of (a) 350, (b) 470, and (c) 1090 km. Reconstructed positions of the Olyutorsky arc (green) and Kronotsky arc (orange) and the associated intraoceanic subduction zones (black with closed triangles) relative to the mantle at 60 Ma (using the mantle reference frame of Doubrovine et al., 2012) are shown in (c).

opposing models have been proposed. One model explains the Japan Sea as a pull-apart basin that formed as a releasing bend between two major dextral strike-slip zones: the Tsushima-Goto and the east Japan Sea fault zones (e.g., Fournier et al., 1994; Jolivet et al., 1994; Jolivet & Tamaki, 1992). If true, this model would require restoring northeast Japan toward the Sea of Okhotsk region, which would then strongly influence the reconstruction of Sakhalin and the East Sakhalin-Nemuro arc. A second model invokes trench-perpendicular extension leading to opposing rotations of the NE and SW Japan blocks (e.g., Martin, 2011; Otofujii et al., 1985). If correct, this model suggests that the Japan Sea and arc have moved mainly relative to Eurasia and restoring these motions does not influence the Okhotsk Sea region much. The second model, with opening of the Japan Sea through opposite rotations of NE and SW Japan, is clearly favored by paleomagnetic constraints (Fig. 6), and is therefore included in our reconstruction.

We model NE and SW Japan as rigid blocks that rotated independently (following, e.g., Kim et al., 2007, 2015; Martin, 2011; Otofujii et al., 1985; Sato, 1994). We reconstruct the onset of rifting between SW Japan and the Korean peninsula at 23 to 18 Ma and follow Kim et al. (2011, 2015) in reconstructing 70 km SE-directed motion of SW Japan relative to the Korean peninsula during this stage, involving 60–70 km of extension at the southeastern margin of Korea to ~100 km between present-day North Korea and the Noto peninsula. For the northeast Japan Sea, we restore up to 100 km of 23–20 Ma extension between NE Honshu and stable Eurasia to represent the southeast-directed motion of NE Japan as a result of initial intra-arc rifting (Van Horne et al., 2017). We model this extension perpendicular to the Japan Trench, consistent with the opening direction of (half-) grabens in the northern Japan Sea (Sato, 1994; van der Werff, 2000).

The remaining extension is reconstructed during the main rifting phase between ~18 and 15 Ma for the southwest and ~20–15 Ma for the northeastern Japan Basin (Kaneoka, 1992; Kim et al., 2015; Martin, 2011; Nohda, 2009; Sato, 1994; Van Horne et al., 2017), complying with the rapid rotations that follow from paleomagnetic data (Fig. 6). We restore up to a maximum of 400 km of extension for both SW and NE Japan (Figs. 10e and 10f), consistent with extension predicted by the crustal thicknesses in the Japan Sea Basin, assuming an initial thickness of 35 km. This results in a total amount of extension close to the 400–500 km of extension in the Japan Sea Basin as estimated by Martin (2011) and Van Horne et al. (2017). The resulting two-step opening of the Japan Sea by the oppositely rotating SW and NE Japan blocks is consistent with paleomagnetic declination data for southwest and northeast Japan (Fig. 6). However, our reconstruction predicts a dextral displacement along the Tsushima-Goto fault zone west of southwestern Honshu of about 30 km between 23 and ~18 Ma, much lower than the maximum estimated 200 km by Jolivet and Tamaki (1992). Our new model shows that a reconstruction of the Japan Sea opening that is consistent with crustal thicknesses and paleomagnetic data does not require large-scale dextral along the strike-slip faults bounding the Japan Sea. In contrast, our model predicts a phase of sinistral transpression in southwesternmost Honshu and the Tsushima and Goto islands from ~17 to 15 Ma, consistent with observed Middle Miocene deformation along the Tsushima-Goto fault system (Fabbri et al., 1996; Son et al., 2015).

A two-step evolution of the Fossa Magna area between 23 and 15 Ma follows from the above reconstruction of NE and SW Japan. We infer a large fault zone between the oppositely rotating rigid blocks that accommodated dextral strike-slip motion during the first part of the opening of the Sea of Japan, similar to the model of Sato (1994). We

model up to ~150 km of right-lateral displacement between 23 and 15 Ma, with most of the motion between 20 and 15 Ma, corresponding to the peak of spreading activity in the Japan and Yamato Basins. The inferred dextral fault zone is not clearly observed in the geological record, probably because it was overprinted by the formation of the Fossa Magna depression and associated basins. The opposite rotation of NE and SW Japan based on extensional records of the Sea of Japan predicts trench-parallel extension in the Fossa Magna region between 17 and 15 Ma. This involves about 30 km of extension in the northernmost part of Fossa Magna, corresponding well with estimated values of ~30–40 km from balanced cross-sections for the northern Fossa Magna Basin (Elouai et al., 2004; H. Sato et al., 2004). Our models predict up to ~200 km of extension in the southernmost part of Fossa Magna, which is equal to the estimate from Martin (2011).

Since ~15 Ma, the southwestern part of the Japanese islands are dominated by inversion tectonics, which may relate to the collision of the Philippine Sea plate due to a change in plate motion associated with a regional plate reorganization (e.g., Kimura et al., 2014; Sibuet et al., 2002; Son et al., 2015). Estimates of the shortening associated with the recent tectonics are in the order of tens of kilometers and are not taken into account in this reconstructed.

7.1.2. Opening of the Kuril Basin

Following from our reconstruction of NE Japan as outlined above, we restored ~170 km of dextral strike slip between the Central Hokkaido and West Sakhalin terranes and Eurasia during the opening of the Japan Sea between 23 and 15 Ma accommodated along offshore faults running through the Tartary Strait (Fournier et al., 1994; Figs. 10e and 10f). We reconstructed 50 km of dextral N-S motion between the island-arc units of eastern Sakhalin and Central Sakhalin, following the estimate of Fournier et al. (1994). We model a similar dextral offset of ~50 km along the Tym-Poronaysk fault between 23 and 9 Ma, synchronous with the opening of the Kuril Basin (Schellart et al., 2003; Takeuchi et al., 1999). In addition, we restore 50 km of extension in the Aniva Trough, which results in ~100 km of dextral motion along the Hidaka Shear Zone.

We then reconstructed the Kuril Basin extension by restoring the Kuril Trench up to ~400 km toward the northeast between 23 and 9 Ma (Figs. 10e–10g). This corresponds to the full width of the bathymetric depression of the Kuril Basin and is ~100 km more than the estimate of Schellart et al. (2003). The geometry of the back-arc basin (Figs. 1 and 2) suggests that this basin opening was associated with a counterclockwise rotation of the Kuril forearc relative to the Okhotsk block north of the Kuril Basin. The Nemuro and Lesser Kuril islands Cretaceous to Paleogene arc fragments as well as the Tokoro belt restore with the Kuril forearc bringing the Tokoro belt adjacent to southeast Sakhalin, consistent with geological observations (Kimura, 1994; Maeda, 1990; Ueda, 2016; Zharov, 2005). After opening of the Kuril Basin, between ~9 Ma and the present, we modeled the eastern parts of Sakhalin and Hokkaido as part of the North American plate. This predicts ~70 km of NE-SW convergence in central Sakhalin to 100 km in southern Hokkaido, consistent with geological shortening estimates (e.g., Iwasaki et al., 2004).

7.1.3. Kronotsky arc collision and opening of the Komandorsky Basin

Magnetic anomalies in the Komandorsky Basin suggest that between ~20 and ~10 Ma, up to ~450 km of NW-SE extension was accommodated by ocean spreading in the SW of

the basin. Toward the north, extension amounts abruptly decrease across two transform faults, and we modeled the 20–10 Ma evolution of the basin by three transform-ridge bounded microplates (SW, Central, and NW Komandorsky microplates) that moved northwest relative to the Shirshov Ridge, subducting below NE Kamchatka (Baranov et al., 1991; Nokleberg et al., 2000; Scholl, 2007; Valyashko et al., 1993; Figs. 9c and 9d). As argued by Scholl (2007), there is no evidence for relative motion between Kamchatka and the Shirshov Ridge during the Neogene. We therefore reconstruct the subduction below northern Kamchatka of oceanic crust that prior to the Neogene floored a proto-Komandorsky Basin. This episode of subduction is consistent with Miocene-Pliocene calc-alkaline volcanism in the Kamchatka isthmus (Hochstaedter et al., 1994; Shapiro & Solov'ev, 2011), as well as the sediment-filled trench on the eastern margin of northern Kamchatka (Avdeiko et al., 2007; Baranov et al., 1991). We modify the interpretation of van der Meer et al. (2018) and correlate the Mayn slab to subduction of the proto-Komandorsky Basin between 20 and 10 Ma, instead of Cenozoic subduction below the Shirshov Ridge, for which there is no compelling evidence (see also section 7.2).

Spreading is inferred to have been accommodated around a pole to the north of the Komandorsky Basin. Stretched arc and an arc-ocean crustal transition was interpreted from geophysical data, but no relics of arc crust that accreted during Miocene subduction are found along eastern Kamchatka. There is thus no positive evidence that prior to the early Miocene the Shirshov Ridge was wider than today, and we model the subducted, proto-Komandorsky Basin as oceanic, with crust whose age is not directly constrained by observations. Restoring the reported marine magnetic anomalies (Baranov et al., 1991) suggests, however, that relict crust of such a proto-Komandorsky Basin may still be present in the northwestern part of the basin (Fig. 9d).

Scholl (2007) suggested that the Komandorsky Basin opened as a forearc sliver, equivalent to, for example, the Andaman Sea. This interpretation is elegant in the light of the observation from the plate circuit that between 20 and 10 Ma, the Pacific-North America motion vector is parallel to the spreading direction of the Komandorsky Basin, and the amount of motion equals the amount of reconstructed spreading, in other words, the southwestern Komandorsky microplate appears to have coupled to the Pacific plate, generating Komandorsky Basin extension (Fig. 9c). We infer that a likely reason for this coupling was the highly oblique collision of the Kronotsky arc: when the collision age of Kronotsky with Kamchatka is modeled as 10 Ma (within the geologically constrained collision age range of 5–10 Ma), the Kronotsky arc couples with the Komandorsky crust around 20 Ma, moves in tandem with the SW Komandorsky microplate and generates proto-Komandorsky Basin subduction below NE Kamchatka (see Fig. 9). Upon Kronotsky-Kamchatka collision, Komandorsky spreading and subduction ceased. The direct interaction of the Kronotsky arc with the Komandorsky crust is consistent with the interpretation that the Komandorsky Islands consist of Kronotsky arc rather than Aleutian arc crust (Alexeiev et al., 2006; Bazhenov et al., 1992; Rostovtseva & Shapiro, 1998; Fig. 9). We model the Komandorsky Islands as a part of the Kronotsky arc that broke off and were left in their current position at ~13 Ma.

7.2. 40 to 25 Ma: Opening of Okhotsk Sea Basin; subduction at Bowers Ridge

The 40 to 25 Ma period covers the time interval following upon the final accretion of the Greater Olyutorsky arc and the final extinction of the Kronotsky arc. The period was

characterized by the opening of the Okhotsk Sea and the enigmatic subduction history forming the Bowers Ridge.

7.2.1. Opening of the Okhotsk Sea Basin

We restore the Late Eocene to Early Miocene opening of the Sea of Okhotsk back-arc basin as a counterclockwise rotation of the Kuril Trench and arc around a pole relative to NE Asia located in south Kamchatka. We model up to 800 km of N-S extension along the transform boundary with Sakhalin (Fig. 10), following Schellart et al. (2003). This requires that the Kuril Trench must have existed and rolled back since at least 40 Ma, and subduction thus starting prior to the oldest dated island-arc rocks from the Kuril volcanic arc that have an Early Oligocene age (De Grave et al., 2016). Our reconstructions suggest that up to 3,000 km of subduction occurred along the Kuril-Kamchatka Trench, consistent with the long slab in the upper and top of the lower mantle, whereby the flat portion of the Kuril-Kamchatka slab (Fig. 8) is similar in length to the amount of extension modeled in the Sea of Okhotsk and Kuril Basin.

Restoring the Okhotsk Sea back-arc basin shows that in Middle Eocene time, just after their obduction onto NE Asia, the East Sakhalin, Nemuro, and Olyutorsky arc segments were oriented at high angles to each other (Fig. 10d). The East Sakhalin arc was oriented ~N-S relative to a fixed Asia. The Nemuro-Kuril forearc segment restores to a NW-SE orientation connecting the northern part of Sakhalin with south Kamchatka, and defined the restored southern margin of the Okhotsk block. The Olyutorsky arc was oriented NE-SW, parallel to Kamchatka (Fig. 10d).

7.2.2. Subduction and spreading in the Bering Sea region

The isolated Bowers Ridge intraoceanic arc within the Aleutian back-arc is one of the most enigmatic features of the northern Pacific tectonic history, but may be understood in terms of arc-arc collision between the Kronotsky and Aleutian arcs. As shown above, modeling the Kronotsky arc as a contiguous part of the Pacific plate after its 40 Ma cessation generates a straightforward Miocene tectonic history of the Komandorsky Basin, and restores the Kronotsky arc southwest of the Bowers Ridge at about 25 Ma, in the center of the Bowers Basin (Fig. 9b). The northern part of the Kronotsky arc, however, overlaps with the modern Aleutian arc by ~150 km. This overlap is generated between ~34 and 26 Ma (Figs. 9a and 9b), that is, in the time period during which the Bowers intraoceanic arc was active (Sato et al., 2016; Wanke et al., 2012). This suggests that subduction below the western Aleutian Trench was temporarily interrupted around 34 Ma due to indentation of the extinct Kronotsky arc, and was instead accommodated by southwestward subduction north of the indenter at the Bowers Ridge. As shown by van der Meer et al. (2018), 34–26 Ma subduction below the Bowers Ridge is fully consistent with the location of the Bering Sea slab.

Our reconstruction of the Bowers Ridge contains similarities with the New Hebrides subduction zone in the SW Pacific. There, a subduction polarity reversal occurred behind the Melanesian arc due to collision of a buoyant indenter formed by the Ontong-Java Plateau (Hall, 2002; Knesel et al., 2008). Our reconstruction of the Bowers Ridge as a result of arc-arc collision predicts that the Bowers Basin, whose age is poorly constrained through direct geological or geophysical observation, was not formed by Eocene-Oligocene back-arc spreading behind the Bowers Ridge as previously suggested (Cooper

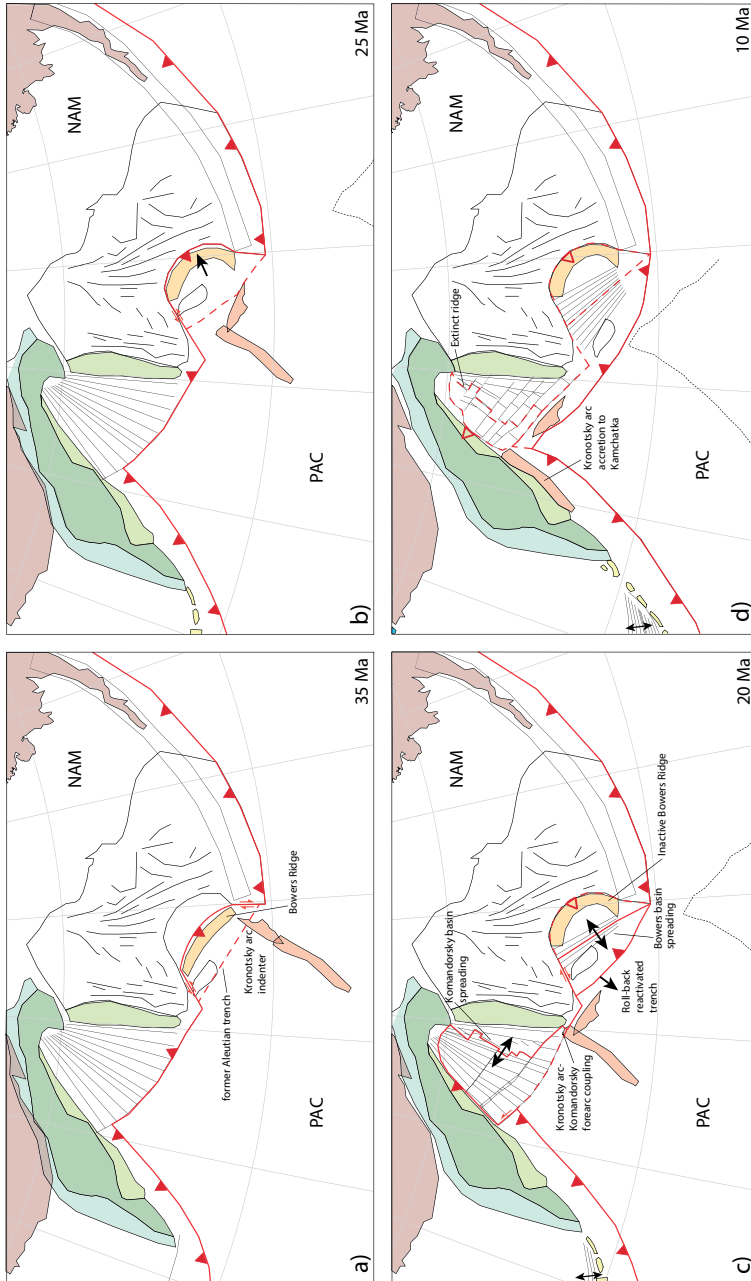


Fig. 9. Snapshots of the plate-kinematic reconstruction of the Bering Sea region at (a) 35, (b) 25, (c) 20, and (d) 10 Ma, relative to a fixed North American plate. The dashed black line represents the reconstructed location of the edge of Pacific plate lithosphere that is presently subducting below the Kuril-Kamchatka and Aleutian Trenches southeast of Kamchatka. Dashed red lines indicate extinct plate boundaries. Red filled/open triangles indicate active/extinct subduction zones. Abbreviations: NAM = North American plate; PAC = Pacific plate.

et al., 1992), but as a result of Miocene southwestward roll-back of the western Aleutian Trench to its modern orientation (Fig. 9c). Fig. 9d shows synthetic marine magnetic anomalies based on a southwestward direction of trench roll-back. The resulting NW-SE to NNW-SSE orientation of these anomalies is not fully consistent with the marine magnetic anomalies in the eastern part of the Bowers Basin as interpreted by Cooper et al. (1976, 1992), which have a N-S orientation instead. If these anomalies represent isochrons, then the roll-back of the Aleutian Trench and the associated back-arc extension may have been more westward, oblique to the modern Aleutian Trench, then modeled here.

Several authors suggested that subduction also occurred below the Shirshov Ridge during the Eocene-Oligocene (e.g., Scholl, 2007; van der Meer et al., 2018; Yogodzinski et al., 1993). There is, however, no convergence between Kamchatka and the Aleutian Basin between 40 and 25 Ma: the Olyutorsky arc did not move relative to Kamchatka after 45 Ma (Solov'ev et al., 2011; Solov'ev, Shapiro, & Garver, 2002) and relative motion between the Aleutian Basin and Alaska at the Beringian margin ceased around 50 Ma (e.g., Scholl, 2007; Worrall, 1991). There is no evidence for arc volcanism of the Shirshov ridge in this time period, and there is no record of Eocene-Oligocene E-W spreading orthogonal to the ridge to the east or west. We therefore model the Shirshov Ridge at its current relative position to Kamchatka between 40 and 25 Ma, contiguous with the lithosphere underlying the Aleutian Basin.

7.3. 60 to 40 Ma: Aligning the East Sakhalin-Nemuro, Olyutorsky, and Shirshov arcs; initiation of Aleutian subduction

Around 60–55 Ma, the distal passive margin of southern Kamchatka started to become involved in subduction below the Olyutorsky arc (Konstantinovskaya, 2001, 2011; Shapiro et al., 2008; Shapiro & Solov'ev, 2009), culminating in final, diachronous obduction at ~50 Ma in south Kamchatka, ~45 Ma in north Kamchatka, and ~45 Ma in East Sakhalin, the arrest of subduction at the Beringian margin around 50 Ma, and the presumed initiation of subduction at the Aleutian trench. In this section, we provide a restoration of the obduction and segmentation of the Olyutorsky-east Sakhalin-Nemuro arc and propose a new scheme to explain the separation of the Shirshov Ridge from the Olyutorsky arc, leading to the opening of a proto-Komandorsky basin and a subduction jump from the Beringian margin to the Aleutian trench. Only few constraints are available on the pre-40 Ma position of the Kronotsky arc, and we will describe its restoration between 40 Ma and the initiation of subduction around 85 Ma in section 7.4.2.

Because of the strong similarities in the composition and age range of arc volcanism, the Olyutorsky-east Sakhalin-Nemuro arc is widely assumed to have been a single, coherent arc (Domeier et al., 2017; Konstantinovskaya, 2001; Nokleberg et al., 2000; Shapiro & Solov'ev, 2009). To arrive at a contiguous belt, we reconstruct a breakup of the Olyutorsky arc into two segments that are separated by a transform fault (Figs. 10b and 10c), following Shapiro et al. (2008). We restore ~80 km of relative sinistral motion between a northern and southern segment between 50 and 45 Ma, that is, the period between the cessation of obduction of both segments. Between 50 and 45 Ma, we restore ~50 km of convergence between the northern segment of the arc and the West Kamchatka zone, accommodated by thrusting along the Vatyn-Lesnaya fault (Solov'ev et al., 2011; Solov'ev, Shapiro, & Garver, 2002).

The Shirshov Ridge appears to be a Cretaceous volcanic arc that is contiguous with the

lithosphere underlying the Aleutian basin (Scholl, 2007). Because of its location close to the Olyutorsky arc and the fact that it is physiogeographically connected to the Olyutorsky arc terrane at Cape Olyutorsky (Figs. 1 and 2), we suggest that the Shirshov Ridge was originally part of the Olyutorsky arc. The modern distance between the Olyutorsky arc and Shirshov Ridge is >500 km, which is unrealistically wide for a volcanic arc, suggesting that an extensional basin—the proto-Komandorsky basin—split the Shirshov Ridge off the Olyutorsky arc leading to the extinction of the Shirshov Ridge. Such a scenario of “arc splitting” may be analogous to the history of the modern Lau basin that split the Tonga arc in two, whereby the trenchward segment remained active (Malahoff et al., 1994). The youngest volcanic rocks dredged from the Shirshov Ridge suggest that this arc splitting occurred after ~65–60 Ma. The proto-Komandorsky basin is a triangular basin, suggesting that its opening was associated with a ~40° counterclockwise rotation of the Shirshov Ridge—and consequently also the Aleutian basin lithosphere—relative to the Olyutorsky arc (Figs. 10b and 10c) around a pole at the position of the Bering Strait. This requires convergence between the Aleutian basin and North America, which was accommodated by northeastward subduction at the Beringian margin until ~50 Ma (Davis et al., 1989; Miller et al., 2018; Scholl, 2007; Worrall, 1991). We therefore model the opening of the proto-Komandorsky basin largely between 60 and 50 Ma. This restoration aligns the marine magnetic anomalies recovered from the Aleutian basin lithosphere with the restored strike of the Olyutorsky arc at and before 60 Ma (Fig. 10b).

Aligning a single Greater Olyutorsky arc at 60 Ma also requires reconstructing a counterclockwise rotation of ~40° of the East Sakhalin-Nemuro arc and now-subducted oceanic crust to its east, between 60 and ~45 Ma, but here around a pole close to Hokkaido. This rotation was guided in the north by a transform fault with a ~800 km dextral displacement along the southwestern margin of the Okhotsk Block. We infer that the E-W-trending part of the Nemuro belt and its eastward continuation into the Lesser Kuril forearc and Vityaz Ridge are segments that were left behind in this transform fault.

It is interesting to note that the shape of the modern Aleutian trench approximates a small circle around the Euler pole that defines the relative Aleutian basin-Olyutorsky arc rotation during the opening of the proto-Komandorsky basin. This may suggest that the Aleutian trench formed initially as a transform fault during the ~60–50 Ma rotation. This transform fault, as well as the one that developed along the southern Okhotsk Block margin, had a strike approximately orthogonal to the trench along the Greater Olyutorsky arc, and may thus have reactivated transform faults or fracture zones in the Greater Olyutorsky back-arc region (Fig. 10b). Convergence between the Aleutian basin lithosphere and North America ceased around 50 Ma upon Olyutorsky arc-Kamchatka collision, which hampered ongoing Aleutian basin-Alaska convergence, and led to the arrest of subduction at the Beringian margin and inception of subduction along the Aleutian trench, inverting the preexisting transform fault.

The onset of rotation of the Aleutian basin and the East Sakhalin-Nemuro arc split the Olyutorsky arc and underlying lithosphere into two plates separated by a transform. We model the lithosphere south (west) of the Aleutian transform/trench (i.e., the remnant Olyutorsky plate, see section 7.4.1) as contiguous with the East Sakhalin arc, which would suggest that subduction polarity reversal behind the southern Olyutorsky arc occurred immediately upon obduction of the arc onto Kamchatka, ~55–50 Ma. This slab was connected to the East Sakhalin-Nemuro arc lithosphere as it rotated and moved toward

Sakhalin, dipping below the south Okhotsk block transform, such that upon arc-continent collision at Sakhalin, a Kuril slab was already present that started retreating southward shortly after at ~40 Ma (Fig. 10d), associated with the large-scale extension in the Okhotsk Sea (section 7.2.1).

The Olyutorsky arc restores above the location of the top of the Agattu slab around the 60–55 Ma inception of obduction and its likely moment of break-off (Fig. 8c). A separate slab segment was not identified by van der Meer et al. (2018) that may have broken off during obduction of the East Sakhalin segment, but we tentatively interpret this slab to form part of the Sakhalin slab, and perhaps the lower part of the horizontal segment of the Kuril-Kamchatka slab. Because the Alaskan orogenic belt underwent major Cretaceous to Eocene translations parallel to North America, and oroclinal buckling (e.g., Johnston, 2001), reconstructing the Beringian margin prior to arrest of subduction around 50 Ma is challenging and not contained in our current reconstruction. If the oroclinal buckling proposed by Johnston (2001) is correct, then the Beringian margin restores >500 km to the east in Late Cretaceous time, making the Yukon slab and the Kluane arc (Nokleberg et al., 2000) possible relics of Beringian subduction.

7.4. 85 to 60 Ma: Intraoceanic subduction initiation and evolution of the Greater Olyutorsky and Kronotsky arcs

The most challenging part of the reconstruction is the intraoceanic subduction history, between ~85–60 Ma for the Greater Olyutorsky arc and ~85–40 Ma for the Kronotsky arc. Absolute positions of the arc may be inferred from paleomagnetic data and seismic tomographic constraints on modern slab positions that may correspond to these arcs. Relative positions versus the Pacific plate may be inferred from the age of ophiolites and accreted oceanic rocks associated with the arcs in combination with restorations of the Izanagi plate reconstructed from its conjugate anomalies on the Pacific plate.

7.4.1. Greater Olyutorsky arc and back-arc

Our ~60 Ma reconstruction reveals a contiguous, 2,500 km-long Greater Olyutorsky arc above a southeasterly dipping intraoceanic subduction zone with the Aleutian Basin, including 13 marine magnetic anomalies interpreted as magnetic polarity reversals (Cooper et al., 1976), oriented roughly parallel to the restored arc and trench, in its overriding plate. The southeastward polarity of subduction below the Greater Olyutorsky arc requires that it converged with Eurasia, but there are different approaches to estimate how much.

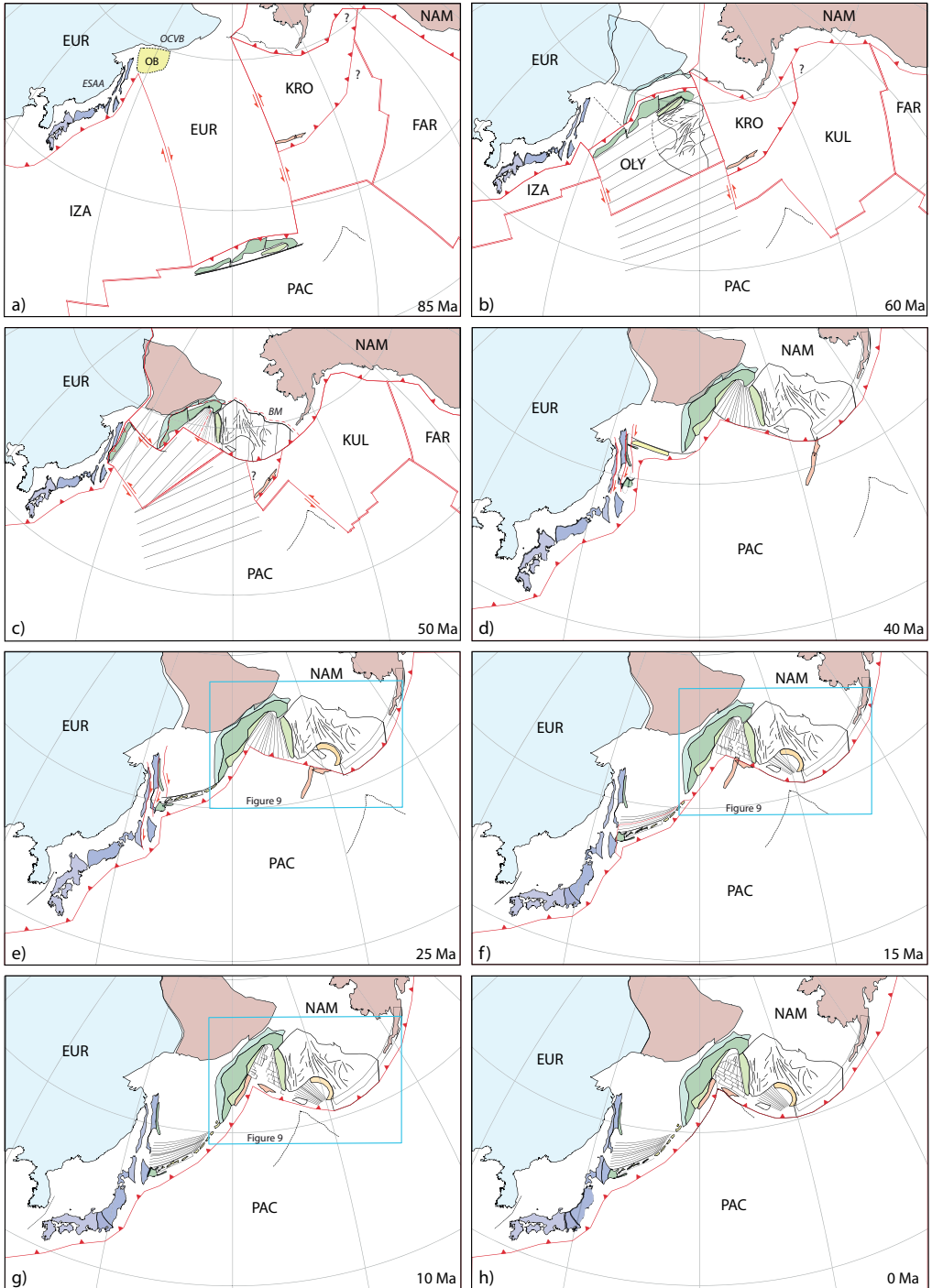
Because many of the paleomagnetic sites from the Olyutorsky arc are derived from sedimentary rocks and tuffs, Domeier et al. (2017) suspected that the inclinations provided by these sites may have shallowed due to compaction. They therefore corrected these data with a widely used average flattening factor of 0.6 (e.g., Torsvik et al., 2012), which would suggest that the paleolatitude of the Greater Olyutorsky arc throughout the Late Cretaceous was ~55°N. They use these corrected data as a basis to reconstruct the paleolocation of the Olyutorsky arc. When placed in a mantle reference frame (Dobrovine et al., 2012), this places the Greater Olyutorsky arc above the southern, deepest imaged portions of the Agattu slab, which they therefore inferred to be the absolute position of the arc at subduction initiation. If correct, the amount of 85–55 Ma convergence between the Pacific plate and NE Asia, and between the Greater Olyutorsky arc and Eurasia, are similar,

that is, the Olyutorsky arc would be part of the Pacific plate. Domeier et al. (2017) inferred that subduction initiation may have started at the Izanagi-Pacific ridge or along oceanic detachment faults adjacent to that ridge, a scenario shown by Maffione et al. (2015) and Maffione and van Hinsbergen (2018) for ophiolites in the Mediterranean region. Such a setting of subduction initiation at a ridge is consistent with the similar ages between the ophiolitic basement and the arc (see section 4.4).

We consider this reconstruction of Domeier et al. (2017) problematic for two reasons. First, the global plate circuit in the mantle reference frame of Doubrovine et al. (2012) shows that the inferred location of the youngest marine magnetic anomaly contained in the modern Pacific plate lithosphere (M0, ~120–126 Ma depending on the time scale used; Cande & Kent, 1995; Gradstein et al., 2012) is located >4,000 km to the south of the Olyutorsky Trench position at subduction initiation predicted by Domeier et al. (2017). This would therefore require full Izanagi-Pacific spreading rates of >20 cm/year for ~35–40 Myr between M0 and the time of subduction initiation, ~85 Ma, much faster than the highest spreading rates reconstructed from the modern ocean floor. Such rates are extremely high, much more than pre-120 Ma spreading rates of ~8 cm/year (Seton et al., 2012), and must have peaked at even higher rates since prior to ridge inversion and subduction initiation, spreading rates must first decrease toward zero. Second, marine geophysical studies of the upper plate behind the Olyutorsky arc, preserved below the Aleutian Basin, interpreted the north-south-trending marine magnetic anomalies in the Aleutian Basin as being formed by seafloor spreading (Cooper et al., 1976, 1992; Scheirer et al., 2016; Steinberger & Gaina, 2007), which if correct, falsifies the scenario of Domeier et al. (2017), in which the upper plate would have entirely formed during the Cretaceous Normal Superchron (Table 1).

We therefore take a different approach, which may be considered an opposite end-member of the Domeier et al. (2017) reconstruction. We follow the suggestion of Domeier et al. (2017) that subduction started at the Izanagi-Pacific ridge, but instead infer the position of that ridge by extrapolating the ~8 cm/year full spreading rates from the Early Cretaceous (Fig. 10a). The southwestward continuation of the trench along the Greater Olyutorsky arc is uncertain. Because subduction below the Japanese islands and Sakhalin continued throughout the Late Cretaceous, we model a right-lateral transform fault between northern Sakhalin and the southwestern termination of the Olyutorsky Trench. As there is no evidence for arc accretion south of Hokkaido during the Cenozoic, we infer that the Izanagi-Pacific ridge remained active between the Pacific plate and the Japan active margin (Figs. 10a and 10b). Further extrapolation of the Early Cretaceous

Fig. 10. Plate boundary configurations of the northwest Pacific region between 85 Ma and present, shown at (a) 85, (b) 60, (c) 50, (d) 40, (e) 25, (f) 15, (g) 10, and (h) 0 Ma, relative to a fixed Eurasian plate. Plate boundaries are shown in red, with filled triangles, arrows and double lines indicating subduction zones, transforms, and spreading ridges, respectively. Straight, black lines indicate oceanic crust formed at the Olyutorsky-Pacific spreading ridge and the approximate orientation of associated magnetic anomalies. The dashed black line represents the reconstructed location of the edge of Pacific plate lithosphere that is presently subducting below the Kuril-Kamchatka and Aleutian Trenches southeast of Kamchatka. Abbreviations: EUR = Eurasian plate; FAR = Farallon plate; BM = Beringian margin; ESAA = East Sikhote-Alin arc; IZA = Izanagi plate; KRO = Kronotsky plate; KUL = Kula plate; NAM = North American plate; OCVB = Okhotsk-Chukotka volcanic belt; PAC = Pacific plate.



a) Name	Predicted age	Age (west)	Age (east)	Age (IODP)	Paleolatitude	Model
Aleutian Basin	~85-60 Ma	~85 Ma	~60 Ma	~78 Ma	<60°, decreasing towards west	This study
	~100-85 Ma	~85 Ma	~100 Ma	~90 Ma	<60°, decreasing towards east	Domeier et al. (2017)
	< 50 Ma	< 50 Ma	< 50 Ma	< 50 Ma	~60-70°	<i>In-situ formation</i>
b) Name	Published ages	Age (this study)	Sources			
Aleutian arc	~46-0 Ma	50-0 Ma	Jicha et al. (2006), Layer et al. (2007)			
Bowers Basin	Eocene-Oligocene	~25-10 Ma	Cooper et al. (1992)			
Bowers Ridge	34-26 Ma	34-26 Ma	Wanke et al. (2012), Sato et al. (2016)			
Komandorsky Basin	~20-10 Ma	20-10 Ma	Valyashko et al. (1993)			
Komandorsky Islands	Paleocene-Eocene*	~85-40 Ma*	Bazhenov et al. (1992), Rostovtseva and Shapiro (1998)			
Shirshov Ridge	L. Cret.-E. Paleog.	~85-60 Ma	Baranov et al. (1991), Hauff et al. (2016)			

Table 1. Model predictions for the Bering Sea region. a) Predicted age and paleolatitude during formation for the Aleutian Basin basement based on three models. Note that our prediction is based on the assumption that the Aleutian Basin crust completely formed on the northern side of the spreading ridge. Predictions for the model of Domeier et al. (2017) are based on the assumption that the Aleutian Basin contains Pacific plate lithosphere formed by Izanagi-Pacific spreading prior to ridge inversion, after which it formed the overriding plate south of the Olyutorsky arc. West and east indicate the western and easternmost parts of the basin. Age (IODP) = predicted age at the proposed sites in the IODP Drilling Proposal 888-full. Estimated paleolatitude for in-situ formation is based on a Paleogene age of formation (between 50 and 23 Ma). b) Ages of the main tectonic features of the Bering Sea region, as published in literature and as adopted in or predicted by this study. Predicted ages are indicated in bold. *The age of the Komandorsky Islands refers to its basement, interpreted to be derived from the Kronotsky (fore)arc.

full spreading rates would lead to the widely inferred subduction of the Izanagi-Pacific ridge below Japan around ~ 60 – 50 Ma (e.g., Liu et al., 2017; Seton et al., 2012; Seton et al., 2015; Whittaker et al., 2007; Figs. 10b and 10c), consistent with geological and seismic tomographical observations such as the presence of MORB basalts intruding wet Paleocene-Lower Eocene foreland basin sediments (Ueda, 2016) and the length of the modern Manchuria slab below Japan (e.g., van der Meer et al., 2018).

Assuming 8 cm/year full Izanagi-Pacific spreading during the Cretaceous Normal Superchron brings the initial location of the Olyutorsky arc at ~ 85 Ma about 2,000–2,500 km farther south than proposed by Domeier et al. (2017). Such a position is consistent with the Late Cretaceous paleolatitudes suggested by paleomagnetic data (Fig. 7b). This reconstruction would require that the Greater Olyutorsky arc underwent faster absolute northward motion than the Pacific plate between ~ 85 and 60–50 Ma, creating $\sim 2,500$ – $3,000$ km of Pacific-Olyutorsky divergence that must have been accommodated by a spreading ridge between an Olyutorsky plate and the Pacific plate. Following the scenarios of Maffione et al. (2015) and van Hinsbergen et al. (2015), we model that the original Izanagi-Pacific ridge, preserved in the forearc above the nascent southward intraoceanic subduction zone, was reactivated and became the Pacific-Olyutorsky plate boundary. The geochemical signatures predicted by such a scenario are found in the suprasubduction zone signature of Upper Cretaceous ophiolites associated with the Olyutorsky arc (Geist et al., 1994; Kravchenko-Berezhnoy & Nazimova, 1991; Tsukanov et al., 2009) and the presence of Paleocene-Upper Eocene MORB-lavas of the Vetlovsky-Govena terrane in the accretionary prism below the Olyutorsky arc nappes in Kamchatka (Bakhteev et al., 1994; Gladenkov, 2016; Zinkevich & Tsukanov, 1993) is straightforwardly explained by a spreading center between the Olyutorsky arc and the Pacific plate. In this scenario, the Olyutorsky-Pacific ridge likely became active shortly after subduction initiation at ~ 85 Ma, and we therefore estimate that seafloor spreading south (east) of the Olyutorsky arc occurred between ~ 85 and 60–50 Ma. The magnetic anomalies predicted by this reconstruction are more or less parallel to the magnetic anomalies of the Aleutian Basin in our restoration at 60 Ma (Fig. 10b). At 60 Ma, the modern easternmost part of the Aleutian Basin lithosphere restores adjacent to the reconstructed Olyutorsky-Pacific ridge, which would be a logical structure bounding the rotating microplate that contained the Aleutian Basin lithosphere during opening of the proto-Komandorsky Basin. Our reconstruction therefore predicts that the Aleutian Basin lithosphere was formed between 85 and 60 Ma by back-arc spreading at the Olyutorsky-Pacific ridge (Table 1). Between 83 and 60 Ma, there are about 15 magnetic polarity reversals, which allows a scenario in which the anomalies interpreted from the Aleutian Basin crust were formed at the northern flank of the spreading ridge. Spreading at the Olyutorsky-Pacific ridge may have continued until the collision of the East Sakhalin-Nemuro arc with Sakhalin, or even longer until it subducted below the fast-retreating Kuril trench.

As far as we can see, this reconstruction explains all key observations and provides a straightforward plate kinematic scenario. It would require, however, that the Agattu slab underwent $\sim 2,000$ km of roll-back from its location of subduction initiation to its modern mantle position. Roll-back of such magnitude may well be possible, but dragging a slab over such a distance through the mantle may be unrealistic—although we note that $>1,200$ km of slab dragging was recently shown for the Tonga slab (van de Lagemaat et al., 2018). Also, the implied rate of roll-back in our model of ~ 10 cm/year is very high. In addition,

while our reconstruction is consistent with reported paleomagnetic paleolatitudes, the (unknown) effects of inclination shallowing are not corrected for in the Olyutorsky arc data and more northerly paleolatitudes are thus permitted. We therefore consider our model an end-member, and we consider a more northerly position of subduction initiation possible. We note, however, that a more northerly position of Olyutorsky subduction initiation requires that the fossil Olyutorsky-Pacific ridge is contained in the Aleutian Basin, which may be tested in future geophysical expeditions. Alternatively, if subduction initiated significantly north of the Izanagi-Pacific ridge, the Izanagi-Pacific ridge may have continued activity for several 10 Myr and may have been responsible for the faster northward motion of the Olyutorsky arc relative to the Pacific plate. However, this scenario is problematic as the preserved magnetic anomalies indicate that the Aleutian Basin crust was formed after the Cretaceous Normal Superchron. Since there is no compelling evidence for major convergence between the Shirshov Ridge and the Aleutian Basin crust, this requires that seafloor spreading occurred at a short distance behind the Shirshov Ridge, that is, the Greater Olyutorsky arc. In any case, if the magnetic anomalies in the Aleutian Basin represent magnetic polarity reversals, this would be consistent with our reconstruction in which the Aleutian Basin was formed by post-83 Ma spreading between the Olyutorsky arc and the Pacific plate (Table 1). We note that we have not been able to develop a kinematically feasible scenario that would allow the anomalies in the Aleutian Basin to be the Upper Jurassic-Lower Cretaceous M-series as tentatively suggested by Cooper et al. (1976). The above shows that any pre-50 Ma reconstruction of the Bering Sea region, including the one presented here, is strongly dependent on the age of the Aleutian Basin crust. We therefore argue that future studies on the age of the basin crust, through marine geophysics or drillings as recently proposed in Drilling Proposal 888 submitted to the International Ocean Discovery Program, are required to test the validity of our reconstruction, or that of Domeier et al. (2017), of the northwest Pacific region between 85 and 50 Ma.

7.4.2. Evolution of the Kronotsky arc

Between ~85 and 40 Ma, the Kronotsky arc was active at a location within the northern Panthalassa Ocean. Our approach of assuming that the arc moved as part of the Pacific plate after its ~40 Ma arrest places it to the east of the Olyutorsky arc (Fig. 10d). This suggests that the two formed adjacent to each other as previously also inferred by Shapiro and Solov'ev (2009), Domeier et al. (2017), and van der Meer et al. (2018), rather than in-sequence as portrayed by Konstantinovskaya (2001).

Like for the Greater Olyutorsky arc, data sets available for determining the absolute location of the Kronotsky arc are paleomagnetism, seismic tomography, and the age of Kronotsky basement and accretionary prism rocks. In particular, the Kamchatka Mys ophiolite and prism of the Kronotsky arc assemblage shows that the arc was either built on ~113–93 Ma ocean crust that spread at a ridge that interacted with the Hawaii-Emperor plume, or that a hotspot seamount of that age accreted below the arc (see section 4.4). In addition, during subduction below the Kronotsky arc, a second subduction zone was active to its north, first at the Beringian margin and after the presumed ~50 Ma switch at the Aleutian Trench. Our new reconstruction of the Kronotsky arc and the Olyutorsky arc and back-arc indeed generates simultaneous convergence across these trenches as well as at the Kronotsky Trench.

Pre-40 Ma paleomagnetic data are sparse, and most predict paleolatitudes for the Kronotsky arc that are lower than for the Pacific reference curve (Fig. 7c). This would require that the Kronotsky arc was located within the current Pacific plate, which is impossible, and it is thus likely that the paleomagnetic data—derived from sedimentary rocks—experienced inclination shallowing. Domeier et al. (2017) therefore suggested that the Kronotsky arc was in a mantle-stationary position above the North Pacific slab, at a location immediately east of a transform fault bounding the Greater Olyutorsky arc. When we place the Kronotsky arc at its inferred 85 Ma inception above the North Pacific slab in the position suggested by Domeier et al. (2017; see Fig. 10a) and construct the marine magnetic anomalies of the Izanagi plate using their conjugate set preserved on the Pacific plate, it follows that the arc was built on ~110-Ma-old Izanagi crust, which is what we adopt in our reconstruction. This is consistent with the age of the Kamchatka Mys ophiolite, but suggests that subduction initiation either did not occur at the Izanagi-Pacific ridge as previously inferred by Domeier et al. (2017), or, if it did, that subduction initiation below the Kronotsky arc occurred much earlier than the inferred ~85 Ma, around 110 Ma.

Domeier et al. (2017) suggested that the Kronotsky Trench accommodated subduction of the Kula plate that broke off Pacific, Izanagi, and Farallon lithosphere around 83 Ma. Anomalies conjugate to the Kula plate are preserved on the Pacific plate to the east of the inferred position of the Kronotsky arc. Domeier et al. (2017) therefore inferred that the Kula-Pacific ridge was located >2,000 km north of the northernmost preserved Pacific lithosphere at 83 Ma, ~1,000 km south of the restored Kronotsky arc position at 40 Ma, and ended at a transform fault with the Olyutorsky plate. The amount of Kula-Pacific spreading between 83 and 40 Ma restored from preserved anomalies on the Pacific plate (Wright et al., 2016) is ~2,000 km. From this it follows that if Domeier et al. (2017) are correct, the Pacific-Kula ridge would have arrived in the Kronotsky subduction zone around 40 Ma, thereby providing an elegant explanation for the arrest of Kronotsky arc volcanism. We include this in our reconstruction (Figs. 10c and 10d).

North American absolute plate motion north of the Kronotsky arc was ~500 km southward between 85 and 60 Ma (Dobrovine et al., 2012). This would generate sufficient convergence between a presumed mantle-fixed Kronotsky arc and North America to drive convergence across the Beringian margin. Between 60 and 40 Ma, northern North America did not move significantly relative to the mantle. In addition, the distance between its inferred position above the North Pacific slab and its 40 Ma position as part of the Pacific plate after its extinction requires that the Kronotsky arc moved ~850 km to the northwest, while rotating ~30° counterclockwise. A similar rotation was constructed for the Kula plate (Wright et al., 2016), although its absolute northwestward motion was higher (~2,000 km). We therefore model trench advance for the Kronotsky arc between 60 and 40 Ma (Figs. 10b and 10c), driving subduction at the late Beringian, and early Aleutian Trenches, and rotate the arc counterclockwise, simultaneously with the Kula plate.

8. Discussion

In the time window of our reconstruction, two major plate reorganizations occurred within the Pacific realm. The ~85 Ma onset of intraoceanic subduction inferred from the geological records of the Olyutorsky and Kronotsky arcs is not an isolated event. Around the same time, the Kula plate broke off the Pacific, Farallon, and Izanagi plates (Woods & Davies, 1982; Wright et al., 2016). In the south, the Hikurangi plateau collided with the

Gondwana margin, merging the Pacific plate with Zealandia, which subsequently broke off Gondwana, effectively merging the Pacific plate for the first time with the global plate circuit (Matthews et al., 2015). A likely driver of subduction initiation at the Olyutorsky arc is the collision of the Okhotsk block with Eurasia (Konstantinovskaya, 2001; Shapiro & Solov'ev, 2009) that led to the ~80 Ma arrest of the Okhotsk-Chukotka arc (Akinin & Miller, 2011; Hourigan & Akinin, 2004; Pease et al., 2018; Tikhomirov et al., 2012; Yang, 2013) and the break-off of the Ushky slab (van der Meer et al., 2018). There is no record of subduction below NE Siberia between ~80 Ma and the onset of the Kuril-Kamchatka arc around 55–45 Ma, and it is thus likely that the segment of original Izanagi lithosphere between the Okhotsk block and the Olyutorsky arc, in our model bounded to the NE and SW by transforms, became part of the Eurasian plate (Fig. 10a). The blocking of subduction at the Eurasian margin then required the formation of a new, Olyutorsky subduction zone. Whether this event also caused the formation of the Kula plate and the Kronotsky subduction zone at ~85 Ma is difficult to assess. The temporal relationship is striking, but at this stage, we do not see a straightforward dynamic link.

The main aim of our research was to assess whether the tectonic evolution of the NW Pacific region may form a straightforward trigger for the ~50–45 Ma plate reorganization, driving the absolute Pacific plate motion from northwest to west. Previous models infer that inception of subduction of Pacific plate lithosphere in the west is a likely driver of this absolute plate motion change (Domeier et al., 2017; Faccenna et al., 2012; Seton et al., 2015; Whittaker et al., 2007), but how and where this Pacific plate started subducting varied between models.

Our reconstruction strongly suggests that the collision of the Greater Olyutorsky arc with NE Asia, resulting in the formation of the Aleutian and Kuril-Kamchatka Trenches, is not a straightforward candidate driver for the ~50 Ma Pacific plate reorganization. This is mainly because the plates that started to subduct below the Aleutian and Kuril-Kamchatka Trenches are not likely to be the Pacific plate as concluded by Domeier et al. (2017), but plates separated from the Pacific plate by ridges and/or trenches. Subduction at the Aleutian Trench at ~50 Ma consumed the Kronotsky plate, separated from the Pacific by the Kronotsky Trench as well as the Kula plate and the Kula-Pacific ridge. Subduction at the Kuril-Kamchatka Trench consumed the Olyutorsky plate, separated by a ridge from the Pacific plate. The subduction jump and the polarity reversal around 50 Ma in the north Pacific thus did not directly involve the Pacific plate (Fig. 10c). If it is possible that dynamic changes affecting neighboring plates propagated across plate boundaries to affect the Pacific plate, which we consider well possible, then there are many other candidates to have driven the Pacific plate motion change. These may include the ~50 Ma onset or acceleration of westward absolute motion of South America forming the Andes (Faccenna et al., 2017; Schellart, 2017; Schepers et al., 2017) or the change in North American plate motion from SW to W driving breaking of the Caribbean plate (Boschman et al., 2014), both affecting the Farallon plate adjacent to the Pacific plate. Whittaker et al. (2007) noted that the Australian plate started accelerating northward around 50 Ma, and even the major India-Asia slowdown around 50 Ma (Copley et al., 2010; van Hinsbergen et al., 2011) may have propagated regionally. If absolute plate motion changes of one plate may propagate across the plate circuit, then these changes may have been dominant over the relatively small-scale collisions and reorganizations of the NW Pacific region.

Other candidates to have accommodated inception of Pacific subduction around 50

Ma is subduction initiation at the Izu-Bonin-Marianas Trench (Faccenna et al., 2012; Ishizuka et al., 2011; Seton et al., 2015) and the Tonga-Kermadec Trench (e.g., Sutherland et al., 2017). However, as there was only very minor Pacific-Australia convergence before 45 Ma, and most if not all such convergence was accommodated at the New Caledonia-Northland subduction zone between the modern Tonga Trench and Australia until 30 Ma Tonga-Kermadec subduction initiation is kinematically quite unlikely to have happened long before 30 Ma (van de Lagemaat et al., 2018). Subduction initiation at the Izu-Bonin-Marianas Trench is widely considered to have started simultaneously with the inception of forearc spreading at 51 Ma (Ishizuka et al., 2011), but this critically hinges on the assumption that subduction initiation was a spontaneous event (Arculus et al., 2015; Stern, 2004; Stern et al., 2012). This assumption is based on a conceptual model that explains how typical suprasubduction zone-type ophiolitic assemblages may result from such spontaneous subduction initiation (Stern & Bloomer, 1992), but Guilmette et al. (2018) recently showed that very similar geological records of the Oman ophiolite must have formed ~10 Myr after the inception of subduction below that ophiolite. Consequently, while the onset of spreading above the Izu-Bonin-Marianas subduction zone may well be related to the events driving the Hawaii-Emperor bend, it may well be the result instead of the cause of the plate reorganization. Moreover, there is considerable debate on the initial orientation of this trench during subduction initiation, which may have been E-W rather than N-S striking during subduction zone infancy, gradually rotating during spreading into its modern orientation (Hall, 2002; Sdrolias et al., 2004; Zahirovic et al., 2014).

If the Pacific plate reorganization occurred as a result of the plate's initial westward subduction, we consider Izanagi-Pacific ridge subduction below Japan the best candidate. Aside from the arguments already provided by Seton et al. (2015), including the arrival of the ridge assuming constant 8 cm/year Izanagi-Pacific spreading rates, and the lull in arc volcanism, we note that the finding of MORB-basalts intruding unconsolidated Paleocene-Lower Eocene foreland basin sediments on west Hokkaido (Ueda, 2016; and references therein) is an elegant geological display of ridge subduction. Our reconstruction, however, demonstrates that the segment over which the Pacific plate may have started to subduct westward is much shorter than previously incorporated in numerical models (Faccenna et al., 2012; Seton et al., 2015), and the Pacific lithosphere that started subducting after ridge subduction was extremely young and hence buoyant, so whether that would provide sufficient slab pull to drive the major 50–45 Ma plate reorganization remains to be tested in future modeling efforts.

9. Conclusions

In this paper, we present a new kinematic reconstruction of the NW Pacific region since the Late Cretaceous based on quantitative geological and marine geophysical data constraints, combined with paleomagnetic data and seismic tomographic images of the mantle. Based on our final model, we conclude the following:

The contiguous NE-SW-trending Greater Olyutorsky intraoceanic island-arc was active from ~85 to 60–50 Ma above a southeasterly dipping subduction zone that consumed oceanic lithosphere of the Eurasian plate, which previously belonged to the Izanagi plate. The subduction culminated in the obduction of the arc and associated ophiolites onto NE Asia at ~55–50 Ma in south Kamchatka, and ~45 Ma in north Kamchatka and east Sakhalin. Obduction of the Olyutorsky arc in south Kamchatka

was followed by a subduction polarity reversal at ~55–50 Ma. In the Okhotsk Sea, slab retreat of a northward-dipping slab started upon collision of the East Sakhalin arc segment with Sakhalin, leading to up to ~800 km of N-S extension of the Okhotsk block and the formation of the present-day geometry of the Kuril-Kamchatka subduction zone.

Olyutorsky subduction likely initiated at a weakness zone at or close to the Izanagi-Pacific ridge, possibly induced by the collision of the Okhotsk Block with NE Siberia. We postulate that the ridge was reactivated, accommodating ~2,500–3,000 km of divergence between the Pacific plate and the Olyutorsky arc from ~85 to 60–50 Ma. We predict that part of this crust is preserved in the present-day Aleutian Basin. At ~60 Ma, the break-up of the Greater Olyutorsky arc led to the opening of the triangular proto-Komandorsky Basin and the formation of the Shirshov Ridge. The rotation of Olyutorsky plate lithosphere behind the Shirshov Ridge between ~60 and 50 Ma was accommodated by oblique subduction below the Beringian margin until around 50 Ma, when the Olyutorsky arc collided with Kamchatka and subduction jumped south to the Aleutian Trench, capturing the ~85–60 Ma oceanic lithosphere that currently underlies the Aleutian Basin. We emphasize that future direct age determination of the Aleutian Basin crust is required to test whether this scenario is correct.

The Kronotsky intraoceanic island-arc formed above a northward-dipping subduction zone northeast of the Greater Olyutorsky arc at ~85 Ma. The Kronotsky subduction zone consumed oceanic lithosphere of the Kula plate until its cessation at around 40 Ma, possibly induced by the arrival of the Kula-Pacific ridge. After 40 Ma, the arc moved passively with the Pacific plate toward the northwest. Oblique collision of the Kronotsky arc with the Aleutian arc induced the formation of the Bowers Ridge between ~34 and 26 Ma. Coupling of the Kronotsky arc with oceanic crust of the proto-Komandorsky Basin generated NW-SE-directed seafloor spreading in the Komandorsky Basin between and subduction of the old proto-Komandorsky Basin crust below north Kamchatka, between ~20 and 10 Ma, until the Kronotsky arc collided with eastern Kamchatka at around 10 Ma.

The polarity reversal following the collision of the Greater Olyutorsky arc with NE Asia is not a straightforward driver for the 50–45 Ma Pacific plate reorganization, as the Pacific plate was still separated from this subduction zone by a ridge. We argue that Izanagi-Pacific ridge subduction below East Asia, limited to the margin south of Sakhalin, is the best candidate driver for the reorganization. Future numerical modeling is required to test whether this subduction would be sufficient to cause a change in the absolute plate motion of the Pacific plate.

2

On pole position: causes of dispersion of the paleomagnetic poles behind apparent polar wander paths

This chapter has been published as:

Vaes, B., Gallo, L. C., & van Hinsbergen, D. J. J. (2022). On pole position: causes of dispersion of the paleomagnetic poles behind apparent polar wander paths. *Journal of Geophysical Research: Solid Earth*, 127(4), e2022JB023953.

Abstract

Paleomagnetic poles used to compute apparent polar wander paths (APWPs) are strongly dispersed, which was recently shown to cause a large fraction (>50%) of these poles to be statistically distinct from the APWP to which they contributed, suggesting that current statistical approaches overestimate paleomagnetic resolution. Here, we analyze why coeval paleopoles are so dispersed, using the paleopoles behind the most recent global APWP and a compilation of paleomagnetic data obtained from <10 Ma volcanic rocks (PSV10). We find that paleopoles derived from sedimentary rocks, or from data sets underrepresenting paleosecular variation (PSV), are more dispersed and more frequently displaced. We show that paleopoles based on a smaller number of paleomagnetic sites are more dispersed than poles based on larger data sets, revealing that the degree to which PSV is averaged is an important contributor to the pole dispersion. We identify as a fundamental problem, however, that the number of sites used to calculate a paleopole, and thus the dispersion of coeval paleopoles, is essentially arbitrary. We therefore explore a different approach in which reference poles of APWPs are calculated from site-level data instead of paleopoles, thereby assigning larger weight to larger data sets. We introduce a bootstrap-based method for comparing a collection of paleomagnetic data with a reference data set on the same hierarchical level, whereby the uncertainty is weighted against the number of paleomagnetic sites. Finally, our study highlights that demonstrating smaller tectonic displacements requires larger paleomagnetic data sets, and that such data sets can strongly improve future APWPs.

Key points

- Paleopoles do not average ‘out’ paleosecular variation, which forms a first-order contributor to the dispersion of coeval paleopoles
- The number of sites used to compute a paleopole and the number of paleopoles calculated from a given data set is essentially arbitrary
- Calculating apparent polar wander paths from site-level data instead of poles allows the weighting of uncertainties and the amount of data

1. Introduction

Apparent polar wander paths (APWPs) are computed to constrain the past position and motion of tectonic plates and continents relative to the Earth's rotation axis. They provide the reference frame for paleogeography, paleoclimate, and paleoenvironment studies, and serve as the reference against which we compare paleomagnetic data collections obtained from deformed terranes to assess relative latitudinal motions or vertical-axis rotations (e.g., Besse & Courtillot, 2002; Butler, 1992; Creer et al., 1954; Irving, 1964; Torsvik et al., 2008, 2012; van Hinsbergen et al., 2015). APWPs are commonly constructed as a sequence of reference poles of different age that are calculated from a collection of coeval paleomagnetic poles (hereafter 'paleopoles'). These paleopoles are assumed to represent stable plate interiors and to provide an accurate representation of the time-averaged geomagnetic field, which is in turn assumed to approximate a geocentric axial dipole (GAD; e.g., Butler, 1992; Creer et al., 1954; Tauxe & Kent, 2004). In the absence of errors in the data, the input paleopoles are expected to plot close to, and be statistically indistinguishable from, the reference pole of the APWP to which they contribute (Butler, 1992; Rowley, 2019; Tauxe et al., 2010). But they do not.

Harrison and Lindh (1982a) and, more recently, Rowley (2019) demonstrated that with commonly used comparison metrics, as much as 50% of the paleopoles used to compute APWPs are statistically distinct from the reference pole to which they contributed (Fig. 1). Rowley (2019) argued that it is inappropriate to determine tectonic displacements from the angular difference and combined uncertainty of a paleopole and a reference pole, as is typically done, because these poles and their confidence limits are calculated on a different hierarchical level (e.g., Bazhenov et al., 2016). Instead, Rowley (2019) pointed out that a geologically meaningful difference can only be interpreted from individual paleopoles that lie beyond the angular dispersion of the paleopoles that underlie the APWP. He proposed that the uncertainty of an APWP should then be determined by the angular distance from the APWP that includes 95% of the input paleopoles (his K95, see Equation 2 in Rowley, 2019), which for the widely used global APWP of Torsvik et al. (2012) is often as large as $\sim 15\text{--}20^\circ$ (Fig. 1). In this approach, the resolution of an APWP is governed by the dispersion of the input paleopoles. Rowley (2019) thus emphasized that the reliable use and future improvement of APWPs requires thorough understanding of the nature and causes of the dispersion of input poles and their possible displacement relative to the APWP.

The sources of uncertainty that likely contribute to the dispersion of paleopoles have so far mostly been sought in the inadequate estimation of individual pole positions (e.g., Domeier et al., 2012; Harrison and Lindh, 1982a; Kent & Muttoni, 2020; Van der Voo, 1990), caused by e.g., inadequate representation of paleosecular variation (PSV), unremoved magnetic overprints, age uncertainties, measurement errors, inclination shallowing in sediments, or unrecognized deformation (e.g., Butler, 1992; Harrison & Lindh, 1982a; Rowley, 2019; Tauxe et al., 2010; Chapter 3). In addition, the dispersion may be enhanced by non-dipole contributions to the paleomagnetic field, or by errors in the relative plate motion reconstructions that were used to transfer paleopoles to a common coordinate frame (e.g., Butler, 1992; Domeier et al., 2012; Tauxe et al., 2010). But even though the problem of the large dispersion of paleopoles has long been acknowledged (e.g., Bazhenov et al., 2016; Harrison and Lindh, 1982a; Van der Voo, 1990), how the above sources of scatter, and any other, contribute to the dispersion of

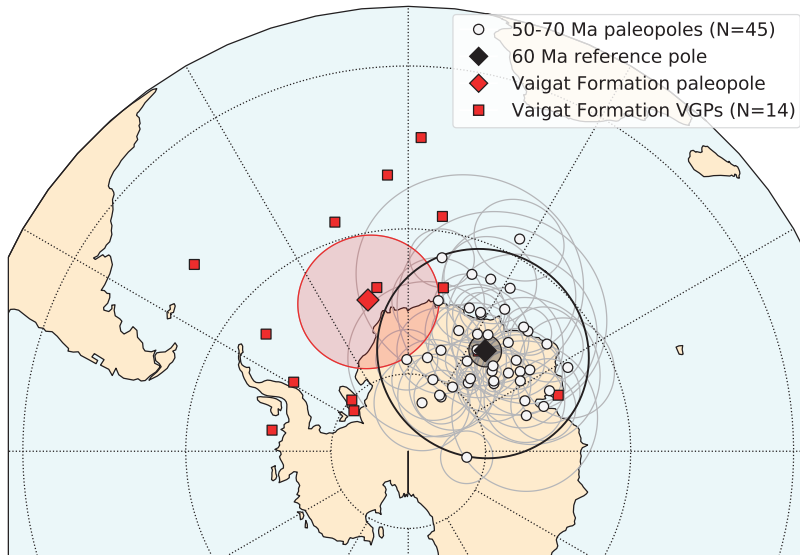


Fig. 1. Orthographic projection of the 50-70 Ma paleopoles (white circles, with 95% confidence ellipses (A_{95}) in grey) used to compute the 60 Ma reference pole (black diamond) of the global APWP of Torsvik et al. (2012). The A_{95} and K_{95} associated with the reference pole are 2.1° and 14.0° and are indicated by the filled and unfilled black circles. The paleopole derived from the Vaigat Formation (Riisager et al., 2003; red diamond, with $A_{95}=9.2^\circ$ in red) is shown as an example of a statistically ‘displaced’ paleopole. The VGPs used to calculate this paleopole are plotted as red squares. Please note that all poles and VGPs are shown in south pole coordinates in a South African coordinate frame.

paleopoles has not been systematically analyzed.

In this study, we investigate to what extent uncertainties and errors in the paleopoles themselves, as well as in the way these poles are defined, may explain pole dispersion. We further examine why a large fraction of those poles is statistically displaced from the APWP to which they contribute using classical comparison metrics. To this end, we analyzed high-quality data sets of volcanic rocks from the last 10 Ma (PSV10; Cromwell et al., 2018), in which plate reconstruction uncertainties, tectonic deformation-induced deviations, and common pitfalls related to sedimentary rocks such as inclination shallowing, play no significant role. We first use this data set to evaluate how the dispersion of paleopoles is influenced by the extent to which PSV is sampled. Then, we analyze which other factors may further enhance the dispersion, and which factors may cause so many paleopoles to be displaced from the reference pole to which they contributed. For this purpose we also used the compilation of paleopoles behind the global APWP of Torsvik et al. (2012) (Fig. 2). Based on our analyses, we explore an optimal approach to calculate APWPs and their use to quantify tectonic displacements, in such a way that statistical differences with an APWP can be used to draw geologically meaningful conclusions.

2. Background: current ways to calculate and use APWPs

The calculation and use of APWPs rely on the fundamental assumption that the time-

averaged geomagnetic field approximates that of a GAD field, whereby the time-averaged geomagnetic pole coincides with the Earth's rotation axis. Through this assumption, APWPs describe the apparent wandering of the rotation axis relative to a geographical reference location through geological time and provide a paleomagnetic reference frame for the paleogeographic reconstruction of continents and geological terranes (e.g., Butler, 1992). APWPs are typically constructed as a sequence of paleomagnetic poles that each represent the geomagnetic pole position relative to a reference (usually a continent, e.g., Africa) for a chosen geological time interval (Fig. 2a).

The first APWP was constructed by Creer et al. (1954), who connected a time series of individual paleopoles obtained from rocks of the British Isles. When more paleopoles became available, reference poles were calculated for selected geological periods by averaging all paleopoles obtained from rocks of that period (e.g., Irving, 1964; Phillips & Forsyth, 1972; Van der Voo & French, 1974). In the last four decades, most APWPs have been constructed using paleopoles as input, in one of two ways: either by a running mean method (e.g., Irving, 1977; Van Alstine & De Boer, 1978), or by fitting a smoothed spline path through a selection of paleopoles (e.g., Jupp & Kent, 1987; Thompson & Clark, 1981, 1982). The presently most widely used reference APWPs were calculated using the running mean method (e.g., Besse & Courtillot, 2002; Torsvik et al., 2012). The main advantage of this method is that it is relatively simple and intuitive, allowing the APWP to be straightforwardly reproduced by other workers. In the running mean approach, a series of reference poles is calculated at a chosen time interval (e.g., 10 Ma) by averaging collections of paleopoles whose mean rock age falls within a chosen time window (e.g., 20 Ma) (e.g., Besse & Courtillot, 2002; Kent & Irving, 2010; Torsvik et al., 2008, 2012, Wu et al. 2021). The input paleopoles may either be derived from a single continent or tectonic plate, yielding a continental/single plate APWP, or from poles obtained from multiple continents and plates after rotating them to a common coordinate frame using relative plate reconstructions, yielding a global (or 'master') APWP (e.g., Besse & Courtillot, 1991, 2002; Phillips & Forsyth, 1972; Torsvik et al. 2008, 2012).

The paleopoles used to calculate an APWP typically represent a 'study mean' paleomagnetic pole, corresponding to the main result of an individual paleomagnetic study (e.g., Hospers, 1954). On the other hand, there are also studies that produce multiple paleopoles and sometimes poles obtained in different studies of the same sedimentary or volcanic sequence are averaged to a single paleopole (e.g., Torsvik et al., 2012). A single paleopole is typically obtained through averaging a set of virtual geomagnetic poles (VGPs) that are each calculated from a site-mean paleomagnetic direction through the assumption of a GAD field (Fig. 1; see Ch. 7 in Butler (1992) for a detailed explanation). A paleomagnetic 'site' is defined as a geological unit that represents an increment of geological time relative to the time scale over which the Earth's magnetic field changes (following McElhinny & McFadden, 2000), such that the corresponding VGP represents a 'spot reading' of the field. Whether or not a rock unit represents an increment of geological time is up to the interpretation of the paleomagnetist: lava flow units are typically assumed to provide such spot readings (e.g., Biggin et al., 2008; Cromwell et al., 2018; Johnson et al., 2008). But whether paleomagnetic directions from sediments provide spot readings, either at sample level or at sedimentary 'bed' level, is more subjective (e.g., Meert et al., 2020; Tauxe & Kent, 2004; Chapter 3). Paleomagnetists aim to acquire a collection of independent spot readings of the paleomagnetic field that is sufficiently

large and contains enough geological time to ‘average out’ PSV. But the minimum number of VGPs (N) required to accurately represent PSV is unclear and depends on the time interval between different sites and the behavior of the geomagnetic field at the time. In practice, the number of VGPs used to compute a paleopole is mostly arbitrary and is often determined by the availability of suitable rocks for sampling, the sampling strategy, or the number of sites or samples that were interpreted to provide reliable paleomagnetic directions. In Chapter 4, we showed the benefits of collecting as many paleomagnetic sites as possible for the determination of a robust paleopole, and emphasized that sampling efforts are better spent on collecting more paleomagnetic sites than on collecting more samples per site. In his widely used list of reliability criteria, Van der Voo (1990) advised using at least 25 paleomagnetic samples to calculate a paleopole, whereas the recently updated ‘Van der Voo’ criteria of Meert et al. (2020) suggested using $N \geq 8$ paleomagnetic sites (each representing a spot reading) for the calculation of a paleopole. On the other hand, a statistical analysis of Tauxe et al. (2003) showed that $N > 100$ may be required for a robust representation of PSV. In practice, each individual paleopole that is included in the calculation of an APWP is assumed to provide an accurate estimate, within its confidence limits, of the time-averaged geomagnetic pole relative to the sampling location, regardless of N.

If the paleopoles obtained from rocks of similar age indeed provide accurate estimates of the time-averaged field, then the scatter of paleopoles around the mean pole should only be caused by non-dipole contributions to the geomagnetic field and plate reconstruction errors (e.g., Butler, 1992; Irving, 1964; Rowley, 2019). In the running mean approach, the pole dispersion may also result, in part, from the apparent polar wander that occurred during the time window (e.g., 20 Ma) from which the input poles have been included (e.g., Van der Voo, 1990). The position of paleopoles may differ substantially if their ages differ by, e.g., > 10 Ma, especially when derived from rapid-moving tectonic plates. By incorporating multiple paleopoles in the calculation of a reference pole of an APWP, paleomagnetists aim to average ‘out’ this scatter (e.g., Irving, 1964), irrespective of its causes. The uncertainty in the position of the reference pole is traditionally expressed by the 95% cone of confidence about the pole ($A_{95,ref}$), which is computed using Fisher (1953) statistics under the implicit assumption that the input paleopoles conform to a Fisher (1953) distribution (Heslop & Roberts, 2019; Rowley, 2019). In this approach, it is common to assign unit weight to each input paleopole, regardless of the uncertainty in the position or age of the pole, or the number of VGPs used to calculate it (e.g., Besse & Courtillot, 2002; Irving & Irving, 1982; Morel & Irving, 1981; Torsvik et al., 2008, 2012).

But already 40 years ago, Harrison and Lindh (1982a) noted that the scatter of poles obtained from stable plate interiors is much larger than expected (see Fig. 1, Fig. 2a) and consequently argued against the uniform weighting of paleopoles in the calculation of APWPs. They suspected that the paleopole scatter resulted, for a large part, from the incomplete averaging of PSV in many paleopoles. To overcome this problem, they proposed a method for calculating APWPs in which individual paleopoles are weighted according to e.g., the number of underlying VGPs and the age range of the sampled rocks. Over the years, different weighting schemes have been proposed, in which individual paleopoles are weighted either quantitatively or against a set of qualitative criteria (e.g., Gallo et al., 2021; Hansma & Tohver, 2020; Harrison & Lindh, 1982a; Le Goff et al., 1992; McFadden & McElhinny, 1995; Musgrave, 1989; Schettino & Scotese, 2005; Swanson-

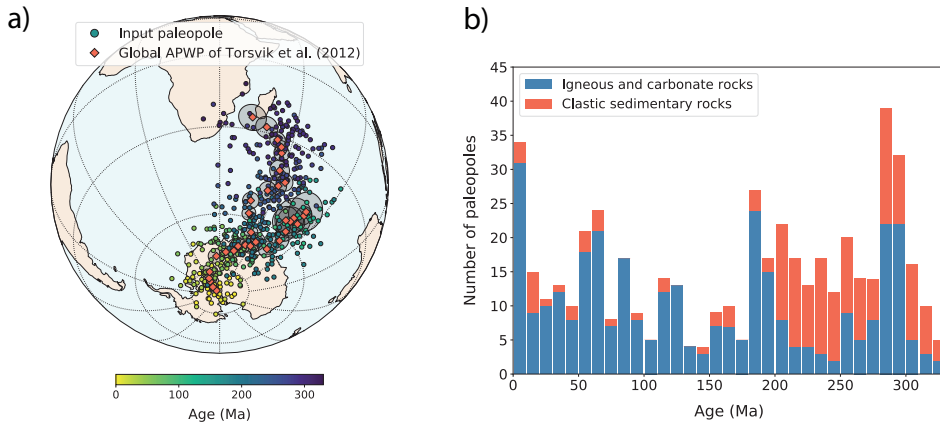


Fig. 2. (a) Orthographic projection of the global APWP of Torsvik et al. (2012) in South African coordinates (black diamonds, each shown with their A_{95}), computed using a running mean approach with a time window of 20 Ma. The input paleopoles are plotted as circles that are colored by age. (b) Histogram of the number of input paleopoles per 10 Ma time interval (after Torsvik et al., 2012).

Hysell et al., 2019; Thompson & Clark, 1981; Torsvik et al., 1992, 1996, 2008, 2012; Wu et al., 2021). Some authors calculated the reference poles of single-continent APWPs by averaging VGPs rather than paleopoles (Hansma & Tohver, 2020; McElhinny et al., 1974; McElhinny & McFadden, 2000; van Hinsbergen et al., 2017), thereby assigning larger weight to larger data sets of independent measurements of the past geomagnetic field. Because the weighting of poles based on a chosen set of criteria inevitably introduces more subjectivity (e.g., Irving & Irving, 1982; Morel & Irving, 1981), the currently most widely used APWPs are still based on a running mean approach in which all poles are weighted equally and in which errors are not propagated (Besse & Courtillot, 2002; Torsvik et al., 2012).

One of the prime applications of APWPs is the identification and quantification of tectonic displacements of tectonic blocks or plates relative to a certain reference continent (see Ch. 11 of Butler (1992) for an extensive review). To determine a tectonic displacement - expressed either as a relative vertical-axis rotation or latitudinal displacement - paleomagnetists typically compare an individual paleopole derived from the studied tectonic block with a reference APWP. If the paleopole is shown to be statistically distinct from the APWP, according to some comparison metric, this is typically interpreted as evidence for a relative vertical-axis rotation and/or latitudinal displacement. To assess whether a paleopole is statistically distinct (or 'discordant') with respect to the reference pole (Butler, 1992; Rowley, 2019), paleomagnetists typically compare the 95% confidence regions about the paleopole with that of a reference pole, even though these are of a different statistical 'rank' (following the terminology of Bazhenov et al., 2016). The uncertainty in the position of the individual paleopole ($A_{95,pp}$) is typically calculated from the distribution of VGPs using Fisher (1953) statistics (see Heslop & Roberts (2019) for a review). In the classical approach, a paleopole is considered statistically displaced if its angular distance to the reference pole exceeds the combined uncertainty of the paleopole and the reference pole, calculated using:

$$\sqrt{A_{95,ref}^2 + A_{95,PP}^2} \quad (1)$$

whereby the $A_{95,ref}$ and the $A_{95,PP}$ are the radius of the 95% confidence circle around the reference pole and the independent paleopole, respectively. It is important to note that the uncertainty in the position of the underlying paleopoles (their $A_{95,PP}$) is typically not propagated in the calculation of the $A_{95,ref}$ which may thus be an underestimate of the uncertainty in the reference pole position (Heslop & Roberts, 2020).

Rowley (2019) showed that, with the above equation, >50% of the paleopoles used in the global APWP of Torsvik et al. (2012) are statistically displaced relative to the APWP itself. He pointed out that a significant difference between an independent paleopole and a reference pole can therefore not be straightforwardly interpreted as a signal of tectonic motion. Instead, he argued, significant tectonic motion can only be concluded if the independent paleopole falls outside the circle that contains 95% of the input paleopoles from which the mean poles of the APWP is computed (which he referred to as the K_{95}). This confidence circle was previously used by Bazhenov et al. (2016) to define ‘alarm bands’ around APWPs, which they used to identify potential remagnetization events. Using the K_{95} as a confidence estimate of the APWP, rather than the $A_{95,ref}$ essentially means that the resolution at which we can discern relative tectonic displacements is for a large part determined by the angular deviation of the paleopoles that lie furthest from the mean pole of the APWP. Increasing the resolution of APWPs for tectonic purposes would then require decreasing the scatter of input poles around the APWP. Below, we therefore analyze what causes the scatter of poles behind an APWP, and what causes their displacement relative to the mean pole to which they contributed.

3. Data and methods

We conduct a series of experiments to explore and identify the main contributors to the dispersion of paleopoles that are used as input for current APWPs and to determine why a large fraction of poles are statistically distinct - in the traditional statistical framework (see Eq. 1) - from the APWP to which they contribute. With this aim, we assess the influence on the pole dispersion, and pole displacement, of a range of parameters associated with each input pole, such as the number of independent measurements of the geomagnetic field used to calculate the pole (N), lithology, the uncertainties in the pole position itself and the age uncertainty of the sampled rocks.

We use two data sets: the PSV10 database, and the compilation of paleopoles used for the Torsvik et al. (2012) global APWP. The PSV10 database contains 83 paleomagnetic data sets (from 81 publications) obtained from volcanic rocks that formed in stable plate interiors in the last 10 Ma, as compiled by Cromwell et al. (2018). This data set is the most recent update of a compilation of paleomagnetic data that fulfill all commonly used quality criteria of volcanic rocks that erupted so recently that age uncertainty, plate motion, tectonic deformation, or artifacts common in sedimentary rocks such as inclination shallowing, are considered negligible. We note that Cromwell et al. (2018) corrected all site locations and VGPs for recent plate motions using the no-net-rotation model of Argus et al. (2011), which only involved small adjustments of up to a few degrees. The PSV10 compilation and its predecessors (e.g., PSVRL; McElhinny & McFadden, 1997) are typically used to study the behavior of the recent geomagnetic field, including paleosecular variation, and serves as the standard of statistical models of the geomagnetic field such

TK03.GAD (Tauxe & Kent, 2004) and BCE19 (Brandt et al., 2020). Each VGP included in the compilation has been interpreted as a nearly 'instantaneous' reading of the magnetic field and is calculated by averaging multiple paleomagnetic directions obtained from the same lava flow unit to decrease the effect of (small) measurement errors. We use the 'original' PSV10 database (that is, not corrected for serial correlation, see section 4 of Cromwell et al., 2018) to assess the influence of representation of PSV on paleopole scatter around a mean for the geomagnetic field of the last 10 Ma. We calculated a paleopole from each paleomagnetic data set included in PSV10 using Fisher (1953) statistics, providing a pole position and associated A_{95} and Fisher precision parameter K (Table S1).

We quantify the dispersion of VGPs or paleopoles using three different statistical parameters: the Fisher (1953) precision parameter K , the angular standard deviation (or VGP scatter) S , and the mean angular distance to the reference S' . S is a widely used measure of the scatter of VGPs and is commonly used to assess PSV in studies of geomagnetic field behavior (see eq. 14.1, Tauxe et al., 2010). S' provides an alternative measure of the dispersion and has the advantage that it is less affected by outliers (Suttie et al., 2015; Doubrovine et al., 2019). In addition, we tested whether the paleopoles whose data were used in the PSV10 database would be deemed statistically displaced according to the traditional comparison metric of Eq. (1). Because tectonic motions of lithology-based artifacts are considered irrelevant for the PSV10 data set, we use the observed scatter of poles about the 'true' mean pole to evaluate the effect of incomplete averaging of PSV, or non-dipole contributions to the geomagnetic field.

Next, we explore to what extent other common sources of error in paleomagnetic data may have further enhanced the dispersion of paleopoles that were used to calculate the global APWP of Torsvik et al. (2012). We first used to entire database of 501 paleopoles that were obtained from 0-330 Ma old rocks to assess the magnitude of pole dispersion, and whether this varies with age and between different lithological groups. Then, for a selection of 167 paleopoles that fall within the 0-110 Ma age range, we compiled additional characteristics of each paleomagnetic data set including the number of paleomagnetic sites used to calculate the pole, the uncertainties in the pole position, and in the age uncertainty of the sampled rocks (Table S2). To assess the influence of specific parameters on the dispersion of individual paleopoles, we used the angular distance of each paleopole to the mean pole of the APWP, following e.g., Harrison & Lindh (1982a). It is worth noting that the mean poles of the global APWP do not represent the 'true' time-averaged pole position, but they provide a useful approximation of the time-averaged pole and are therefore used as the reference poles in our analyses. In addition, to quantify the clustering of poles that fall within a specific time interval of, e.g., 20 Ma, we used the Fisher (1953) precision parameter, analogous to K for distributions of VGPs. We performed these calculations using a set of inhouse-developed Python codes, for which we made extensive use of the functions and programs from the freely available paleomagnetic software package PmagPy (Tauxe et al., 2016). The Python codes used for this study are publicly available through the online repository on Zenodo (see Data availability statement).

4. Results

4.1. Analysis of PSV10

The 83 paleomagnetic data sets included in the PSV10 database (Table S1) vary in size from $N=3$ to $N=128$ VGPs, with an average N of ~ 29 , and from each of these collections

of VGPs we computed a paleopole (Fig. 3a). We calculated the time-averaged ‘reference’ geomagnetic pole for the last 10 Ma by computing the Fisher (1953) mean of all 2401 VGPs, as well as by averaging the paleopoles without taking their uncertainties into account, as is common when computing APWPs (Fig. 3a). The angular distance between the two reference poles (0.6°) is statistically insignificant; the VGP-based mean has an $A_{95, \text{VGPs}}=0.7^\circ$ and pole-based mean has $A_{95, \text{poles}}=1.2^\circ$. We use these data-based reference poles to enable the application of the comparison metrics and to ensure consistency with the analyses in the next section. We note that using the geographic pole instead of these reference poles hardly influences the results described below (see Fig. S1).

As a measure of the dispersion of VGPs and paleopoles, we calculated the angular distance of each VGP and each paleopole to the respective reference pole positions (Fig. 3b). The dispersion of the paleopoles, each averaging a different number of VGPs that were obtained within a single study, is, logically, smaller than that of the individual VGPs. The total distribution of VGPs has $K=17.1$, $S=20.1^\circ$ and $S'=15.6^\circ$, compared to the distribution of paleopoles which has $K=172.3$, $S=6.2^\circ$, and $S'=5.2^\circ$. The 95% angular deviation of the population of VGPs is 33.8° (calculated using eq. 2 in Rowley, 2019), whereas that of the population of paleopoles, corresponding to the K_{95} , is 10.7° . So even though averaging collections of VGPs to paleopoles considerably decreases the scatter, some of the ‘study mean’ paleopoles are still significantly dispersed around the reference pole (Fig. 3a, b).

To assess to what extent PSV underlies this pole scatter, we first conducted a numerical simulation in which we generated sets of synthetic paleomagnetic poles by randomly sampling (with replacement) N VGPs from the PSV10 database. For every second value of N (from 2 to 70) we generated 5000 pseudosamples from which we calculated synthetic poles along with their angular distance to the reference pole. We note that the magnitude of VGP dispersion is latitude-dependent, at least for the last 10 Ma (e.g., Biggin et al., 2008; Cox, 1962, 1970; Doubrovine et al., 2019; McFadden et al., 1991), but because paleopoles used to calculate APWPs are often derived from a wide latitude range, we draw VGPs from the entire data set in our experiment. Fig. 3c shows how the scatter of these synthetic paleopoles decreases with N , with the mean angular distance to the reference pole (S') gradually decreasing from almost 9° for $N=4$ to $\sim 2^\circ$ for $N=70$. The observed angular distances of the paleopoles calculated from the PSV10 data sets clearly follow the trend obtained for the synthetic poles (Fig. 3c). Also, we find that the majority (75%) of the paleopoles that are at a relatively large angular distance to the reference pole, that is larger than the mean value of 5.2° (S'), have $N < 25$ (Fig. 3c). Overall, these results illustrate that PSV is never averaged ‘out’: larger data sets simply provide a more accurate estimate of the grand mean pole position.

Next, we estimated the expected pole dispersion resulting from PSV by randomly distributing the 2401 VGPs over 83 collections of VGPs with the same N as the data sets that contributed to PSV10. We then determined the mean angular distance to the reference pole (S') of the 83 paleopoles that were calculated from those 83 collections of VGPs. We repeated this procedure 5000 times and obtained an average S' of 3.9° (with 95% bootstrap confidence bounds of 3.4° and 4.4°) instead of the 5.2° obtained from the published data sets. This suggests that the majority ($\sim 4^\circ$) of the dispersion of poles in the PSV10 database is a signal of PSV and that a relatively small contribution to the scatter ($\sim 1.3^\circ$) results from other artifacts that may affect a data set of a particular study (e.g., local deformation, erroneous structural corrections, unremoved magnetic overprints,

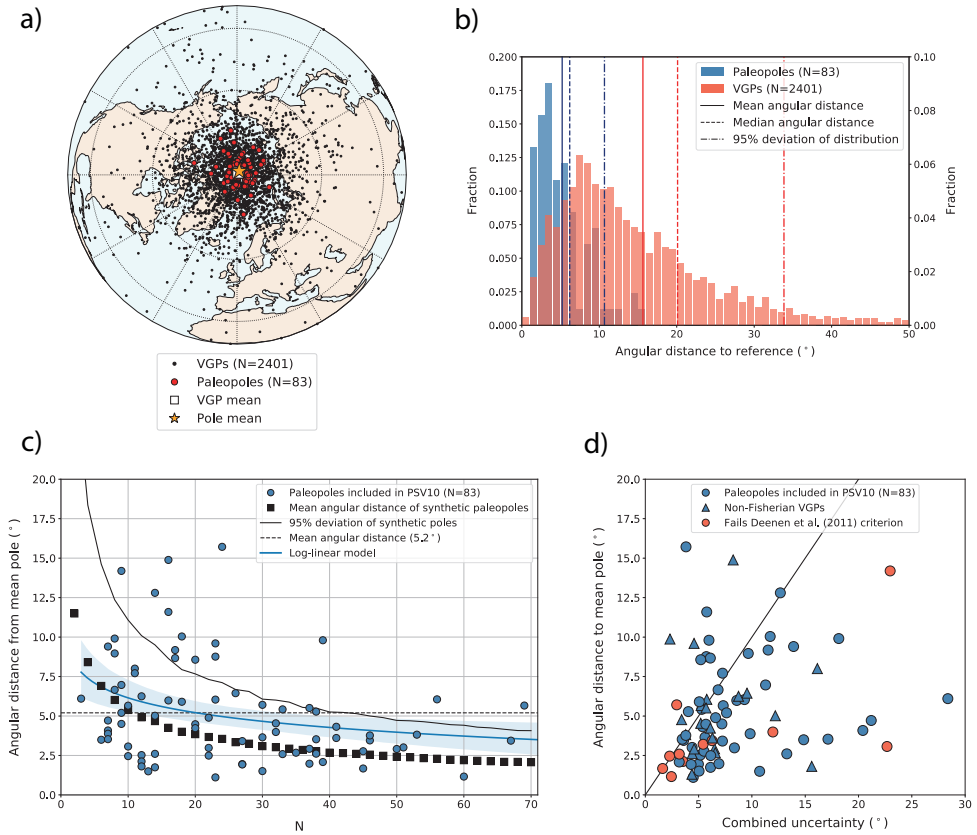


Fig. 3. (a) Orthographic projection of the VGPs included in the PSV10 database (Cromwell et al., 2018). The paleopoles computed from the 83 data sets of PSV10 are plotted as red circles. The reference poles calculated from the VGPs and paleopoles are shown by the white square and orange star, respectively. (b) Histogram of the angular distance to their reference pole of the VGPs and paleopoles shown in (a). (c) Angular distance to the mean pole of the 83 paleopoles versus the number of VGPs (N). The mean angular distance and 95% deviation of the 5000 synthetic paleopoles, which are computed for every second value of N , are depicted by black squares (see text for explanation). A log-linear regression curve computed for the paleopoles included in PSV10 is shown in blue (with bootstrapped 95% confidence regions). (d) Plot of the angular distance of each paleopole against the combined uncertainty, as calculated using Eq. 1 (after Rowley, 2019). Poles that do not satisfy the Deenen et al. (2011) criterion or whereby the underlying distribution of VGPs is not consistent with a Fisher (1953) distribution are plotted as red circles or blue triangles, respectively.

measurement errors).

Finally, we tested whether the poles calculated for the PSV10 data set are statistically displaced from the mean pole position, using Eq. 1. We find that 26.5% (22 out of 83) of the paleopoles that are used in the PSV10 data set are, under this comparison statistic, distinct from the mean pole (Fig. 3d). This result cannot be entirely attributed to the relatively low A_{95} of 1.2° ; even if we would use an A_{95} of 3.0° instead, which is a typical A_{95}

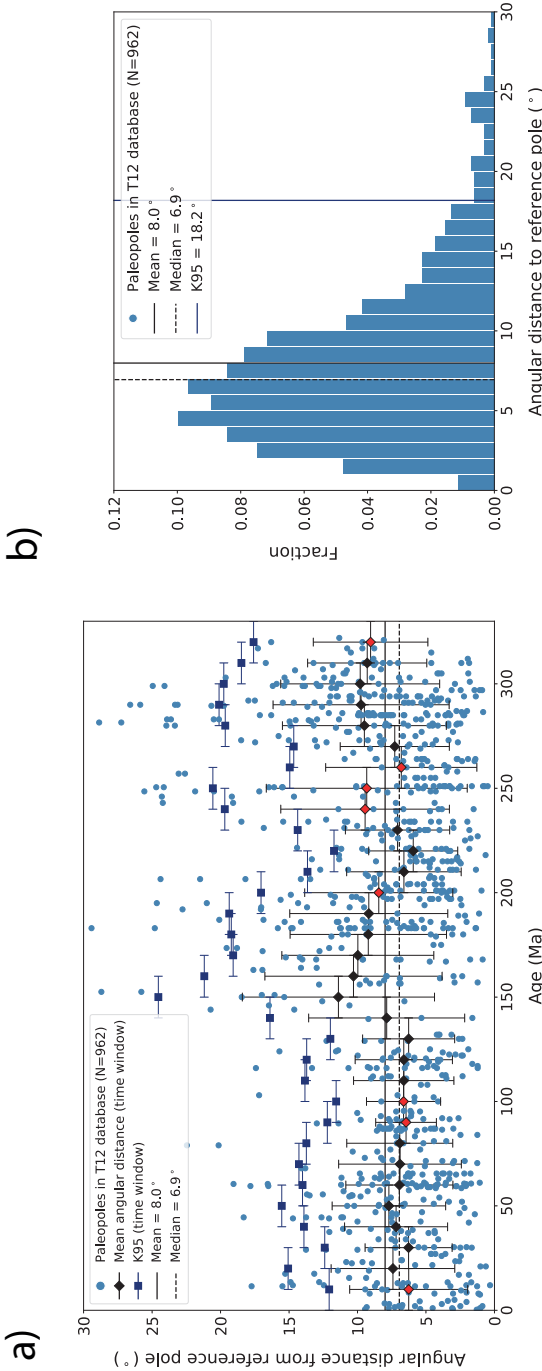


Fig. 4. (a) Angular distance to the reference pole of all 0-330 Ma paleopoles used to compute the global APWP (in South African coordinates) of Torsvik et al. (2012). The reference poles are computed as running mean poles with a 20 Ma time window. The mean angular distance and K_{95} computed from the paleopoles included in each 20 Ma time window are plotted as black diamonds and blue squares, respectively. The mean angular distance is plotted in red if the distribution of paleopoles is not consistent with a Fisher (1953) distribution. (b) Histogram of the angular distance to the reference pole for all paleopoles in the database. Note that because in most paleopoles are used twice in the running mean approach, the number of poles in this figure is higher than the actual number of paleopoles (501).

value for a mean pole of the global APWP of Torsvik et al. (2012), then 15.7% (13 out of 83) of the poles would still be displaced. We find that the data set used to compute three of the 22 displaced poles may have undersampled PSV, as indicated by their A_{95} values that are smaller than the lower limit of the $A_{95\text{min-max}}$ envelope of Deenen et al. (2011) (Fig. 3d, Table S1). In addition, seven of the displaced poles do not conform to a Fisher (1953) distribution, as indicated by the quantile-quantile method of Fisher et al. (1987). The other 12 poles pass all common reliability criteria, however. If we would exclude all data sets that do not pass these additional criteria, we find that 23.5% is statistically displaced according to Eq. 1. This illustrates that even in the PSV10 data set, which should contain little artifacts, a significant fraction of poles are statistically displaced from the reference pole calculated from all 83 paleopoles.

4.2. Analysis of the paleopoles used for the global APWP

The mean (median) angular distance to the reference pole of the 962 paleopoles (most poles count twice) used for the global APWP for the last 320 Ma of Torsvik et al. (2012) is 8.0° (6.9°) (Fig. 4, Table S2). This is higher than for the PSV10 data set, suggesting that there are additional sources of scatter. This trend is also obvious from the 95% angular deviation (K_{95}) of the total population of paleopoles of 18.2° (Fig. 4a). The magnitude of pole dispersion is relatively constant with time with an average angular distance of $\sim 7^\circ$, and up to $9\text{--}10^\circ$ between 140–200 Ma and 280–330 Ma (Fig. 4b). The K_{95} of the paleopoles for the majority of 20 Ma time windows is around $12\text{--}15^\circ$, but the time windows with increased dispersion yield K_{95} values of up to $\sim 20^\circ$ (Fig. 4b). For most time windows, the application of the quantile-quantile method of Fisher et al. (1987) indicates that the input paleopoles are consistent with a Fisher (1953) distribution around the reference pole (Fig. 4b). This suggests that the contribution of polar wander to the pole dispersion, which is expected to cause an elliptical distribution of the paleopoles within a time window, is relatively small. We also find that using a smaller time window of 10 Ma instead of 20 Ma only leads to a minor decrease in the pole dispersion (mean and median angular distance of 7.5° and 6.5° , see Fig. S2), which supports the above interpretation. In the following, we assess the potential relationships between the observed dispersion of paleopoles and specific characteristics of the paleomagnetic data sets used to calculate those poles.

The adequate sampling and averaging of the PSV are key requirements for determining an accurate paleopole (Deenen et al., 2011; Meert et al., 2020; Van der Voo, 1990). Paleomagnetic poles based on a larger number of independent measurements of the geomagnetic field should provide a more accurate estimate of the time-averaged geomagnetic field and thus lie closer to the position of the ‘true’ time-averaged geomagnetic pole. We compiled the number paleomagnetic sites (N) used for the calculation of the 167 paleopoles included for the 0–110 Ma segment of the global APWP of Torsvik et al. (2012). The number of sites used to calculate a pole varies widely between different studies, from $N=3$ to $N=507$, with a median value of 20 (Fig. 5a). For sedimentary rocks, the number of sites may represent individual samples, but sometimes also averages of multiple samples from one or multiple beds. Notably, 12% of the poles (20 in total) are calculated from less than the minimum of eight paleomagnetic sites formulated by Meert et al. (2020) in their recent update of the Van der Voo (1990) criteria. Fig. 5b shows the angular distance of each paleopole against the number of sites used to compute that pole. For this compilation of paleopoles, we observe a general decrease of

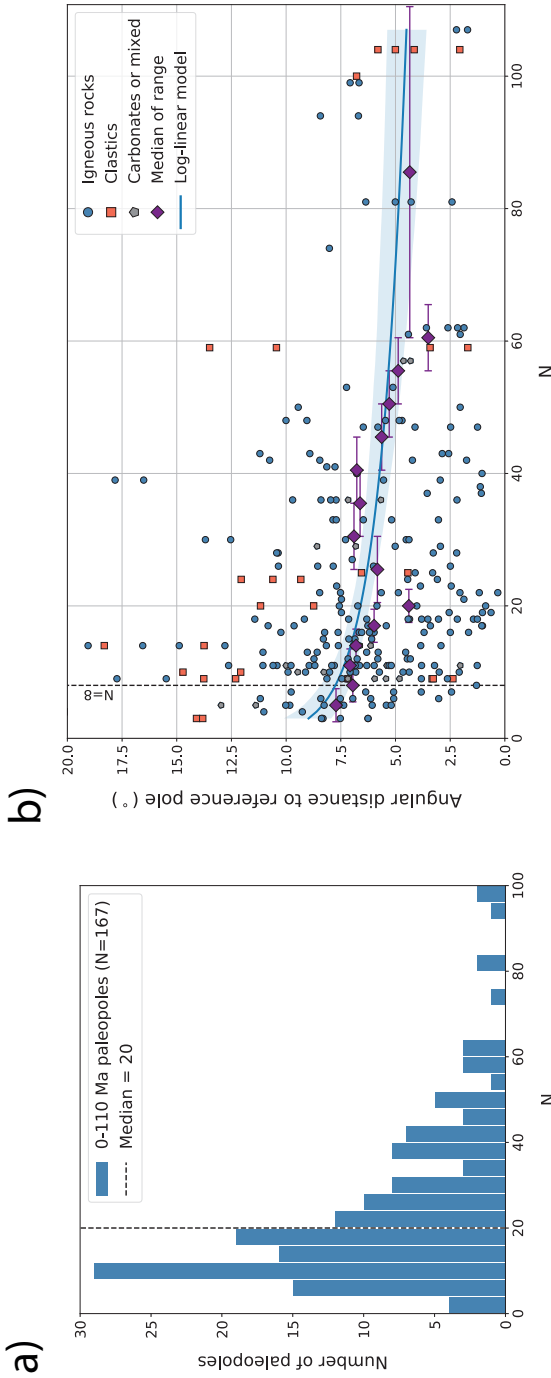


Fig. 5. (a) Histogram of the number of VGPs (N) used to compute each of the 0-110 Ma paleopoles behind the global APWP of Torsvik et al. (2012). **(b)** Angular distance of each paleopole to the reference pole versus N . Each paleopole is plotted by their lithology. The reference poles are computed as running mean poles with a 20 Ma time window. The median angular distance is computed for 15 ranges of N and shown as purple diamonds. A log-linear regression curve (blue, with bootstrapped 95% confidence region) highlights the trend.

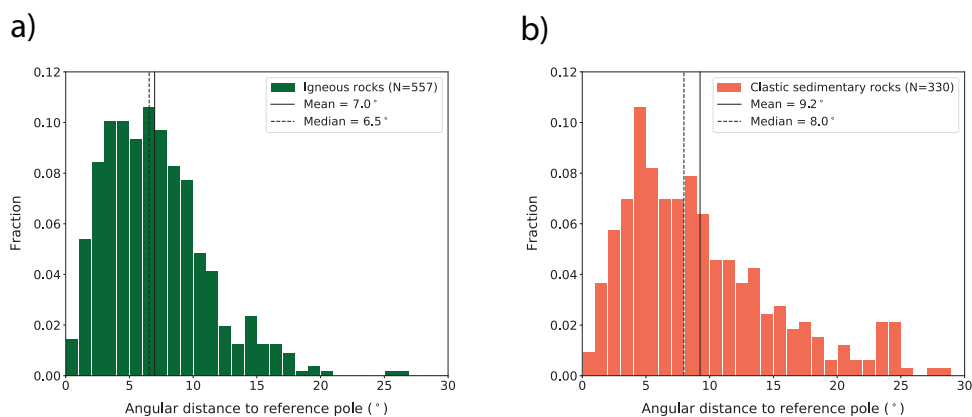


Fig. 6. Histograms of the angular distance to the reference pole of all 0-330 Ma paleopoles that are derived from igneous and carbonate rocks (a) and clastic sedimentary rocks (b). The poles derived from the latter rocks are corrected for inclination shallowing using a ‘blanket’ flattening factor of $f=0.6$, following Torsvik et al. (2012). The mean (median) values are indicated by the vertical straight (dashed) lines.

the angular distance of paleopoles to the reference pole with increasing N , from $\sim 8^\circ$ for $N < 8$ to $\sim 5^\circ$ for $N > 50$. This trend is similar to that observed for the PSV10 database (Fig. 3c) and reflects the degree to which PSV is represented by the data. The mean angular distance is, however, a few degrees higher which may reflect additional sources of scatter, which we analyze below.

Contrary to the PSV10 database, the global APWP also contains poles from intrusive igneous rocks, carbonate rocks and clastic sedimentary rocks. Differences exist between these broad lithological groups in terms of how they record the past geomagnetic field and the properties and robustness of paleomagnetic data derived from them. Clastic sedimentary rocks are typically considered to be less reliable paleomagnetic recorders than igneous rocks because of their weaker remanent magnetization and the common shallowing of the paleomagnetic inclination, caused by syn- and post-depositional processes (e.g., Bilardello et al., 2013; King, 1955; Kodama, 2012; Tauxe & Kent, 2004; Chapter 3). The mean (median) angular distance of paleopoles derived from clastic sedimentary rocks is indeed larger (9.2° (8.0°)) than those derived from igneous rocks (7.0° (6.5°)) (Fig. 6).

Torsvik et al. (2012) corrected the poles derived from clastic sedimentary rocks by applying a so-called ‘blanket’ flattening factor of $f=0.6$, except for poles that were calculated from data sets on which the original authors already applied an inclination shallowing-correction. We find that the application of this ‘blanket’ correction factor does not significantly reduce the dispersion of paleopoles derived from clastic sedimentary rocks. The paleopoles that were corrected with this flattening factor have a mean (median) angular distance of 9.5° (8.2°), whereas the uncorrected poles have a mean (median) angular distance of 9.7° (8.3°) to the reference pole of the APWP, which was re-calculated using the uncorrected sediment-derived paleopoles. We note that Torsvik et al. (2012) did not apply an inclination shallowing correction to paleopoles derived from carbonate rocks, even though they may also be affected by inclination error (e.g., Muttoni et al.,

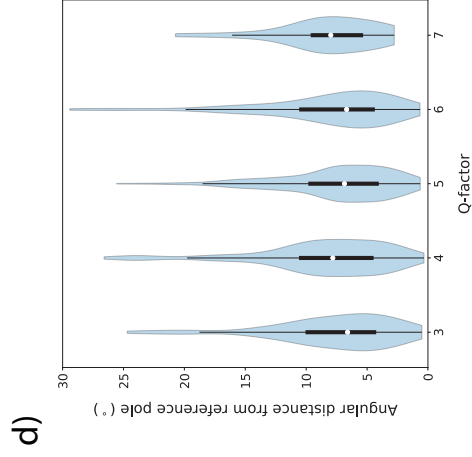
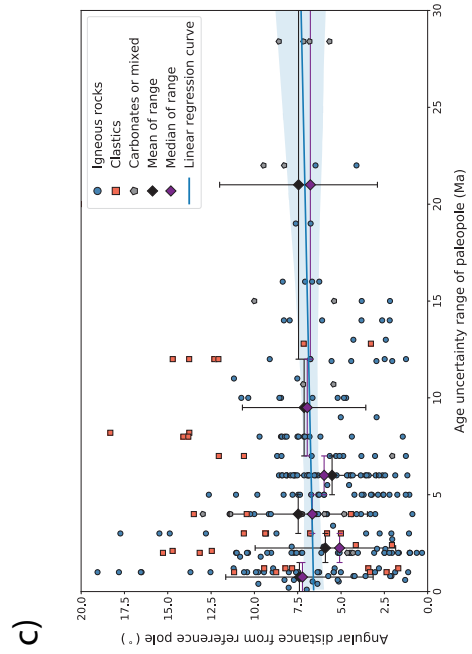
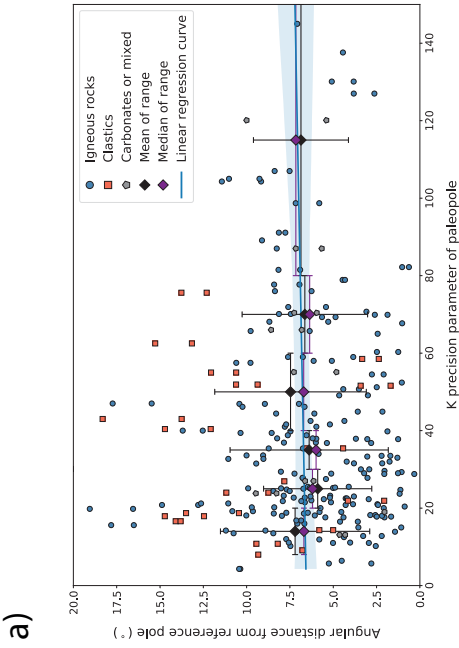
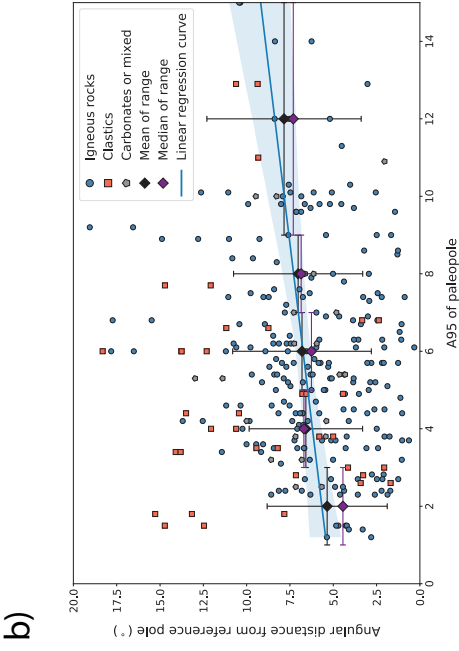


Fig. 7. Angular distance to the reference pole for all 0-110 Ma paleopoles in the compilation of Torsvik et al. (2012) against the Fisher (1953) precision parameter K (a), A_{95} (b) and the age uncertainty range (c). The median angular distance is computed for several intervals and shown as purple diamonds. A log-linear regression curve (blue, with bootstrapped 95% confidence region) highlights the trend for each parameter. (d) Boxplots showing the median angular distance and its distribution of the 0-330 Ma paleopoles behind the global APWP with a given Q-factor (Van der Voo, 1990).

2013; Chapter 3). The number of paleopoles in the Torsvik et al. (2012) database that were derived either from carbonate rocks or from clastic sediments that were corrected for inclination shallowing by the original authors is, however, too low for a meaningful calculation of the mean angular distance.

Next, we evaluate the relationship between the dispersion of paleopoles and the commonly used statistical parameters K and A_{95} . The range of K values thought to be representative for PSV is ~ 10 -50 (Deenen et al., 2011) or 10-70 (Meert et al., 2020) and collections of VGPs with higher values likely underrepresent PSV. The angular distance of igneous-based poles relative to the reference pole is $\sim 6^\circ$ at K -values of 20-40, increasing to a slightly higher value of $\sim 7^\circ$ at K -values higher than 80 (Fig. 7a). We also find that the angular distance increases with increasing A_{95} (Fig. 7b). The A_{95} confidence circle is a function of both K and N and considering the observed trends in K (Fig. 7a) and N (Fig. 5b), these results suggest that although the dispersion increases with a tighter clustering of VGPs, this effect is counteracted by the decrease in dispersion with increasing N . These combined effects may explain the relatively low mean angular distance for paleopoles with relatively small A_{95} values.

There does not seem to be a clear correlation between the angular distance and age uncertainty of paleopoles (Fig. 7c), whether derived from igneous or sedimentary rocks. We note, however, that the rocks sampled to compute the 0-110 Ma paleopoles have age uncertainties rarely exceeding 15 Ma, which may be higher for poles from lower Mesozoic and Paleozoic rocks. We also find no strong relationship between the difference in age of the reference pole and the mean age of the input paleopole (Fig. S2), indicating that the effect on the pole dispersion of polar wander on timescales of <10 Ma is relatively small.

A common selection criterion to include poles into an APWP is the Q-factor of Van der Voo (1990), whose underlying quality criteria were recently updated by Meert et al. (2020). The Q-factor ranges from 1-7, indicating how many of each of the seven quality criteria of Van der Voo (1990) are satisfied by the paleomagnetic data set. In the calculation of some recent APWPs, such as the spline paths of Torsvik et al. (2012) and the APWPs of Wu et al. (2021), larger statistical weight was assigned to paleopoles with a higher Q-factor compared to those with low Q. We used the entire data set of Torsvik et al. (2012) from 0-330 Ma, which only included paleopoles with $Q \geq 3$, to assess whether there is a correlation between the Q-factor and its angular distance to the mean pole to which it contributes. We find no correlation between the quality factor Q and the angular distance of these poles (Fig. 7d). Our finding confirms the analysis by Van der Voo (1990) based on his compilation of Phanerozoic poles from Europe and North America, based on which he showed that there was no substantial decrease in the mean angular distance for $Q > 2$ (see Fig. 7 of Van der Voo, 1990).

According to the traditional comparison approach (eq. 1) we find that 52.2% of the 0-110 Ma paleopoles used for the 0-100 Ma segment of the global APWP of Torsvik et

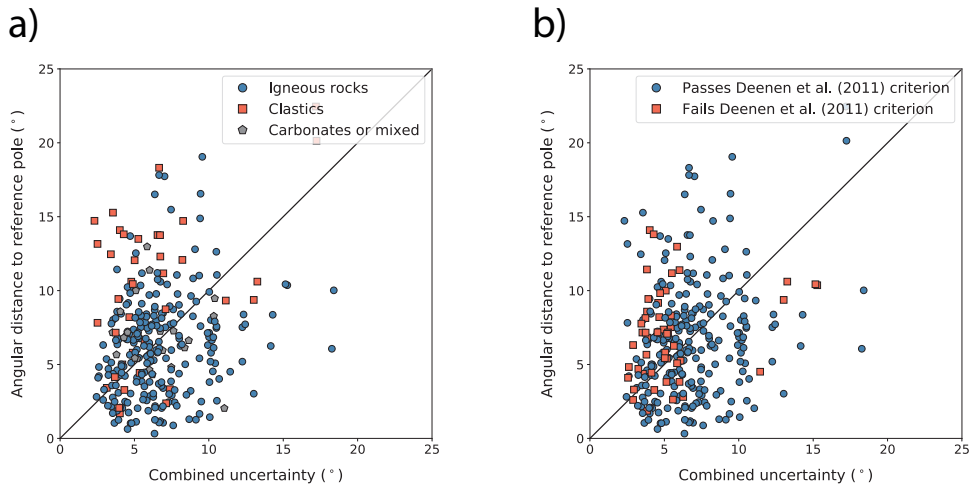


Fig. 8. Plots of the angular distance of each paleopole against the combined uncertainty, as calculated using Eq. 1 (after Rowley, 2019). Poles are colored by lithology (a) or by whether the underlying VGPs conform to a Fisher (1953) distribution (b).

al. (2012) is statistically different from the reference pole to which they contribute, i.e., the angular distance to the reference pole exceeds the combined uncertainty of both poles (Fig. 8). Paleopoles derived from clastic sedimentary rocks are not only more scattered around the reference pole to which they contribute (Fig. 6) but are also more often statistically displaced than paleopoles derived from igneous rocks (Fig. 8a). Nearly 80% (30 of 39) of the clastic sedimentary poles are displaced compared to ~48% (113 of 235) of the igneous poles.

Finally, of all paleopoles that have an A_{95} that falls outside of the N-dependent reliability envelope of Deenen et al. (2011), which assesses whether the scatter is straightforwardly explained by PSV alone, 72% is found to be statistically displaced (Fig. 8b), mostly because of low scatter of the underlying VGPs, yielding an $A_{95} < A_{95,\min}$. This supports the conclusion of Harrison & Lindh (1982a) that underrepresentation of PSV by the paleomagnetic data set is an important cause of individual paleopoles to be statistically displaced from the reference pole to which they contribute. Together with the trend that poles with higher K-values have larger angular distances to the reference pole, this shows that undersampling of PSV increases the dispersion of paleopoles used in current APWPs, and the number of statistically displaced poles.

5. Discussion

5.1. The problem of using paleopoles

Rowley (2019) argued that the traditional method used to determine a statistically significant difference between independent paleopoles and an APWP is flawed, because a large fraction of input poles is statistically ‘displaced’ from the reference pole to which they contribute. Such statistical differences therefore do not necessarily represent the tectonically meaningful difference that is commonly interpreted from them (e.g., Butler, 1992; Coe et al., 1985; Harrison & Lindh, 1982a; Rowley, 2019). What causes these

paleopoles to be displaced (according to the traditional statistical framework)? Our analysis in part confirms the widely held suspicion that common errors and uncertainties in paleomagnetic data contribute to this. We find that paleopoles are more often statistically distinct when derived from data sets in which PSV is likely underrepresented (indicated by high K values (e.g., $K > 70$; Meert et al., 2020), and an A_{95} that is below the $A_{95, \min}$ of the reliability envelope of Deenen et al. (2011)), or from clastic sedimentary rocks, regardless of whether they are corrected for inclination shallowing using a ‘blanket’ correction factor of 0.6 or not (*sensu* Torsvik et al., 2012). Excluding paleopoles based on such data sets may thus decrease the dispersion of paleopoles. We also find, however, that the dispersion of paleopoles, and their statistical difference with the reference pole to which they contribute, cannot solely be attributed to the ‘insufficient’ quality of the paleopoles themselves.

Our analysis reveals that even when paleomagnetic data sets pass stringent and widely applied quality criteria, the paleopoles derived from them are frequently statistically different from the reference pole to which they contribute. Our analysis of 0-110 Ma paleopoles behind the APWP of Torsvik et al. (2012) shows that ~50% of the igneous-based paleopoles, that have a high Q -factor and that satisfy the criterion of Deenen et al. (2011), are statistically displaced from the reference pole to which they contribute. Moreover, ~26% of the paleopoles obtained from the high-quality data sets of recently erupted lavas included in PSV10 are statistically displaced from the mean pole calculated for the recent (<10 Ma) geomagnetic field. These findings illustrate that the accuracy at which we can determine the time-averaged geomagnetic pole position using a single paleopole is not as high as our statistical metrics suggest, and that the formal confidence region (the A_{95}) may underestimate the true uncertainty of an individual paleopole (e.g., Coe et al., 1985; Harrison & Lindh, 1982a; Rowley, 2019). This may be partly explained by the fact that uncertainties are typically not propagated through each hierarchical level in standard paleomagnetic analyses (Heslop & Roberts, 2020). Our results show that there are often sources of scatter that cause poles to be displaced that cannot be, or at least were not, recognized by the paleomagnetists that collected the data sets, and that cannot be straightforwardly identified using commonly applied quality criteria. Such sources of dispersion may include non-dipole contributions to past geomagnetic field, errors in tilt correction and/or unrecognized intra-plate deformation (e.g., Besse & Courtillot, 2002; Butler, 1992). Overall, our results support the notion from Rowley (2019) that the observed dispersion may be inherent to paleomagnetic data, and the paleopoles derived from them. But because the dispersion of coeval paleopoles is not accounted for in the traditional statistical framework, Rowley (2019) proposed an alternative approach in which the uncertainty of an APWP is directly determined by the dispersion of input poles, irrespective of the sources of the dispersion. The magnitude of dispersion depends, however, on subjective choices, which we illustrate below.

Our results show that the number of VGP's used to compute paleopoles (N) is a first-order contributor to the dispersion of coeval paleopoles (Fig. 3c, 5a). And this introduces a fundamental problem: there is no definition of the amount of paleomagnetic data that defines paleopole. Widely used quality criteria only include a minimum amount of data needed to calculate a reliable paleopole: Van der Voo (1990) proposed a minimum of 25 samples, to which Meert et al. (2020) recently added that these samples should preferably be derived from $N \geq 8$ paleomagnetic sites. Because these values only provide

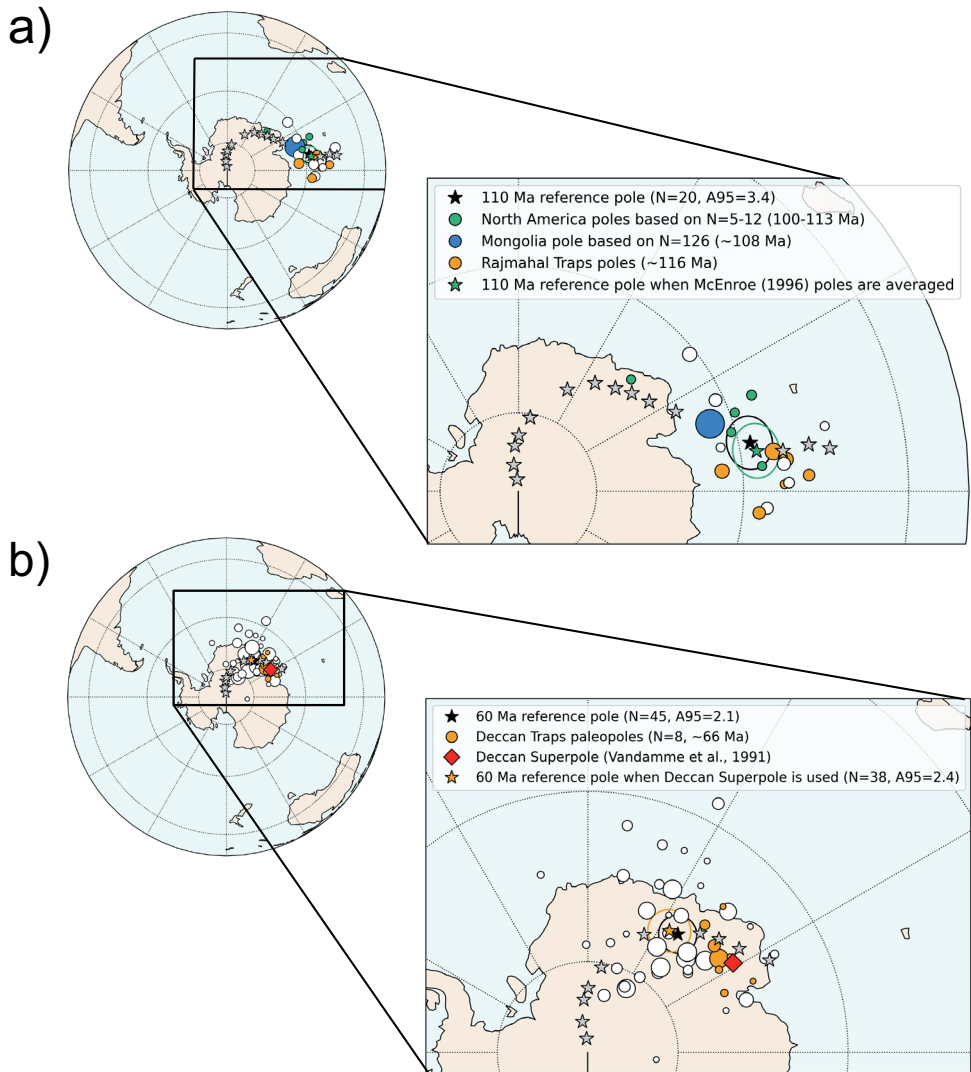


Fig. 9. Examples of how subjective choices related to the definition and inclusion of certain paleopoles may influence the reference pole position and associated parameters. See text for discussion. **(a)** Orthographic projection of the 100-120 Ma paleopoles used to compute the 110 Ma reference pole of the global APWP of Torsvik et al. (2012). Two reference poles are plotted: computed from all paleopoles (black star) or if the McEnroe (1996) poles are replaced by a 'study mean' pole (green star). The difference between the reference poles is 1.2° . **(b)** Same as **(a)**, but this time showing the 50-70 Ma paleopoles used to compute the 60 Ma reference pole. Again, two reference poles are plotted: computed from all paleopoles (black star) or if the Deccan Traps poles are replaced by the Deccan Superpole of Vandamme et al. (1991). The difference between the reference poles is 1.0° .

a minimum, this allows the calculation, and inclusion in an APWP, of paleopoles based on a highly variable number of paleomagnetic data, as illustrated by the poles used in the most recent global APWP (Fig. 5a). Although the number of VGPs behind a paleopole is often simply determined by the amount of ‘reliable’ paleomagnetic data presented in a single study, multiple paleopoles from the same study are sometimes included as separate poles in the calculation of an APWP, or a single ‘grand’ mean pole is computed from data obtained in different studies of the same volcanic or sedimentary sequence. For example, in the global APWP of Torsvik et al. (2012), a Cretaceous paleomagnetic pole from Mongolia was calculated from $N=126$ lava sites (van Hinsbergen et al., 2008), whereas 42 sites from North American intrusive rocks of approximately the same age (McEnroe, 1996) were used to compute five different input poles of $N=5-12$ (Fig. 9a). Likewise, that APWP includes seven poles from seven published data sets of the Deccan Traps of India constrained by N varying from 3 to 130 (Fig. 9b), whereas these data sets could instead be combined into a single mean pole for the Deccan Traps, as done by Vandamme et al. (1991).

If the number of paleomagnetic sites/VGPs (N) behind a single paleopole is essentially arbitrary, as illustrated above, and N is a first-order contributor to the dispersion of poles, then the K_{95} value is dependent on arbitrary choices as well. Given a data set of VGPs, we may calculate reference poles of an APWP with low A_{95} and high K_{95} by including many paleopoles based on low N , or with high A_{95} and low K_{95} by combining the same data over a few paleopoles with high N . Below we will therefore explore the alternative avenue of calculating a reference APWP from VGP-level data directly, instead of from paleopoles that each represent an average of an arbitrarily defined collection of VGPs.

5.2. Towards a VGP-based comparison method

Calculating a reference data set from VGPs instead of paleopoles allows the comparison with an independent paleomagnetic data set of VGPs on the same hierarchical level and avoids subjective choices regarding the amount of paleomagnetic data that is used to determine a single paleopole. VGP-based APWPs have been constructed before, for e.g., Australia (Hansma & Tohver, 2020; McElhinny et al., 1974), Iberia (van Hinsbergen et al., 2017), and Laurentia (Swanson-Hysell et al., 2019), and for all major continents by McElhinny & McFadden (2000). Also, paleomagnetic data from different studies and locations have been combined on the VGP level in studies of geomagnetic field behavior (e.g., Brandt et al. 2021; Cromwell et al., 2018). Calculating APWPs from VGPs poses several challenges, however. First, a method needs to be designed to avoid the ‘displacement’ problem highlighted by Rowley (2019). Second, for many published paleomagnetic data sets, individual VGPs have not been reported and estimates need to be developed from published statistical descriptions of the data.

The problem of displaced paleopoles that follows from the application of the traditional comparison metric (Eq. 1) will be even more prominent for VGP-based APWPs. Because the total number of VGPs (N) is much higher than the number of paleopoles, the A_{95} calculated from all individual VGPs is even smaller than that calculated from the associated paleopoles. With so many paleopoles already statistically displaced from the APWP using classical comparison metrics (see Eq. 1), this problem will also exist or be even larger for VGP-based APWPs. To illustrate this: for the PSV10 data set, the A_{95} calculated from the ‘study mean’ poles that contributed to the PSV10 data set is 1.2° , and

from the VGPs is 0.7° . Using the VGP-based A_{95} as the $A_{95, \text{ref}}$ instead of the pole-based A_{95} , the number of displaced poles determined with Eq. 1 increases from 22 to 23. This shows that a different measure needs to be developed that ensures that $\sim 95\%$ of the input data sets do not statistically differ from the reference data set. Below, we use the PSV10 data set to explore such an alternative approach.

Our analysis shows that the angular difference between a paleopole and a reference pole decreases with an increasing number of VGPs (N) (Fig. 3c, 5a). We therefore introduce a new comparison metric between paleopoles and reference data sets that takes N into account. Central to this approach is an alternative expression for the confidence limit of the reference pole (of an APWP), which we refer to as the ‘ B_{95} ’. The B_{95} is an estimate of the 95% confidence limit that the reference data set, represented by a reference pole, would have had if it had been constrained by the same N as the studied paleopole. In other words, the B_{95} represents a prediction of the pole position of a paleopole with given N , if that paleopole would have sampled N VGPs from the total cloud of ‘reference’ VGPs. This way, the resolution of a comparison between a reference data set and a collection of VGPs obtained by a paleomagnetic study is directly dependent on the N of the latter data set, and thus naturally reflects the amount of information included in the statistical comparison.

To determine the B_{95} , we use a bootstrap approach: for each bootstrap run we compute a pseudopole from N randomly drawn VGPs from the reference data cloud. By repeating this procedure a few thousand times, we obtain thousands of pseudopoles, each derived from the same amount of VGPs as included in the studied paleomagnetic data set. Next, we calculate the B_{95} as the angular distance from the principal vector of the cloud of pseudopoles that contains 95% of the pseudopoles (Fig. 10a, b). Evidently, the B_{95} becomes larger when these pseudopoles are calculated from a smaller number of VGPs and is thus directly proportional to the number of VGPs included in the studied data set. This approach makes no a priori assumptions about the behavior or statistical properties of the geomagnetic field, but simply predicts where poles based on N VGPs could lie, as a function of the scatter in the reference data set, regardless of the sources of this scatter. We now assess how this equal- N approach performs by determining the number of ‘displaced’ paleomagnetic data sets included in the PSV10 database. To this end, we compute the B_{95} for each ‘study mean’ pole using its underlying number of VGPs, and then replace the $A_{95, \text{ref}}$ by the B_{95} in Eq. 1. Again, we consider a data set statistically distinct from the reference if the angular distance of the study mean pole exceeds the combined uncertainty, which in this approach is a function of the B_{95} of the reference and the A_{95} of the compared paleopole. We find that this comparison method reduces the percentage of displaced poles from 26.5% to 8.4% (7 out of the 83 data sets, Fig. 10d). Some of these data sets are thus still ‘displaced’, also according to our proposed comparison metric. We note, however, that four of these data sets were almost entirely derived from a sequence of successive lava flows, which led Cromwell et al. (2018) to discard most of the VGPs in their filtered PSV10 data sets, since those VGPs may not have provided entirely independent spot readings of the field.

The above results suggest that replacing the $A_{95, \text{ref}}$ with the bootstrapped B_{95} in Eq. 1 may provide an alternative solution for the ‘displacement’ problem pointed out by Rowley (2019). The application of this approach requires, however, that the reference data set (of an APWP) is calculated from VGPs, which are not always available.

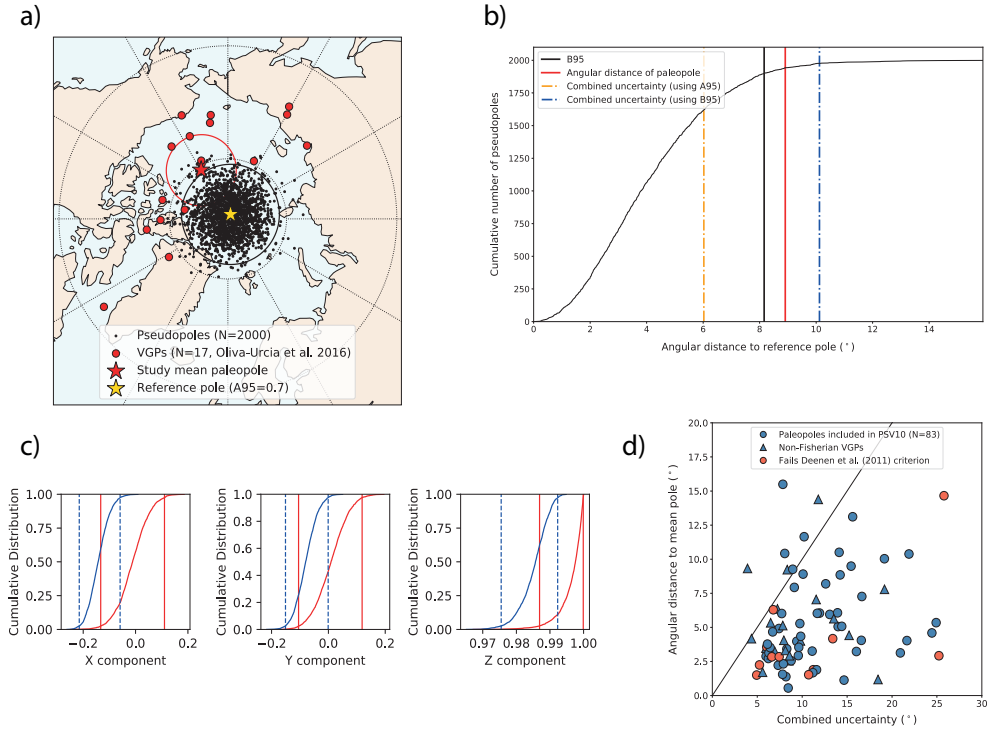


Fig. 10. Example of the proposed VGP-based comparison method (see text for discussion). **(a)** Orthographic projection of the paleomagnetic data set of Oliva-Urcia et al. (2016) that was included in PSV10. The VGPs and the paleopole computed from those VGPs are plotted as red circles and the red star (with A_{95}), respectively. To assess whether this paleopole is statistically distinct from the reference data set, 2000 pseudopoles are computed by randomly drawing the same number of VGPs ($N=17$) from the total data set (small black dots). The B_{95} is then defined as the 95% angular deviation of these pseudopoles from the principal vector of the distribution of pseudopoles and is indicated by the black circle. **(b)** Cumulative distribution of the pseudopoles plotted against the angular distance from the reference pole. Vertical lines show the angular distance of the paleopole, the B_{95} and the combined uncertainty computed (i) following the traditional framework (see Eq. 1) and (ii) by replacing the $A_{95,ref}$ with the B_{95} . This figure indicates that the studied paleopole is not statistically ‘displaced’ according to our new metric, whereas it is displaced according to the traditional statistical framework. **(c)** Bootstrap common mean test of Tauxe et al. (2010) applied to the studied data set (blue), showing that the data set is not statistically different on the 95% confidence level from the set of pseudopoles (red). The three subplots each show the cumulative distribution of bootstrapped means in the three Cartesian coordinates x , y and z . **(d)** Plot of the angular distance of each paleopole against the combined uncertainty for all data sets included in PSV10, whereby the combined uncertainty is computed after replacing the $A_{95,ref}$ in Eq. 1 by the B_{95} (see also Table S1). Using the VGP-based approach, the number of displaced poles decreases from 22 to 7 (out of 83).

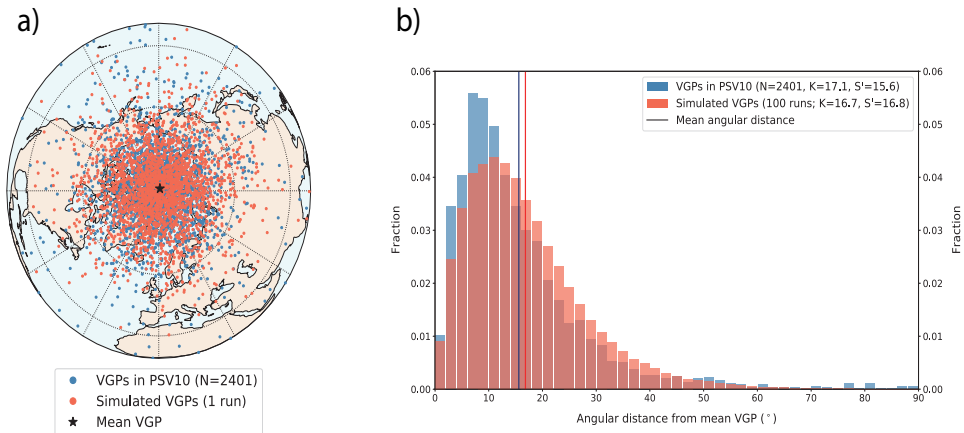


Fig. 11. Comparison between the VGPs included in the PSV10 compilation and the parametrically sampled VGPs derived from the paleopoles and their statistical parameters. **(a)** Orthographic projection of the VGPs included in PSV10 (blue dots) and parametrically sampled VGPs (red dots) from one simulation whereby these VGPs were generated for each data set of PSV10 from a Fisher (1953) distribution around the paleopole and described by the K value of the underlying VGPs. **(b)** Histogram of the angular distance from the reference pole of the published VGPs (blue) and parametrically sampled VGPs (obtained from 100 simulations). The mean angular distance of the simulated VGPs (red line) is slightly larger than that of the published VGPs (blue line).

5.3. Parametric re-sampling of VGPs

Paleomagnetic data sets available for computation of APWPs have not always been reported on the VGP level, but only per paleopole, and the vast majority of published paleomagnetic data has not been included in modern paleomagnetic databases (e.g., MagIC (Jarboe et al., 2012), Paleomagnetism.org (Koymans et al., 2020)). To overcome this problem, we may parametrically re-sample VGPs from the paleopoles given the published statistical properties of these poles. Similar approaches of parametrically re-sampling paleopoles or VGPs have been frequently used for paleomagnetic data analyses and simulations (e.g., Cromwell et al., 2018; Gallo et al., 2021; Koymans et al., 2016; Rowley, 2019; Smirnov & Tarduno, 2010; Swanson-Hysell et al., 2014; Tauxe et al., 1991). To evaluate whether this approach is appropriate here, we reproduce the PSV10 data set by parametrically re-sampling VGPs from the ‘study mean’ poles and their statistical parameters (referred to as a ‘parametric bootstrap’, following Tauxe et al., 2010). For each data set included in PSV10, we created the same number of VGPs as included in the published data set from a Fisher (1953) distribution around the ‘study mean’ pole and its associated precision parameter K , which were both calculated from the published VGPs. The parametrically sampled data cloud is very similar to that of the published VGPs (Fig. 11a), with little difference in the associated statistical parameters. We observe a slightly larger dispersion of the parametrically sampled VGPs (indicated by a lower K and higher S' value) compared to the published VGPs (Fig. 11b). This is explained by the outlying VGPs in the published data sets that lower the K value for that data set, such that when these data sets are parametrically re-sampled, a larger fraction of the simulated VGPs are

between $\sim 15^\circ$ and $\sim 50^\circ$ from the mean pole of all VGPs (Fig. 11a).

We now test whether the data sets that contributed to the PSV10 database are displaced relative to a reference data set consisting of parametrically re-sampled VGPs instead of the published VGPs. From the collection of 2401 parametrically sampled VGPs, we compute a pseudopole by drawing the required N , which is again equal to the N that is behind the investigated data set included in PSV10. We then repeated this procedure 2000 times, each time generating a new set of parametrically sampled VGPs, to obtain the set of pseudopoles from which we compute the B_{95} . We find that this B_{95} is typically $\sim 0.1\text{--}0.4^\circ$ larger than that obtained from the published VGPs (Table S1). This illustrates that using parametrically sampled VGPs instead of the ‘real’ VGPs is slightly more conservative, making it thus slightly more difficult to demonstrate a significant displacement between a paleopole and the reference data set. We find that using parametrically sampled VGPs to compute the B_{95} makes no difference for the data sets included in PSV10: the number of ‘displaced’ paleopoles remains the same (7 out of 83; Table S1). This therefore opens the opportunity to compute future APWPs, including a global APWP, from VGP-level data, even if all the original VGPs are not available.

5.4 Outlook: future APWPs and their application

We show here that calculating APWPs from VGP-level data may provide an alternative solution to the ‘displacement’ problem in current pole-based APWPs, whereby subjective choices related to the definition of individual paleopoles are avoided and paleomagnetic data can be compared with a chosen reference on the same hierarchical level. Computing APWPs from VGPs has more benefits: it allows the incorporation and propagation of key uncertainties and errors in paleomagnetic data, such as age uncertainty, as demonstrated by the bootstrap or Monte Carlo-based methods recently developed by Swanson-Hysell et al. (2019) and Hansma & Tohver (2020). The uncertainty in the position of a ‘study mean’ paleopole, which is determined by the number and scatter of the underlying VGPs, is automatically accounted for in a VGP-based approach. To incorporate age uncertainty, a reference pole and its B_{95} can be computed from only those VGPs that fall in a chosen age range. Age uncertainty could then be weighed by parametrically sampling VGPs from all reference paleopoles that overlap in age with the chosen time window and assigning a random age within the age range of the reference paleopole to each VGP. Each pseudopole from which the reference pole position and its B_{95} is computed is then drawn from only those VGPs whose ages fall within the time window. When comparing an independent paleomagnetic data set with a VGP-based APWP, the age range may be equated to the age range of the sampled rocks, thereby accounting for both the number of VGPs that data set and its age uncertainty.

On the other hand, the VGP-based approach also comes with a necessity for larger data scrutiny, particularly for large data sets. In the VGP-approach unit weight is assigned to each VGP, such that largest weight is assigned to largest paleomagnetic data sets. This essentially means that the accuracy of each paleopole is assumed to be a function of N alone; with increasing N , PSV and other sources of noise are increasingly averaged. However, some paleomagnetic data sets may be affected by systematic bias that is unrelated to N , such as local deformation, errors in tilt correction, systematic magnetic overprints, a local/regional magnetic field anomaly, inclination shallowing, and undersampling of PSV. The majority of input paleopoles of the global APWP of Torvsik et al. (2012) that

are displaced according to classical comparison metrics likely suffer from one or more of these artifacts. To identify a potential bias in future VGP-based APWPs caused by such artifacts requires a careful analysis of statistical differences between different input data sets, with particular focus on the data sets with largest N . In general, it will be important to apply stringent and objective selection criteria, such as those from Meert et al. (2020) and Chapter 3, for inclusion of data into the APWP.

We foresee that VGP-based APWPs, which have confidence intervals that better reflect the scatter of the underlying paleomagnetic data and do not depend on subjective choices, will provide more accurate and robust paleomagnetic reference frames, at shorter time intervals, to underpin paleogeography studies (e.g., van Hinsbergen et al., 2015), or e.g., true polar wander calculations (e.g., Kulakov et al., 2021; Muttoni & Kent, 2019; Torsvik et al., 2012). At the same time, the B_{95} makes that the resolution of the reference is adjusted to the resolution of the paleomagnetic data set that is compared with the reference, such that demonstrating smaller statistical differences requires larger data sets. It also opens novel opportunities to compute high-resolution reference poles for specific times of rapid Earth system change by collecting large, well-dated paleomagnetic data sets. We emphasize that for VGP-based APWPs, it is of key importance that the paleomagnetic community makes all their published data publicly available, e.g., in databases such as MagIC (Jarboe et al., 2012) or paleomagnetism.org (Koymans et al., 2020), as this will strongly improve future APWPs and contribute to solving detailed Earth system problems.

6. Conclusions

In this study, we investigated the causes of the large dispersion of paleopoles obtained from similar aged rocks that causes a large fraction of these poles to be statistically displaced from the mean pole to which they contribute. To this end, we used a previously compiled global data set from <10 Ma old volcanic rocks (PSV10) without tectonics-induced pole dispersion, and the compilation of paleopoles used to compute the most recent global APWP of Torsvik et al. (2012). Based on our analyses, we conclude the following:

- The dispersion of paleopoles, defined by their angular distance to the reference pole to which they contribute, decreases with an increasing number of VGPs from which they are calculated. Individual paleopoles, which are commonly based on a few dozen VGPs, do not average ‘out’ PSV and their angular distance to the reference pole is, in part, dependent on the extent to which PSV has been sampled by the underlying paleomagnetic data set.
- Paleopoles that are statistically displaced from the reference pole of the APWP, according to the traditional statistical framework, are more often derived paleomagnetic data sets in which PSV is likely underrepresented, or from clastic sedimentary rocks, regardless of whether they are corrected for inclination shallowing using a ‘blanket’ correction factor.
- The dispersion of paleopoles, and their statistical difference with a given reference pole, cannot only be attributed to the insufficient quality of the paleopoles. This is indicated by the absence of a correlation between the Q -factor of Van der Voo (1990) and the pole dispersion, as well as the high percentage (~26%) of displaced paleopoles derived from the data sets included in PSV10. The high percentage of displaced poles indicates that the formal confidence region (the A_{95}) of individual paleopoles

may underestimate the true uncertainty in pole position. This implies that sources of uncertainty cause poles to be displaced that are not straightforwardly identified by applying common quality criteria, which may include non-dipole contributions, erroneous tilt corrections or unrecognized intra-plate deformation.

- There is no clear definition of the amount of paleomagnetic data that underpins a single paleopole. Although all input paleopoles are typically assigned equal weight in APWP computation, they are an average of a collection of VGPs of essentially arbitrary size, and the number of VGPs that underlie paleopoles varies considerably. Also, the number of paleopoles derived from a single paleomagnetic data set or from a specific volcanic or sedimentary sequence is often determined by subjective choices. Such choices may potentially bias the position of reference poles of an APWP and the size of its confidence regions.
- Calculating a reference data set from VGP-level data avoids the problem of arbitrarily defined paleopoles. We explored a bootstrap-based approach to comparing a given paleomagnetic data set against such a VGP-based reference data set, whereby the resolution is determined by the number of VGPs in the studied data set. We show that this comparison metric significantly reduces the percentage of displaced data sets included in PSV10 (from ~24% to ~8%) and may thus provide an alternative solution to the problem of displaced paleopoles in current pole-based APWPs highlighted by Rowley (2019).
- Constructing APWPs from VGP-level data instead of from paleopoles allows giving more weight to larger data sets and incorporating uncertainties on the position and in the age of the paleopole. This enables the comparison of paleomagnetic data sets with a reference APWP on the same hierarchical level, such that physically meaningful differences and associated uncertainties may be determined. Such an approach also implies that constraining smaller relative tectonic displacements requires larger, better dated paleomagnetic data sets. Moreover, future APWPs may thus be strongly improved by collecting large, high-quality data sets from stable plate interiors.

Data availability statement

No new paleomagnetic data is used in this study. The paleomagnetic data sets are derived from previous compilations by Torsvik et al. (2012) and Cromwell et al. (2018), and can be found both in the original publications as well as in the tables of the Supporting Information. The Python codes used for our analyses are publicly available on Zenodo: <https://doi.org/10.5281/zenodo.6366399>.

3

Reliability of paleomagnetic poles from sedimentary rocks

This chapter has been published as:

Vaes, B., Li, S., Langereis, C. G., & van Hinsbergen, D. J. J. (2021). Reliability of paleomagnetic poles from sedimentary rocks. *Geophysical Journal International*, 225(2), 1281-1303.

Abstract

Paleomagnetic poles form the building blocks of apparent polar wander paths and are used as primary input for quantitative paleogeographic reconstructions. The calculation of such poles requires that the short-term, paleosecular variation (PSV) of the geomagnetic field is adequately sampled and averaged by a paleomagnetic dataset. Assessing to what extent PSV is recorded is relatively straightforward for rocks that are known to provide spot readings of the geomagnetic field, such as lavas. But it is unknown whether and when paleomagnetic directions derived from sedimentary rocks represent spot readings of the geomagnetic field and sediments are moreover suffering from inclination shallowing, making it challenging to assess the reliability of poles derived from these rocks. Here, we explore whether a widely used technique to correct for inclination shallowing, known as the elongation-inclination method (E/I), allows us to formulate a set of quality criteria for (inclination shallowing-corrected) paleomagnetic poles from sedimentary rocks. The E/I method explicitly assumes that a sediment-derived dataset provides, besides flattening, an accurate representation of PSV. We evaluate the effect of perceived pitfalls for this assumption using a recently published dataset of 1275 individual paleomagnetic directions of a >3 km-thick succession of ~69-41.5 Ma red beds from the Gonjo Basin (eastern Tibet), as well as synthetic data generated with the TK03.GAD field model. The inclinations derived from the uncorrected dataset are significantly lower than previous estimates for the basin, obtained using coeval lavas, by correcting inclination shallowing using anisotropy-based techniques, and by predictions from tectonic reconstructions. We find that the E/I correction successfully restores the inclination to values predicted by these independent datasets if the following conditions are met: the number of directions N is at least 100, the A95 cone of confidence falls within a previously defined A95_{min-max} reliability envelope, no negative reversal test is obtained and vertical-axis rotation differences within the dataset do not exceed 15°. We propose a classification of three levels (A, B, and C) that should be applied after commonly applied quality criteria for paleomagnetic poles are met. For poles with classification 'A', we find no reasons to assume insufficient quality for tectonic interpretation. Poles with classification 'B' could be useful, but have to be carefully assessed, and poles with classification 'C' provide unreliable paleolatitudes. We show that application of these criteria for datasets of other sedimentary rock types classifies datasets whose reliability is independently confirmed as 'A' or 'B', and that demonstrably unreliable datasets are classified as 'C', confirming that our criteria are useful, and conservative. The implication of our analysis is that sediment-based datasets of quality 'A' may be considered statistically equivalent to datasets of site-mean directions from rapidly cooled igneous rocks like lavas and provide high-quality paleomagnetic poles.

1. Introduction

Paleomagnetic poles are extensively used as input for paleogeographic reconstructions and models of regional tectonic deformation, and for the construction of apparent polar wander paths (APWPs) (e.g., Besse & Courtillot 2002; Torsvik et al. 2008, 2012; Kent & Irving 2010; Wu et al. 2020; Kent & Muttoni 2020). These APWPs describe the motion of plates and continents relative to the Earth's spin axis and thereby provide the reference frame for paleogeography, -climate, -biology and -oceanography studies (e.g., van Hinsbergen et al. 2015). Each paleomagnetic pole is assumed to provide an accurate representation of the time-averaged geomagnetic field that existed during the formation of the rock, and that this field is approximately a geocentric axial dipole (GAD) field (e.g., Creer et al. 1954; Tauxe & Kent 2004). To evaluate the reliability of a pole, the paleomagnetic community widely uses a set of seven criteria, originally formulated by van der Voo (1990) and recently updated by Meert et al. (2020). A fundamental requirement for a reliable pole is that the short-term, paleosecular variation (PSV) of the geomagnetic field is adequately sampled, such that it can be averaged 'out' to obtain an accurate estimate of the GAD field (e.g., Butler 1992, Deenen et al. 2011; Meert et al. 2020).

To assess to what extent PSV is recorded by a dataset, the observed dispersion of virtual geomagnetic poles (VGPs) is commonly evaluated against statistics-based criteria that are derived from reference models of the geomagnetic field (e.g., Butler 1992; Deenen et al. 2011, 2014; Meert et al. 2020). These models are calibrated against paleomagnetic measurements obtained from fast-cooled, young (<5 Ma) igneous rocks, whose within-site directional reproducibility is checked against quantitative criteria (typically sites with $k > 50$ are considered reliable spot readings, e.g. Johnson et al. 2008; Biggin et al. 2008), and whereby the thermal remanent magnetization acquired during rapid cooling provides, in principle, an 'instantaneous' record of the ambient field (e.g., McElhinny & McFadden 1997; Tauxe & Kent 2004; Johnson et al. 2008; Cromwell et al. 2018; Doubrovine et al. 2019). Statistics-based quality criteria derived from these models thus apply to datasets whereby each VGP represents a spot reading of the geomagnetic field, such as those obtained from lavas and thin dykes (e.g., Meert et al. 2020). But, for sedimentary rocks, it is often unclear whether individual directions (or VGPs) provide spot readings of the geomagnetic field. On the one hand, sediment samples represent some geological time and partial averaging of PSV may occur in a single paleomagnetic sample, depending on the rate of sediment accumulation and the duration of acquisition of the remanent magnetization (Kodama 2012). On the other hand, because sedimentary beds do not form geologically instantaneously, like lavas do, there are currently no objective criteria to assess whether a sediment-based paleomagnetic direction is reproducible and whether it may be considered a spot reading. For instance, Meert et al. (2020) recommended taking at least three samples per horizon but provide no definition of a horizon or a statistical criterion to test the internal consistency of a sedimentary site. As a result, the chance of including erroneous directions is thus larger for sediments than for lavas. This makes it challenging to test whether the scatter of directions (and associated VGPs) in a sediment-based dataset is representative for PSV, such that an accurate paleomagnetic pole may be determined.

Despite these problems, a method that is widely used in the paleomagnetic community to correct for the notorious problem of inclination shallowing explicitly assumes that each paleomagnetic direction obtained from a sedimentary rock closely represents a spot reading of the geomagnetic field: the so-called elongation-inclination (E/I) method

of Tauxe & Kent (2004). In sedimentary rocks that suffer from inclination shallowing, the observed inclination is shallower than the inclination of the geomagnetic field in which the rocks were initially magnetized (King 1955). Inclination shallowing is widely observed in clastic sedimentary rocks, and particularly in hematite-bearing red beds, but has also been documented for carbonate rocks (e.g., Dallanave et al. 2009, 2012; Meijers et al. 2010a, b; Muttoni et al. 2013, 2018). When unnoticed, inclination shallowing may lead to major underestimations of the primary paleomagnetic inclination (and associated paleolatitude) of up to 25-30° (e.g., Kodama 2012). Inclination shallowing may thus cause a substantial bias in paleogeographic reconstructions or (reference) APWPs, for which paleomagnetic poles from sedimentary rocks are widely used as input (e.g., Kent & Irving 2010; Domeier et al. 2011; Torsvik et al. 2012; Muttoni et al. 2013; Wu et al. 2017, 2020; Kent & Muttoni 2020). Therefore, this artefact must be corrected for before a sediment-based pole is included in such models, and the E/I method is widely used to this end.

Importantly, the E/I method critically relies on the assumption that the observed distribution of paleomagnetic directions provides, besides flattening, an accurate representation of PSV (Tauxe & Kent 2004; Tauxe et al. 2008). The method has been shown to successfully restore inclinations to values confirmed by independent datasets that were obtained using anisotropy-based inclination shallowing corrections or from lava-based datasets (e.g., Kent & Tauxe 2005; Tauxe et al. 2008; Bilardello et al. 2011; Huang et al. 2013, 2015). Nevertheless, there are several perceived pitfalls that could make it difficult to distinguish the scatter related to PSV from other sources of noise, e.g., resulting from syn-sedimentary rotations (Kodama 2012; Li & Kodama 2016; Meng et al. 2017), secondary magnetic overprints (Channell et al. 2010; Bilardello et al. 2018), misorientations of particles (Jezek et al. 2012; Bilardello 2013; Bilardello et al. 2013), partial averaging of PSV in a sample (Kodama 2012; Li & Kodama 2016), tectonic strain (Dallanave & Kirscher 2020), or measuring errors. Importantly, if the observed scatter in the paleomagnetic dataset does not accurately represent PSV, the E/I correction yields erroneous inclination shallowing corrections. However, if the E/I method indeed restores the correct primary inclination, then the assumption that the data scatter represents PSV is apparently a correct approximation. In that case, a reliable, inclination shallowing-corrected paleomagnetic pole is obtained. Despite the identification of potential pitfalls such as those listed above, there are currently no (quantitative) guidelines for the robust application of the E/I correction.

In this paper, we investigate under which circumstances the E/I method accurately corrects for inclination shallowing. As a basis for our analysis, we use an exceptionally large dataset of 1275 individual paleomagnetic directions from a >3 km-thick succession of red beds from the Gonjo Basin of eastern Tibet (Fig. 1), covering a magnetostratigraphically constrained ~27.5 Ma time interval (~69-41.5 Ma, Li et al. 2020a, b). Li et al. (2020a, b) showed that the sampled sedimentary sequence contains commonly quoted potential pitfalls for the E/I correction method (e.g., Kodama 2012; Li & Kodama 2016): intervals with syn-sedimentary vertical-axis rotations, large variations in sedimentation rate (of <10 to >25 cm/ka), intervals with low magnetic intensity, and intervals with stronger and weaker anisotropy of magnetic susceptibility (AMS) fabrics, amidst segments without such potential pitfalls. We assess how these parameters affect the results of the E/I correction. In addition, we test the influence of partial averaging of PSV, the application of commonly used cut-offs, and the number of directions used for the E/I

correction, by using both the Gonjo Basin dataset as well as synthetic datasets drawn from the TK03.GAD field model of Tauxe & Kent (2004). Based on our analysis, we propose a set of reliability criteria for the successful application of the E/I correction. We then use an extensive compilation of previously published E/I corrected datasets to evaluate whether our new criteria correctly classify datasets that were independently demonstrated to be reliable or unreliable. We discuss how the new criteria, which form an extension of the widely applied criteria as formulated by Meert et al. (2020), may be used to evaluate the reliability of sediment-based paleomagnetic poles. Finally, we discuss the implications of our analysis for the use and statistical treatment of paleomagnetic data from sedimentary rocks and the poles derived from those.

2. Background of the E/I method

Inclination shallowing was first recognized some 65 years ago by King (1955) and results either from depositional processes (e.g., Griffiths et al. 1960; Tauxe & Kent 1984; Tauxe et al. 2006) and/or post-depositional compaction (e.g., Anson & Kodama 1987; Kodama 1997). More recently, it was shown by both numerical and lab experiments that particle misalignment due to processes that occur in the water column may provide a significant contribution to shallow inclinations (e.g., Jezek et al. 2012; Bilardello 2013; Bilardello et al. 2013). Paleomagnetic directions that suffer from inclination shallowing are well-documented, for instance from Cenozoic clastic sedimentary rocks in Central Asia (e.g., Gilder et al. 2001; Tan et al. 2003; Dupont-Nivet et al. 2010; Li et al. 2013; Huang et al. 2013, 2015). The problem of inclination shallowing is not restricted to a specific type of sedimentary rocks, and has been reported for hematite-bearing red beds (e.g., Tauxe & Kent 1984; Garcés et al. 1996; Gilder et al. 2001; Tan & Kodama 2002; Kent & Tauxe 2005; Bilardello & Kodama 2010a), magnetite-bearing (marine) clastic sediments (e.g., Ali et al. 2003; Tamaki et al. 2008; van Hinsbergen et al. 2010; Huang et al. 2015) and carbonate rocks (e.g., Dallanave et al. 2009, 2012; Meijers et al. 2010a, b; Channell et al. 2010; Muttoni et al. 2013, 2018).

Presently, two different approaches are routinely used to correct for inclination shallowing: the paleomagnetic direction-based elongation/inclination (E/I) method (Tauxe & Kent 2004) and the sedimentary fabric-based methods that use magnetic anisotropy of susceptibility and remanence (e.g., Jackson et al. 1991; Kodama 1997, 2009; Tan & Kodama 2003). The anisotropy-based corrections focus on the assemblage of individual magnetic particles themselves, providing direct physical evidence for compaction-induced strain, and infer from this the magnitude of inclination shallowing. The E/I method, on the other hand, relies on the comparison of the observed distribution of paleomagnetic directions with the expected ratio of elongation versus mean inclination, as predicted by the TK03.GAD giant Gaussian process (GGP) model of the geomagnetic field (Tauxe & Kent, 2004). Although the two approaches have previously provided very similar results where they were both applied to the same sample collection (Tauxe et al. 2008; Bilardello et al. 2011; Huang et al. 2013, 2015; Tong et al. 2017; Westerweel et al. 2019), the E/I method has several important advantages: it requires no additional time-consuming (rock) magnetic experiments other than straightforward demagnetization, it is relatively easy to use, and it is routinely incorporated in paleomagnetic software packages (e.g., Tauxe et al. 2016; Koymans et al. 2016, 2020).

The E/I method forms one of the main applications of the TK03.GAD statistical

model of geomagnetic secular variation (Tauxe & Kent 2004). The TK03.GAD model parameters were configured to fit a compilation of paleomagnetic data by McElhinny & McFadden (1997), whereby each of the >2500 paleomagnetic directions (and associated VGPs) represented a multi-specimen average of a spot reading of the geomagnetic field obtained from a single lava flow or thin dyke that erupted during the last 5 million years. Although the compilation of McElhinny & McFadden (1997) is now outdated, the TK03.GAD model still provides an adequate fit with the more recent PSV10 database by Cromwell et al. (2018), at least for latitudes up to 70° (Brandt et al. 2020). Importantly, by using the TK03.GAD model, and therefore also the E/I method, one implicitly assumes that the past time-averaged geomagnetic field behaved similar to that of the last 5 Myr and closely resembles that of a geocentric axial dipole (GAD) field (Tauxe & Kent 2004; Tauxe 2005). The E/I method has been shown to produce robust results when applied to datasets derived from Mesozoic and Upper Paleozoic rocks (e.g., Kent & Tauxe 2005; Tauxe et al. 2008; Bilardello et al. 2011), suggesting that the technique may be reliably applied to rocks much older than 5 Ma.

The TK03.GAD model generates circularly symmetric distributions of virtual geomagnetic poles (VGPs), which give directional distributions that are elongated along the meridian, i.e., in the north-south direction. This elongation of paleomagnetic directions was already described more than 50 years ago and varies as a function of latitude (Creer et al. 1959; Creer 1962; Cox 1970; Tanaka 1999). The degree of elongation can be expressed by the elongation parameter E , which is defined as the ratio of the intermediate and minimum eigenvalues (τ_2/τ_3) of a tensor fit to the distribution of directions (Tauxe 1998). In the TK03.GAD model, the elongation decreases with increasing latitude (and hence increasing inclination) from about 3 at the equator to close to 1 at the poles (Tauxe & Kent 2004). The E/I method exploits this relationship between the elongation and inclination to both detect and correct for inclination shallowing.

Inclination shallowing processes like post-depositional compaction may result in a ‘flattening’ of the distribution of paleomagnetic directions from sedimentary rocks, reducing both the (north-south) elongation (E) and mean inclination (I). In principle, the E/I method assumes that any deviations from the elongation versus inclination curve, as predicted by the TK03.GAD model, are purely the result of inclination shallowing and that this shallowing follows the equation of King (1955): $\tan I_0 = f \tan I_p$, where f is the so-called flattening factor and I_0 and I_p are the observed and applied field inclination, respectively. This relationship indicates that the effect of inclination shallowing is the greatest for rocks formed at intermediate latitudes, whereby observed inclinations may be up to 25-30° too shallow (e.g., Kodama 2012). Notably, it has been shown that there is no characteristic flattening factor for either hematite- or magnetite-bearing sediments, and the magnitude of inclination shallowing may vary significantly between different sedimentary successions or lithologies (e.g., Kent & Tauxe, 2005; Bilardello & Kodama, 2010b; Kodama, 2012), indicating that the magnitude of flattening depends on the specific lithological and rock magnetic characteristics of the sampled rocks. We note, however, that the E/I method assumes that the paleomagnetic directions used for the correction have the same average flattening factor (Tauxe et al. 2008), regardless of the lithological variations throughout the sampled stratigraphy. For hematite-bearing rocks such as (most) red beds, obtained flattening factors are often within the range of $f=0.4-0.7$ (Kent & Tauxe 2005; Bilardello & Kodama 2010b; Kodama 2012).

The E/I method relies on the assumption that the scatter in the paleomagnetic dataset on which it is applied is representative of PSV. Based on Monte Carlo simulations, an estimated minimum number of 100 readings of the geomagnetic field are required to accurately represent secular variation and to provide a reliable inclination shallowing correction (Tauxe et al. 2003, 2008). The method is thus particularly well suited on large datasets, such as those derived from magnetostratigraphic studies. To correct for inclination shallowing, a stepwise unflattening of the distribution is applied by using different values for f , starting with $f=1$ (no flattening) and decreasing toward $f=0$ (complete flattening). The 'original' field inclination is then estimated by calculating the ratio of elongation versus mean inclination, until it matches the predicted E/I curve (Fig. 2; Tauxe & Kent 2004). Confidence bounds are subsequently obtained by performing a bootstrap resampling technique on the dataset, whereby the 95% confidence bounds are given by the interval of inclinations in which 95% percent of the (e.g., 1000) bootstrapped pseudo-samples lie (Fig. 2).

3. Dataset

We use the extensive paleomagnetic dataset from a high-resolution magnetostratigraphy study by Li et al. (2020a) from a section covering the 69–41.5 Ma time interval. Sampling was performed along a 3325 m thick section in the Gonjo Basin (30.85°N, 98.3°E, Fig. 1a), located in the eastern part of the Qiangtang terrane, eastern Tibet. The >200 km-long NW-SE-oriented Gonjo Basin is one of many thrust-bounded basins in central and eastern Tibet and is interpreted to have formed as a syn-contractual basin in the footwall of the Yangla fold-thrust system (Studnicki-Gizbert et al. 2008; Tang et al. 2017). The sedimentary strata of the basin are now exposed in an asymmetric syncline, and mainly consist of red-colored mudstones, sandstones, and rare conglomerates, reaching a total thickness of >3500 m (Studnicki-Gizbert et al. 2008; Tang et al. 2017).

Paleomagnetic samples were collected in the field with an average interval of ~2 m. Rock magnetic analysis suggested that hematite is the main carrier of magnetic remanence in the Gonjo Basin rocks, with a small contribution of magnetite for the bottom part of the section (Li et al. 2020a, b). After progressive stepwise thermal demagnetization up to a maximum temperature of 690 °C on 1766 paleomagnetic samples, a total of 1317 characteristic remanent magnetization (ChRM) directions were identified, of which 42 directions were determined using the great circle approach of McFadden & McElhinny (1988). Because great circle-determined directions are not direct measurements of the paleomagnetic field, but best-fit approximations, we exclude these from the dataset. This gives a total of 1275 paleomagnetic directions that were used for the analysis presented here (Fig. 1b; Table S1, Supplementary Materials A). A positive fold test (Tauxe & Watson 1994) and positive reversal test of the non-rotated intervals support a primary origin of the remanent magnetization for the sampled succession (see Li et al. 2020a), consistent with previous paleomagnetic studies of the same basin (Tong et al. 2017; Zhang et al. 2018).

Li et al. (2020a) showed that the sampled sedimentary sequence of the Gonjo Basin records two syn-depositional vertical-axis rotation phases: a ~10° counterclockwise rotation from 69 to 67 Ma and a ~30° clockwise rotation from 52 to ~48 Ma (Fig. 1c). In addition, correlation of the observed magnetozones with the geomagnetic polarity timescale revealed two phases with a higher sediment accumulation rate of ~20 cm/

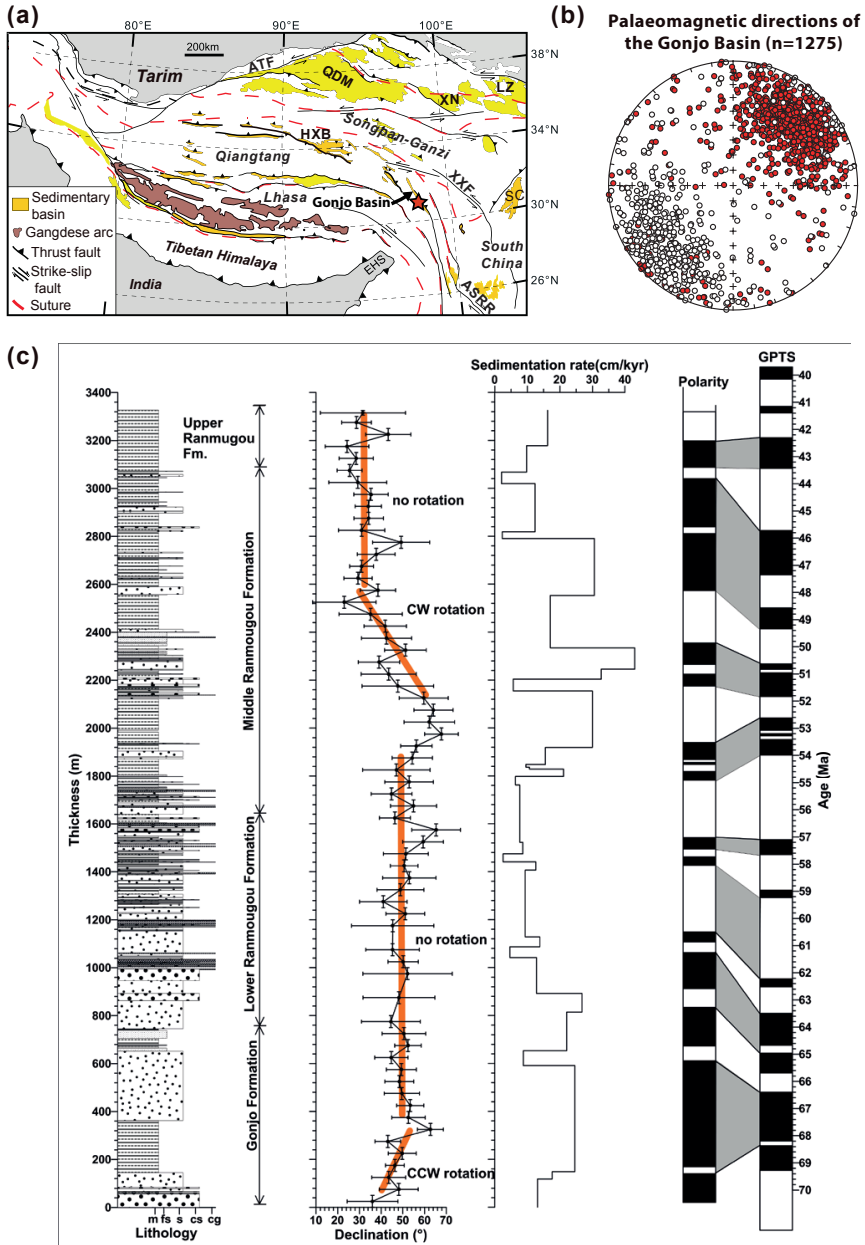


Fig. 1. (a) Simplified tectonic map of the Tibetan region after Li et al. (2020a). The location of the sampled section (30.85°N, 98.3°E) is indicated by a red star. For more details on the basins and faults, please see Li et al. (2020a). (b) All 1275 palaeomagnetic directions of the Gonjo Basin from Li et al. (2020a, b) that are used in this study. (c) Comparison of lithology, paleomagnetic declination and sedimentation rate against stratigraphic level in the Gonjo Basin section, modified after Li et al. (2020a, b). The interpreted magnetozones and their correlation with the geomagnetic polarity timescale is also shown. The orange curve shows the vertical-axis rotations identified by Li et al. (2020a).

kyr, at 69-64 Ma and 52-48 Ma, amidst rates of 7-8 cm/kyr for the other time intervals (Fig. 1c). These phases with rapid sedimentation are largely coeval with the observed rotations, leading Li et al (2020a) to suggest that they reflect two distinct pulses of crustal shortening. This interpretation is supported by a subsequent study on the anisotropy of magnetic susceptibility (AMS) of the same sedimentary succession, which showed the presence of a 'pencil structure' fabric (e.g., Parés et al. 1999) in the ~52-41.5 Ma interval of the section, indicating an increase in tectonic strain at ~52 Ma (Li et al. 2020b). Here, we make extensive use of the detailed information on the sampled sedimentary succession of the Gonjo Basin provided by these previous studies, and we refer the reader to Li et al. (2020a, b) for details on demagnetization, rock magnetism, AMS and field tests.

4. Methods

We perform a series of experiments to test under which circumstances the E/I method produces robust and reproducible results, and how the technique may be used to assess whether PSV is adequately sampled by the paleomagnetic dataset. We assess how the results may be affected by vertical-axis rotations, variations in sedimentation rate, the presence of non-PSV-induced scatter, the effect of cut-offs, and the number of directions used for the correction. In each experiment described below, we apply the E/I correction for inclination shallowing (Tauxe & Kent 2004) to collections of paleomagnetic directions selected from the total dataset of 1275 directions. The size of each collection depends on the question addressed, but sample sets were drawn in consecutive stratigraphic order. In addition, we use synthetic datasets of directions generated from the TK03.GAD model of Tauxe & Kent (2004). We developed a number of Python codes to perform our calculations and to visualize our results, whereby we made extensive use of several key functions and programs from the freely available paleomagnetic software package PmagPy (Tauxe et al. 2016). In particular, we used the 'find_ei' and 'tk03' programs from this package to perform the E/I correction and to generate synthetic data from the TK03.GAD model, respectively. The E/I correction uses the principal direction of the data, corresponding to the eigenvector associated with the maximum eigenvalue of a tensor fit to the distribution of paleomagnetic directions (Tauxe & Kent 2004; Tauxe 2005). For consistency, we express the average paleomagnetic direction of each collection of paleomagnetic directions by the principal direction, rather than the Fisher (1953) mean direction. It has long been shown that Fisher (1953) statistics should not be applied to paleomagnetic directions (e.g., Creer et al. 1959; Cox 1970; Tauxe & Kent 2004), but may be applied to VGPs instead (Deenen et al. 2011). In the following, we only use Fisher (1953) statistics for the calculation of two commonly used statistical parameters related to the observed distribution of VGPs: the radius of the 95% confidence circle about the mean (A_{95}) and the Fisher precision parameter (K).

As a reference to test the E/I corrected inclination values against, we use three independent estimates of the inclination (and paleolatitude) for (the eastern part of) the Qiangtang terrane (Fig. 3). First, we use the result of the anisotropy-based inclination shallowing correction method of Hodych & Buchan (1994) performed by Tong et al. (2017) on Gonjo Basin sediments, revealing a corrected inclination of 41.6° ($\alpha_{95}=3.2^\circ$), corresponding to a paleolatitude of $23.9 \pm 1.9^\circ$. They obtained similar values by applying the E/I method to separate datasets from two limbs of a large fold, yielding corrected inclinations of 40.3° ($34.0\text{-}45.3^\circ$) and 40.4° ($33.5\text{-}46.7^\circ$), respectively. The age

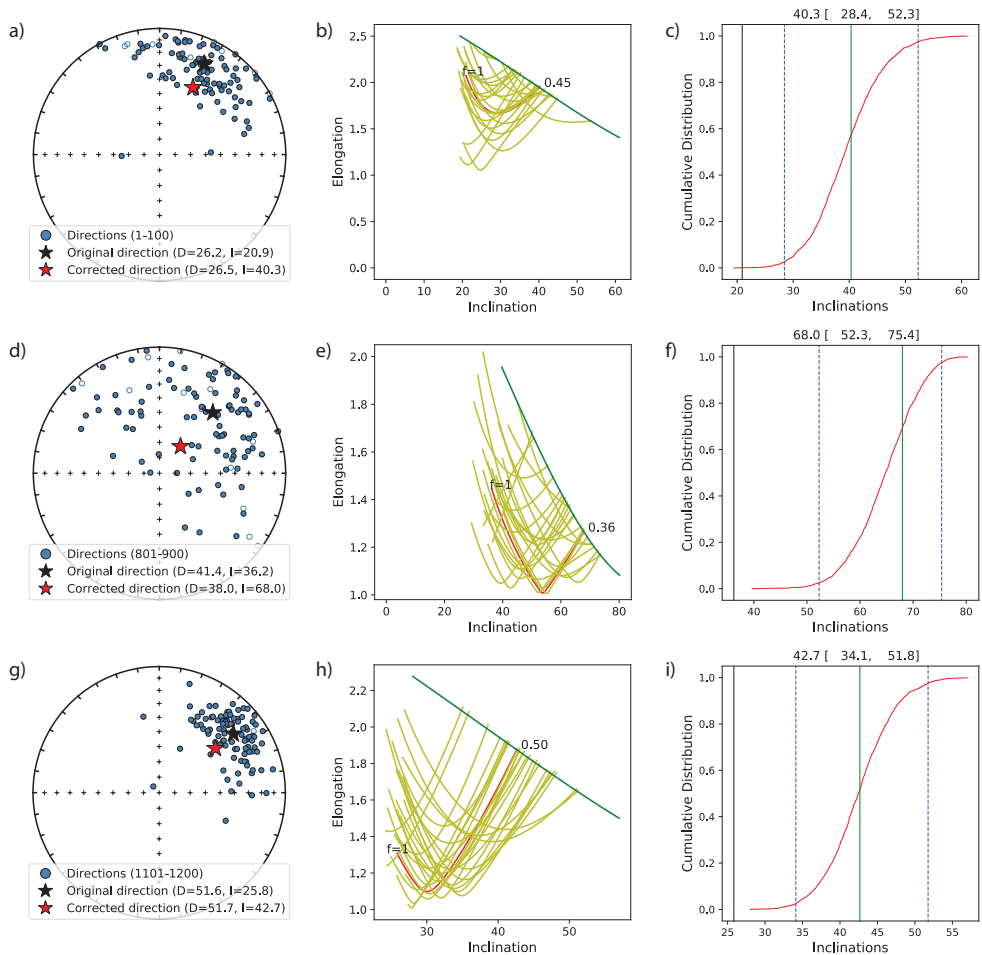


Fig. 2. Examples of three groups of 100 successive paleomagnetic directions from the Gonjo Basin dataset. The stereographic plots (**a**, **d**, **g**) show the uncorrected paleomagnetic directions (converted to normal polarity, blue circles), the principal direction (black star) and the E/I corrected mean direction (red star) for the three different groups. (**b**, **e**, **h**) Application of the E/I method to the directional dataset. The red curves show the elongation versus inclination upon stepwise unflattening of the dataset by gradually decreasing the flattening factor (f). The dark green curve is the elongation versus inclination curve predicted by the TK03.GAD model (Tauxe & Kent 2004). The intersection between these two curves gives the flattening factor used in the correction for inclination shallowing, as indicated in the plots. The light green curves show the results of stepwise unflattening of 25 bootstrap pseudo-samples. (**c**, **f**, **i**) Plots of the cumulative distribution of the corrected inclination as calculated in 2000 bootstrap runs (red). The black and green vertical lines show the uncorrected and corrected inclination, respectively. Confidence bounds that contain 95% of the bootstrap results are shown as two dashed, blue lines.

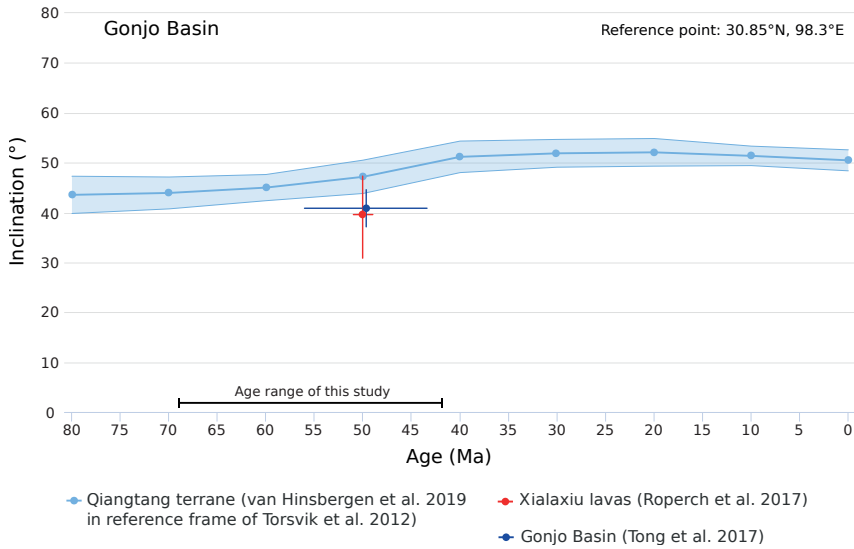


Fig. 3. Estimated inclination for the eastern Qiangtang terrane at reference coordinate 30.85°N, 98.3°E based on previously published paleomagnetic results: the 51-49 Ma lavas of the Xialaxiu area (Roperch et al. (2017) and the inclination shallowing-corrected result for the Gonjo Basin red beds (Tong et al., 2017), which are shown in red and blue, respectively. The expected inclination for the Gonjo Basin based on the kinematic reconstruction of the Tibetan region by van Hinsbergen et al. (2019), placed in the paleomagnetic reference frame of Torsvik et al. (2012), is depicted by the light blue curve (with confidence region). This figure was created using paleomagnetism.org (Koymans et al. 2016, 2020).

of the sampled succession was initially estimated as 43.2-56.0 Ma by Tong et al. (2017), but is likely younger than the end of the $\sim 30^\circ$ clockwise rotation (~ 48 Ma), based on a comparison of the observed mean declination of $\sim 35^\circ$ with the declination curve from Li et al. (2020a). Second, Roperch et al. (2017) reported a mean inclination of 41.6° ($\alpha_{95}=8.0^\circ$), corresponding to an in situ paleolatitude of $23.9 \pm 6.5^\circ$, from 21 sites in 49-51 Ma lavas of the Xialaxiu area, located ~ 250 km to the north-northwest of the Gonjo basin. Third, we use estimates of the inclination of the (eastern) Qiangtang terrane as predicted by kinematic restorations of eastern Tibet based on structural geological constraints on intra-Tibetan shortening and extrusion (van Hinsbergen et al. 2019) placed in the global paleomagnetic reference frame of Torsvik et al. (2012) (Fig. 3). We note that the observed inclination values of Tong et al. (2017) and Roperch et al. (2017) are ~ 5 - 8° lower than the expected values based on the global APWP of Torsvik et al. (2012), in line with previous reports of persistently low inclinations for East Asia for the 50-20 Ma time interval (e.g., Cogné et al., 1999, 2013, Hankard et al. 2007; Dupont-Nivet al. 2010). For the ~ 41.5 -50 Ma time interval, we therefore use the results obtained by Tong et al. (2017) and Roperch et al. (2017) as the primary reference against which we compare our corrected inclinations.

5. Results

5.1. Reproducibility of the results of the E/I method

First, we test the reproducibility of the E/I method by applying the correction to groups

of 100 successive paleomagnetic directions selected from the total dataset (see examples in Fig. 2). We select these directions by using a sliding window with an interval of 25 directions. By doing so, we obtain 48 groups of 100 directions, and compute the inclination before and after E/I correction (Fig. 4). The uncorrected group-mean inclinations mostly fall within the range of 20-30°, with some outliers of >30° (Fig. 4a). These are significantly (~10-20°) lower than the primary inclinations estimated by Tong et al. (2017) and Roperch et al. (2017), and the predicted inclination for the eastern Qiangtang terrane (section 4; Fig. 3). The E/I correction yields mean inclinations that are generally ~10-25° higher than the observed inclinations. The associated flattening factors are generally between $f=0.40$ to $f=0.65$ (Fig. 4b), with a mean of $f=0.50$ and a standard deviation of 0.10, consistent with previously obtained values for hematite-bearing rocks (Kent & Tauxe 2005; Bilardello & Kodama 2010b; Kodama 2012). The median uncorrected and corrected inclination are 27.0° and 45.0°, respectively, and approximately 60% of the corrected inclinations fall within 5 degrees from this median value. The results for the youngest part of the succession, with an age of <50 Ma, are in agreement with the estimated primary inclination of 41.6° from Tong et al. (2017) and Roperch et al. (2017) and are thus somewhat lower than predicted by the reference APWP of Torsvik et al. (2012). However, for seven groups the E/I correction yields anomalously high inclinations of >55°, some 25-35° higher than the original group-mean inclinations, and entirely inconsistent with independent estimates or tectonic reconstructions (Fig. 4a). In the following, we evaluate to what extent selected potential pitfalls may explain these mismatches.

5.2. Syn-sedimentary rotations

Vertical-axis rotation phases that occur during sediment deposition leads to a wider spread of paleomagnetic declinations than caused by paleosecular variation alone, and thus affects the elongation of the distribution of directions (e.g., Kodama 2012; Tong et al. 2015; Meng et al. 2017; Zhang et al. 2018). To quantify the effect of syn-sedimentary rotations, we created datasets of paleomagnetic directions generated with the TK03. GAD field model. We used 200 directions to obtain more precise corrections compared to when using the required minimum of 100 directions, although we note that the latter produces very similar results. We first simulated inclination shallowing by applying a flattening factor of 0.6 to the synthetic data, after which we rotated half of the directions with a predefined rotation angle, followed by the application of the E/I method to retrieve the original inclination. Fig. 5 shows that increased elongation caused by the vertical-axis rotation leads to an overcorrection of the original inclination. Unsurprisingly, this overcorrection increases with increasing rotation angle. We note that the results are independent of the applied flattening factor, however. The simulations predict an overestimation of the original inclination of <3° for vertical-axis rotations up to 10°. Also, the magnitude of the rotation-induced overcorrection is dependent on the latitude (and thus, inclination) for which the synthetic data were generated. The largest effect of the simulated syn-sedimentary rotations is observed for the latitude range of ~10-30° (Fig. 5). For low latitudes, overcorrections of >10° may be expected for rotations >20°. For higher latitudes (>50°), the effects of vertical-axis rotations are relatively limited.

Within our dataset, most groups in the interval that recorded the ~30° clockwise rotation phase (~52-48 Ma; Figs 4a and c) do not yield a significant overestimation of the

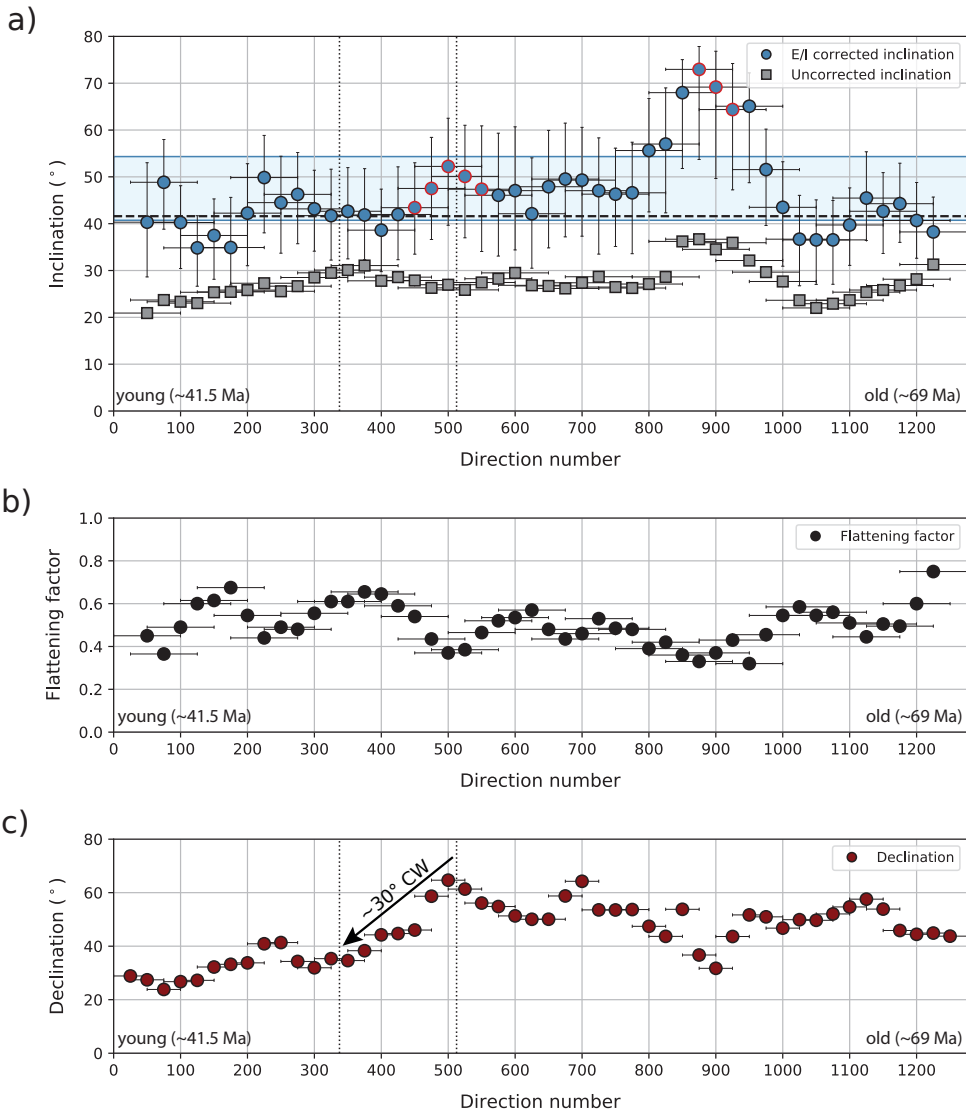


Fig. 4. (a) Uncorrected (grey squares) and E/I corrected (blue circles) inclinations for groups of directions of the Gonjo Basin dataset. Circles with a red border denote groups with a negative bootstrap reversal test. The E/I method of Tauxe & Kent (2004) is applied to groups of 100 successive directions, using a sliding window with a step of 25. Note that the age of the sampled rocks increases with increasing direction number. As a reference, the inclination of 41.6° obtained from an anisotropy-based inclination shallowing correction by Tong et al. (2017) is shown by the dashed black line. The light blue band shows the range of expected inclinations as predicted by the model of van Hinsbergen et al. (2019) placed in the reference frame of Torsvik et al. (2012). (b) Flattening factors per group of 100 directions as determined by the E/I correction. (c) Mean declination of 50 successive directions calculated using a sliding window with an interval of 25. The $\sim 30^\circ$ clockwise rotation identified by Li et al. (2020a) is highlighted by the black arrow.

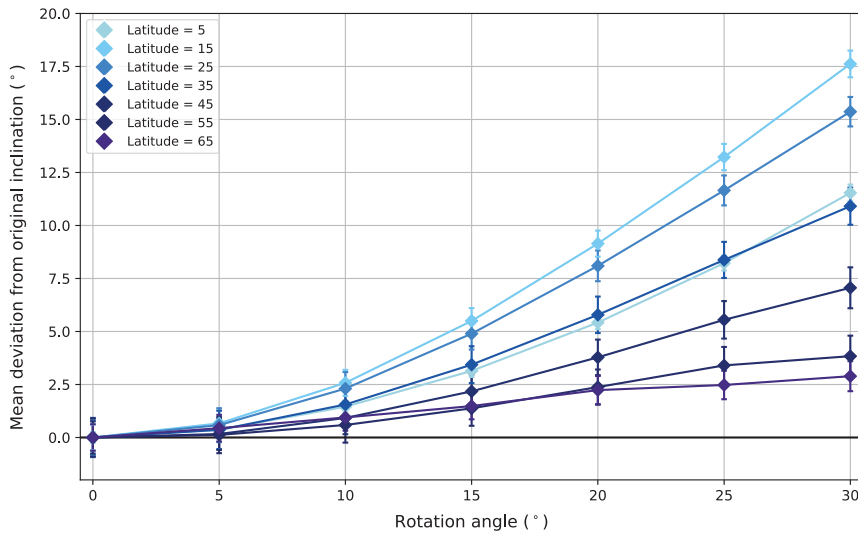


Fig. 5. Effect of vertical-axis rotations on the E/I correction. The curves show the average difference between the corrected and original inclination, i.e., prior to flattening, versus the rotation angle. The average difference is calculated from 100 runs whereby the 200 directions generated from the TK03. GAD statistical model are flattened with a flattening factor of 0.6, followed by a rotation of half of the dataset with the specified angle and by the application of the E/I correction. Each curve corresponds to the specific latitude for which the directions are initially simulated with the TK03.GAD model. Error bars represent two standard error of the mean.

initial inclination, although it should be noted that the rotation phase covers an interval of ~ 160 directions: collections of 100 samples in this case thus only record part of the rotation. Only the groups that consist mostly of directions numbered 450 to 500, the interval of successive samples for which we observe a change in declination of $\sim 20^\circ$, give an overcorrection of $\sim 5\text{-}10^\circ$. A larger effect is, however, observed for datasets that cover the entire rotation phase. In section 5.6, where we will test the effect of increasing N , we will return to this topic. We note that the $\sim 52\text{-}48$ Ma deformation phase also coincides with the development of a ‘pencil structure’ AMS fabric, which appears in the sediments of ~ 52 Ma and younger (Li et al. 2020b). The presence of a (strong) tectonic fabric may affect the elongation of the directional distribution, as recently shown by Dallanave and Kirscher (2020), and thus also contribute to the observed overestimations of the primary inclination for this interval. However, the ‘pencil structure’ fabric is also observed for the $\sim 48\text{-}41.5$ Ma interval (Li et al. 2020b), which yielded corrected inclinations that are consistent with independent results (Fig. 4a), suggesting that the influence of the tectonic fabric on our results is limited. Finally, we find that the $\sim 10^\circ$ counterclockwise rotation recorded by the lowermost part of the sampled sequence ($\sim 69\text{-}67$ Ma) does not seem to significantly affect the results of the E/I method, in line with the results of the simulations described above.

As a third experiment, we tested the effect of a vertical-axis rotation by using the dataset obtained by Gilder et al. (2001) of $N=222$ paleomagnetic directions from Oligo-Miocene red beds of the Subei area (western China), which was used for the original E/I

correction by Tauxe & Kent (2004). Gilder et al. (2001) found that the upper part of the section may have rotated $\sim 15^\circ$ relative to the lower part. Not correcting for this rotation yielded a minor overcorrection in the inclination of 1.2° (Fig. S1, Supplementary Materials B). Because the rotation of 15° is an estimate with an uncertainty, the magnitude of which depends on the number of samples averaged, and the interpretation of which data are pre- and post-rotation, the rotation correction may add more uncertainty than that it solves.

Overall, these results demonstrate that the effect of vertical-axis rotations of up to 15° on the results of the E/I correction are often limited ($<3^\circ$ for most latitudes, and up to 5° at latitudes of $10\text{--}30^\circ$). Also, we note that the observed outliers in the results of the E/I method applied to 100 directions of the Gonjo Basin dataset (Figs 4a and c) cannot be explained by the effects of vertical-axis rotations. Instead, significant overcorrections of $>5^\circ$ of the primary inclination are only expected for vertical-axis rotations of $>15^\circ$.

5.3. Sedimentation rate and averaging of PSV

The sedimentation rate controls, for a large part, the amount of time and thus PSV that is recorded in a single paleomagnetic sample. Decreasing sedimentation rates could lead to an increase in the amount of averaging of PSV that occurs within each sample, reducing the scatter of paleomagnetic directions/VGPs. Although it is not directly evident that this also affects the elongation of the distribution, it has been suggested that low sedimentation rates may cause an underestimation of the primary inclination obtained from the E/I correction (e.g., Kodama 2012; Li & Kodama 2016). The Gonjo Basin section contains an order of magnitude variations in sedimentation rate (Fig. 1c and 6) from >20 cm/kyr to as low as 2–10 cm/kyr (Li et al., 2020a). We note, however, that the calculated sedimentation rates correspond to an average rate for a stratigraphic interval of tens to hundreds of meters, and the true accumulation rate for an individual bed may be highly variable (e.g., Opdyke & Channell 1996). Nevertheless, our results reveal no correlation between sedimentation rate and the E/I corrected inclination (Fig. 6). The intervals with relatively low sedimentation rates, at $\sim 900\text{--}1800\text{m}$ and $\sim 2800\text{--}3325\text{m}$, do not correlate with anomalously low corrected inclinations. Instead, some of the lowest (corrected) inclination values correspond to an interval ($\sim 400\text{--}600\text{m}$) with a high sedimentation rate of >20 cm/kyr. In addition, we observe no correlation between sedimentation rate and the observed scatter of paleomagnetic directions/VGPs, as indicated by A95 and K (Fig. 6). The intervals with low(er) sedimentation rate do not correlate with reduced scatter, suggesting that the averaging of PSV is not significantly increased compared to intervals with high(er) sedimentation rate.

To assess how the averaging of PSV may influence the observed distribution of directions (or VGPs), we applied the E/I correction to sets of 100 artificially created ‘sites’, whereby each site is the average of 3 successive paleomagnetic directions from the Gonjo Basin dataset (Figs 7a and b). The corrected inclinations for collections of 100 of such ‘sites’ are, on average, only 1.1° (median of 1.8° and standard deviation of 3.5°) lower than the corrected inclinations obtained from the 300 individual directions that were used to create the sites (Fig. 7b). In addition, we applied the E/I correction to sets of 100 ‘sites’ of $N=3, 5$ and 10 directions generated with the TK03.GAD model, after we applied a flattening factor of $f=0.6$ to the site-mean directions (see example in Fig. 7c). Again, the effect of averaging multiple directions is limited: the corrected inclinations calculated using the sites are, on average, $\sim 2^\circ$ lower than those whereby the E/I correction is applied

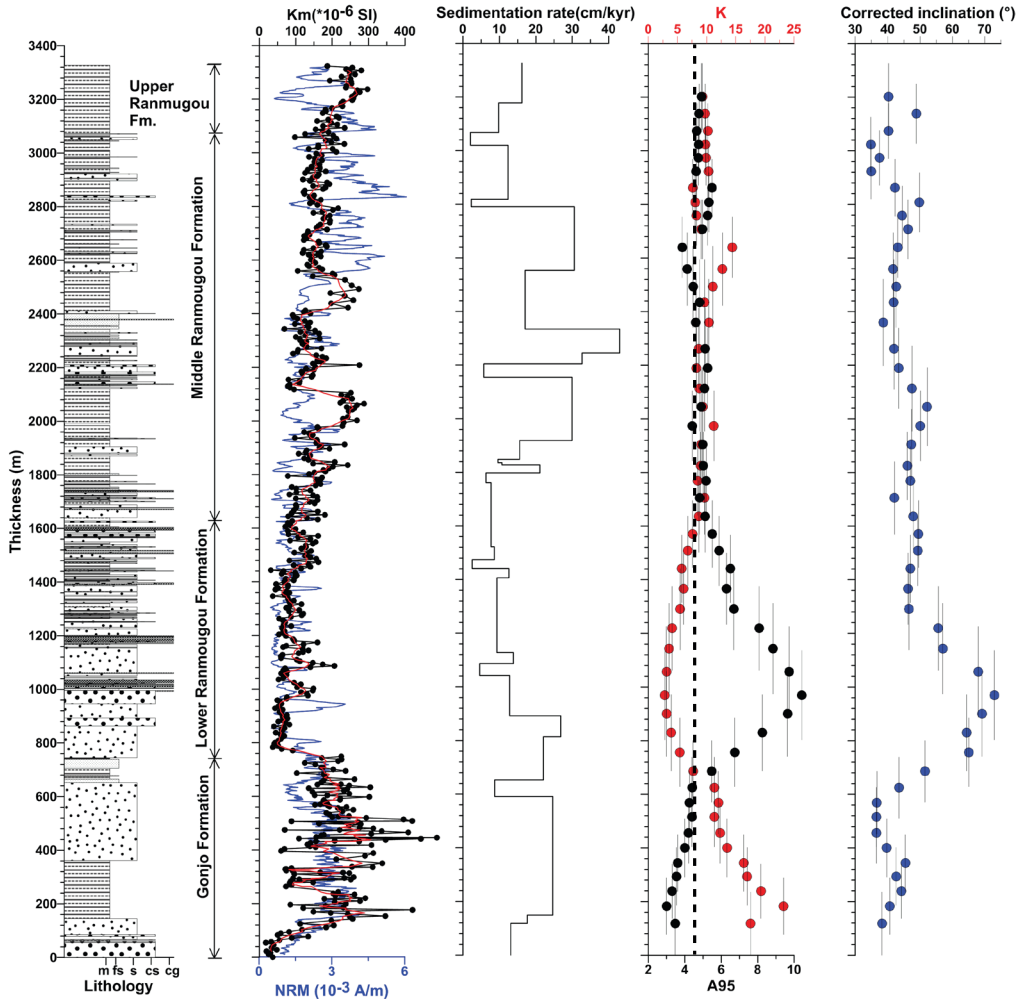


Fig. 6. Comparison of (a) lithology, (b) mean magnetic susceptibility (Km, black) and intensity of the natural remanent magnetisation (NRM, blue) and (c) sedimentation rate against stratigraphic level in the Gonjo Basin section, after Li et al. (2020a, b). (d) A_{95} (black circles) and K (red circles) calculated from the distribution of VGPs obtained from 100 successive paleomagnetic directions of the Gonjo Basin dataset. The dashed, black line shows the A_{95max} calculated for $N=100$, following the reliability criterion of Deenen et al. (2011). (e) E/I corrected inclinations per group of 100 successive directions, using a sliding window with a step of 25, as also plotted in Fig. 4a.

to the sets of $N=300$, 500 and 1000 individual directions (see Figs 7c and d). The increased elongation as a result of inclination shallowing processes is thus not significantly reduced by partial averaging of PSV. This demonstrates that although partial averaging of PSV may indeed result in a slight underestimation of the primary inclination, its effect is small, and the E/I method still provides accurate estimates of the primary inclination.

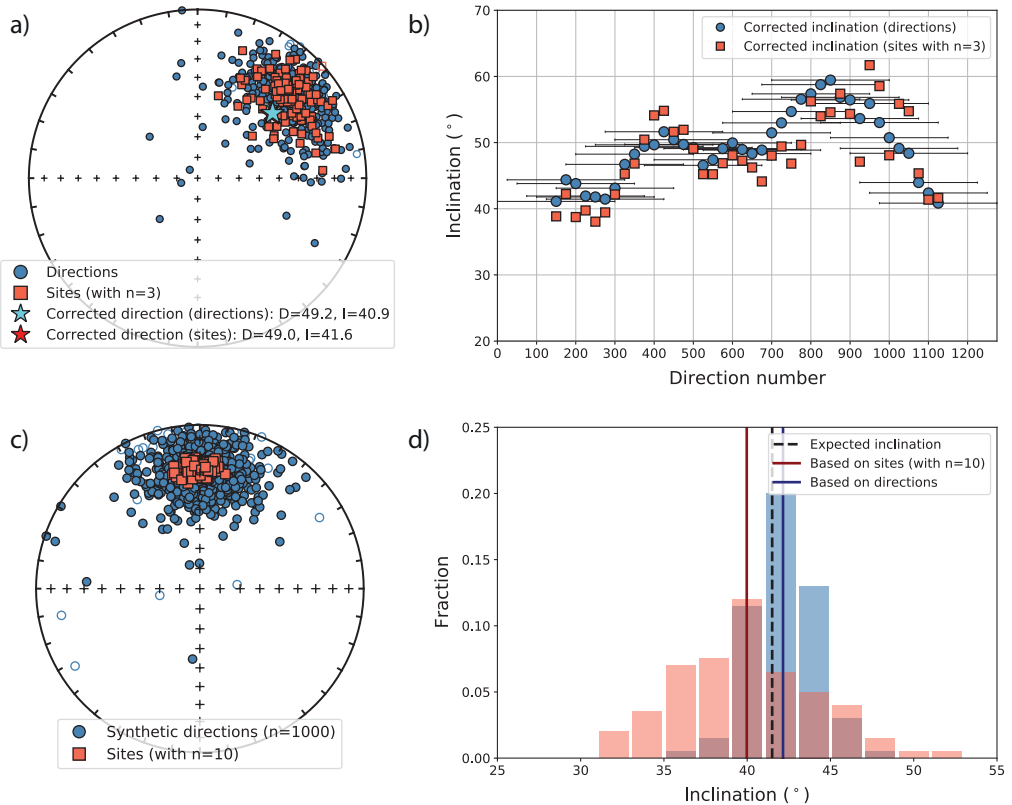


Fig. 7. (a) Stereographic plot of 300 paleomagnetic directions from the Gonjo Basin dataset, converted to normal polarity (directions numbered 975-1275, blue circles). 100 'sites' calculated by averaging three successive directions are shown by orange squares. The E/I corrected direction based on the individual directions and 'sites' are indicated by the cyan and red stars, respectively. (b) E/I corrected inclinations calculated from groups of 300 individual directions of the Gonjo Basin dataset (blue circles) and from 'sites' based on three successive directions (orange squares). (c) Stereographic plot of 1000 synthetic directions generated with the TK03.GAD statistical model (Tauxe & Kent 2004) for a latitude of 25° (blue circles). The directions are flattened using a flattening factor of $f=0.6$ (blue circles). Artificial 'sites' based on 10 directions are plotted as orange squares. (d) Histogram of the E/I corrected inclinations of 100 simulated datasets of 1000 individual directions (blue) and 100 'sites' (of $N=10$ directions). The mean inclinations are depicted by the vertical blue and red lines. The expected inclination (for a latitude of 25°) is plotted by the dashed, black line.

5.4. Scatter of directions unrelated to PSV

The E/I method assumes that the scatter of directions is exclusively due to geomagnetic field behavior (PSV and geomagnetic excursions), whereby each direction is considered a spot reading ('site') of the past geomagnetic field (e.g., Tauxe et al. 2008). Also, it assumes that the distribution of directions was solely distorted by inclination shallowing, following the relation of King (1955) (section 2). To test whether non-PSV-induced scatter affects our results of the E/I method, we first apply the bootstrap reversal test of Tauxe (2010) to the 28 (out of 48) groups of 100 directions which include at least 20 normal or

reverse polarity directions. Even though a reversal test for the two non-rotated intervals was positive (Li et al. 2020a), we obtain a negative result for eight of the 28 groups (highlighted in Fig. 4a). Four of these groups (partly) cover the interval that recorded the $\sim 30^\circ$ clockwise rotation, and three groups yielded very high corrected inclinations of $>60^\circ$. The latter groups correspond to the stratigraphic intervals from which most great circle directions were determined, suggesting that some magnetic overprints may not be entirely removed. The failed reversal tests of these groups show that the normal and reverse polarity directions are not antipodal, and thus indicate that for some intervals of the Gonjo Basin dataset the directional distribution is likely affected by a significant contribution of non-PSV-induced scatter, for instance related to unremoved magnetic overprints or rotations.

To further evaluate this, we use the reliability criterion developed by Deenen et al. (2011) which informs whether the observed distribution of paleomagnetic data may be explained by PSV. They defined an N-dependent A_{95} envelope, whereby an observed distribution of VGPs having an A_{95} that falls inside this envelope, between the $A_{95,\min}$ and $A_{95,\max}$, may in principle be straightforwardly explained by PSV alone. Values higher than $A_{95,\max}$ likely include sources of scatter other than PSV, whereas values below $A_{95,\min}$ indicate an underrepresentation of PSV.

We use this reliability envelope to evaluate whether the principal assumption that the scatter represents solely geomagnetic field behavior, is met. For $N=100$ directions, the $A_{95,\min}$ and $A_{95,\max}$ are 1.90° and 4.51° , respectively. We calculated the A_{95} from the VGPs that correspond to the uncorrected directions. We note that this is a rather lenient approach, as the A_{95} calculated before the E/I correction is, on average, 0.20° (standard deviation of 0.19°) lower than calculated after the correction (Fig. S2, Supplementary Materials B). A total of 13 out of the 48 groups has an A_{95} value - calculated prior to the E/I correction - that falls within the A_{95} envelope defined by Deenen et al. (2011), including the lowermost part of the sampled sequence (Fig. 6; Fig. S2, Supplementary Materials B). For these groups, there is no statistical ground to suspect a significant contribution of scatter from sources other than PSV. The majority of groups have an A_{95} that falls just above ($<1^\circ$) the $A_{95,\max}$ value, suggesting a small contribution of non-PSV-induced scatter. However, the groups that include directions from the interval ~ 750 - 1250 m have an A_{95} that is $>2^\circ$ higher than the $A_{95,\max}$, with values up to $\sim 10^\circ$. Importantly, this is the interval for which the E/I correction yielded anomalously high inclinations of $>55^\circ$ (section 5.1).

The high A_{95} values for this interval suggest that there is a large contribution of non-PSV-induced scatter affecting the distribution of directions (and associated VGPs). The large scatter is equivalent to very low K values of ~ 3 - 5 for these groups (Fig. 6). Despite this clear evidence for a large contribution of non-PSV-induced scatter in these subsets of directions, only 3 of these 8 groups do not pass the reversal test. In other words, a reversal test alone is insufficient to determine whether the scatter in a dataset is predominantly the result of PSV, and the Deenen et al. (2011) criterion appears to provide a better assessment (see also Meert et al. 2020).

The interval of large scatter correlates with an interval of relatively coarse-grained sediments (Fig. 6b), which may be more affected by random misorientation of the (large) grains (e.g., Tauxe 2006) and are more prone to weathering and subsequent remagnetization/overprinting. Notably, both a relatively low intensity of the natural remanent magnetization (NRM) and low magnetic susceptibility is observed for this

interval (Fig. 6b). These factors may contribute to a less efficient acquisition of the NRM, and result in an additional source of scatter, unrelated to PSV, to the distribution of directions. In cases where the non-PSV-induced scatter is significant, as indicated by a high A_{95} value, the E/I correction may thus give a large overestimation of the primary inclination.

5.5. Cut-offs

It is common practice in paleomagnetism to apply a cut-off to remove outliers that may distort the distribution of directions. Such cut-offs remove directions from the dataset that do not represent PSV but result from e.g., orientation errors or lightning strikes instead. The cut-offs thus aim to make the dataset more representative of PSV. However, applying cut-offs also removes transitional or excursions directions from the dataset that are representative of geomagnetic field behavior and such directions are included in most field models like TK03.GAD (Tauxe & Kent 2004; Tauxe et al. 2008). For this reason, Tauxe et al. (2008) argue that cut-offs should preferably not be used when comparing datasets with field models such as TK03.GAD. Despite this, however, cut-offs have regularly been applied prior to the E/I correction (e.g., Gong et al. 2008; Meijers et al. 2010a, b; Dupont-Nivet et al. 2010; Huang et al. 2015; Muttoni et al. 2018; Milanese et al. 2019). Here, we investigate the influence of two commonly used cut-offs on the E/I correction: a fixed 45° cut-off (e.g., Johnson et al. 2008) and the variable Vandamme (1994) cut-off. For the Vandamme (1994) cut-off, the cut-off angle is a function of the obtained initial scatter of the dataset and increases with larger scatter.

First, we applied both cut-offs to datasets of synthetic paleomagnetic directions generated with the TK03.GAD field model. In these synthetic datasets, all outliers removed by the cut-off are an integral part of geomagnetic field behavior and should thus not be corrected for when applying the E/I method (Tauxe & Kent 2004). We use the cut-offs on datasets of 200 synthetic directions that were previously flattened with a flattening factor of 0.6. Subsequently, we apply the E/I correction to estimate the original inclination. Our tests show that when no cut-off is applied the original mean inclination of the synthetic dataset is accurately approximated by the E/I method, particularly for the latitude range of 0–45°, whereas the original inclination for higher latitudes is somewhat underestimated, by ~1.5–2° (Fig. 8a). However, the application of a cut-off, either the fixed 45° or the Vandamme (1994) cut-off, leads to a systematic underestimation of the inclination, particularly for mid-latitudes of 30–40°. The fixed 45° cut-off yields inclinations that are ~1.5–3° lower than when no cut-off is applied, for latitudes of 15–60° (Fig. 8a). For this latitude range, the application of the Vandamme (1994) cut-off yields inclinations that are some 3–5° lower compared to when no cut-off is applied. This clearly argues for the application of the E/I correction without a cut-off.

Second, we applied both cut-offs to the 48 groups of 100 directions of the Gonjo Basin dataset (Fig. 8b). In most cases, the E/I method gives lower inclinations when a cut-off is applied. The difference between the corrected inclination calculated with and without a cut-off vary strongly, depending on the number of directions that fall outside of the cut-off angle and are excluded. Notably, the overcorrected inclination values from the ~750–1250m interval that have A_{95} values well above $A_{95,max}$ are corrected to much lower values of 31–43° when the fixed 45° cut-off is applied (Fig. 8b). The variable Vandamme (1994) cut-off does not lead to an improved fit because the large scatter of directions greatly

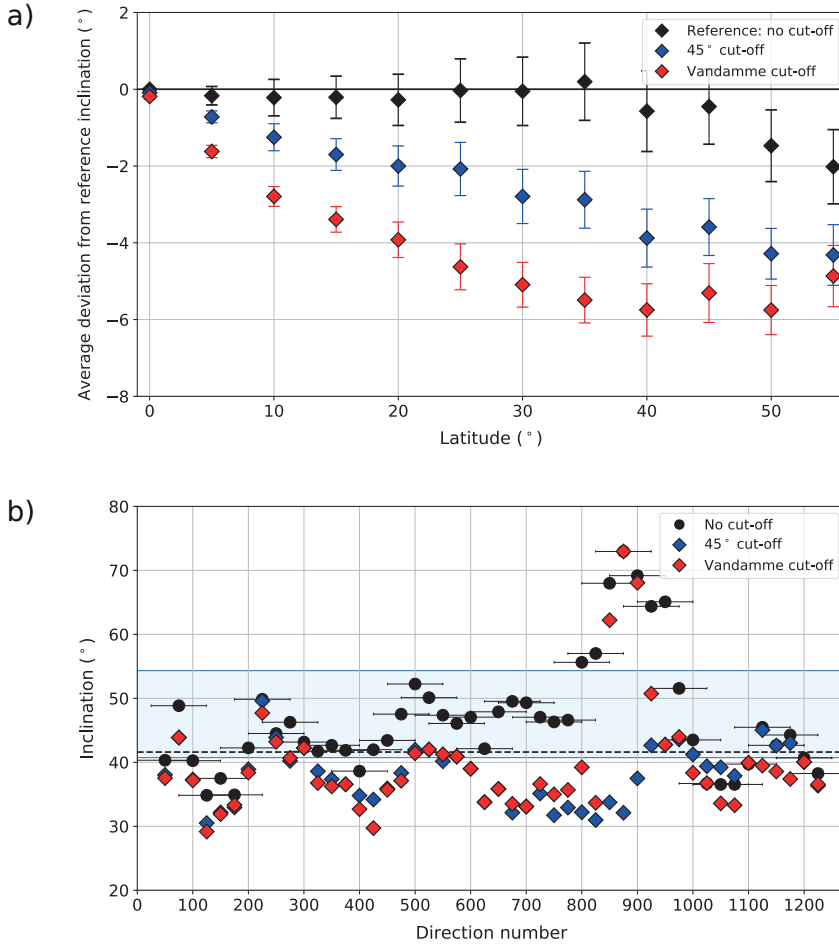


Fig. 8. (a) Effect of cut-offs on the E/I correction. Each diamond represents the average deviation from the expected inclination (calculated with the dipole formula for the given latitude) of 100 E/I corrected datasets of 200 directions generated with TK03.GAD. Each dataset is flattened with a flattening factor of $f=0.6$ followed by the application of the cut-off and the correction. Results for no cut-off, the fixed 45° cut-off and Vandamme (1994) cut-off are shown by in black, blue and red, respectively. Error bars represent two standard error of the mean. **(b)** E/I corrected inclinations for groups of 100 directions of the Gonjo Basin dataset, calculated without cut-off (black circles, same as in Fig. 4a) and with a fixed 45° cut-off (blue diamonds) or Vandamme (1994) cut-off (red diamonds) applied prior to the correction. Reference data are plotted as in Fig. 4a.

increases the (variable) cut-off angle for these cases. Apart from this interval with the overcorrection, the median corrected inclination is 38.5° when the 45° cut-off is applied before the E/I correction and 36.9° for the Vandamme (1994) cut-off. This is much lower than the median value of 43.3° based on the results for which no cut-off was applied, as well as the reference inclinations, indicating that the application of either cut-off may lead

to systematically and significantly lower estimates of the original inclination. Only for some, but not all groups that sample the interval showing a large dispersion of directions, likely as a result of non-PSV-induced scatter, the application of the 45° cut-off leads to an improved estimate of the primary inclination.

5.6. Number of directions

As final test, we evaluate the effect of the number of directions used on the results of the E/I correction. To this end, we applied the E/I method to collections of 150, 200 and 300 directions, drawn in consecutive stratigraphic order, again using a sliding window with an interval of 25 directions. As expected, the variation in the corrected inclinations decreases with a larger number of directions (Fig. 9). Also, using larger N results in a lower variation in the obtained flattening factors, particularly when 200 or 300 directions are used, whereby $f=0.40-0.55$ for the large majority of groups. However, increasing the number of directions (N) leads to an increase in the overcorrection of the inclination for the groups that record (part of) the ~30° clockwise rotation phase. Collections with 200 or 300 directions yield inclinations that are up to 8-10° higher than when 100 directions are used (Figs 9b and c). This is readily explained: with N=150 or more, these groups contain (almost) all directions of the ~160 sample interval that recorded the rotation, thus encompassing the full distortion of the distribution due to the ~30° rotation. In addition, the effect of the interval with excess, non-PSV-induced scatter and the associated overcorrection relative to the expected inclination is more widely distributed and observed for a larger number of groups. The application of cut-offs to these groups with larger N yields similar results as described in section 5.5 for groups with N=100: the E/I corrected inclinations are systematically lower than the inclinations calculated without using a cut-off, and mostly fall below the range of expected values, except for those groups for which limited (<5%) directions were rejected (Fig. S3, Supplementary Materials B). These results indicate that although the variation in corrected inclinations decreases with increasing N, the distribution of directions is more likely to be affected by processes unrelated to PSV and inclination flattening, and the fit with expected directions is not significantly improved with higher N.

6. Discussion

6.1. Reliability criteria for the application of the E/I correction

Based on our analyses, we present a set of criteria and recommendations for the application of the E/I correction for inclination shallowing (Table 1). The reliable use of the E/I correction requires, first and foremost, that the distribution of paleomagnetic directions provides an accurate representation of PSV, and that the observed flattening of the distribution is the result of inclination shallowing alone. Our results demonstrate that if these requirements are not fulfilled, the E/I method may provide substantial (>5-10°) under- or over-estimation of the primary inclination. As a first criterion, we cite the minimum of 100 independent readings of the past geomagnetic field that were estimated by Tauxe and Kent (2004) and Tauxe et al. (2008) to be required to sample the full variation of the geomagnetic field and obtain a robust estimate of the elongation of the distribution.

Second, our analyses reveal that of all studied pitfalls, a large contribution of non-PSV-induced scatter to the distribution of paleomagnetic directions is most important.

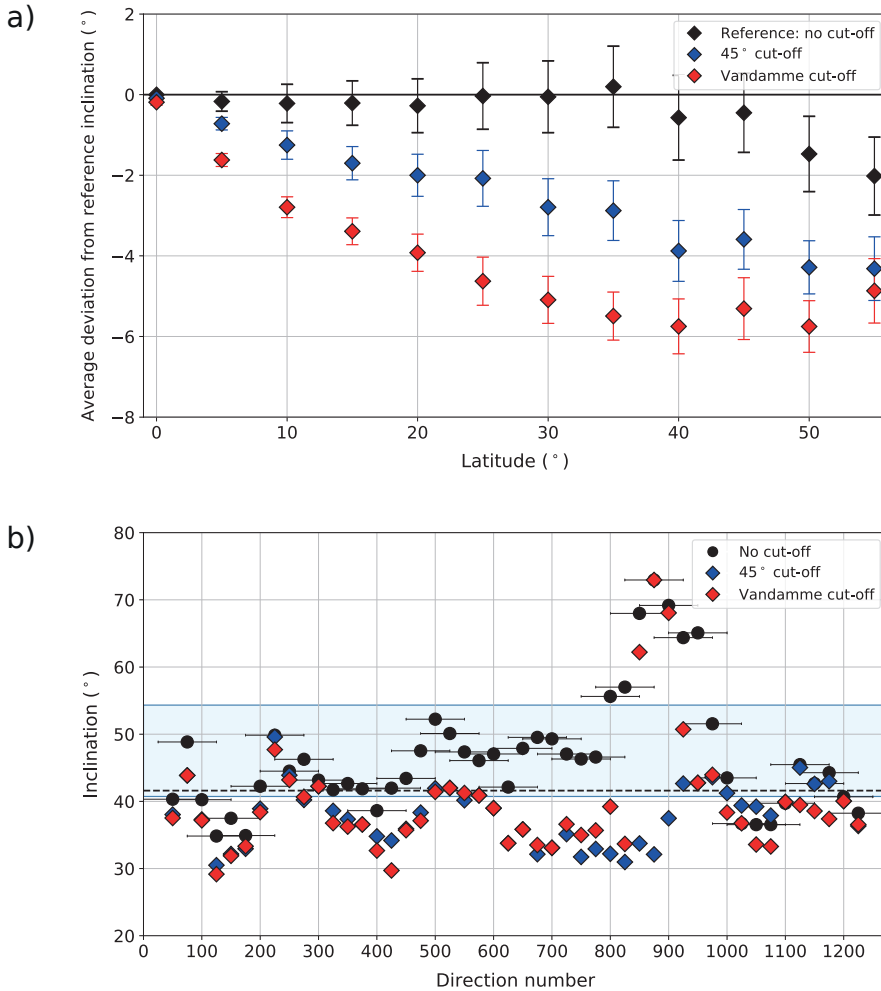


Fig. 9. Effect of the number of paleomagnetic directions used for the E/I correction. Results are shown for a sliding window with (a) 150, (b) 200 and (c) 300 successive directions from the Gonjo Basin dataset. Corrected inclinations for groups of 100 directions (see also Fig. 4a) are plotted as a reference (black). Also, the corrected inclination obtained from an anisotropy-based inclination shallowing correction by Tong et al. (2017) of 41.6° is shown by the dashed grey line. Reference data are plotted as in Fig. 4a.

We find that the reliability envelope of Deenen et al. (2011) is a successful means to identify datasets whereby the observed scatter cannot be straightforwardly explained by PSV alone (section 5.4). We include this criterion to evaluate whether the principal assumption that the observed scatter of directions/VGPs is an adequate representation of PSV, is met. An A_{95} higher than $A_{95,max}$ (see eq. 3 in Deenen et al. (2014)) indicates that the paleomagnetic dataset is affected by a significant contribution of non-PSV-induced sources of scatter. Nevertheless, our results indicate that for cases where the A_{95} is only slightly ($<1^\circ$ for $N \geq 100$) above the $A_{95,max}$, corresponding to K values of $\sim 8-11$, the E/I

method may still provide a reliable correction of the inclination (section 5.4). But, if the A_{95} is well above this upper limit ($>2^\circ$ for $N \geq 100$), indicating a large contribution of other sources of scatter, the E/I correction tends to yield a substantial ($>10^\circ$) overestimation of the primary inclination. In cases where the A_{95} is below the $A_{95, \min}$, PSV is likely underrepresented by the paleomagnetic dataset. This may result from (re)magnetization in a short time interval, from the acquisition of a chemical remanent magnetization (CRM) after deposition, or from significant averaging of PSV in each paleomagnetic sample, for instance for sediments with very low sedimentation rates (Deenen et al. 2011). Our experiments indicate that the E/I correction may still provide an accurate estimate of the primary inclination if PSV is already partially averaged, whereby A_{95} may be below $A_{95, \min}$, as long as the dispersion is predominantly the result of PSV and the excess elongation of the distribution results from flattening (section 5.3). However, if the cause(s) of such low scatter cannot be straightforwardly determined from a set of directions/VGPs or, alternatively, from sediment properties and the NRM acquisition mechanism, we advise not to use datasets with $A_{95} < A_{95, \min}$.

Evidently, the fact that a dataset satisfies the Deenen et al. (2011) criterion - or any other statistics-based criterion - does not preclude the presence of non-PSV-induced scatter, which may directly affect the elongation of the directional distribution. A dataset with an A_{95} value that falls within the $A_{95, \min-\max}$ range may represent a 'false positive' and be obtained, for instance, from remagnetized rocks with noisy demagnetization behavior, and thus provide a meaningless E/I correction. Contributions of various sources of noise, e.g., related to measurement errors or low magnetic intensity, are inherently present in each paleomagnetic dataset and are often difficult to quantify and distinguish from PSV. This is particularly the case for data from sediments, for which no well-established quantitative criteria exist to test the reproducibility of paleomagnetic directions. We emphasize that if the Deenen et al. (2011) criterion is met, there is no statistical basis to reject a dataset, but it is not conclusive of PSV being adequately recorded by the dataset, or of a primary magnetization. A number of careful checks for a primary magnetization, however, are included in the commonly applied quality criteria of van der Voo (1990) and Meert et al. (2020), and we strongly recommend the application of those prior to the use of the E/I correction (see Table 1). These criteria include the application of a reversal test, if a sufficient number of normal and reversed polarity directions are available. We note that although our analysis shows that a positive reversal test may be obtained for datasets whereby the E/I correction did not yield an accurate result (section 5.4), it provides a useful instrument to evaluate whether a dataset may be contaminated by non-PSV-induced sources of noise, e.g., due to not entirely removed magnetic overprints.

Our criteria for the application of the E/I correction, however, replace some of the statistical requirements previously formulated for a quantitative assessment of PSV. Van der Voo (1990) argued that at least 25 spot readings are needed to test whether PSV is sufficiently recorded by the dataset, whereas Meert et al. (2020) recommends at least eight spot readings (with a minimum of three samples per site). While those may well contain valuable information when based on rocks that are unaffected by inclination shallowing such as lavas or dykes, $N \geq 100$ is recommended to adequately correct for inclination shallowing (using the E/I method) and to assess whether the distribution of directions/VGPs represents PSV or not. In addition, we note that for such large N the Deenen et al. (2011) criterion is more conservative than the statistics-based criterion of $10 \leq K \leq 70$

Reliability criteria

Criterion	Description
	General reliability criteria (based on criteria defined by Meert et al. 2020), which include: <ul style="list-style-type: none"> - Well-determined rock age - Evidence for a primary remanent magnetisation (provided by field tests) - Application of modern demagnetisation techniques
0	<ul style="list-style-type: none"> - Analysis of directional data using Zijdeveld (1967) diagrams and principal component analysis (Kirschvink 1980) - Characterisation of the magnetic carriers - Application of a magnetic reversal test (if sufficient directions of both polarities are available)
1	≥100 individual paleomagnetic directions
2	Deenen et al. (2011) criterion passed: $A_{95,\min} < A_{95} < A_{95,\max}$
3	No vertical-axis rotations of >15° within the dataset

Recommendations for the E/I correction

1. No application of a cut-off
2. Exclusion of poorly defined ChRM directions (e.g., directions determined using the great circle method (McFadden & McElhinny 1988))
3. Testing the reproducibility of the results using a sliding window approach

Quality grade	Criteria	Interpretation and application
A	All the criteria listed above are passed	Reliable, inclination shallowing-corrected pole: suitable as input for high-resolution APWPs and paleogeographic reconstructions
B	<ol style="list-style-type: none"> 1. Criteria 0, 2 and 3 passed and $75 \leq N < 100$ 2. Criterion 0, 1 and 3 passed and $8 < K < 100$ 	Less reliable, but provide a useful estimate of the primary inclination and paleolatitude
C	Datasets that do not satisfy the criteria defined for a quality grade 'A' or 'B'	Insufficient quality for inclusion in APWPs or as primary input for paleogeographic reconstructions

Table 1. Overview of our proposed criteria for the reliable application of the E/I correction, and for the calculation of E/I corrected paleomagnetic poles derived from sedimentary rocks. N = number of individual paleomagnetic directions; K= Fisher (1953) precision parameter of the distribution of VGPs; A_{95} = radius of the 95% confidence circle about the mean of the VGP distribution.

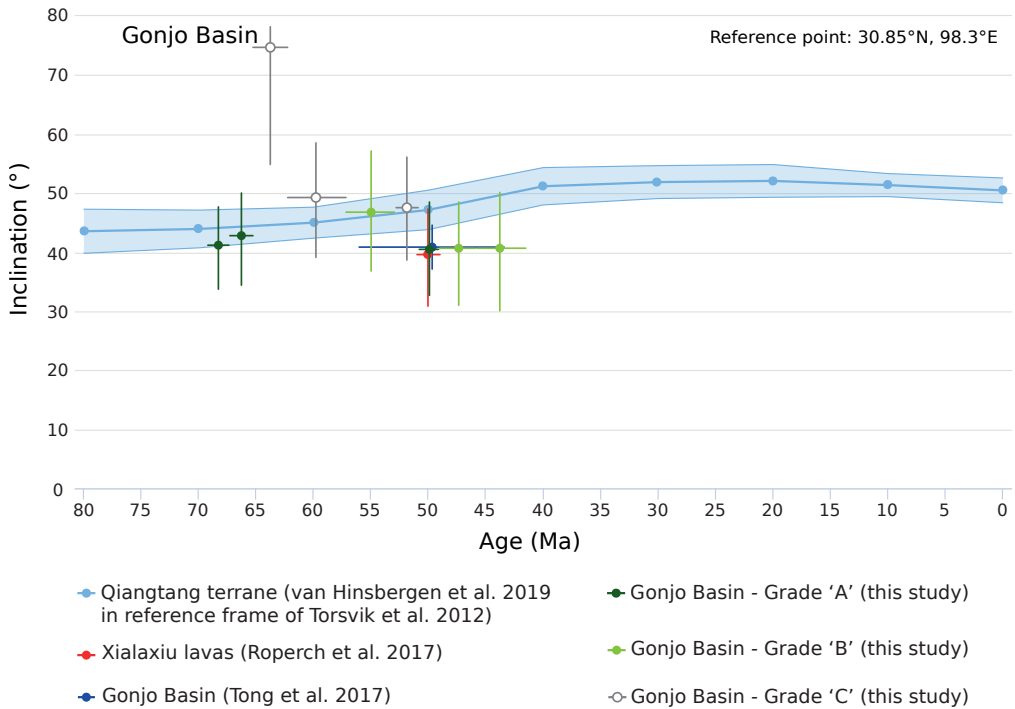


Fig. 10. E/I corrected inclinations for the 9 groups of paleomagnetic directions from the Gonjo Basin dataset as listed in Table 2. Horizontal error bars indicate the age range of the selected directions. Vertical error bars correspond to the 95% bootstrap confidence bounds. The colour of the data points indicates the quality grade of the result based on the reliability criteria presented in Table 1. Reference data provided by previous results for the 51-49 Ma lavas of the Xialaxiu area (Roperch et al. (2017) and the inclination shallowing-corrected result for the Gonjo Basin red beds (Tong et al., 2017) are shown in red and blue, respectively. The expected inclination based on the kinematic reconstruction of the Tibetan region by van Hinsbergen et al. (2019), placed in the paleomagnetic reference frame of Torsvik et al. (2012), is depicted by the light blue curve (with confidence region). This figure was created using paleomagnetism.org (Koymans et al. 2016, 2020).

proposed by Meert et al. (2020). For instance, for $N=100$, the reliability envelope of Deenen et al. (2011) yields an $A_{95,\min}$ and $A_{95,\max}$ of 1.90 and 4.51, corresponding to K values of 56.2 and 10.8.

To reduce the effects of non-PSV-induced scatter, it is common to remove outliers from a paleomagnetic dataset by manual filtering or by employing cut-offs, such as the fixed 45° and Vandamme (1994) cut-offs. However, this directly influences (the elongation of) the distribution of paleomagnetic directions, and our results indicate that the application of a cut-off leads to a systematic underestimation of the primary inclination (section 5.5, Fig. 8), which offsets the benefit of removing non-PSV-induced outliers. We thus advise against the application of cut-offs prior to the E/I correction. Paleomagnetic directions that are obviously not representing PSV, e.g., due to lightning strikes (see e.g., Strik et al. 2003, their fig. 7), or directions estimated through the great

circle method (McFadden & McElhinny 1988), should manually be excluded from the dataset. A potential source for non-PSV induced scatter is the distortion of the directional distribution resulting from vertical-axis rotations that occurred during deposition. Our experiments show that syn-sedimentary rotations of $>15\text{-}20^\circ$ may lead to significant overcorrections of the primary inclination of $>10^\circ$ (section 5.2). It may however require much larger rotations to drive A_{95} beyond $A_{95,\text{max}}$ and it is well possible that a rotation-induced increase of the elongation cannot be detected by using the Deenen et al. (2011) criterion alone. We thus recommend that prior to the application of the E/I correction, the paleomagnetic dataset is checked, e.g., using a moving average as in Li et al. (2020a), for systematic changes in declination with age/stratigraphic position that may indicate syn-sedimentary vertical-axis rotations. Previously, the effects of a rotation on the results have sometimes been corrected (see section 5.2; Meng et al. 2017), but as we pointed out before, determining the exact magnitude of the rotation and propagating its associated uncertainty is not straightforward. Correcting rotations estimated from paleomagnetic data alone (instead of e.g., bedding strike variations) may thus add more uncertainty than that it solves. Data from intervals that record rotations smaller than 15° typically result in overcorrections of $<5^\circ$ (Fig. 5). We recommend to not use data for the E/I correction, or for the calculation of paleomagnetic poles, from stratigraphic intervals in which vertical-axis rotations beyond 15° are recorded or suspected. In such cases, the E/I correction is best applied to data from each of the non-rotated intervals.

Finally, we advocate testing the reproducibility of the inclination shallowing-corrected inclination for datasets with $N > \sim 150$, by applying the E/I method to multiple subsets of ~ 100 directions, e.g., using the sliding window approach we performed in this study. Although a larger dataset would ideally be used to capture the entire variability of the field to better constrain the elongation and to perform a more robust E/I correction, there is a greater chance that the distribution is contaminated by intervals that contain significant non-PSV-induced scatter or are affected by rotations. Also, for large datasets that provide a record of more than ~ 5 Myr, the distribution of directions may be distorted by plate motion (Tauxe & Kodama 2009). Lastly, we note that because the E/I method applies a single average flattening factor to all paleomagnetic directions, applying the method to subsets of directions may help to discern variations in the magnitude of flattening, for instance due to lithological variations. Evidently, if the results are shown to be internally consistent, then the E/I correction may be reliably applied to all directions, providing a robust estimate of the primary inclination.

Based on the criteria discussed above, we propose three quality grades that indicate whether a paleomagnetic dataset obtained from sedimentary rocks is appropriate to use for the E/I correction and for the calculation of an inclination shallowing-corrected paleomagnetic pole (Table 1). We assign datasets that pass all criteria a quality grade 'A', indicating that the E/I method may be reliably used to correct the dataset for inclination shallowing and to obtain a shallowing-corrected pole. For datasets that meet all other criteria but have $75 \leq N < 100$ or that have an A_{95} that falls outside the $A_{95,\text{min-max}}$ envelope but have $8 < K < 100$, we assign a quality grade 'B' (Table 1). We define this quality grade 'B' based on the observation that datasets with an A_{95} that falls just above the envelope of Deenen et al. (2011) still provide accurate estimates of the primary inclination (see Fig. 4, 6), suggesting that the $A_{95,\text{max}}$ (corresponding to K values of $\sim 11\text{-}14$ for $N=100\text{-}300$) may be a bit overly strict for datasets from (clastic) sedimentary rocks. We specify a range of

#	Interval (m)	Age (Ma)	N	Dec (°)	Inc ₀ (°)	Inc _{EI} (°)	Inc _{low} (°)	Inc _{hi} (°)	f	K	A ₉₅ (°)	A _{95,max} (°)	RT	Rot. >15°	Grade
1	3325.4-3020.5	43.6 (41.5-45.7)	128	26.2	21.5	40.8	30.1	50.5	0.46	8.3	4.6	3.9	p		B
2	3018.5-2701.2	47.35 (45.7-49.0)	145	36.1	25.7	40.8	31.0	48.5	0.56	8.8	4.2	3.6	n/a		B
3	2699.2-2337.2	49.8 (49.0-50.6)	129	35.1	28.6	40.6	32.9	48.8	0.61	12.6	3.6	3.8	p		A
4	2331.2-1919.6	51.6 (50.6-52.6)	137	56.1	27.4	47.8	39.0	56.3	0.45	8.9	4.3	3.7	n	x	C
5	1917.6-1519.6	54.85 (52.6-57.1)	156	53.3	27.5	47.1	36.9	57.4	0.49	8.7	4.1	3.4	p		B
6	1514.8-1123.5	59.65 (57.1-62.2)	133	52.0	27.1	49.4	39.4	58.7	0.45	5.2	5.9	3.8	p		C
7	1119.5-762.0	63.75 (62.2-65.3)	113	40.1	37.0	74.8	54.9	78.4	0.29	2.9	9.7	4.2	n		C
8	757.0-384.2	66.25 (65.3-67.2)	167	50.7	26.0	43.0	34.9	50.1	0.51	11.9	3.3	3.3	p		A
9	382.2-0	68.20 (67.2-69.2)	167	48.5	29.5	41.0	34.0	48.1	0.62	16.0	2.8	3.3	p		A

Table 2. Results for selected groups of paleomagnetic directions from the Gonjo Basin dataset. N = number of individual paleomagnetic directions; Dec = declination; Inc₀/Inc_{EI} = inclination before/after E/I correction; Inc_{low}/Inc_{hi} = 95% bootstrap confidence bounds for the E/I corrected inclination; f = flattening factor; K = Fisher (1953) precision parameter of the distribution of VGPs; A₉₅ = radius of the 95% confidence circle about the mean of the VGP distribution; A_{95,max} = upper limit of N-dependent A95 envelope of Deenen et al. (2011); RT = results of bootstrap reversal test (Tauxe 2010); p is positive, n is negative, n/a indicates that no robust test could be performed due to the limited number of directions of one polarity; Rot. >15° = rotation of >15° recorded by dataset; Grade = quality grade assigned to the directional group, based on the criteria listed in Table 1.

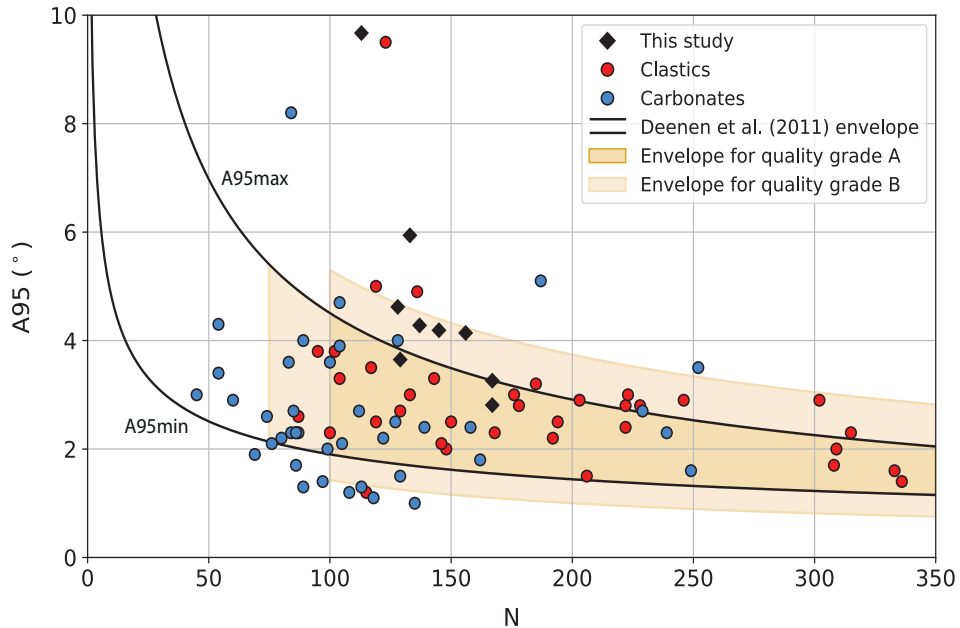


Fig. 11. A_{95} versus N for a compilation of paleomagnetic datasets on which the E/I correction has been performed. Datasets derived from clastic and carbonate rocks are shown by the red and blue circles, respectively. The A_{95} values for the 9 groups of this study (listed in Table 2) are plotted as black diamonds. The N -dependent A_{95} envelope is plotted by the black lines. The coloured areas indicate the criteria with respect to A_{95} and N required for a quality grade ‘A’ or ‘B’, as defined by the reliability criteria presented in Table 1. The data compilation and references are provided in Table S2 (Supplementary Materials C).

values for K rather than A_{95} , for the simple reason that K is independent of N . The upper limit of $K < 100$ is chosen based on the reliable results that were obtained from datasets whereby PSV was already partially averaged and for which A_{95} was slightly below $A_{95,\min}$ (section 5.3, Fig. 7). Also, we assign this grade to datasets that satisfy all criteria but have $75 \leq N < 100$, considering that the suggested minimum of 100 independent directions is to some extent arbitrary and that previous studies have shown that the E/I correction may provide accurate results with slightly lower N (section 6.2). We emphasize that although datasets that are assigned a quality grade ‘B’ are in principle less reliable, they may well provide a meaningful estimate of the primary inclination and thus paleolatitude after application of the E/I method. Finally, we assign a quality grade ‘C’ for datasets that do not satisfy the criteria for a grade ‘A’ or ‘B’, indicating that datasets do not provide a reliable E/I corrected result. In addition, we assign this quality grade to datasets whereby no fit with the TK03.GAD model is obtained upon stepwise unflattening, suggesting that the directional distribution is significantly distorted.

6.2. The applicability of the reliability criteria and its limitations

To illustrate how our criteria perform, we first applied them to groups of paleomagnetic directions from the Gonjo Basin dataset (Table 2). To this end, we selected nine sample collections of >100 directions to which we applied the E/I correction (see Figs S4, S5 and S6, Supplementary Materials B). Most of these groups include directions corresponding to several successive polarity chrons, so that the age range can be accurately determined. For groups #1-3 that cover the ~40-50 Ma time interval, groups #1-2 are assigned quality 'B' and group #3 is assigned quality 'A'. They provide corrected inclinations that are identical to those previously obtained from lavas by Roperch et al. (2017) and from an anisotropy-based correction by Tong et al. (2017) and reinforce their conclusions for the paleolatitude of the (eastern) Qiangtang terrane in the Eocene (Fig. 10). These results suggest that our criteria for quality grade 'A' may be somewhat conservative and that paleomagnetic results that are assigned grade 'B' may indeed provide a useful estimate of the primary inclination (and thus paleolatitude). A quality grade 'C' is assigned to group #4. This interval recorded the ~30° clockwise rotation documented by Li et al. (2020a) and also does not pass the bootstrap reversal test (Table 2). This group yields a corrected inclination that is ~6-8° higher than the results of groups #1-3. It is, however, consistent with the predictions for the Qiangtang terrane placed in the paleomagnetic reference frame of Torsvik et al. (2012) (Fig. 10), but as noted earlier, this may provide predicted values that are too high for East Asia for the ~40-50 Ma time interval. Groups #6 and #7 are assigned grade 'C' and correspond to the interval with very large VGP scatter, whereby the $A95$ is >5° above $A95_{max}$. The two 'A' grade poles for the ~65-69 Ma time interval yield very similar primary inclinations, which are consistent with predicted values for the Qiangtang terrane. Finally, we note that the grade 'A' poles come from the base of the studies section where the AMS fabric reveals a compaction-dominated fabric, and from the top of the section, which has a tectonic fabric (Li et al., 2020b). We find that the results of groups #1-3, corresponding to the stratigraphic interval with a 'pencil structure' AMS fabric, are nearly identical to those obtained from independent datasets of Roperch et al. (2017) and Tong et al. (2017) (Fig. 10). Although it has recently been shown that a strong tectonic fabric (corresponding to weak or strong cleavage state) may lead to erroneous results of the E/I correction (Dallanave & Kirscher 2020), our results illustrate that the presence of a less strong tectonic fabric, such as a 'pencil structure' fabric, does not necessarily lead to unreliable results of the E/I correction.

Our case study of the Gonjo Basin applies to clastic sediments with relatively high sedimentation rates, to which the E/I method has previously been mostly applied. To evaluate to what extent our criteria are successful in isolating reliable datasets from other sedimentary lithologies and rock magnetic characteristics, we compiled 78 datasets on which the E/I correction has been applied, which were published in 33 different studies (Table S2, Supplementary Materials C). This compilation includes datasets that are derived from a variety of lithologies, depositional environments, and magnetic mineralogies and were obtained from rocks with an age ranging from the Carboniferous to the Neogene. Although sampling strategies varied between studies, we note that in most studies a single sample was collected per stratigraphic level, similar to the sampling strategy employed by Li et al. (2020a, b). For several of these datasets, the E/I corrected inclination is supported by independent estimates obtained from nearby sedimentary sections, volcanic rocks, or anisotropy-based correction methods. We note that nearly all E/I corrected datasets

(unless explicitly indicated) were considered in the original publication to provide a reliable estimate of the paleolatitude or paleomagnetic pole, which were often used as input for a paleogeographic reconstruction or APWP.

We evaluate all datasets against our new reliability criteria, assigning each dataset one of the quality grades defined in the previous section (see Table S2, Supplementary Materials C). To visualize whether the datasets meet the statistical requirements defined in Table 1, we plotted the A_{95} against the number of individual measurements for each dataset (Fig. 11). The majority of datasets (52 from 78) have an A_{95} that falls within the reliability envelope of Deenen et al. (2011). Most of these datasets that are based on $N \geq 100$ are assigned quality grade 'A', provided that they meet all the 'general' criteria of Meert et al. (2020) and did not record any vertical-axis rotations of $>15^\circ$. Notably, most datasets of clastic rocks that fall outside of the Deenen et al. (2011) envelope have an $A_{95} > A_{95,\max}$, whereas datasets based on carbonate rocks more often yield an A_{95} that is below $A_{95,\min}$. This suggests that paleomagnetic records from clastic sedimentary rocks are more prone to sources of scatter unrelated to PSV, whereas datasets derived from carbonate rocks are more prone to partial averaging of PSV, possibly due to their typically lower sedimentation rates, or because of the acquisition of a chemical or post-depositional remanent magnetization after early compaction and dewatering.

The data compilation shows that the E/I correction, if the criteria are satisfied, provides reliable and reproducible results for a range of lithologies, magnetic mineralogies and rock ages, as indicated by independent data from nearby sedimentary sequences of the same age, anisotropy-based corrections and from coeval igneous rocks. We find that nearly all E/I corrected datasets that would be assigned a quality grade 'A' yield an estimate of the paleolatitude or pole that is confirmed by independent datasets, as shown in the original publication. Importantly, the few (published) datasets for which the original authors indicated that the E/I correction did not provide a reliable result would indeed be assigned a grade 'C', either because the dataset does not satisfy our statistical criteria or because it recorded vertical-axis rotations of $>15^\circ$ (Table S2, Supplementary Materials C). We find, however, that independently confirmed results at times are classified as grade 'B' (or even 'C'), indicating that our criteria for a grade 'A' may be overly conservative in some cases. This also indicates that datasets that are assigned a quality grade 'B' may well provide a useful estimate of the primary inclination, as previously shown by the results for the Gonjo Basin. Several datasets from carbonate rocks that are assigned a grade 'C' provided results that were shown to be reproducible, based on datasets from nearby sedimentary sequences that span the same time interval. But considering that these results are obtained from particularly small datasets ($N < 75$) or datasets whereby $K > 100$, we do not recommend such datasets to be used as primary input for paleogeographic reconstructions or APWPs. On the other hand, datasets that do not pass the criteria for a reliable E/I corrected paleomagnetic pole may still be used to construct a well-determined magnetostratigraphy, as this merely requires adequate identification of the magnetic polarity. Also, for studies aiming to determine the magnitude and/or timing of vertical-axis rotations, inclination shallowing is not important, and data that do not pass the criteria presented here may still be meaningful to determine such rotations.

We emphasize that our proposed criteria - like any other set of criteria - cannot unequivocally determine whether a paleomagnetic result is reliable or not. The E/I technique itself has some inherent limitations, which may place some restrictions on

the applicability of our criteria. For instance, the validity of the E/I correction relies for a large part on whether the TK03.GAD model accurately predicts the behavior of the geomagnetic field for the time interval in which the sampled rocks acquired their remanent magnetization (see section 2). Although the E/I correction appears successful for rocks of Early Mesozoic or Late Paleozoic age (e.g., Kent & Tauxe, 2005; Haldan et al., 2009; Meijers et al. 2010a; Bilardello et al., 2011), it is unclear whether the elongation-inclination curve predicted by the TK03.GAD model is accurate for time intervals for which it has not been thoroughly tested, such as the Early Paleozoic and Precambrian. Tauxe & Kodama (2009) showed that the elongation versus inclination of a dataset from ~1.1 Ga old lava flows matches those predicted by the TK03.GAD model, but future efforts are likely needed to confirm the validity of the model for ancient times. We envisage, however, that new models of the geomagnetic field, such as the GGP models recently presented by Brandt et al. (2019) and Bono et al. (2020), may potentially replace the TK03.GAD model to refine the E/I method, either to enhance the accuracy of the method in general, or for specific time intervals.

At present, some alternative strategies may be employed in cases where the age of the rocks or the limited number of directions precludes a robust inclination shallowing correction by the E/I method. For instance, the magnitude of flattening may be assessed through alternative analyses of the shape of the distribution of directions (e.g., Levashova et al. 2013; 2015) or VGPs (Domeier et al. 2011). In addition, anisotropy-based methods may provide a valid alternative for the correction of inclination shallowing, as previously demonstrated (e.g., Tauxe et al. 2008; Bilardello et al. 2011; Huang et al. 2013, 2015). Because these methods are independent of a statistical model of the geomagnetic field, they may be particularly useful to correct datasets obtained from Precambrian sedimentary rocks (e.g., Rapalini 2006; Schmidt et al. 2009). But if possible, we recommend applying the E/I method in addition to an anisotropy-based correction, as was done in previous studies (e.g., Bilardello et al. 2011; Huang et al. 2013, 2015; Tong et al. 2017; Westerweel et al. 2019), to assess the robustness of the inclination shallowing correction and to evaluate - using the criteria presented here - whether PSV is adequately sampled.

6.3. Implications for paleomagnetic poles derived from sedimentary rocks

The calculation of an accurate paleomagnetic pole from sedimentary rocks requires that PSV is adequately sampled and averaged, and that the dataset is corrected for inclination shallowing (if present). The E/I correction provides a means to not only correct for inclination shallowing, but also to assess whether the observed scatter of paleomagnetic directions predominantly results from PSV. Our analysis implies that if a sediment-based, E/I corrected dataset passes all quality criteria the observed distribution of directions (and associated VGPs) can be considered comparable - in terms of both the shape and magnitude of scatter - to a distribution of site-mean directions/VGPs from fast-cooled igneous rocks like lavas. In other words, even though the consistency of the individual paleomagnetic directions from such a sediment-based dataset cannot be independently confirmed, as is possible for lavas, the dataset as a whole behaves as a collection of spot readings of the paleomagnetic field. Such a data collection thus provides an inclination shallowing-corrected paleomagnetic pole that averages PSV based on ≥ 100 independent measurements of the field, and can be used with equal weight as poles based on igneous

rocks when used as input for paleogeographic reconstructions and APWPs.

A large fraction of the sediment-based paleomagnetic poles that are currently used as input for paleogeographic reconstructions or APWPs have not been corrected for inclination shallowing in the original publication. For most of these poles, the E/I correction cannot be reliably applied because of the small (<100) number of paleomagnetic directions or because the individual directions were not published or included in online appendices or in databases such as MagIC (Jarboe et al. 2012) or paleomagnetism.org (Koymans et al. 2020). In such cases, many authors apply a single ‘blanket’ flattening factor, typically $f=0.6$ for clastic sediments, to correct such poles for inclination shallowing (e.g., Torsvik et al. 2008, 2012; Wu et al. 2017, 2020; Jeong & Yu 2019). However, the range of flattening factors of ~ 0.4 - 0.65 obtained in this study illustrates that the magnitude of shallowing may vary significantly even for a single sedimentary sequence. In addition, our compilation of E/I corrected datasets show that the magnitude of flattening may vary substantially for datasets derived from similar lithologies (Table S2, Supplementary Materials C). These observations support previous notions that inclination shallowing is largely dependent on the specific lithological and rock magnetic properties of the sampled rocks (e.g., Bilardello & Kodama 2010b; Kodama 2012). Notably, the application of the E/I method to carbonate rocks show that significant inclination shallowing (with estimated flattening factors ranging from 0.4 to 0.7) is not restricted to clastic sedimentary rocks, but may also affect e.g., (clay-rich) limestones and marls (Table S2, Supplementary Materials C) (e.g., Agnini et al. 2011; Dallanave et al. 2012; Muttoni et al. 2013, Muttoni & Kent 2019). This further suggests that the use of a ‘blanket’ flattening factor (applied to clastic sediments only) may not provide an optimal correction for all sediment-based datasets and should be treated with caution.

Importantly, poles from sedimentary rocks on which the E/I correction cannot be applied and that have previously been corrected for inclination shallowing by a ‘blanket’ flattening factor do not pass our proposed criteria, and our criteria thus place large restrictions on the sedimentary poles that are used as input in paleogeographic reconstructions and APWPs. We note that the above concerns have led some authors to only use poles that were based on datasets specifically corrected using the E/I technique or anisotropy-based methods as input for their APWPs (e.g., Kent & Irving 2010; Kent & Muttoni 2020). But to what extent a ‘blanket’ correction affects the scatter of poles used for, or causes bias in APWPs remains to be investigated. We envisage, however, that our (conservative) quality criteria will stimulate researchers to critically evaluate (E/I corrected) paleomagnetic poles derived from sedimentary rocks and will help unlocking sedimentary archives as a prime contributor to future, high-resolution APWPs and paleomagnetic reference frames based on those.

7. Conclusions

Paleomagnetic poles from sedimentary rocks are extensively used as input for APWPs and paleogeographic reconstructions. Obtaining an accurate pole from sedimentary rocks requires that PSV is well-sampled by the paleomagnetic dataset, other sources of scatter are minimal, and that potential inclination shallowing is corrected for. However, there are currently no well-established criteria for sediment-based datasets to evaluate whether the observed scatter of paleomagnetic directions may be representative for PSV alone, making it challenging to assess the reliability of a sediment-based pole. The elongation-inclination

(E/I) method by Tauxe & Kent (2004) is widely used to correct for inclination shallowing and explicitly assumes that a large, sediment-based dataset provides an accurate representation of PSV. Thus, if the E/I method accurately restores the primary inclination, the assumption that PSV is adequately recorded may be a correct approximation.

In this study, we examined under which conditions the elongation-inclination (E/I) method of Tauxe & Kent (2004) provides a robust correction for inclination shallowing. To this end, we analyzed a large (N=1275) dataset from red beds of the Gonjo Basin (eastern Tibet) that contains most known artefacts that are thought to hamper the application of the E/I method and the calculation of a reliable paleomagnetic pole, together with synthetic datasets created with the TK03.GAD field model. We proposed criteria for the reliable use of the E/I correction as an extension of already commonly used quality criteria for paleomagnetic data. Using these criteria, we defined three quality grades that indicate whether a sediment-based dataset may provide a reliable E/I corrected paleomagnetic pole. Using an extensive compilation of previously published E/I corrected datasets, obtained from a variety of lithologies (including limestones and marls), we showed that our new criteria successfully classify datasets that were previously demonstrated to provide erroneous results as unreliable, and classify datasets whose reliability is confirmed by independent results as reliable.

An important implication of our study is that E/I corrected datasets that satisfy all reliability criteria have a distribution of directions (and associated VGPs) that can be considered comparable in scatter and shape to a dataset based on site-means from rapidly cooled igneous rocks like lavas. Such datasets provide reliable inclination shallowing-corrected poles that average PSV based on a large dataset of independent measurements of the field, and can be used as input for paleogeographic reconstructions and APWPs in addition to high-quality poles based on igneous rocks. Our analysis also illustrates that the application of a 'blanket' correction factor to uncorrected datasets from (clastic) sediments may not provide an optimal correction for inclination shallowing. Paleomagnetic poles that are corrected using a 'blanket' flattening factor do not pass our requirements for a reliable sediment-based pole and our criteria thus place restrictions on the use of paleomagnetic records from sediments as prime input for paleogeographic reconstructions and APWPs. We foresee, however, that our proposed criteria will provide a useful instrument for the selection and determination of sediment-based paleomagnetic poles that can be reliably used for future, high-resolution APWPs and paleogeographic reconstructions.

4

Influence of data filters on the position and precision of paleomagnetic poles: what is the optimal sampling strategy?

This chapter has been published as:

Gerritsen, D., Vaes, B., & van Hinsbergen, D. J. J. (2022). Influence of data filters on the position and precision of paleomagnetic poles: what is the optimal sampling strategy? *Geochemistry, Geophysics, Geosystems*, 23(4), e2021GC010269.

Abstract

To determine a paleopole, the paleomagnetic community commonly applies a loosely defined set of quantitative data filters that were established for studies of geomagnetic field behavior. These filters require costly and time-consuming sampling procedures, but whether they improve the precision and influence the position of paleopoles has not yet been systematically analyzed. In this study, we performed a series of experiments on four datasets which consist of 73–125 lava sites with 6–7 samples per lava. The datasets are from different regions and ages, and are large enough to represent paleosecular variation, yet include demonstrably unreliable paleomagnetic directions. We show that the systematic application of data filters based on within-site scatter (a maximum angular deviation filter on individual directions, a k -cutoff, a minimum number of samples per site, and eliminating the farthest outliers per site) cannot identify unreliable directions. We find instead that excluding unreliable directions relies on the subjective interpretation of the expert, highlighting the importance of making all data available following the FAIR principles. In addition, data filters that decrease the number of sites even have an adverse effect; they decrease the precision of the paleopole. Between-site scatter often outweighs within-site scatter, and when collecting paleomagnetic poles, the extra efforts put into collecting multiple samples per site are more effectively spent on collecting more single-sample sites.

Key points

- Within-site data filters (maximum angular deviation cutoff, minimum k or n , eliminating outliers) do not significantly improve paleopole precision or position
- The precision of paleomagnetic poles is dominated by between-site scatter; within-site scatter has minimal contribution
- For paleopoles, efforts put into collecting multiple samples per site are more effectively spent on collecting more single-sample sites

1. Introduction

Paleomagnetic poles, or paleopoles, quantify the past position of rocks relative to the geomagnetic pole and constrain tectonic reconstructions and apparent polar wander paths (APWPs; e.g., Besse & Courtillot, 2002; Torsvik et al., 2012). The calculation of paleopoles relies on the assumption that the time-averaged geomagnetic field approximates a geocentric axial dipole (GAD), but is complicated by short-term deviations from this field (e.g., Cromwell et al., 2018; Oliveira et al., 2021) known as paleosecular variation (PSV). To obtain a paleopole, paleomagnetists therefore average virtual geomagnetic poles (VGPs), whereby every VGP is then assumed a ‘spot reading’: an instantaneous reading of the past geomagnetic field collected from a rock unit (‘site’) that represents an increment of geological time, such as a lava flow (Butler, 1992; Tauxe et al., 2010). However, not every VGP represents an accurate spot reading because artifacts may be introduced by measuring errors or remagnetization (e.g., Bilardello et al., 2018; Butler, 1992; Irving, 1961, 1964). Therefore, the paleomagnetic community commonly uses a set of data filters to acquire a set of reliable spot readings and to objectively eliminate outliers and unreliable data. However, these filters vary between authors and were not determined by studies aiming to constrain paleopoles.

The studies that established the data filter rules, investigated PSV and geomagnetic field behavior by determining the between-site scatter of a set of VGPs (e.g., Cromwell et al., 2018; de Oliveira et al., 2021; Johnson & Constable, 1996; Johnson et al., 2008; Tauxe et al., 2003). To this end, these studies aim to correct for within-site scatter induced by measuring errors and typically require well-determined directions with a low maximum angular deviation (MAD) and a minimum number of readings per site, although the cutoff values for these criteria vary between authors (e.g., Asefaw et al., 2021; Biggin et al., 2008; Cromwell et al., 2018; Doubrovine et al., 2019; Johnson et al., 2008). The resulting paleomagnetic directions are then averaged to a site-mean direction which is converted to a VGP if the site passes a criterion for the minimum within-site precision value (‘cutoff’), typically expressed as a Fisher (1953) precision parameter k . This value also varies between authors, for example, $k \geq 50$ or $k \geq 100$ (e.g., Biggin et al., 2008; Cromwell et al., 2018; Johnson et al., 2008; Tauxe et al., 2003). Subsequently, similar procedures have become common for calculation of paleopoles (e.g., Butler, 1992; Lippert et al., 2014; Meert et al., 2020). However, does this time- and data-intensive procedure improve the precision and influence the position of paleopoles?

In this study, we analyze to what extent commonly applied paleomagnetic data filters established for PSV studies affect the position and precision of paleopoles. To this end, we study four large paleomagnetic datasets obtained from lava sequences from the Cretaceous of Mongolia, the Permian of Norway, the Miocene of Turkey, and the Quaternary of Antarctica. These datasets are large enough to represent PSV, but contain additional between-site and within-site scatter of varying magnitude due to measurement errors, lightning-induced remagnetization, and/or tectonic deformation. We perform a series of experiments to examine the effects of the systematic application of data filters on the position and precision of paleopoles. We evaluate whether these filters can exclude outliers and filter non-PSV induced scatter from the paleomagnetic datasets. We then assess how a given number of paleomagnetic directions is optimally distributed over a collection of paleomagnetic sites to acquire the best-constrained paleopole position. We discuss to what extent the filters used in PSV studies influence paleopole position and precision. Our

results aim to aid paleomagnetists to optimize their sampling and data filtering strategies.

2. Background

When evaluating the reliability of a paleopole, it is common to apply certain criteria aimed at identifying whether the underlying paleomagnetic data set is representative of PSV (e.g., Butler, 1992; Irving, 1961; McElhinny, 1973; van Alstine & de Boer, 1978). In his landmark paper, van der Voo (1990) proposed a set of such reliability criteria that became widely adopted by the paleomagnetic community, and was only recently updated (Meert et al., 2020). van der Voo (1990) recommended to average a minimum set of 25 samples or sites (i.e., spot readings) for a paleopole, and formulated loosely defined filters using Fisher (1953) statistics. Those statistics are used to describe a paleomagnetic data set and can be applied to either directional data or VGPs. Three parameters are of importance in this statistical approach: the radius of the 95% confidence cone around the mean (α_{95} for directions and A_{95} for VGPs), the precision parameter (k for directions and K for VGPs), and the circular standard deviation (S) that quantifies the angular between-site dispersion of VGPs. van der Voo (1990) suggested filters for these parameters: α_{95} or $A_{95} \leq 16^\circ$, and k or $K \geq 10$. In later studies, filters were added to determine the reliability of each VGP based on quality filters used in PSV studies, such as $n > 4$ and $k > 50$ (e.g., Lippert et al., 2014).

For obtaining paleopoles, paleomagnetists usually sample multiple sites at a locality, where every site likely represents a spot reading of the paleomagnetic field. Lava flow units, which cool geologically instantaneously, are commonly such “spot reading recorders”. Sediment samples are usually treated as spot readings (e.g., Tauxe & Kent, 2004; Chapter 3), but do average some geological time, and whether directions from the same sedimentary horizon represent the same spot reading is difficult to establish. Our analysis below thus focuses on lava sites.

Each paleomagnetic direction represents a paleomagnetic component determined with the principal component analysis of Kirschvink (1980) that is interpreted by the expert as the characteristic remanent magnetization (ChRM). Each of these components comes with a maximum angular deviation (MAD) value that describes component uncertainty, and MAD values of 15° are typically used as reliability filter (McElhinny & McFadden, 2000), although smaller angles (e.g., 5° , Asefaw et al. (2021)) are also used. The total scatter in a paleomagnetic data set then consists of within-site and between-site scatter (McElhinny & McFadden, 1997), whereby the uncertainties in paleomagnetic directions or VGPs are typically not propagated through the different levels of the hierarchical framework and directions/VGPs are typically given unit weight in the calculation of a mean direction/paleopole (e.g., Heslop & Roberts, 2020; Irving, 1964). Paleomagnetists collect multiple samples per site to test whether a paleomagnetic direction is reproducible and to average measurements and other random errors (e.g., Meert et al., 2020; van der Voo, 1990). A quality check for within-site precision is a k -cutoff (Tauxe et al., 2003), where sites with a k value lower than an arbitrary value of 50 or 100 are discarded (e.g., Biggin et al., 2008; Johnson et al., 2008; Lippert et al., 2014). Furthermore, outliers are often subjectively discarded from sites based on the ‘expert eye’ and experience of the interpreter. How many samples should be collected per site is not widely agreed upon. Based on Monte Carlo simulations, a minimum number of five independently oriented samples was deemed necessary to estimate k reliably (Tauxe et al., 2003). Others suggest that three (Meert et al.,

2020), four (Cromwell et al., 2018; Lippert et al., 2014), or six (Asefaw et al., 2021) samples are needed. Most paleomagnetic studies collected six to eight samples per lava site.

To average between-site scatter, assumed predominantly to be the result of PSV, multiple sites are collected, but the minimum number of sites required for a ‘good’ average, that is, the paleopole, is not well defined (Tauxe et al., 2010). Instead of providing such a minimum number, Deenen et al. (2011) provided a measure to identify whether the between-site scatter of a data set is straightforwardly explained by PSV alone, using a range of reconstructed values from detailed PSV studies. If datasets indeed represent PSV, the accuracy of the position of a paleopole is expected to increase with increasing number of underlying VGPs, which was recently shown to be true for the paleopoles behind the most recent global APWP (Chapter 2). Meert et al. (2020) suggested eight sites are sufficient to determine a paleopole, provided that each site is constrained by at least three samples. Based on a statistical simulation of PSV, Tauxe et al. (2003) showed that a minimum of approximately 100 sites may be required to fully sample PSV. However, this number is rarely obtained due to limited availability of sites and because resources are consumed by sampling a high number of samples for each site. Below, we analyze the effect of these different sampling and filtering strategies on the position and precision of the resulting paleopole.

3. Datasets and approach

3.1. Datasets

As basis for our analysis, we use four paleomagnetic datasets derived from lavas from Mongolia (van Hinsbergen et al., 2008), Norway (Haldan et al., 2014), Turkey (van Hinsbergen et al., 2010), and Antarctica (Asefaw et al., 2021). We chose these datasets because they consist of a particularly large number of paleomagnetic sites (with $n \geq 6$ samples per site) and cover a broad range of paleolatitudes and ages. The results were previously published, but for the purpose of this study, we reinterpreted the demagnetization diagrams of all samples. We did this by identifying the characteristic remanent magnetization (ChRM) by principal component analysis (Kirschvink, 1980), using the online paleomagnetic analysis platform Paleomagnetism.org (Koymans et al., 2016, 2020). We have thereby not forced interpreted components through the origin, and we have not used the remagnetization great-circle method of McFadden and McElhinny (1988), as was occasionally done in the original interpretations. All interpretable diagrams were interpreted, and no samples were discarded based on obviously outlying directions, such as those with abnormally high intensities and rapid low-temperature decay that are suggestive of lightning strikes (Strik et al., 2003). In other words, we deliberately kept directions that an experienced paleomagnetist would likely immediately discard as unreliable. We also did not exclude sites that were collected from tectonically deformed regions. As a result, the datasets contain larger noise and a higher between-site scatter (lower K value) than the published values. This allows us to assess whether the quality filters alone can clean the data set from outliers, or whether this relies on a subjective ‘expert eye’. The sites from Mongolia, Norway, and Turkey were sampled with a minimum of seven samples per site, and the sites from Antarctica with a minimum of six. Only sites with seven (or six, for Antarctica) interpretable directions are used in our analysis. If sites contain more samples, only the first seven (or six, for Antarctica) samples are used. All uninterpreted data are publicly available in the MagIC database (see Data availability

Comparison between paleopoles of this study and published paleopoles

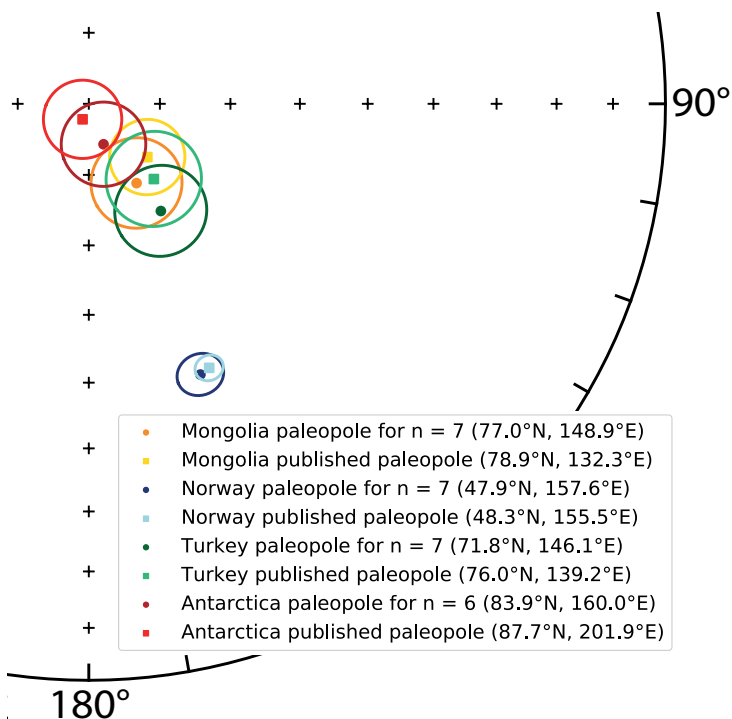


Fig. 1. Equal angle projection showing the paleopoles and their A_{95} following from our reinterpretation (used as reference paleopoles in this study), calculated with all sites and $n = 7$ (or $n = 6$, in case of Antarctica), and the published paleopoles and their A_{95} of Mongolia, Norway, Turkey, and Antarctica. All paleopoles are plotted on the upper hemisphere, whereby the longitude increases clockwise and the center represents the northern geographic pole.

statement). Our reinterpretations are provided in the supplementary information (Table S1) to this paper, but because our interpretations are (deliberately) not better than the original interpretations, we will not upload these to the MagIC database to avoid confusion. All paleopole positions from this study differ from the published paleopole positions, but still fall within the 95% confidence region of the respective published paleopoles (Fig. 1). In the following, we use these paleopole positions, which followed from our reinterpretation and were calculated with all sites and $n = 7$ (or $n = 6$, in case of Antarctica), as our reference paleopoles.

After the reinterpretation, we arrive at a total of 108 sites with $n = 7$ of lower Cretaceous lavas, corresponding to the base of the Cretaceous Normal Superchron, from the NE Gobi Altai mountain range of southern Mongolia, which erupted at a paleolatitude of $\sim 50^\circ\text{N}$ (van Hinsbergen et al., 2008; vH08). We do not include samples from the Artz Bogd area from the original data set because these appear systematically rotated due to tectonic deformation. Furthermore, only the sites acquired by van Hinsbergen et al. (2008) are included. Our reinterpreted data set (G22) leads to a higher scatter than the original interpretation of van Hinsbergen et al. (2008) for reasons outlined above ($A_{95, \text{vH08}} = 5.3^\circ$ vs.

$A_{95,G22} = 6.4^\circ$, $K_{vH08} = 9.1$ vs. $K_{G22} = 5.5$). Most sites have limited within-site scatter and high k values, as expected for lava sites.

We arrive at a total of 73 sites with $n = 7$ from lavas of Permian age from the Oslo Graben in Norway, which erupted at a paleolatitude of $\sim 20^\circ\text{N}$ (Haldan et al., 2014; H14). This data set contains lavas from the Permo-Carboniferous Reversed Superchron (PCRS). Interestingly, the between-site scatter is much lower than for the other three localities (Brandt et al., 2021; Handford et al., 2021). The within-site scatter of this data set, however, is higher. Our reinterpretation contains more scatter than the interpretation of Haldan et al. (2014) ($A_{95,H14} = 1.9^\circ$ vs. $A_{95,G22} = 3.1^\circ$, $K_{H14} = 52.2$ vs. $K_{G22} = 29.4$).

A total of 125 sites with $n = 7$ of lower to middle Miocene lavas and ignimbritic tuffs come from basins in the northern Menderes Massif in western Turkey, which formed at a paleolatitude of $\sim 35^\circ\text{N}$ (van Hinsbergen et al., 2010; vH10). This data set was acquired in a tectonically active area and contains basins that were interpreted to be tectonically coherent, and basins that were interpreted by van Hinsbergen et al. (2010) to be internally tectonically disturbed (later confirmed and mapped out in detail by Uzel et al. (2015, 2017)). It also contained sites acquired by preceding studies, but only the sites acquired by van Hinsbergen et al. (2010) are included in our data set. Our re-interpreted data set contains a comparable scatter as the data set of van Hinsbergen et al. (2010) ($A_{95,vH10} = 6.7^\circ$ vs. $A_{95,G22} = 6.4^\circ$, $K_{vH10} = 4.6$ vs. $K_{G22} = 4.8$).

Finally, we use 107 sites with $n = 6$ from lavas of Plio-Pleistocene age of the Erebus volcanic province in Antarctica at a latitude of $\sim 75^\circ\text{S}$ (Asefaw et al., 2021; A21). We did not reinterpret this data set and use the published interpretations, but only use sites with $n = 6$. We note that Asefaw et al. (2021) combined some sites; in our analysis, however, we still use the original, uncombined sites. Furthermore, we do not use the age constraint of < 5 Ma and k -cutoff. Our reinterpretation does not significantly differ from the published one of Asefaw et al. (2021) ($A_{95,A21} = 5.5^\circ$ vs. $A_{95,G22} = 5.9^\circ$, $K_{A21} = 7.7$ vs. $K_{G22} = 6.3$).

3.2. Approach

We perform a series of experiments to study the effect on paleopole position and precision of filters that one may use when multiple samples per site are available. These filters are: (a) a MAD cutoff; (b) a k -cutoff; (c) the number of samples per site (n), and (d) discarding outliers of within-site dispersion. In addition, we assess how a given number of paleomagnetic directions may be optimally distributed over a collection of paleomagnetic sites (N) to acquire the best-constrained paleopole position. We tested whether the distributions of VGPs conform to a Fisher (1953) distribution by applying the quantile-quantile (Q-Q) method described by Fisher et al. (1987). We found that all studied datasets have circularly symmetric distributions of VGPs. The VGPs of the data set from Turkey are Fisherian, whereas the datasets from Norway and Mongolia conform to a Fisher distribution only after application of a 45° cutoff and the Antarctica data set after application of a Vandamme (1994) cutoff. Therefore, we will be using the standard Fisher (1953) parameters in our analyses: the radius of the 95% confidence cone around the paleopole (A_{95}), the precision parameter (K) and the circular standard deviation (S). Furthermore, we calculate the angular distance to the reference paleopole, which is shown in Fig. 1. We perform experiments using a Python code, which we developed making extensive use of the freely available paleomagnetic software package PmagPy (Tauxe et al., 2016). We perform the calculations 1000 times, and each time different samples and/or

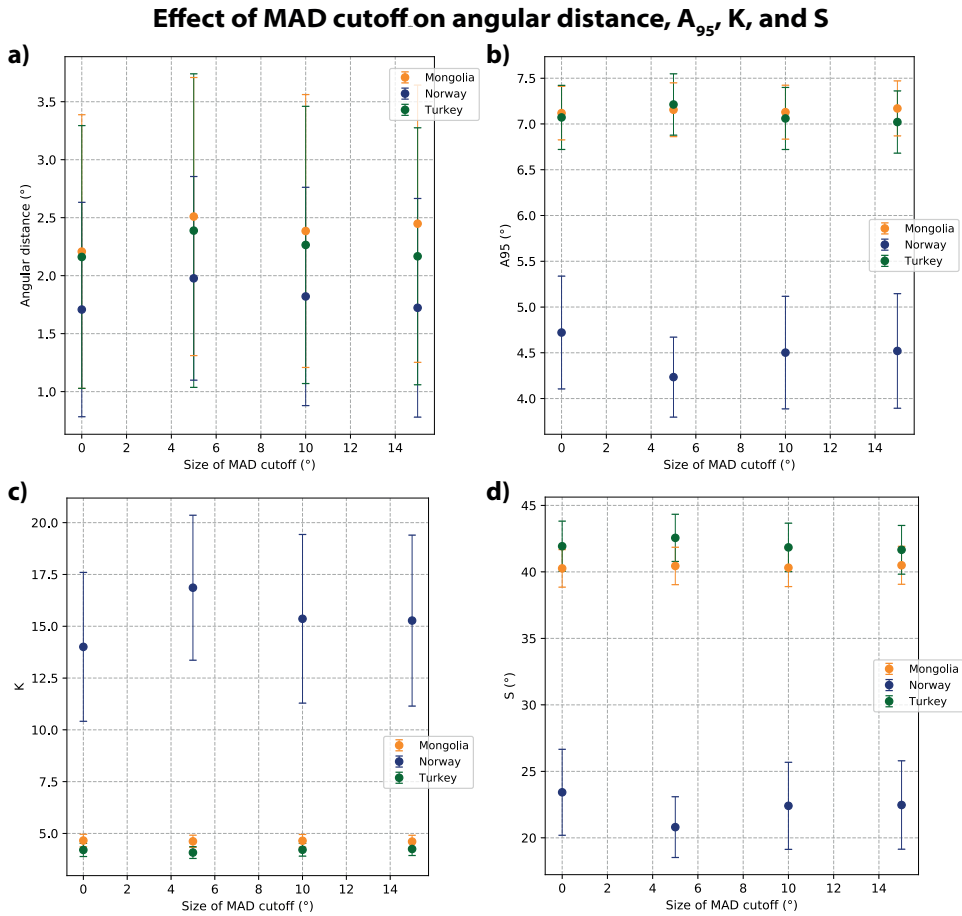


Fig. 2. Effect of a MAD cutoff on the (a) angular distance of the acquired paleopole to the reference paleopole whereby all sites have $n = 7$ (or 6, for Antarctica), and the (b) A_{95} , (c) K, and (d) S of the acquired paleopole. Every datapoint represents 1000 calculations, with error bars indicating the 95% confidence interval of these 1000 calculations. Each calculation, one random sample per site was selected, such that $n = 1$ and N is constant.

sites are selected from the population. We then calculate the mean and standard deviation of the parameters (angular distance to the reference paleopole, A_{95} , K, and S). Our Python code is available on Zenodo (see Data availability statement).

4. Results

4.1. Effect of MAD Cutoff

First, we analyze whether application of a maximum angular deviation (MAD) cutoff improves paleopole precision. We apply MAD cutoffs of 5°, 10°, and 15° on each of our datasets. The Antarctica data are very well determined, and all data pass these filters. We thus concentrate our analysis on the data from Mongolia (6%–32% eliminated), Norway (7%–52% eliminated), and Turkey (3%–12% eliminated). After applying the filter, we

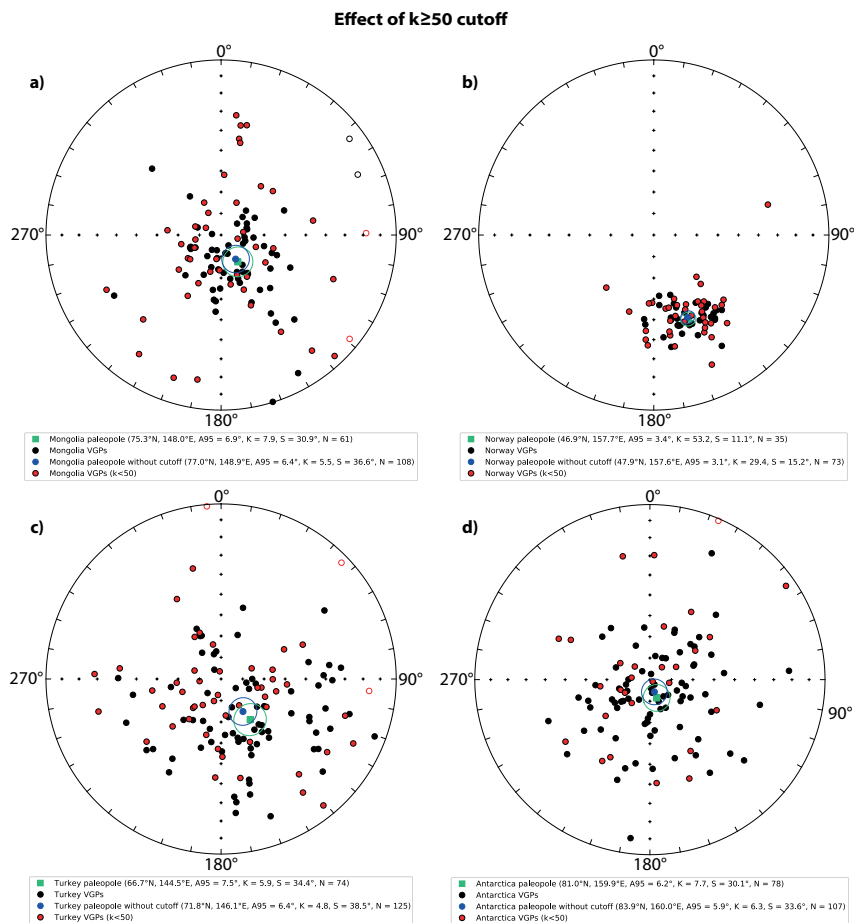


Fig. 3. Equal angle projections showing the VGPs of the data set from (a) Mongolia whereby each site has $n = 7$, (b) Norway whereby each site has $n = 7$, (c) Turkey whereby each site has $n = 7$, and (d) Antarctica whereby each site has $n = 6$. Solid (open) symbols are plotted on the upper (lower) hemisphere, whereby the longitude increases clockwise. The center of each subplot represents the northern geographic pole. Sites discarded by a $k \geq 50$ cutoff are indicated in red. In green, the paleopole and its A_{95} with application of the cutoff are indicated. In blue, the reference paleopole and its A_{95} (without application of the cutoff) are indicated.

randomly select one direction from each site such that $n = 1$, convert it to a VGP using the corresponding site longitude and latitude, and compute the paleopole with all sites for each analyzed filter. In no case the MAD cutoff eliminates all directions from a site, thus N is constant. Each analysis is conducted 1000 times, and we compute the average angular distance to the reference paleopole with $n = 7$, A_{95} , K , and S , and their 95% confidence interval. The results show that applying a MAD cutoff does not significantly change the position and precision of the paleopole (Fig. 2).

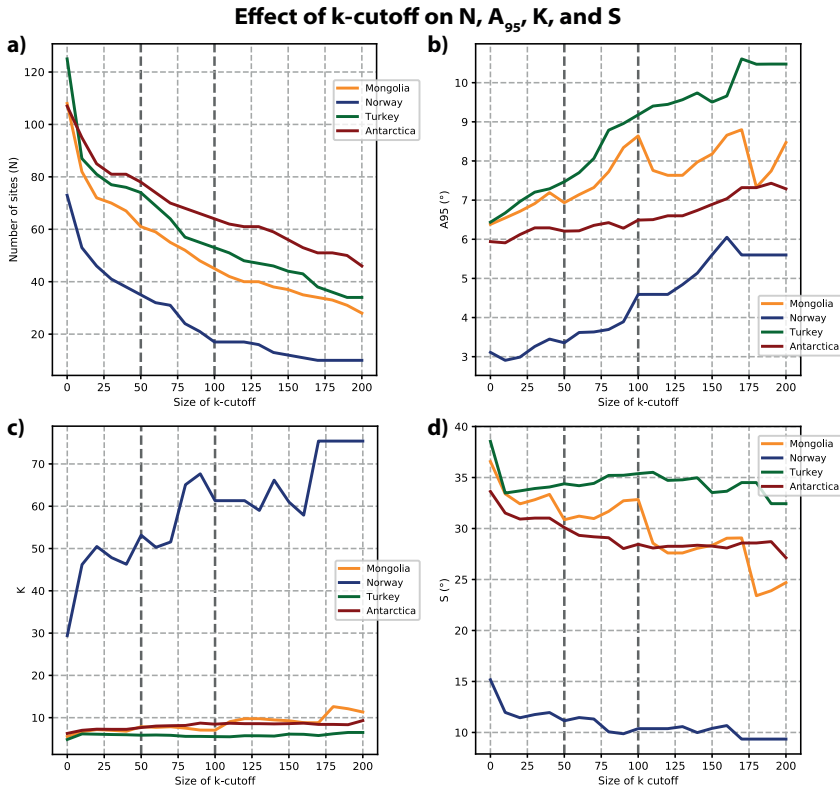


Fig. 4. Effect of the size of the k-cutoff on (a) the number of sites (N) remaining in the data set after application of the cutoff, and the (b) A_{95} , (c) K , and (d) S of the acquired paleopole. Commonly applied cutoff sizes of 50 and 100 are indicated with gray dashed lines.

4.2. Effect of a k-cutoff

A widely used filter to establish site-mean directions that represent spot readings of the paleomagnetic field is to check for high within-site scatter by applying a k-cutoff to the distribution of within-site directions. The Fisher (1953) precision parameter (k) is computed for the collection of ChRM directions per site, which are, in principle, expected to conform to a Fisher distribution, under the assumption that the within-site scatter results from randomly distributed errors such as measuring errors. The k-cutoff aims to eliminate sites that may not be representative of a spot reading, and sites with k values below a certain cutoff value are therefore discarded. We analyze the effect of the k-cutoff size on between-site scatter, and we test whether the eliminated sites indeed represent outliers. We apply the k-cutoff to all sites and increase its value by increments of ten. Afterward, we convert all remaining site-mean directions to VGP's using the corresponding site longitude and latitude, and from that calculate the paleopole (Fig. 3; Fig. S1) and its N , A_{95} , K , and S (Fig. 4). The paleopole positions do not significantly change when applying a k-cutoff (Fig. 3; Fig. S1). When a low $k \geq 10$ cutoff is applied, the number of sites remaining in the data set decreases by approximately 15%–30% (Fig.

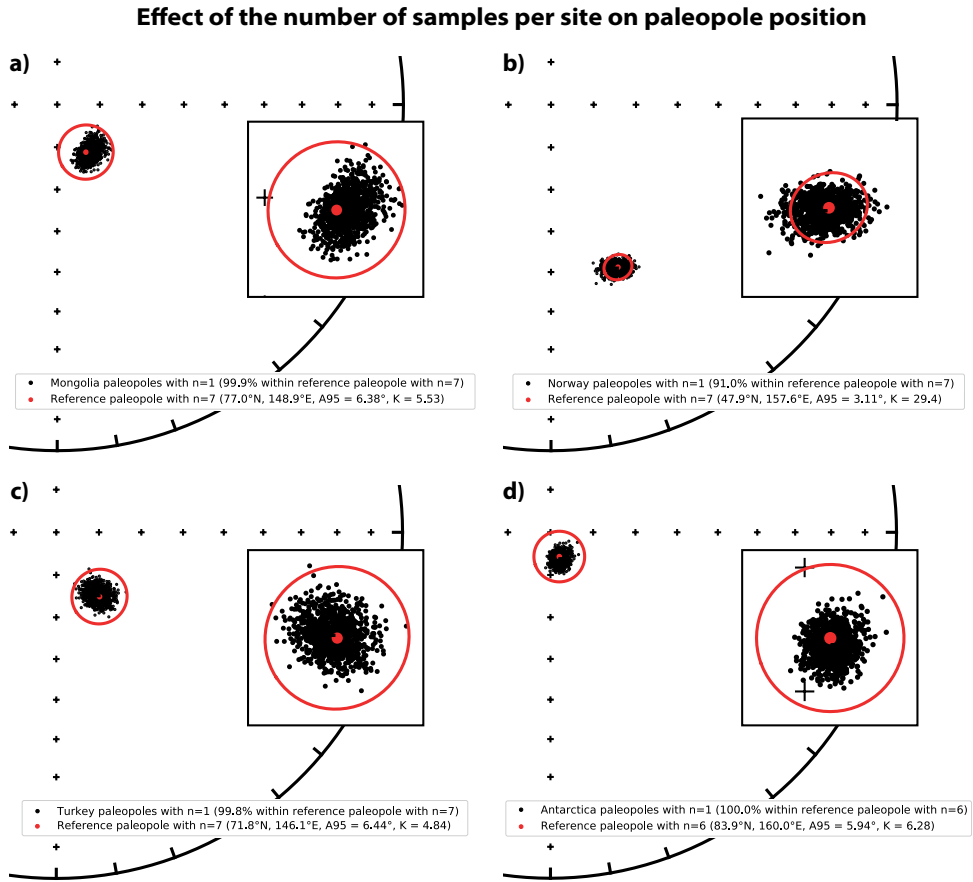


Fig. 5. Equal angle projection with in black 1000 paleopole positions whereby all sites have $n = 1$ and in red the reference paleopole position and its A_{95} whereby all sites have $n = 7$ (or 6, for Antarctica) for (a) Mongolia, (b) Norway, (c) Turkey, and (d) Antarctica. All paleopoles are plotted on the upper hemisphere, whereby the longitude increases clockwise. The center of each subplot represents the northern geographic pole. Inset shows a zoom-in on the data.

4a), omitting sites with near-random direction distributions. Increasing the cutoff size beyond 20, the decay in sites decreases. The A_{95} increases with increasing k -cutoff due to a decrease in N (Fig. 4b). As expected, discarding sites with high within-site scatter leads to a higher K and lower S , although the effects are small (Figs. 4c and 4d), except in the data set from Norway where K rises from 30 to 75. We note the K value of the data set from Mongolia approximately doubles from 6 to 11 when a k -cutoff of 200 is applied, but $\sim 75\%$ of the data is excluded while doing so. No major improvement becomes apparent in any of the variables at the commonly used cutoff sizes of 50 and 100. In addition, the elimination of sites is not demonstrably filtering outliers (Fig. 3). Importantly, although the application of a k -cutoff may subtly decrease S and increase K , the decrease in N leads to an increase of the A_{95} , and thus to a decrease in precision of the paleopole when a k -cutoff is applied, whereas the paleopole position remains approximately the same.

Effect of the number of samples per site on angular distance, A_{95} , K , and S

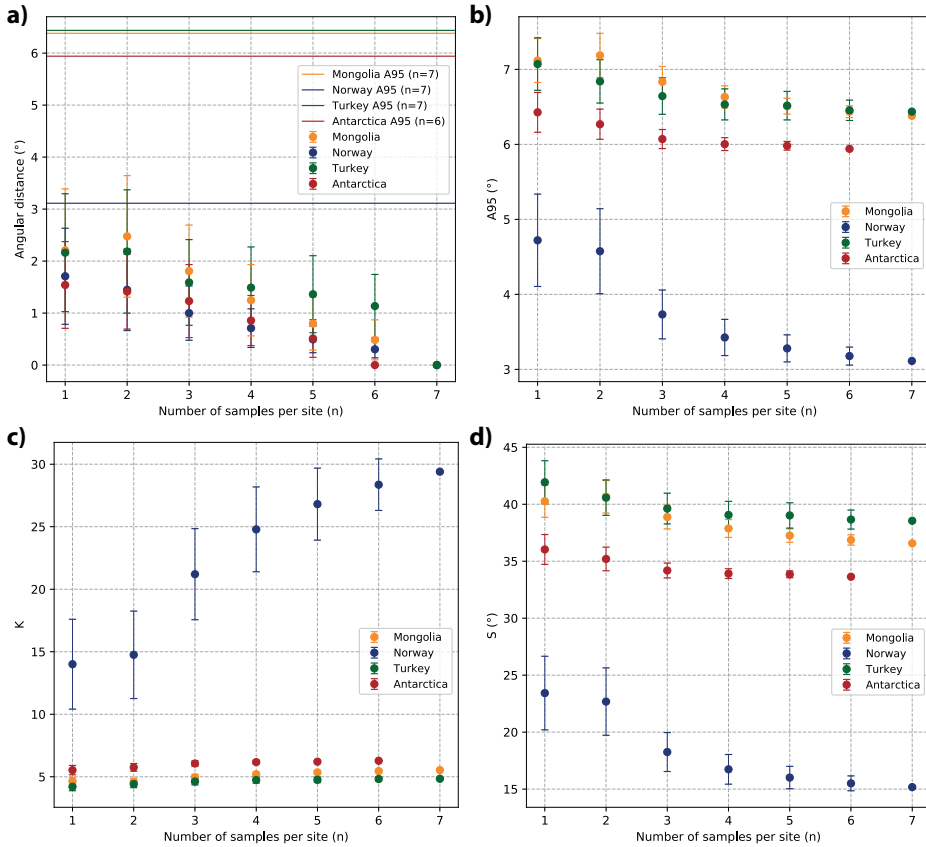


Fig. 6. Effect of the number of samples per paleomagnetic site (n) on the (a) angular distance of the acquired paleopole to the reference paleopole whereby all sites have $n = 7$ (or 6, for Antarctica), and the (b) A_{95} , (c) K , and (d) S of the acquired paleopole. Every datapoint represents 1000 calculations, with error bars indicating the 95% confidence interval of these 1000 calculations.

4.3 Effect of the number of samples per site (n)

Next, we analyze the benefits of collecting multiple samples per site to average within-site or between-sample errors. To this end, we study the influence of the number of samples per site (n) on the paleopole of a data set (Fig. 5) and its angular distance to the reference paleopole with $n = 7$ (or 6, for Antarctica), A_{95} , K , and S (Fig. 6). For each n , we perform the calculations 1000 times. Each calculation randomly collects n different samples from the total collection of samples per site. For each calculation, we compute a site-mean direction from these n samples, convert it to a VGP using the corresponding site longitude and latitude, and compute the paleopole by averaging N sites (Fig. 5). We then calculate the mean and standard deviation of each parameter (angular distance to the reference paleopole, A_{95} , K , and S) from the 1000 values obtained for each of the paleopoles (Fig. 6). The paleopole position calculated with $n = 1$ falls within the A_{95} of the reference paleopole calculated with $n = 7$ in 100% of the calculations for the datasets from Mongolia,

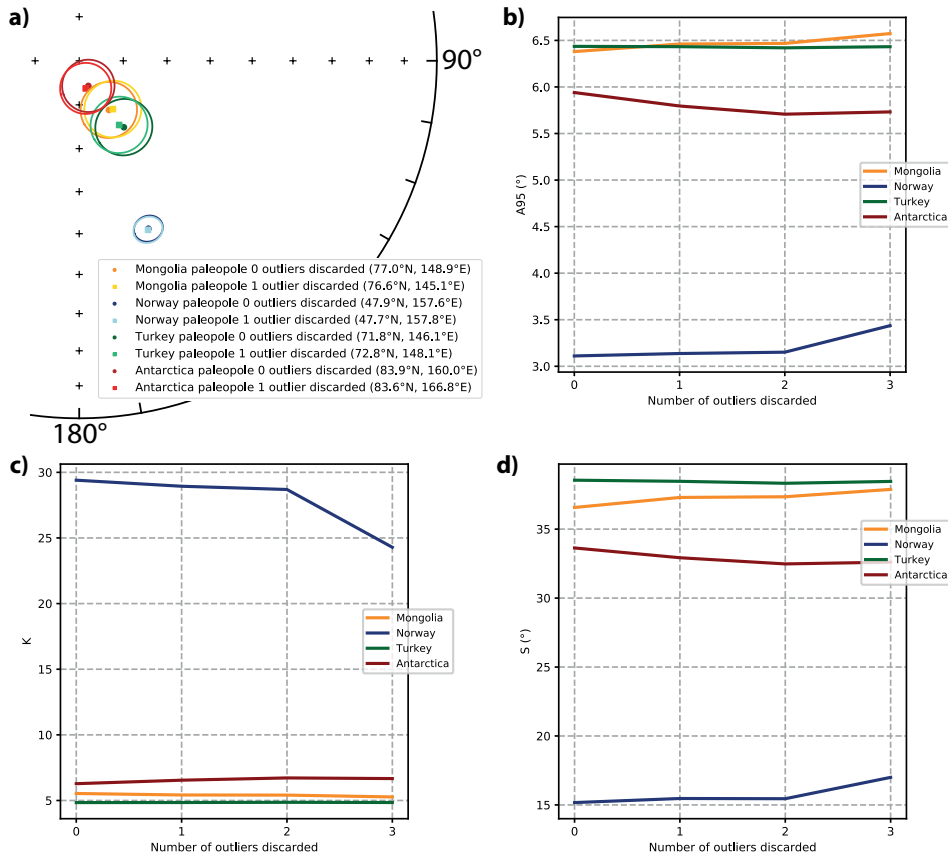
Effect of discarding outliers on paleopole position, A_{95} , K , and S


Fig. 7. Effect of the number of samples discarded per paleomagnetic site on (a) paleopole position in equal angle projection, shown without outliers discarded and with one outlier discarded, and the (b) A_{95} , (c) K , and (d) S of the acquired paleopole. All paleopoles in subplot (a) are plotted on the upper hemisphere, whereby the longitude increases clockwise and the center represents the northern geographic pole.

Turkey, and Antarctica (Fig. 5). For the Norwegian data set, this is the case for 91% of the calculations. In other words, the paleopole position is barely influenced by the number of samples per site (Fig. 6a) and stays within the 95% confidence interval. The influence on the A_{95} is small, but there is a slight decrease in the A_{95} when within-site scatter is averaged by increasing n (Fig. 6b). This varies from less than 0.5°–1.5°, with the largest effect occurring for the data set from Norway, whose sites have the largest within-site scatter. We find that the number of samples per site has a minor influence on K and S (Figs. 6c and 6d). Only Norway shows an increase in K from approximately 14 to 29 and a decrease in S from 23° to 16°. This experiment shows that the effect of the number of samples per site on determining a paleopole position is surprisingly small, even if between-site scatter is somewhat decreasing.

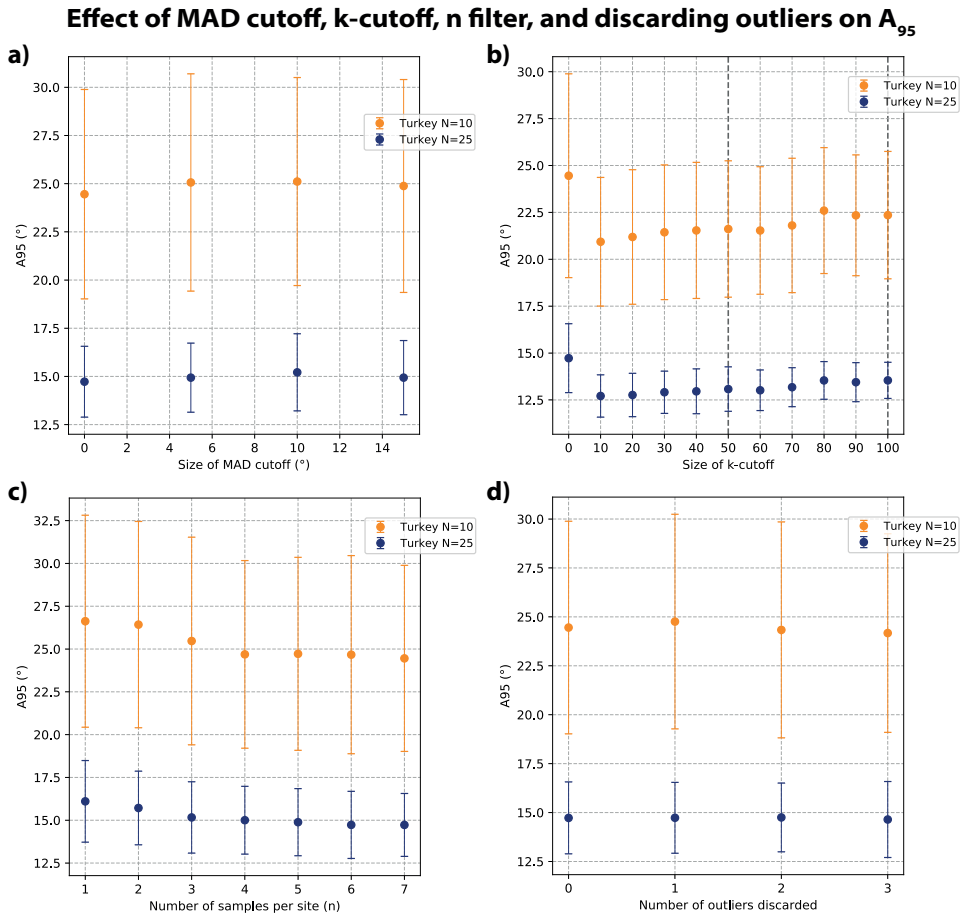


Fig. 8. Effect of (a) a MAD cutoff, (b) a k-cutoff, (c) varying the number of samples per site (n), and (d) discarding outliers on the A_{95} of the obtained paleopole, when taking $N = 10$ or $N = 25$ from the total collection of sites of the Turkey N_{95} data set. Every datapoint represents 1000 calculations, with error bars indicating the 95% confidence interval of these 1000 calculations.

4.4. Effect of discarding outliers on site level

One potential benefit of having multiple samples per site is to discard outliers, commonly done in the paleomagnetic community based on the “expert eye” of the interpreter. Here, we study the effect of discarding outliers on site level, by eliminating the farthest directions from the site mean. We do this three times, eliminating the one, two, or three most outlying directions. Interestingly, we find generally no effect of eliminating within-site outliers on paleopole position and its A_{95} , K , and S (Fig. 7), and for the Norway data set, the between-site scatter even increases. This is because VGP positions do not systematically shift toward or away from the paleopole (Figs. S2-S5). As a result, decreasing the within-site scatter by removing outlying directions has little effect on the between-site dispersion of VGPs.

4.5. Effect of filters on small data collections

The datasets that we analyzed above are unusually large. In most cases, paleomagnetic datasets are much smaller due to either the limited availability of lavas, or due to time constraints and the choice to collect multiple samples per site, rather than more sites with lower n . We thus briefly illustrate whether the filters we applied above on the large datasets yield different results for small datasets. To this end, we analyze the Turkey data set, which has the largest scatter. We again test the effect of a MAD cutoff, k -cutoff, minimum n per site, and number of outliers discarded on A_{95} , but now based on randomly choosing $N = 10$ or $N = 25$ from the total collection of sites (Fig. 8; for the effects on angular deviation, K , and S see Figs. S6-8). As for the large datasets, a MAD cutoff, eliminating the farthest outliers, or a minimum n per site, has no significant influence on paleopole precision (Figs. 8a, 8c and 8d). A marginal improvement of A_{95} value is obtained when eliminating sites with $k < 10$, but more stringent k filters have no significant effect (Fig. 8b).

4.6. Effect of sample distribution over sites

To average between-site scatter, it is common to collect multiple sites at a locality. The minimum number of sites recommended for determining a paleopole varies between authors (e.g., Meert et al., 2020; van der Voo, 1990), but as shown by (Chapter 2), paleopoles with larger N tend to plot closer to a best estimate of the time-averaged paleopole. We perform experiments varying the number of samples per site and the number of sites, with combinations chosen such that the total amount of paleomagnetic samples remains approximately 100. We study the effect on angular distance to the reference paleopole, A_{95} , K , and S (Fig. 9) of the acquired paleopole. The means are calculated from 1000 runs of the specific number of samples per site and number of sites, where the number of samples and sites is randomly selected from the total population during each run.

The paleopole position is strongly influenced by the distribution of samples over sites in case of Mongolia, Turkey, and Antarctica, and lies further from the reference paleopole if the samples are distributed over fewer sites (Fig. 9a). There also is a major effect on the A_{95} . For all datasets, the A_{95} is by far the smallest when it is constrained by 100 sites of $n = 1$, and the highest when it is constrained by 15 sites of $n = 7$ (Fig. 9b). The effect on K and S is small, except in the data set from Norway (Figs. 9c and 9d). In that data set, K is highest and S is lowest for 15 sites with $n = 7$. Nonetheless, the paleopole position is far better determined when taking many sites with few samples.

5. Discussion and conclusions

The results above show that none of the widely used data filters and cutoffs that aim to eliminate outliers and unreliable data, significantly improves paleopole precision. The application of these filters may even have an adverse effect; because these filters eliminate data, the filtered paleopoles often have lower N , and thus higher uncertainty without a significant change in position. Below, we briefly discuss why these filters do not have the desired effect.

The datasets we analyzed are all lava-based, and demagnetization behavior is typically stable, leading to ChRM directions with low MAD values. High MAD values may thus be considered suspect. Nonetheless, filtering of data with high MAD values led to no improvement in paleopole precision (Fig. 2). From this we may infer that the noise due

to higher MAD values does not significantly influence between-site scatter. Moreover, the farthest outliers are not systematically correlated with high MAD values. These farthest outliers are often very well determined directions with high intensities and stable demagnetization behavior, and their strong deviation from the reference direction was by the original authors interpreted as a lightning strike, which presents a common problem in lava sites (e.g., Strik et al., 2003). Such strongly overprinted outliers pass all MAD cutoffs.

In our reinterpretation of the data, we closed our “expert eye” and included sites that were excluded in the original studies because of subjective interpretations such as lightning struck sites. Our analysis illustrates that systematic application of filters, such as a k -cutoff, a minimum number of samples per site, or eliminating the farthest outliers per site, is incapable of filtering these unreliable VGPs. We point out that in absence of a demonstrable improvement of paleopole precision above a particular threshold, the choice of such a threshold is essentially arbitrary. The subjective judgment of the expert is needed to determine which samples and sites are included in the calculation of the paleopole, which should be explained in a paper describing the analysis (and all data should be made available following the FAIR principles (Wilkinson et al., 2016)).

Our analysis next shows that for the three datasets with high between-site scatter and low within-site scatter (i.e., Turkey, Mongolia, and Antarctica), applying the within-site scatter-based criteria leads to a marginal increase in data clustering (i.e., an increase in K and decrease in S). For the Norwegian data set, which has the rare combination of high within-site scatter and low between-site scatter, these criteria even lead to significantly higher clustering of the data. This deviation might be explained by the formation of the lavas during a long period of dominantly single polarity in the Permo-Carboniferous Reversed Superchron (PCRS; Haldan et al., 2014; Handford et al., 2021). This improvement may lend support to using these data filters for PSV studies.

But applying these filters when calculating paleopoles often leads to a decrease in paleopole precision (i.e., an increase in A_{95}), as demonstrated by the decrease in N that is caused by applying data filters and the corresponding decrease in paleopole precision (Fig. 9). Our experiments thus show that the effect of between-site scatter on paleopole precision is often dominant over within-site scatter. Because the accuracy of paleopoles generally decreases with decreasing N , as illustrated in Chapter 2 for the paleopoles behind the global APWP of Torsvik et al. (2012), applying within-site scatter filters may systematically decrease paleopole accuracy as well as precision (see also Fig. 9).

Our analysis shows that - for a fixed number of samples - collecting and averaging multiple samples per site leads to a relatively small improvement of the overall precision of the paleopole, whereas distributing the same number of samples over single-sample sites generates a much larger increase in paleopole precision (compare Fig. 6 with Fig. 9). Likewise, increasing the number of samples per site only leads to statistically insignificant changes in the position of the paleopole (Figs. 5 and 6a), whereas the position of a paleopole is much better constrained by increasing the number of sites (Fig. 9a), even when those sites are based on only a single sample. These results demonstrate a major benefit of collecting more sites instead of collecting more samples from the same site with the aim of reproducing the same spot reading multiple times. This suggests that also for sediment-based paleomagnetic datasets, reproduction of a spot reading, which is much more difficult to establish, is not essential. Datasets derived from long magnetostratigraphies, in which $n = 1$ per site is common, are thus in principle well-suited

Effect of sample distribution over sites on angular distance, A_{95} , K , and S

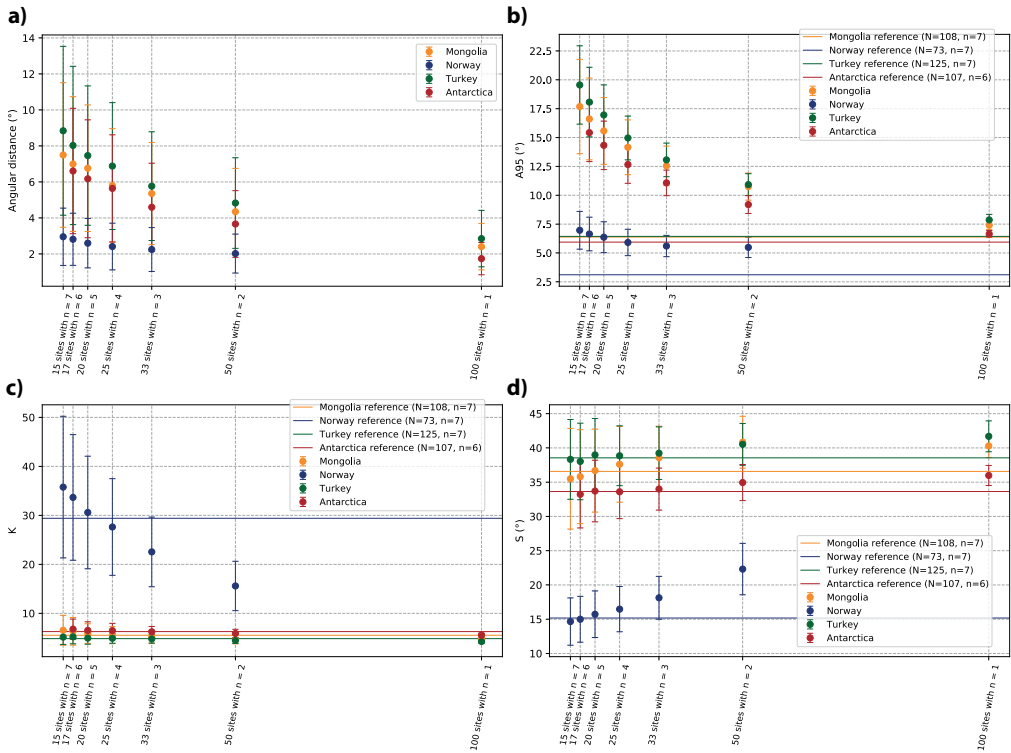


Fig. 9. Effect of distributing 100 paleomagnetic samples over a varying number of paleomagnetic sites on the (a) angular distance of the acquired paleopole to the reference paleopole whereby all sites have $n = 7$ (or 6, for Antarctica), and the (b) A_{95} , (c) K , and (d) S of the acquired paleopole. Every datapoint represents 1000 calculations of a distribution, with error bars indicating the 95% confidence interval of these 1000 calculations.

to calculate paleomagnetic poles from, provided common sedimentary artifacts such as inclination shallowing are corrected for (Kent & Tauxe, 2005; Tauxe & Kent, 2004; Chapter 3).

In case only few sites are available, or there is reason to question data quality, collecting multiple samples per site, as recommended by Meert et al. (2020), may still be a useful strategy. However, even for data collections with a low number of sites, we find that applying filters does not improve the resulting paleopole (Fig. 8). Therefore, we do not recommend collecting more samples per site to allow for the application of the data filters studied in this paper. Nonetheless, demonstrating the reproducibility of a paleomagnetic direction within a lava site may help a paleomagnetist to confirm that these sites have the tight clustering of data expected for spot readings and support the reliability of the paleomagnetic data. Rather than demonstrating this for each site, we recommend to apply this on a small selection of sites, which may serve as a field test in addition to for example, a fold, reversal, and/or conglomerate test.

Key information on the reliability of a paleomagnetic pole may be better determined using data distributions. For instance, the common problem of inclination shallowing (e.g., Tauxe & Kent, 2004), as well as suspected remagnetization may be identified from a non-Fisherian, elongated distribution of VGPs (e.g., Beck, 1999; Bilardello, 2020; Bilardello et al., 2018; Schmidt, 1990). Accurate determination of the shape of such data distributions requires large datasets (e.g., >100 sites; Tauxe et al., 2003; Tauxe & Kent, 2004; Chapter 3). However, the number of sites used to compute a paleomagnetic pole is often relatively low; the average number of sites behind the >8000 paleopoles of the global paleomagnetic database (GPMDB; Pisarevsky, 2005) is only ~15, and the median number of sites that underlie the 0–110 Ma paleopoles behind the global APWP of Torsvik et al. (2012) is 20 (Chapter 2). For future calculation of paleomagnetic poles, the extra efforts put into collecting multiple samples per site are thus more effectively spent on collecting more single-sample sites.

Data availability statement

All uninterpreted paleomagnetic data are publicly available in the MagIC database (Tauxe et al., 2016); Mongolia data set: <https://earthref.org/MagIC/19428>, Norway data set: <https://earthref.org/MagIC/19429>, Turkey data set: <https://earthref.org/MagIC/19430>, and Antarctica data set: <https://earthref.org/MagIC/17076>. The Python code used for our analysis is available on Zenodo (Gerritsen, 2022): <https://doi.org/10.5281/zenodo.6323434>.

5

A global apparent polar wander path for the last 320 Ma calculated from site-level paleomagnetic data

This chapter has been submitted for publication in Earth-Science Reviews as:

Vaes, B., van Hinsbergen, D. J. J., van de Lagemaat, S. H. A., van der Wiel, E., Lom, N., Advokaat, E. L., Boschman, L. M., Gallo, L. C., Greve, A., Guilmette, C., Li, S., Lippert, P. C., Montheil, L., Qayyum, A. & Langereis, C. G. A global apparent polar wander path for the last 320 Ma calculated from site-level paleomagnetic data.

Abstract

Apparent polar wander paths (APWPs) calculated from paleomagnetic data describe the motion of tectonic plates relative to the Earth's rotation axis through geological time, providing a quantitative paleogeographic framework for studying the evolution of Earth's interior, surface, and atmosphere. Previous APWPs were typically calculated from collections of paleomagnetic poles, with each pole computed from collections of paleomagnetic sites, and each site representing a spot reading of the paleomagnetic field. It was recently shown that the choice of how sites are distributed over poles strongly determines the confidence region around APWPs and possibly the APWP itself, and that the number of paleomagnetic data used to compute a single paleomagnetic pole varies widely and is essentially arbitrary. Here, we use a recently proposed method to overcome this problem and provide a new global APWP for the last 320 million years that is calculated from simulated site-level paleomagnetic data instead of from paleopoles, in which spatial and temporal uncertainties of the original datasets are incorporated. We provide an updated global paleomagnetic database scrutinized against quantitative, stringent quality criteria, and use an updated global plate motion model. The new global APWP follows the same trend as the most recent pole-based APWP but has smaller uncertainties. This demonstrates that the first-order geometry of the global APWP is robust and reproducible, indicating that paleomagnetism provides a reliable reference frame as basis for reconstructing, for instance, paleogeography and paleoclimate. Moreover, we find that previously identified peaks in APW rate disappear when calculating the APWP from site-level data and correcting for a temporal bias in the underlying data. Finally, we show that a higher-resolution global APWP frame may be determined for time intervals with high data density, but that this is not yet feasible for the entire 320-0 Ma time span. Future collection of large and well-dated paleomagnetic datasets from stable plate interiors are needed to improve the quality and resolution of the global APWP, which may contribute to solving detailed Earth scientific problems that rely on a paleomagnetic reference frame.

Key points

- New paleomagnetic reference frame for the last 320 million years
- Global apparent polar wander path computed from site-level data rather than poles
- First-order geometry similar to previous models but with smaller uncertainties
- Peaks in apparent polar wander may result from a temporal bias in the data
- Future improvement of the reference frame requires new, high-quality data

1. Introduction

Paleomagnetism provides one of the principal tools for the quantitative reconstruction of Earth's paleogeography. Paleomagnetic data are used to construct apparent polar wander paths (APWPs) that describe the apparent motion of the paleomagnetic pole relative to a fixed continent or tectonic plate through time (e.g., Creer et al., 1954). Assuming that the time-averaged geomagnetic pole coincides with the Earth's spin axis allows the translation of an APWP into the motion of a continent or plate relative to the geographic pole. By combining paleomagnetic data from all major plates using reconstructions of relative plate motions, a global APWP may be constructed that places a global model of relative plate motions into an 'absolute' reference frame (e.g., Phillips & Forsyth, 1972; Besse & Courtillot, 1991; 2002; Torsvik et al., 2008; 2012). Such a paleomagnetic reference frame is widely used by paleomagnetists to determine relative paleolatitudinal motions or vertical-axis rotations (e.g., Demarest, 1983; Butler, 1992) and also allows the estimation of the paleolatitude (through time) of any given location on Earth (e.g., van Hinsbergen et al., 2015), providing key input for paleoclimate, paleoenvironment, and paleobiology interpretation. These applications rely on the quality of the underlying global APWP and the robust quantification of its confidence limits. However, there is increasing recognition that the statistical approach used to calculate the widely used (global) APWPs and their uncertainty, which has changed little over the last >60 years, has several shortcomings.

First, the paleomagnetic poles (or paleopoles) that are used as input for APWP construction are commonly assigned equal weight, regardless of the uncertainties in the position of the paleopole or in the age of the rocks from which they were derived. Second, such paleopoles are calculated from widely different, and essentially arbitrary numbers of paleomagnetic sites (Chapter 2), whereby each site is interpreted to represent a 'spot reading' of the past geomagnetic field (e.g., McElhinny & McFadden, 2000). In previous APWPs, each input paleopole was assumed to have averaged 'out' the paleosecular variation (PSV) of the geomagnetic field, but Chapter 2 showed that the dispersion of input paleopoles around the most recent global APWP becomes larger with a smaller number of sites, creating a bias towards poles based on smaller datasets with larger uncertainty. Thus, the classical approach allows the calculation of non-unique APWPs with different uncertainties using the same underlying data depending on the subjective choice of how to distribute data over paleopoles (Chapter 2).

To overcome these problems, APWPs may instead be computed from site-level paleomagnetic data, that is, from virtual geomagnetic poles (VGPs) (e.g., McElhinny et al., 1974; Hansma & Tohver, 2020; van Hinsbergen et al., 2017, Chapter 2), or by weighting paleopoles against the number of sites (McFadden & McElhinny, 1995). In these approaches, equal weight is assigned to each 'spot reading' of the past geomagnetic field (that is, a site) rather than to each paleopole based on some collection of site-level data (Fig. 1). However, building a database with site-level data for the many hundreds of studies that reported relevant input data is not straightforward as paleomagnetic data is not always reported at the site-level, particularly in older publications, and it would require an enormous effort to compile those that are only listed in the original publication and not in databases such as MagIC (Jarboe et al., 2012). In Chapter 2, we introduced an alternative approach: they showed that when site-level data are parametrically re-sampled from reported paleopoles and their statistical parameters, a distribution of synthetic VGPs may be obtained that provides an accurate, albeit conservative approximation (i.e.,

with a somewhat larger dispersion) of the original data. This approach thus provides a promising avenue to use published paleomagnetic poles to compute APWPs from site-level data, allowing the incorporation of key uncertainties in the construction of APWPs as well as the weighting of datasets against the number of sites. Although recent studies have incorporated key sources of uncertainty, such as spatial and age uncertainties, in the computation of an APWP (e.g., Swanson-Hysell et al., 2019; Hansma & Tohver, 2020; Gallo et al., 2021; Wu et al., 2021), this has not yet been applied to the computation of a global APWP.

In this study, we compute the first global apparent polar wander from site-level paleomagnetic data, for the last 320 Ma, in which the key uncertainties in the underlying paleomagnetic datasets, in position and age, are incorporated and weighted. To transfer paleomagnetic data to a common reference plate, we use an updated global plate circuit that includes the most recent marine geophysics-based ocean basin reconstructions. We also provide an updated paleomagnetic database that updates the compilation of Torsvik et al. (2012). We have filtered that database using stringent, statistics-based, quantitative quality criteria and have extended the database with new, high-quality paleomagnetic datasets from stable plate interiors that have been published in the last decade. We also compiled data from regions that were previously not incorporated, such as the China Blocks, Iberia, and the Antarctic Peninsula, for the time period during which their motions relative to major tectonic plates are determined independently of paleomagnetism. We compute a global APWP from parametrically re-sampled VGPs at a 10 Ma resolution using a 20 Ma time window. We first evaluate whether there is reason to suspect that the obtained distributions of re-sampled VGPs are affected by biases in the underlying data (e.g., due to overlooked tectonic rotations or plate reconstruction errors). Next, we compare the new APWP with previous global APWPs that were based on paleopoles and highlight differences between them. In addition, we evaluate how the geometry of the new global APWP, and the rates of apparent polar wander, are influenced by the chosen temporal resolution of the path. Finally, we provide an outlook for the future construction of APWPs and highlight opportunities for improving the quality and resolution of the paleomagnetic reference frame.

2. Background

2.1. History of APWP computation

The paleogeographic and tectonic applications of paleomagnetism rely on the key assumption that the Earth's time-averaged magnetic field closely resembles that of a geocentric axial dipole (GAD) field, such that the position of the geomagnetic pole coincides with the Earth's rotation axis (e.g., Runcorn, 1959; Butler, 1992; Johnson & McFadden, 2007). The GAD hypothesis was already applied by Hospers (1954) and Creer et al. (1954) to determine the position of the past paleomagnetic pole relative to the sampling locations of rocks from different geological periods. One of the main advantages of assuming a dipolar field structure is that it provides a simple relationship between the paleomagnetic inclination and the paleolatitude of the location from which the paleomagnetic samples are derived: the so-called dipole formula (e.g., Runcorn, 1959; Irving, 1964). Most studies that investigated the nature of the past geomagnetic field find that the Earth's magnetic field is not a perfect geocentric axial dipole, and non-dipolar contributions to the past geomagnetic field have been estimated to be on the order of up

to 5% (e.g., Butler, 1992; Besse & Courtillot, 2002; Bono et al., 2020). However, the axial dipole contribution to the field is considered to be dominant, and it has now been widely accepted that the time-averaged geomagnetic field is well-approximated by a GAD field since at least mid-Carboniferous times (e.g., Butler, 1992; McElhinny & McFadden, 2000; Johnson & McFadden, 2007; Biggin et al., 2020).

The application of the GAD assumption allows the determination of the position of the geographic pole relative to a fixed plate or continent. When the position of the time-averaged paleomagnetic pole, as a proxy for the geographic pole, is plotted for different moments in the geological past, it seems to ‘wander’ relative to the present-day geographic pole position, as first observed by Creer et al. (1954). This ‘apparent’ polar wander reflects the motion of the plate or continent relative to the Earth’s rotation axis, providing an ‘absolute’ frame of reference for past plate tectonic motions. This motion is the combined result of two processes: plate tectonic motion relative to the rotation axis and the rotation of the entire crust-mantle system relative to the rotation axis; the latter known as true polar wander (TPW, e.g., Goldreich & Toomre, 1969; Gordon & Livermore, 1987; Evans, 2003). It is important to note that while APWPs provide quantitative constraints on the paleolatitude and azimuthal orientation of tectonic plates and continents through geological time, they do not provide any constraints on paleolongitude, due to the symmetrical structure of the assumed GAD field.

Apparent polar wander paths are constructed as a time series of paleomagnetic reference poles relative to the coordinate frame of a chosen reference plate (Fig. 1). Calculating an APWP requires a method to compute these reference poles by combining, averaging, or fitting available paleomagnetic data derived from rocks of different ages (e.g., McElhinny & McFadden, 2000; Tauxe et al., 2010). Creer et al. (1954) constructed the first APWP by connecting a sequence of individual paleomagnetic poles derived from rocks of different geological epochs sampled on the British Isles. But with the publication of an increasing number of ‘study mean’ paleopoles from rocks with overlapping ages in the following decades, reference poles were calculated by averaging available paleopoles from a given geological period (e.g., Irving, 1964, Phillips & Forsyth, 1972, Van der Voo & French, 1974). Since the late 1970s, the continuous increase in the amount of data allowed the construction of APWPs at a higher resolution by averaging paleopoles that fall within a chosen time window that was shorter than (most) geological time periods using a running mean (or sliding window) (e.g., Irving, 1977, 1979; Van Alstine & De Boer, 1978, Harrison & Lindh, 1982). This approach is appealing because of its simplicity and reproducibility (e.g., Torsvik et al., 2008), and was also used to compute the most widely used global APWPs of the last two decades (Besse and Courtillot, 2002; Kent and Irving, 2010; Torsvik et al., 2008; 2012). These APWPs were calculated at a 10 Ma interval by averaging paleopoles whose mean rock age falls within a 20 Ma sliding window centered on that age. The paleomagnetic data used to compute an APWP may be derived either from a single continent, tectonic plate, or geological terrane, or from multiple continents or plates. The advent of high-resolution global plate tectonic reconstructions enabled paleomagnetists to rotate paleomagnetic data from all the major tectonic plates and continents into a common reference plate, providing a ‘global’ APWP that describes the motion of all plates and geological terranes that are linked by the plate motion model relative to a fixed rotation axis (e.g., Phillips & Forsyth, 1972; Besse & Courtillot, 1991; 2002; Torsvik et al., 2008; 2012). South Africa, or the African plate, is typically used as reference plate for

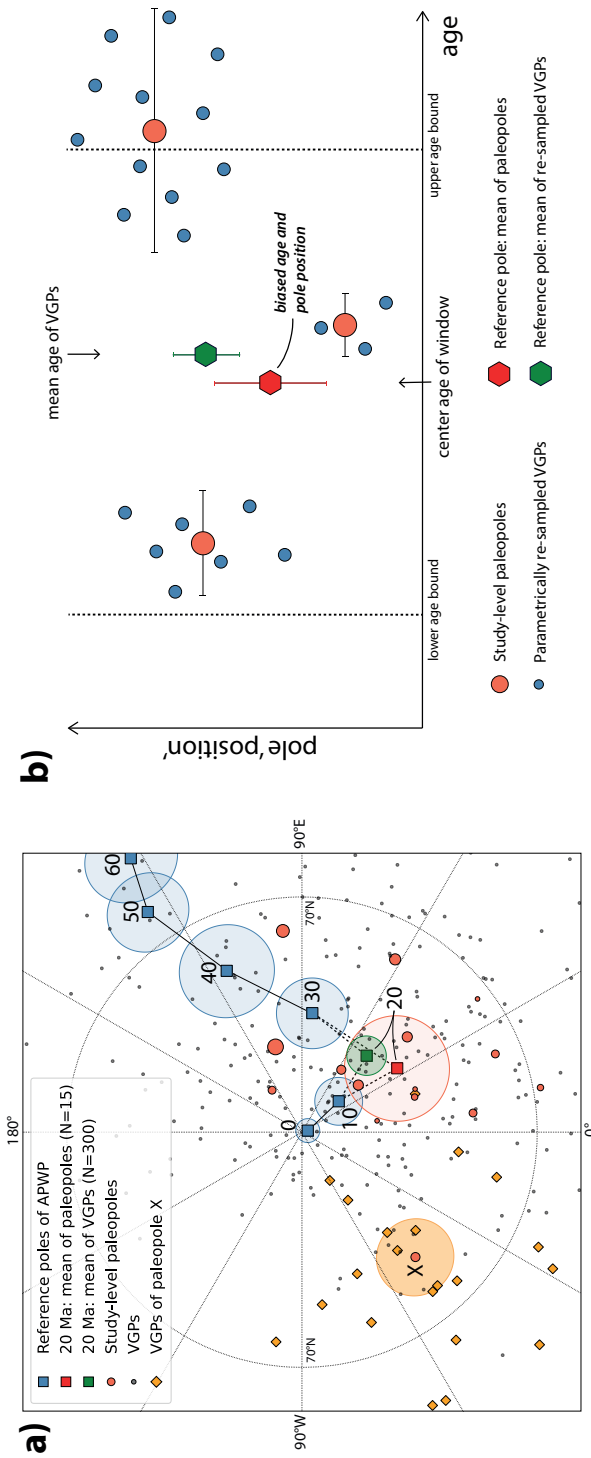


Fig. 1. (a) Example of an apparent polar wander path for the last 60 Ma (blue squares, with 95% confidence regions). The 20 Ma reference pole is computed in two ways: by taking the mean of the 15 paleopoles (light red circles) – as done in the conventional approach to calculating APWPs – or by taking the mean of 300 VGPs (grey dots) that were used to calculate those paleopoles. Note the difference in the reference pole position (green versus red square) and the size of its 95% confidence region. The size of the paleopoles corresponds to the number of VGPs from which that paleopole is derived, ranging between 5 and 60. Paleopole X and the 20 VGPs from which it was calculated are highlighted in orange. **(b)** Schematic comparison between the pole-based approach to calculating APWPs and the VGP-based approach developed in Chapter 2. Note that the oldest study-level paleopole does not contribute to the reference pole in the pole-based approach, but that nearly half of its VGPs are used in the calculation of the reference pole in the VGP-based approach. This way, both the number of sites behind each paleopole and its spatial and temporal uncertainties are taken into account in the computation of the reference poles of an APWP. In the VGP-based approach used in this study, the mean age of the (re-sampled) VGPs is used for the reference pole, rather than the center age of the time window.

the computation of a global APWP (Besse & Courtillot, 2002; Torsvik et al., 2008; 2012), because it is considered to have been relatively stationary (also longitudinally) for the last few 100 Ma, as it has been surrounded mostly by spreading ridges since the breakup of Pangea (e.g., Torsvik et al., 2008).

2.2. Shortcomings of conventional approaches, and alternatives

The conventional approach to calculating APWPs has several important limitations. First, known sources of uncertainty, such as uncertainties in the position or age of the input paleopoles, are typically not taken into account during the calculation of the APWP (Fig. 1b). In standard paleomagnetic procedures, directional uncertainties are quantified firstly at the level of individual paleomagnetic directions (often expressed as the maximum angular deviation; see e.g., Tauxe et al., 2010), secondly, at the level of individual site-mean directions (with an α_{95} confidence cone around the Fisher (1953) mean direction), and thirdly, at the level of paleomagnetic poles (with an A_{95} confidence cone around the Fisher (1953) mean of the input VGPs). However, these uncertainties are traditionally not propagated through this hierarchical framework (Heslop & Roberts, 2016; 2020). By computing an APWP from paleopoles without error propagation, it is implicitly assumed that the uncertainties and random biases in the individual paleomagnetic poles are effectively averaged 'out' by averaging up to a few dozen coeval paleopoles in the calculation of the reference poles of the APWP (e.g., Irving, 1964; Torsvik et al., 2008; 2014).

We showed in Chapter 2 that the assumption that paleopoles used to compute recent (global) APWPs average 'out' PSV is invalid. In fact, the dispersion of paleopoles around an APWP increases with a decreasing number of sites underpinning each paleopole. Despite the fact that the number of VGPs that underlie each input paleopole varies substantially (Chapter 2), each input paleopole is assigned equal weight in the classical running mean approach. Hence, the position and statistical properties of pole-based APWPs may be strongly affected by subjective choices in how data are distributed over poles. For example, site-level paleomagnetic data from multiple paleomagnetic studies of the same volcanic or sedimentary sequence may either be included in the computation of an APWP as a single paleopole (after combining the data on the site-level) or as separate entries. Hansma and Tohver (2020) explained that there is, in fact, no phenomenological basis for first averaging a certain number of VGPs to a 'study mean' pole to average PSV, and to then average the resulting poles again in the determination of an APWP.

It is important to note that there have been many previous efforts to propagate or weight uncertainties in the computation of apparent polar wander, for instance using a weighted running mean or spherical spline (e.g., Thompson & Clark, 1981; Harrison & Lindh, 1982; Torsvik et al., 1996; Schettino & Scotese, 2005; Swanson-Hysell et al., 2019; Wu et al., 2021; Gallo et al., 2021; Rose et al., 2022). However, the majority of the APWPs computed in these studies were still derived from paleopole-level data, and these weighting methods did not account for the subjectivity in the choice of the number of data underpinning each paleopole.

The approach chosen in this paper is aimed at overcoming these problems: we compute an APWP from site-level paleomagnetic data instead of from paleopoles (e.g., McElhinny & McFadden, 1974; Hansma & Tohver, 2020; Chapter 2). In this approach, equal weight is given to each VGP that is determined for a single 'site'. We here define a paleomagnetic

'site' as a geological unit that was formed in a short period of time relative to the time scale over which the geomagnetic field changes, such that the site mean direction represents a 'spot reading' of the paleomagnetic field (e.g., the site-mean direction from a lava flow, or a thin dyke) (see e.g., McElhinny & McFadden, 2000). Although it is often difficult to estimate the amount of geological time contained in a single sedimentary bed, individual samples obtained from sedimentary rocks may also provide independent readings of the past geomagnetic field (Tauxe & Kent, 2004; Bilardello & Kodama, 2010b). Demonstrating this may be challenging for small sediment-based datasets, but in Chapter 3 we formulated a stringent set of criteria to determine whether large paleomagnetic datasets ($n > 80$ directions) derived from sediments represent collections of paleomagnetic spot readings. Site-level data referred to hereafter in this manuscript thus includes site-mean directions from lavas flows or thin dykes, as well as individual directions obtained from a single sedimentary horizon or bed. The use of site-level data rather than paleopoles better reflects the underlying paleomagnetic data by assigning larger weight to larger datasets of independent measurements of the past geomagnetic field and avoids the subjectivity surrounding the definition of a paleopole.

3. Methods

3.1. Calculating apparent polar wander from site-level data

We developed an approach to compute a global APWP for the last 320 Ma from site-level paleomagnetic data. To obtain a paleomagnetic dataset at the site-level, we use an iterative, parametric re-sampling approach (Fig. 2). Although it would be possible to calculate a global APWP directly from published site-level data, compiling these from the many hundreds of studies with relevant input data would require a major effort and is complicated by the fact that not all these studies have reported their data at the site-level. Recent analysis, however, showed that parametric re-sampling of VGPs from a set of reported paleopoles and their statistical parameters provides an accurate approximation of the original distribution of VGPs, albeit with a slightly larger dispersion (Chapter 2). To generate a site-level dataset, we first compiled a database of 'classical' paleomagnetic poles as reported in literature, with statistical properties that describe the number of underlying paleomagnetic sites and their dispersion, the sampling location, uncertainties associated with inclination shallowing correction, and age (see section 5). Using this database, we generate synthetic site-level paleomagnetic data from each paleopole included in our compilation and repeat this procedure 2000 times (Fig. 2). This large number of iterations ensures the robustness of the resulting APWP and allows the propagation of both spatial and temporal uncertainties in the confidence bounds of the APWP. For each iteration, we parametrically re-sample a set of pseudo-VGPs from a Fisher (1953) distribution that is centered around the paleopole and defined by its Fisher (1953) precision parameter K . We generate the same number of VGPs as the number of sites that was included in the calculation of the paleopole (or grand mean paleomagnetic direction) reported in the original publication. In our approach, equal weight is thus assigned to each (pseudo-) VGP rather than to each paleopole, and the weight of each paleomagnetic dataset directly depends on its number of sites.

In our workflow, we also address the important source of uncertainty in the computation of APWPs that is known as 'inclination shallowing', which affects paleomagnetic datasets derived from sedimentary rocks. A 'blanket' correction factor

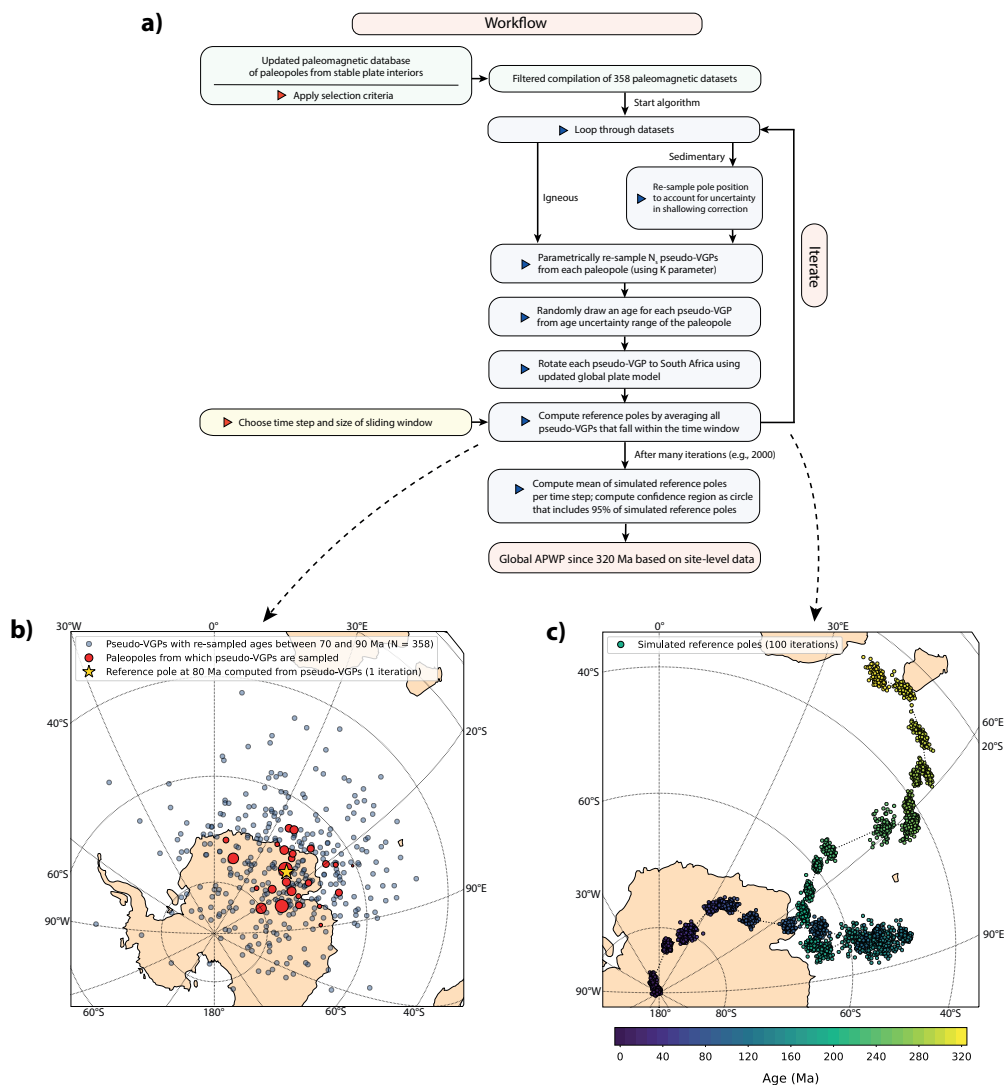


Fig. 2. (a) Workflow for the computation of the new global APWP. (b) Orthographic plot of the parametrically re-sampled VGPs with ages between 70 and 90 Ma (blue circles), which are derived from the paleopoles (red circles, size corresponds to number of VGPs sampled from pole) and used to compute a reference pole at 80 Ma. c) Orthographic plot showing the simulated reference poles obtained by 100 iterations.

(of $f=0.6$ in Torsvik et al., 2012) has often been used in the computation of APWPs (e.g., Torsvik et al., 2012; Wu et al., 2021; Kulakov et al., 2021) but this underestimates the natural variation in the magnitude of inclination shallowing and assumes that all sediments are affected by shallowing which is not always the case (e.g., Bilardello & Kodama, 2010a; Bilardello et al., 2011; Kodama, 2012; Gallo et al., 2017; Kent & Muttoni,

2020; Chapter 3; Pierce et al., 2022). In the computation of our global APWP, we only include datasets from sedimentary rocks to which an inclination shallowing correction has been applied and whereby the uncertainty in the correction is quantified. Except for two datasets that were corrected using an anisotropy-based correction technique (Kodama, 2009; Brandt et al., 2019), all sedimentary datasets were corrected for inclination shallowing using the elongation-inclination (E/I) method of Tauxe and Kent (2004).

To incorporate the uncertainty in the shallowing correction in our workflow, we build upon the recent work of Pierce et al. (2022). These authors developed a way to express the uncertainty of the E/I correction as an uncertainty in paleomagnetic pole position along the great-circle between the paleopole and the sampling locality, i.e., in the co-latitude direction. Using the ensemble of flattening factor obtained from the bootstrapped ensemble of paleomagnetic directions, they computed the ensemble of possible paleomagnetic pole positions, each with a different paleomagnetic paleo- and co-latitude. Pierce et al. (2022) noted that the distribution of estimated paleolatitudes approximates that of a normal distribution. Here, we assume that the distribution of paleolatitudes, and thus the co-latitudes, approximates a normal distribution, and use this to incorporate the extra uncertainty in the co-latitude direction resulting from inclination shallowing. To this end, we compute the standard deviation of the colatitude distribution for every inclination shallowing corrected dataset in our compilation. We obtain this value either by applying the E/I correction to the individual paleomagnetic directions that were published in the original paper or provided to us by the authors. If we were unable to obtain the directional dataset, we derived the standard deviation from the reported 95% confidence regions on the inclination or paleolatitude by taking these confidence regions as two standard deviations. For the two datasets corrected by an anisotropy-based approach, we use the reported confidence regions on the correction to obtain this value. For each iteration in our workflow, we first re-sample the paleomagnetic co-latitude from a normal distribution with a mean corresponding to the co-latitude of the shallowing-corrected pole and the listed standard deviation. We then compute a new position of the paleopole – along the great-circle between the sampling location and the reported shallowing-corrected paleopole – using this re-sampled co-latitude and the paleomagnetic declination computed from the original shallowing-corrected pole. This procedure yields a new position of each sediment-derived paleopole, thereby incorporating the additional uncertainty in the co-latitude direction resulting from inclination shallowing. Next, pseudo-VGPs are generated from this new paleopole position, following the workflow outlined above (Fig. 2a).

The second step in our workflow is to propagate the uncertainties in the age of the sampled rocks. To this end, we randomly draw an age for each pseudo-VGP from a uniform distribution that corresponds to the age uncertainty range listed for each paleopole in the database. Quantifying the age uncertainty by a uniform distribution is intuitive for sediment-derived datasets, whose age uncertainty range is often determined by bio- and/or magnetostratigraphy, and a uniform distribution may straightforwardly be defined by the upper and lower age limit of the geological time period or interpreted magnetozones. The age of igneous rocks, on the other hand, is often based on radiometric dating, for which the uncertainty on individual age determinations is often reported as one or two standard deviation(s), and a Gaussian distribution could thus be used to quantify the uncertainty in age (see e.g., Swanson-Hysell et al., 2019; Wu et al., 2021,

Gallo et al., 2021; Rose et al., 2022). However, because the age of sampled igneous rocks is typically determined by multiple radiometric ages, either from multiple dated samples or determined for the regional magmatic activity (e.g., for a large igneous province (LIP)), it is difficult to use a Gaussian distribution for the age uncertainty for all igneous datasets. We therefore choose a slightly more conservative approach and also use a uniform distribution between the upper and lower limit reported for the age of the paleomagnetic datasets that were derived from igneous rocks.

In the third step of our workflow, we transfer the obtained collection of pseudo-VGPs to the same coordinate frame, for which we use an updated global model of relative plate motions (see section 4 and Tables 1 and S1). For each tectonic plate included in the plate circuit, we computed the Euler rotation poles per million years relative to a given reference plate, interpolating between reported total reconstruction poles assuming constant rotation rates. Here, we use South Africa as our main reference plate, as is commonly done in the construction of global APWPs (e.g., Besse & Courtillot, 2002; Torsvik et al., 2008, 2012). We use this plate model to rotate each individual pseudo-VGP to South Africa coordinates after rounding its assigned age to the nearest integer. This procedure thus propagates the effect of uncertainties in age on the relative plate motion and position of the tectonic plates from which the paleomagnetic data is derived.

In the fourth step, we determine a reference pole of the global APWP at a chosen interval (we use an interval of 10 Ma) and with a chosen sliding window (here, 20 Ma). Because datasets cannot constrain variations that are smaller than the uncertainties of that dataset, we only include data collections in the analysis with an age uncertainty that is smaller than the chosen sliding window. The reference pole is computed based on all pseudo-VGPs whose assigned age falls within the chosen age window of the pole (Fig. 2b). In cases where the age uncertainty of a paleopole overlaps only partially with the time window of a reference pole, only the pseudo-VGPs are used that were assigned an age that falls in that time window. The contribution of each paleomagnetic dataset to a given reference pole of the APWP is thus weighted against the overlap between the age range of the dataset and the time window of the reference pole. Because in each iteration, the pseudo-VGPs are redrawn and are assigned a new random age, the number of VGPs that falls within the chosen time window will differ between iterations. So, although the total number of pseudo-VGPs that are generated for the entire APWP is equal for each iteration, the exact number of VGPs that is used to compute each reference pole will vary due to the re-sampling of ages.

We compute each reference pole by taking the Fisher (1953) mean of the pseudo-VGPs that fall within the time window, yielding a reference pseudo-pole that provides an estimate of the time-averaged paleomagnetic pole position – and thus the rotation axis – in a South African coordinate frame. In addition, we compute a range of statistical parameters from the distribution of pseudo-VGPs, including the number of VGPs (N), the Fisher (1953) precision parameter (K), the 95% confidence region (A_{95}), the circular standard deviation (S) and the elongation parameter (E , computed as the ratio of eigenvalues τ_2/τ_3 , see Tauxe et al., 2004). We use these statistical parameters to assess the robustness and identify potential biases in the distributions of re-sampled VGPs that underlie the reference poles.

Finally, we repeat the above procedure 2000 times to average the variation in the obtained reference poles resulting from parametric re-sampling and to allow the

determination of confidence regions for the global APWP (see Fig. 2c). We compute the final reference poles of the APWP by taking the Fisher (1953) mean of the 2000 reference pseudo-poles for each time step. We define the confidence region of the reference poles of the global APWP by the circle that includes 95% of the 2000 reference pseudo-poles, which we refer to as the P95.

In this approach to calculating global apparent polar wander and its confidence, we thus incorporate a number of key uncertainties, including spatial and temporal uncertainties in the paleomagnetic datasets, the uncertainty associated with the E/I correction for inclination shallowing of sedimentary rocks, as well as uncertainties in the rotation of the VGPs to the reference coordinate system that results from uncertainties in age. All these uncertainties are reflected in the dispersion of the pseudo-VGPs, which is largely controlled by the between-pole dispersion of the coeval paleopoles and their K values that are used to parametrically re-sample the pseudo-VGPs. Other incidental errors in the dataset, such as incorrect age assignments, unrecognized regional vertical-axis rotations, or unrecognized magnetic overprints, cannot be explicitly taken into account or corrected for, but such errors would likely lead to increased dispersion in the pseudo-VGPs per time window. We will compare the average scatter, elongation, and Fisher (1953) precision parameter of the pseudo-VGPs with values expected from PSV to assess whether and which reference poles may suffer from such errors.

3.2. Selection criteria

We applied a number of selection criteria during the compilation of the paleomagnetic datasets that were used for construction of the global APWP (see section 5 for more details on the compilation). First, we re-compiled the data that were included in the compilation of Torsvik et al. (2012) from the original publications. We excluded data for which evidence was reported that it does not represent a reliable estimate of the time-averaged field at the time of formation of the sampled rocks, as concluded by the original authors or by others in more recent work that evaluated that particular dataset. We also rejected datasets for which no modern demagnetization techniques were used, as is common procedure (van der Voo, 1990a; Meert et al., 2020). In addition, we removed duplicates: in some cases, the paleomagnetic data used to compute a paleopole that was included in the Torsvik et al. (2012) database were also used (and combined with other or newer data) to compute more recently published paleopoles. Reasons for exclusion are provided in Table S2 and include, for instance, evidence for remagnetization or unremoved magnetic overprints, local or regional vertical-axis rotations, erroneous structural corrections, or poor age control. We note that paleomagnetic datasets that were not originally compiled by Torsvik et al. (2012), e.g., because they were published after their compilation, and that did not satisfy the above criteria, were immediately rejected, and are not included in Table 2.

We then applied the following criteria to all paleomagnetic datasets:

- 1) We exclude datasets derived from less than 5 sites that are interpreted as independent spot readings of the past geomagnetic field. This number is essentially arbitrary but establishing whether such small datasets accurately represent PSV is difficult, and in our site-level computation of the APWP, the impact of such small datasets is negligible. We do not require that sites are based on averages of multiple samples, as this was shown to have minor effects on paleopole position or precision (Chapter 4).

2) We exclude paleomagnetic datasets from igneous rocks if their A_{95} values fall outside of the N-dependent reliability envelope of Deenen et al. (2011). This criterion evaluates whether the dispersion of VGPs is consistent with what may be expected from secular variation. If the reported A_{95} cone of confidence of the paleopole falls outside of the $A_{95, \text{min-max}}$ reliability envelope, this suggests that the dataset is likely affected by one or more sources of additional scatter that are unrelated to PSV (if $A_{95} > A_{95, \text{max}}$), or that PSV was insufficiently sampled by the dataset (if $A_{95} < A_{95, \text{min}}$), for instance, due to the limited temporal coverage of the sampled sites (see Deenen et al. (2011) for a detailed explanation).

3) We only include sediment-derived datasets whereby the paleopole and statistical parameters were calculated from a collection of paleomagnetic directions that approximately represent independent readings of the past geomagnetic field, and whereby these directions were corrected for potential inclination shallowing. To select such datasets, we use the reliability criteria formulated in Chapter 3, which assess under which conditions sedimentary datasets may be reliably corrected for inclination shallowing by the E/I correction, while satisfying the underlying assumption of that method that each of the paleomagnetic directions may be considered an independent reading of the past geomagnetic field. We only include E/I-corrected sedimentary datasets that would receive a grade 'A' or 'B' according to the evaluation scheme of Chapter 3. In addition, we have included two datasets that satisfy these criteria but were corrected for inclination shallowing using an anisotropy-based approach (Kodama, 2009; Brandt et al., 2019). We note that these criteria for sedimentary rocks are far more stringent than in previous compilations for the computation of APWPs, and only 29 sediment-derived datasets are used in the computation of the global APWP.

4) As a final selection criterion, we only include datasets with an age uncertainty range of <20 Ma: datasets with larger age uncertainties can only be included in APWPs with sliding windows larger than 20 Ma, which we do not compute here, and which would lead to needless smoothing of the global APWP.

4. Global plate model

The global apparent polar wander path is computed from paleomagnetic data from all stable plate interiors after rotating them relative to a single tectonic plate using a global model of relative plate motions. These relative plate motions are quantitatively described by Euler rotation poles that are mostly derived from marine magnetic anomaly identifications and fracture zone data. In the global plate model, each tectonic plate is linked – either directly or via a chain of neighboring plates – to the reference plate South Africa. We only include the major plates and continental blocks whose motions relative to South Africa are well-established, such that the available paleomagnetic data may be reliably combined to construct a global APWP. A schematic representation of the global plate circuit is shown in Fig. 3.

In our global plate model, we incorporate recently published Euler rotation poles based on the highest-resolution marine geophysical records. The original sources of the rotation poles for each tectonic plate are listed in Table 1, and we provide all rotation poles in Table S1. We note that many of these rotation poles were already used for the construction of previous global APWPs (e.g., Kent & Irving, 2010; Torsvik et al., 2008, 2012), as well as in global plate models (Seton et al., 2012; Torsvik & Cocks, 2016; Müller et al., 2016,

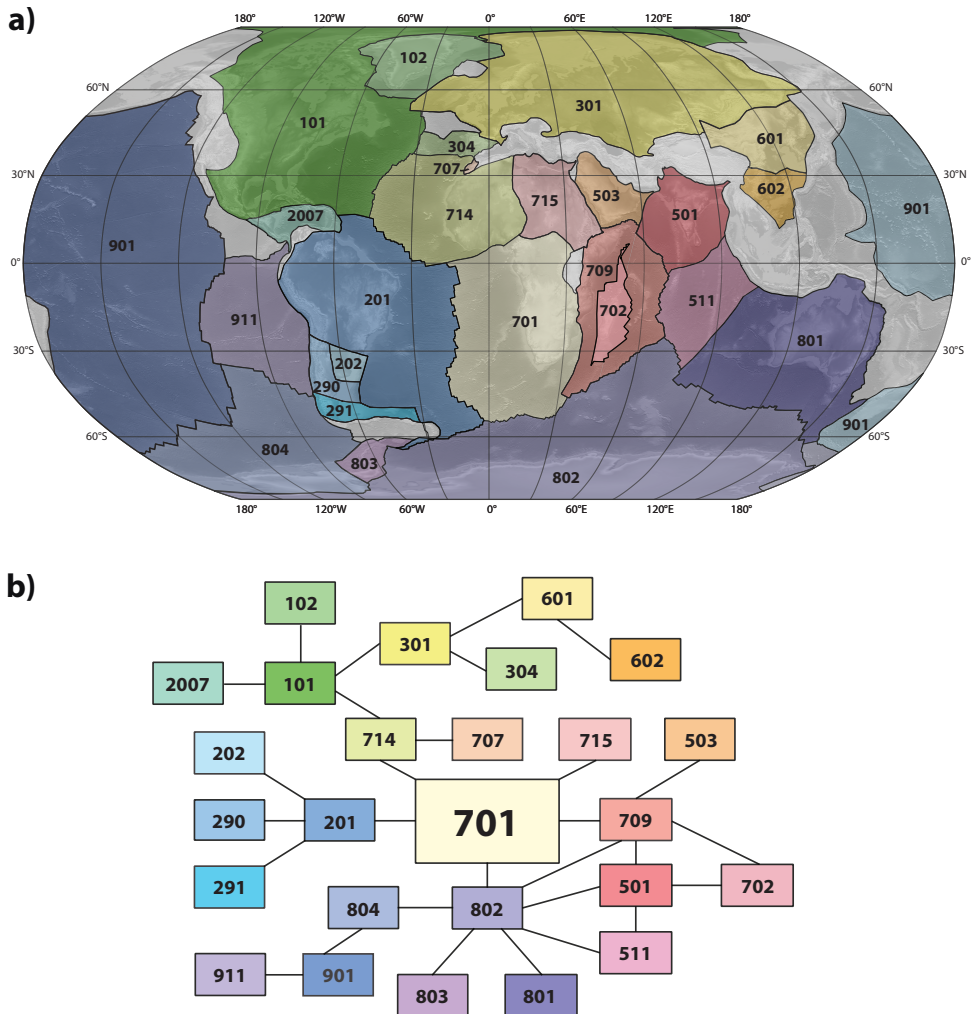


Fig. 3. (a) Simplified global map of the tectonic plates from which the paleomagnetic data used for the global APWP is derived. (b) Schematic representation of plate circuit. See Table 1 and S1 for more details. Modified from van Hinsbergen et al. (2015).

2019). The latest updates have mostly added more detail to the plate motion histories (e.g., DeMets & Merkouriev, 2021), but do not significantly change the long-term motions. Importantly, we have converted the ages of all the interpreted magnetic anomalies to the most recent geological time scale of Gradstein et al. (2020), which may shift the age of anomalies by up to a few million years compared to the ages assigned by the original authors.

Our global APWP uses data from the following tectonic plates or lithospheric fragments (with plate identification number) whose relative motions are constrained for the entire time period from which data were compiled for our global APWP, i.e., the

last 330 Ma (Fig. 3): North America (101), Greenland (102), South America/Amazonia (201), Parana (202), Colorado (290), Patagonia (291), Eurasia (301), India (501), Arabia (503), South Africa (701), Madagascar (702), Moroccan Meseta (707), Somalia (709), Northwest Africa (714), Northeast Africa (715), Australia (801), and East Antarctica (802). In addition, we have added several tectonic plates and blocks to our plate circuit, which were not included in the previous data compilation of Torsvik et al. (2012). The motions of these plates relative to South Africa are not sufficiently well-constrained (e.g., by marine geophysical data) for the entire time period covered by our global APWP but are well-constrained for a more limited time period. We thus include them for the period for which their motions relative in the global plate model are determined independently from paleomagnetic data (Table 1).

We have included paleomagnetic data from Iberia (304) for times after chron 34n (~83.65 Ma, the end of the Cretaceous Normal Superchron; CNS). Although marine magnetic anomaly-based Euler rotations are available for Iberian motion before the superchron, we do not incorporate data from this time because the interpretation and robustness of the underlying anomalies are under debate (e.g., Bronner et al., 2011; Tucholke & Sibuet, 2012). We have included data from the North and South China Blocks (601, 602) for times younger than 130 Ma, corresponding to the youngest age estimates for the cessation of significant motion along the Mongol-Okhotsk suture zone (e.g., van der Voo et al., 2015; Yang et al., 2015). We have included paleomagnetic data from the Antarctic Peninsula and neighboring islands (803) for the last 140 Ma, for which time it was rigidly attached to East Antarctica (van de Lagemaat et al., 2021). We include the Caribbean plate (2007) back to 38 Ma, for which time there is no relative motion of the Cuba segment relative to North America and relative Caribbean-North America motions are constrained by marine magnetic anomalies on the oceanic crust that underlies the Cayman Trough (Leroy et al., 2000; Boschman et al., 2014). Finally, we have included the Pacific (901) and Nazca (911) Plates in our plate circuit (for which marine magnetic anomaly data are available for times after 83.65 and 22.34 Ma, respectively), allowing us to rotate the paleomagnetic data obtained from young volcanic rocks (<10 Ma) to South Africa. The Nazca Plate is reconstructed relative to the Pacific Plate using the Euler rotation poles from Tebbens and Cande (1997) that were updated by Wright et al. (2016). The Pacific Plate (901) is linked to the 'main' plate circuit of the major continent-hosting plates via a relative plate motion chain through Marie Byrd Land (using rotation poles of Croon et al., 2008; Wright et al., 2016) and East Antarctica (Cande & Stock, 2004; Granot et al., 2013; Granot & Dymment, 2018).

In contrast to Torsvik et al. (2012), we have excluded data from the Colorado Plateau from North America for times before 40 Ma. After 40 Ma, widespread extension affected the western USA forming the Basin and Range province, but a detailed kinematic restoration of this extension of McQuarrie and Wernicke (2005) showed that the rotation of the Colorado Plateau relative to North America in this time window was no more than ~1°, which we consider negligible. For times prior to 40 Ma, the Colorado Plateau moved relative to North America during shortening in the Laramide and Sevier fold-thrust belts (Yonkee & Weil, 2015; Arkula et al., 2023), and these motions have only been quantified based on paleomagnetically determined rotations, with an estimated rotation of the Colorado Plateau relative to North America ranging from ~5 to ~13° (e.g., Bryan & Gordon, 1990; Molina-Garza et al., 1998; Steiner, 2003; Kent & Witte, 1993). Including

Plate	ID	Moves relative to	Age range (Ma)	References	Notes
North America	101	Northwest Africa	0 - 203	DeMets et al. (2015), Müller et al. (1999, 2008), Gürer et al. (2022), van Hinsbergen et al. (2020), Sahabi et al., (2004), Labails et al. (2010)	Fixed to Northwest Africa from 203 to 330 Ma*
Greenland	102	North America	0 - 125	Gaina and Jakob (2019), Torsvik et al., (2008a), Roest and Srivastava (1989), Torsvik et al. (2012)	Fixed to North America from 125 to 330 Ma*
South America	201	South Africa	0 - 133.6	DeMets and Merkouriev (2019), Müller et al. (1999), Granot and Dymant (2015), Gaina et al. (2013), Torsvik et al. (2009)	Fixed to South Africa from 133.6 to 330 Ma*
Parana	202	South America	0 - 150	Torsvik et al. (2009)	Fixed to South America from 150 to 330 Ma*
Colorado	290	South America	0 - 150	Torsvik et al. (2009)	Fixed to South America from 150 to 330 Ma*
Patagonia	291	South America	0 - 190	Torsvik et al. (2009)	Fixed to South America from 190 to 330 Ma*
Eurasia	301	North America	0 - 220	DeMets et al. (2015), Vissers and Meijer (2012a, b), Srivastava and Roest (1989, 1996), Torsvik et al. (2008a), Alvey (2009)	Fixed to North America from 220 to 330 Ma*
Iberia	304	Eurasia	0 - 83.65 [^]	Visser and Meijer (2012a, b)	
India	501	Somalia	0 - 59.237	DeMets and Merkouriev (2021)	Correction for motion since ~16 Ma between Capricorn plate and India (see DeMets and Merkouriev, 2021)
		Capricorn	59.237 - 83.65	Bull et al. (2010)	
		Madagascar	83.65 - 126.51	Gibbons et al. (2013)	
		Antarctica	126.51 - 160	Gibbons et al. (2013)	Fixed to Antarctica from 160 to 330 Ma
Arabia	503	Somalia	0 - 35	DeMets and Merkouriev (2016), Fourmier et al. (2010)	Fixed to Northeast Africa from 35 to 330 Ma
Capricorn	511	India	0 - 59.237	Bull et al. (2010)	Fixed to India between ~16 to ~59 Ma
		Antarctica	59.237 - 83.65 [^]	Cande and Patriat (2015)	
North China	601	Eurasia	0 - 130 [^]	Torsvik and Cocks (2016)	Assumed fixed to Eurasia
South China	602	North China	0 - 130 [^]	Replumaz and Taponnier (2003)	Fixed to North China from 10 to 130 Ma
Madagascar	702	Somalia	0 - 170	Gaina et al. (2013)	Fixed to Somalia from 170 to 330 Ma
Moroccan Meseta	707	Northwest Africa	0 - 50	Van Hinsbergen et al. (2020)	Fixed to Northwest Africa from 50 to 330 Ma
Somalia	709	South Africa	0 - 19.535	DeMets and Merkouriev (2016)	Fixed to South Africa from ~20 to 330 Ma
Northwest Africa	714	South Africa	120 - 133.565	Torsvik et al. (2009)	Fixed to South Africa after 120 Ma and before 133.565 Ma*
Northeast Africa	715	South Africa	83.65 - 121.4	Torsvik et al. (2004)	Fixed to South Africa after 83.65 Ma and before 121.4 Ma*
Australia	801	Antarctica	0 - 136.657	Cande and Stock (2004), Whittaker et al. (2007, 2013), Williams et al. (2011)	Fixed to Antarctica from ~136 to 330 Ma
Antarctica	802	South Africa	0 - 51.724	DeMets et al. (2021)	
		Somalia	51.724 - 182	Cande and Patriat (2015), Mueller and Jokat (2019)	Fixed to Somalia from 182 to 330 Ma
Antarctic Peninsula	803	Antarctica	0 - 140	Van de Lagemaat et al. (2021)	Fixed to Antarctica from ~140-0 Ma
Marie Byrd Land	804	Antarctica	0 - 83.65 [^]	Granot and Dymant (2018), Granot et al. (2013a, b), Cande and Stock (2004)	Fixed to Antarctica from ~62 Ma to 83.65 Ma (Van de Lagemaat et al., 2021)
Pacific	901	Marie Byrd Land	0 - 83.65 [^]	Groon et al. (2008), Wright et al. (2015, 2016)	
Nazca	911	Pacific	0 - 22.34 [^]	Tebbens and Cande (1997), Wright et al. (2016)	
Caribbean	2007	North America	0 - 38 [^]	Leroy et al. (2000), Boschman et al. (2014)	Relative motion of Caribbean plate to Southern Cuba (North America) constrained by Cayman Trough anomalies

Table 1. Overview of the global plate circuit used to transfer paleomagnetic data to a single reference plate. See Fig. 3 for a graphical overview. Full rotation parameters, chrons and references per Euler rotation pole are listed in Table S1. * = fit in Pangea same as in Torsvik et al. (2012), ^ = maximum age to which plate is connected to South Africa (701) in plate circuit.

data from this block using a paleomagnetism-based rotation correction would thus introduce circular reasoning.

Adria has often been proposed to be part of stable Africa and is rich in paleomagnetic data, which has led several authors to use Adria-derived paleomagnetic data as input for APWP computation (e.g., Muttoni et al., 2013; Kent & Muttoni, 2020; Channell et al., 2022). However, there is unequivocal evidence for rotation in GPS measurements today, and Adria must have experienced both a Neogene rotation during the extension in the Sicily Channel, as well as a Triassic-Jurassic rotation during the opening of the oceanic eastern Mediterranean basin whose ocean floor is preserved in the Ionian Sea today (van Hinsbergen et al., 2020, and references therein). While these rotations of Adria relative to Africa may have been small (5-10° in the reconstruction of van Hinsbergen et al., 2020), the arguments for and against inclusion of Adria are based on the paleomagnetic data itself (Channell et al., 2022; van Hinsbergen et al., 2014), and using this data would thus introduce circular reasoning. Data for Adria are therefore not used in our compilation.

Finally, for times prior to ~270 Ma, there is an ongoing debate about whether Pangea may be considered a single continent (e.g., Domeier et al., 2012) or was cut by an enigmatic and unpreserved megashear (e.g., Muttoni & Kent, 2019). The latter model is based on paleomagnetic arguments, and its predicted relative plate motions can therefore not be used as an independent basis for computing a global APWP from paleomagnetic data from all major plates. For this reason, we compute a global APWP for the 330-270 Ma time period under the assumption of a Pangea A configuration (i.e., a single plate from ~320 Ma, following Torsvik et al., 2008; 2012), which is obtained by closing the oceanic basins between the major continents using marine geophysical constraints. In section 7, we evaluate whether the data from the northern and southern continents, or from the mobile belts that formed during Pangea formation as recently suggested by Pastor-Galán (2022), display systematic mismatches. Similar to the Pangea debate, Cogné et al. (2013) suggested that Asia and Europe moved in Cenozoic time over ~10° or more back and forth along enigmatic faults in the Ural and eastern Europe, to explain differences in paleomagnetic data from East Asia and the global APWP of Besse and Courtillot (2002). However, in absence of geological evidence for major Cenozoic cross-cutting fault zones, we treat Eurasia as a single plate in the Cenozoic.

5. Paleomagnetic database

We present here an updated database of paleomagnetic datasets for the tectonic plates and continental blocks described in the previous section (see Fig. 4, Table 2). Our compilation builds upon the efforts of the many paleomagnetists that collected, evaluated, and tabulated paleomagnetic results from hundreds of paleomagnetic studies of the last ~60 years, overviews of which have been published in a series of seminal papers (e.g., Irving, 1964, 1977; Irving & Irving, 1982; Van der Voo, 1990b; Lock & McElhinny, 1991; Torsvik et al., 2008; 2012). In this study, we used the data compilation presented in Torsvik et al. (2012) as a starting point. We have expanded this database by adding high-quality

paleomagnetic results from undeformed or mildly folded regions that may be considered part of the stable plate interior, and that were published from 2012 to 2022, i.e., after the database of Torsvik et al. (2012) was compiled, as well as newly compiled datasets from the additional regions. We have also included datasets that were published prior to 2012 that were not incorporated by Torsvik et al. (2012), but that were included in recent compilations of ‘cratonic’ paleopoles (e.g., Gallo et al., 2021; Kulakov et al., 2021; González et al., 2022). For transparency, we have included all paleomagnetic data that were published from stable plate interiors and that fit the basic criteria for inclusion (primary magnetization, modern demagnetization techniques, principal component analysis). When these data were subsequently excluded based on the Deenen et al. (2011) criteria (for igneous rocks), the criteria presented in Chapter 3 (for sedimentary rocks) or for its large age uncertainty, this is indicated in the database (Table S2).

For the last 10 Ma, we have limited our data compilation to the paleomagnetic datasets that were included in the PSV10 database (Cromwell et al., 2018). This database consists of 83 paleomagnetic datasets that are obtained from volcanic rocks that formed in the last 10 Ma. Not all of these datasets were used for the calculation of the global APWP, however, as some do not satisfy the selection criteria described in section 3.2. We note that not all of these datasets are obtained from regions that would be considered as ‘stable’ plate interiors. Following Cromwell et al. (2018), we assume that regional deformation has not significantly influenced the paleomagnetic results from these young rocks (predominantly <3 Ma) and assign each dataset to the most appropriate tectonic plate that is included in the global plate circuit as described in section 4 (e.g., a PSV10 dataset from Alaska is considered to be derived from North America). The paleomagnetic data in the PSV10 database is compiled on the site-level and contains 2401 VGPs. Instead of using the published site-level data, we have calculated the paleomagnetic poles from each dataset and generate synthetic VGPs from those poles, to ensure consistency in our parametric re-sampling approach. We note that the application of this approach to the PSV10 database yields a distribution of (synthetic) VGPs that mimics that of the published VGPs, as shown in Chapter 2.

We have compiled metadata and statistical parameters for each paleomagnetic dataset (Table 2), based on the information provided in the original publications. For the application of our selection criteria, we have classified the lithology of the sampled rocks as either igneous or sedimentary. We have listed the paleopole (latitude, longitude) for each entry in our database in south pole coordinates. When available, we used the paleopole from the original publication (if provided) or computed the pole by taking the Fisher (1953) mean of the reported site-level VGPs. If the authors only provided the grand mean paleomagnetic direction, we used the mean sampling location to determine the position of the associated paleopole. We have listed the statistical parameters that underlie our sampling approach in Table 2, which include the number of sites, the Fisher (1953) precision parameter K and the A_{95} cone of confidence about the paleopole. These parameters were either obtained from the original publication or from other reported statistical parameters from which the missing values may be determined. If the number of sites and either the Fisher (1953) precision parameter K or the 95% cone of confidence (A_{95}) is provided, the other parameter was calculated if it was not reported (see e.g., Ch. 11 in Tauxe et al., 2010). For studies in which Fisher (1953) statistics have been applied to the site-level paleomagnetic directions instead of the VGPs – yielding a mean paleomagnetic

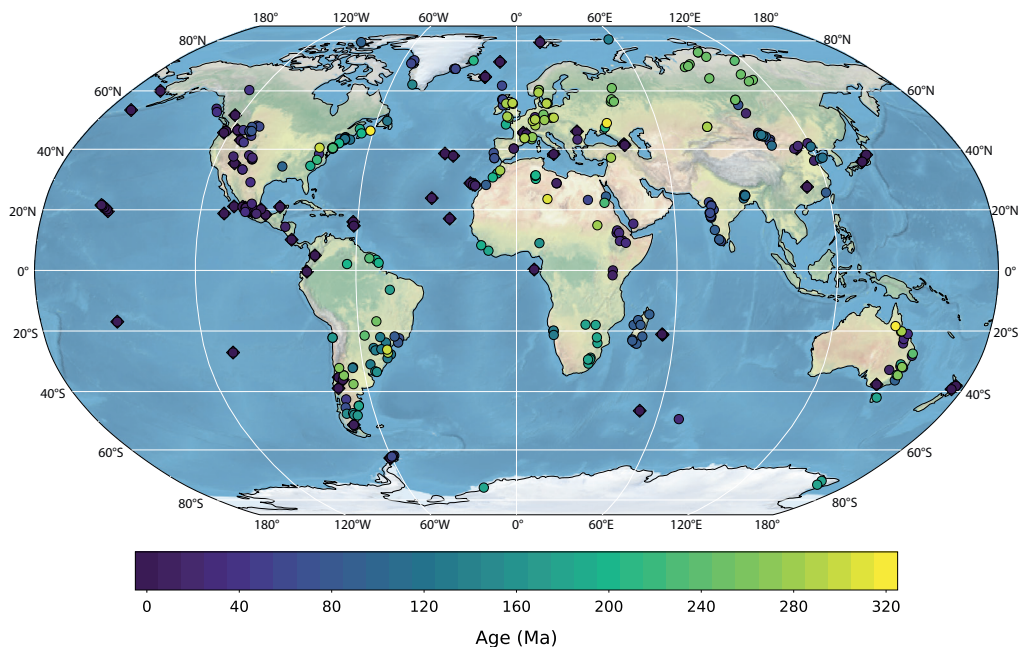


Fig. 4. Sampling locations of the 350 paleomagnetic datasets used for the calculation of the global APWP. Locations are colored by the mean age of the rocks. Diamonds indicate datasets from the PSV10 database (Cromwell et al., 2018).

direction with an α_{95}/k and an elliptical confidence region on the paleopole described by the parameters dp/dm (e.g., Butler, 1992) - we use the analytical formula of Cox (1970) to convert the k (and associated α_{95}) to K (and A_{95}), after estimating the paleolatitude using the reported mean paleomagnetic inclination (see Deenen et al., 2011 for more details).

For each paleomagnetic dataset, we have listed an age range that describes the uncertainty of the age determination of the sampled rocks, whereby we mostly follow the age assignment of the original authors. This may correspond to the uncertainty of an individual radiometric age, to the mean computed from multiple radiometric age determinations, or to a certain age interval from which the rocks are derived. For biostratigraphically or magnetostratigraphically dated sediments, we have updated the numerical ages using the most recent geological timescale, of Gradstein et al. (2020), which was also used for the plate model. When new age constraints were available, we have updated the ages of individual database entries, e.g., for data from LIPs. We emphasize here that not all age determinations are without controversy and that there are likely revised age determinations that we were not aware of during the compilation of our database. Finally, we note that additional details on the age determination, statistical parameters and the dominant lithology of the sampled rocks are provided in the extended database in Table S2.

name	min_age	max_age	age	slat	slon	N	K	A95	plat	plon	plateID	lithology	authors	DB
Praado section, Teruel, Spain	9.1	10.3	9.7	40.3	-1.1	246	16.5	2.3	-84.4	341.0	304	sedimentary	Abals et al. (2009)	T12
Casacante, Spain	9.4	10.6	10.0	40.2	-1.1	81	15.4	4.1	-79.0	293.9	304	sedimentary	Abdali-Azz et al. (2004)	T12
Jesus Maria and Antonico lavas	9.2	11.9	10.6	20.6	257.0	29	39.7	4.3	-80.7	292.3	301	igneous	Gogutchaichvili et al. (2011)	this study
Volcanics, Jebel Soda, Libya	10.0	13.0	11.5	28.7	15.6	12	35.4	7.4	-78.4	16.1	715	igneous	Schult and Soffel (1973)	T12
Volcanics, Jebel Soda, Libya	10.0	13.0	11.5	28.8	15.5	9	47.0	6.8	-69.0	4.0	715	igneous	Adel-Hall et al. (1975)	T12
East African volcanics, Kenya and Tanzania	11.0	13.0	12.0	0.0	36.0	22	28.8	6.1	-86.5	6.6	709	igneous	Reilly et al. (1976)	T12
Taasym Gool 3, Mongolia	12.1	13.3	12.7	45.5	10.1	7	14.5	16.4	-71.6	358.0	301	igneous	Hankard et al. (2007a)	this study
Ethiopian traps, Debre Sina	10.6	14.9	12.8	9.9	39.8	30	27.7	5.1	-83.8	26.9	715	igneous	Lhuillier & Gilder (2018)	this study
Miocene volcanics, Canary Islands	5.0	21.0	13.0	28.0	344.0	99	16.0	3.5	-81.9	294.4	714	igneous	Watkins (1973)	T12
Volcanics, Kenya	12.0	15.0	13.5	-1.6	35.9	14	20.8	8.9	-80.1	214.3	709	igneous	Patel and Raja (1979)	T12
Pedre Miguel Ignimbrite Suite, Honduras	14.3	16.3	15.3	14.4	272.9	33	24.5	5.2	-80.0	322.9	2007	igneous	Molina-Garza et al. (2012)	this study
Hongshya	14.0	18.0	16.0	36.2	118.5	9	57.8	6.8	-84.3	53.5	601	igneous	Zhao et al. (1994)	this study
Leucitite	15.0	17.2	16.1	-32.84	146.45	17	20.5	8.6	-80.2	95.4	801	igneous	Hansma and Tohver (2018)	this study
Trosky volcano, Czech Republic	15.7	17.3	16.5	50.52	152.33	11	21.5	10.1	-76.9	261.1	301	igneous	Petronis et al. (2015)	this study
Hannoba	15.0	24.0	19.5	40.2	112.7	16	36.3	6.2	-83.7	52.3	601	igneous	Pan et al. (2005)	this study
Ust-Bokson, Mongolia	19.5	20.3	19.9	52.1	100.3	9	32.1	9.2	-69.8	6.5	301	igneous	Hankard et al. (2007a)	this study
Janetico granodiorites & Tepexco volcanics	18.8	22.8	20.8	18.7	261.3	26	17.4	7.0	-78.4	4.28	101	igneous	Duarte et al. (2015)	this study
Stoddard Mountain lacolith	20.0	22.0	21.0	37.6	246.6	19	54.3	4.6	-82.9	346.2	101	igneous	Petronis et al. (2004)	T12
Suhindol volcanics	19.4	23.5	21.5	43.23	25.15	11	25.2	9.3	-84.1	242.1	301	igneous	van Hinsbergen et al. (2008a)	this study
Dinan Bay lavas	18.9	24.4	21.7	53.7	227.3	13	19.0	9.8	-82.7	30.7	101	igneous	Irving et al. (2000)	T12
Younger plations	22.0	23.0	22.5	36.6	254.5	11	34.8	7.8	-87.1	189.5	101	igneous	Hagstrum and Johnson (1986)	T12
Pingzhuang	22.0	23.0	22.5	42.0	119.2	17	49.9	5.1	-88.0	300.0	601	igneous	Shi et al. (2002)	this study
Lake City Caldera	22.0	24.0	23.0	38.0	252.7	17	9.2	12.4	-76.4	30.3	101	igneous	Reynolds et al. (1986)	T12
Main Range Volcano and Tweed Volcano	20.2	26.7	23.5	-28.20	153.00	56	22.5	4.1	-74.2	74.8	801	igneous	Wellman (1975)	this study
Latir volcanics	21.0	26.0	23.5	36.8	254.6	43	14.2	6.0	-80.9	331.2	101	igneous	Hagstrum and Lippman (1986)	T12
Volcanics Germany	18.0	30.0	24.0	50.8	8.0	40	15.4	6.0	-77.8	310.8	301	igneous	Schreiber and Botsch (1998)	T12
Zhangjiakou	17.0	33.0	25.0	41.1	114.7	8	9.0	19.5	-84.4	233.2	601	igneous	Zheng (1991)	this study
Conjejos and Hinsdale Formation	23.0	29.0	26.0	37.2	254.4	23	15.2	8.0	-79.7	342.6	101	igneous	Brown and Golombek (1997)	T12
Kerguelen islands (Antarctic Plate)	24.0	30.0	27.0	-49.3	69.5	233	16.5	2.3	-85.5	9.3	802	igneous	Camps et al. (2007)	T12
Springsure Volcano	27.3	28.9	28.1	-24.10	148.10	18	13.7	9.7	-70.5	120.6	801	igneous	Hansma and Tohver (2019)	this study
Igimbritia Panaillo Superior	24.8	31.3	28.1	22.0	259.0	41	27.4	3.6	-68.6	338.1	101	igneous	Gonzalez-Naranjo et al. (2012)	this study
Afro-Arabian flood volcanic province, Yemen	27.0	31.0	29.0	15.4	44.1	48	33.6	3.6	-74.2	69.1	503	igneous	Rissager et al. (2005)	T12
Peak Range	28.2	31.2	29.7	22.66	147.97	29	10.1	8.8	-64.6	111.8	801	igneous	Hansma and Tohver (2019)	this study
Ethiopian traps, Belesa	29.2	30.5	29.9	12.4	37.7	42	44.9	3.3	-80.5	60.6	715	igneous	Lhuillier & Gilder (2018)	this study
Lima Limo section, Ethiopian Traps	29.4	30.4	29.9	13.2	37.9	79	22.7	3.4	-78.2	33.0	715	igneous	Ahn et al. (2021)	this study
Mongolon-Datil volcanics	24.0	36.0	30.0	33.3	252.1	61	17.6	4.5	-81.9	323.6	101	igneous	McIntosh et al. (1992)	T12
Mongolon-Datil volcanics	24.0	36.0	30.0	33.3	252.2	39	21.0	5.1	-82.8	316.2	101	igneous	McIntosh et al. (1992)	T12
Ethiopian Traps, Ethiopia	29.0	31.0	30.0	12.4	38.6	53	28.9	3.7	-77.0	28.0	715	igneous	Rochette et al. (1998)	T12
Ethiopian Flood basalts, Ethiopia	29.0	31.0	30.0	9.7	38.8	16	17.8	9.0	-83.0	13.3	715	igneous	Kidane et al. (2002)	T12
Mongolia, Iram Plateau and Bogd Plateaus	30.2	30.4	30.3	44.8	100.7	13	25.1	8.4	-81.6	94.5	301	igneous	Dupont-Nivet et al. (2011)	this study
Hillsborough Volcano	33.1	34.1	33.6	-20.98	149.00	14	32.2	7.1	-67.1	121.4	801	igneous	Hansma and Tohver (2019)	this study
Liverpool Volcano	33.0	34.4	33.7	-31.70	150.20	36	25.7	4.8	-71.1	95.5	801	igneous	Wellman (1969)	this study
Southern Plateau volcanics, Ethiopia	30.0	38.0	34.0	9.1	41.0	22	24.4	6.4	-75.1	350.3	709	igneous	Schult (1974)	T12

A global apparent polar wander path for the last 320 Ma calculated from site-level paleomagnetic data

Tealithan Dikes	33.2	36.8	35.0	19.3	257.0	12	30.8	8.0	-75.7	346.6	101	igneous	Rosas-Eguera et al. (2011)	this study
Mariscal Mountain Gabbro	35.0	39.0	37.0	29.1	256.8	18	42.5	5.4	-80.0	5.3	101	igneous	Harlan et al. (1995)	T12
Ramsay Island lavas	36.0	41.0	38.5	52.5	228.7	11	41.0	7.0	-78.2	299.9	101	igneous	Irving et al. (2000)	T12
Takerna Member lavas	38.0	40.0	39.0	70.4	305.2	13	32.7	7.4	-76.3	21.5	102	igneous	Schmidt et al. (2005)	T12
Mongolia, Khatoon Sudal	38.8	40.0	39.4	44.5	101.3	7	45.1	9.1	-76.7	60.1	301	igneous	Dupont-Nivet et al. (2011)	this study
Khatoon Sudal, Mongolia	38.8	40.0	39.4	44.5	101.4	8	61.5	7.1	-71.9	22.6	301	igneous	Hankard et al. (2007a)	this study
Beaver River albaltic complex	41.5	42.5	42.0	60.3	234.7	21	39.8	5.1	-79.2	325.8	101	igneous	Symons et al. (2003)	T12
Monterey intrusives	42.0	47.0	44.5	38.4	280.6	11	12.3	13.6	-85.5	63.7	101	igneous	Resetter and Martin (1980)	T12
Rattlesnake Hills volcanics	42.0	50.0	46.0	42.3	248.1	18	13.9	9.6	-79.4	326.2	101	igneous	Sheriff and Shive (1980)	T12
Bitterroot Dome dike swarm	44.0	51.0	47.0	46.4	245.2	11	34.9	7.8	-72.0	341.6	101	igneous	Doughly and Sheriff (1992)	T12
Eocene volcanics Patagonia	42.0	49.0	49.0	-42.6	290.0	36	18.0	5.7	-81.0	337.4	291	igneous	Somoza (2007)	T12
Robinson Anticline intrusives	48.0	52.0	50.0	46.2	248.5	16	26.6	7.3	-77.1	325.8	101	igneous	Harlan et al. (1988)	T12
Aboaroko volcanics	45.0	55.0	50.0	44.5	249.8	42	13.5	6.2	-83.1	326.3	101	igneous	Harlan and Morgan (2010)	T12
Combined Eocene intrusives	47.0	54.0	50.5	47.9	249.9	94	18.6	3.5	-82.7	347.2	101	igneous	Diehl et al. (1983)	T12
Ezcara Inlet & Point Hennesquin groups	47.8	56.0	51.9	-62.1	301.7	22	16.7	7.8	-79.0	48.0	803	igneous	Watts et al. (1984)	this study
Barrington Volcano, New South Wales	52.0	54.0	53.0	43.2	151.4	33	23.2	5.3	-70.5	125.6	801	igneous	Wellman et al. (1969)	T12
Nuussuaq lavas, Kaniat Member	53.0	55.0	54.0	70.7	305.5	20	11.1	10.3	-74.6	339.4	102	igneous	Risager et al. (2003b)	T12
South Shetland Islands	52.2	56.5	54.4	-62.2	301.0	15	8.0	14.4	-82.1	2.6	803	igneous	Guo et al. (2018)	this study
Kangerdlugssuaq dykes, Irminger	53.0	54.0	54.5	68.2	329.0	11	31.8	8.2	-62.9	0.4	102	igneous	Faller and Soper (1979)	T12
Skaergaard Intrusion	55.0	56.0	55.5	68.2	328.3	30	25.1	5.4	-61.0	345.0	102	igneous	Schwarz et al. (1979)	T12
Khuts Uul, Mongolia	56.3	57.9	57.1	43.2	104.6	14	34.9	6.8	-69.6	328	301	igneous	Hankard et al. (2008)	this study
Svartehak lavas	54.0	61.5	57.8	71.4	305.5	30	9.3	9.1	-62.0	349.7	102	igneous	Chauvet et al. (2019)	this study
Jacobson Fjord dykes	53.0	60.0	59.0	68.2	329.0	22	33.3	5.5	-67.7	357.7	102	igneous	Faller and Soper (1979)	T12
East Giff Kebir Plateau basalts	57.3	60.7	59.0	23.3	27.3	13	80.0	4.7	-71.7	23.5	715	igneous	Lotfy and Odah (2015)	this study
Arran dikes, Scotland	58.8	60.0	59.4	55.6	354.8	41.3	17.8	1.7	-81.7	339.8	301	igneous	Dagley et al. (1978)	T12
Jacobson Fjord basalts	59.0	60.0	59.5	68.2	329.0	39	11.1	7.2	-56.0	3.0	102	igneous	Faller and Soper (1979)	T12
Arran intrusives and extrusives	58.0	61.0	59.5	55.5	354.8	165	27.4	2.1	-80.2	339.6	301	igneous	Hodgson et al. (1990)	T12
Ardaamurchan complex, Scotland	59.6	60.4	60.0	56.7	353.8	62	23.8	3.8	-77.0	355.0	301	igneous	Dagley et al. (1984)	T12
Faeroe flood volcanics	59.5	60.7	60.1	61.9	353.1	43	14.2	6.0	-71.4	334.7	301	igneous	Risager et al. (2002)	T12
Svartehak lavas, Vaigat Formation	60.0	61.0	60.5	71.6	305.9	10	25.1	9.8	-76.2	37.9	102	igneous	Risager et al. (2003b)	T12
Nuussuaq and Disko lavas, Vaigat Formation	60.0	61.0	60.5	70.3	305.1	14	19.8	9.2	-64.8	321.5	102	igneous	Risager et al. (2003a)	T12
Rhum and Gama igneous, Scotland	59.7	61.7	60.7	57.0	355.5	107	15.7	3.6	-81.0	359.0	301	igneous	Dagley and Mussett (1981)	T12
Mull lavas, Scotland	59.7	62.0	60.9	56.3	353.9	26	23.3	6.0	-73.3	346.2	301	igneous	Garned et al. (2008)	T12
Torris, Snow, Half Moon lavas and intrusions	56.0	66.0	61.0	-62.4	300.3	10	19.8	11.1	-82.7	355.2	803	igneous	Poblete et al. (2011)	this study
Antrim Lava, Ireland	59.6	62.6	61.1	54.9	353.9	37	15.0	6.3	-78.9	347.0	301	igneous	Garned et al. (2010)	T12
Muck and Egg igneous	60.9	61.4	61.2	56.9	353.8	133	13.0	3.5	-74.0	351.0	301	igneous	Dagley and Mussett (1986)	T12
Sumber Uul - Tuiga, Mongolia	56.2	68.0	62.1	43	104	14	85.0	4.3	-85.2	272.5	301	igneous	Hankard et al. (2008)	this study
Combined Paleocene intrusions	59.0	67.0	63.0	47.6	251.1	36	20.2	5.4	-81.8	1.4	101	igneous	Diehl et al. (1983)	T12
Mount Pavagath Traps, Gujarat, India	60.0	68.0	64.0	22.5	73.5	16	52.5	5.1	-39.2	105.6	501	igneous	Verma and Mital (1974)	T12
Deccan Traps, Mahabaleshwar, India	64.0	67.0	65.5	17.9	73.6	28	12.8	7.4	-40.0	96.0	501	igneous	Kono et al. (1972)	T12
Deccan Traps, Nagpur to Bombay traverse, India	64.0	67.0	65.5	20.0	75.0	16	37.9	6.1	-38.4	102.4	501	igneous	Vandamme et al. (1991)	T12
Deccan dyke swarms, western India	64.0	67.0	65.5	21.5	74.3	11	23.0	9.7	-37.2	99.5	501	igneous	Prasad et al. (1996)	T12
Khumbarli Ghat, Mahabaleshwar Plateau, India	64.0	67.0	65.5	17.4	73.7	15	24.6	7.9	-44.7	107.8	501	igneous	Jay et al. (2009)	T12
Varandah Ghat, Mahabaleshwar Plateau, India	64.0	67.0	65.5	18.1	73.6	15	28.8	7.2	-33.5	106.7	501	igneous	Jay et al. (2009)	T12

Wai-Panchgani, Mahabeshwar Plateau, India	64.0	67.0	65.5	17.9	73.8	16	14.7	10.0	-36.8	85.9	501	igneous	Jay et al. (2009)	T12
Kelgri, Mahabeshwar Plateau, India	64.0	67.0	65.5	17.9	73.7	16	21.2	8.2	-42.3	96.6	501	igneous	Jay et al. (2009)	T12
Taposa, Mahabeshwar Plateau, India	64.0	67.0	65.5	17.8	73.7	17	17.1	8.9	-38.2	95.5	501	igneous	Jay et al. (2009)	T12
Matheran Ghat, Mahabeshwar Plateau, India	64.0	67.0	65.5	19.0	73.3	17	36.0	6.0	-36.6	108.4	501	igneous	Jay et al. (2009)	T12
Ambemali Ghat, Mahabeshwar Plateau, India	64.0	67.0	65.5	17.9	73.6	34	16.8	6.2	-38.8	104.5	501	igneous	Jay et al. (2009)	T12
Nandurbar-Dhule dykes, India	63.0	68.4	65.7	21.3	74.3	13	13.5	11.7	-40.5	104.5	501	igneous	Das et al. (2021)	this study
Western Ghats, Deccan Traps, India	64.0	68.5	66.3	19.0	73.5	50	28.7	3.8	-37.8	102.6	501	igneous	Chenet et al. (2009)	this study
Late Cretaceous mafic dikes in Kerala	65.0	70.0	67.5	10.2	76.1	10	56.8	6.5	-37.7	107.0	501	igneous	Radhakrishna et al. (2012)	this study
Central Kerala dykes, India	68.0	70.0	69.0	9.7	76.7	6	33.4	11.8	-34.6	94.0	501	igneous	Radhakrishna et al. (1994)	T12
Itaitia and Pasa Quatro Complexes, Brazil	67.0	74.0	70.5	-22.4	315.2	18	37.8	5.7	-79.5	0.0	201	igneous	Montes-Laurar et al. (1995)	T12
Patagonian Plateau basalts, Chile, Argentina	64.0	79.0	71.5	-45.3	288.7	18	31.6	6.3	-78.7	358.4	291	igneous	Butler et al. (1991)	T12
Lisbon Basalts 1969, Portugal	70.0	74.0	72.0	38.83	-91.8	5	72.3	9.1	-73.7	19.6	304	igneous	van der Voo (1969)	this study
Moncheque Syenite I	70.0	74.0	72.0	37.06	-88.2	8	104.9	5.4	-73.5	344.6	304	igneous	van der Voo (1969)	this study
Moncheque Syenite II	70.0	74.0	72.0	37.06	-88.2	27	47.8	4.1	-77.1	347.1	304	igneous	Storetvedt et al. (1990)	this study
Add Mountain volcanics	71.0	81.0	76.0	47.5	248.1	26	16.7	7.2	-83.4	20.9	101	igneous	Gunderson and Sheriff (1991)	T12
Minusa trough intrusions, Siberia	74.0	79.0	76.5	55.0	99.2	16	37.5	6.1	-82.8	8.5	301	igneous	Mietkin et al. (2007)	this study
Dobery Mountain sills	76.5	77.5	77.0	45.9	248.1	5	33.6	13.4	-80.8	338.1	101	igneous	Harlan et al. (2008)	T12
Elkhorn Mountains	77.0	83.0	80.0	46.1	248.0	15	16.8	9.6	-80.3	9.5	101	igneous	Diehl (1991)	T12
Mauldow Formation welded tuffs	75.0	85.0	80.0	46.1	248.9	11	22.7	9.8	-69.8	27.8	101	igneous	Swenson and McWilliams (1989)	T12
Sao Sebastiao Island Intrusions, Brazil	78.0	84.0	81.0	-23.8	314.7	18	50.7	4.9	-79.4	331.9	201	igneous	Montes-Laurar et al. (1995)	T12
Pocos de Caldas Alkaline Complex, Brazil	78.0	90.0	84.0	-21.8	313.5	47	60.3	2.7	-83.2	320.1	201	igneous	Montes-Laurar et al. (1995)	T12
Volcanics, Massif d'Androy Andria	84.0	90.0	87.0	-24.2	46.0	6	36.0	11.3	-64.0	63.0	702	igneous	Andriamirado and Roche (1969)	T12
Volcanics, Malaka Andria	84.0	90.0	87.0	-18.0	44.4	10	35.2	8.3	-70.3	63.1	702	igneous	Andriamirado (1971)	T12
Volcanics, Mangoby-Anilaby Andria	84.0	90.0	87.0	-22.8	44.3	11	21.8	10.0	-73.7	73.1	702	igneous	Andriamirado (1971)	T12
Volcanics, Antanmenia Andria	84.0	90.0	87.0	-16.4	46.0	12	48.7	6.3	-66.1	49.7	702	igneous	Andriamirado (1971)	T12
Volcanics, Southeast Coast Andria	84.0	90.0	87.0	-21.8	48.0	14	42.1	6.2	-65.8	35.6	702	igneous	Andriamirado (1971)	T12
Volcanics, Southwest Madagascar	84.0	90.0	87.0	-23.2	44.3	41	68.1	2.7	-76.8	68.2	702	igneous	Torsvik et al. (1998)	T12
Dolerites, east Madagascar	84.0	90.0	87.0	-18.0	47.0	16	38.8	6.0	-65.5	38.0	702	igneous	Storetvedt et al. (1992)	T12
Late Cretaceous mafic dikes in Kerala	85.0	90.0	87.5	10.2	76.1	6	42.1	10.4	-26.8	113.1	501	igneous	Radhakrishna et al. (2012)	this study
Yongai	87.9	88.6	88.3	25.7	119.0	19	76.5	3.9	-83.1	332.6	602	igneous	Huang et al. (2012)	this study
St. Mary Islands, western India	91.0	91.4	91.2	13.4	74.7	7	42.1	9.4	-14.2	117.8	501	igneous	Torsvik et al. (2000)	T12
d'Anjala complex	91.3	91.9	91.6	-14.5	50.1	5	41.6	12.0	-66.7	43.5	702	igneous	Meert and Thirrat (2006)	T12
Amna Fatma section, Morocco	89.4	93.9	91.7	28.2	348.2	88	38.7	2.5	-64.3	76.3	707	igneous	Ruiz-Martinez et al. (2011)	this study
Wadi Natash volcanics, Egypt	86.0	100.0	93.0	24.4	34.3	15	44.4	5.8	-69.3	78.1	715	igneous	Schult et al. (1981)	T12
Kharnum Ul. - Shovon basalts, Mongolia	90.8	96.0	93.4	44.2	103.4	23	22.2	6.6	-84.7	15.0	301	igneous	Hankar et al. (2007b)	this study
Mount Dromedary Intrusion	92.0	96.0	94.0	-36.30	150.70	22	11.5	9.5	-55.9	138.6	801	igneous	Robertson (1963)	this study
Axel Heiberg lavas	93.2	97.2	95.2	79.4	267.6	36	15.0	6.4	-70.4	17.0	101	igneous	Tarduno et al. (2002)	this study
Magnet Cove and other intrusions	98.0	102.0	100.0	34.3	267.5	20	34.0	5.7	-74.1	12.5	101	igneous	Gleberman and Irving (1988)	T12
Cattingsville	99.7	100.3	100.0	43.5	287.1	5	50.2	10.9	-72.1	17.0	101	igneous	McEnroe (1996)	T12
Tsost Magmatic Field, Mongolia	94.7	107.0	100.9	44.3	102.2	7	19.2	14.1	-82.1	324.9	301	igneous	van Hinsbergen et al. (2008b)	this study
Little Battlesnake Complex	108.0	114.0	111.0	43.0	288.9	12	71.2	5.2	-71.5	2.6	101	igneous	McEnroe (1996)	T12
Pleasant Mountain	111.7	112.5	112.1	44.0	289.2	5	88.5	8.2	-77.4	5.0	101	igneous	McEnroe (1996)	T12
Subongu	110.6	114.1	112.4	41.2	104.1	31	64.4	3.2	-80.3	20.3	601	igneous	Ren et al. (2004); Zhu et al. (2008)	this study
Burnt Meadow Mountains	112.4	112.8	112.6	43.9	289.1	10	51.9	6.8	-75.7	28.5	101	igneous	McEnroe (1996)	T12

A global apparent polar wander path for the last 320 Ma calculated from site-level paleomagnetic data

Cretaceous Lamproites	109.1	116.6	112.9	23.8	87.0	11	30.5	8.4	-14.9	107.6	501	igneous	Radhakrishna et al. (2017)	this study
Rajmahal Traps, West Bengal and Bihar, India	115.0	117.0	116.0	24.8	87.7	16	91.0	6.0	-3.2	117.5	501	igneous	McDougall and McElhinny (1970)	T12
Rajmahal Traps, Bihar, India	115.0	117.0	116.0	24.6	87.7	25	29.8	5.4	-7.0	117.0	501	igneous	Kloerwijk (1971)	T12
Rajmahal Traps, West Bengal, India	115.0	117.0	116.0	25.0	87.4	19	10.6	10.8	-9.3	124.8	501	igneous	Das et al. (1996)	T12
Rajmahal Traps, North Rajmahal Hills, India	115.0	117.0	116.0	24.7	87.5	8	52.8	7.7	-6.5	120.2	501	igneous	Tardano et al. (2001)	T12
Hongyan	114.0	118.0	116.0	36.9	121.2	11	27.3	8.9	-86.5	341.1	601	igneous	Charles et al. (2012)	this study
Rajmahal Traps, Bihar, India	116.0	118.0	117.0	24.7	87.7	34	53.7	3.4	-9.4	116.6	501	igneous	Rao and Rao (1996)	T12
South-East Ariz Begd, Mongolia	115.4	119.3	117.4	44.4	102.5	24	38.1	4.9	-75.6	312.3	301	igneous	van Hinsbergen et al. (2008b)	this study
Weidshah	116.0	120.0	118.0	37.2	122.4	9	33.7	9.0	-80.1	0.1	601	igneous	Charles et al. (2011)	this study
Jiangchang	117.0	121.0	119.0	40.9	119.8	5	31.5	7.6	-81.1	49.2	601	igneous	Qin et al., 2008	this study
Alfred Complex	118.0	122.0	120.0	43.5	289.3	14	64.1	5.0	-74.0	29.8	101	igneous	McEnroe (1996b)	T12
Cape Neddick	120.2	121.0	120.6	43.2	291.4	12	67.5	5.3	-74.8	354.8	101	igneous	McEnroe (1996b)	T12
Volcanics Cerro Colorado Formation, Cordoba, Argentina	115.0	127.0	121.0	-32.0	-64.0	6	27.5	13.0	-81.0	14.0	202	igneous	Valencio (1972)	T12
South-East Ih Begd, Mongolia	118.2	124.3	121.3	44.8	100.7	21	34.3	5.7	-83.7	16.4	301	igneous	van Hinsbergen et al. (2008b)	this study
Tatic Complex	120.0	124.0	122.0	43.3	289.3	10	65.2	6.0	-65.9	27.8	101	igneous	McEnroe (1996b)	T12
Floripolis dykes, Santa Catarina Island, Brazil	119.0	128.3	123.7	-27.7	311.5	65	47.3	2.6	-89.1	3.3	201	igneous	Raposo et al. (1998)	T12
South-East Baga Begd, Mongolia	122.7	124.7	123.7	44.8	101.9	29	18.8	6.3	-79.9	339.9	301	igneous	van Hinsbergen et al. (2008b)	this study
El Salto-Almoharte lavas, Cordoba, Argentina	119.0	129.0	124.0	-32.2	-64.2	15	39.4	6.2	-72.0	25.0	202	igneous	Mendia (1978)	T12
Lebanon diorite	122.0	128.0	125.0	43.4	289.2	5	70.9	9.1	-71.0	16.9	101	igneous	McEnroe (1996b)	T12
Notre Dame Bay dikes	122.0	136.0	129.0	49.5	304.6	10	99.5	4.9	-67.2	30.8	101	igneous	Lapointe (1979)	T12
Ponta Grossa dykes, Brazil	129.2	131.4	130.3	-24.5	310.0	115	43.8	2.0	-82.4	30.3	201	igneous	Raposo and Ernesto (1995)	T12
Ponta Grossa dykes	129.2	131.4	130.3	-23.8	310.0	24	35.7	5.0	-88.1	222.0	201	igneous	Cervantes-Solano et al. (2015)	this study
Serra Geral basalts, Brazil	131.0	135.0	133.0	-29.0	310.0	37	40.4	3.7	-84.6	115.4	202	igneous	Pacca and Hiedo (1976)	T12
Kenko lavas, Namibia	131.0	136.0	133.5	-20.0	14	40	59.3	3.0	-48.3	86.6	701	igneous	Gidskehaug et al. (1975)	T12
Etendeka, Namibia	131.0	136.0	133.5	-19.9	14.1	21	26.1	6.3	-47.5	88.9	701	igneous	Owen-Smith et al. (2019)	this study
Etendeka LIP (upper), Namibia	131.0	136.0	133.5	-21.3	14.2	37	26.2	4.7	-52.3	91.7	701	igneous	Dodd et al. (2015)	this study
Parana flood basalt, Paraguay	132.0	136.0	134.0	-25.6	-54.9	18	65.0	4.3	-86.2	359.2	201	igneous	Gogutchaivili et al. (2013)	this study
Posadas Formation, Parana flood basalts	132.0	136.0	134.0	-26.4	-54.3	26	45.6	4.2	-89.7	339.1	201	igneous	Mena et al. (2010)	this study
Arapey volcanics, Uruguay	132.0	136.0	134.0	-31.0	303.0	29	42.0	4.2	-84.8	95.8	202	igneous	Cervantes-Solano et al. (2010)	this study
Central Parana Magmatic Province	132.0	136.0	134.0	-26.0	308.0	96	34.3	2.5	-84.1	69.2	201	igneous	Owen-Smith et al. (2019)	this study
Northern Parana Magmatic Province, Brazil	132.0	136.0	134.0	-22.0	308.0	128	48.0	1.8	-82.7	84.5	201	igneous	Ernesto et al. (2021)	this study
Franz Josef Land LIP	125.0	145.0	135.0	80.7	56.0	40	26.2	4.5	-68.9	357.5	301	igneous	Abshiev et al. (2018)	this study
Southwest Greenland dykes	144.2	151.0	147.6	62.3	310.2	40	25.1	4.6	-69.3	5.0	102	igneous	Kiriakov et al. (2021)	this study
La Negra south	151.2	154.0	152.8	-22.2	289.8	18	11.2	10.8	-84.5	76.4	290	igneous	Fu et al. (2020)	this study
Posadas and Sierra Colorado ignimbrites, Argentina	153.0	157.0	155.0	-47.4	-71.8	16	24.5	7.6	-81.0	172.0	291	igneous	Iglesias-Llanos et al. (2003)	T12
Chon Aike Formation, Argentina	151.5	158.5	155.0	-47.2	-69.0	23	13.3	8.6	-84.3	191.3	291	igneous	Ruiz Gonzalez et al. (2019)	this study
La Mafilde Formation, Patagonia	156.7	158.1	157.4	-47.8	291.2	10	13.6	13.6	-84.1	179.2	291	igneous	Ruiz Gonzalez et al. (2022)	this study
Nico Perez dykes, Uruguay	154.6	160.6	157.6	-33.3	-55.6	8	30.0	10.2	-87.0	197.3	202	igneous	Lossada et al. (2014)	this study
Zapican dike swarm, Uruguay	154.6	160.6	157.6	-33.5	-55.0	19	22.7	7.2	-86.4	178.9	202	igneous	Cervantes-Solano et al. (2020)	this study
Intrusive rocks, Nigeria	150.0	170.0	160.0	9.0	8.6	6	27.8	13.0	-62.5	61.6	714	igneous	Marron and Marron (1976)	T12
La Negra north	162.2	169.4	165.8	-22.2	289.8	28	13.8	7.6	-84.3	180.9	290	igneous	Fu et al. (2020)	this study
Chon Aike Formation, Patagonia	166.0	170.0	168.0	-48.0	292.6	13	10.3	13.5	-81.2	207.7	291	igneous	Yizan (1998)	this study
Gingebullen Dolerite	167.0	177.0	172.0	-34.5	150.3	7	9.2	21.0	-52.0	153.0	801	igneous	Thomas et al. (2000)	this study

1730	177.0	175.0	-6.4	-47.4	15	31.8	6.9	-85.3	262.5	201	igneous	Schult and Guerreiro (1979)	T12
1770	183.0	180.0	-31.0	150.0	14	16.8	10.0	-46.1	175.2	801	igneous	Schmidt (1976)	T12
1775	183.3	180.4	-17.9	26.2	5	27.4	14.9	-63.9	80.6	701	igneous	Jones et al. (2001)	T12
1795	182.5	181.0	-17.8	162.0	8	28.0	9.3	-72.0	236.0	802	igneous	Rolf & Henjes-Kunst (2003)	this study
1795	182.5	181.0	-73.3	162.9	22	22.9	7.0	-66.4	222.7	802	igneous	Lemna et al. (2016)	this study
1770	185.0	181.0	-44.8	-65.7	25	12.2	8.7	-80.5	203.5	291	igneous	Vizan (1998)	this study
1801	182.8	181.5	-30.76	28.04	15	30.8	7.0	-76.0	88.8	701	igneous	Moulin et al. (2011)	this study
1801	182.8	181.5	-28.8	28.7	29	27.9	5.2	-65.3	87.9	701	igneous	Moulin et al. (2017)	this study
1790	187.0	183.0	-24.0	31.0	10	16.4	12.3	-65.4	75.1	701	igneous	McElhinny and Jones (1965)	T12
1790	187.0	183.0	-18.0	30.0	9	42.4	8.0	-57.0	84.0	701	igneous	McElhinny et al. (1968)	T12
1790	187.0	183.0	-42.0	147.5	21	38.3	5.2	-50.7	174.5	801	igneous	Schmidt and McDougall (1977)	T12
1790	187.0	183.0	-74.5	342.0	15	59.5	5.5	-47.8	225.5	802	igneous	Lanza and Zanello (1993)	T12
1790	187.0	183.0	-29.3	28.6	47	32.6	3.7	-71.6	93.5	701	igneous	Kosterov and Perrin (1996)	T12
1780	188.0	183.0	-44.8	65.6	10	19.2	11.3	-83.0	138.0	290	igneous	Iglesias-Llanos et al. (2003)	T12
1790	187.0	183.0	-29.4	27.8	15	15.2	10.1	-63.7	88.5	701	igneous	Prevot et al. (2003)	this study
1780	191.0	184.5	55.5	14.0	21	16.4	8.1	-69.0	283.0	301	igneous	Bylund and Halvorsen (1993)	T12
1835	188.1	185.8	6.5	349.5	25	31.0	5.3	-68.5	62.4	714	igneous	Dhrymprie et al. (1975)	T12
1890	186.0	185.0	-22.1	30.7	8	47.5	8.1	-70.7	106.7	701	igneous	Brock (1968)	T12
1890	193.0	191.0	46.8	294.0	8	36.4	9.3	-74.9	256.0	101	igneous	Hodych and Hayatsu (1988)	T12
1900	196.0	193.0	48.3	355.5	7	36.0	10.2	-61.3	238.8	301	igneous	Sichler and Perrin (1993)	T12
1900	196.0	193.0	8.3	346.8	13	55.8	5.6	-82.9	32.7	714	igneous	Hargraves et al. (1999)	T12
1900	198.0	194.0	34.5	278.5	20	24.5	6.8	-67.9	275.3	101	igneous	Dooley and Smith (1982)	T12
1903	200.3	195.3	3.5	307.5	26	50.7	4.0	-81.2	235.1	201	igneous	Nomade et al. (2000)	T12
1927	202.0	197.4	2.5	308.5	17	48.0	5.2	-79.8	208.6	201	igneous	Ernesto et al. (2003)	this study
1980	202.0	200.0	30.2	7.5	23	55.0	4.1	-73.0	64.7	707	igneous	Ernesto et al. (2003)	T12
1995	201.4	200.5	45.3	295.3	9	26.0	10.3	-66.4	251.9	101	igneous	Palencia-Ortiz et al. (2011)	T12
1996	202.0	200.8	42.0	287.4	315	12.9	2.3	-66.6	268.2	101	igneous	Hodych and Hayatsu (1988)	T12
1990	203.0	201.0	32.0	352.5	27	16.7	7.0	-71.0	36.0	707	igneous	Kent and Olsen (2008)	T12
1990	203.0	201.0	31.2	7.3	5	16.9	19.1	-73.0	61.3	707	igneous	Barclon et al. (1973)	T12
1990	203.0	201.0	30.7	350.8	13	48.0	6.0	-69.2	55.5	707	igneous	Knigh et al. (2004)	T12
1990	203.0	201.0	31.4	7.5	99	31.4	2.6	-60.0	61.6	707	igneous	Ruiz-Martinez et al. (2012)	T12
1993	209.5	204.4	40.6	285.4	302	8.8	2.9	-67.8	276.1	101	igneous	Font et al. (2011)	T12
2054	208.6	207.0	40.2	285.4	246	10.6	2.9	-66.6	266.5	101	igneous	Kent and Tauxe (2005)	T12
2070	211.0	209.0	71.5	337.3	222	16.1	2.4	-52.5	279.0	102	igneous	Kent and Tauxe (2005)	T12
202.6	217.7	210.2	47.3	37.4	12	47.9	6.3	-50.0	286.4	301	igneous	Kent and Tauxe (2005)	T12
208.6	213.4	211.0	40.5	285.4	309	17.0	2.0	-61.7	275.3	101	igneous	Yuan et al. (2011)	T12
2130	215.0	214.0	40.5	285.6	336	31.0	1.4	-60.1	277.1	101	igneous	Kent and Tauxe (2005)	T12
2150	219.0	217.0	40.3	285.1	308	23.2	1.7	-59.9	279.5	101	igneous	Kent and Tauxe (2005)	T12
2185	224.0	221.0	40.3	285.2	194	17.3	2.5	-60.5	281.6	101	igneous	Kent and Tauxe (2005)	T12
2170	225.0	221.0	36.5	280.5	333	25.2	1.6	-59.0	279.6	101	igneous	Kent and Tauxe (2005)	T12
2210	233.0	227.0	40.4	285.4	148	34.6	2.0	-54.2	286.6	101	igneous	Kent and Tauxe (2005)	T12
2270	229.2	228.1	74.8	100.6	11	74.7	5.3	-47.1	301.6	301	igneous	Walderhaug et al. (2005)	T12
2240	234.0	229.0	22.3	33.6	10	75.5	5.6	-54.6	46.2	715	igneous	Lotfy & Elaat (2018)	this study

A global apparent polar wander path for the last 320 Ma calculated from site-level paleomagnetic data

2270	Dolerite dykes, Suriname	237.0	232.0	4.0	305.0	10	61.3	6.2	-82.0	320.0	201	igneous	Veldkamp et al. (1971)	T12
2320	Udzh, Siberian Platform	245.0	238.5	71.4	115.3	18	10.5	11.2	-60.3	332.4	301	igneous	Veselovskiy et al. (2012)	this study
240.0	Alto Paraguay Province, Paaguany/Brazil	242.8	241.5	-21.5	-57.9	26	23.0	6.0	-78.0	319.0	201	igneous	Ernesto et al. (2015)	this study
2370	Brisbane Tuffs	247.1	-27.47	242.1	-27.47	6	31.7	12.1	-56.5	153.1	801	igneous	Robertson (1963)	this study
235.3	Puesto Viejo Formation Volcanics, Mendoza	254.7	245.0	-34.6	-68.3	14	30.6	7.3	-76.7	312.4	290	igneous	Dometer et al. (2011c)	T12
242.5	Taimyr basalts, Siberia	254.5	245.5	74.9	106.5	10	12.0	14.5	-59.3	325.8	301	igneous	Waldorhaug et al. (2005)	T12
2484	Kotuy River Siberian Traps, Siberia	251.6	250.0	73.0	102.4	5	31.0	13.9	-52.7	328.4	301	igneous	Veselovskiy et al. (2003)	T12
2484	Siberian Traps Mean recalculated, Siberia	251.6	250.0	66.1	111.6	5	19.5	17.7	-52.8	334.4	301	igneous	Kravchinsky et al. (2002)	T12
250.4	Siberian Traps, YG locality	252.4	251.4	64.0	115.0	9	36.2	8.7	-65.2	329.0	301	igneous	Konstantinov et al. (2014)	this study
250.4	Siberian Traps, Nizhnedudinsk-Otyubskiy group	252.4	251.4	56.8	99.4	9	14.9	13.8	-44.5	329.1	301	igneous	Latsyhev et al. (2018)	this study
250.4	Siberian Traps, Tura lavas	252.4	251.4	56.8	99.4	12	11.5	13.4	-45.5	312.8	301	igneous	Latsyhev et al. (2018)	this study
250.4	Siberian Traps, RD locality	252.4	251.4	63.5	112.5	19	15.4	8.8	-53.0	313.5	301	igneous	Konstantinov et al. (2014)	this study
250.4	Kulumber river intrusions, Siberia	252.4	251.4	68.9	86.4	33	13.4	7.1	-47.4	323.1	301	igneous	Latsyhev et al. (2021b)	this study
250.4	Siberian Traps, Nizhnyaya Tunguska river	252.4	251.4	64.6	94.4	35	24.5	5.0	-56.2	313.6	301	igneous	Latsyhev et al. (2018)	this study
250.4	Siberian Traps, Norilsk-Marymecha-Kotuy	252.4	251.4	70.0	90.0	49	23.2	4.3	-52.9	327.1	301	igneous	Pavlov et al. (2019)	this study
251.3	Norilsk region intrusions, Siberia	252.3	251.8	69.3	88.5	31	24.7	5.3	-54.5	320.8	301	igneous	Latsyhev et al. (2021a)	this study
246.7	East European Platform, Zhukov	259.5	253.1	56.2	42.6	106	17.3	3.4	-53.2	349.5	301	sedimentary	Fetisova et al. (2017)	this study
246.7	East European Platform, Puchezh	259.5	253.1	57.0	43.2	157	19.7	2.6	-41.0	326.3	301	sedimentary	Fetisova et al. (2017)	this study
252.2	Araguainha impact structure, Brazil	257.2	254.7	-16.8	-53.0	28	83.5	3.6	-84.2	326.6	201	igneous	Yokoyama et al. (2014)	this study
251.9	East European Platform, Sukhona	259.5	255.7	61.0	45.0	210	13.9	2.7	-49.2	345.9	301	sedimentary	Fetisova et al. (2018)	this study
251.9	East European Platform, Nelben	259.5	255.7	51.7	11.7	82	34.5	2.7	-57.3	341.7	301	sedimentary	Fetisova et al. (2018)	this study
254.2	SW England, Aylesbeare Mudstone	264.3	259.3	50.6	-3.4	81	22.4	3.4	-65.6	325.9	301	sedimentary	Hounslow et al. (2016)	this study
259.4	Confamur 1, Lodeve	264.3	261.9	43.3	6.3	118	69.1	1.6	-54.0	348.9	301	igneous	Evans et al. (2014)	this study
261.0	Sierra Chica, La Pampa	264.6	263.0	-37.5	-65.3	35	54.9	3.3	-80.1	349.0	290	igneous	Dometer et al. (2011b)	T12
261.5	Upper Choyoi Group, Mendoza	265.5	263.5	-34.7	-68.3	40	31.4	4.1	-73.7	315.6	290	igneous	Dometer et al. (2011c)	T12
263.5	Gerrigong Volcanics	265.1	264.3	-34.6	150.8	17	16.3	9.1	-56.9	154.8	801	igneous	Belica et al. (2017)	this study
263.4	Werric Basalt	269.4	266.4	-31.9	151.0	9	10.8	16.4	-61.2	128.7	801	igneous	Klootwijk et al. (2003)	this study
259.6	Tambillo, Uspallate Basin, Argentina	274.4	267.0	-32.2	290.5	16	33.5	6.5	-78.9	319.6	290	igneous	Rapalini and Vilas (1991)	T12
268.3	Lammer dikes, Norway	274.7	271.0	60.3	10.5	8	103.8	5.5	-52.9	344.4	301	igneous	Tosvick et al. (1988)	T12
268.3	Lammer dikes, Norway	274.7	271.0	60.3	10.5	25	68.7	3.5	-50.9	343.6	301	igneous	Dominguez et al. (2011)	T12
269.2	Dome de Barrot, France	274.4	271.8	44.0	6.6	206	41.8	1.5	-47.2	324.5	301	sedimentary	Haldan et al. (2009)	this study
264.3	Lodeve basin redbeds	283.3	273.8	43.7	3.4	146	33.3	2.1	-41.7	336.7	301	sedimentary	Haldan et al. (2009)	this study
275.0	Bohemian Massif igneous, Germany	280.0	277.5	49.8	12.0	9	65.4	6.4	-42.3	345.9	301	igneous	Sofed and Harzer (1991)	T12
278.0	Scania mafhyre dikes, Sweden	282.0	278.0	55.7	13.7	8	35.9	9.4	-54.0	351.5	301	igneous	Bylund (1974)	T12
278.0	Jebel Neboud Ring Complex, Kordofan, Sudan	282.0	280.0	14.9	30.5	8	102.7	5.5	-40.8	71.3	715	igneous	Bachhede et al. (2002)	T12
280.0	Trachytes, Ukraine	282.2	282.6	37.2	37.8	19	54.9	4.6	-49.4	339.7	301	igneous	Yuan et al. (2011)	T12
280.0	Exeter Lavas, UK	291.0	285.5	51.0	356.0	9	62.5	6.6	-48.0	343.0	301	igneous	Dometer et al. (2020)	this study
277.0	Western Meseta, Morocco	294.6	285.8	33.0	353.6	18	27.1	6.8	-41.4	52.1	707	igneous	Kornad and Nairn (1972)	T12
281.0	Black Forest volcanics, Germany	291.0	286.0	48.0	8.0	7	82.1	6.7	-51.6	359.6	301	igneous	Harcumbe-Smea et al. (1996)	T12
279.0	Mauchline lavas, Scotland	293.0	286.0	55.5	-4.6	5	36.4	12.8	-46.2	348.0	301	igneous	Clark and Jackle (2003)	this study
280.0	Mount Leysion Intrusive Complex, Australia	292.0	286.0	-20.3	146.3	34	16.4	6.3	-43.2	137.3	801	igneous	Clark and Jackle (2003)	this study
280.0	Tuckers Igneous Complex, Australia	292.0	286.0	-20.1	146.5	42	11.5	6.8	-47.5	143.0	801	igneous	Clark and Jackle (2003)	this study
282.8	NE Kazakhstan lavas 1	289.8	286.3	47.5	80.7	65	48.8	2.5	-33.2	338.2	301	igneous	Bazhenov et al. (2014)	this study

NE Kazakhstan lavas 2	283.8	290.8	287.3	47.5	80.7	88	48.0	2.2	-44.1	340.6	301	igneous	Bazhenov et al. (2016)	this study
Oslo Graben, Krokstøgen and Vestfold	284.0	292.0	288.0	59.4	10.2	104	52.2	1.9	-48.2	335.5	301	igneous	Haldan et al. (2014)	this study
Lodeve basin redbeds	283.3	293.5	288.4	43.7	3.4	143	98.2	1.2	-47.1	333.9	301	sedimentary	Haldan et al. (2009)	this study
Saar-Nahe volcanics, Germany	288.0	293.0	290.5	49.5	7.0	11	20.8	10.2	-41.1	349.2	301	igneous	Berthold et al. (1965)	T12
Nahe volcanics, Germany	288.0	293.0	290.5	50.0	8.0	5	104.8	7.5	-46.0	347.0	301	igneous	Nijenhuis (1961)	T12
Irarare Group, Parana Basin, Brazil	283.3	298.9	291.1	-27.2	310.4	119	32.7	2.3	-63.2	347.5	201	sedimentary	Franco et al. (2012)	this study
Scania dolerite dikes, Sweden	287.0	300.0	293.5	55.5	13.5	6	85.6	7.3	-37.0	354.0	301	igneous	Mulder (1971)	T12
Alnækk Sill, High Green dykes, UK	292.0	296.0	294.0	55.4	-1.6	17	47.1	7.7	-47.1	337.1	301	igneous	Liss et al. (2004)	T12
Holy Island Sill and Dyke (Whin Sill), UK	292.0	296.0	294.0	55.7	-1.8	20	36.2	5.5	-35.4	346.8	301	igneous	Liss et al. (2004)	T12
Silesia volcanics, Poland	285.0	305.0	295.0	50.6	16.1	8	41.0	8.8	-43.0	354.0	301	igneous	Birkenmajer et al. (1968)	T12
Glenshaw Formation	298.9	307.0	303.0	40.5	280.0	23	16.1	7.8	-27.9	294.5	101	sedimentary	Kodama (2009)	T12
Maïra Formation, Brazil	298.9	307.0	303.0	-26.1	310.2	111	55.9	1.8	-51.9	344.3	201	sedimentary	Brandt et al. (2019)	this study
Moscovian, Murzuq basin, Algeria	307.0	315.2	311.1	23.6	11.9	113	25.4	2.7	-22.3	53.5	715	sedimentary	Annema et al. (2014)	this study
Tashkivska Dombas, Ukraine	315.2	323.4	319.3	48.8	38.6	84	35.4	2.6	-38.4	339.5	301	sedimentary	Meijers et al. (2010)	T12
Newcastle range volcanics	315.6	328.2	321.9	-18.4	143.8	15	26.2	7.6	-63.4	125.0	801	igneous	Anderson et al. (2003)	T12
Magdalen Basin	315.2	330.3	322.8	46.2	298.7	262	12.4	2.6	-27.9	299.5	101	sedimentary	Opdyke et al. (2014)	this study

Table 2. Paleomagnetic database used to compute the global apparent polar wander path for the last 320 Ma. NB: Data for the last 10 Ma from the PSV10 database are not included in this table. For the complete database, see Table S2. Abbreviations: min_age and max_age = lower and upper boundaries of age uncertainty range; slat/slom = latitude and longitude of (mean) sampling location; N = number of paleomagnetic sites used to compute the paleopole; A_{95} = radius of the 95% confidence circle about the mean of the distribution of VGPs; K = Fisher (1953) precision parameter of the distribution of VGPs; plat/plon = paleopole latitude and longitude (south pole); plateID = plate identification number (see Fig. 2 and Table 1); DB = database in which entry is listed (T12 = Torsvik et al. (2012), PSV10 = Cromwell et al. (2018) or added in this study).

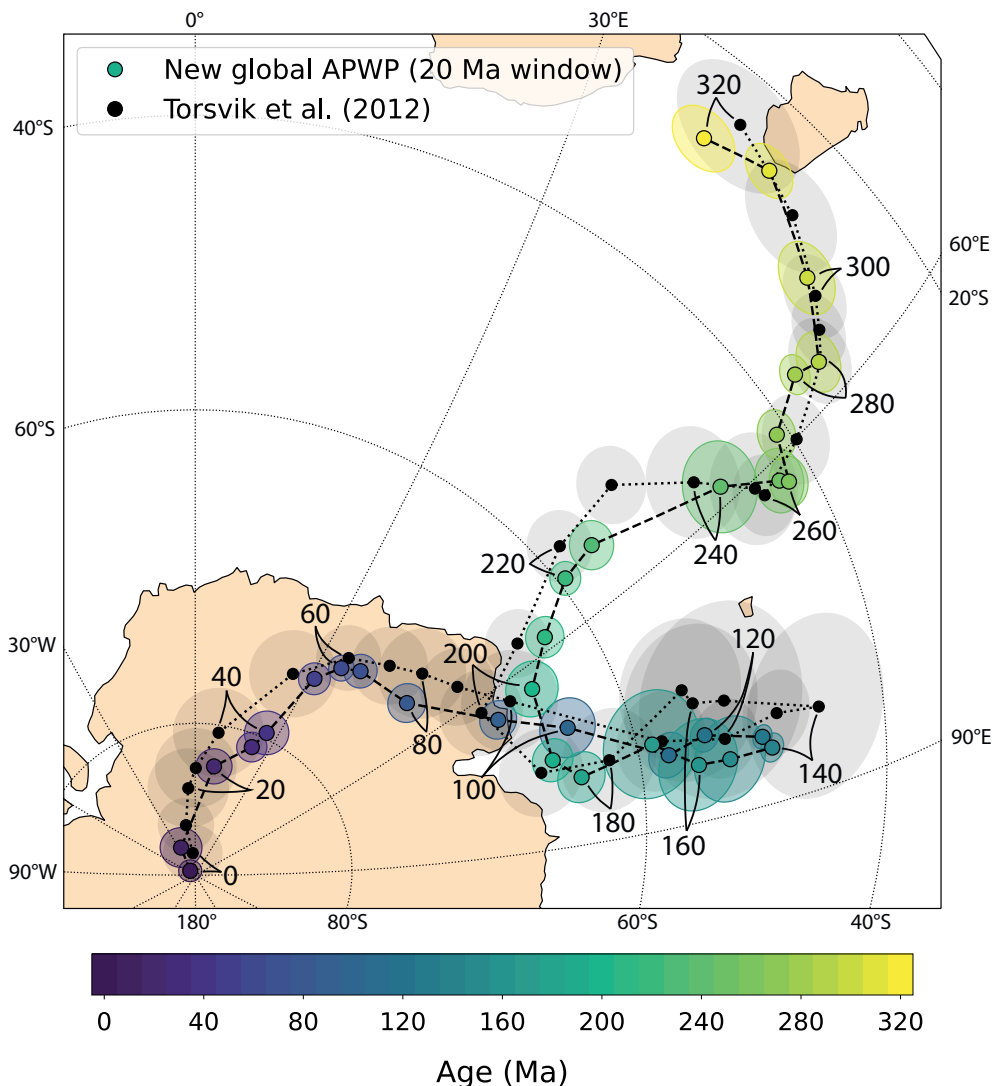


Fig. 5. Orthographic plot of the new global APWP for the last 320 Ma in South African coordinates, calculated using a 20 Ma sliding window. Reference poles and 95% confidence regions are colored by their age. Global APWP of Torsvik et al. (2012) is plotted with black circles (and light grey A95 confidence circles). Numbers indicate the center age of the time windows and are shown per 20 Ma.

6. Results

We computed a global APWP for the last 320 Ma using a 10 Ma time interval and a 20 Ma sliding window. The APWP is based on a total of 13737 parametrically re-sampled VGPs that are derived from 350 different paleomagnetic datasets (Table 2), yielding a mean and median number of sites per dataset of ~39 and 19, respectively. Of these datasets, 162 were included in the compilation of Torsvik et al. (2012), 71 in the PSV10 database

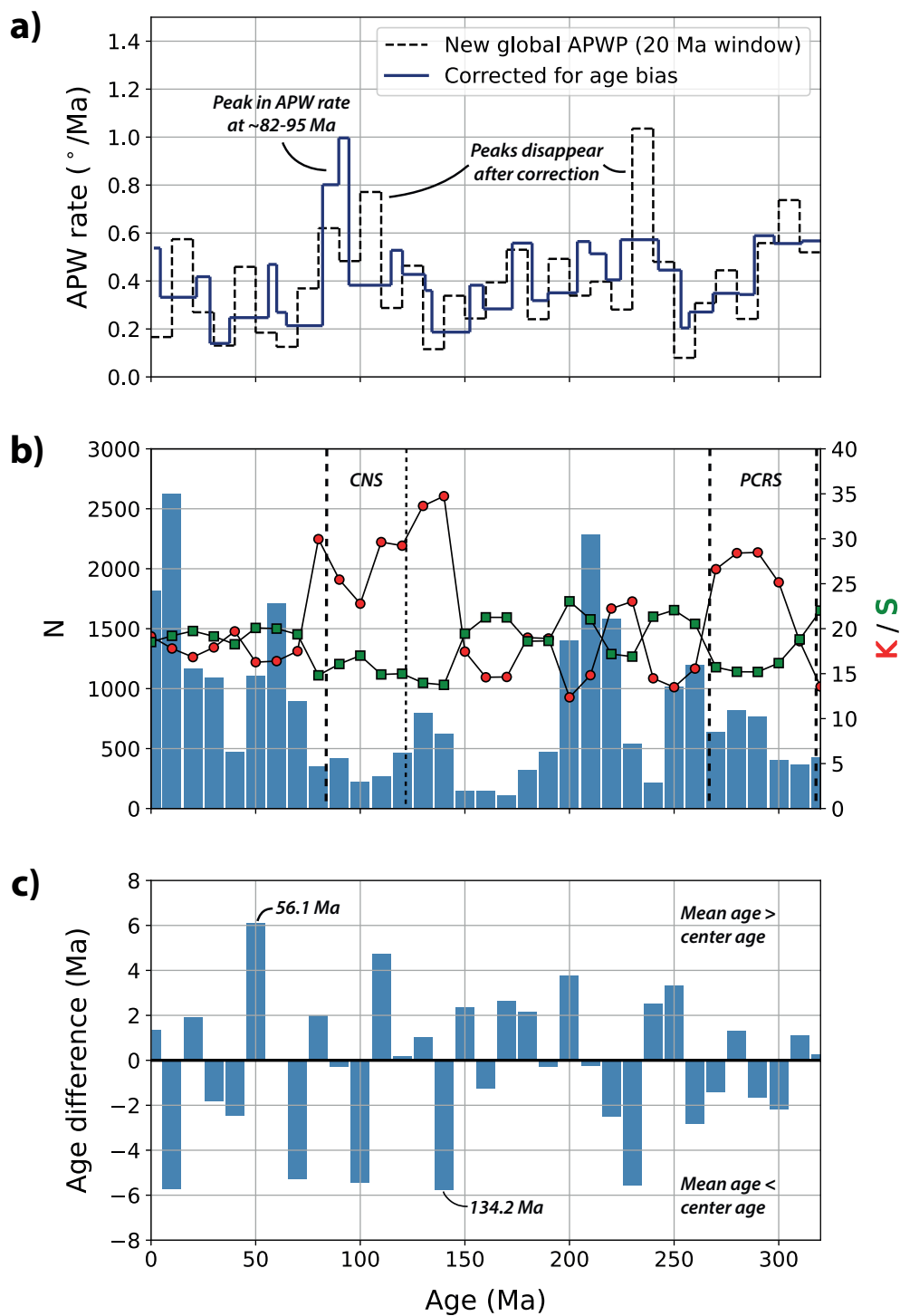
(Cromwell et al., 2018) and 117 were added during our data compilation (most of which were published post-2011). The new global APWP is shown in Fig. 5 as reference poles per 10 Ma that are plotted as south poles in South African coordinates (see also Table 3). The global APWP in the coordinate frame of other major tectonic plates, including North America, South America, Eurasia, India, Australia, Antarctica and the Pacific is given in Table 4. Because the pseudo-VGPs are not necessarily evenly distributed around the center age of the sliding window, we also report the average age of the re-sampled VGPs behind each reference pole in Table 3. In the following, we describe the geometry and statistical parameters of the global APWP as calculated for a South African coordinate frame (see also Figs. 5 and 6).

The reference poles of the global APWP in South African coordinates plot along smooth path segments intervened by sharp cusps (Fig. 5). The APWP shows a relatively smooth path from the present back to an Early Cretaceous (140 Ma) cusp that was also observed in previous global APWPs in South Africa coordinates (Besse & Courtillot, 2002; Schettino & Scotese, 2005; Torsvik et al., 2008; 2012). The reference poles of the 140-230 Ma segment of the APWP form another relatively smooth path, except for the 170 Ma pole which defines a minor ‘kink’ in the path. Notably, the reference poles at 230 and 240 Ma (Early Triassic) show a large angular difference of $\sim 10.4^\circ$. This is in large contrast to the 250 and 260 Ma reference poles which are separated by only $\sim 0.8^\circ$ and define another ‘cusp’ in our global APWP. The oldest (320-260 Ma) part of the APWP forms two segments that are separated by a kink defined by the 290 Ma reference pole, although we note that the oldest 320-300 Ma segment has the largest uncertainties of our APWP.

The 95% confidence regions of the global APWP are defined by the circle that includes 95% of the pseudo-poles computed for 2000 iterations (the P95). The size of the confidence regions ranges from 0.7° to 3.5° (for the 0 and 170 Ma reference poles, respectively), with an average (and standard deviation) of 1.6° (0.7°) (Table 3). The reference poles of the APWP are computed from, on average, 813 parametrically re-sampled VGPs. The lowest data density is observed for the Late Jurassic, with only ~ 110 -150 sites per time window. As expected, the highest data density is obtained for the last 10 Ma, provided by the large number of sites included in the PSV10 dataset. Additionally, the early Cenozoic (50-60 Ma) and Late Triassic (200-220 Ma) segments of the APWP are also based on large datasets of re-sampled VGPs.

For each time window, we computed the mean values of the Fisher (1953) precision parameter (K), the circular standard deviation (CSD) and elongation (E) for each iteration from the distribution of re-sampled VGPs that were included in that window (Table 3, Fig. 6b). The values for K are on average 20.9, ranging between 12.4 and 34.7. We obtain an average angular standard deviation for all time windows of 18.3° , with minimum and maximum values of 13.8° and 23.1° . The elongation ranges from 1.07 to 1.42 (Table 3),

Fig. 6. (a) APW rates derived from the new global APWP per 10 Ma age interval (black, dashed line). Rates computed using the mean ages of the pseudo-VGPs are shown by the blue line. (b) Mean number of sites (N), K and VGP dispersion (S) of the pseudo-VGPs that fall within each time window. The age range of the Cretaceous Normal Superchron (CNS) and Permo-Carboniferous Reversed Superchron (PCRS) are indicated. (c) Age difference between the mean age of the pseudo-VGPs and the center age of the time window.



with an average value of 1.16, indicating that the distribution of pseudo-VGPs that fall within the same time window is approximately circularly symmetric (see also Fig. 2a).

We calculated the rate of apparent polar wander per 10 Ma time period from the great-circle distance between reference poles of successive age (Fig. 6a). We obtain an average APW rate of $0.40 \pm 0.21^\circ/\text{Ma}$ (one standard deviation). Except for a notable spike in APW rate of $1.04^\circ/\text{Ma}$ between 230 and 240 Ma and two peaks of $\sim 0.8^\circ/\text{Ma}$ at 100-110 Ma and 300-310 Ma, all APW rates are $\sim 0.6^\circ/\text{Ma}$ or lower. There seems to be no clear correlation between the APW rate and age, and age bins with relatively low APW rates alternate with slightly faster APW throughout the studied time span of the pole path. On the other hand, the observed APW rates and position of the reference poles may be influenced by an uneven temporal distribution of the re-sampled VGPs. For example, a large dataset with relatively tight age constraints may 'pull' a reference pole toward the paleopole with large N. This temporal bias may be identified from a relatively large difference between the center age of the window and the mean age of the re-sampled VGPs that fall within that time window (see Fig. 6c). For example, the high APW rate between 230 and 240 Ma may be explained by the difference in mean age of the re-sampled VGPs of ~ 18 Ma. To correct for this effect, we have also computed the APW rates per 10 Ma time interval by dividing the angular distance by the difference in mean age of the re-sampled VGPs (Fig. 6a). Although the average APW rate (with one standard deviation) remains similar ($0.42 \pm 0.18^\circ/\text{Ma}$), all the peaks in APW rate mentioned above disappear. Instead, we now observe a single peak in the APW rate of 0.8 - $1.0^\circ/\text{Ma}$ between 82 to ~ 95 Ma. Whether the observed spikes in APW rate are robust features of our global APWP will be discussed in section 7.2.

7. Discussion

7.1. Robustness of the global APWP

Our approach to compute a global APWP from site-level paleomagnetic data critically builds on the assumption that the dominant sources of uncertainty in paleomagnetism are (more) effectively averaged by assigning equal weight to each paleomagnetic site rather than to a paleopole that is an average of an arbitrary collections of those sites (Chapter 2). On the one hand, our approach allows us to straightforwardly propagate uncertainties in the age of the sampled rocks and the uncertainty caused by paleosecular variation of the past magnetic field. On the other hand, there are multiple sources of uncertainty and error that are independent of the number of sites, e.g., due to unremoved magnetic overprints or remagnetization, dating errors, or non-rigidity of assumed rigid plates. Besse and Courtillot (2002) suspected that because some degree of deformation is often necessary for rocks to be exposed at the surface, unrecognized local deformation (such as local rotations caused by plunging fold axes) may be an important source of noise in APWPs. In the conventional approach in which each paleopole is assigned equal weight, the bias resulting from a single dataset that is affected by one or more of the above artifacts is unlikely to be large. However, if such a dataset has a large number of sites, its relatively large weight may cause considerable bias in the APWP calculated from site-level data.

We first evaluate the influence of large datasets on the global APWP by parametrically re-sampling only 50 VGPs for all paleomagnetic datasets that are based on more than 50 sites. The resulting APWP is very similar to the one presented in the previous section (Fig. 7). As expected, the confidence regions for many reference poles are larger, as they are

Window	Age	N	P ₉₅	Longitude	Latitude	Mean K	Mean CSD	Mean E
0	1.3	1811.5	0.7	313.2	-89.6	19.1	18.5	1.07
10	4.4	2609.7	1.3	334.1	-87.9	17.8	19.2	1.06
20	21.7	1156.7	1.1	9.4	-82.7	17.0	19.7	1.10
30	28.2	1091.0	1.0	23.2	-80.8	17.9	19.1	1.09
40	37.5	475.0	1.4	26.1	-79.6	19.6	18.3	1.14
50	56.1	1101.3	1.0	31.0	-75.2	16.3	20.1	1.11
60	60.0	1707.5	0.8	35.2	-73.7	16.4	20.0	1.08
70	64.7	896.5	1.1	39.1	-73.1	17.5	19.4	1.12
80	82.0	350.1	1.3	51.5	-72.6	29.9	14.8	1.16
90	89.7	412.9	1.2	64.9	-68.2	25.5	16.1	1.17
100	94.6	217.3	1.9	71.5	-64.2	22.8	17.0	1.21
110	114.7	259.5	1.5	80.7	-57.9	29.6	14.9	1.26
120	120.2	458.1	1.1	80.0	-55.0	29.3	15.0	1.18
130	131.0	798.2	0.8	82.7	-50.7	33.6	14.0	1.10
140	134.2	621.8	0.9	84.1	-50.0	34.7	13.8	1.12
150	152.4	144.3	2.8	83.7	-53.4	17.5	19.4	1.24
160	158.7	148.9	3.0	83.1	-55.8	14.6	21.2	1.24
170	172.6	112.5	3.5	78.6	-58.9	14.7	21.2	1.28
180	182.1	319.5	1.7	79.5	-64.2	19.0	18.6	1.29
190	189.7	470.1	1.4	75.3	-65.8	18.9	18.7	1.18
200	203.7	1399.0	1.8	63.5	-65.4	12.4	23.1	1.09
210	209.7	2287.7	1.3	58.1	-62.9	14.8	21.0	1.06
220	217.5	1583.0	1.1	53.8	-59.5	22.2	17.2	1.07
230	224.4	543.6	1.6	53.1	-56.7	23.0	16.9	1.12
240	242.5	215.4	2.9	58.3	-46.8	14.5	21.4	1.21
250	253.3	1017.2	2.1	61.7	-42.7	13.5	22.1	1.08
260	257.2	1200.3	1.6	62.4	-42.1	15.6	20.5	1.08
270	268.6	637.2	1.6	58.5	-41.0	26.6	15.7	1.13
280	281.3	819.1	1.3	56.2	-36.9	28.4	15.2	1.11
290	288.4	763.9	2.0	57.0	-34.6	28.4	15.2	1.18
300	297.8	405.8	2.5	52.1	-30.8	25.1	16.2	1.26
310	311.1	368.0	1.9	45.3	-26.6	18.6	18.8	1.42
320	320.3	427.9	2.4	39.8	-28.2	13.6	22.0	1.33

Table 3. Global APWP for the last 320 Ma in South African coordinates, calculated using a 20 Ma window. The center age of the window and the mean age of the re-sampled VGPs in that window are listed. N and P₉₅ are the average number of re-sampled VGPs that fall within the time window and the 95% confidence region of the reference pole (in degrees). Mean K, CSD and E are the average Fisher (1953) precision parameter, circular standard deviation and elongation of the re-sampled VGPs.

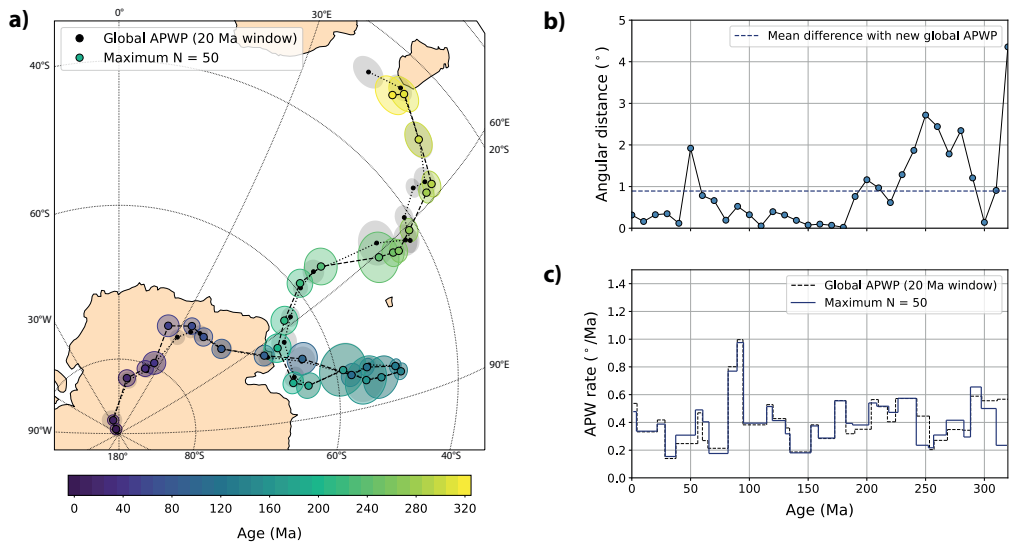


Fig. 7. (a) Global APWP calculated with a maximum of $N=50$ per dataset. The global APWP of Fig. 5 is plotted with the black circles. (b) Angular difference between the two APWPs. (c) Comparison of APW rates.

based on fewer sites. We observe two main differences. First, the 50 and 70 Ma poles are at a large angular distance from the 60 Ma pole, as they are pulled less towards the larger datasets with ages of ~ 60 Ma. Second, the 240–300 Ma segment of the APWP becomes a smoother path. This shows that although no major differences are observed, large datasets indeed alter some segments of the APWP. However, since we do not know the ‘true’ APWP, it is difficult to assess whether the influence of a large datasets represents a bias in the path or provides improved constraints on the position of the ‘true’ time-average pole. The most straightforward way of testing the robustness of these features of the global APWP is by collecting more large high-quality datasets for these time intervals.

In addition, we assess the robustness of the new global APWP using a set of statistical parameters that describe the distribution of the re-sampled VGPs per time window (see Table 4, Fig. 6b). The dispersion of pseudo-VGPs – as quantified by K or CSD – is shown to be similar to what may be expected from ‘normal’ PSV. Typical values for K range from 10 to 70 (e.g., Deenen et al., 2011; Meert et al., 2020) and for CSD (or VGP scatter, S) from 10 to 25 (e.g., Butler, 1992; Cromwell et al., 2018; Doubrovine et al., 2019). The mean K and CSD values obtained for each time window of the global APWP all fall within these ranges (Fig. 6b). In addition, the mean elongation of the pseudo-VGPs that fall within each age bin show that the re-sampled VGPs have a nearly circular symmetric distribution (Table 3), similar to what may be expected from PSV (e.g., Tauxe and Kent, 2004). Interestingly, the time intervals with the lowest dispersion of pseudo-VGPs approximately coincide with the Cretaceous Normal Superchron (~ 83 –121 Ma, Gradstein et al., 2020) and Permo-Carboniferous Reversed Superchron (~ 267 –318 Ma, Gradstein et al., 2020). Even though these dispersion values are not obtained from ‘real’ VGP-level data, we hypothesize that this may reflect a suppression in the magnitude of PSV during these

intervals with stable magnetic field polarity, as was previously proposed (e.g., Brandt et al., 2019; Handford et al., 2021). We note, however, that the lowest dispersion of pseudo-VGPs is observed for the age windows centered at 130 and 140 Ma, whereby the majority of the input data is derived from large igneous datasets of South America and southern African that are associated with the Parana-Etendeka LIP. This low dispersion of pseudo-VGPs may be explained by the fact that the data is obtained from rocks of a relatively short age interval and is likely less affected by noise resulting from unrecognized local deformation or plate reconstruction errors.

In summary, the statistical parameters obtained for the global APWP indicate that the errors that undoubtedly exist in our dataset due to e.g., unresolved overprints, unrecognized tectonic deformation, plate circuit errors, or age errors, do not form a major contribution to the scatter of the data that drives the dispersion beyond values that typically represent PSV. This suggests that the global APWP presented here is robust and that it represents the time-averaged paleomagnetic field for each interval.

7.2. Comparison to previous global APWPs

Because of the fundamentally different approach used here, it is interesting to evaluate how the site-level-based path compares to previous global APWPs that were computed using the conventional running mean approach applied to paleopoles. We find that our new global APWP has a mean angular difference (with one standard deviation) of $2.5 \pm 1.1^\circ$ when compared to the global APWP of Torsvik et al. (2012) (Fig. 8a). This difference is similar to the mean angular difference of 2.6° between the global APWP (in South African coordinates) of Besse and Courtillot (2002) and Torsvik et al. (2012), but notably smaller than the difference between the APWP of Torsvik et al. (2012) and those of Torsvik et al. (2008) and Kent and Irving (2010), which yielded average angular differences of 3.9° and 4.1° , respectively. These APWPs were all computed using the same running mean approach with a time step of 10 Ma and a sliding window of 20 Ma, and the observed differences thus resulted from differences between the compilations of paleopoles and plate reconstruction parameters. But even though we constructed our path using (i) parametrically re-sampled VGPs instead of paleopoles, (ii) an updated paleomagnetic database obtained with more stringent selection criteria and (iii) an updated global plate circuit, we obtain a path that is, to first-order, similar to the most recent pole-based APWP of Torsvik et al. (2012) (see Fig. 5a). This clearly shows that the overall geometry of the path is well-constrained, and strengthens confidence that paleomagnetism provides a reliable and reproducible reference frame as basis for paleogeography and paleoclimate for the last 320 Ma.

One of the main differences between our VGP-based APWP and the pole-based APWP of Torsvik et al. (2012) is the size of the 95% confidence regions (Fig. 5a). Particularly for time intervals with high data density, such as for the Cenozoic, Early Cretaceous and Late Triassic, the confidence regions of the new global APWP are $<1.5^\circ$, compared to A_{95} values of $\sim 2\text{--}3^\circ$ of the Torsvik et al. (2012) path for those intervals. The smaller confidence regions may seem counterintuitive, since the approach used for the VGP-based path incorporates both temporal and spatial uncertainties that were set to zero in the computation of the APWP of Torsvik et al. (2012). We interpret this as simply the result of the significant increase in data points from dozens of paleopoles to hundreds or even thousands of re-sampled pseudo-VGPs. The increase in independent data points

thus outweighs the larger dispersion of simulated VGPs (with a K of ~ 15 -35) compared to that of coeval paleopoles (with K values of ~ 100 , see Rowley, 2019; Chapter 2). The smaller confidence regions obtained from using site-level data instead of paleopoles was previously observed for the PSV10 dataset in Chapter 2. This suggests that the resolution and precision obtained with paleomagnetic data has long been underestimated by artificially decreasing the number of data points underlying APWPs due to the averaging of arbitrarily defined collections of sites into paleopoles.

Although the first-order geometry of our new global APWP is similar to that of Torsvik et al. (2012), there are several time intervals for which there are notable differences. For instance, the reference poles of the 30-40, 90-100 and 310-320 Ma segments of the path, as well as the poles at 200 and 230 Ma, are at an angular distance of $>3^\circ$ (Fig. 8a). We interpret these differences as being mainly caused by our site-level approach and the updated paleomagnetic database, to which we added recently published data but from which we also excluded many paleomagnetic datasets due to the application of our more stringent selection criteria.

The largest difference between our new global APWP and that of Torsvik et al. (2012) is observed for the 140-170 Ma segment, yielding an angular difference of $\sim 4^\circ$ (Fig. 5, 8a). This segment of the APWP of Torsvik et al. (2012) was based on relatively few paleopoles (<20 per time window), and the observed differences may partly be explained by the inclusion of recently published datasets in our database, e.g., those from Cervantes-Solano et al. (2020) and Kulakov et al. (2021). Despite these differences, our new APWP is similar to that of Torsvik et al. (2012) in that it does not include a phase of rapid polar wander between ~ 165 and 140 Ma as shown in the APWP of Kent and Irving (2010). This rapid polar shift is often referred to as the 'Jurassic monster polar shift' and has been interpreted as fast true polar wander (e.g., Kent et al., 2015; Muttoni and Kent, 2019; Yi et al., 2019). Our new global APWP does not support such anomalously fast polar wander in the Late Jurassic, consistent with recently published paleomagnetic results (Kulakov et al., 2021; Gao et al., 2021). We note, however, that our APWP does not rule out the occurrence of a phase of relatively 'slow' TPW in the late Jurassic.

Another notable difference is the $\sim 4^\circ$ angular distance between our reference pole at 100 Ma and that of Torsvik et al. (2012), yielding a very different estimate of the APW rate at mid-Cretaceous times. The 110-100 Ma spike in APW rate observed by Torsvik et al. (2012) is much less pronounced in our global APWP and disappears entirely when correcting for the 'effective' age difference between successive reference poles (Fig. 8b). We find that the re-sampled VGPs that fall in the age windows centered on 100 Ma and 110 Ma have mean ages of ~ 95 Ma and ~ 115 Ma, respectively (Fig. 6c, Table 3), indicating that the spike in uncorrected APW rate may be the result from an uneven age distribution of the input data. This suggests that previous estimates of APW rate based on the center ages of each time window may be influenced by temporal biases and shows the importance of taken into account the uncertainties in ages and their distribution.

Intriguingly, after applying a correction for the effective age difference between successive reference poles, the APW rates calculated for South Africa for the last 320 Ma show only a single spike at ~ 82 -95 Ma. Although a detailed analysis of this phase of rapid APW is beyond the scope of this paper, we note that this spike coincides with a ~ 80 -92 Ma peak in the convergence rate during a counterclockwise rotation of Africa relative to Eurasia, as part of a recently proposed tectonic chain reaction (Gürer et al., 2022). The

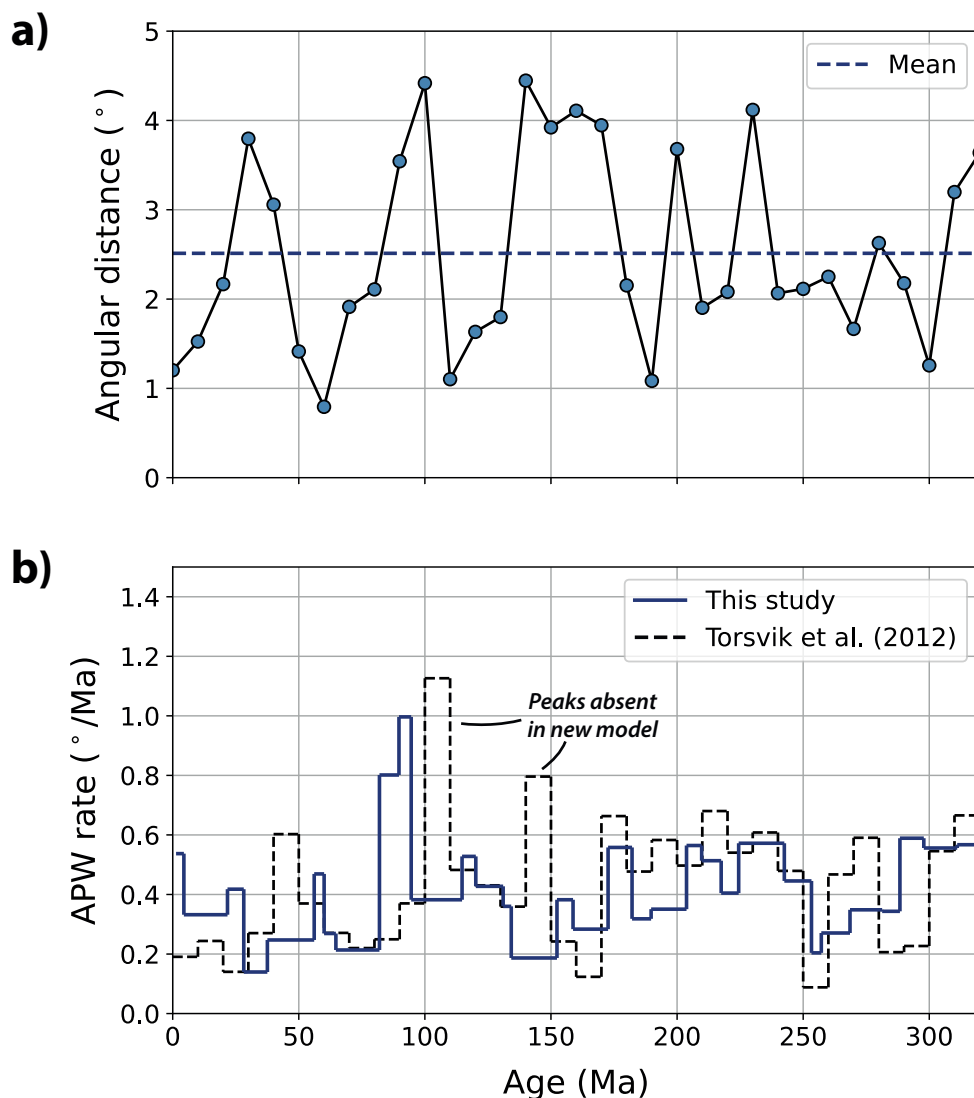


Fig. 8. (a) Angular difference between the new VGP-based global APWP and the pole-based APWP of Torsvik et al. (2012), both in South African coordinates. The dashed blue line is the mean angular distance of 2.5°. (b) APW rates determined in this study compared to those derived from the global APWP of Torsvik et al. (2012).

spike in APW rate observed in our APWP may thus be related to a phase of relatively rapid plate motion of (South) Africa.

Finally, we note that there are a number of previously inferred and long-debated ‘anomalies’ in paleomagnetic data, such as those between the major continents of Gondwana, Laurentia, and Baltica for ~320–250 Ma which underpin the Pangea A vs B controversy (e.g., Domeier et al., 2012; 2021; Gallo et al., 2017; Kent & Muttoni, 2020,

Kent et al., 2021; Pastor-Galan, 2022), or the ‘east Asian inclination anomaly’ in the Paleogene (e.g., Cogné et al., 2013). The observed mismatches between paleomagnetic data and APWPs of different continents and tectonic plates have generally been based on analyses using pole-level data. These discrepancies may be re-evaluated using a site-level approach, in which spatial and temporal uncertainties are explicitly incorporated, which have often been omitted in comparative analyses. Evaluating whether previously inferred anomalies still exist when using our site-level approach requires a detailed review of the underlying data, which is beyond the scope of this paper. We note, however, that there is no systematic increase in the dispersion of re-sampled VGPs that underlie our site-based global APWP in the time intervals of the long-standing debates. We thus find no reason to infer a significant error in the relative plate motion model in these time intervals (e.g., Muttoni et al., 2003, Cogné et al., 2013), or a systematic time-dependent non-dipole field (e.g., Torsvik & van der Voo, 2002, Dupont-Nivet et al., 2010).

7.3. Resolution of the global APWP

We calculated the reference poles of the global APWP at a resolution of 10 Ma using a sliding window of 20 Ma, similar to previously published global APWPs of Besse and Courtillot (2002), Kent and Irving (2010) and Torsvik et al. (2008; 2012). The use of such overlapping time windows results in the smoothing of the pole path and is expected to increase the extent to which random biases and noise in the underlying data are averaged. On the other hand, too much smoothing could cause the removal of short-duration features in the APWP that may be real (e.g., Muttoni et al., 2005; Dupont-Nivet et al., 2010), as illustrated, for instance, by the spherical spline path of Torsvik et al. (2008) that smoothed ‘away’ a peak in APW rate. To assess the influence of the temporal resolution on the shape of the global APWP, we also computed the path at a higher resolution, using a time step of 5 Ma and a sliding window of 10 Ma (Fig. 9). The geometry of the path is notably more irregular than the APWP calculated using a 20 Ma sliding window, showing more distinct features such as relative standstills and cusps that separate segments of the path covering shorter time intervals. For example, while the 10 Ma-resolution-APWP showed a relative smooth path for the last 140 Ma, the 5 Ma-resolution-APWP shows a relative stand-still during the 30-50 Ma interval (Fig. 9a). For time intervals with relatively high APW rates, such as from 180 to 230 Ma, the 5 Ma-resolution-path is nearly identical to the 10 Ma-resolution-path. This finding is consistent with that of Besse and Courtillot (2002) who also computed their global APWP at a 5 Ma resolution (with a 10 Ma window) and who illustrated the large similarities between both paths in the coordinate frame of the relatively fast-moving Indian plate, noting that all the ‘essential’ features were captured by both paths. The use of a smaller time window leads to a decrease in the degree of smoothing of the path, resulting in $\sim 40\%$ higher APW rates with an average of $0.58 \pm 0.30^\circ/\text{Ma}$ (after correcting for the effective age) and seven intervals of 5 Ma that yield an APW rate of $>1.0^\circ/\text{Ma}$ (Fig. 9b). Notably, the peak in APW rate observed for the 10 Ma-resolution-APWP between 82 and ~ 95 Ma is also identified for the 5-Ma-resolution-APWP, which shows a $\sim 1.2^\circ/\text{Ma}$ APW rate between 86 and ~ 94 Ma.

The reference poles of the 5 Ma-resolution-APWP are, unsurprisingly, based on about half as many re-sampled VGPs (417 versus 813) compared to the 10 Ma-resolution-APWP. Notably, $\sim 17\%$ of the reference poles have a mean number of sites of <100 (see Fig. 9c, Table S3). The reduced number of sites behind each reference pole leads to larger

Window	Age	P ₉₅	North America		South America		Eurasia		India		Australia		Antarctica		Pacific	
			Plat	Plon	Plat	Plon	Plat	Plon	Plat	Plon	Plat	Plon	Plat	Plon	Plat	Plon
0	1.3	0.7	313.2	-89.6	313.2	-89.6	313.2	-89.6	313.2	-89.6	313.2	-89.6	313.2	-89.6	313.2	-89.6
10	4.4	1.3	330.3	-87.5	290.2	-87.7	309.8	-87.6	90.4	-88.0	135.2	-86.3	298.1	-87.6	231.7	-86.6
20	21.7	1.1	356.6	-82.3	332.1	-84.6	350.3	-83.5	67.6	-81.7	98.5	-81.4	345.5	-84.2	277.7	-86.0
30	28.2	1.0	2.8	-80.9	329.1	-84.4	357.3	-82.8	88.9	-76.8	108.5	-75.1	353.4	-84.2	251.7	-86.0
40	37.5	1.4	355.2	-80.3	313.3	-83.5	345.0	-82.7	101.7	-72.7	114.7	-71.2	341.0	-84.4	238.3	-82.3
50	56.1	1.0	0.5	-76.5	328.3	-81.1	352.9	-79.7	101.2	-63.3	110.3	-68.1	3.9	-83.0	239.0	-80.0
60	60.0	0.8	7.1	-74.5	337.2	-80.8	354.3	-79.3	96.3	-52.6	112.9	-66.8	9.5	-83.8	220.7	-78.3
70	64.7	1.1	7.5	-74.7	337.2	-81.2	351.9	-79.6	98.8	-39.0	116.6	-65.9	13.0	-85.2	202.9	-73.0
80	82.0	1.3	12.6	-76.7	337.8	-84.1	359.3	-81.8	103.2	-31.8	125.7	-63.4	66.3	-88.9	187.1	-65.7
90	89.7	1.2	17.8	-77.8	9.2	-85.7	359.4	-83.1	111.7	-23.3	130.6	-58.9	150.0	-85.8		
100	94.6	1.9	14.6	-77.2	36.5	-84.3	357.9	-82.2	114.0	-17.6	135.6	-56.3	167.4	-82.8		
110	114.7	1.5	22.4	-74.5	57.7	-80.2	18.2	-80.9	116.0	-9.9	139.1	-51.2	166.3	-78.0		
120	120.2	1.1	12.1	-74.4	65.6	-85.4	4.3	-79.6	114.6	-8.2	145.5	-52.2	187.2	-76.9		
130	131.0	0.8	8.5	-71.7	70.4	-85.3	5.9	-76.6	115.7	-0.1	146.0	-47.0	178.6	-73.1		
140	134.2	0.9	4.7	-72.4	66.4	-83.9	359.9	-76.6	120.0	1.8	150.3	-44.5	183.5	-69.6		
150	152.4	2.8	349.1	-74.9	89.7	-86.7	338.6	-76.3	124.9	-2.6	160.2	-44.8	198.1	-65.4		
160	158.7	3.0	330.3	-75.8	137.6	-87.8	320.9	-74.4	128.8	-5.5	167.4	-44.3	205.8	-61.5		
170	172.6	3.5	303.0	-74.1	221.2	-86.5	303.0	-67.0	129.7	-9.8	173.0	-46.1	214.0	-59.8		
180	182.1	1.7	275.6	-73.9	215.1	-81.2	284.0	-67.0	133.7	-14.6	181.7	-45.1	220.2	-54.7		
190	189.7	1.4	268.0	-71.0	224.5	-79.4	280.2	-63.6	133.1	-17.0	184.3	-46.7	224.4	-54.5		
200	203.7	1.8	268.4	-65.3	247.2	-77.4	286.0	-58.7	128.6	-19.7	185.2	-51.6	231.8	-57.1		
210	209.7	1.3	273.0	-62.5	262.4	-76.9	294.0	-56.8	125.0	-19.7	182.6	-54.6	234.9	-60.1		
220	217.5	1.1	278.5	-59.5	278.6	-75.8	303.0	-54.8	120.8	-19.0	178.2	-57.7	238.3	-63.8		
230	224.4	1.6	283.2	-58.1	289.9	-75.4	307.5	-53.7	118.3	-17.5	173.4	-59.0	238.8	-66.6		
240	242.5	2.9	301.7	-55.8	330.2	-74.4	324.8	-52.9	113.4	-8.3	154.2	-57.0	222.3	-75.5		
250	253.3	2.1	310.1	-55.1	346.6	-73.0	332.7	-53.0	112.5	-3.7	147.4	-54.1	203.6	-77.6		
260	257.2	1.6	311.5	-55.0	349.2	-72.7	334.0	-53.0	112.4	-3.0	146.6	-53.5	199.9	-77.7		
270	268.6	1.6	309.6	-52.1	343.8	-70.2	333.0	-50.0	109.5	-4.1	143.6	-56.1	207.1	-80.5		
280	281.3	1.3	312.1	-48.0	345.9	-65.8	336.4	-46.2	105.4	-2.4	135.7	-56.9	196.1	-84.8		
290	288.4	2.0	315.2	-46.8	350.1	-64.2	339.6	-45.3	104.3	-0.3	132.1	-55.5	168.6	-85.3		
300	297.8	2.5	314.3	-41.2	346.5	-58.8	339.8	-39.7	98.7	-0.4	122.9	-57.8	72.4	-87.5		
310	311.1	1.9	311.9	-34.1	341.3	-52.1	338.5	-32.4	91.4	-1.8	109.8	-60.9	20.4	-81.4		
320	320.3	2.4	306.0	-32.4	333.2	-50.8	333.0	-30.1	89.4	-6.6	106.9	-65.9	354.2	-78.7		

Table 4. Global APWP (20 Ma window) rotated into the coordinate frame of other major tectonic plates. See Table 3 for more information.

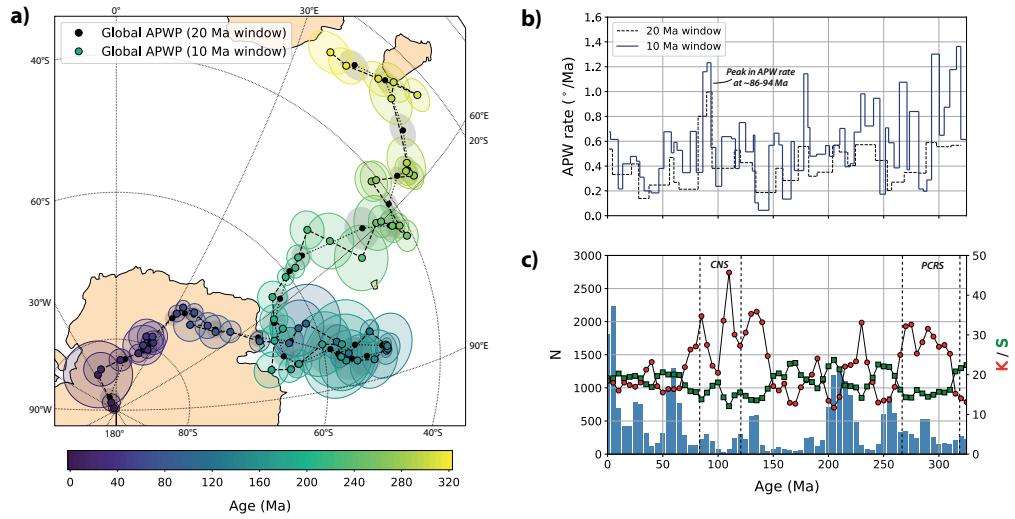


Fig. 9. (a) Global APWP for the last 325 Ma (in South African coordinates) computed at a 5 Ma resolution with a 10 Ma window. The path calculated using a 20 Ma window is plotted with the black circles. (b) Comparison of APW rates. (c) Statistical parameters for the 5 Ma-resolution-APWP; see Fig. 6 for more information.

confidence regions that have an average (and standard deviation) of 2.5° (1.2°) compared to 1.6° (0.7°) for the 10 Ma-resolution-APWP (Fig. 9a).

Intriguingly, the distribution of re-sampled VGPs shows a very similar mean dispersion, with a K value of 22.2 for the 5 Ma-resolution-APWP compared to 20.9 for the 10 Ma-resolution-APWP, further supporting that the distributions of re-sampled VGPs underpinning our global APWP provide a robust approximation of the dispersion expected from PSV (Fig. 9c). But because of the lower number of re-sampled VGPs per time window, the APWP and associated APW rates are more likely to be biased by random noise or an uneven temporal distribution of the re-sampled VGPs.

7.4. Outlook

The calculation of a global APWP based on parametrically re-sampled VGPs provides a next step in the propagation of key sources of uncertainty in the computation of APWPs, building on previous efforts and approaches aimed to incorporate uncertainties in paleopoles or APWPs (e.g., McFadden & McElhinny, 1995; Swanson-Hysell et al., 2019; Hansma & Tohver, 2020; Gallo et al., 2021; Chapter 2; Pierce et al., 2022). Future improvements in the propagation of errors may concentrate on some of the following aspects. First, errors in the Euler rotation poles that are used to rotate the VGPs to a common coordinate frame are not yet propagated. Although methods have been developed to propagate such uncertainties throughout a plate circuit (Dobrovine & Tarduno, 2008), the uncertainties of many Euler rotation poles computed from ocean floor anomalies have not been reported and the size of error ellipses of marine magnetic anomaly-derived are typically an order of magnitude smaller than uncertainties induced by PSV (e.g., DeMets & Merkouriev, 2021). We foresee that the propagation of these errors

will provide only marginal gains.

Second, a statistical framework for the full propagation of the errors through the hierarchical levels of paleomagnetic data, that is from the individual demagnetization steps to the VGP or paleopole - has yet to be developed. Recent advances in the statistical treatments of paleomagnetic data (Heslop and Roberts, 2016; 2020) or directional statistics (e.g., Scealy et al., 2022) may provide promising avenues for improved propagation of these fundamental uncertainties behind paleomagnetic data. Ideally, future APWPs could be computed from 'real' site-level data rather than from parametrically re-sampled VGPs. Such an approach would avoid the necessity of adopting a pre-defined distribution of VGPs, such as the assumed Fisher (1953) distribution used here. When using a parametric re-sampling approach, the Fisher (1953) distribution is essentially the only option, however, for the simple reason that statistical parameters describing the paleomagnetic data distributions have traditionally been reported in the framework of Fisher (1953). Building the database from the 'real' VGPs would also allow the systematic application of selection criteria and data filters on the site-level. Apart from the fact that not all site-level data is available for the studies included in the data compilations that underlie global APWPs, the compilation of more than ten thousand sites from hundreds of publications would require an enormous effort. Whether the calculation of an APWP from the published VGPs would yield different results from our re-sampling approach remains to be investigated. To enable the computation of VGP-based APWPs in the future, we strongly recommend paleomagnetists to archive their published data, e.g., in the MagIC database (Jarboe et al., 2012) or the Paleomagnetism.org data library (Koymans et al., 2020).

We emphasize that the calculation of a reference APWP from site-level data provides opportunities to significantly improve intervals of the global APWP by collecting large datasets of independent readings of the past geomagnetic field (e.g., from thick sequences of lava flows or sedimentary rocks), particularly for time intervals that have a relative low data coverage. Moreover, Dupont-Nivet et al. (2010) already argued that the precision and temporal resolution of reference APWPs provides a limiting factor in the analysis of detailed tectonic problems, such as the estimation of convergence rates between tectonic terranes that are not included in a plate circuit. They therefore tried to stimulate the paleomagnetic community to focus part of their efforts on collecting datasets from stable plate interiors that may improve the accuracy and precision of the global APWP. We suggest here that rock formations that have provided reliable paleomagnetic data in the past but that include, as of yet, only a relatively limited number of sites may provide particularly useful sampling locations for this purpose. In addition, we highlight that our new approach allows the comparison of independent paleomagnetic datasets against the global APWP at the site-level, which may improve the robustness of future determinations of relative tectonic displacements such as paleolatitudinal motions and vertical-axis rotations (see Chapter 2). Finally, we note the site-level approach holds great promise to optimize the resolution of APWPs for key time intervals, such as those containing mass extinctions or climate crises: collecting data from such well-dated intervals allows computing a high-resolution paleomagnetic reference frame that may be used as input for detailed studies of such events. We foresee that the continuous improvement of the global APWP, both in terms of data coverage and uncertainty incorporation, will enable Earth Scientists to place better quantitative constraints on, for instance, orogenic evolution, the

rate and magnitude of TPW, plate tectonic reconstructions and the paleogeographical influence on paleoclimate, paleoenvironment and paleobiology.

8. Conclusions

In this study, we presented a global apparent polar wander path for the last 320 Ma calculated from simulated site-level paleomagnetic data, using an updated paleomagnetic database and relative plate motion model. Based on our new APWP, we conclude the following:

- A parametric re-sampling approach allows the straightforward incorporation of both spatial and temporal uncertainties in the paleomagnetic data, as well as uncertainty in the widely used E/I correction for inclination shallowing. Even though these uncertainties are taken into account in our approach, the 95% confidence regions of the site-level APWP are smaller than that of previously computed global APWPs because the much larger number of re-sampled VGPs per time window compared to the number of paleopoles in the conventional approach outweighs the larger dispersion of synthetic VGPs compared to paleopoles.
- The distributions of parametrically re-sampled VGPs that fall within a given age bin resemble the dispersion of VGPs expected for normal geomagnetic field behavior (that is, PSV) in the last few hundred Ma. This indicates that there are no major sources of noise that significantly enhance the dispersion beyond expected values for PSV and that would bias the global APWP.
- The first-order geometry of the new global APWP is similar to the most recent pole-based APWP of Torsvik et al. (2012), with an average angular difference of 2.8° between similar-aged reference poles. The average APW rate for South Africa is $0.38^\circ \pm 0.23^\circ$ (1σ), slightly lower than the $0.43^\circ \pm 0.22^\circ$ obtained by Torsvik et al. (2012). The similarity between the previous pole-based global APWP and our APWP computed from site-level data, using more stringent selection criteria, an updated database and global plate model, indicates that the global APWP is robust and reproducible.
- Peaks in APW rate may result from a temporal bias in paleomagnetic data. By correcting for the mean age of the re-sampled VGPs that underlie each reference pole, we observe that previously identified spikes in APW rate (for South Africa) disappear, while a new peak in APW rate is identified between 100-80 Ma.
- The calculation of the global APWP at a higher resolution using a time step of 5 Ma and a sliding window of 10 Ma results in a more irregular path with time intervals that show standstills that alternate with segments with relatively high APW rates. We find that the data coverage is certainly high enough to compute a reliable path at this resolution for some time intervals, but not for the entire 320-0 time period.
- Calculating APWPs from site-level data provides opportunities to significantly improve the temporal resolution and robustness of the global APWP by collecting large high-quality paleomagnetic datasets from stable plate interiors, particularly from rocks derived from age intervals and/or tectonic plates that are underrepresented in the current database. Finally, we emphasize that such datasets may also contribute to future re-assessments of previously observed systematic differences between similarly aged paleomagnetic data from different tectonic plates (e.g., the Pangea controversy), or provide a better-constrained paleomagnetic reference frame for time intervals of rapid Earth system change, such as climate crises and mass extinctions.

Data availability statement

No new paleomagnetic and marine magnetic anomaly data is used in this study. The paleomagnetic data compilation includes datasets from previously published peer-reviewed articles and builds on compilations by Torsvik et al. (2012) and Cromwell et al. (2018). The complete database can be found in Table S2. The global plate circuit presented in this study consists of previously published Euler rotation poles that are provided in Table S1. The Python codes used for the computation of the global APWP, its statistical parameters and the associated figures will be made publicly available on Github and archived on Zenodo upon acceptance of this manuscript.

6

APWP-online.org: a global reference database and open-source tools for calculating apparent polar wander paths and relative paleomagnetic displacements

This chapter has been submitted for publication in *Tektonika* as:

Vaes, B., van Hinsbergen, D. J. J., Paridaens, J. APWP-online.org: a global reference database and open-source tools for calculating apparent polar wander paths and relative paleomagnetic displacements.

Abstract

Paleomagnetism provides a quantitative tool for estimating paleogeographic displacements of rock units relative to the Earth's spin axis and is widely used to determine relative tectonic displacements (vertical-axis rotations and paleolatitudinal motions). These relative displacements are commonly determined by comparing a study-mean paleomagnetic pole with a reference pole provided by an apparent polar wander path (APWP), even though these poles are calculated by averaging paleomagnetic data from different hierarchical levels. This conventional approach was recently shown to strongly overestimate the resolution at which paleomagnetic displacements can be determined. This problem was recently overcome by comparing paleomagnetic poles computed at the same hierarchical level, whereby the uncertainty of the reference pole is weighed against the number of datapoints underlying the study-mean pole. To enable the application of this approach, a new global APWP was calculated for the last 320 Ma from (simulated) site-level paleomagnetic data. Applying this method requires a computationally more intensive procedure, however. Here, we therefore present the online, open-source environment APWP-online.org that provides user-friendly tools to determine relative paleomagnetic displacements and to compute APWPs from site-level paleomagnetic data. In addition, the website hosts the curated paleomagnetic database used to compute the most recent global APWP and includes an interface for adding new high-quality paleomagnetic data that may be used for future iterations of the global APWP. We illustrate how the tools can be used through two case studies: the vertical-axis rotation history of the Japanese Islands and the paleolatitudinal motion of the intra-oceanic Olyutorsky arc exposed on Kamchatka.

1. Introduction

Paleomagnetic data – obtained from measurements of the remanence magnetization recorded in rocks – provide a quantitative tool for studying the paleogeographic history and interpreting the relative and absolute motions of tectonic plates and smaller, fault-bounded terranes (e.g., Cox & Hart, 1986; Butler, 1992). One of the main tectonic applications of paleomagnetism is the identification and quantification of two types of relative displacements: vertical-axis rotations and paleolatitudinal motions. To quantify such displacements, paleomagnetists typically compare a study-mean paleomagnetic direction or pole from a studied geological record, e.g., a fault-bounded block – with a reference direction or pole that represents a nearby stable tectonic plate, often provided by an apparent polar wander path (APWP) (e.g., Demarest, 1983; Coe et al., 1985; Butler, 1992). Conventional APWPs, computed by averaging a collection of study-mean paleopoles whose mean age fall into a fixed time window, provide reference poles with an A_{95} cone of confidence that allow a straightforward comparison with a study-mean pole and its A_{95} , computed instead by averaging a collection ‘spot readings’ of the past geomagnetic field. Statistical differences between a study-mean pole and a reference pole (from an APWP) are routinely interpreted as evidence for relative tectonic motions. However, Rowley (2019) recently showed that more than half of the study-mean poles that were used to compute the widely used global APWP of Torsvik et al. (2012) are statistically distinct (or ‘discordant’) from the reference pole position to which they contributed. This shows that the conventional approach to determine paleomagnetic displacements cannot reliably demonstrate tectonically meaningful displacements (Rowley, 2019).

Chapter 2 showed that the underlying problem is that conventional APWPs have been computed from paleomagnetic data at a different hierarchical level than study-mean poles: the reference direction or pole is computed from site-means, whereas the study-level direction or pole is instead computed from a collection of spot readings (i.e., paleomagnetic sites). These authors demonstrated that an alternative approach computing APWPs on site-level paleomagnetic data, rather than pole-level data, offers a solution to this problem. They showed that when the uncertainty of the reference pole is weighted against the number of site-level datapoints in the study-mean pole, a statistical difference can be interpreted as geologically meaningful. In this approach, the reference pole position and its uncertainty are determined from a large number (>1000) of synthetic reference poles that are calculated from the same number of sites in the studied paleomagnetic dataset. The resolution at which a statistical difference, and thus a tectonic displacement, may be determined is thus directly controlled by the size of the studied dataset. In contrast to the conventional approach, the methodology developed in Chapter 2 also weights the spatial and temporal uncertainties in the underlying paleomagnetic data in the computation of the reference pole and its confidence region. Building on this study, Chapter 5 presented a global APWP (combining all paleomagnetic data from stable plate interiors whose relative motions are well-constrained, e.g., by ocean basin reconstructions (Besse & Courtillot, 2002; Torsvik et al., 2008, 2012) calculated from parametrically re-sampled site-level data. This provides a new reference frame that allows the determination of paleomagnetic displacements by comparing paleomagnetic data on the same hierarchical level. However, this new approach requires a bootstrapped approach to determine the reference pole and its uncertainty, which is computationally more complex than the conventional approach.

APWP-online.org

[Home](#)
[APWP Tool](#)
[RPD Tool](#)
[Reference database](#)
[About](#)

APWP-online

User-friendly tools to compute apparent polar wander paths (APWPs) from site-level paleomagnetic data and to determine relative paleomagnetic displacements.

You will also find the curated paleomagnetic database used to compute the most recent global APWP of Vaas et al. (2023). Do you have new high-quality paleomagnetic data to add to future iterations of the global APWP, let us know!



APWP TOOL

Compute a custom Apparent Polar Wander Paths based on site-level paleomagnetic data



RPD TOOL

Determine Relative Paleomagnetic Displacements to quantify vertical-axis rotations and paleolatitudinal motions through time



REFERENCE DATABASE

The reference database that underpins the global APWP for the last 320 Ma from Vaas et al. (2023).

APWP-ONLINE

[Home](#)
[APWP Tool](#)
[RPD Tool](#)
[Reference database](#)
[About](#)

CONTACT

info@apwp-online.org Department of Earth Sciences
 Utrecht University,
 Vening Meinesz Building A,
 Princetonlaan 8A,
 3584 CB Utrecht, Netherlands

SUPPORTED BY




© 2022 – 2023, version 0.3

Fig. 1. Overview of the homepage of APWP-online.org.

Here, we present the online and open-source environment APWP-online.org that provides a set of tools to compute relative paleomagnetic displacements and custom APWPs using the approaches presented Chapters 2 and 5. This web application also includes a portal providing access to the curated paleomagnetic database that was used to compute the global APWP of Chapter 5, together with an interface where paleomagnetists can request the addition of new high-quality paleomagnetic data, or revision of age constraints, that may be used for future updates of the global APWP. We illustrate how these two portals may contribute to solving tectonic problems by applying them to two case-studies: the timing and magnitude of the Neogene rotations of the Japanese islands and the paleolatitudinal evolution of the Late Cretaceous-Paleogene intra-oceanic Olyutorsky arc (Kamchatka).

2. Tools

2.1. APWP tool

The APWP tool allows users to compute an APWP based on site-level paleomagnetic data using the approach of Chapter 5. The APWP is calculated from virtual geomagnetic poles (VGPs) that are parametrically re-sampled from a custom-provided collection of paleopoles, rather than from those paleopoles itself. To compute the APWP, the user first

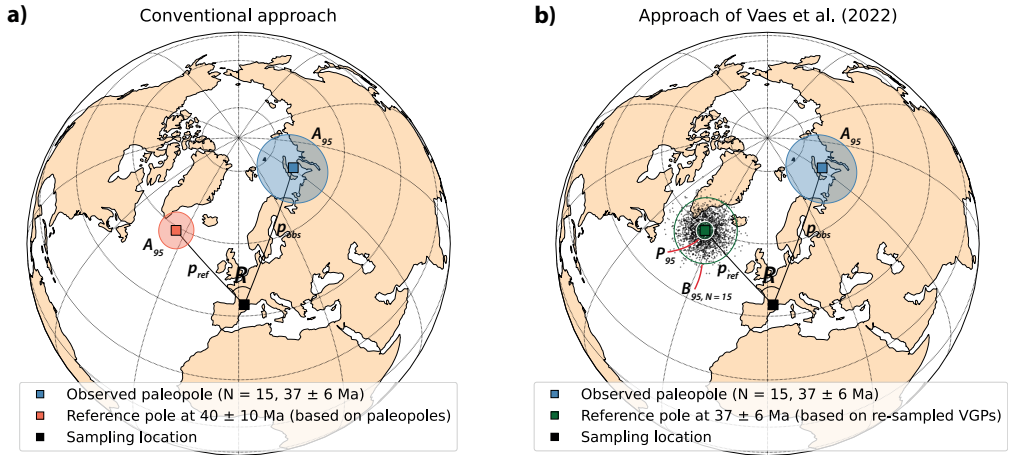


Fig. 2. Comparison between the conventional approach and the recently developed approach in Chapter 2 for the determination of relative tectonic displacements.

needs to specify the age range for the APWP, size of the time window and the time step at which the reference poles of the APWP are computed (Fig. 3). This tool can be used to construct an APWP for any plate or terrane regardless of the age of rocks from which the data are derived, as long as the input data are provided in the coordinate system of the same plate or terrane. The website includes a tool to rotate paleopoles into the coordinates of a different plate based on user-provided relative Euler rotation poles (Fig. 3). Prior to initializing the APWP tool, the user can also choose the number of iterations used for the computation of the path and the estimation of its 95% confidence region (the P_{95} of Chapter 5, see Fig. 2b), like the Relative Paleomagnetic Displacement tool described in the next section. It is important to note that a very large number (1000s) of iterations will significantly slow down the computation time.

For each iteration of the APWP computation, the re-sampled VGPs are assigned a random age within the age uncertainty range of the pole from which they are generated. Next, a sliding window is applied to the VGPs, computing an estimate of the reference pole for each time step by averaging the pseudo-VGPs that fall within the time window centered on that age. The final APWP is computed as the average of the simulated reference poles per time window, with the P_{95} confidence region defined as the circle that includes 95% of those simulated reference poles. For a more detailed explanation of the workflow, we refer the reader to section 3 of Chapter 5.

The tool also facilitates the straightforward reproduction of the global APWP presented in Chapter 5 and can be directly applied to the reference database that is available under the Reference database portal (see section 5). Moreover, it allows users to compute custom APWPs from a filtered set of paleopoles included in that database. For instance, one may calculate an APWP solely based on the data derived from a chosen plate, e.g., South America, using a different window size and time step as used in Chapter 5. Researchers may also apply this tool to evaluate the effect of a new paleomagnetic dataset on the global APWP.

APWP Tool

This tool allows you to compute an APWP based on site-level paleomagnetic data using the approach of Vaes et al. (2023).

Show more ▾

LOAD INPUT FILES 📄 data will be stored and processed locally on your own machine.

+

Add your dataset
.xlsx or .csv

Load in demo data

[or download the example input file](#)

NEJ
NEJ.csv (3.2 kB)
37 poles

This set is active

SWJ
SWJ.csv (3.2 kB)
37 poles

Use this set

CALCULATIONS 📄 calculations will done locally on your own machine.

Window length (Ma) Time step (Ma)

Minimum age (Ma) Maximum age (Ma)

Number of iterations

Calculate APWP

NEJ
NEJ.csv (3.2 kB)
37 poles

This set is active

CALCULATED APWP

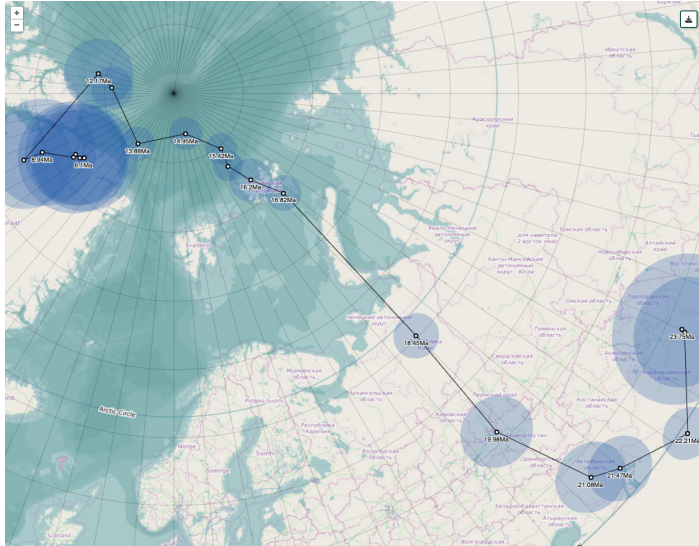


Fig. 3. Overview of the APWP tool.

2.2. Relative Paleomagnetic Displacement (RPD) tool

The second tool of APWP-online.org (Fig. 4) allows the determination of a relative paleomagnetic displacement (RPD) using the comparison metric that was introduced Chapter 2. Central to this approach is the comparison between an observed paleopole and a reference pole in which the number of paleomagnetic sites used to compute the paleopole is taken into consideration. The 95% confidence region of the reference pole (the B_{95}) is estimated as if it had been derived from the same number of sites as the observed paleopole (N_s) (see Fig. 2). To determine the reference and the B_{95} we use the parametric bootstrap approach described in Chapter 2. For each run the tool computes a single estimate for the position of the reference pole – a pseudopole – using two steps. First, VGPs are generated by parametric re-sampling of all paleopoles included in the reference database, whose age uncertainty range overlaps with that of the studied dataset. For each paleopole, VGPs are re-sampled from a Fisher (1953) distribution centered on the paleopole position and defined by the reported precision parameter K , whereby the number of VGPs corresponds to the number of sites used by the original authors to compute that pole. Next, a pseudopole is computed by averaging N_s randomly drawn VGPs whose age falls within the age uncertainty range of the studied dataset. A distribution of pseudopoles is then obtained after repeating this procedure hundreds to thousands of times (as specified by the user, see Fig. 4). In Chapter 2, we defined the B_{95} as the radius of the circle about the principal vector of the pseudopoles that includes 95% of those pseudopoles (Fig. 2). The size of the B_{95} is directly dependent on the N_s and becomes larger with decreasing N_s , such that the resolution of the statistics comparison is adjusted to the amount of information contained in the studied dataset. This way, the reference pole and the B_{95} simply show the uncertainty in the position of the reference pole, predicting where it could be located if it would have been calculated from the same number of VGPs as included in the studied dataset.

The reference data used to compute the relative paleomagnetic displacements can be chosen by the user (Fig. 4). To determine the displacements of a collection of paleopoles relative to a large tectonic plate (North America, South America, Eurasia, Iberia, Africa, India, Antarctica, Australia, Pacific), the reference pole position is computed from the database underlying the global APWP of Chapter 5. To this end, all re-sampled VGPs are rotated to the chosen reference plate using pre-calculated Euler rotation poles that are derived from the global plate circuit presented in Chapter 5. For each input paleopole, a default age range of 10 Ma around the mean age of the pole is used. This age range can be modified by the user (Fig. 4), e.g., to exactly match the age range of the observed paleopole. With age uncertainties of a few to ten million years, this is not likely to affect the result, but this can be evaluated for each individual case by the user.

The user may also upload a custom reference database to the RPD tool, allowing the determination of RPDs using reference poles computed from this database. This can be done by choosing the right uploaded file under ‘Choose reference’ (Fig. 4). It is important to note that the reference data should be provided using the template input file (see section 2.3), hence consisting of a collection of paleopoles whereby relevant parameters such as age, age uncertainty range, number of sites and the Fisher (1953) precision parameter K are provided. This allows the determination of the reference pole position and its B_{95} following the procedures described above. Alternatively, the user may also compute the RPDs relative to the geographic pole. The estimated vertical-axis rotation for each

observed paleopole then simply corresponds to the absolute paleomagnetic declination at the chosen reference location based on that paleopole (Figs. 5a, b). The relative paleolatitudinal displacement corresponds to the absolute difference between the observed paleolatitude and the present-day latitude of the reference location. Because the position of the geographic pole has no uncertainty, the uncertainty of these results is determined by the A_{95} of the observed pole.

We quantify the relative paleomagnetic displacements as relative rotation (R) and latitudinal displacement (L) based on the difference in pole position between an observed paleopole and reference pole, calculated using a spherical triangle (Fig. 2). The rotation R (following the nomenclature of, for instance, Beck (1980) and Demarest (1983)) and is quantified by the angle between the great-circle segments that connect the sampling location with both paleopoles, which is identical to the difference between the paleomagnetic declinations predicted by the poles at the sampling location. To determine whether the rotation is clockwise or counterclockwise needs to be inferred from these declination values, as the angle in rotation space does not contain this information (see Butler (1992) for more detail). The paleolatitudinal displacement (L) is then determined by the difference between the angular distances p_{ref} and p_{obs} (i.e., the paleomagnetic colatitude of both poles) of the two great-circle segments, where $L = p_{\text{ref}} - p_{\text{obs}}$. A positive displacement value thus indicates that the paleomagnetic latitude of the observed pole is larger than that of the reference pole. Please note that L has the opposite sign of the poleward transport (P) defined by Butler (1992), whereby a positive value indicates a northward motion toward the reference pole, corresponding instead to a lower paleolatitude of the observed pole than predicted by the reference pole. We found the resulting plots counterintuitive, and therefore plot a more northerly (southerly) paleolatitude than expected from the reference pole position above (below) the 0° reference line (Fig. 7), following e.g., Kent and Irving (2010, their Figure 8). To quantify the uncertainties on relative paleomagnetic displacements, we follow the square-root formulas developed by Demarest (1983) and defined by Butler (1992) for a pole-space approach (see equations A.66 and A.76 in the Appendix), whereby the 95% confidence region on the reference pole ($A_{95, \text{ref}}$) is replaced by the B_{95} .

2.3. Input and output

The input for the APWP and RPD tools should be provided through the template file that can be downloaded from the website ('Download the example input file'). This comma-separated values (CSV) file consists of a header with column names under which the relevant data and metadata should be added. Each entry that is included in the input file should contain the following parameters: the age and age uncertainty range of the sampled rocks, the longitude and latitude of the mean sampling location, the longitude and latitude of the paleopole, the number of paleomagnetic sites (N, i.e., the number of spot readings of the paleomagnetic field), the Fisher (1953) precision parameter (K) and the 95% cone of confidence about the pole (A_{95}). For the global APWP of Chapter 5, we only used sediment-derived paleopoles that were corrected for inclination shallowing using the elongation-inclination (E/I) correction of Tauxe and Kent (2004) and that satisfied the criteria proposed in Chapter 3. This avoided the variable bias posed by potential inclination shallowing and allows propagating the uncertainty associated with the E/I correction in the calculation of the APWP (following the approach of Pierce et

RPD Tool

The relative paleomagnetic displacement (RPD) tool allows the determination of displacements using the comparison metric that was introduced by Vaes et al. (2022).

Show more ▾

LOAD INPUT FILES data will be stored and processed locally on your own machine.

Add your dataset
.xlsx or .csv

Load in demo data

or download the example input file

NEJ
NEJ.csv (2.2 kB)
37 poles

This set is active

SWJ
SWJ.csv (3.2 kB)
37 poles

Use this set

CALCULATIONS calculations will done locally on your own machine.

input dataset

Use dataset

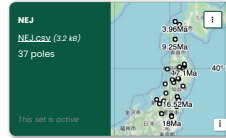
Number of iterations Time window (Ma)

Reference location

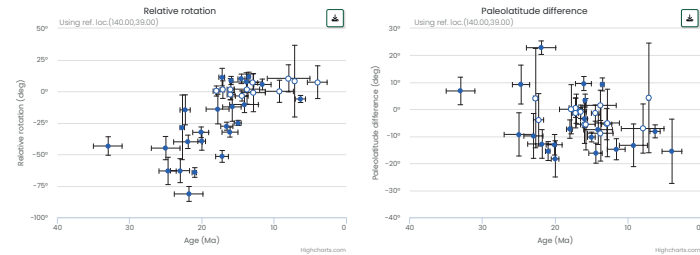
Set a custom single loc

Choose reference Reference plate

Calculate displacements



CALCULATED ROTATION AND DISPLACEMENT



APWP-ONLINE

Home
APWP Tool
RPD Tool
Reference database
About

CONTACT

info@apwp-online.org Department of Earth Sciences
Utrecht University
Vening Meinesz Building A,
Princetonlaan 8A,
3584 CB Utrecht, Netherlands

SUPPORTED BY



Fig. 4. Overview of the relative paleomagnetic displacement (RPD) tool.

al. (2022); see section 3 in Chapter 5 for more details). The input file thus includes an optional column for the uncertainty of the E/I correction. This source of uncertainty can be accounted for in the computation of a custom APWP by adding the mean difference between the shallowing-corrected paleolatitude estimate and the associated 95% confidence limits.

The output of the APWP tool consists of a plot of the APWP on a northern hemisphere map projection. The age and relevant parameters of each reference pole of the APWP is easily inspected by hovering the mouse over the path. The custom APWP may be visually compared to the global APWP of Chapter 5 – in the reference frame of a chosen plate – by adding a reference APWP to the map using the ‘Add reference APWP’ button. The output APWP may be directly downloaded from the web interface as a CSV file that contains the longitude and latitude values of the APWP, the center age of the window, the mean age and number of the re-sampled VGPs for each time window, as well as the P_{95} values and all other relevant statistical parameters. The custom APWP may be used directly in the RPD portal to determine the relative paleomagnetic displacements between the studied tectonic plate or terrane and a chosen reference plate (see examples in section 4).

For the computation of the RPDs in the RPD tool, the user may specify a few input parameters, similar to the APWP tool. The number of iterations and time window (default is 10 Ma) used to compute the reference pole position and its uncertainty (the B95) can be provided as direct input on-screen. Instead of using the sampling location of each entry in the input file, a reference location may instead be chosen by the user to compute the RPDs (Fig. 4). Note that specifying a reference location is required when using a custom APWP as input for this tool. As described in the previous section, the user may choose the reference against which the uploaded input data are compared. The output of the RPD tool consists of two figures on the web interface that show the relative vertical-axis rotations and paleolatitudinal displacement computed for each input paleopole, which can be downloaded as raster (PNG) or vector (SVG) image. As for the APWP tool, the output results may also be downloaded as a CSV file.

3. Reference database portal

The final portal of APWP-Online.org hosts the reference database that underpins the global APWP for the last 320 Ma from Chapter 5. Through this web interface (Fig. 8), the most recent version of the global APWP – in the coordinate frame of all major tectonic plates - may be accessed and downloaded, as well as the paleomagnetic database and the global plate circuit, which underlie the computation of the APWP. This portal provides a platform where future updates of the global APWP will be made available. We refer the reader to Chapter 5 for a detailed description of the methodology and plate circuit. Any future updates of the APWP will be described in a change log on the website and indicated with a version number (see Fig. 8), and any major future updates will be accompanied by a peer-reviewed publication.

We intend to update the paleomagnetic database that underlies the computation of the global APWP on an annual basis. The database is intended as a community effort, and a steering committee of specialists will be maintained that will meet on an annual basis to evaluate new entries (see APWP-online.org for the latest composition of the committee). Moreover, the database will be coupled to the MagIC database (Jarboe et al., 2012).

We encourage researchers to submit new datasets that may contribute to the

improvement of the database. First, we welcome any new, high-quality paleomagnetic data obtained from stable plate interiors – after publication in a peer-reviewed journal – that may be included in the database. New data will be reviewed and against the reliability criteria described in Chapter 5. For sedimentary data, these criteria require that the collection of paleomagnetic directions is corrected for potential inclination shallowing (see e.g., Paleomagnetism.org (Koymans et al., 2016; 2020). Inclusion of sediment-based data will be evaluated using the quality criteria proposed in Chapter 3.

Second, we also welcome new age data that provides better constraints on the rock and/or magnetization age of the paleomagnetic data that is included in the database. Any suggestions for updating the age of specific paleopoles are highly appreciated and may be submitted through the query form. We note that many of the age uncertainty ranges quoted in the current database correspond to available age constraints at the time of the original publication of the paleomagnetic data. Therefore, useful age data may also be provided by peer-reviewed articles that were already published before the database of Chapter 5 was compiled. Finally, we welcome any corrections to mistakes in our database, as well as new insights or doubts related to the reliability of certain paleomagnetic datasets.

4. Application to case studies

We illustrate the functionalities of the two main tools of the APWP-online.org application by applying them to two different case studies: the opening of the Japan Sea and the paleolatitudinal motion of the intra-oceanic Olyutorsky arc (Figs. 5-7). We revisit the paleomagnetic data analyses performed in Chapter 1 that was used to test their plate-kinematic reconstruction of the northwest Pacific region.

In Chapter 1, we reconstructed the motions of tectonic blocks relative to major plates (e.g., Pacific, North America, or Eurasia) based on marine magnetic and structural geological data, and by placing their reconstruction in a paleomagnetic reference frame (of Torsvik et al., 2012), they predicted the declination and paleolatitude for these tectonic blocks through time, at 10 Ma intervals. They then compared the predicted declinations or paleolatitudes against paleomagnetic data from these tectonic blocks and adjusted the reconstruction where required by paleomagnetic data and permitted by structural data (see also Li et al., 2017 for procedures). Rather than comparing such predictions against observed data, we show here how the APWP and RPD tools may be used to directly quantify the magnitude, timing, and uncertainty of vertical-axis rotations and paleolatitudinal motions relative to a chosen reference.

The opening of the Sea of Japan since ~25 Ma is well-known to have led to opposite rotations of the northeastern and southwestern parts of Japan (e.g., Otofujii et al., 1985; Martin, 2011), and an extensive paleomagnetic database has been collected over the years (see Chapter 1). Using the RPD tool, we may plot the individual study-mean poles compiled in Chapter 1 relative to the north geographic pole (i.e., only the declination and the associated uncertainty are shown) (Fig. 5a, b). Next, we may plot these data relative to the global APWP of Chapter 5 in the coordinates of Eurasia, because these are the values that are relevant for kinematic restoration of the opening of the Japan Sea (Fig. 5c, d). The difference between Figs. 5a-b and 5c-d are minor as Eurasia did not rotate much relative to the north pole in the last 25 Ma, but the confidence regions are slightly larger in Fig. 5c-d as the uncertainty in the position of the reference pole contributes to the overall uncertainty. While the general amount and timing of the coherent rotation of northeast

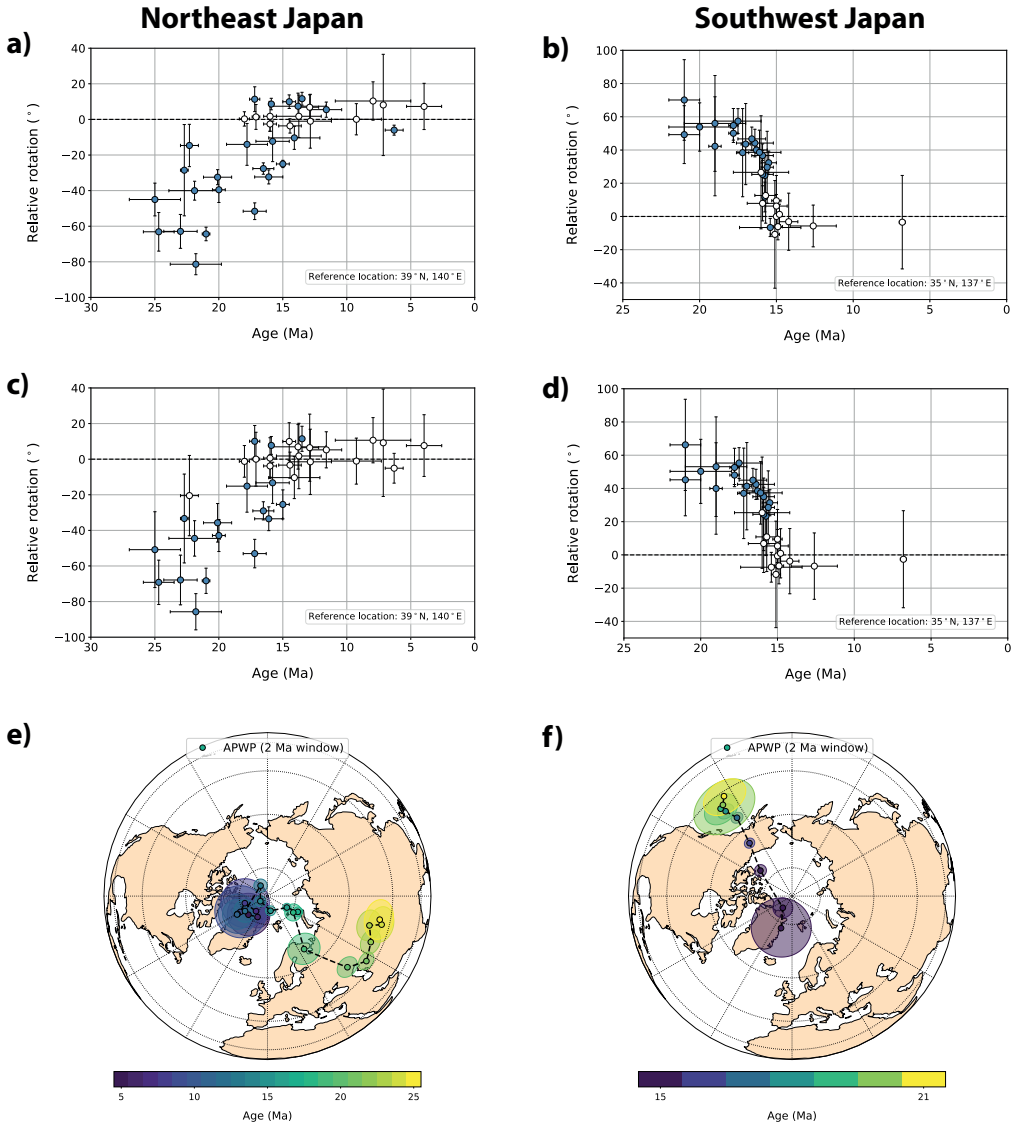
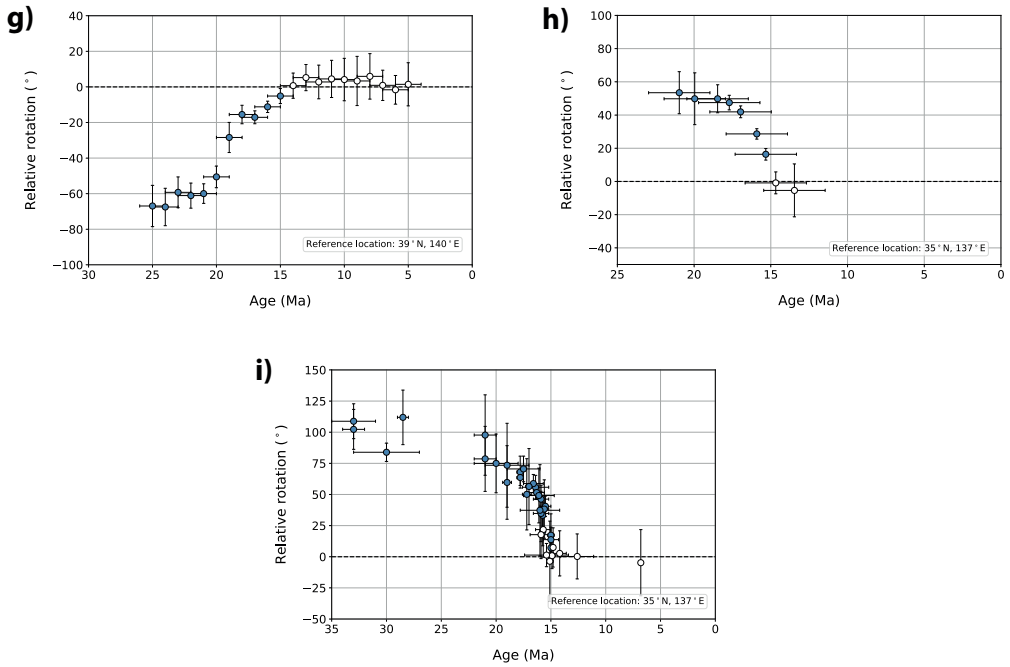


Fig. 5. Application of the APWP and RPD tools to the northeast and southwest Japan blocks. Vertical-axis rotations of each dataset relative to the geographic pole are shown in (a) and (b). A positive value indicates a clockwise rotation since that time. Rotations relative to Eurasia – using the global APWP presented in Chapter 5 – are shown in (c) and (d). Custom APWPs computed with the APWP tool, using a time window of 2 Ma and a temporal resolution of 1 Ma, are shown on orthographic plots in (e) and (f). Vertical-axis rotations relative to Eurasia are computed using these APWPs in (g) and (h). Finally, the rotation through time of southwest Japan relative to northeast Japan is shown in (i).



Japan is easily estimated from these plots, the dispersion of the study-mean poles is large, owing to the limited number (<10) of paleomagnetic directions underpinning many of these study-mean poles (see Chapters 2 and 4) and, potentially, to minor differential rotations of smaller blocks (Yamaji et al., 1999).

To obtain a better estimate of the magnitude and timing of the counterclockwise rotation, we constructed an APWP for the Japan blocks using the APWP tool: for the period of 25 to 5 Ma for northeast Japan and of 21 to 13 Ma for southwest Japan. The underlying database is identical as the one used for the plots of Figs. 5a-d. The high data density allows the computation of the APWP using a time step of only 1 Ma and a sliding window of 2 Ma. This is a much higher temporal resolution than typically used in the construction of (global) APWPs, which often have a resolution of 10 Ma (e.g., Besse & Courtillot, 2002; Torsvik et al., 2008, 2012; Chapter 5). For the northeast Japan block, The APWP shows a phase of rapid polar wander between ~20 and 15 Ma followed by a stillstand of the paleomagnetic pole position after ~14 Ma (Fig. 5e). Likewise, southwest Japan reveals a rapid phase of polar wander between ~21-13 Ma, but data density before and after is insufficient for a meaningful APWP calculation (Fig. 5f). We assess whether these polar wander phases indeed correspond to a relative rotation by using the custom APWPs as input in the RPD tool and compute the vertical-axis rotation through time relative to Eurasia, which tightly constrains the timing and amount of the vertical-axis rotation phases (Fig. 5g, h). For illustration, we also compared the compilation of study-mean paleopoles from southwest Japan to the database of northeast Japan, by adding the latter as a ‘custom reference database’ in the RPD tool (Fig. 5i). The results reveal a relative rotation of ~100° during the opening of the Sea of Japan until ~15 Ma. Finally,

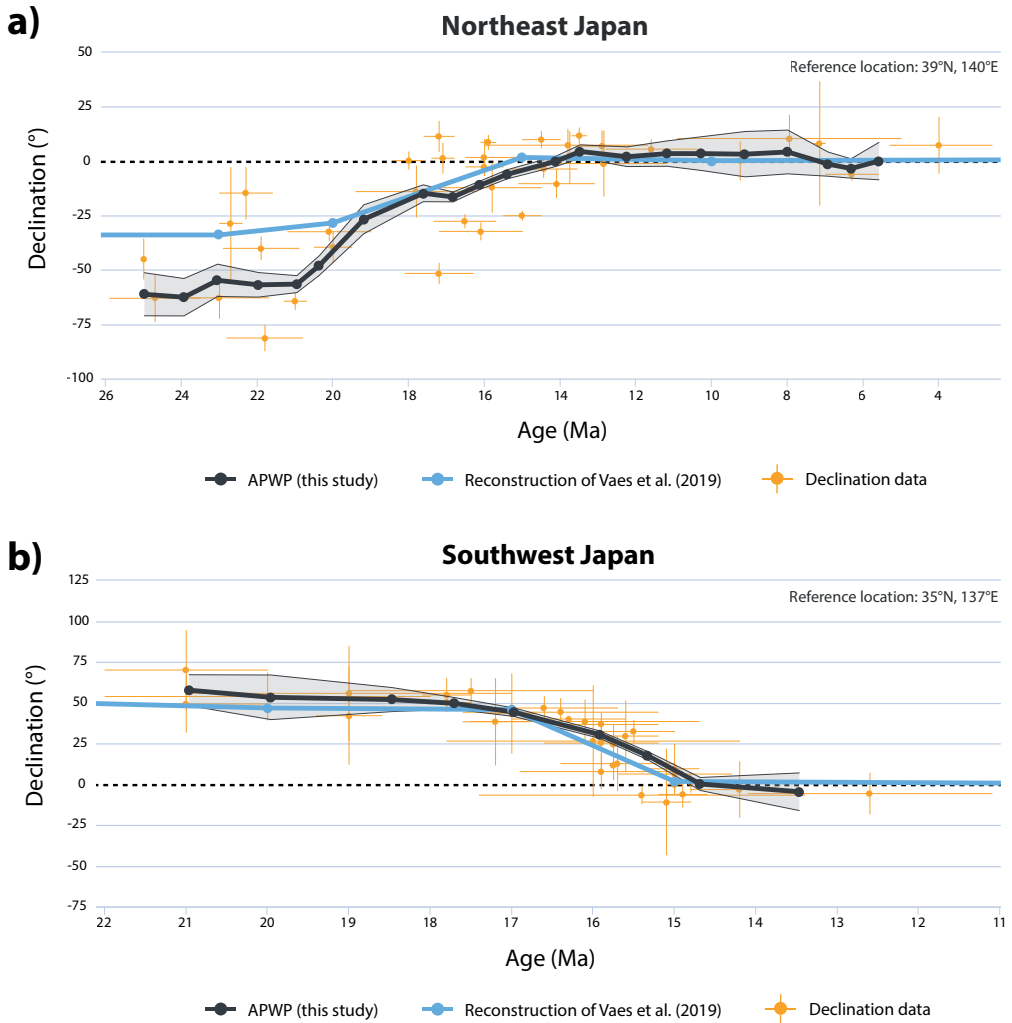


Fig. 6. Comparison of the declination curves predicted for northeast Japan (a) and southwest Japan (b) for a chosen reference location using the APWPs computed in this study (Figs. 5e, f) and using the plate-kinematic reconstruction of Chapter 1.

we uploaded the new APWPs for northeast and southwest Japan in the Geography Portal of Paleomagnetism.org 2.0 (Koymans et al., 2020) to show how the declination values predicted by these APWPs compare to the declination curves predicted from the plate reconstruction developed in Chapter 1 (Fig. 6). The main difference between the curves obtained in Chapter 1 and those presented here is that the latter are purely based on paleomagnetic data and are computed at a much finer temporal resolution, providing tight paleomagnetic constraints on the rotation history of the Japanese islands during the Miocene opening of the Japan Sea.

We illustrate the application of the paleolatitudinal displacement (L) tool using a case

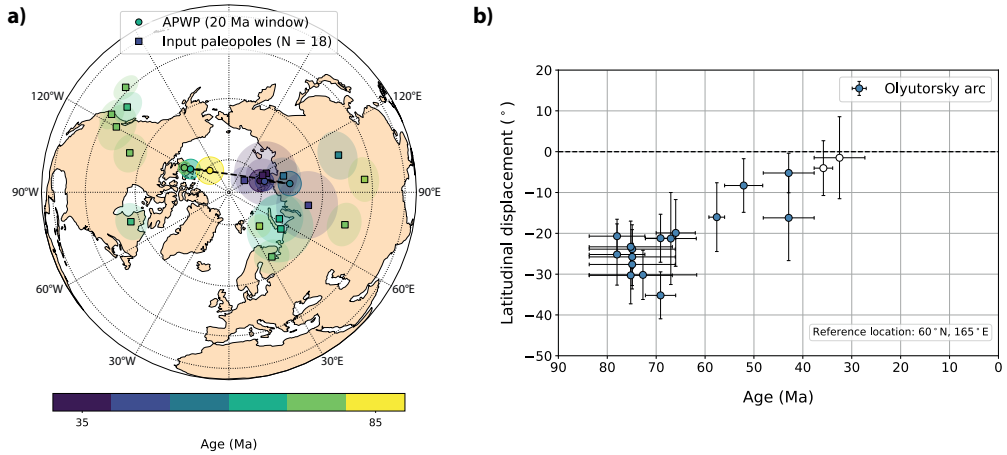


Fig. 7. (a) Custom APWP computed for the data compilation of the Olyutorsky arc. (b) Latitudinal displacement against age, relative to the North American plate.

study of the Olyutorsky arc (Fig. 7). The Olyutorsky arc is an extensive intra-oceanic arc complex that was emplaced onto continental crust of Kamchatka in the Eocene (~55–45 Ma, see review in Chapter 1). Paleomagnetic data reveal that the arc was located far south of its present-day location (e.g., Kovalenko, 1996; Levashova et al., 1997, 1998, Konstantinovskaya, 2001; Shapiro & Soloviev, 2009; Domeier et al., 2017, Chapter 1). In Fig. 7a, we show the relative paleolatitudinal displacement relative to the stable North American plate (of which the Kamchatka peninsula is currently part). In this case, computing an APWP for Olyutorsky is not meaningful, because sediment-derived datasets that have not been corrected for inclination shallowing and datasets have been strongly rotated relative to each other (see strongly scattered poles in Fig. 7b). Nonetheless, the data reveal a systematic decrease in the paleolatitude relative to North America of ~20–30° between the onset of arc magmatism around ~85–80 Ma and the obduction age of ~50 Ma (Fig. 7a), which is more informative for plate kinematic reconstruction purposes than the absolute paleolatitudes of the study-mean poles and the global APWP in North American coordinates that was used in Chapter 1.

5. Availability, data storage and license

The APWP-online.org application (<https://www.apwp-online.org>) can be freely accessed with the latest versions of commonly used internet browsers, such as Google Chrome, Mozilla Firefox, and Safari. The source codes of the web applications and the Python scripts that are used to perform the calculations will be made publicly available on Github and archived on Zenodo upon submission of the manuscript. All processing of paleomagnetic data and calculations are performed locally on the machine of the user. No imported data or results are stored externally on a server or sent over the internet, ensuring the integrity of the data and user. The input data and results are instead stored locally within the local storage of the browser, and thus allow the user to continue using the webtools offline. The local storage may also be downloaded by pressing the ‘Download session’ button, enabling users to continue working with the input data and results at any

APWP-online.org

[Home](#)
[APWP Tool](#)
[BPD Tool](#)
[Reference database](#)
[About](#)

Reference Database

This portal hosts the reference database that underpins the global APWP for the last 320 Ma from Voes et al. (2023).

Below, the most recent version of the global APWP – in the coordinate frame of all major tectonic plates – can be accessed and downloaded, as well as the paleomagnetic database and the global plate circuit, which underlie the computation of the APWP. This portal provides a platform where future updates of the global APWP will be made available.

Version history Global APWP

Name	Publication date	Authors	DOI	Download model
gAPWP23	16 January 2023 (Preprint)	Bram Voes et al.	doi: 10.1123/x55368	Download zip (352 kb)

Contribute to the next global APWP

We encourage researchers to submit new new, high-quality paleomagnetic data obtained from stable plate interiors – after publication in a peer-reviewed journal – that may be included in the database. We also welcome new age data that provides better constraints on the rock and/or magnetization age of the paleomagnetic data that is included in the database.

Any suggestions for updating the age of specific paleopoles are highly appreciated and may be submitted through this query form.

Your name

Affiliated institute

Email address

Description of the data

Reference/link to publication

Add your dataset
.xlsx or .csv

APWP-ONLINE

[Home](#)

[APWP Tool](#)

[BPD Tool](#)

[Reference database](#)

[About](#)

CONTACT

info@apwp-online.org

Department of Earth Sciences
Utrecht University,
Vening Meinesz Building A,
Princetonlaan 8A,
3584 CB Utrecht, Netherlands

SUPPORTED BY

© 2022 – 2023, version 0.3

Fig. 8. Overview of the ‘Reference database’ portal.

later moment by re-uploading this file. In addition, the local storage file may be shared among colleagues or added as a supplementary file to a paper to facilitate evaluation and reproducibility of the analyses by peers. APWP-online.org is an open-source web application licensed under the GNU General Public License v3.0.

6. Conclusions

APWP-online.org is an online, open-source application that enables paleomagnetists to compute custom apparent polar wander paths and relative paleomagnetic displacements (RPD) using a statistical approach that was recently developed in Chapters 2 and 5. The application consists of three different portals: the APWP portal, the RPD portal and the Reference Database portal. The APWP portal enables researchers to compute a custom APWP from site-level paleomagnetic from a collection of paleopoles, using a chosen temporal resolution. The resulting APWP can then be compared to a reference APWP using the RPD tool to determine the relative paleomagnetic displacements through time. The RPD tools allow the identification and quantification of vertical-axis rotations and paleolatitudinal displacements relative to a chosen APWP or pole, in which temporal and spatial uncertainties are propagated and in which the uncertainty of the reference pole is weighted against the number of paleomagnetic sites used to compute the studied paleomagnetic direction or paleopole. Finally, the Global Database portal provides an up-to-date version of the global APWP for the last 320 Ma in the coordinate frame of all major plates, as well as the paleomagnetic database and plate circuit that underlie its computation. We invite paleomagnetists to submit new, high-quality paleomagnetic data, or recommend modification of the existing database (e.g., the revision of age constraints) through the query form included in this portal, such that the global APWP can be regularly updated in the future. An international steering committee will update the database and the global APWP behind APWP-online.org on an annual basis. We foresee that the accessible and easy-to-use tools of APWP-online.org will enable specialist users to apply state-of-the-art methods for computing apparent polar wander paths and tectonic displacements, which may contribute to solving detailed tectonic or paleogeographic problems.

Data availability statement

No new paleomagnetic data were used in this study. The paleomagnetic datasets used to illustrate the applications of the tools were previously compiled in Chapter 1 and the original sources are cited in the text of the current paper. We refer the reader to Chapter 1 – and to Table S1 – for more details.

7

The wandering pole: improved paleomagnetic constraints on true polar wander during the last 320 Ma

Abstract

On geological timescales, the rotation of the Earth's crust and mantle relative to its spin axis, named true polar wander (TPW), is driven by the redistribution of mantle density heterogeneities within the mantle. Kinematically constrained estimates of the magnitude and rate of TPW provide a window into the dynamics of the Earth's interior through geological time, as these are largely controlled by the density distribution and rheology of the mantle. Here, we provide new estimates of the magnitude and rate of TPW during the last 320 Ma by comparing existing mantle reference frames and a new paleomagnetic reference frame with improved uncertainty quantification. We obtain an average TPW rate for the last 320 Ma of $0.38^{\circ} \pm 0.15^{\circ}/\text{Ma}$ (1σ), with a maximum rate of up to $\sim 0.8^{\circ}$. Our results show that TPW rotations predominantly occurred about two equatorial axes that are approximately orthogonal, with one axis close to the present-day TPW rotation axis at $\sim 10^{\circ}\text{E}$, whose location is inferred to be controlled by large basal mantle structures. Our findings suggests that, for time intervals including much of the late Cretaceous and Cenozoic, the distribution and flux of subduction dominate Earth's moment of inertia, such that the TPW axis is located at a large distance from these lower mantle structures, causing them to rotate relatively to the spin axis. We show that the improved paleomagnetic reference frame, and the quantification of age bias therein, provides a key step forward in quantifying TPW, and we identify the development of purely kinematic mantle reference frames with uncertainty quantification as the next desired step forward in using TPW as kinematic constraint on mantle dynamics.

1. Introduction

Determining the rate of convection of the Earth's mantle is key in deciphering the drivers of plate tectonics and volcanism but is notoriously difficult to quantify from kinematic observations alone. True polar wander (TPW) provides an avenue to kinematically constrain mantle convective processes. TPW is the rotation of the entire solid Earth relative to the spin axis, such that the axis of maximum nonhydrostatic moment of inertia remains closely aligned with the spin axis. On geological timescales, the reorientation of the Earth's mantle and crust relative to the spin axis is driven by the redistribution of density anomalies within the Earth's mantle (e.g., Goldreich & Toomre, 1969; Gordon, 1987; Evans, 2003), such as sinking subducted slabs or rising mantle plumes. The magnitude and rate at which TPW occurs is primarily determined by the spatial distribution of excess masses and mass deficits and is ultimately controlled by the viscosity of the mantle (e.g., Sabadini & Yuen, 1989; Spada et al., 1992; Steinberger & Torsvik, 2010; Fu et al., 2022). Long-term (≥ 10 Ma) TPW is often kinematically quantified through the comparison of paleomagnetic reference frames, derived from apparent polar wander paths (APWPs) that track the motion of the spin axis relative to a tectonic plate, and mantle reference frames that record plate tectonic motions relative to the ambient mantle (e.g., Morgan, 1981; Harrison & Lindh, 1982a; Livermore et al., 1984; Andrews, 1985; Courtillot & Besse, 1987; Besse & Courtillot, 1991, 2002, Doubrovine et al., 2012). The difference between these models thus provides a direct estimate of the motion between the spin axis and the 'mean' mantle, i.e., TPW. However, the robustness of these estimates relies on the accuracy and precision of both the paleomagnetic and mantle reference frames, which are based on very different underlying philosophies, datasets, and error propagation schemes.

Previously published TPW curves were generally obtained using conventional, pole-based apparent polar wander paths, in which spatial and temporal uncertainties in the underlying data were not incorporated (e.g., Besse & Courtillot, 2002; Torsvik et al., 2012; Doubrovine et al., 2012; see Chapters 2 and 5 for details). The novel global APWP presented in Chapter 5 is the first in which these sources of uncertainty were propagated. One of the key steps forward of that global APWP is that estimates of APW rates may now be corrected for temporal bias, by computing the 'effective' age of the reference pole positions from the age distribution of the (re-sampled) site-level paleomagnetic data used as input for those poles. In Chapter 5, we showed that observed peaks in APW rate that have previously been interpreted as phases of relatively rapid TPW, such a spike between 110 and 100 Ma (Steinberger & Torsvik, 2008; Torsvik et al., 2012; Doubrovine et al., 2012), disappeared after correcting for the 'effective' age difference between successive reference pole of the APWP.

In this chapter, we derive new quantitative estimates of the magnitude and rate of true polar wander by comparing the new global APWP with previously published mantle reference frames. We compute true polar wander paths that show the motion of the time-averaged paleomagnetic pole relative to the deep mantle using three different mantle frames based on hotspots that go back to ~ 120 Ma, and, for the first time one back to 320 Ma using the recent mantle reference frame of Müller et al. (2022) that is based on a set of tectonic 'rules'. We re-assess whether phases of rapid TPW (or TPW 'events') inferred from fast polar shifts, such as the 'Jurassic monster polar shift' (e.g., Kent & Irving, 2010; Kent et al., 2015; Yi et al., 2019; Muttoni & Kent, 2019) and a proposed, short-lived TPW event at ~ 84 Ma (Gordon, 1983; Sager & Koppers, 2000; Mitchell et al., 2021), may truly represent

rapid TPW or rather may represent noise (e.g., Cottrell & Tarduno, 2000; Kulakov et al., 2021; Gao et al., 2021) induced by age uncertainty or the use of paleopoles in determining polar wander. We discuss the implications of our results for mantle dynamics and the role of deep-mantle structure in determining the axis of TPW. Finally, we present an outlook for future identification and quantification of true polar wander as kinematic constraint on the dynamics of the Earth's interior.

2. Methods

We construct true polar wander paths (TPWPs) using four different mantle reference frames: the Indo-Atlantic fixed hotspot reference frame of Müller et al. (1993), the Indo-Atlantic moving hotspot reference frame of Torsvik et al. (2008), the global moving hotspot reference frame of Doubrovine et al. (2012), and the recently published mantle reference frame of Müller et al. (2022) that was constructed using an optimization approach based on a set of 'tectonic rules'. We computed each TPWP as an apparent polar wander path in a coordinate frame in which the mantle is kept fixed, following the approach of many previous workers (e.g., Livermore et al., 1984; Andrews, 1985; Courtillot & Besse, 1987; Doubrovine et al., 2012). This path then describes the motion of the time-averaged paleomagnetic pole relative to the ambient mantle, in the same way as a conventional APWP describes the motion of the pole relative to a fixed tectonic plate. We computed the TPWPs using the paleomagnetic database, global plate circuit and approach presented in Chapter 5. To enable the computation of a TPWP, we added the Euler rotation poles to the plate circuit which describe the motion of the South African plate relative to the mantle, as provided by the original authors for each mantle reference frame. In the computation of the TPWP, we rotated each parametrically re-sampled VGP to the coordinate frame of the mantle, using the Euler rotation pole for the corresponding tectonic plate relative to the mantle at the age which was assigned to that VGP. This allows the propagation of temporal uncertainties, and its effect on the time-dependent position of the plate relative to the mantle, into the confidence regions of the TPWP, as described in detail in Chapter 5. We quantify the 95% confidence regions of the TPWP by the P_{95} cone of confidence, which includes 95% of the pseudo-poles computed for each time window, following the approach outlined in Chapter 5.

It is important to note that in our computation of the TPWP, the uncertainties associated with the mantle reference frames are not (yet) incorporated. The uncertainties of the rotation poles for Africa relative to the mantle were not quantified for the reference frames of Müller et al. (1993) and Müller et al. (2022). 95% confidence regions for the two moving hotspot reference frames were provided by Doubrovine et al. (2012) and Torsvik et al. (2008), although the latter did not tabulate the uncertainty values but only showed them in a figure. In addition, we note that the plate circuit and time scale used to determine the mantle reference frames differs between all four models and is also different from the updated plate circuit as well as the time scale (of Gradstein et al., 2020) used for the construction of the global APWP in Chapter 5. Because the four reference frames are based on different input datasets, underlying assumptions, and methodologies, they each provide a different perspective on the motion of South Africa relative to the deep mantle. We note that a detailed description of each of the mantle frames is beyond the scope of this chapter, and we refer to the original papers for more detail.

The three hotspot-based mantle frames used here determine the 'absolute' motion of

tectonic plates relative to the deep mantle using hotspot tracks: linear chains of intraplate volcanoes that show a clear progression of eruption ages (e.g., Wilson, 1963; Morgan, 1971; 1981). The geometry and age progression of these hotspot tracks have been widely used to reconstruct lithospheric motions relative to mantle upwellings (or ‘plumes’, Morgan, 1971), which are either assumed to be stationary in a ‘mean mantle’ frame (i.e., a fixed hotspot reference frame, e.g., Morgan, 1981; Duncan & Clague, 1985; Müller et al., 1993) or corrected for slow relative motions inferred to result from mantle convection (i.e., a moving hotspot reference frame; e.g., O’Neill et al., 2005; Torsvik et al., 2008; Doubrovine et al., 2012). A moving hotspot reference frame essentially corresponds to a mean mantle reference frame, in which convective motions are globally averaged such that there is no net horizontal flow (Steinberger & O’Connell, 1998; Doubrovine et al., 2012). This class of mantle reference frames, however, does not provide independent kinematic constraints on mantle dynamics because a mantle convection model, constrained by a global model of plate tectonic motions and mantle density heterogeneities, is used as input, after which the reference frame is iteratively constructed to fit hotspot tracks (e.g., Torsvik et al., 2008; Doubrovine et al., 2008). The disadvantage of hotspot reference frames is that the availability of linear hotspot tracks only allows the robust determination of plate motions relative to hotspots since the Late Cretaceous (~120 Ma).

The recent mantle reference frame of Müller et al. (2022) was constructed in an entirely different way, using an iterative approach in which the absolute plate motion of the reference plate Africa is obtained by optimizing a global plate model using four different criteria. These criteria include the minimization of the net lithospheric rotation rate, the minimization of global trench migration velocities, a global continental median plate velocity below 6.0 cm/a, and the minimization of the spatio-temporal misfit between observed and model-predicted hotspot tracks (only for the last 80 Ma). Using the global plate model for the last billion years of Merdith et al. (2021) as input for their model, Müller et al. (2022) constructed an ‘optimized’ mantle reference frame since 1000 Ma. This therefore allows to construct a TPWP from 320 Ma to present, using the global APWP for the last 320 Ma presented in chapter 5.

3. Results

We first computed four true polar wander paths for the last 120 Ma using the four different mantle reference frames (Fig. 1). The paths show the motion of the paleomagnetic pole relative to a fixed mantle, plotted on the northern hemisphere. The time-averaged paleomagnetic pole position, which is assumed to coincide with the spin axis, was calculated using a 10 Ma time interval and a 20 Ma sliding window. The TPWPs thus visualize the motion of the spin axis in a fixed mantle frame, providing direct estimates of the magnitude, rate, and direction of TPW. We report the positions of the spin axis using the effective age of each paleomagnetic reference pole, derived from averages of the re-sampled site-level paleomagnetic data that fall within each time window (see Chapter 5). The 95% confidence regions of these poles were computed using 1000 iterations and reflect the uncertainties in the paleomagnetic data that underly the global APWP. The size of the P_{95} confidence circles is nearly identical for each TPWP, and ranges from 0.7° to 2.3° for the 0 and 100 Ma pole positions (effective ages of 1.3 and 94.6 Ma), respectively.

The four TPWPs show a similar first-order geometry for the last 120 Ma (Fig. 1). For this time span, the poles plot along three segments that are intervened by sharp cusps.

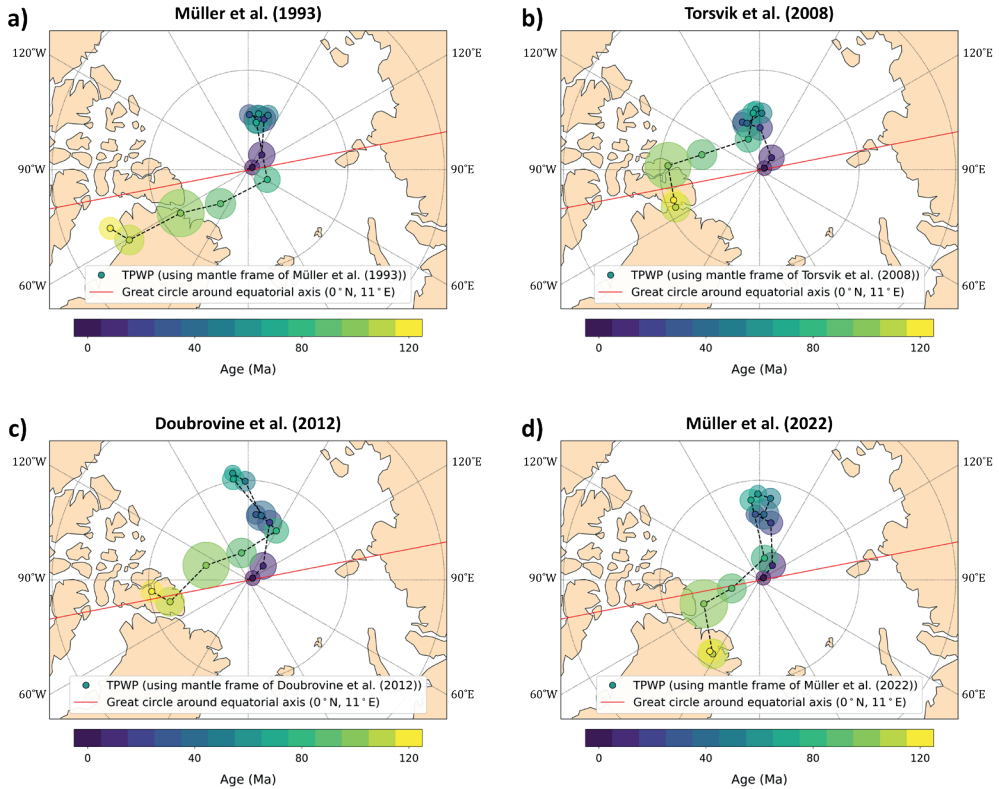


Fig. 1. True polar wander paths for the last 120 Ma, computed using four different mantle reference frames, with a 20 Ma time window. The colored circles represent the 95% confidence regions (P_{95}). The color of the poles indicates the center of the age window. The red line shows the great circle around an equatorial rotation axis at 11°E , corresponding to the longitude of the preferred TPW axis of Torsvik et al. (2012, 2014).

All four paths show a back-and-forth motion of the spin axis during the last 80 Ma, roughly along the 180° meridian, although this is somewhat less pronounced in the TPWP constructed using the Torsvik et al. (2008) model. In the paths computed using the Müller et al. (1993) and Müller et al. (2022) reference frames, the position of the pole at ~ 80 Ma is close to the geographic pole (in a fixed mantle frame). The net angle of TPW of $>10^\circ$ at ~ 50 Ma is notably larger for the Doubrovine et al. (2012) model than the $\sim 6^\circ$ for Müller et al. (1993) and Torsvik et al. (2008) models. All four TPWPs show a nearly linear segment between 80 and 100 Ma that is sub-parallel to the great circle around an equatorial axis at 11°E . This segment extends to the pole computed at 110 Ma for the TPWPs computed using the Müller et al. (1993) and Doubrovine et al. (2012) frames. The geometry of the Torsvik et al. (2008) and Müller et al. (2022) paths are nearly identical for the 100–120 Ma segments, showing a $\sim 100^\circ$ angle between the 80–100 Ma segments and the 100–120 Ma segment that runs parallel to the $\sim 15^\circ\text{E}$ meridian.

The TPWP computed for the last 320 Ma (Fig. 2a), using the frame of Müller et al. (2022), shows two smooth segments between ~ 140 –200 and ~ 200 –250 Ma that are nearly

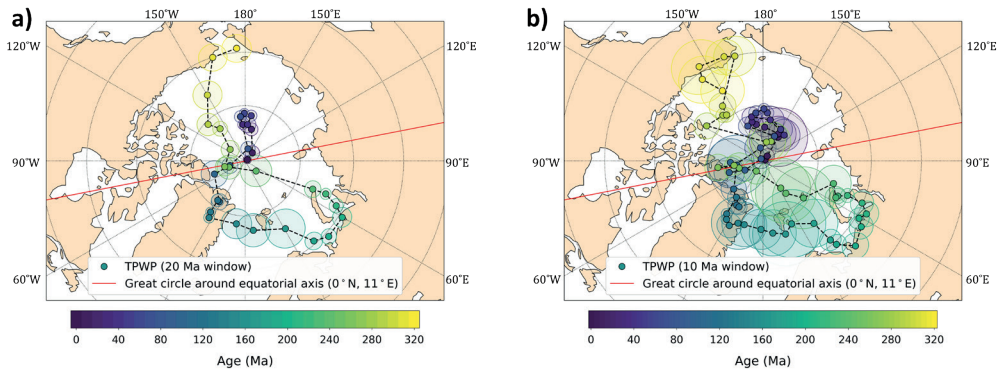


Fig. 2. True polar wander paths for the last 320 Ma, computed using the ‘tectonic rules’-based mantle reference frame of Müller et al. (2022). The path is calculated with at a 5 (a) and 10 Ma (b) resolution, using a 10 and 20 Ma time window, respectively. See Fig. 1 for more details.

parallel. During both these time spans, the pole position moves $\sim 24^\circ$. These paths would correspond to a rotation around an equatorial axis located at $\sim 10\text{--}15^\circ\text{W}$. The oldest part of the TPWP, from 260 to 320 Ma runs roughly parallel to the 180° meridian, similar to the 0–80 Ma segments. Notably, the position of the rotation axis returns to the geographic pole at ~ 250 Ma. The largest net TPW angle of approximately 21° is observed at $\sim 190\text{--}200$ Ma and $\sim 310\text{--}320$ Ma. The path computed at a 5 Ma resolution shows a similar overall trend, but is more irregular and has much larger confidence regions (because the amount of data per interval is lower, and only poles are used with age uncertainties <10 Ma; see also Chapter 5). The main difference with the 10 Ma-resolution TPWP is that there are two back-and-forth motions of the pole instead of one, between 80 and 10 Ma. However, whether these motions are truly representative of TPW is questionable considering the large and often overlapping confidence regions.

We calculated the rate of true polar wander through time by dividing the great-circle distance between successive pole positions by the effective age difference of those poles (Fig. 3). We observe very similar TPW rates for all four paths. For most of the last 120 Ma, the rates are between $0.1^\circ/\text{Ma}$ and $0.4^\circ/\text{Ma}$. All models show a peak in TPW rate between ~ 82 and 95 Ma, with rates of $0.6\text{--}0.8^\circ/\text{Ma}$. The confidence intervals of all curves indicate that the TPW rate is higher than $0.4^\circ/\text{Ma}$ at the 95% confidence level. The TPW rates computed for the last 320 Ma using the Müller et al. (2022) model are below $0.7^\circ/\text{Ma}$ for this entire time span, with an average of $0.38^\circ \pm 0.15^\circ/\text{Ma}$ (1σ). However, much higher rates are obtained from the TPWP computed at a 5 Ma resolution, showing eight peaks with a $>1.0^\circ/\text{Ma}$ TPW rate between 230 and 320 Ma. It should be noted, however, that the confidence regions are notably large, such that these spikes are not statistically significant.

4. Discussion

4.1. True polar wander during the last 320 Ma

We have quantified the motion of the time-averaged paleomagnetic pole relative to the fixed mantle using the new global APWP presented in Chapter 5. If these motions correspond to the movement of the Earth’s spin axis relative to the mantle, they quantify the magnitude, rate, and direction of TPW. The similarities between the first-order

geometry of the four TPWPs for the last 120 Ma indicates that the observed trends in polar motion are reproducible, even though these paths were constructed using mantle reference frames based on different datasets and approaches. The back-and-forth polar motion during the last 80 Ma seems to be a robust feature in these TPWPs (Fig. 1) and was previously observed by Doubrovine et al. (2012) in a comparison of their moving hotspot frame and the global APWP of Torsvik et al. (2012). Intriguingly, the direction of polar motion is nearly orthogonal to the great circle about an equatorial axis at 11°E (Fig. 1), which is the axis of TPW rotation that would be expected if the Earth's moment of inertia is mainly controlled by the basal mantle structures referred to as large low shear-wave velocity provinces (LLSVPs; Steinberger & Torsvik, 2008; Torsvik et al., 2012, 2014) and that is close to the present-day TPW axis (e.g., Pavoni, 2008). Our TPWPs do not show any polar motion parallel to this great circle for the last 40 Ma as observed by Doubrovine et al. (2012), not even in the TPWP constructed using their mantle reference frame (Fig. 1c). The absence of TPW rotation about this axis for the last 80 Ma is consistent with the findings of Torsvik et al. (2014), who modelled no significant TPW rotations around 0°N/11°E for the last 100 Ma.

However, we observe polar motion between ~82 and 95 Ma (or even back to 120 Ma, see Figs. 1a, c) along the great circle associated with the 0°N/11°E axis in all TPWPs for the last 120 Ma. The timing of this phase of polar wander is slightly different compared to a similar TPW rotation obtained by Doubrovine et al. (2012) and Torsvik et al. (2014), who identified TPW rotations about an axis at ~0°N/11°E at 120-100 Ma and 110-100 Ma, respectively. The TPWP based on the fixed hotspot frame of Müller et al. (1993) shows the largest rotation of ~15° about this axis, between ~82 and 120 Ma, although we note that the fixed hotspot model prior to 80 Ma is considered much less reliable (e.g., Torsvik et al., 2008). The previously identified phase of relative fast TPW (~0.8°/Ma) at 110-100 Ma (Steinberger & Torsvik, 2008; Torsvik et al., 2012, 2014) is, however, absent in our TPWPs (Fig. 3a, c). We showed in chapter 5 that a spike in APW between 110 and 100 Ma in the global APWP of Torsvik et al. (2012) was likely the result of temporal bias, and we therefore interpret this inferred 110-100 Ma TPW event as a result of this artifact in the paleomagnetic reference frame used to constrain it.

The TPWP computed for the last 320 Ma using our new global APWP placed in the reference frame of Müller et al. (2022) shows that the motion of the spin axis relative to the mantle before 120 Ma has two main directions: one parallel to the ~10-15°E meridian and one roughly parallel to the 0-180° meridian (Fig. 2a). Remarkably, the timing and magnitude of true polar wander along the first direction are very similar to the TPW rotations determined by Torsvik et al. (2012, 2014) based on paleomagnetic data alone, which built upon earlier work by Steinberger & Torsvik (2008). Our new TPWP shows a polar motion of 24° away from the geographic pole between 250 and 200 Ma, and back parallel to the same great circle and with similar magnitude between ~190 and 140 Ma (Fig. 2). The inferred rotation axes for these phases of TPW would lie approximately at longitude 10-15°W, close to the estimated axes by Steinberger & Torsvik (2008), Torsvik et al. (2012) and Mitchell et al. (2012). These motions of the spin axis relative to the mantle would correspond to a coherent counterclockwise rotation of the solid earth relative to the spin axis between 250 and 200 Ma, followed by a clockwise rotation between 190 and 140 Ma, consistent with the findings of Torsvik et al. (2014). The net TPW angle of ~21° at ~200 Ma is statistically indistinguishable from the 22° estimated by Torsvik et al. (2014).

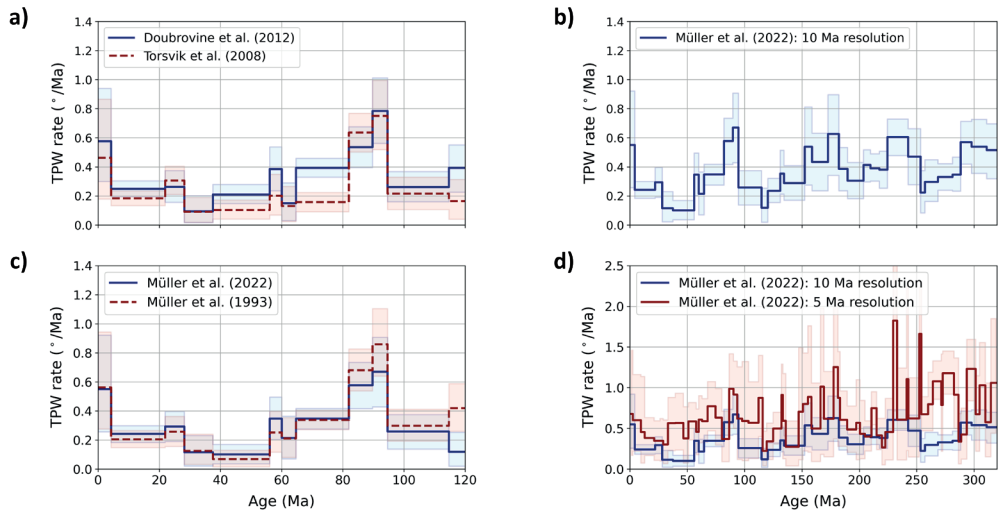


Fig. 3. True polar wander rates derived from the four mantle reference frames shown in Figs. 1 and 2. Estimated rates for the last 120 Ma are compared in (a) and (c). 95% confidence regions were empirically determined by computing the TPW rate from the great-circle distance and effective age of for each of the 1000 iterations and represent the range that includes 95% of the obtained values. TPW rates for the last 320 Ma are shown in (b) and (d), for the paths shown in Fig. 2. Note the different scale on the y axis in (d).

Our results confirm previous inferences by Torsvik et al. (2012, 2014) that cumulative TPW for the last 250 Ma is close to zero. We find, however, a deviation of the spin axis from the geographic pole (fixed to the mantle) of $\sim 20^\circ$ for the Late Carboniferous (~ 320 – 310 Ma). Using the mantle reference frame of Müller et al. (2022), the observed motion of the pole parallel to the 0 – 180° meridian and towards the geographic pole indicates a TPW-induced $\sim 20^\circ$ northward motion of Pangea between 320 and 260 Ma, corresponding to a northward total motion of all continents that was previously interpreted as purely caused by plate motion relative to the spin axis (Steinberger & Torsvik, 2008; Torsvik et al., 2012).

For the last 120 Ma, all TPWPs show a peak in TPW rate for the ~ 82 – 95 Ma time period, with a rate of ~ 0.6 – $0.8^\circ/\text{Ma}$ (Fig. 3a, c). Intriguingly, this peak coincides with the peak in APW rate of ~ 0.8 – $1.0^\circ/\text{Ma}$ observed for the global APWP in South African coordinates (chapter 5). This suggests that the spike in APW rate may be largely the result of relatively rapid TPW. It is probably not entirely the result of rapid TPW, since the timing of this peak also coincides with a recently demonstrated acceleration of Africa relative to Eurasia (Gürer et al., 2022; see discussion in Chapter 5). A phase of rapid TPW has previously been proposed for this time interval. Sager and Koppers (2000) proposed fast TPW (3 – $10^\circ/\text{Ma}$) at around 84 Ma based on data paleomagnetic poles from Pacific seamounts, although these results are not without controversy (Cottrell & Tarduno, 2000, 2003). A recent study by Mitchell et al. (2021) argued for a phase of rapid, oscillatory TPW ($\sim 3^\circ/\text{Ma}$) between ~ 86 and 78 Ma, based on high-resolution paleomagnetic records from two partly overlapping stratigraphic sections in northern Italy. Their TPW rates are much higher than obtained in this study, however. This may be explained by the use of a

20 Ma time window for the construction of the global APWP that underlies the TPWPs presented here, causing it to smooth or obscure potential short-term (<10 Ma) and/or small-amplitude phases of polar wander (e.g., Muttoni et al., 2005; Mitchell et al., 2021).

Phases of rapid TPW are frequently proposed based on rapid shifts in paleomagnetic pole positions that are often derived from rocks of a single tectonic plate. The existence of episodic, and possibly oscillatory, phases of rapid TPW are actively investigated by the paleomagnetic community. Whether such fast polar shifts, such as the Jurassic monster polar shift (e.g., Kent & Irving, 2010; Kent et al., 2015; Yi et al., 2019; Muttoni & Kent, 2019), truly represent rapid TPW is not always straightforwardly determined, and it may often be difficult to distinguish signal from noise (e.g., Cottrell & Tarduno, 2000; Evans, 2003; Kulakov et al., 2021; Gao et al., 2021). Our results do not provide any robust evidence for rapid ($>1.0^\circ/\text{Ma}$) TPW during the last 320 Ma. The peaks in TPW rate of more than $1.0^\circ/\text{Ma}$ observed for the 5 Ma-resolution TPWP (Fig. 3d) are not statistically significant, and we conservatively interpret these as noise rather than a true 'signal'. The use of TPWPs to establish whether short (<5 Ma) phases of fast TPW have occurred since the Late Paleozoic requires an increase in the resolution of the paleomagnetic reference frame, and the quantification of the uncertainty of the mantle reference frames. Before these become available, such rapid changes in pole position may instead be identified by collecting well-dated, paleomagnetic datasets from sedimentary sequences with a high sampling resolution, which provide high-resolution records of shifts in the paleomagnetic declination and inclination (e.g., Li et al., 2020; Mitchell et al., 2021; Chapter 3). By obtaining such records from multiple plates, the reproducibility of these events may be tested, to confirm whether a rapid polar shift may indeed represent TPW.

4.2. Linking true polar wander and mantle dynamics

The rate of TPW provides first-order kinematic constraints on the rate mantle convection, particularly on the velocity at which density anomalies, such as sinking lithospheric slabs, move through the Earth's mantle. Fu et al. (2022) presented a compilation of paleomagnetically estimated TPW rates since the late Mesoproterozoic (~1100 Ma), proposing a direct link between the secular change of the TPW rate and the thermal structure and nature of convection in the mantle. Fast TPW ($>1^\circ/\text{Ma}$) has often been inferred for pre-Pangean TPW, suggesting a different geodynamic regime that may correlate with the supercontinent cycle (e.g., Evans, 2003; Mitchell et al., 2014; Fu et al., 2022). For instance, Jing et al. (2022) recently proposed a very large ($\sim 50^\circ$) wholesale rotation of the solid earth relative to the spin axis in only ~10 Ma, between ca. 450-440 Ma. Testing pre-Mesozoic TPW hypotheses is not straightforward, as plate motion-induced polar wander may be difficult to distinguish from TPW and thus obscure past TPW signals (Evans, 2003; Torsvik et al., 2014). Rapid polar shifts during the Ediacaran have also been attributed to TPW (e.g., Mitchell et al., 2011; Robert et al., 2017, 2018), but may also alternatively be explained by unusual geomagnetic field behavior (Abrajevitch & Van der Voo, 2010; Bono et al., 2019)

Reproducing observed TPW by numerical modeling has also proven difficult, as this requires detailed knowledge on the structure of the mantle, such as the volumes and distribution of subducted lithospheric slabs (see Steinberger & Torsvik, 2010). Paleomagnetism-based estimates of TPW rates are frequently compared to TPW speed limits inferred from geodynamic modelling. However, these predictions vary substantially:

for instance, Tsai and Stevenson (2007) provide a TPW speed limit of $2.5^\circ/\text{Ma}$, whereas Greff-Lefftz and Besse (2014) argue that TPW may occur at rates of up to $10^\circ/\text{Ma}$ for larger mass reorganizations. These estimates heavily rely on the choice of rheological parameters, which are poorly constrained, particularly for deep geological time (Steinberger & Torsvik, 2010; Mitchell et al., 2021). Moreover, whether such geodynamical models used to determine the magnitude and rate of TPW have slab sinking rates that are consistent with independent kinematic constraints on the slab sinking velocity versus depth, such as those obtained from seismic tomographic images of subducted slabs (van der Meer et al., 2010, 2018), it not always clear (Steinberger & Torsvik, 2010).

Recent modelling studies show that TPW rotations are likely stabilized by the contribution to the moment of inertia by the two antipodal LLSVPs, with important contributions from subducted slabs, whose relative contribution to the moment of inertia strongly change with depth (e.g., Steinberger & Torsvik, 2010; Steinberger et al., 2017). Observed TPW rotations about an axis of minimum moment of inertia that is close to the combined center of mass of the LLSVPs suggests that TPW is mainly controlled by these structures (Torsvik et al., 2012; 2014). TPW rotations along an axis nearly orthogonal to this $0^\circ\text{N}/11^\circ\text{E}$ axis instead indicates that the reorientation of the solid earth is controlled by other contributions to the moment of inertia tensor, e.g., resulting from large density anomalies caused by subducting slabs at relatively high latitudes $\sim 90^\circ$ from this alternative axis.

Identifying the role of subduction as driver of TPW on Earth is, however, complicated by the continuously changing flux and distribution of subduction through geological time. First, the position of density anomalies associated with lithospheric slabs relative to the mantle change through time due to trench advance, retreat or by the passive dragging through the mantle of a subducted slab along with the subducting lithospheric plate (i.e., ‘slab dragging’, Spakman et al., 2018; examples of slabs that were horizontally displaced over >1000 km in latitude during subduction include Tonga (van de Lagemaat et al., 2018) and Burma (Parsons et al., 2021)). Second, the latitude distribution of subducted or subducting slabs are time-dependent, with high-latitude subduction contributing much stronger to the Earth’s moment of inertia tensor (Steinberger & Torsvik, 2010). Third, the contribution of a particular subducting slab to the moment of inertia tensor is directly influenced by the age of the subducting lithosphere, the length of slab, and the rate of subduction (Steinberger and Torsvik, 2010), with faster subduction expected to lead to an increased slab volume in the upper mantle due to increased buckling (e.g., Sigloch & Mihalynuk, 2013). We expect that tectonic events, such as changes in the global flux and distribution of subduction, e.g., associated with (global) plate tectonic reorganizations, or global increases of plate production rate (van der Meer et al., 2014) should have an effect on the moment of inertia, and thus may trigger phases of TPW (e.g., Doubrovine et al., 2012).

Steinberger and Torsvik (2010) proposed that the observed motion of the spin axis relative to the mantle could be explained by changes in the distribution and amount of subduction in the Pacific realm. On the other hand, Steinberger et al. (2017) more recently noted that establishing direct causal links between TPW and potential geodynamics triggers is far from straightforward, particularly because amounts of subduction are increasingly poorly constrained back in geological time. A recent study by Lin et al. (2022) highlighted that using plate-kinematic reconstructions of the Pacific realm that

incorporated intra-oceanic subduction zones (e.g., Chapter 1; Boschman et al., 2021) may provide very different models of the past geoid and mantle structure than those in which these subduction zones were not included. They demonstrated that geodynamic models that include intra-oceanic subduction provided a much better match with the present-day geoid, dynamic topography and mantle structure. We note that the largest changes in the TPWPs for the last 120 Ma, at ~50 Ma and ~82 Ma, coincide with the ~50 Ma and ~85 Ma plate reorganizations (Chapter 1; van de Lagemaat et al., 2023). However, interpreting the direction and rate of polar motion in the context of the many changes that occurred during these reorganization ‘events’ is too complex for an intuitive analysis and requires a quantitative analysis that is beyond the scope of this study.

5. Conclusions and outlook

In this chapter, we presented new quantitative estimates of true polar wander (TPW) using the new global APWP for the last 320 Ma presented in Chapter 5. We have constructed, for the first time, a TPW path (TPWP) for the last 320 Ma, without any assumptions on the axis of TPW rotation or the stability and influence of basal mantle structures on the moment of inertia tensor. Our novel TPWP yields an average TPW rate for the last 320 Ma of $0.38 \pm 0.15^\circ/\text{Ma}$ (1σ), with a maximum rate of up to $\sim 0.8^\circ/\text{Ma}$, suggesting that no fast TPW ‘events’ of >5 Ma occurred during this time span. Our results show that TPW rotations predominantly occurred about two equatorial axes that are approximately orthogonal. We observe TPW rotations during the ~80-100, 140-190 and 200-250 Ma time intervals along an axis that is located close to a previously inferred rotation axis that is dominated by the contribution of the two LLSVPs. In contrast, the new TPWP indicates that the spin axis rotated relative to the mantle about an axis that is approximately located at ~90-100°E during the last ~80 Ma and during the 110-140 and 260-320 Ma time intervals. This implies that other contributions to the moment of inertia, such as those exerted by subducting lithospheric slabs, controlled to nature of TPW, causing the entire solid Earth, including the LLSVPs, to rotate relatively to the spin axis at an axis approximately orthogonal to the present-day center of mass of the LLSVPs. Since all the mantle reference frames tested in this study show polar motion around such an axis for the last 80 Ma, this observation seems robust, unless there are major problems with these mantle reference frames, which we consider unlikely.

We emphasize that to establish whether the observed TPW is statistically significant, and to assess the robustness of TPW rates and its implications for mantle dynamics, it is key to improve the quantification and incorporation uncertainties in future mantle reference frames. To derive kinematically-based estimates of TPW, a mantle reference frame is needed that integrates observational data and is independent from dynamic interpretations and modelling, i.e., it does not rely on a mantle convection model with a subjectively chosen rheology and boundary conditions. Hotspot tracks and subducted slabs may provide such data, but alternative avenues may be provided by the minimization or ‘optimization’ of kinematic parameters (see Müller et al., 2022), e.g., minimizing the global trench-parallel component of subduction (slab dragging). Although already more than 20 years old, we echo Besse and Courtillot (2002) in that there is much more exciting work to be done to identify possible links between episodes of TPW, plate tectonic reorganizations and mantle dynamics. We foresee that with the increase in temporal resolution of paleomagnetic reference frames, for which Chapter 5 provides the

quantitative basis, and with the development of purely kinematic mantle reference frames that include uncertainties, the recent advances in our understanding of the subducting history and structure will allow key strides forward in our understanding of the properties of the Earth's mantle through TPW analysis. Moreover, this will gain better understanding of the relationship between TPW and Earth's climate, life, and mantle dynamics through geological time.

Supplementary information to chapters

Supplementary information to each chapter of this thesis can be accessed through a Google Drive folder with the following link:

<https://drive.google.com/drive/folders/1p4S-mqb2hGc3-kO5wxY6kCzN6OAbFZJs?usp=sharing>

This folder contains a set of subfolders for every chapter that has supplementary texts, figures, and/or data files (Chapters 1-5). For chapters that have been published as peer-reviewed articles, this corresponds to the published version of the files that was provided with the publication.

References

- Abdul Aziz, H., van Dam, J., Hilgen, F. J., & Krijgsman, W. (2004). Astronomical forcing in Upper Miocene continental sequences: implications for the Geomagnetic Polarity Time Scale. *Earth and Planetary Science Letters*, 222(1), 243-258.
- Abels, H. A., Aziz, H. A., Ventra, D., & Hilgen, F. J. (2009). Orbital Climate Forcing in Mudflat to Marginal Lacustrine Deposits in the Miocene Teruel Basin (Northeast Spain). *Journal of Sedimentary Research*, 79(11), 831-847. doi:10.2110/jsr.2009.081
- Abels, H. A., Hilgen, F. J., Krijgsman, W., Kruk, R. W., Raffi, I., Turco, E., & Zachariasse, W. J. (2005). Long-period orbital control on middle Miocene global cooling: Integrated stratigraphy and astronomical tuning of the Blue Clay Formation on Malta. *Paleoceanography*, 20(4).
- Abrajevitch, A., & van der Voo, R. (2010). Incompatible Ediacaran paleomagnetic directions suggest an equatorial geomagnetic dipole hypothesis. *Earth and Planetary Science Letters*, 293(1-2), 164-170.
- Agnini, C., Fornaciari, E., Giusberti, L., Grandesso, P., Lanci, L., Luciani, V., ... & Stefani, C., 2011. Integrated biomagnetostratigraphy of the Alano section (NE Italy): A proposal for defining the middle-late Eocene boundary. *Geol. Soc. Am. Bull.*, 123(5-6), 841-872.
- Ahn, H.-S., Kidane, T., Otofujii, Y.-i., Yamamoto, Y., Ishikawa, N., and Yoshimura, Y. (2021). High-resolution paleomagnetic results of Ethiopian trap series from Lima Limo section: implications for the Oligocene geomagnetic field behaviour and timing of volcanism. *Geophysical Journal International*, 225(1), 311-328.
- Akinin, V.V., Miller, E.L., 2011. Evolution of calc-alkaline magmas of the Okhotsk-Chukotka volcanic belt. *Petrology* 19, 237-277.
- Alexeiev, D.V., Gaedicke, C., Tsukanov, N.V., Freitag, R., 2006. Collision of the Kronotskiy arc at the NE Eurasia margin and structural evolution of the Kamchatka–Aleutian junction. *International Journal of Earth Sciences* 95, 977-993.
- Ali, J. R., Ward, D. J., King, C., & Abrajevitch, A., 2003. First Paleogene sedimentary rock paleomagnetic pole from stable western Eurasia and tectonic implications. *Geophys. J. Int.*, 154(2), 463-470.
- Alvey, A. D. (2009). Using crustal thickness and continental lithosphere thinning factors form gravity inversion to refine plate reconstruction models for the Arctic & North Atlantic (Doctoral dissertation, University of Liverpool).
- Amaru, M., 2007. Global travel time tomography with 3-D reference models. Utrecht University.
- Ando, H., 2003. Stratigraphic correlation of Upper Cretaceous to Paleocene forearc basin sediments in Northeast Japan: cyclic sedimentation and basin evolution. *Journal of Asian Earth Sciences* 21, 921-935.
- Andrews, J. A. (1985). True polar wander: an analysis of Cenozoic and Mesozoic paleomagnetic poles. *Journal of Geophysical Research: Solid Earth*, 90(B9), 7737-7750.
- Anson, G. L., & Kodama, K. P., 1987. Compaction-induced inclination shallowing of the post-depositional remanent magnetization in a synthetic sediment. *Geophys J. Int.*, 88(3), 673-692.
- Arculus, R.J., Ishizuka, O., Bogus, K.A., Gurnis, M., Hickey-Vargas, R., Aljadhali, M.H., Bandini-Maeder, A.N., Barth, A.P., Brandl, P.A., Drab, L., do Monte Guerra, R., Hamada, M., Jiang, F., Kanayama, K., Kender, S., Kusano, Y., Li, H., Loudin, L.C., Maffione, M., Marsaglia, K.M., McCarthy, A., Meffre, S., Morris, A., Neuhaus, M., Savov, I.P., Sena, C., Tepley Iii, F.J., van der Land, C., Yagodinski, G.M., Zhang, Z., 2015. A record of spontaneous subduction initiation in the Izu–Bonin–Mariana arc. *Nature Geoscience* 8, 728-733.
- Argus, D. F., Gordon, R. G., & DeMets, C. (2011). Geologically current motion of 56 plates relative to the no-net-rotation reference frame. *Geochemistry, Geophysics, Geosystems*, 12(11).
- Arkula, C., Lom, N., Wakabayashi, J., Rea-Downing, G., Qayyum, A., Dekkers, M. J., ... and van Hinsbergen, D. J. (2023). The forearc ophiolites of California formed during trench-parallel spreading: Kinematic reconstruction of the western USA Cordillera since the Jurassic. *Earth-Science Reviews*, 237, 104275.
- Asefaw, H., Tauxe, L., Koppers, A. A. P., & Staudigel, H. (2021). Four-Dimensional Paleomagnetic

- Dataset: Plio-Pleistocene Paleodirection and Paleointensity Results From the Erebus Volcanic Province, Antarctica. *Journal of Geophysical Research: Solid Earth*, 126(2), 1–22. <https://doi.org/10.1029/2020JB020834>
- Audin, L., Quidelleur, X., Coulié, E., Courtillot, V., Gilder, S., Manighetti, I., . . . Kidane, T. (2004). Paleomagnetism and K-Ar and $^{40}\text{Ar}/^{39}\text{Ar}$ ages in the Ali Sabieh area (Republic of Djibouti and Ethiopia): constraints on the mechanism of Aden ridge propagation into southeastern Afar during the last 10 Myr. *Geophysical Journal International*, 158(1), 327–345. doi:10.1111/j.1365-246X.2004.02286.x
- Avdeiko, G., Savelyev, D., Palueva, A., Popruzhenko, S., 2007. Evolution of the Kurile-Kamchatkan volcanic arcs and dynamics of the Kamchatka-Aleutian Junction. *Volcanism and Subduction: The Kamchatka Region*, 37–55.
- Baba, A.K., Matsuda, T., Itaya, T., Wada, Y., Hori, N., Yokoyama, M., Eto, N., Kamei, R., Zaman, H., Kidane, T., 2007. New age constraints on counter-clockwise rotation of NE Japan. *Geophysical Journal International* 171, 1325–1341.
- Bakhteev, M., Ben'yamovskii, V., Bragin NYu, V.D., Morozov, O., Sineĭnikova, V., Tikhomirova, S., Shatser, A., 1994. New data on Mesozoic-Cenozoic stratigraphy of the Eastern Kamchatka (Valaginsky Range). *Stratigr Geol Correlation* 2, 555–562.
- Bakhteev, M., Morozov, O., Tikhomirova, S., 1997. Structure of the Eastern Kamchatka Ophiolite-free Collisional Suture--Grechishkin Thrust. *Geotectonics* 31, 236–246.
- Baranov, B., Seliverstov, N., Murav'ev, A., Muzurov, E., 1991. The Komandorsky Basin as a product of spreading behind a transform plate boundary. *Tectonophysics* 199, 237–269.
- Baranov, B., Wong, H.K., Dozorova, K., Karp, B., Lüdmann, T., Karnaukh, V., 2002. Opening geometry of the Kurile Basin (Okhotsk Sea) as inferred from structural data. *Island Arc* 11, 206–219.
- Barnes, D., 1992. Sedimentology, phenocryst chemistry, and age-Miocene "Blue Tuff": Sites 794 and 796, Japan Sea, Proc. ODP Scientific Results, pp. 115–130.
- Batanova, V., Lyaskovskaya, Z., Savelieva, G., Sobolev, A., 2014. Peridotites from the Kamchatsky Mys: evidence of oceanic mantle melting near a hotspot. *Russian Geology and Geophysics* 55, 1395–1403.
- Bazhenov, M. L., Levashova, N. M., & Meert, J. G. (2016). How well do Precambrian paleomagnetic data agree with the Phanerozoic apparent polar wander path? A Baltica case study. *Precambrian Research*, 285, 80–90.
- Bazhenov, M., Burtman, V., Krezhovskikh, O., Shapiro, M., 1992. Paleomagnetism of Paleogene rocks of the Central—East Kamchatka and Komandorsky Islands: tectonic implications. *Tectonophysics* 201, 157–173.
- Bazhenov, M.L., Burtman, V.S., 1994. Upper Cretaceous paleomagnetic data from Shikotan Island, Kuril Arc: implications for plate kinematics. *Earth and Planetary Science Letters* 122, 19–28.
- Bazhenov, M.L., Zharov, A.E., Levashova, N.M., Kodama, K., Bragin, N.Y., Fedorov, P.I., Bragina, L.G., Lyapunov, S.M., 2001. Paleomagnetism of a Late Cretaceous island arc complex from South Sakhalin, East Asia: Convergent boundaries far away from the Asian continental margin? *Journal of Geophysical Research: Solid Earth* 106, 19193–19205.
- Beck Jr, M. E. (1980). Paleomagnetic record of plate-margin tectonic processes along the western edge of North America. *Journal of Geophysical Research: Solid Earth*, 85(B12), 7115–7131.
- Beck, M. E. (1976). Discordant paleomagnetic pole positions as evidence of regional shear in the western Cordillera of North America. *American Journal of Science*, 276(6), 694–712.
- Beck, M. E. (1999). On the shape of paleomagnetic data sets. *Journal of Geophysical Research: Solid Earth*, 104(B11), 25427–25441. <https://doi.org/10.1029/1999jb900225>
- Beniamovsky, V.N., Fregatova, N., Spirina, L., Boyarinova, M., Volobueva, V., Gladenkov, Y.B., 1992. Zonation of planktonic and benthic foraminifera in Paleogene deposits of East Kamchatka. *Izvestiya Akademii Nauk SSSR Seriya Geologicheskaya* 1, 100–113.
- Bernard, A., Munschy, M., Rotstein, Y., Sauter, D.J.G.J.I., 2005. Refined spreading history at the Southwest Indian Ridge for the last 96 Ma, with the aid of satellite gravity data. 162, 765–778.
- Besse, J., and Courtillot, V. (1991). Revised and synthetic apparent polar wander paths of the African, Eurasian, North American and Indian plates, and true polar wander since 200 Ma. *Journal of Geophysical Research: Solid Earth*, 96(B3), 4029–4050.
- Besse, J., and Courtillot, V. (2002). Apparent and true polar wander and the geometry of the geomagnetic field over the last 200 Myr. *Journal of Geophysical Research: Solid Earth*, 107(B11), EPM-6. Biedermann, A. R., Bilardello, D., Jackson, M., Tauxe, L., & Feinberg, J. M., 2019. Grain-size-dependent remanence

- anisotropy and its implications for paleodirections and paleointensities—Proposing a new approach to anisotropy corrections. *Earth Planet. Sci. Lett.*, 512, 111-123.
- Biggin, A. J., Bono, R. K., Meduri, D. G., Sprain, C. J., Davies, C. J., Holme, R., and Doubrovine, P. V. (2020). Quantitative estimates of average geomagnetic axial dipole dominance in deep geological time. *Nature communications*, 11(1), 1-9.
- Biggin, A. J., van Hinsbergen, D. J., Langereis, C. G., Straathof, G. B., & Deenen, M. H. (2008). Geomagnetic secular variation in the Cretaceous Normal Superchron and in the Jurassic. *Physics of the Earth and Planetary Interiors*, 169(1-4), 3-19.
- Biggin, A.J., Strik, G.H., Langereis, C.G., 2008. Evidence for a very-long-term trend in geomagnetic secular variation. *Nature Geoscience* 1, 395.
- Bilardello, D. (2020). Comment on “New Late Pennsylvanian Paleomagnetic Results From Paraná Basin (Southern Brazil): Is the Recent Giant Gaussian Process Model Valid for the Kiaman Superchron?” by Brandt et al. *Journal of Geophysical Research: Solid Earth*, 125(7). <https://doi.org/10.1029/2019JB018556>
- Bilardello, D., 2013. Understanding DRM acquisition of plates and spheres: a first comparative experimental approach. *Geophys. J. Int.*, 195(1), 148-158.
- Bilardello, D., and Kodama, K. P. (2010a). Paleomagnetism and magnetic anisotropy of Carboniferous red beds from the Maritime Provinces of Canada: evidence for shallow paleomagnetic inclinations and implications for North American apparent polar wander. *Geophysical Journal International*, 180(3), 1013-1029.
- Bilardello, D., and Kodama, K. P. (2010b). Rock magnetic evidence for inclination shallowing in the early Carboniferous Deer Lake Group red beds of western Newfoundland. *Geophysical Journal International*, 181(1), 275-289.
- Bilardello, D., Callebert, W. C., & Davis, J. R. (2018). Evidence for widespread remagnetizations in south america, case study of the itararé group rocks from the state of São Paulo, Brazil. *Frontiers in Earth Science*, 6, 182. <https://doi.org/10.3389/feart.2018.00182>
- Bilardello, D., Jezek, J., & Gilder, S. A. (2013). Role of spherical particles on magnetic field recording in sediments: experimental and numerical results. *Physics of the Earth and Planetary Interiors*, 214, 1-13.
- Bilardello, D., Jezek, J., and Kodama, K. P. (2011). Propagating and incorporating the error in anisotropy-based inclination corrections. *Geophysical Journal International*, 187(1), 75-84.
- Bindeman, I., Vinogradov, V., Valley, J., Wooden, J., Natal'in, B., 2002. Archean protolith and accretion of crust in Kamchatka: SHRIMP dating of zircons from Sredinny and Ganal Massifs. *The Journal of geology* 110, 271-289.
- Blackett, P. M. S. (1961). Comparison of ancient climates with the ancient latitudes deduced from rock magnetic measurements. *Proceedings of the Royal Society of London. Series A. Mathematical and Physical Sciences*, 263(1312), 1-30.
- Bogdanov, N., Khain, V., 2000. *The Tectonic Map of the Sea of Okhotsk Region, Scale 1: 2500000*. Moscow: Institute of the Lithosphere of Marginal Seas of RAS 1.
- Bono, R. K., Biggin, A. J., Holme, R., Davies, C. J., Meduri, D. G., and Bestard, J. (2020). Covariant giant Gaussian process models with improved reproduction of paleosecular variation. *Geochemistry, Geophysics, Geosystems*, 21(8), e2020GC008960.
- Bono, R. K., Tarduno, J. A., Nimmo, F., & Cottrell, R. D. (2019). Young inner core inferred from Ediacaran ultra-low geomagnetic field intensity. *Nature Geoscience*, 12(2), 143-147.
- Boschman, L. M., van Hinsbergen, D. J., Langereis, C. G., Flores, K. E., Kamp, P. J., Kimbrough, D. L., ... & Spakman, W. (2021). Reconstructing lost plates of the Panthalassa Ocean through paleomagnetic data from circum-Pacific accretionary orogens. *American Journal of Science*, 321(6), 907-954.
- Boschman, L.M., van Hinsbergen, D.J.J., Torsvik, T.H., Spakman, W. and Pindell, J.L., (2014). Kinematic reconstruction of the Caribbean region since the Early Jurassic. *Earth-Science Reviews*, 138: 102-136.
- Boyd, T.M., Creager, K.C., 1991. The geometry of Aleutian subduction: Three-dimensional seismic imaging. *Journal of Geophysical Research: Solid Earth* 96, 2267-2291.
- Boyden, J.A., Müller, R.D., Gurnis, M., Torsvik, T.H., Clark, J.A., Turner, M., Ivey-Law, H., Watson, R.J., Cannon, J.S., 2011. Next-generation plate-tectonic reconstructions using GPlates.
- Brandt, D., Constable, C., & Ernesto, M. (2020). Giant Gaussian process models of geomagnetic paleosecular variation: a directional outlook. *Geophysical Journal International*, 222(3), 1526-1541.
- Brandt, D., Ernesto, M., & Constable, C. (2021). Consistent and Contrasting Aspects of the Geomagnetic Field Across Epochs With Distinct Reversal Frequencies Revealed by Modeling the Kiaman Superchron.

- Geochemistry, Geophysics, Geosystems, 22(7), 1–24. <https://doi.org/10.1029/2021GC009866>
- Brandt, D., Ernesto, M., Constable, C., Franco, D. R., Carlos Weinschutz, L., de Oliveira Carvalho Rodrigues, P., ... and Zhao, X. (2019). New late Pennsylvanian paleomagnetic results from Paraná Basin (Southern Brazil): is the recent giant Gaussian process model valid for the Kiaman superchron?. *Journal of Geophysical Research: Solid Earth*, 124(7), 6223–6242.
- Brenner, A. R., Fu, R. R., Evans, D. A., Smirnov, A. V., Trubko, R., & Rose, I. R. (2020). Paleomagnetic evidence for modern-like plate motion velocities at 3.2 Ga. *Science Advances*, 6(17), eaaz8670.
- Brenner, A. R., Fu, R. R., Kylander-Clark, A. R., Hudak, G. J., & Foley, B. J. (2022). Plate motion and a dipolar geomagnetic field at 3.25 Ga. *Proceedings of the National Academy of Sciences*, 119(44), e2210258119.
- Brenner, A. R., Fu, R. R., Kylander-Clark, A. R., Hudak, G. J., & Foley, B. J. (2023). Reply to Mitchell and Jing: True polar wander alone is insufficient to drive measured Paleoproterozoic lithospheric motions. *Proceedings of the National Academy of Sciences*, 120(1), e2219560120.
- Bronner, A., Sauter, D., Manatschal, G., Péron-Pinvidic, G. and Munsch, M., (2011). Magmatic breakup as an explanation for magnetic anomalies at magma-poor rifted margins. *Nature Geoscience*, 4(8): 549–553.
- Brown, L. L., & Golombek, M. P. (1997). Tectonic stability of the San Luis Hills, Northern Rio Grande Rift, Colorado: Evidence from paleomagnetic measurements. *Geophysical Research Letters*, 24(4), 473–476. doi:10.1029/97gl00127
- Brown, L. L., Singer, B. S., & Gorrying, M. L. (2004). Paleomagnetism and ⁴⁰Ar/³⁹Ar Chronology of Lavas from Meseta del Lago Buenos Aires, Patagonia. *Geochemistry, Geophysics, Geosystems*, 5(1), n/a-n/a. doi:10.1029/2003gc000526
- Bryan, P., & Gordon, R. G. (1990). Rotation of the Colorado Plateau: An updated analysis of paleomagnetic poles. *Geophysical Research Letters*, 17(10), 1501–1504.
- Bull, J. M., DeMets, C., Krishna, K. S., Sanderson, D. J., & Merkouriev, S. (2010). Reconciling plate kinematic and seismic estimates of lithospheric convergence in the central Indian Ocean. *Geology*, 38(4), 307–310.
- Burke, K., & Torsvik, T. H. (2004). Derivation of large igneous provinces of the past 200 million years from long-term heterogeneities in the deep mantle. *Earth and Planetary Science Letters*, 227(3–4), 531–538.
- Butler, R. F. (1992). *Paleomagnetism: magnetic domains to geologic terranes* (Vol. 319). Boston: Blackwell Scientific Publications.
- Butler, R. F., & Taylor, L. H., 1978. A middle Paleocene paleomagnetic pole from the Nacimiento Formation, San Juan Basin, New Mexico. *Geology*, 6(8), 495–498.
- Butler, R. F., Hervé, F., Munizaga, F., Beck, M. E., Burmester, R. F., & Oviedo, E. S. (1991). Paleomagnetism of the Patagonian Plateau Basalts, southern Chile and Argentina. *Journal of Geophysical Research: Solid Earth*, 96(B4), 6023–6034. doi:10.1029/90jb02698
- Butterworth, N., Talsma, A., Müller, R., Seton, M., Bunge, H.-P., Schuberth, B., Shephard, G., Heine, C., 2014. Geological, tomographic, kinematic and geodynamic constraints on the dynamics of sinking slabs. *Journal of Geodynamics* 73, 1–13.
- Camps, P., Henry, B., Nicolaysen, K., & Plenier, G. (2007). Statistical properties of paleomagnetic directions in Kerguelen lava flows: Implications for the late Oligocene paleomagnetic field. *Journal of Geophysical Research*, 112(B6). doi:10.1029/2006jb004648
- Cande, S. C., & Patriat, P. (2015). The anticorrelated velocities of Africa and India in the Late Cretaceous and early Cenozoic. *Geophysical Journal International*, 200(1), 227–243.
- Cande, S. C., & Stock, J. M. (2004). Pacific—Antarctic—Australia motion and the formation of the Macquarie Plate. *Geophysical Journal International*, 157(1), 399–414.
- Cande, S.C., Kent, D.V., 1995. Revised calibration of the geomagnetic polarity timescale for the Late Cretaceous and Cenozoic. *Journal of Geophysical Research: Solid Earth* 100, 6093–6095.
- Cande, S.C., Patriat, P., Dymment, J.J.G.J.I., 2010. Motion between the Indian, Antarctic and African plates in the early Cenozoic. 183, 127–149.
- Cervantes Solano, M., Goguitchaichvili, A., Mena, M., Alva-Valdivia, L., Morales Contreras, J., Cejudo Ruiz, R., ... & Urrutia-Fucugauchi, J. (2015). Paleomagnetic pole positions and geomagnetic secular variation from the Cretaceous Ponta Grossa Dike Swarm (Brazil). *Geofísica internacional*, 54(2), 167–178.
- Cervantes-Solano, M., Goguitchaichvili, A., Bettucci, L. S., Morales-Contreras, J., Gogorza, C., & Núñez,

- P. (2020). An integrated paleomagnetic and multispecimen paleointensity study from the late Jurassic Zapicán dike swarm (Uruguay). *Journal of South American Earth Sciences*, 104, 102815.
- Channell, J. E. T., & Erba, E., 1992. Early Cretaceous polarity chrons CM0 to CM11 recorded in northern Italian land sections near Brescia. *Earth Planet. Sci. Lett.*, 108(4), 161-179.
- Channell, J. E. T., Bralower, T. J., & Grandesso, P., 1987. Biostratigraphic correlation of Mesozoic polarity chrons CM1 to CM23 at Capriolo and Xausa (Southern Alps, Italy). *Earth Planet. Sci. Lett.*, 85(1-3), 203-221.
- Channell, J. E. T., Casellato, C. E., Muttoni, G., & Erba, E., 2010. Magnetostratigraphy, nanofossil stratigraphy and apparent polar wander for Adria-Africa in the Jurassic–Cretaceous boundary interval. *Paleogeogr. Paleoclimatol. Paleocool.*, 293(1-2), 51-75.
- Channell, J. E. T., Erba, E., & Lini, A., 1993. Magnetostratigraphic calibration of the Late Valanginian carbon isotope event in pelagic limestones from Northern Italy and Switzerland. *Earth Planet. Sci. Lett.*, 118(1-4), 145-166.
- Channell, J. E. T., Erba, E., Muttoni, G., & Tremolada, F., 2000. Early Cretaceous magnetic stratigraphy in the APTICORE drill core and adjacent outcrop at Cisono (Southern Alps, Italy), and correlation to the proposed Barremian-Aptian boundary stratotype. *Geol. Soc. Am. Bull.*, 112(9), 1430-1443.
- Channell, J. E. T., Muttoni, G., and Kent, D. V. (2022). Adria in Mediterranean paleogeography, the origin of the Ionian Sea, and Permo-Triassic configurations of Pangea. *Earth-Science Reviews*, 230, 104045.
- Chekhovich, V.D., Sukhov, A.N., 2015. Geodynamics of the formation of the Paleogenic island arc of the Bauers submarine ridge (Bering Sea). *Doklady Earth Sciences* 461, 221-225.
- Chekhovich, V.D., Sukhov, A.N., Sheremet, O.G., Kononov, M.V., 2012. Cenozoic geodynamics of the Bering Sea region. *Geotectonics* 46, 212-231.
- Chenet, A.-L., Courtillot, V., Fluteau, F., Gérard, M., Quidelleur, X., Khadri, S. F. R., et al. (2009). Determination of rapid Deccan eruptions across the Cretaceous-Tertiary boundary using paleomagnetic secular variation: 2. Constraints from analysis of eight new sections and synthesis for a 3500-m-thick composite section. *Journal of Geophysical Research*, 114(B6).
- Cheon, Y., Cho, H., Ha, S., Kang, H.-C., Kim, J.-S., Son, M., 2018. Tectonically controlled multiple deformations along the Yangsan Fault Zone, SE Korea, since Late Cretaceous. *Journal of Asian Earth Sciences*.
- Chertova, M., Spakman, W., Geenen, T., Berg, A., Hinsbergen, D., 2014. Underpinning tectonic reconstructions of the western Mediterranean region with dynamic slab evolution from 3-D numerical modeling. *Journal of Geophysical Research: Solid Earth* 119, 5876-5902.
- Cho, H.M., Kim, H.J., Jou, H.T., Hong, J.K., Baag, C.E., 2004. Transition from rifted continental to oceanic crust at the southeastern Korean margin in the East Sea (Japan Sea). *Geophysical Research Letters* 31.
- Christeson, G.L., Barth, G.A., 2015. Aleutian basin oceanic crust. *Earth and Planetary Science Letters* 426, 167-175.
- Clark, D. A., & Lackie, M. A. (2003). Paleomagnetism of the Early Permian Mount Leyshton intrusive complex and tuckers igneous complex, North Queensland, Australia. *Geophysical Journal International*, 153(3), 523-547.
- Clyde, W. C., Hamzi, W., Finarelli, J. A., Wing, S. L., Schankler, D., & Chew, A. (2007). Basin-wide magnetostratigraphic framework for the Bighorn Basin, Wyoming. *Geological Society of America Bulletin*, 119(7-8), 848-859. doi:10.1130/b26104.1
- Clyde, W. C., Krause, J. M., De Benedetti, F., Ramezani, J., Cúneo, N. R., Gandolfo, M. A., et al. (2021). New South American record of the Cretaceous–Paleogene boundary interval (La Colonia Formation, Patagonia, Argentina). *Cretaceous Research*, 126.
- Coe, R. S., Globberman, B. R., Plumley, P. W., & Thrupp, G. A. (1985). Paleomagnetic results from Alaska and their tectonic implications.
- Cogné, J. P., Besse, J., Chen, Y., and Hankard, F. (2013). A new Late Cretaceous to Present APWP for Asia and its implications for paleomagnetic shallow inclinations in Central Asia and Cenozoic Eurasian plate deformation. *Geophysical Journal International*, 192(3), 1000-1024.
- Cogné, J. P., Halim, N., Chen, Y., & Courtillot, V., 1999. Resolving the problem of shallow magnetizations of Tertiary age in Asia: insights from paleomagnetic data from the Qiangtang, Kunlun, and Qaidam blocks (Tibet, China), and a new hypothesis. *J. Geophys. Res.*, 104(B8), 17715-17734.
- Cojan, I., & Moreau, M. G. (2006). Correlation of Terrestrial Climatic Fluctuations with Global Signals During the Upper Cretaceous-Danian in a Compressive Setting (Provence, France). *Journal of*

- Sedimentary Research, 76(3), 589-604. doi:10.2110/jsr.2006.045
- Cooper, A., Marlow, M., Scholl, D., 1987. Geologic framework of the Bering Sea crust.
- Cooper, A., Marlow, M., Scholl, D., Stevenson, A., 1992. Evidence for Cenozoic crustal extension in the Bering Sea region. *Tectonics* 11, 719-731.
- Cooper, A.K., Marlow, M.S., Ben-Avraham, Z., 1981. Multichannel seismic evidence bearing on the origin of Bowers Ridge, Bering Sea. *Geological Society of America Bulletin* 92, 474-484.
- Cooper, A.K., Marlow, M.S., Scholl, D.W., 1976. Mesozoic magnetic lineations in the Bering Sea Marginal Basin. *Journal of Geophysical Research* 81, 1916-1934.
- Copley, A., Avouac, J.P., Royer, J.Y., 2010. India-Asia collision and the Cenozoic slowdown of the Indian plate: Implications for the forces driving plate motions. *Journal of Geophysical Research: Solid Earth* 115.
- Cottrell, R. D., & Tarduno, J. A. (2000). Late Cretaceous true polar wander: not so fast. *Science*, 288(5475), 2283-2283.
- Cottrell, R. D., & Tarduno, J. A. (2003). A Late Cretaceous pole for the Pacific plate: implications for apparent and true polar wander and the drift of hotspots. *Tectonophysics*, 362(1-4), 321-333.
- Courtillot, V., & Besse, J. (1987). Magnetic field reversals, polar wander, and core-mantle coupling. *Science*, 237(4819), 1140-1147.
- Cox, A. (1962). Analysis of present geomagnetic field for comparison with paleomagnetic results. *Journal of geomagnetism and geoelectricity*, 13(3-4), 101-112.
- Cox, A. (1970). Latitude dependence of the angular dispersion of the geomagnetic field. *Geophysical Journal International*, 20(3), 253-269.
- Cox, A., Hart, R.B., (2009). Plate tectonics: how it works. John Wiley & Sons.
- Creer, K. M., & Irving, E. (2012). Testing continental drift: constructing the first paleomagnetic path of polar wander (1954). *Earth Sciences History*, 31(1), 111-145.
- Creer, K. M., 1962. The dispersion of the geomagnetic field due to secular variation and its determination for remote times from paleomagnetic data. *J. Geophys. Res.*, 67(9), 3461-3476.
- Creer, K. M., Irving, E., & Nairn, A. E. M., 1959. Paleomagnetism of the Great Whin sill. *Geophys. J. Int.*, 2(4), 306-323.
- Creer, K. M., Irving, E., and Runcorn, S. K. (1954). The direction of the geomagnetic field in remote epochs in Great Britain. *Journal of Geomagnetism and Geoelectricity*, 6(4), 163-168.
- Cromwell, G., Johnson, C. L., Tauxe, L., Constable, C. G., & Jarboe, N. A. (2018). PSV10: A global data set for 0–10 Ma time-averaged field and paleosecular variation studies. *Geochemistry, Geophysics, Geosystems*, 19(5), 1533-1558.
- Croon, M. B., Cande, S. C., & Stock, J. M. (2008). Revised Pacific-Antarctic plate motions and geophysics of the Menard Fracture Zone. *Geochemistry, Geophysics, Geosystems*, 9(7).
- Cukur, D., Kim, S.-P., Horozal, S., Ryu, B.-J., Kim, G.-Y., Kong, G.-S., 2015. Seismic stratigraphy and structural analysis of the western South Korea Plateau (WSKP), East Sea. *Quaternary International* 384, 145-159.
- Dallanave, E., & Kirscher, U., 2020. Testing the reliability of sedimentary paleomagnetic dataset for paleogeographic reconstructions. *Front. Earth Sci.*, 8, 618.
- Dallanave, E., Agnini, C., Bachtadse, V., Muttoni, G., Crampton, J. S., Strong, C. P., ... & Slotnick, B. S., 2015. Early to middle Eocene magneto-biochronology of the southwest Pacific Ocean and climate influence on sedimentation: Insights from the Mead Stream section, New Zealand. *Geol. Soc. Am. Bull.*, 127(5-6), 643-660.
- Dallanave, E., Agnini, C., Muttoni, G., & Rio, D., 2012. Paleocene magneto-biostratigraphy and climate-controlled rock magnetism from the Belluno Basin, Tethys Ocean, Italy. *Paleogeogr. Paleoclimatol. Paleocol.*, 337, 130-142.
- Dallanave, E., Agnini, C., Muttoni, G., Rio, D., 2009. Magneto-biostratigraphy of the Cicogna section (Italy): implications for the late Paleocene-Early Eocene time scale. *Earth Planet. Sci. Lett.*, 285, 39–51.
- Dallanave, E., Kirscher, U., Hauck, J., Hesse, R., Bachtadse, V., & Wortmann, U. G., 2018. Paleomagnetic time and space constraints of the Early Cretaceous Rhenodanubian Flysch zone (Eastern Alps). *Geophys. J. Int.*, 213(3), 1804-1817.
- Das, A., Mallik, J., & Shajahan, R. (2021). Geodynamics related to late-stage Deccan volcanism: Insights from paleomagnetic studies on Dhule-Nandurbar (DND) dyke swarm. *J. Ind. Geophys. Union*, 25(6), 28-44.

- Davis, A.S., Pickthorn, L.-B.G., Valuer, T.L., Marlow, M.S., 1989. Petrology and age of volcanic-arc rocks from the continental margin of the Bering Sea: implications for Early Eocene relocation of plate boundaries. *Canadian Journal of Earth Sciences* 26, 1474-1490.
- De Grave, J., Zhimulev, F.I., Glorie, S., Kuznetsov, G.V., Evans, N., Vanhaecke, F., McInnes, B., 2016. Late Paleogene emplacement and late Neogene–Quaternary exhumation of the Kuril island-arc root (Kunashir island) constrained by multi-method thermochronometry. *Geoscience Frontiers* 7, 211-220.
- De Kock, M. O., and Abubakre, A. O. (2022). Permian Magnetostratigraphy and End of the Kiaman Reverse Polarity Superchron From the Southeast Karoo Basin, South Africa. *Journal of Geophysical Research: Solid Earth*, 127(6).
- De Oliveira, W. P., Hartmann, G. A., Terra-Nova, F., Brandt, D., Biggin, A. J., Engbers, Y. A., et al. (2021). Paleosecular variation and the time-averaged geomagnetic field since 10 Ma. *Geochemistry, Geophysics, Geosystems*.
- Deenen, M. H., Langereis, C. G., van Hinsbergen, D. J., and Biggin, A. J. (2011). Geomagnetic secular variation and the statistics of paleomagnetic directions. *Geophysical Journal International*, 186(2), 509-520.
- Demarest Jr, H. H. (1983). Error analysis for the determination of tectonic rotation from paleomagnetic data. *Journal of Geophysical Research: Solid Earth*, 88(B5), 4321-4328.
- DeMets, C., & Merkouriev, S. (2016). High-resolution estimates of Nubia–Somalia plate motion since 20 Ma from reconstructions of the Southwest Indian Ridge, Red Sea and Gulf of Aden. *Geophysical Journal International*, 207(1), 317-332.
- DeMets, C., & Merkouriev, S. (2019). High-resolution reconstructions of South America plate motion relative to Africa, Antarctica and North America: 34 Ma to present. *Geophysical Journal International*, 217(3), 1821-1853.
- DeMets, C., & Merkouriev, S. (2021). Detailed reconstructions of India–Somalia Plate motion, 60 Ma to present: implications for Somalia Plate absolute motion and India–Eurasia Plate motion. *Geophysical Journal International*, 227(3), 1730-1767.
- DeMets, C., Iaffaldano, G., & Merkouriev, S. (2015). High-resolution Neogene and quaternary estimates of Nubia-Eurasia-North America plate motion. *Geophysical Journal International*, 203(1), 416-427.
- DeMets, C., Merkouriev, S., & Sauter, D. (2021). High resolution reconstructions of the Southwest Indian Ridge, 52 Ma to present: implications for the breakup and absolute motion of the Africa plate. *Geophysical Journal International*, 226(3), 1461-1497.
- Diehl, J. F. (1991). The Elkhorn Mountains revisited: New data for the Late Cretaceous paleomagnetic field of North America. *Journal of Geophysical Research*, 96(B6). doi:10.1029/91jb00959
- Diehl, J. F., Beck, M. E., Beske-Diehl, S., Jacobson, D., & Hearn, B. C. (1983). Paleomagnetism of the Late Cretaceous-Early Tertiary north-central Montana Alkalic Province. *Journal of Geophysical Research: Solid Earth*, 88(B12), 10593-10609. doi:10.1029/JB088iB12p10593
- Diehl, J. F., McClannahan, K. M., & Bornhorst, T. J. (1988). Paleomagnetic results from the Mogollon-Datil Volcanic Field, southwestern New Mexico, and a refined Mid-Tertiary Reference Pole for North America. *Journal of Geophysical Research: Solid Earth*, 93(B5), 4869-4879. doi:10.1029/JB093iB05p04869
- Domeier, M., & Torsvik, T. H. (2014). Plate tectonics in the late Paleozoic. *Geoscience Frontiers*, 5(3), 303-350.
- Domeier, M., Doubrovine, P. V., Torsvik, T. H., Spakman, W., & Bull, A. L. (2016). Global correlation of lower mantle structure and past subduction. *Geophysical Research Letters*, 43(10), 4945-4953.
- Domeier, M., Font, E., Youbi, N., Davies, J., Nemkin, S., van der Voo, R., ... & Torsvik, T. H. (2021). On the Early Permian shape of Pangea from paleomagnetism at its core. *Gondwana Research*, 90, 171-198.
- Domeier, M., Shephard, G. E., Jakob, J., Gaina, C., Doubrovine, P. V., & Torsvik, T. H. (2017). Intraoceanic subduction spanned the Pacific in the Late Cretaceous-Paleocene. *Sciences Advances*, 3. eaao2303.
- Domeier, M., van der Voo, R., & Denny, F. B., (2011a). Widespread inclination shallowing in Permian and Triassic paleomagnetic data from Laurentia: support from new paleomagnetic data from Middle Permian shallow intrusions in southern Illinois (USA) and virtual geomagnetic pole distributions. *Tectonophysics*, 511(1-2), 38-52.
- Domeier, M., van der Voo, R., and Torsvik, T. H. (2012). Paleomagnetism and Pangea: the road to reconciliation. *Tectonophysics*, 514, 14-43.
- Domeier, M., van der Voo, R., Tomezzoli, R. N., Tohver, E., Hendriks, B. W., Torsvik, T. H., . . . Dominguez,

- A. (2011c). Support for an “A-type” Pangea reconstruction from high-fidelity Late Permian and Early to Middle Triassic paleomagnetic data from Argentina. *Journal of Geophysical Research: Solid Earth*, 116(B12).
- Domeier, M., Van der Voo, R., Tohver, E., Tomezzoli, R. N., Vizan, H., Torsvik, T. H., & Kirshner, J. (2011b). New Late Permian paleomagnetic data from Argentina: Refinement of the apparent polar wander path of Gondwana. *Geochemistry, Geophysics, Geosystems*, 12(7).
- Dobrovine, P. V., Steinberger, B., & Torsvik, T. H. (2012). Absolute plate motions in a reference frame defined by moving hot spots in the Pacific, Atlantic, and Indian oceans. *Journal of Geophysical Research: Solid Earth*, 117(B9).
- Dobrovine, P. V., Veikkolainen, T., Pesonen, L. J., Piispa, E., Ots, S., Smirnov, A. V., et al. (2019). Latitude dependence of geomagnetic paleosecular variation and its relation to the frequency of magnetic reversals: observations from the Cretaceous and Jurassic. *Geochemistry, Geophysics, Geosystems*, 20(3), 1240-1279.
- Dobrovine, P.V. and Tarduno, J.A., (2008). Linking the Late Cretaceous to Paleogene Pacific plate and the Atlantic bordering continents using plate circuits and paleomagnetic data. *Journal of Geophysical Research*, 113(B7).
- Duncan, R. A., & Clague, D. A. (1985). Pacific plate motion recorded by linear volcanic chains. *The Ocean Basins and Margins: Volume 7A The Pacific Ocean*, 89-121.
- Dupont-Nivet, G., Sier, M., Campisano, C. J., Arrowsmith, J. R., DiMaggio, E., Reed, K., . . . Hüsing, S. (2008). Magnetostratigraphy of the eastern Hadar Basin (Ledi-Geraru research area, Ethiopia) and implications for hominin paleoenvironments. In *The Geology of Early Humans in the Horn of Africa*.
- Dupont-Nivet, G., van Hinsbergen, D. J., & Torsvik, T. H. (2010). Persistently low Asian paleolatitudes: Implications for the India-Asia collision history. *Tectonics*, 29(5).
- Elouai, D., Sato, H., Hirata, N., Kawasaki, S., Takeshita, T., Kato, N., Takeda, T., 2004. Deep seismic reflection profiling across the Northern Fossa Magna: The ERI 1997 and the JNOC 1996 seismic lines, active faults and geological structures. *Earth, planets and space* 56, 1331-1338.
- Engbers, Y. A., Biggin, A. J., & Bono, R. K. (2020). Elevated paleomagnetic dispersion at Saint Helena suggests long-lived anomalous behavior in the South Atlantic. *Proceedings of the National Academy of Sciences*, 117(31), 18258-18263.
- Engelbreton, D. C., Cox, A., & Gordon, R. G. (1985). Relative motions between oceanic and continental plates in the Pacific basin.
- Ernesto, M., Bellieni, G., Piccirillo, E. M., Marques, L. S., De Min, A., Pacca, I. G., ... & Macedo, J. W. P. (2003). Paleomagnetic and geochemical constraints on the timing and duration of the CAMP activity in northeastern Brazil. *GEOPHYSICAL MONOGRAPH-AMERICAN GEOPHYSICAL UNION*, 136, 129-150.
- Ernesto, M., Comin-Chiaromonti, P., & Gomes, C. d. B. (2015). The Early Triassic magmatism of the Alto Paraguay Province, Central South America: Paleomagnetic and ASM data. *Open Geosciences*, 7(1). doi:10.1515/geo-2015-0022
- Ernesto, M., Demarco, P. N., Xavier, P., Sanchez, L., Schultz, C., & Piñeiro, G. (2020). Age constraints on the Paleozoic Yaguari-Buena Vista succession from Uruguay: paleomagnetic and paleontologic information. *Journal of South American Earth Sciences*, 98. doi:10.1016/j.jsames.2019.102489
- Ernesto, M., Zaffani, L. A., & Caminha-Maciel, G. (2021). New paleomagnetic data from the Paraná Magmatic Province: Brief emplacement time and tectonism. *Journal of South American Earth Sciences*, 106. doi:10.1016/j.jsames.2020.102869
- Evans, D. A. (2003). True polar wander and supercontinents. *Tectonophysics*, 362(1-4), 303-320.
- Evans, D. A. (2006). Proterozoic low orbital obliquity and axial-dipolar geomagnetic field from evaporite paleolatitudes. *Nature*, 444(7115), 51-55.
- Evans, D. A. (2013). Reconstructing pre-Pangean supercontinents. *Bulletin*, 125(11-12), 1735-1751.
- Evans, D. A., & Pisarevsky, S. A. (2008). Plate tectonics on early Earth? Weighing the paleomagnetic evidence. *When did plate tectonics begin on planet Earth*, 440, 249-263.
- Fabbri, O., Charvet, J., Fournier, M., 1996. Alternate senses of displacement along the Tsushima fault system during the Neogene based on fracture analyses near the western margin of the Japan Sea. *Tectonophysics* 257, 275-295.
- Faccenna, C., Becker, T.W., Lallemand, S., Steinberger, B., 2012. On the role of slab pull in the Cenozoic motion of the Pacific plate. *Geophysical Research Letters* 39.

- Faccenna, C., Oncken, O., Holt, A.F., Becker, T.W., 2017. Initiation of the Andean orogeny by lower mantle subduction. *Earth and Planetary Science Letters* 463, 189-201.
- Filatova, N.I., 2013. New data on the structure and history of formation of the conjunction zone between the Middle Cretaceous Okhotsk-Koryak and Cenozoic Olyutor-Kamchatka Orogen belts (Vatyn-Ukelayat Suture Zone). *Doklady Earth Sciences* 448, 7-11.
- Fisher, N. I., Lewis, T., & Embleton, B. J. (1993). *Statistical analysis of spherical data*. Cambridge University Press.
- Fisher, R. A. (1953). Dispersion on a sphere. *Proceedings of the Royal Society of London. Series A. Mathematical and Physical Sciences*, 217(1130), 295-305.
- Font, E., Ernesto, M., Silva, P. F., Correia, P. B., & Nascimento, M. A. L. (2009). Paleomagnetism, rock magnetism and AMS of the Cabo Magmatic Province, NE Brazil, and the opening of South Atlantic. *Geophysical Journal International*, 179(2), 905-922. doi:10.1111/j.1365-246X.2009.04333.x
- Fournier, M., Chamot-Rooke, N., Petit, C., Huchon, P., Al-Kathiri, A., Audin, L., ... & Merkuriev, S. (2010). Arabia-Somalia plate kinematics, evolution of the Aden-Owen-Carlsberg triple junction, and opening of the Gulf of Aden. *Journal of Geophysical Research: Solid Earth*, 115(B4).
- Fournier, M., Jolivet, L., Huchon, P., Sergeev, K.F., Ostorbin, L.S., 1994. Neogene strike-slip faulting in Sakhalin and the Japan Sea opening. *Journal of Geophysical Research: Solid Earth* 99, 2701-2725.
- Franco, D. R., Ernesto, M., Ponte-Neto, C. F., Hinnov, L. A., Berquó, T. S., Fabris, J. D., & Rosière, C. A. (2012). Magnetostratigraphy and mid-paleolatitude VGP dispersion during the Permo-Carboniferous Superchron: results from Paraná Basin (Southern Brazil) rhythmites. *Geophysical Journal International*, no-no. doi:10.1111/j.1365-246X.2012.05670.x
- Fu, H., Zhang, S., Condon, D. J., & Xian, H. (2022). Secular change of true polar wander over the past billion years. *Science Advances*, 8(41), eabo2753.
- Fu, R. R., Kent, D. V., Hemming, S. R., Gutiérrez, P., and Creveling, J. R. (2020). Testing the occurrence of Late Jurassic true polar wander using the La Negra volcanics of northern Chile. *Earth and Planetary Science Letters*, 529.
- Fujiwara, Y., Ohtake, T., 1974. Paleomagnetism of late Cretaceous alkaline rocks in the Nemuro peninsula, Hokkaido, NE Japan. *Journal of geomagnetism and geoelectricity* 26, 549-558.
- Fujiwara, Y., Sugiyama, R., 1986. Post-Oligocene tectonic rotation of southeast Hokkaido. *Rock Magnetism and Paleogeophysics*, 15.
- Fukuma, K., Shinjoe, H., Hamano, Y., 1998. Origin of the absence of magnetic lineations in the Yamato Basin of the Japan Sea: Magnetic properties of mafic rocks from Ocean Drilling Program Hole 794 D. *Journal of Geophysical Research: Solid Earth* 103, 17791-17805.
- Funicello, F., Faccenna, C., Heuret, A., Lallemand, S., Di Giuseppe, E., Becker, T., 2008. Trench migration, net rotation and slab-mantle coupling. *Earth and Planetary Science Letters* 271, 233-240.
- Gaina, C., & Jakob, J. (2019). Global Eocene tectonic unrest: Possible causes and effects around the North American plate. *Tectonophysics*, 760, 136-151.
- Gaina, C., Roest, W., Müller, R.J.E., Letters, P.S., 2002. Late Cretaceous-Cenozoic deformation of northeast Asia. 197, 273-286.
- Gaina, C., Torsvik, T. H., van Hinsbergen, D. J., Medvedev, S., Werner, S. C., & Labails, C. (2013). The African Plate: A history of oceanic crust accretion and subduction since the Jurassic. *Tectonophysics*, 604, 4-25.
- Gallo, L. C., Farjat, A. D., Tomezzoli, R. N., Calvagno, J. M., and Hernández, R. M. (2021). Sedimentary evolution of a Permo-Carboniferous succession in southern Bolivia: Responses to icehouse-greenhouse transition from a probabilistic assessment of paleolatitudes. *Journal of South American Earth Sciences*, 106, 102923.
- Gallo, L. C., Tomezzoli, R. N., & Cristallini, E. O. (2017). A pure dipole analysis of the Gondwana apparent polar wander path: Paleogeographic implications in the evolution of Pangea. *Geochemistry, Geophysics, Geosystems*, 18(4), 1499-1519.
- Ganerød, M., Smethurst, M. A., Rouse, S., Torsvik, T. H., & Prestvik, T. (2008). Reassembling the Paleogene-Eocene North Atlantic igneous province: New paleomagnetic constraints from the Isle of Mull, Scotland. *Earth and Planetary Science Letters*, 272(1-2), 464-475. doi:10.1016/j.epsl.2008.05.016
- Ganerød, M., Smethurst, M. A., Torsvik, T. H., Prestvik, T., Rouse, S., McKenna, C., ... Hendriks, B. W. H. (2010). The North Atlantic Igneous Province reconstructed and its relation to the Plume Generation Zone: the Antrim Lava Group revisited. *Geophysical Journal International*, no-no. doi:10.1111/j.1365-246X.2010.04620.x

- Gao, Y., Zhang, S., Zhao, H., Ren, Q., Yang, T., Wu, H., & Li, H. (2021). North China block underwent simultaneous true polar wander and tectonic convergence in late Jurassic: New paleomagnetic constraints. *Earth and Planetary Science Letters*, 567, 117012.
- Garcés, M., Parés, J. M., & Cabrera, L., 1996. Further evidence for inclination shallowing in red beds. *Geophys. Res. Lett.*, 23(16), 2065-2068.
- Garver, J., Soloviev, A., Bullen, M., Brandon, M., 2000. Towards a more complete record of magmatism and exhumation in continental arcs, using detrital fission-track thermochrometry. *Physics and Chemistry of the Earth, Part A: Solid Earth and Geodesy* 25, 565-570.
- Garza, R. S. M., Acton, G. D., & Geissman, J. W. (1998). Carboniferous through Jurassic paleomagnetic data and their bearing on rotation of the Colorado Plateau. *Journal of Geophysical Research: Solid Earth*, 103(B10), 24179-24188.
- Geist, E.L., Vallier, T.L., Scholl, D.W., 1994. Origin, transport, and emplacement of an exotic island-arc terrane exposed in eastern Kamchatka, Russia. *Geological Society of America Bulletin* 106, 1182-1194.
- Gerritsen, D., Vaes, B., and van Hinsbergen, D. J. (2022). Influence of data filters on the position and precision of paleomagnetic poles: what is the optimal sampling strategy?. *Geochemistry, Geophysics, Geosystems*, e2021GC010269.
- Gibbons, A. D., Whittaker, J. M., & Müller, R. D. (2013). The breakup of East Gondwana: Assimilating constraints from Cretaceous ocean basins around India into a best-fit tectonic model. *Journal of geophysical research: solid earth*, 118(3), 808-822.
- Gilder, S. A., Gomez, J., Chen, Y., & Cogné, J. P., 2008. A new paleogeographic configuration of the Eurasian landmass resolves a paleomagnetic paradox of the Tarim Basin (China). *Tectonics*, 27(1).
- Gilder, S., Chen, Y., & Sen, S., 2001. Oligo-Miocene magnetostratigraphy and rock magnetism of the Xishuigou section, Subei (Gansu Province, western China) and implications for shallow inclinations in central Asia. *J. Geophys. Res.*, 106(B12), 30505-30521.
- Gladenkov, Y.B., 2016. Paleogene and Neogene reference sections of Eastern Kamchatka. *Stratigraphy and Geological Correlation* 24, 58-74.
- Globerman, B. R., & Irving, E. (1988). Mid-Cretaceous paleomagnetic reference field for North America: Restudy of 100 Ma intrusive rocks from Arkansas. *Journal of Geophysical Research*, 93(B10). doi:10.1029/JB093iB10p11721
- Glorie, S., Alexandrov, I., Nixon, A., Jepson, G., Gillespie, J., Jahn, B.-M., 2017. Thermal and exhumation history of Sakhalin Island (Russia) constrained by apatite U-Pb and fission track thermochronology. *Journal of Asian Earth Sciences* 143, 326-342.
- Gnibidenko, H.S., Khvedchuk, I.I., 1982. The tectonics of the Okhotsk Sea. *Marine Geology* 50, 155-197.
- Goldreich, P., and Toomre, A. (1969). Some remarks on polar wandering. *Journal of Geophysical Research*, 74(10), 2555-2567.
- Gong, Z., Langereis, C. G., & Mullender, T. A. T., 2008. The rotation of Iberia during the Aptian and the opening of the Bay of Biscay. *Earth Planet. Sci. Lett.*, 273(1-2), 80-93.
- González, V. R., Renda, E., Vizán, H., Ganerød, M., Puigdomenech, C., & Zaffarana, C. (2022). Deformation along the Deseado Massif (Patagonia, Argentina) during the Jurassic Period and its relationship with the Gondwana breakup: paleomagnetic and geochronological constraints. *Tectonophysics*, 834, 229389.
- Gorbatov, A., Widiyantoro, S., Fukao, Y., Gordeev, E., 2000. Signature of remnant slabs in the North Pacific from P-wave tomography. *Geophysical Journal International* 142, 27-36.
- Gordon, R. G. (1983). Late Cretaceous apparent polar wander of the Pacific plate: evidence for a rapid shift of the Pacific hotspots with respect to the spin axis. *Geophysical Research Letters*, 10(8), 709-712.
- Gordon, R. G. (1987). Polar wandering and paleomagnetism. *Annual Review of Earth and Planetary Sciences*, 15(1), 567-593.
- Gordon, R. G., and Livermore, R. A. (1987). Apparent polar wander of the mean-lithosphere reference frame. *Geophysical Journal International*, 91(3), 1049-1057.
- Gradstein, F. M., Ogg, J. G., Schmitz, M. D., & Ogg, G. M. (2020). *Geologic time scale 2020*: Elsevier.
- Gradstein, F.M., Ogg, J.G., Schmitz, M., Ogg, G., (2012). *The geologic time scale 2012*. elsevier.
- Grannik, V.M., 2012. East Sakhalin island arc paleosystem of the Sea of Okhotsk region. *Doklady Earth Sciences* 445, 934-938.
- Granot, R., & Dymant, J. (2015). The Cretaceous opening of the South Atlantic Ocean. *Earth and Planetary Science Letters*, 414, 156-163.
- Granot, R., and Dymant, J. (2018). Late Cenozoic unification of East and West Antarctica. *Nature*

- Communications, 9(1), 1-10.
- Granot, R., Cande, S., Stock, J., & Damaske, D. (2013). Revised Eocene-Oligocene kinematics for the West Antarctic rift system. *Geophysical Research Letters*, 40(2), 279-284.
- Greff-Lefftz, M., & Besse, J. (2014). Sensitivity experiments on True Polar Wander. *Geochemistry, Geophysics, Geosystems*, 15(12), 4599-4616.
- Griffiths, D. H., King, R. F., Rees, A. I., & Wright, A. E., 1960. The remanent magnetism of some recent varved sediments. *Proceedings of the Royal Society of London. Series A. Mathematical and Physical Sciences*, 256(1286), 359-383.
- Guilmette, C., Smit, M., Hinsbergen, D., Gürer, D., Corfu, F., Maffione, M., Savard, D., 2018. Forced subduction initiation revealed by crust-sole couple geochronology of the Semail ophiolite of Oman. *Nature Geoscience*, under review.
- Gunderson, J. A., & Sheriff, S. D. (1991). A new Late Cretaceous paleomagnetic pole from the Adel Mountains, west central Montana. *Journal of Geophysical Research*, 96(B1). doi:10.1029/90jb01963
- Gürer, D., Granot, R., & van Hinsbergen, D. J. (2022). Plate tectonic chain reaction revealed by noise in the Cretaceous quiet zone. *Nature Geoscience*, 15(3), 233-239.
- Hagstrum, J. T., & Lipman, P. W. (1986). Paleomagnetism of the structurally deformed Latir volcanic field, northern New Mexico: Relations to formation of the Questa caldera and development of the Rio Grande rift. *Journal of Geophysical Research: Solid Earth*, 91(B7), 7383-7402. doi:10.1029/JB091iB07p07383
- Haldan, M. M., Langereis, C. G., Biggin, A. J., Dekkers, M. J., & Evans, M. E., 2009. A comparison of detailed equatorial red bed records of secular variation during the Permo-Carboniferous Reversed Superchron. *Geophys. J. Int.*, 177(3), 834-848.
- Haldan, M. M., Meijers, M. J. M., Langereis, C. G., Larsen, B. T., & Heyer, H. (2014). New paleomagnetic results from the Oslo Graben, a Permian Superchron lava province. *Geophysical Journal International*, 199(3), 1554-1571. <https://doi.org/10.1093/gji/ggu351>
- Hall, R., 2002. Cenozoic geological and plate tectonic evolution of SE Asia and the SW Pacific: computer-based reconstructions, model and animations. *Journal of Asian Earth Sciences* 20, 353-431.
- Handford, B., Biggin, A., Haldan, M., & Langereis, C. (2021). Analyzing Triassic and Permian Geomagnetic Paleosecular Variation and the Implications for Ancient Field Morphology. *Geochemistry, Geophysics, Geosystems*, 22(11), e2021GC009930.
- Hankard, F., Cogné, J. P., Kravchinsky, V. A., Carporzen, L., Bayasgalan, A., & Lkhagvadorj, P., 2007. New Tertiary paleomagnetic poles from Mongolia and Siberia at 40, 30, 20, and 13 Ma: Clues on the inclination shallowing problem in central Asia. *J. Geophys. Res.*, 112(B2).
- Hansma, J., and Tohver, E. (2020). Southward drift of eastern Australian hotspots in the paleomagnetic reference frame is consistent with global true polar wander estimates. *Frontiers in Earth Science*, 489.
- Harbert, W., Heiphetz, A., Savostin, L., 1994. Reconnaissance paleomagnetism of the Olyutorsky superterrane, northeast Russia, *Proceedings, International Conference on Arctic Margins*, MMS 94-0040. University of Pittsburgh, pp. 223-228.
- Harbert, W., Kepezhinskas, P., Krylov, K., Grigoriev, V., Sokolov, S., Aleksuitin, M., Heiphetz, A., Layer, P., 1998. Paleomagnetism and tectonics of the Kamchatka region, northeastern Russia: Implications for the development and evolution of the northwest Pacific basin. *Polarforschung* 68, 297-308.
- Harbert, W., Tsukanov, N., Alexeiev, D., Gaedicke, C., Freitag, R., Baranov, B., Skolotnev, S., Kramer, W., Seifert, W., 2009. Paleomagnetism of the Cretaceous rocks from Cape Kronotskiy, East Kamchatka and reconstruction of terrane trajectories in the NE Pacific area. *Stephan Mueller Special Publication Series* 4, 313-327.
- Hargraves, R. B. (1989). Paleomagnetism of mesozoic kimberlites in southern Africa and the cretaceous apparent polar wander curve for Africa. *Journal of Geophysical Research*, 94(B2). doi:10.1029/JB094iB02p01851
- Harlan, S. S., & Morgan, L. A. (2010). Paleomagnetic results from Tertiary volcanic strata and intrusions, Absaroka Volcanic Supergroup, Yellowstone National Park and vicinity: Contributions to the North American apparent polar wander path. *Tectonophysics*, 485(1-4), 245-259. doi:10.1016/j.tecto.2009.12.025
- Harlan, S. S., Geissman, J. W., Whisner, S. C., & Schmidt, C. J. (2008). Paleomagnetism and geochronology of sills of the Doherty Mountain area, southwestern Montana: Implications for the timing of fold-and-thrust belt deformation and vertical-axis rotations along the southern margin of the Helena salient. *Geological Society of America Bulletin*, 120(9-10), 1091-1104. doi:10.1130/b26313.1

- Harrison, C. G. A., and Lindh, T. (1982a). A polar wandering curve for North America during the Mesozoic and Cenozoic. *Journal of Geophysical Research: Solid Earth*, 87(B3), 1903-1920.
- Harrison, C. G. A., & Lindh, T. (1982b). Comparison between the hot spot and geomagnetic field reference frames. *Nature*, 300(5889), 251-252.
- Hassan, R., Müller, R.D., Gurnis, M., Williams, S.E., Flament, N., 2016. A rapid burst in hotspot motion through the interaction of tectonics and deep mantle flow. *Nature* 533, 239.
- Hauff, F., Werner, R., Portnyagin, M., Baranov, B., Yogodzinski, G., Botcharnikov, R., Hoernle, K., Silantsev, S., van den Bogaard, P., 2016. Exploring the Origin of the Bering Sea: Initial Results of Cruise SO249-2 (17th July-13th August 2016), AGU Fall Meeting Abstracts.
- Hayashida, A., 1986. Timing of rotational motion of Southwest Japan inferred from paleomagnetism of the Setouchi Miocene Series. *Journal of geomagnetism and geoelectricity* 38, 295-310.
- Hayashida, A., Ito, Y., 1984. Paleoposition of Southwest Japan at 16 Ma: implication from paleomagnetism of the Miocene Ichishi Group. *Earth and planetary science letters* 68, 335-342.
- Heslop, D., & Roberts, A. P. (2019). Quantifying the similarity of paleomagnetic poles. *Journal of Geophysical Research: Solid Earth*, 124(12), 12388-12403.
- Heslop, D., and Roberts, A. P. (2016). Estimation and propagation of uncertainties associated with paleomagnetic directions. *Journal of Geophysical Research: Solid Earth*, 121(4), 2274-2289.
- Heslop, D., and Roberts, A. P. (2020). Uncertainty propagation in hierarchical paleomagnetic reconstructions. *Journal of Geophysical Research: Solid Earth*, 125(6), e2020JB019488.
- Hess, H. H., (1962). History of ocean basins. In Engle, E. A. J. (ed.), *Petrologic Studies*. New York: Geological Society of America.
- Hirata, N., Karp, B.Y., Yamaguchi, T., Kanazawa, T., Suyehiro, K., Kasahara, J., Shiobara, H., Shinohara, M., Kinoshita, H., 1992. Oceanic crust in the Japan Basin of the Japan Sea by the 1990 Japan-USSR Expedition. *Geophysical Research Letters* 19, 2027-2030.
- Hirata, N., Tokuyama, H., Chung, T.W., 1989. An anomalously thick layering of the crust of the Yamato Basin, southeastern Sea of Japan: the final stage of back-arc spreading. *Tectonophysics* 165, 303-314.
- Hiroki, Y., Matsumoto, R., 1999. Magnetostratigraphic correlation of Miocene regression-and-transgression boundaries in central Honshu, Japan. *Jour. Geol. Soc. Japan* 105, 87-107.
- Hirooka, K., Sakai, H., Takahashi, T., Kinoto, H., Takeuchi, A., 1986. Tertiary tectonic movement of central Japan inferred from paleomagnetic studies. *Journal of geomagnetism and geoelectricity* 38, 311-323.
- Hirooka, K., Yamada, R., Yamashita, M., Takeuchi, A., 1990. Paleomagnetic evidence of the rotation of central Japan and the paleoposition of Japan. *Paleogeography, Paleoclimatology, Paleoecology* 77, 345-354.
- Hisada, K.i., Takashima, S., Arai, S., Lee, Y.I., 2008. Early Cretaceous paleogeography of Korea and Southwest Japan inferred from occurrence of detrital chromian spinels. *Island Arc* 17, 471-484.
- Hochstaedter, A.G., Kepezshinskas, P.K., Defant, M.J., Drummond, M.S., Bellon, H., 1994. On the tectonic significance of arc volcanism in northern Kamchatka. *The Journal of Geology* 102, 639-654.
- Hodych, J. P., & Buchan, K. L., 1994. Early Silurian paleolatitude of the Springdale Group redbeds of central Newfoundland: a paleomagnetic determination with a remanence anisotropy test for inclination error. *Geophys. J. Int.*, 117(3), 640-652.
- Hoernle, K., Werner, R., Portnyagin, M., Yogodzinski, G., Hauff, F., Baranov, B., Silantsev, S., 2016. New Insights into the Origin of the Bering Sea from SO201 and SO249 cruises, AGU Fall Meeting Abstracts.
- Horner-Johnson, B.C., Gordon, R.G., Argus, D.F.J.o.G.R.S.E., 2007. Plate kinematic evidence for the existence of a distinct plate between the Nubian and Somalian plates along the Southwest Indian Ridge. 112.
- Hoshi, H., Kato, D., Ando, Y., Nakashima, K., 2015. Timing of clockwise rotation of Southwest Japan: constraints from new middle Miocene paleomagnetic results. *Earth, Planets and Space* 67, 92.
- Hoshi, H., Matsubara, T., 1998. Early Miocene paleomagnetic results from the Ninohe area, NE Japan: Implications for arc rotation and intra-arc differential rotations. *Earth, planets and space* 50, 23-33.
- Hoshi, H., Sano, M., 2013. Paleomagnetic constraints on Miocene rotation in the central Japan Arc. *Island Arc* 22, 197-213.
- Hoshi, H., Takahashi, M., 1997. Paleomagnetic constraints on the extent of tectonic blocks and the location of their kinematic boundaries: Implications for Miocene intra-arc deformation in Northeast Japan. *Jour. Geol. Soc. Japan* 103, 523-542.
- Hoshi, H., Takahashi, M., 2013. Refined Paleomagnetic Direction of the Miocene Motegi Formation,

Tochigi Prefecture, Central Honshu.

- Hoshi, H., Tanaka, D., Takahashi, M., Yoshikawa, T., 2000. Paleomagnetism of the Nijo Group and its implication for the timing of clockwise rotation of southwest Japan. *Journal of Mineralogical and Petrological Sciences* 95, 203-215.
- Hoshi, H., Teranishi, Y., 2007. Paleomagnetism of the Ishikoshi Andesite: a Middle Miocene paleomagnetic pole for northeastern Japan and tectonic implications. *Earth, planets and space* 59, 871-878.
- Hoshi, H., Yokoyama, M., 2001. Paleomagnetism of Miocene dikes in the Shitara basin and the tectonic evolution of central Honshu, Japan. *Earth, planets and space* 53, 731-739.
- Hosoi, J., Okada, M., Gokan, T., Amano, K., Martin, A.J., 2015. Early to Middle Miocene rotational tectonics of the Ou Backbone Range, northeast Japan. *Island Arc* 24, 288-300.
- Hospers, J. (1954). Rock magnetism and polar wandering. *Nature*, 173(4416), 1183-1184.
- Hourigan, J.K., Akinin, V.V., 2004. Tectonic and chronostratigraphic implications of new $^{40}\text{Ar}/^{39}\text{Ar}$ geochronology and geochemistry of the Arman and Malan-Ola volcanic fields, Okhotsk-Chukotka volcanic belt, northeastern Russia. *Geological Society of America Bulletin* 116, 637-654.
- Hourigan, J.K., Brandon, M.T., Soloviev, A.V., Kirmasov, A.B., Garver, J.L., Stevenson, J., Reiners, P.W., 2009. Eocene arc-continent collision and crustal consolidation in Kamchatka, Russian Far East. *American Journal of Science* 309, 333-396.
- Huang, W., Dupont-Nivet, G., Lippert, P. C., van Hinsbergen, D. J., & Hallot, E., 2013. Inclination shallowing in Eocene Linzizong sedimentary rocks from Southern Tibet: correction, possible causes and implications for reconstructing the India-Asia collision. *Geophys. J. Int.*, 194(3), 1390-1411.
- Huang, W., van Hinsbergen, D. J., Dekkers, M. J., Garzanti, E., Dupont-Nivet, G., Lippert, P. C., ... & Guo, Z., 2015. Paleolatitudes of the Tibetan Himalaya from primary and secondary magnetizations of Jurassic to Lower Cretaceous sedimentary rocks. *Geochem. Geophys. Geosyst.*, 16(1), 77-100.
- Hussain, A. G., Schult, A., & Soffel, H. (1979). Paleomagnetism of the basalts of Wadi Abu Tereifiya, Mandisha and dioritic dykes of Wadi Abu Shihat, Egypt. *Geophysical Journal International*, 56(1), 55-61.
- Ikeda, Y., Stern, R.J., Kagami, H., Sun, C.H., 2000. Pb, Nd, and Sr isotopic constraints on the origin of Miocene basaltic rocks from northeast Hokkaido, Japan: Implications for opening of the Kurile back-arc basin. *Island Arc* 9, 161-172.
- Ingle Jr, J.C., 1992. Subsidence of the Japan Sea: stratigraphic evidence from ODP sites and onshore sections, *Proc. ODP Scientific Results*, pp. 1197-1218.
- Irving, E. (1956). Paleomagnetic and paleoclimatological aspects of polar wandering. *Geofisica pura e applicata*, 33(1), 23-41.
- Irving, E. (1961). Paleomagnetic Methods: A Discussion of a Recent Paper by A. E. M. Nairn. *The Journal of Geology*, 69(2), 226-231. <https://doi.org/10.1086/626733>
- Irving, E. (1964). *Paleomagnetism and its application to geological and geophysical problems*. New York: Wiley.
- Irving, E. (1977). Drift of the major continental blocks since the Devonian. *Nature*, 270(5635), 304-309.
- Irving, E. (1979). Paleopoles and paleolatitudes of North America and speculations about displaced terrains. *Canadian Journal of Earth Sciences*, 16(3), 669-694.
- Irving, E., & Irving, G. (1982). Apparent polar wander paths Carboniferous through Cenozoic and the assembly of Gondwana. *Geophysical Surveys*, 5(2), 141-188.
- Isezaki, N., 1986. A magnetic anomaly map of the Japan Sea. *Journal of geomagnetism and geoelectricity* 38, 403-410.
- Ishikawa, N., 1997. Differential rotations of north Kyushu Island related to middle Miocene clockwise rotation of SW Japan. *Journal of Geophysical Research: Solid Earth* 102, 17729-17745.
- Ishizuka, O., Tani, K., Reagan, M.K., Kanayama, K., Umino, S., Harigane, Y., Sakamoto, I., Miyajima, Y., Yuasa, M., Dunkley, D.J., 2011. The timescales of subduction initiation and subsequent evolution of an oceanic island arc. *Earth and Planetary Science Letters* 306, 229-240.
- Isozaki, Y., Aoki, K., Nakama, T., Yanai, S., 2010. New insight into a subduction-related orogen: A reappraisal of the geotectonic framework and evolution of the Japanese Islands. *Gondwana Research* 18, 82-105.
- Isozaki, Y., Maruyama, S., Furuoka, F., 1990. Accreted oceanic materials in Japan. *Tectonophysics* 181, 179-205.
- Ito, T., 2002. Active faulting, lower crustal delamination and ongoing Hidaka arc-arc collision, Hokkaido, Japan. *Seismotectonics in Convergent Plate Boundary*, 219-224.

- Itoh, Y., 1988. Differential rotation of the eastern part of southwest Japan inferred from paleomagnetism of Cretaceous and Neogene rocks. *Journal of Geophysical Research: Solid Earth* 93, 3401-3411.
- Itoh, Y., Doshida, S., Kitada, K., Danhara, T., 2001. Paleomagnetism and fission-track ages of the Mt. Wasso moonstone rhyolitic welded tuff in the Ishikawa Prefecture, central Japan. *Bulletin of the Geological Survey of Japan* 52, 573-580.
- Itoh, Y., Hayakawa, H., 1988. Magnetostratigraphy of Neogene rocks around the Yatsuo area in Toyama Prefecture, Japan. *Jbun Geol. Jour. Geol. Soc. Japan* 94, 515-525.
- Itoh, Y., Ito, Y., 1989. Confined ductile deformation in the Japan arc inferred from paleomagnetic studies. *Tectonophysics* 167, 57-73.
- Itoh, Y., Kitada, K., 2003. Early Miocene rotational process in the eastern part of south-west Japan inferred from paleomagnetic studies. *Island Arc* 12, 348-356.
- Itoh, Y., Tsuru, T., 2006. A model of late Cenozoic transcurrent motion and deformation in the fore-arc of northeast Japan: Constraints from geophysical studies. *Physics of the Earth and Planetary Interiors* 156, 117-129.
- Iwasaki, T., Adachi, K., Moriya, T., Miyamachi, H., Matsushima, T., Miyashita, K., Takeda, T., Taira, T., Yamada, T., Ohtake, K., 2004. Upper and middle crustal deformation of an arc-arc collision across Hokkaido, Japan, inferred from seismic refraction/wide-angle reflection experiments. *Tectonophysics* 388, 59-73.
- Iwasaki, T., Levin, V., Nikulin, A., Iidaka, T., 2013. Constraints on the Moho in Japan and Kamchatka. *Tectonophysics* 609, 184-201.
- Jackson, M. J., Banerjee, S. K., Marvin, J. A., Lu, R., & Gruber, W., 1991. Detrital remanence, inclination errors, and anhysteretic remanence anisotropy: quantitative model and experimental results. *Geophys. J. Int.*, 104(1), 95-103.
- Jarboe, N. A., Koppers, A. A., Tauxe, L., Minnett, R., and Constable, C. (2012). The online MagIC Database: data archiving, compilation, and visualization for the geomagnetic, paleomagnetic and rock magnetic communities. In *AGU Fall Meeting Abstracts* (Vol. 2012, pp. GP31A-1063).
- Jay, A. E., Niocaill, C. M., Widdowson, M., Self, S., & Turner, W. (2009). New paleomagnetic data from the Mahabaleshwar Plateau, Deccan Flood Basalt Province, India: implications for the volcanostratigraphic architecture of continental flood basalt provinces. *Journal of the Geological Society*, 166(1), 13-24.
- Jeong, D., & Yu, Y., 2019. Apparent polar wander path for East Asia and implications for paleomagnetic low inclination in sedimentary rocks. *Phys. Earth Planet. Inter.*, 289, 63-72.
- Jezeq, J., Gilder, S., & Bilardello, D., 2012. Numerical simulation of inclination shallowing by rolling and slipping of spherical particles. *Comput Geosci.*, 49, 270-277.
- Jiang, G., Zhao, D., Zhang, G., 2009. Seismic tomography of the Pacific slab edge under Kamchatka. *Tectonophysics* 465, 190-203.
- Jicha, B.R., Scholl, D.W., Singer, B.S., Yogodzinski, G.M., Kay, S.M., 2006. Revised age of Aleutian Island Arc formation implies high rate of magma production. *Geology* 34, 661.
- Jing, X., Yang, Z., Mitchell, R. N., Tong, Y., Zhu, M., & Wan, B. (2022). Ordovician–Silurian true polar wander as a mechanism for severe glaciation and mass extinction. *Nature Communications*, 13(1), 7941.
- Johnson, C. L., & Constable, C. G. (1996). Paleosecular variation recorded by lava flows over the past five million years. *Philosophical Transactions of the Royal Society A: Mathematical, Physical and Engineering Sciences*, 354(1704), 89–141. <https://doi.org/10.1098/rsta.1996.0004>
- Johnson, C. L., and McFadden, P. (2007). Time-averaged field and paleosecular variation. *Geomagnetism*, 5, 417-453.
- Johnson, C. L., Constable, C. G., Tauxe, L., Barendregt, R., Brown, L. L., Coe, R. S., ... & Stone, D. B. (2008). Recent investigations of the 0–5 Ma geomagnetic field recorded by lava flows. *Geochemistry, Geophysics, Geosystems*, 9(4).
- Johnston, S.T., 2001. The Great Alaskan Terrane Wreck: reconciliation of paleomagnetic and geological data in the northern Cordillera. *Earth and Planetary Science Letters* 193, 259-272.
- Jolivet, L., Huchon, P., 1989. Crustal-scale strike-slip deformation in Hokkaido, northern Japan. *Journal of structural geology* 11, 509-522.
- Jolivet, L., Miyashita, S., 1985. The Hidaka Shear Zone (Hokkaido, Japan): Genesis during a right-lateral strike-slip movement. *Tectonics* 4, 289-302.
- Jolivet, L., Tamaki, K., 1992. Neogene kinematics in the Japan Sea region and volcanic activity of the

- Northeast Japan Arc, Proc. ODP Scientific Results, pp. 1311-1331.
- Jolivet, L., Tamaki, K., Fournier, M., 1994. Japan Sea, opening history and mechanism: A synthesis. *Journal of Geophysical Research: Solid Earth* 99, 22237-22259.
- Jupp, P. E., & Kent, J. T. (1987). Fitting smooth paths to spherical data. *Journal of the Royal Statistical Society: Series C (Applied Statistics)*, 36(1), 34-46.
- Kanamatsu, T., Nanayama, F., Iwata, K., Fujiwara, Y., 1992. Pre-Tertiary Systems on the western side of the Abashiri Tectonic Line in the Shiranuka area, eastern Hokkaido, Japan: implications to the tectonic relationship between the Nemuro and Tokoro Belts. *The Journal of the Geological Society of Japan* 98, 1113-1128.
- Kaneoka, I., 1992. $^{40}\text{Ar}/^{39}\text{Ar}$ analysis of volcanic rocks recovered from the Japan Sea floor: Constraints on the age of formation of the Japan Sea. *Proceedings of the Ocean Drilling Program, Scientific Results*, 1992 127, 819-836.
- Kano, K., Uto, K., Ohguchi, T., 2007. Stratigraphic review of Eocene to Oligocene successions along the eastern Japan Sea: Implication for early opening of the Japan Sea. *Journal of Asian Earth Sciences* 30, 20-32.
- Kapwar, M. R., and Mamilla, V. (2020). Paleomagnetism and rock magnetism of early Cretaceous Rajmahal basalts, NE India: Implications for paleogeography of the Indian subcontinent and migration of the Kerguelen hotspot. *Journal of Asian Earth Sciences*, 201.
- Kato, H., 1992. Fossa Magna-A masked border region separating southwest and northeast Japan. *Bulletin of the Geological Survey of Japan* 43, 1-30.
- Kato, N., Sato, H., Orito, M., Hirakawa, K., Ikeda, Y., Ito, T., 2004. Has the plate boundary shifted from central Hokkaido to the eastern part of the Sea of Japan? *Tectonophysics* 388, 75-84.
- Kawai, N., Ito, H., Kume, S., 1961. Deformation of the Japanese Islands as inferred from rock magnetism. *Geophysical Journal International* 6, 124-130.
- Kemkin, I., Khanchuk, A., Kemkina, R., 2016. Accretionary prisms of the Sikhote-Alin Orogenic Belt: Composition, structure and significance for reconstruction of the geodynamic evolution of the eastern Asian margin. *Journal of Geodynamics* 102, 202-230.
- Kent, D. V., & Clemmensen, L. B., 1996. Paleomagnetism and cycle stratigraphy of the Triassic Fleming Fjord and Gipsdalen Formations of East Greenland. *Bull. Geol. Soc. Den.*, 42(2), 121-136.
- Kent, D. V., & Irving, E. (2010). Influence of inclination error in sedimentary rocks on the Triassic and Jurassic apparent pole wander path for North America and implications for Cordilleran tectonics. *Journal of Geophysical Research: Solid Earth*, 115(B10).
- Kent, D. V., & Olsen, P. E., 1999. Astronomically tuned geomagnetic polarity timescale for the Late Triassic. *J. Geophys. Res.*, 104(B6), 12831-12841.
- Kent, D. V., & Olsen, P. E., 2008. Early Jurassic magnetostratigraphy and paleolatitudes from the Hartford continental rift basin (eastern North America): Testing for polarity bias and abrupt polar wander in association with the central Atlantic magmatic province. *J. Geophys. Res.*, 113(B6).
- Kent, D. V., & Tauxe, L. (2005). Corrected late triassic latitudes for continents adjacent to the North Atlantic. *Science*, 307(5707), 240-244.
- Kent, D. V., & Witte, W. K. (1993). Slow apparent polar wander for North America in the Late Triassic and large Colorado Plateau rotation. *Tectonics*, 12(1), 291-300.
- Kent, D. V., and Irving, E. (2010). Influence of inclination error in sedimentary rocks on the Triassic and Jurassic apparent pole wander path for North America and implications for Cordilleran tectonics. *Journal of Geophysical Research: Solid Earth*, 115(B10).
- Kent, D. V., and Muttoni, G. (2020). Pangea B and the late paleozoic ice age. *Paleogeography, Paleoclimatology, Paleoecology*, 553, 109753.
- Kent, D. V., Kjarsgaard, B. A., Gee, J. S., Muttoni, G., & Heaman, L. M. (2015). Tracking the Late Jurassic apparent (or true) polar shift in U-Pb-dated kimberlites from cratonic North America (Superior Province of Canada). *Geochemistry, Geophysics, Geosystems*, 16(4), 983-994.
- Kent, D. V., Olsen, P. E., & Witte, W. K., 1995. Late Triassic-earliest Jurassic geomagnetic polarity sequence and paleolatitudes from drill cores in the Newark rift basin, eastern North America. *J. Geophys. Res.*, 100(B8), 14965-14998.
- Kent, D. V., Olsen, P. E., Muttoni, G., & Et-Touhami, M. (2021). A Late Permian paleopole from the Ikakern Formation (Argana basin, Morocco) and the configuration of Pangea. *Gondwana Research*, 92, 266-278.

- Khanchuk, A., 2006. Geodynamics, Magmatism and Metallogeny of the Eastern Russia. *Dal'nauka, Vladivostok* 1, 1-572.
- Khotin, M.Y., Shapiro, M.N., 2006. Ophiolites of the Kamchatsky Mys Peninsula, eastern Kamchatka: Structure, composition, and geodynamic setting. *Geotectonics* 40, 297-320.
- Kidane, T., Carlot, J., Courtillot, V., Gallet, Y., Quidelleur, X., Gillot, P. Y., & Haile, T. (1999). Paleomagnetic and geochronological identification of the Réunion subchron in Ethiopian Afar. *Journal of Geophysical Research: Solid Earth*, 104(B5), 10405-10419. doi:10.1029/1999jb900014
- Kidane, T., Courtillot, V., Manighetti, I., Audin, L., Lahitte, P., Quidelleur, X., . . . Haile, T. (2003). New paleomagnetic and geochronologic results from Ethiopian Afar: Block rotations linked to rift overlap and propagation and determination of a 2 Ma reference pole for stable Africa. *Journal of Geophysical Research: Solid Earth*, 108(B2). doi:10.1029/2001jb000645
- Kim, G.B., Yoon, S.H., Chough, S.K., Kwon, Y.K., Ryu, B.J., 2011. Seismic reflection study of acoustic basement in the South Korea Plateau, the Ulleung Interplain Gap, and the northern Ulleung Basin: Volcano-tectonic implications for Tertiary back-arc evolution in the southern East Sea. *Tectonophysics* 504, 43-56.
- Kim, H.-J., Han, S.-J., Lee, G.H., Huh, S., 1998. Seismic study of the Ulleung Basin crust and its implications for the opening of the East Sea (Japan Sea). *Marine Geophysical Researches* 20, 219-237.
- Kim, H.-J., Jou, H.-T., Cho, H.-M., Bijwaard, H., Sato, T., Hong, J.-K., Yoo, H.-S., Baag, C.-E., 2003. Crustal structure of the continental margin of Korea in the East Sea (Japan Sea) from deep seismic sounding data: evidence for rifting affected by the hotter than normal mantle. *Tectonophysics* 364, 25-42.
- Kim, H.-J., Lee, G.H., Choi, D.-L., Jou, H.-T., Li, Z., Zheng, Y., Kim, G.-Y., Lee, S.-H., Kwon, Y.K., 2015. Back-arc rifting in the Korea Plateau in the East Sea (Japan Sea) and the separation of the southwestern Japan Arc from the Korean margin. *Tectonophysics* 638, 147-157.
- Kim, H.-J., Lee, G.H., Jou, H.-T., Cho, H.-M., Yoo, H.-S., Park, G.-T., Kim, J.-S., 2007. Evolution of the eastern margin of Korea: Constraints on the opening of the East Sea (Japan Sea). *Tectonophysics* 436, 37-55.
- Kimura, G., 1994. The latest Cretaceous-Early Paleogene rapid growth of accretionary complex and exhumation of high pressure series metamorphic rocks in northwestern Pacific margin. *Journal of Geophysical Research: Solid Earth* 99, 22147-22164.
- Kimura, G., Hashimoto, Y., Kitamura, Y., Yamaguchi, A., Koge, H., 2014. Middle Miocene swift migration of the TTT triple junction and rapid crustal growth in southwest Japan: A review. *Tectonics* 33, 1219-1238.
- Kimura, G., Sakakibara, M., Ofuka, H., Ishizuka, H., Miyashita, S., Okamura, M., Melnikov, O.A., Lushchenko, V., 1992. A deep section of accretionary complex: Susunai complex in Sakhalin island, northwest Pacific margin. *Island Arc* 1, 166-175.
- King, R. F. (1955). The remanent magnetism of artificially deposited sediments. *Geophysical Supplements to the Monthly Notices of the Royal Astronomical Society*, 7(3), 115-134.
- Kirmasov, A., Solov'ev, A., Hourigan, J., 2004. Collision and postcollision structural evolution of the Andrianovka Suture, Sredinny Range, Kamchatka. *Geotectonics* 38, 294-316.
- Kirschvink, J. L. (1980). The least-squares line and plane and the analysis of paleomagnetic data. *Geophysical Journal of the Royal Astronomical Society*, 62(3), 699-718. <https://doi.org/10.1111/j.1365-246X.1980.tb02601.x>
- Knesel, K.M., Cohen, B.E., Vasconcelos, P.M., Thiede, D.S., 2008. Rapid change in drift of the Australian plate records collision with Ontong Java plateau. *Nature* 454, 754.
- Kodama, K. P., (2009). Simplification of the anisotropy-based inclination correction technique for magnetite- and haematite-bearing rocks: a case study for the Carboniferous Glenshaw and Mauch Chunk Formations, North America. *Journal of Geophysical Research.*, 114(2), 467-477.
- Kodama, K. P., (2012). *Paleomagnetism of sedimentary rocks: Process and interpretation*. John Wiley and Sons.
- Kodama, K. P., 1997. A successful rock magnetic technique for correcting paleomagnetic inclination shallowing: case study of the nacimiento formation, New Mexico. *J. Geophys Res.*, 102(B3), 5193-5205.
- Kodama, K., Takeuchi, T., Ozawa, T., 1993. Clockwise tectonic rotation of Tertiary sedimentary basins in central Hokkaido, northern Japan. *Geology* 21, 431-434.
- Kojima, S., Tsukada, K., Otoh, S., Yamakita, S., Ehiro, M., Dia, C., Kirillova, G.L., Dymovich, V.A., Eichwald, L.P., 2008. Geological relationship between Anyui metamorphic complex and Samarka terrane, Far

- East Russia. *Island Arc* 17, 502-516.
- Kojima, T., Okada, M., Ohira, H., Tokieda, K., Komuro, H., Amano, K., 2001. Paleomagnetism and fission-track ages of Oki-Dogo Island in Southwest Japan. *Earth, planets and space* 53, 45-54.
- Konstantinovskaya, E. (2001). Arc–continent collision and subduction reversal in the Cenozoic evolution of the Northwest Pacific: An example from Kamchatka (NE Russia). *Tectonophysics*, 333, 75–94.
- Konstantinovskaya, E., 2011. Early Eocene arc–continent collision in Kamchatka, Russia: structural evolution and geodynamic model, *Arc-Continent Collision*. Springer, pp. 247-277.
- Koulakov, I.Y., Dobretsov, N., Bushenkova, N., Yakovlev, A., 2011. Slab shape in subduction zones beneath the Kurile–Kamchatka and Aleutian arcs based on regional tomography results. *Russian Geology and Geophysics* 52, 650-667.
- Kovalenko, D., 1992. Paleomagnetism in the Paleogene Suites of the Il'pinskiy Peninsula, Kamchatka. *Geotectonics* 26, 408-421.
- Kovalenko, D., 1993. Paleomagnetism of Paleogene complexes at the Ilpinsky Peninsula (the South Koryak Plateau). *Fizika Zemli*, 72-80.
- Kovalenko, D., 1996. Paleomagnetism and Kinematics of the Central Olyutorsky Range, Koryak Highland. *Geotectonics* 30, 243.
- Kovalenko, D., Chernov, E., Kurilov, D., 2002. Paleomagnetism of Upper Cretaceous and Cenozoic Geological Complexes in the Western and Eastern Kamchatka Areas. *Fizika Zemli* 38, 469-484.
- Kovalenko, D., Kravchenko-Berezhnoy, I., 1999. Paleomagnetism and tectonics of Karaginsky Island, Bering Sea. *Island Arc* 8, 426-439.
- Kovalenko, D., Remizova, L., 1997. Paleomagnetism of the Northwestern Olyutorskii Zone, Southern Koryak Upland. *Izvestiya Physics of the Solid Earth* 33, 589-598.
- Koymans, M. R., Langereis, C. G., Pastor-Galán, D., & van Hinsbergen, D. J. J. (2016). Paleomagnetism.org: An online multi-platform open source environment for paleomagnetic data analysis. *Computers & Geosciences*, 93, 127-137.
- Koymans, M. R., van Hinsbergen, D. J. J., Pastor-Galán, D., Vaes, B., & Langereis, C. G. (2020). Towards FAIR paleomagnetic data management through Paleomagnetism.org 2.0. *Geochemistry, Geophysics, Geosystems*, 21(2), e2019GC008838.
- Kravchenko-Berezhnoy, I., Nazimova, Y., 1991. The Cretaceous Ophiolite of Karaginsky Island (the Western Bering Sea). *Ofoliti* 16, 79-110.
- Krijgsman, W., & Tauxe, L., 2006. E/I corrected paleolatitudes for the sedimentary rocks of the Baja British Columbia hypothesis. *Earth Planet. Sci. Lett.*, 242(1-2), 205-216.
- Kristjánsson, L., Gudmundsson, M. T., Smellie, J. L., McIntosh, W. C., & Esser, R. (2005). Paleomagnetic, ⁴⁰Ar/³⁹Ar, and stratigraphical correlation of Miocene–Pliocene basalts in the Brandy Bay area, James Ross Island, Antarctica. *Antarctic Science*, 17(3), 409-417. doi:10.1017/s0954102005002853
- Kulakov, E. V., Torsvik, T. H., Doubrovine, P. V., Slagstad, T., Ganerød, M., Silkoset, P., & Werner, S. C. (2021). Jurassic fast polar shift rejected by a new high-quality paleomagnetic pole from southwest Greenland. *Gondwana Research*.
- Labails, C., Olivet, J. L., Aslanian, D., & Roest, W. R. (2010). An alternative early opening scenario for the Central Atlantic Ocean. *Earth and Planetary Science Letters*, 297(3-4), 355-368.
- Lanci, L., Tohver, E., Wilson, A., and Flint, S. (2013). Upper Permian magnetic stratigraphy of the lower Beaufort Group, Karoo Basin. *Earth and Planetary Science Letters*, 375, 123-134.
- Lander, A.V., Shapiro, M.N., 2007. The origin of the modern Kamchatka subduction zone. *Volcanism and Subduction: The Kamchatka Region*, 57-64.
- Latyshev, A. V., Lapkovskii, A. A., Veselovskiy, R. V., Fetisova, A. M., and Krivolutskaya, N. A. (2021b). Paleomagnetism of the Permian–Triassic Siberian Traps Intrusions from the Kulumbe River Valley, Northwestern Siberian Platform. *Izvestiya, Physics of the Solid Earth*, 57(3), 375-394.
- Latyshev, A., Krivolutskaya, N., Ulyakhina, P., Fetisova, A., Veselovskiy, R., Pasenko, A., et al. (2021a). Paleomagnetism of the Permian-Triassic intrusions from the Norilsk region (the Siberian platform, Russia): Implications for the timing and correlation of magmatic events, and magmatic evolution. *Journal of Asian Earth Sciences*, 217.
- Layer, P., Scholl, D., Newberry, R., 2007. Ages of Igneous Basement From the Komandorsky Islands, Far Western Aleutian Ridge, AGU Fall Meeting Abstracts.
- Le Goff, M., Henry, B., & Daly, L. (1992). Practical method for drawing a VGP path. *Physics of the earth and planetary interiors*, 70(3-4), 201-204.

- Lee, G.H., Kim, B., 2002. Infill history of the Ulleung Basin, East Sea (Sea of Japan) and implications on source rocks and hydrocarbons. *Marine and Petroleum Geology* 19, 829-845.
- Lee, G.H., Kim, H.J., Han, S.J., Kim, D.C., 2001. Seismic stratigraphy of the deep Ulleung Basin in the East Sea (Japan Sea) back-arc basin. *Marine and Petroleum Geology* 18, 615-634.
- Lee, G.H., Yoon, Y., Nam, B.H., Lim, H., Kim, Y.-S., Kim, H.J., Lee, K., 2011. Structural evolution of the southwestern margin of the Ulleung Basin, East Sea (Japan Sea) and tectonic implications. *Tectonophysics* 502, 293-307.
- Lelikov, E., Emelyanova, T., 2011. Geology and volcanism of the underwater Vityaz Ridge (Pacific slope of the Kuril Island Arc). *Oceanology* 51, 315-328.
- Lelikov, E., Pugachev, A., 2016. Granitoid magmatism of the Japan and Okhotsk seas. *Petrology* 24, 196-213.
- Lemaux, J., Gordon, R.G., Royer, J.-Y.J.G., 2002. Location of the Nubia-Somalia boundary along the Southwest Indian ridge. 30, 339-342.
- Leroy, S., Mauffret, A., Patriat, P. and Mercier de Lépinay, B., (2000). An alternative interpretation of the Cayman trough evolution from a reidentification of magnetic anomalies. *Geophysical Journal International*, 141(3): 539-557.
- Levashova, N. M., Bazhenov, M. L., & Shapiro, M. N. (1997). Late Cretaceous paleomagnetism of the East Ranges island arc complex, Kamchatka: Implications for terrane movements and kinematics of the northwest Pacific. *Journal of Geophysical Research*, 102(B11).
- Levashova, N. M., Bazhenov, M. L., Meert, J. G., Danukalov, K. N., Golovanova, I. V., Kuznetsov, N. B., & Fedorova, N. M., 2015. Paleomagnetism of upper Ediacaran clastics from the South Urals: Implications to paleogeography of Baltica and the opening of the Iapetus Ocean. *Gondwana Res.*, 28(1), 191-208.
- Levashova, N. M., Bazhenov, M. L., Meert, J. G., Kuznetsov, N. B., Golovanova, I. V., Danukalov, K. N., & Fedorova, N. M., 2013. Paleogeography of Baltica in the Ediacaran: Paleomagnetic and geochronological data from the clastic Zigán Formation, South Urals. *Precambrian Res.*, 236, 16-30.
- Levashova, N. M., Shapiro, M. N., & Bazhenov, M. L. (1998). Late Cretaceous paleomagnetic data from the Median Range of Kamchatka, Russia: Tectonic implications. *Earth and Planetary Science Letters*, 163(1-4), 235-246.
- Levashova, N.M., Shapiro, M.N., Beniamovsky, V.N., Bazhenov, M.L., 2000. Paleomagnetism and geochronology of the Late Cretaceous-Paleogene island arc complex of the Kronotsky Peninsula, Kamchatka, Russia: Kinematic implications. *Tectonics* 19, 834-851.
- Li, S., Advokaat, E. L., van Hinsbergen, D. J., Koymans, M., Deng, C., & Zhu, R. (2017). Paleomagnetic constraints on the Mesozoic-Cenozoic paleolatitudinal and rotational history of Indochina and South China: Review and updated kinematic reconstruction. *Earth-Science Reviews*, 171, 58-77.
- Li, S., Deng, C., Yao, H., Huang, S., Liu, C., He, H., ... & Zhu, R., 2013. Magnetostratigraphy of the Dali Basin in Yunnan and implications for late Neogene rotation of the southeast margin of the Tibetan Plateau. *J. Geophys. Res.*, 118(3), 791-807.
- Li, S., van Hinsbergen, D. J., Najman, Y., Liu-Zeng, J., Deng, C., & Zhu, R. (2020). Does pulsed Tibetan deformation correlate with Indian plate motion changes?. *Earth and Planetary Science Letters*, 536, 116144.
- Li, S., van Hinsbergen, D. J., Shen, Z., Najman, Y., Deng, C., & Zhu, R., 2020b. Anisotropy of magnetic susceptibility (AMS) analysis of the Gonjo Basin as an independent constraint to date Tibetan shortening pulses. *Geophys. Res. Lett.*, 47(9).
- Li, Y. X., & Kodama, K. P., 2016. Detecting and correcting for paleomagnetic inclination shallowing of sedimentary rocks: A review. *Front. Earth Sci.*, 4, 7.
- Li, Z. X., Liu, Y., & Ernst, R. (2023). A dynamic 2000–540 Ma Earth history: From cratonic amalgamation to the age of supercontinent cycle. *Earth-Science Reviews*, 104336.
- Liao, J.-P., Jahn, B.-M., Alexandrov, I., Chung, S.-L., Zhao, P., Ivin, V., Usuki, T., 2018. Petrogenesis of Mid-Eocene granites in South Sakhalin, Russian Far East: Juvenile crustal growth and comparison with granitic magmatism in Hokkaido and Sikhote-Alin. *Journal of Asian Earth Sciences*.
- Liao, J.P., Alexandrov, I., Jahn, B.-m., 2016. Eocene Granitoids of the Okhotsk Complex in Sakhalin Island, Russian Far East: Petrogenesis and tectonic implications from zircon U-Pb ages, geochemical and Sr-Nd isotopic characteristics, EGU General Assembly Conference Abstracts, p. 6720.
- Lin, Y. A., Colli, L., & Wu, J. (2022). NW Pacific-Panthalassa Intra-Oceanic Subduction During Mesozoic Times From Mantle Convection and Geoid Models. *Geochemistry, Geophysics, Geosystems*, 23(11),

e2022GC010514.

- Linares, E., & Valencio, D. A. (1975). Paleomagnetism and K-Ar ages of some trachybasaltic dikes from Río de Los Molinos, Province of Córdoba, Republic of Argentina. *Journal of Geophysical Research*, 80(23), 3315-3321. doi:10.1029/JB080i023p03315
- Lippert, P. C., van Hinsbergen, D. J. J., & Dupont-Nivet, G. (2014). Early Cretaceous to present latitude of the central proto-Tibetan Plateau: A paleomagnetic synthesis with implications for Cenozoic tectonics, paleogeography, and climate of Asia. *Special Paper of the Geological Society of America*, 507, 1–21. [https://doi.org/10.1130/2014.2507\(01\)](https://doi.org/10.1130/2014.2507(01))
- Liu, X., Zhao, D., Li, S., Wei, W., 2017. Age of the subducting Pacific slab beneath East Asia and its geodynamic implications. *Earth and Planetary Science Letters* 464, 166-174.
- Livermore, R. A., Vine, F. J., & Smith, A. G. (1984). Plate motions and the geomagnetic field—II. Jurassic to Tertiary. *Geophysical Journal International*, 79(3), 939-961.
- Lock, J., and McElhinny, M. W. (1991). Database design. In *The Global Paleomagnetic Database* (pp. 317-327). Springer, Dordrecht.
- Lotfy, H., & van der Voo, R. (2007). Tropical northeast Africa in the middle–late Eocene: Paleomagnetism of the marine-mammals sites and basalts in the Fayum province, Egypt. *Journal of African Earth Sciences*, 47(3), 135-152. doi:10.1016/j.jafrearsci.2006.12.005
- Luchitskaya, M.V., Solov'ev, A.V., Hourigan, J.K., 2008. Two stages of granite formation in the Sredinnyi Range, Kamchatka: Tectonic and geodynamic setting of granitic rocks. *Geotectonics* 42, 286-304.
- Luchitskaya, M.V., Soloviev, A.V., 2012. Early Eocene magmatism in the Sredinnyi Range, Kamchatka: Composition and geodynamic aspects. *Petrology* 20, 147-187.
- Maeda, J.I., 1990. Opening of the Kuril Basin deduced from the magmatic history of Central Hokkaido, North Japan. *Tectonophysics* 174, 235-255.
- Maffione, M., Hinsbergen, D.J., 2018. Reconstructing plate boundaries in the Jurassic Neo-Tethys from the East and West Vardar Ophiolites (Greece, Serbia). *Tectonics*.
- Maffione, M., Thieulot, C., van Hinsbergen, D.J., Morris, A., Plümpner, O., Spakman, W., 2015. Dynamics of intraoceanic subduction initiation: 1. Oceanic detachment fault inversion and the formation of supra-subduction zone ophiolites. *Geochemistry, Geophysics, Geosystems* 16, 1753-1770.
- Malahoff, A., Kroenke, L.W., Cherkis, N., Brozena, J., 1994. Magnetic and tectonic fabric of the North Fiji Basin and Lau Basin. Basin formation, ridge crest processes, and metallogenesis in the North Fiji Basin. Springer, pp. 49-61.
- Mankinen, E. A. (2008). Paleomagnetic study of late Miocene through Pleistocene igneous rocks from the southwestern USA: Results from the historic collections of the U.S. Geological Survey Menlo Park laboratory. *Geochemistry, Geophysics, Geosystems*, 9(5), n/a-n/a. doi:10.1029/2008gc001957
- Mankinen, E. A., & Cox, A. (1988). Paleomagnetic investigation of some volcanic rocks from the McMurdo volcanic province, Antarctica. *Journal of Geophysical Research*, 93(B10). doi:10.1029/JB093iB10p11599
- Maron, M., Rigo, M., Bertinelli, A., Katz, M. E., Godfrey, L., Zaffani, M., & Muttoni, G., 2015. Magnetostratigraphy, biostratigraphy, and chemostratigraphy of the Pignola-Abriola section: New constraints for the Norian-Rhaetian boundary. *Geol. Soc. Am. Bull.*, 127(7-8), 962-974.
- Martin-Short, R., Allen, R.M., Bastow, I.D., 2016. Subduction geometry beneath south central Alaska and its relationship to volcanism. *Geophysical Research Letters* 43, 9509-9517.
- Martin, A. K. (2011). Double saloon door tectonics in the Japan Sea, Fossa magna, and the Japanese Island arc. *Tectonophysics*, 498(1-4), 45-65.
- Martynov, A.Y., Kimura, J.I., Martynov, Y.A., Rybin, A.V., 2010. Geochemistry of late Cenozoic lavas on Kunashir Island, Kurile arc. *Island Arc* 19, 86-104.
- Martynov, Y.A., Khanchuk, A.I., Grebennikov, A.V., Chashchin, A.A., Popov, V.K., 2017. Late Mesozoic and Cenozoic volcanism of the East Sikhote-Alin area (Russian Far East): A new synthesis of geological and petrological data. *Gondwana Research* 47, 358-371.
- Matthews, K.J., Williams, S.E., Whittaker, J.M., Müller, R.D., Seton, M., Clarke, G.L., 2015. Geologic and kinematic constraints on Late Cretaceous to mid Eocene plate boundaries in the southwest Pacific. *Earth-Science Reviews* 140, 72-107.
- McElhinny, M. W., & McFadden, P. L. (1997). Paleosecular variation over the past 5 Myr based on a new generalized database. *Geophysical Journal International*, 131(2), 240-252.
- McElhinny, M. W., and McFadden, P. L. (2000). *Paleomagnetism: continents and oceans*. Elsevier.

- McElhinny, M. W., Embleton, B. J. J., and Wellman, P. (1974). A synthesis of Australian Cenozoic paleomagnetic results. *Geophysical Journal International*, 36(1), 141-151.
- McEnroe, S. A. (1996). North America during the Lower Cretaceous: New paleomagnetic constraints from intrusions in New England. *Geophysical Journal International*, 126(2), 477-494.
- McFadden, P. L., & McElhinny, M. W. (1988). The combined analysis of remagnetization circles and direct observations in paleomagnetism. *Earth and Planetary Science Letters*, 87(1-2), 161-172. [https://doi.org/10.1016/0012-821X\(88\)90072-6](https://doi.org/10.1016/0012-821X(88)90072-6)
- McFadden, P. L., and McElhinny, M. W. (1995). Combining groups of paleomagnetic directions or poles. *Geophysical Research Letters*, 22(16), 2191-2194.
- McFadden, P. L., Merrill, R. T., McElhinny, M. W., & Lee, S. (1991). Reversals of the Earth's magnetic field and temporal variations of the dynamo families. *Journal of Geophysical Research: Solid Earth*, 96(B3), 3923-3933.
- McQuarrie, N., & Wernicke, B. P. (2005). An animated tectonic reconstruction of southwestern North America since 36 Ma. *Geosphere*, 1(3), 147-172.
- Meert, J. G., & Tamrat, E. (2006). Paleomagnetic evidence for a stationary Marion hotspot: Additional paleomagnetic data from Madagascar. *Gondwana Research*, 10(3-4), 340-348. doi:10.1016/j.gr.2006.04.008
- Meert, J. G., Pivarunas, A. F., Evans, D. A., Pisarevsky, S. A., Pesonen, L. J., Li, Z. X., ... and Salminen, J. M. (2020). The magnificent seven: a proposal for modest revision of the quality index. *Tectonophysics*, 790, 228549.
- Meijers, M. J., Hamers, M. F., van Hinsbergen, D. J., van der Meer, D. G., Kitchka, A., Langereis, C. G., & Stephenson, R. A., 2010a. New late Paleozoic paleopoles from the Donbas Foldbelt (Ukraine): Implications for the Pangea A vs. B controversy. *Earth Planet. Sci. Lett.*, 297(1-2), 18-33.
- Meijers, M. J., Kaymakci, N., van Hinsbergen, D. J., Langereis, C. G., Stephenson, R. A., & Hippolyte, J. C., 2010b. Late Cretaceous to Paleocene oroclinal bending in the central Pontides (Turkey). *Tectonics*, 29(4).
- Meijers, M. J., Smith, B., Kirscher, U., Mensink, M., Sosson, M., Rolland, Y., ... & Müller, C., 2015. A paleolatitude reconstruction of the South Armenian Block (Lesser Caucasus) for the Late Cretaceous: Constraints on the Tethyan realm. *Tectonophysics*, 644, 197-219.
- Mejia, V., Böhnell, H., Opdyke, N. D., Ortega-Rivera, M. A., Lee, J. K. W., & Aranda-Gomez, J. J. (2005). Paleosecular variation and time-averaged field recorded in late Pliocene-Holocene lava flows from Mexico. *Geochemistry, Geophysics, Geosystems*, 6(7), n/a-n/a. doi:10.1029/2004gc000871
- Meng, J., Coe, R. S., Wang, C., Gilder, S. A., Zhao, X., Liu, H., ... & Li, S., 2017. Reduced convergence within the Tibetan Plateau by 26 Ma? *Geophys. Res. Lett.*, 44(13), 6624-6632.
- Merdith, A. S., Collins, A. S., Williams, S. E., Pisarevsky, S., Foden, J. D., Archibald, D. B., ... & Müller, R. D. (2017). A full-plate global reconstruction of the Neoproterozoic. *Gondwana Research*, 50, 84-134.
- Merdith, A. S., Williams, S. E., Collins, A. S., Tetley, M. G., Mulder, J. A., Blades, M. L., ... & Müller, R. D. (2021). Extending full-plate tectonic models into deep time: Linking the Neoproterozoic and the Phanerozoic. *Earth-Science Reviews*, 214, 103477.
- Merrill, R. T., & McFadden, P. L. (2003). The geomagnetic axial dipole field assumption. *Physics of the Earth and Planetary Interiors*, 139(3-4), 171-185. <https://doi.org/10.1016/j.pepi.2003.07.016>
- Metelkin, D. V., Kazansky, A. Y., Bragin, V. Y., Tsel'movich, V. A., Lavrenchuk, A. V., and Kungurtsev, L. V. (2007). Paleomagnetism of the Late Cretaceous intrusions from the Minusa trough (southern Siberia). *Russian Geology and Geophysics*, 48(2), 185-198.
- Milanese, F., Rapalini, A., Slotznick, S. P., Tobin, T. S., Kirschvink, J., & Olivero, E., 2019. Late Cretaceous paleogeography of the Antarctic Peninsula: New paleomagnetic pole from the James Ross Basin. *J. S. Am. Earth Sci.*, 91, 131-143.
- Miller, E.L., Meisling, K.E., Akinin, V.V., Brumley, K., Coakley, B.J., Gottlieb, E.S., Hoiland, C.W., O'Brien, T.M., Soboleva, A., Toro, J., 2018. Circum-Arctic Lithosphere Evolution (CALE) Transect C: displacement of the Arctic Alaska–Chukotka microplate towards the Pacific during opening of the Amerasia Basin of the Arctic. Geological Society, London, Special Publications 460, 57-120.
- Minyuk, P., Stone, D., 2009. Paleomagnetic determination of paleolatitude and rotation of Bering Island (Komandorsky Islands) Russia: Comparison with rotations in the Aleutian Islands and Kamchatka. Stephan Mueller Special Publication Series 4, 329-348.
- Mitchell, R. N. (2014). True polar wander and supercontinent cycles: Implications for lithospheric elasticity

- and the triaxial Earth. *American Journal of Science*, 314(5), 966-979.
- Mitchell, R. N., & Jing, X. (2023). Paleoproterozoic plate motion: Not so fast. *Proceedings of the National Academy of Sciences*, 120(1), e2218383120.
- Mitchell, R. N., Kilian, T. M., & Evans, D. A. (2012). Supercontinent cycles and the calculation of absolute paleolongitude in deep time. *Nature*, 482(7384), 208-211.
- Mitchell, R. N., Kilian, T. M., Raub, T. D., Evans, D. A., Bleeker, W., & Maloof, A. C. (2011). Sutton hotspot: Resolving Ediacaran-Cambrian Tectonics and true polar wander for Laurentia. *American Journal of Science*, 311(8), 651-663.
- Mitchell, R. N., Thissen, C. J., Evans, D. A., Slotznick, S. P., Coccioni, R., Yamazaki, T., & Kirschvink, J. L. (2021). A Late Cretaceous true polar wander oscillation. *Nature Communications*, 12(1), 3629.
- Molina-Garza, R. S., Acton, G. D., and Geissman, J. W. (1998). Carboniferous through Jurassic paleomagnetic data and their bearing on rotation of the Colorado Plateau. *Journal of Geophysical Research: Solid Earth*, 103(B10), 24179-24188.
- Molina-Garza, R. S., van Hinsbergen, D. J. J., Rogers, R. D., Ganerød, M., and Dekkers, M. J. (2012). The Padre Miguel Ignimbrite Suite, central Honduras: Paleomagnetism, geochronology, and tectonic implications. *Tectonophysics*, 574-575, 144-157.
- Morel, P., & Irving, E. (1981). Paleomagnetism and the evolution of Pangea. *Journal of Geophysical Research: Solid Earth*, 86(B3), 1858-1872.
- Morgan, W. J. (1971). Convection plumes in the lower mantle. *Nature*, 230, 42-43.
- Morgan, W. J. (1981). Hotspot tracks and the opening of the Atlantic and Indian Oceans. *The Sea*, vol. 7, *The Oceanic Lithosphere*, 443-487.
- Mortimer, N., van den Bogaard, P., Hoernle, K., Timm, C., Gans, P., Werner, R., Riefstahl, F., 2019. Late Cretaceous oceanic plate reorganization and the breakup of Zealandia and Gondwana. *Gondwana Research* 65, 31-42.
- Moulin, M., Fluteau, F., Courtillot, V., Marsh, J., Delpech, G., Quidelleur, X., et al. (2011). An attempt to constrain the age, duration, and eruptive history of the Karoo flood basalt: Naude's Nek section (South Africa). *Journal of Geophysical Research*, 116(B7).
- Moulin, M., Fluteau, F., Courtillot, V., Marsh, J., Delpech, G., Quidelleur, X., & Gérard, M. (2017). Eruptive history of the Karoo lava flows and their impact on early Jurassic environmental change. *Journal of Geophysical Research: Solid Earth*, 122(2), 738-772.
- Mueller, C. O., & Jokat, W. (2019). The initial Gondwana break-up: a synthesis based on new potential field data of the Africa-Antarctica Corridor. *Tectonophysics*, 750, 301-328.
- Müller, R. D., Flament, N., Cannon, J., Tetley, M. G., Williams, S. E., Cao, X., ... & Merdith, A. (2022). A tectonic-rules-based mantle reference frame since 1 billion years ago—implications for supercontinent cycles and plate–mantle system evolution. *Solid Earth*, 13(7), 1127-1159.
- Muller, R. D., Royer, J. Y., & Lawver, L. A. (1993). Revised plate motions relative to the hotspots from combined Atlantic and Indian Ocean hotspot tracks. *Geology*, 21(3), 275-278.
- Müller, R. D., Royer, J. Y., Cande, S. C., Roest, W. R., & Maschenkov, S. (1999). New constraints on the Late Cretaceous/Tertiary plate tectonic evolution of the Caribbean. *Sedimentary basins of the world*, 4, 33-59.
- Müller, R. D., Sdrolias, M., Gaina, C., & Roest, W. R. (2008). Age, spreading rates, and spreading asymmetry of the world's ocean crust. *Geochemistry, Geophysics, Geosystems*, 9(4).
- Müller, R. D., Seton, M., Zahirovic, S., Williams, S. E., Matthews, K. J., Wright, N. M., ... and Cannon, J. (2016). Ocean basin evolution and global-scale plate reorganization events since Pangea breakup. *Annual Review of Earth and Planetary Sciences*, 44(1), 107-138.
- Müller, R. D., Zahirovic, S., Williams, S. E., Cannon, J., Seton, M., Bower, D. J., . . . Liu, S. (2019). A global plate model including lithospheric deformation along major rifts and orogens since the Triassic. *Tectonics*, 38(6), 1884-1907.
- Musgrave, R. J. (1989). A weighted least-squares fit of the Australian apparent polar wander path for the last 100 Myr. *Geophysical Journal International*, 96(2), 231-243.
- Muttoni, G., and Kent, D. V. (2019). Jurassic monster polar shift confirmed by sequential paleopoles from Adria, promontory of Africa. *Journal of Geophysical Research: Solid Earth*, 124(4), 3288-3306.
- Muttoni, G., Dallanave, E., & Channell, J. E. T. (2013). The drift history of Adria and Africa from 280 Ma to Present, Jurassic true polar wander, and zonal climate control on Tethyan sedimentary facies. *Paleogeography, Paleoclimatology, Paleocology*, 386, 415-435.

- Muttoni, G., Erba, E., Kent, D. V., & Bachtadse, V. (2005). Mesozoic Alpine facies deposition as a result of past latitudinal plate motion. *Nature*, 434(7029), 59-63.
- Muttoni, G., Kent, D. V., Garzanti, E., Brack, P., Abrahamsen, N., & Gaetani, M. (2003). Early permian pangea 'B' to late permian pangea 'A' Earth and Planetary Science Letters, 215(3-4), 379-394.
- Muttoni, G., Visconti, A., Channell, J. E., Casellato, C. E., Maron, M., & Jadoul, F., 2018. An expanded Tethyan Kimmeridgian magneto-biostratigraphy from the S'Adde section (Sardinia): Implications for the Jurassic timescale. *Paleogeogr. Paleoclimatol. Paleocol.*, 503, 90-101.
- Nakahigashi, K., Shinohara, M., Yamada, T., Uehira, K., Mochizuki, K., Kanazawa, T., 2013. Seismic structure of the extended continental crust in the Yamato Basin, Japan Sea, from ocean bottom seismometer survey. *Journal of Asian Earth Sciences* 67-68, 199-206.
- Nakajima, T., 2013. Late Cenozoic tectonic events and Intra-arc Basin development in northeast Japan, Mechanism of Sedimentary Basin Formation-Multidisciplinary Approach on Active Plate Margins. InTech.
- Nakajima, T., Hirooka, K., 1986. Clockwise rotation of Southwest Japan inferred from paleomagnetism of Miocene rocks in Fukui Prefecture. *Journal of geomagnetism and geoelectricity* 38, 513-522.
- Nishisaka, H., Shinohara, M., Sato, T., Hino, R., Mochizuki, K., Kasahara, J., 2001. Crustal structure of the Yamato basin and the margin of the northeastern Japan Sea using ocean bottom seismographs and controlled sources. *Journal of the Seismological Society of Japan* 54, 365-379.
- Nohda, S., 2009. Formation of the Japan Sea basin: reassessment from Ar–Ar ages and Nd–Sr isotopic data of basement basalts of the Japan Sea and adjacent regions. *Journal of Asian Earth Sciences* 34, 599-609.
- Nokleberg, W.J., Parfenov, L.M., Monger, J.W., Baranov, B.V., Byalobzhesky, S.G., Bundtzen, T.K., Fenney, T.D., Fujita, K., Gordey, S.P., Grantz, A., 1996. Summary Circum-North Pacific tectonostratigraphic terrane map. US Geological Survey.
- Nokleberg, W.J., Parfenov, L.M., Monger, J.W., Norton, I.O., Khanchuk, A.I., Stone, D.B., Scotese, C.R., Scholl, D.W., Fujita, K., 2000. Phanerozoic tectonic evolution of the Circum-North Pacific.
- O'Connor, J.M., Steinberger, B., Regelous, M., Koppers, A.A., Wijbrans, J.R., Haase, K.M., Stoffers, P., Jokat, W., Garbe-Schönberg, D., 2013. Constraints on past plate and mantle motion from new ages for the Hawaiian-Emperor Seamount Chain. *Geochemistry, Geophysics, Geosystems* 14, 4564-4584.
- O'Neill, C., Müller, D., & Steinberger, B. (2005). On the uncertainties in hot spot reconstructions and the significance of moving hot spot reference frames. *Geochemistry, Geophysics, Geosystems*, 6(4).
- Ogg, J.G., Ogg, G., Gradstein, F.M., 2016. A concise geologic time scale: 2016. Elsevier.
- Oliva-Urcia, B., Gil-Peña, I., Maestro, A., López-Martínez, J., Galindo-Zaldívar, J., Soto, R., et al. (2016). Paleomagnetism from Deception Island (South Shetlands archipelago, Antarctica), new insights into the interpretation of the volcanic evolution using a geomagnetic model. *International Journal of Earth Sciences*, 105(5), 1353-1370.
- Oncken, O., Hindle, D., Kley, J., Elger, K., Victor, P., Schemmann, K., 2006. Deformation of the central Andean upper plate system—Facts, fiction, and constraints for plateau models, *The Andes*. Springer, pp. 3-27.
- Opdyke, M. D., & Channell, J. E., 1996. *Magnetic stratigraphy*. Academic Press.
- Otofujii, Y. I., Matsuda, T., & Nohda, S. (1985). Opening mode of the Japan Sea inferred from the paleomagnetism of the Japan Arc. *Nature*, 317(6038), 603-604.
- Otofujii, Y.-i., Itaya, T., Matsuda, T., 1991. Rapid rotation of southwest Japan—paleomagnetism and K-Ar ages of Miocene volcanic rocks of southwest Japan. *Geophysical Journal International* 105, 397-405.
- Otofujii, Y.-i., Kambara, A., Matsuda, T., Nohda, S., 1994. Counterclockwise rotation of Northeast Japan: Paleomagnetic evidence for regional extent and timing of rotation. *Earth and Planetary Science Letters* 121, 503-518.
- Otofujii, Y.-i., Matsuda, T., 1983. Paleomagnetic evidence for the clockwise rotation of Southwest Japan. *Earth and Planetary Science Letters* 62, 349-359.
- Otofujii, Y.-i., Matsuda, T., 1984. Timing of rotational motion of Southwest Japan inferred from paleomagnetism. *Earth and Planetary Science Letters* 70, 373-382.
- Otofujii, Y.-i., Nishizawa, Y., Tamai, M., Matsuda, T., 1997. Paleomagnetic and chronological study of Miocene welded tuffs in the northern part of Central Japan: tectonic implications for the latest stage of arc formation of Japan. *Tectonophysics* 283, 263-278.
- Otofujii, Y.I., 1996. Large tectonic movement of the Japan Arc in late Cenozoic times inferred from paleomagnetism: Review and synthesis. *Island Arc* 5, 229-249.

- Owen-Smith, T. M., Ganerød, M., van Hinsbergen, D. J., Gaina, C., Ashwal, L. D., & Torsvik, T. H. (2019). Testing early cretaceous Africa–South America fits with new paleomagnetic data from the Etendeka Magmatic Province (Namibia). *Tectonophysics*, 760, 23-35.
- Parés, J. M., van der Pluijm, B. A., & Dinarès-Turell, J., 1999. Evolution of magnetic fabrics during incipient deformation of mudrocks (Pyrenees, northern Spain). *Tectonophysics*, 307(1-2), 1-14.
- Parfenov, L., Badarch, G., Berzin, N., Khanchuk, A., Kuzmin, M., Nokleberg, W., Prokopiev, A., Ogasawara, M., Yan, H., 2009. Summary of Northeast Asia geodynamics and tectonics. *Stephan Mueller Special Publication Series* 4, 11-33.
- Parfenov, L., Natal'in, B., 1986. Mesozoic tectonic evolution of northeastern Asia. *Tectonophysics* 127, 291-304.
- Parfenov, L.M., Nokleberg, W.J., Berzin, N.A., Badarch, G., Dril, S.I., Gerel, O., Goryachev, N.A., Khanchuk, A.I., Obolenskiy, M.I.K.m., Alexander, A., 2011. Tectonic and metallogenic model for northeast Asia. *US Geological Survey*.
- Parsons, A. J., Sigloch, K., & Hosseini, K. (2021). Australian Plate Subduction is Responsible for Northward Motion of the India-Asia Collision Zone and 1,000 km Lateral Migration of the Indian Slab. *Geophysical Research Letters*, 48(18), e2021GL094904.
- Pastor-Galán, D. (2022). From supercontinent to superplate: Late Paleozoic Pangea's inner deformation suggests it was a short-lived superplate. *Earth-Science Reviews*, 226, 103918.
- Pavoni, N. (2008). Present true polar wander in the frame of the Geotectonic Reference System. *Swiss Journal of Geosciences*, 101, 629-636.
- Pease, V., Miller, E., Wyld, S.J., Sokolov, S., Akinin, V., Wright, J.E., 2018. U–Pb zircon geochronology of Cretaceous arc magmatism in eastern Chukotka, NE Russia, with implications for Pacific plate subduction and the opening of the Amerasia Basin. *Geological Society, London, Special Publications* 460, 159-182.
- Pechersky, D.M., Levashova, N.M., Shapiro, M.N., Bazhenov, M.L., Sharonova, Z.V., 1997. Paleomagnetism of Paleogene volcanic series of the KamchatskyMys Peninsula, East Kamchatka: The motion of an active island arc. *Tectonophysics* 273, 219-237.
- Phillips, J. D., and Forsyth, D. (1972). Plate tectonics, paleomagnetism, and the opening of the Atlantic. *Geological Society of America Bulletin*, 83(6), 1579-1600.
- Pierce, J., Zhang, Y., Hodgin, E. B., & Swanson-Hysell, N. L. (2022). Quantifying Inclination Shallowing and Representing Flattening Uncertainty in Sedimentary Paleomagnetic Poles. *Geochemistry, Geophysics, Geosystems*, 23(11), e2022GC010682.
- Piip, V., Rodnikov, A., 2004. The Sea of Okhotsk crust from deep seismic sounding data. *Russian Journal of Earth Sciences* 6.
- Piper, J. D. A. (1974). Proterozoic crustal distribution, mobile belts and apparent polar movements. *Nature*, 251(5474), 381-384.
- Pisarevsky, S. A. (2005). New edition of the global paleomagnetic database. *EOS Transactions, American Geophysical Union*, 86, 170.
- Piskarev, A., Butsenko, V., Poselov, V., Savin, V., 2012. Deep structure of the crust beneath the Sea of Okhotsk inferred from 3D seismic density modeling. *Oceanology* 52, 411-421.
- Portnyagin, M., Hoernle, K., Savelyev, D., 2009. Ultra-depleted melts from Kamchatkan ophiolites: Evidence for the interaction of the Hawaiian plume with an oceanic spreading center in the Cretaceous? *Earth and Planetary Science Letters* 287, 194-204.
- Portnyagin, M., Savelyev, D., Hoernle, K., Hauff, F., Garbe-Schönberg, D., 2008. Mid-Cretaceous Hawaiian tholeiites preserved in Kamchatka. *Geology* 36, 903.
- Qi, C., Zhao, D., Chen, Y., 2007. Search for deep slab segments under Alaska. *Physics of the Earth and Planetary Interiors* 165, 68-82.
- Rapalini, A. E., 2006. New Late Proterozoic paleomagnetic pole for the Rio de la Plata craton: implications for Gondwana. *Precambrian Res.*, 147(3-4), 223-233.
- Raznitsin, Y.N., 2012. Geodynamics of ophiolites and formation of hydrocarbon fields on the shelf of eastern Sakhalin. *Geotectonics* 46, 1-15.
- Replumaz, A., & Tapponnier, P. (2003). Reconstruction of the deformed collision zone between India and Asia by backward motion of lithospheric blocks. *Journal of Geophysical Research: Solid Earth*, 108(B6).
- Reynolds, R. L., Hudson, M. R., & Hon, K. (1986). Paleomagnetic evidence for the timing of collapse and resurgence of the Lake City Caldera, San Juan Mountains, Colorado. *Journal of Geophysical Research*,

- 91(B9). doi:10.1029/JB091iB09p09599
- Riisager, J., Perrin, M., Riisager, P., & Ruffet, G. (2000). Paleomagnetism, paleointensity and geochronology of Miocene basalts and baked sediments from Velay Oriental, French Massif Central. *Journal of Geophysical Research: Solid Earth*, 105(B1), 883-896. doi:10.1029/1999jb900337
- Riisager, J., Riisager, P., & Pedersen, A. K. (2003). Paleomagnetism of large igneous provinces: case-study from West Greenland, North Atlantic igneous province. *Earth and Planetary Science Letters*, 214(3-4), 409-425.
- Riisager, J., Riisager, P., & Pedersen, A. K. (2003). The C27n-C26r geomagnetic polarity reversal recorded in the west Greenland flood basalt province: How complex is the transitional field? *Journal of Geophysical Research: Solid Earth*, 108(B3).
- Riisager, P., Knight, K. B., Baker, J. A., Ukstins Peate, I., Al-Kadasi, M., Al-Subbary, A., & Renne, P. R. (2005). Paleomagnetism and ⁴⁰Ar/³⁹Ar Geochronology of Yemeni Oligocene volcanics: Implications for timing and duration of Afro-Arabian traps and geometry of the Oligocene paleomagnetic field. *Earth and Planetary Science Letters*, 237(3-4), 647-672. doi:10.1016/j.epsl.2005.06.016
- Rikhtyer, A., 1995. Structure of the metamorphic complex of the Central Kamchatka Massif. *Geotectonics* 29, 65-72.
- Robert, B., Besse, J., Blein, O., Greff-Lefftz, M., Baudin, T., Lopes, F., ... & Belbadaoui, M. (2017). Constraints on the Ediacaran inertial interchange true polar wander hypothesis: A new paleomagnetic study in Morocco (West African Craton). *Precambrian Research*, 295, 90-116.
- Robert, B., Greff-Lefftz, M., & Besse, J. (2018). True polar wander: A key indicator for plate configuration and mantle convection during the late Neoproterozoic. *Geochemistry, Geophysics, Geosystems*, 19(9), 3478-3495.
- Rodnikov, A.G., Sergeyeva, N.A., Zabarinskaya, L.P., 2013. Ancient subduction zone in Sakhalin Island. *Tectonophysics* 600, 217-225.
- Roest, W. R., & Srivastava, S. P. (1989). Sea-floor spreading in the Labrador Sea: A new reconstruction. *Geology*, 17(11), 1000-1003.
- Roperch, P., Dupont-Nivet, G., Guillot, S., Goussin, F., Huang, W., Replumaz, A., ... & Song, B., 2017. Paleomagnetic constraints on early collisional deformation along the eastern margin of the Qiantang terrane (Tibetan plateau) at 50 and 37 Ma. In EGU General Assembly Conference Abstracts, 19, 9476.
- Rose, I. R., Zhang, Y., and Swanson-Hysell, N. L. (2022). Bayesian paleomagnetic Euler pole inversion for paleogeographic reconstruction and analysis. *Journal of Geophysical Research: Solid Earth*, 127(10), e2021JB023890.
- Rostovtseva, Y.V., Shapiro, M., 1998. Provenance of the Paleocene-Eocene clastic rocks of the Komandorsky Islands. *Sedimentology* 45, 201-216.
- Rowley, D. B. (2019). Comparing paleomagnetic study means with apparent wander paths: A case study and paleomagnetic test of the Greater India versus Greater Indian Basin hypotheses. *Tectonics*, 38(2), 722-740.
- Royer, J.Y., Chang, T.J.J.o.G.R.S.E., 1991. Evidence for relative motions between the Indian and Australian plates during the last 20 my from plate tectonic reconstructions: Implications for the deformation of the Indo-Australian plate. 96, 11779-11802.
- Rubenstone, J.L., 1984. Geology and geochemistry of early Tertiary submarine volcanic rocks of the Aleutian Islands, and their bearing on the development of the Aleutian Island Arc.
- Ruiz González, V., Renda, E. M., Vizán, H., Ganerød, M., Puigdomenech, C. G., and Zaffarana, C. B. (2022). Deformation along the Deseado Massif (Patagonia, Argentina) during the Jurassic Period and its relationship with the Gondwana breakup: paleomagnetic and geochronological constraints. *Tectonophysics*, 834.
- Ruiz-Martínez, V. C., Urrutia-Fucugauchi, J., & Osete, M. L. (2010). Paleomagnetism of the Western and Central sectors of the Trans-Mexican volcanic belt-implications for tectonic rotations and paleosecular variation in the past 11 Ma. *Geophysical Journal International*, 180(2), 577-595.
- Runcorn, S. K. (1959). On the hypothesis that the mean geomagnetic field for parts of geological time has been that of a geocentric axial multipole. *Journal of Atmospheric and Terrestrial Physics*, 14(1-2), 167-174.
- Runcorn, S. K., (1956). Paleomagnetic comparisons between Europe and North America. *Proceedings of the Geological Association of Canada*, 8, 77-85.
- Sabadini, R., & Yuen, D. A. (1989). Mantle stratification and long-term polar wander. *Nature*, 339(6223),

- Sager, W. W., & Koppers, A. A. A. (2000). Late Cretaceous polar wander of the Pacific plate: evidence of a rapid true polar wander event. *Science*, 287(5452), 455-459.
- Sahabi, M., Aslanian, D., & Olivet, J. L. (2004). A new starting point for the history of the central Atlantic. *Comptes Rendus Geoscience*, 336(12), 1041-1052.
- Sato, H., 1994. The relationship between Late Cenozoic tectonic events and stress field and basin development in northeast Japan. *Journal of Geophysical Research: Solid Earth* 99, 22261-22274.
- Sato, H., Iwasaki, T., Ikeda, Y., Takeda, T., Matsuta, N., Imai, T., Kurashimo, E., Hirata, N., Sakai, S.i., Elouai, D., 2004a. Seismological and geological characterization of the crust in the southern part of northern Fossa Magna, central Japan. *Earth, planets and space* 56, 1253-1259.
- Sato, K., Kawabata, H., W. Scholl, D., Hyodo, H., Takahashi, K., Suzuki, K., Kumagai, H., 2016. 40 Ar– 39 Ar dating and tectonic implications of volcanic rocks recovered at IODP Hole U1342A and D on Bowers Ridge, Bering Sea. *Deep Sea Research Part II: Topical Studies in Oceanography* 125-126, 214-226.
- Sato, T., No, T., Kodaira, S., Takahashi, N., Kaneda, Y., 2014. Seismic constraints of the formation process on the back-arc basin in the southeastern Japan Sea. *Journal of Geophysical Research: Solid Earth* 119, 1563-1579.
- Sato, T., Shinohara, M., Karp, B.Y., Kulinich, R.G., Isezaki, N., 2004b. P-wave velocity structure in the northern part of the central Japan Basin, Japan Sea with ocean bottom seismometers and airguns. *Earth, planets and space* 56, 501-510.
- Sato, T., Takahashi, N., Miura, S., Fujie, G., Kang, D.-H., Kodaira, S., Kaneda, Y., 2006. Last stage of the Japan Sea back-arc opening deduced from the seismic velocity structure using wide-angle data. *Geochemistry, Geophysics, Geosystems* 7, n/a-n/a.
- Savostin, L., Zonenshain, L., Baranov, B., 1983. *Geology and plate tectonics of the Sea of Okhotsk. Geodynamics of the Western Pacific-Indonesian Region*, 189-221.
- Sawada, Y., Mishiro, Y., Imaoka, T., Yoshida, K., Inada, R., Hisai, K., Kondo, H., Hyodo, M., 2013. K-Ar ages and paleomagnetism of the Miocene in the Izumo Basin, Shimane Prefecture. *Journal of the Geological Society of Japan* 119, 267-284.
- Scealy, J. L., Heslop, D., Liu, J., & Wood, A. T. (2022). Directions Old and New: Paleomagnetism and Fisher (1953) Meet Modern Statistics. *International Statistical Review*, 90(2), 237-258.
- Scheirer, D., Barth, G., Scholl, D., Stern, R., 2016. Geophysical Evidence for the Origin of the Aleutian Basin, AGU Fall Meeting Abstracts.
- Schellart, W., 2017. Andean mountain building and magmatic arc migration driven by subduction-induced whole mantle flow. *Nature communications* 8, 2010.
- Schellart, W., Stegman, D., Freeman, J., 2008. Global trench migration velocities and slab migration induced upper mantle volume fluxes: Constraints to find an Earth reference frame based on minimizing viscous dissipation. *Earth-Science Reviews* 88, 118-144.
- Schellart, W.P., Jessell, M.W., Lister, G.S., 2003. Asymmetric deformation in the backarc region of the Kuril arc, northwest Pacific: New insights from analogue modeling. *Tectonics* 22, n/a-n/a.
- Schepers, G., van Hinsbergen, D.J., Spakman, W., Kosters, M.E., Boschman, L.M., McQuarrie, N., 2017. South-American plate advance and forced Andean trench retreat as drivers for transient flat subduction episodes. *Nature communications* 8, 15249.
- Schettino, A., and Scotese, C. R. (2005). Apparent polar wander paths for the major continents (200 Ma to the present day): a paleomagnetic reference frame for global plate tectonic reconstructions. *Geophysical Journal International*, 163(2), 727-759.
- Schmidt, P. W., Williams, G. E., & McWilliams, M. O., 2009. Paleomagnetism and magnetic anisotropy of late Neoproterozoic strata, South Australia: implications for the paleolatitude of late Cryogenian glaciation, cap carbonate and the Ediacaran System. *Precambrian Res.*, 174(1-2), 35-52.
- Schmidt, V. A. (1990). Circularity of paleomagnetic data sets: an aid in the recognition of contaminating secondary overprints. *Tectonophysics*, 184(1), 11–20. [https://doi.org/10.1016/0040-1951\(90\)90117-Q](https://doi.org/10.1016/0040-1951(90)90117-Q)
- Scholl, D.W., 2007. Viewing the Tectonic Evolution of The Kamchatka-Aleutian (KAT) Connection with an Alaska Crustal Extrusion Perspective. *Volcanism and Subduction: The Kamchatka Region*, 3-35.
- Scholl, D.W., Buffington, E.C., Marlow, M.S., 1975. Plate tectonics and the structural evolution of the Aleutian–Bering Sea region, GSA Special Papers. The Geological Society of America, pp. 1-31.
- Sdrolias, M., Roest, W.R., Müller, R.D., 2004. An expression of Philippine Sea plate rotation: the Parece Vela and Shikoku basins. *Tectonophysics* 394, 69-86.

- Seama, N., Isezaki, N., 1990. Sea-floor magnetization in the eastern part of the Japan Basin and its tectonic implications. *Tectonophysics* 181, 285-297.
- Sears, J. W. (2022). Challenging the dipolar paradigm for Proterozoic Earth.
- Seton, M., Flament, N., Whittaker, J., Müller, R.D., Gurnis, M., Bower, D.J., 2015. Ridge subduction sparked reorganization of the Pacific plate-mantle system 60–50 million years ago. *Geophysical Research Letters* 42, 1732-1740.
- Seton, M., Müller, R. D., Zahirovic, S., Gaina, C., Torsvik, T., Shephard, G., ... and Chandler, M. (2012). Global continental and ocean basin reconstructions since 200 Ma. *Earth-Science Reviews*, 113(3-4), 212-270.
- Shapiro, M. N., & Solov'ev, A. V. (2009). Formation of the Olyutorsky–Kamchatka foldbelt: A kinematic model. *Russian Geology and Geophysics*, 50, 668–681.
- Shapiro, M., Gladenkov, Y.B., Shants'er, A., 1996. Regional angular unconformities in the Cenozoic sequences of Kamchatka. *Stratigr. Geol. Correlation* 4, 567-579.
- Shapiro, M., Solov'ev, A., Garver, G., Shcherbinina, E., Ledneva, G., Brandon, M., 2004. Age of Terrigenous Rocks of Northeastern Karaginskioe Island (Eastern Kamchatka). *Stratigraphy and geological correlation* 12, 188-198.
- Shapiro, M.N., Solov'ev, A.V., 2011. Cenozoic volcanic rocks of North Kamchatka: In search of subduction zones. *Geotectonics* 45, 210-224.
- Shapiro, M.N., Solov'ev, A.V., Hourigan, J.K., 2008. Lateral structural variability in zone of eocene island-arc-continent collision, Kamchatka. *Geotectonics* 42, 469-487.
- Sharp, W.D., Clague, D.A., 2006. 50-Ma initiation of Hawaiian-Emperor bend records major change in Pacific plate motion. *Science* 313, 1281-1284.
- Shive, P. N., & Frerichs, W. E. (1974). Paleomagnetism of the Niobrara Formation in Wyoming, Colorado, and Kansas. *Journal of Geophysical Research*, 79(20), 3001-3007. doi:10.1029/JB079i020p03001
- Shive, P. N., & Pruss, E. F. (1977). A paleomagnetic study of basalt flows from the Absaroka Mountains, Wyoming. *Journal of Geophysical Research*, 82(20), 3039-3048. doi:10.1029/JB082i020p03039
- Sibuet, J.-C., Hsu, S.-K., Le Pichon, X., Le Formal, J.-P., Reed, D., Moore, G., Liu, C.-S., 2002. East Asia plate tectonics since 15 Ma: constraints from the Taiwan region. *Tectonophysics* 344, 103-134.
- Siglöch, K., & Mihalyuk, M. G. (2013). Intra-oceanic subduction shaped the assembly of Cordilleran North America. *Nature*, 496(7443), 50-56.
- Sillitoe, R., 1977. Metallogeny of an Andean-type continental margin in South Korea: Implication for opening of the Japan Sea. Island arcs, deep sea trenches and back arc basins., 303-310.
- Skolotnev, S., Tsukanov, N., Sidorov, E., 2018. New Data on the Composition of Ophiolite Complexes on Karaginskii Island (Eastern Kamchatka), *Doklady Earth Sciences*. Springer, pp. 290-294.
- Smirnov, A. V., & Tarduno, J. A. (2010). Co-location of eruption sites of the Siberian Traps and North Atlantic Igneous Province: implications for the nature of hotspots and mantle plumes. *Earth and Planetary Science Letters*, 297(3-4), 687-690.
- Solov'ev, A., Brandon, M., Garver, J., Shapiro, M., 2001. Kinematics of the Vatyn-Lesnaya Thrust Fault (Southern Koryakia). *Geotectonics* 35, 471-489.
- Solov'ev, A., Hourigan, J., Brandon, M., Garver, J., Grigorenko, E., 2004. The age of the Baraba Formation inferred from the U/Pb (SHRIMP) dating (Sredinnyi Range, Kamchatka): geological consequences. *Stratigr. Geol. Correlation* 12, 418-424.
- Solov'ev, A., Shapiro, M., Garver, J., 2002a. Lesnaya nappe, northern Kamchatka. *Geotectonics* 36, 469-482.
- Solov'ev, A., Shapiro, M., Garver, J., Shcherbinina, E., Kravchenko-Berezhnoy, I., 2002b. New age data from the Lesnaya Group: A key to understanding the timing of arc-continent collision, Kamchatka, Russia. *Island Arc* 11, 79-90.
- Solov'ev, A.V., Garver, J.I., Shapiro, M.N., Brandon, M.T., Hourigan, J.K., 2011. Eocene arc-continent collision in northern Kamchatka, Russian Far East. *Russian Journal of Earth Sciences* 12, 1-13.
- Solov'ev, A., Palechek, T., 2004. New Data on the Age of the Andrianovka Formation, Sredinnyi Range in Kamchatka: Structure of Metamorphic Complexes in Accretion Zone, Proceedings of the Youth School-Conference of XXXVII Tectonic Conference, pp. 86-89.
- Solov'ev, A., Shapiro, M., Garver, J., Lander, A., 2004. Formation of the east Kamchatkan accretionary prism based on fission-track dating of detrital zircons from terrigenous rocks. *Russian Geology and Geophysics* 45, 1237-1247.
- Solov'ev, A.V., Palechek, T.N., Shapiro, M.N., Johnston, S.A., Garver, J.I., Ol'shanetskii, D.M., 2007. New

- data on the Baraba Formation age (the Sredinnyi Range of Kamchatka). *Stratigraphy and Geological Correlation* 15, 112-119.
- Somoza, R. (2007). Eocene paleomagnetic pole for South America: Northward continental motion in the Cenozoic, opening of Drake Passage and Caribbean convergence. *Journal of Geophysical Research*, 112(B3). doi:10.1029/2006jb004610
- Somoza, R., & Zaffarana, C. B. (2008). Mid-Cretaceous polar standstill of South America, motion of the Atlantic hotspots and the birth of the Andean cordillera. *Earth and Planetary Science Letters*, 271(1-4), 267-277. doi:10.1016/j.epsl.2008.04.004
- Somoza, R., Singer, S., & Coira, B. (1996). Paleomagnetism of upper Miocene ignimbrites at the Puna: An analysis of vertical-axis rotations in the Central Andes. *Journal of Geophysical Research: Solid Earth*, 101(B5), 11387-11400. doi:10.1029/95jb03467
- Somoza, R., Singer, S., & Tomlinson, A. (1999). Paleomagnetic study of upper Miocene rocks from northern Chile: Implications for the origin of Late Miocene-Recent tectonic rotations in the southern Central Andes. *Journal of Geophysical Research: Solid Earth*, 104(B10), 22923-22936. doi:10.1029/1999jb900215
- Son, M., Song, C.W., Kim, M.C., Cheon, Y., Cho, H., Sohn, Y.K., 2015. Miocene tectonic evolution of the basins and fault systems, SE Korea: dextral, simple shear during the East Sea (Sea of Japan) opening. *Journal of the Geological Society* 172, 664-680.
- Spada, G., Ricard, Y., & Sabadini, R. (1992). Excitation of true polar wander by subduction. *Nature*, 360, 452-454.
- Spakman, W., Chertova, M. V., van den Berg, A., & van Hinsbergen, D. J. (2018). Puzzling features of western Mediterranean tectonics explained by slab dragging. *Nature Geoscience*, 11(3), 211-216.
- Spakman, W., Stein, S., van der Hilst, R., Wortel, R., 1989. Resolution experiments for NW Pacific subduction zone tomography. *Geophysical Research Letters* 16, 1097-1100.
- Srivastava, S. P., & Roest, W. R. (1996). Comment on "Porcupine plate hypothesis" by MF Gerstell and JM Stock (*Marine Geophysical Researches* 16, pp. 315-323, 1994). *Marine Geophysical Researches*, 18(5), 589-593.
- Steinberger, B., & O'Connell, R. J. (1998). Advection of plumes in mantle flow: implications for hotspot motion, mantle viscosity and plume distribution. *Geophysical Journal International*, 132(2), 412-434.
- Steinberger, B., & Torsvik, T. H. (2008). Absolute plate motions and true polar wander in the absence of hotspot tracks. *Nature*, 452(7187), 620-623.
- Steinberger, B., & Torsvik, T. H. (2010). Toward an explanation for the present and past locations of the poles. *Geochemistry, Geophysics, Geosystems*, 11(6).
- Steinberger, B., Gaina, C., 2007. Plate-tectonic reconstructions predict part of the Hawaiian hotspot track to be preserved in the Bering Sea. *Geology* 35, 407.
- Steinberger, B., Seidel, M. L., & Torsvik, T. H. (2017). Limited true polar wander as evidence that Earth's nonhydrostatic shape is persistently triaxial. *Geophysical Research Letters*, 44(2), 827-834.
- Steiner, M. B. (2003). A cratonic Middle Jurassic paleopole: Callovian-Oxfordian stillstand (J-2 cusp), rotation of the Colorado Plateau, and Jurassic North American apparent polar wander. *Tectonics*, 22(3).
- Stern, R.J., 2004. Subduction initiation: spontaneous and induced. *Earth and Planetary Science Letters* 226, 275-292.
- Stern, R.J., Bloomer, S.H., 1992. Subduction zone infancy: examples from the Eocene Izu-Bonin-Mariana and Jurassic California arcs. *Geological Society of America Bulletin* 104, 1621-1636.
- Stern, R.J., Reagan, M., Ishizuka, O., Ohara, Y., Whattam, S., 2012. To understand subduction initiation, study forearc crust: To understand forearc crust, study ophiolites. *Lithosphere* 4, 469-483.
- Strik, G., Blake, T. S., Zegers, T. E., White, S. H., & Langereis, C. G. (2003). Paleomagnetism of flood basalts in the Pilbara Craton, Western Australia: Late Archaean continental drift and the oldest known reversal of the geomagnetic field. *Journal of Geophysical Research: Solid Earth*, 108(B12). <https://doi.org/10.1029/2003JB002475>
- Strik, G., Blake, T.S., Zegers, T.E., White, S.H. & Langereis, C.G., 2003. Paleomagnetism of flood basalts in the Pilbara Craton, Western Australia: Late Archaean continental drift and the oldest known reversal of the geomagnetic field. *J. Geophys. Res.*, 108(B12).
- Studnicki-Gizbert, C., Burchfiel, B. C., Li, Z., & Chen, Z., 2008. Early Tertiary Gonjo basin, eastern Tibet: Sedimentary and structural record of the early history of India-Asia collision. *Geosphere*, 4(4), 713-735.

- Sukhov, A.N., Chekhovich, V.D., Lander, A.V., Presnyakov, S.L., Lepekhina, E.N., 2011. Age of the Shirshov submarine ridge basement (Bering Sea) based on the results of investigation of zircons using the U-Pb SHRIMP method. *Doklady Earth Sciences* 439, 926-932.
- Sun, Z., Pei, J., Li, H., Xu, W., Jiang, W., Zhu, Z., ... & Yang, Z., 2012. Paleomagnetism of late Cretaceous sediments from southern Tibet: Evidence for the consistent paleolatitudes of the southern margin of Eurasia prior to the collision with India. *Gondwana Res.*, 21(1), 53-63.
- Sutherland, R., Collot, J., Bache, F., Henrys, S., Barker, D., Browne, G., Lawrence, M., Morgans, H., Hollis, C., Clowes, C., 2017. Widespread compression associated with Eocene Tonga-Kermadec subduction initiation. *Geology* 45, 355-358.
- Suttie, N., Biggin, A., & Holme, R. (2015). Robust estimators of paleosecular variation. *Geophysical Journal International*, 200(2), 1046-1051.
- Swanson-Hysell, N. L., Ramezani, J., Fairchild, L. M., and Rose, I. R. (2019). Failed rifting and fast drifting: Midcontinent Rift development, Laurentia's rapid motion and the driver of Grenvillian orogenesis. *Bulletin*, 131(5-6), 913-940.
- Swanson-Hysell, N. L., Vaughan, A. A., Mustain, M. R., & Asp, K. E. (2014). Confirmation of progressive plate motion during the Midcontinent Rift's early magmatic stage from the Osler Volcanic Group, Ontario, Canada. *Geochemistry, Geophysics, Geosystems*, 15(5), 2039-2047.
- Symons, D. T. A., Erdmer, P., & McCausland, P. J. A. (2003). New 42 Ma cratonic North American paleomagnetic pole from the Yukon underscores another Cordilleran paleomagnetism-geology conundrum. *Canadian Journal of Earth Sciences*, 40(10), 1321-1334. doi:10.1139/e03-047
- Takahashi, M., Hoshi, H., Yamamoto, T., 1999. Miocene counterclockwise rotation of the Abukuma Mountains, Northeast Japan. *Tectonophysics* 306, 19-31.
- Takeuchi, A., 2004. Basement-involved tectonics in North Fossa Magna, central Japan. *Earth, planets and space* 56, 1261-1269.
- Takeuchi, T., Kodama, K., Ozawa, T., 1999. Paleomagnetic evidence for block rotations in central Hokkaido-south Sakhalin, Northeast Asia. *Earth and Planetary Science Letters* 169, 7-21.
- Tamaki, K., Suyehiro, K., Allan, J., Ingle Jr., J.C., Pisciotto, K.A., 1992. Tectonic synthesis and implications of Japan Sea ODP drilling, *Proc. ODP Scientific Results*. College Station, pp. 1333-1348.
- Tamaki, M., Itoh, Y., Watanabe, M., 2006. Paleomagnetism of the Lower to Middle Miocene Series in the Yatsuo area, eastern part of southwest Japan: clockwise rotation and marine transgression during a short period. *Bulletin of the Geological Survey of Japan* 57, 73-88.
- Tamaki, M., Kusumoto, S., Itoh, Y., 2010. Formation and deformation processes of late Paleogene sedimentary basins in southern central Hokkaido, Japan: paleomagnetic and numerical modeling approach. *Island Arc* 19, 243-258.
- Tamaki, M., Oshimbe, S., & Itoh, Y., 2008. A large latitudinal displacement of a part of Cretaceous forearc basin in Hokkaido, Japan: paleomagnetism of the Yezo Supergroup in the Urakawa area. *J. Geol. Soc. Japan*, 114(5), 207-217.
- Tan, X., & Kodama, K. P., 2002. Magnetic anisotropy and paleomagnetic inclination shallowing in red beds: Evidence from the Mississippian Mauch Chunk Formation, Pennsylvania. *J. Geophys. Res.*, 107(B11), EPM-9.
- Tan, X., & Kodama, K. P., 2003. An analytical solution for correcting paleomagnetic inclination error. *Geophys. J. Int.*, 152(1), 228-236.
- Tan, X., Gilder, S., Kodama, K. P., Jiang, W., Han, Y., Zhang, H., ... & Zhou, D., 2010. New paleomagnetic results from the Lhasa block: revised estimation of latitudinal shortening across Tibet and implications for dating the India-Asia collision. *Earth Planet. Sci. Lett.*, 293(3-4), 396-404.
- Tan, X., K.P., Kodama, H., Chen, D., Fang, D., Sun, & Li, Y., 2003. Paleomagnetism and magnetic anisotropy of Cretaceous red beds from the Tarim basin, northwest China: Evidence for a rock magnetic cause of anomalously shallow paleomagnetic inclinations from central Asia. *J. Geophys. Res.*, 108(B2).
- Tanaka, H., 1999. Circular asymmetry of the paleomagnetic directions observed at low latitude volcanic sites. *Earth Planets Space*, 51(12), 1279-1286.
- Tanaka, H., Tsunakawa, H., Yamagishi, H., Kimura, G., 1991. Paleomagnetism of the Shakotan Peninsula, West Hokkaido, Japan. *Journal of geomagnetism and geoelectricity* 43, 277-294.
- Tang, J., Xu, W., Niu, Y., Wang, F., Ge, W., Sorokin, A., Chekryzhov, I., 2016. Geochronology and geochemistry of Late Cretaceous-Paleocene granitoids in the Sikhote-Alin Orogenic Belt: Petrogenesis and implications for the oblique subduction of the paleo-Pacific plate. *Lithos* 266, 202-212.

- Tang, M., Liu-Zeng, J., Hoke, G. D., Xu, Q., Wang, W., Li, Z., ... & Wang, W., 2017. Paleoelevation reconstruction of the Paleocene-Eocene Gonjo basin, SE-central Tibet. *Tectonophysics*, 712, 170-181.
- Tararin, I., 2008. Granulites of the Kolpakovskaya Series in the sredinny range, Kamchatka: A myth or reality? *Petrology* 16, 193-209.
- Tararin, I., Badredinov, Z., Markovsky, B., Slyadnev, B., 2012. U-Pb SHRIMP dating of zircons from metamorphic complexes in eastern Kamchatka. *Russian Journal of Pacific Geology* 6, 114-130.
- Tarduno, J., Bunge, H.-P., Sleep, N., Hansen, U., 2009. The bent Hawaiian-Emperor hotspot track: Inheriting the mantle wind. *Science* 324, 50-53.
- Tarduno, J.A., Duncan, R.A., Scholl, D.W., Cottrell, R.D., Steinberger, B., Thordarson, T., Kerr, B.C., Neal, C.R., Frey, F.A., Torii, M., 2003. The Emperor Seamounts: Southward motion of the Hawaiian hotspot plume in Earth's mantle. *Science* 301, 1064-1069.
- Tauxe, L., & Kent, D. V. (2004). A simplified statistical model for the geomagnetic field and the detection of shallow bias in paleomagnetic inclinations: was the ancient magnetic field dipolar? *Geophysical Monograph Series*, 145, 101-155.
- Tauxe, L., & Kent, D. V., 1984. Properties of a detrital remanence carried by haematite from study of modern river deposits and laboratory redeposition experiments. *Geophys. J. Int.*, 76(3), 543-561.
- Tauxe, L., & Kodama, K. P., 2009. Paleosecular variation models for ancient times: Clues from Keweenaw lava flows. *Phys. Earth Planet. Inter.*, 177(1-2), 31-45.
- Tauxe, L., & Watson, G. S., 1994. The fold test: an eigen analysis approach. *Earth Planet. Sci. Lett.*, 122(3-4), 331-341.
- Tauxe, L., 1998. *Paleomagnetic Principles and Practice*, Kluwer Academic Publishers.
- Tauxe, L., 2005. Inclination flattening and the geocentric axial dipole hypothesis. *Earth Planet. Sci. Lett.*, 233(3-4), 247-261.
- Tauxe, L., and Kent, D. V. (2004). A simplified statistical model for the geomagnetic field and the detection of shallow bias in paleomagnetic inclinations: was the ancient magnetic field dipolar? *Geophysical Monograph Series*, 145, 101-155.
- Tauxe, L., Banerjee, S. K., Butler, R. F., and van der Voo, R. (2010). *Essentials of paleomagnetism*. Berkeley, CA: University of California Press.
- Tauxe, L., Constable, C., Johnson, C. L., Koppers, A. A., Miller, W. R., & Staudigel, H., 2003. Paleomagnetism of the southwestern USA recorded by 0–5 Ma igneous rocks. *Geochem. Geophys. Geosyst.*, 4(4).
- Tauxe, L., Gans, P., & Mankinen, E. A. (2004). Paleomagnetism and 40Ar/39Ar ages from volcanics extruded during the Matuyama and Brunhes Chrons near McMurdo Sound, Antarctica. *Geochemistry, Geophysics, Geosystems*, 5(6). doi:10.1029/2003gc000656
- Tauxe, L., Kodama, K. P., & Kent, D. V., 2008. Testing corrections for paleomagnetic inclination error in sedimentary rocks: a comparative approach. *Phys. Earth Planet. Inter.*, 169(1-4), 152-165.
- Tauxe, L., Kylstra, N., & Constable, C. (1991). Bootstrap statistics for paleomagnetic data. *Journal of Geophysical Research: Solid Earth*, 96(B7), 11723-11740.
- Tauxe, L., Luskin, C., Selkin, P., Gans, P., & Calvert, A. (2004). Paleomagnetic results from the Snake River Plain: Contribution to the time-averaged field global database. *Geochemistry, Geophysics, Geosystems*, 5(8). doi:10.1029/2003gc000661
- Tauxe, L., Shaar, R., Jonestrask, L., Swanson-Hysell, N. L., Minnett, R., Koppers, A. A. P., et al. (2016). PmagPy: Software package for paleomagnetic data analysis and a bridge to the Magnetics Information Consortium (MagIC) Database. *Geochemistry, Geophysics, Geosystems*, 17(6), 2450–2463. <https://doi.org/10.1002/2016GC006307>
- Tauxe, L., Steindorf, J. L., & Harris, A., 2006. Depositional remanent magnetization: Toward an improved theoretical and experimental foundation. *Earth Planet. Sci. Lett.*, 244(3-4), 515-529.
- Tebbens, S. F., and Cande, S. C. (1997). Southeast Pacific tectonic evolution from early Oligocene to present. *Journal of Geophysical Research: Solid Earth*, 102(B6), 12061-12084.
- Terekhov, E., Mozherovsky, A., Gorovaya, M., Tsoy, I., Vashchenkova, N., 2010. Composition of the rocks of the Kotikovo Group and the main stages in the Late Cretaceous-Paleogene evolution of the Terpeniya Peninsula, Sakhalin Island. *Russian Journal of Pacific Geology* 4, 260-273.
- Thompson, R., & Clark, R. M. (1982). A robust least-squares Gondwanan apparent polar wander path and the question of paleomagnetic assessment of Gondwanan reconstruction. *Earth and Planetary Science Letters*, 57(1), 152-158.
- Thompson, R., and Clark, R. M. (1981). Fitting polar wander paths. *Physics of the Earth and Planetary*

Interiors, 27(1), 1-7.

- Tikhomirov, P.L., Kalinina, E.A., Moriguti, T., Makishima, A., Kobayashi, K., Cherepanova, I.Y., Nakamura, E., 2012. The Cretaceous Okhotsk–Chukotka Volcanic Belt (NE Russia): Geology, geochronology, magma output rates, and implications on the genesis of silicic LIPs. *Journal of Volcanology and Geothermal Research* 221-222, 14-32.
- Tong, Y. B., Yang, Z., Gao, L., Wang, H., Zhang, X. D., An, C. Z., ... & Han, Z. R., 2015. Paleomagnetism of Upper Cretaceous red-beds from the eastern Qiangtang Block: Clockwise rotations and latitudinal translation during the India–Asia collision. *J. Asian Earth Sci.*, 114, 732-749.
- Tong, Y., Yang, Z., Mao, C., Pei, J., Pu, Z., & Xu, Y., 2017. Paleomagnetism of Eocene red-beds in the eastern part of the Qiangtang Terrane and its implications for uplift and southward crustal extrusion in the southeastern edge of the Tibetan Plateau. *Earth Planet. Sci. Lett.*, 475, 1-14.
- Torsvik, T. H., and Cocks, L. R. M. (2016). *Earth history and paleogeography*. Cambridge University Press.
- Torsvik, T. H., Eide, E. A., Redfield, T. F., Lundin, E., Smethurst, M. A., & Ebbing, J. (2004). South Atlantic reconstructions: a self-consistent model. *NGU Report* 2004.024, 100.
- Torsvik, T. H., Müller, R. D., van der Voo, R., Steinberger, B., and Gaina, C. (2008a). Global plate motion frames: toward a unified model. *Reviews of Geophysics*, 46(3).
- Torsvik, T. H., Rouse, S., Labails, C., & Smethurst, M. A. (2009). A new scheme for the opening of the South Atlantic Ocean and the dissection of an Aptian salt basin. *Geophysical Journal International*, 177(3), 1315-1333.
- Torsvik, T. H., Smethurst, M. A., Meert, J. G., van der Voo, R., McKerrow, W. S., Brasier, M. D., et al. (1996). Continental break-up and collision in the Neoproterozoic and Paleozoic—a tale of Baltica and Laurentia. *Earth-Science Reviews*, 40(3-4), 229-258.
- Torsvik, T. H., Smethurst, M. A., van der Voo, R., Trench, A., Abrahamsen, N., & Halvorsen, E. (1992). Baltica. A synopsis of Vendian-Permian paleomagnetic data and their paleotectonic implications. *Earth-Science Reviews*, 33(2), 133-152.
- Torsvik, T. H., Steinberger, B., Cocks, L. R. M., & Burke, K. (2008). Longitude: linking Earth's ancient surface to its deep interior. *Earth and Planetary Science Letters*, 276(3-4), 273-282.
- Torsvik, T. H., van der Voo, R., Doubrovine, P. V., Burke, K., Steinberger, B., Ashwal, L. D., ... & Bull, A. L. (2014b). Deep mantle structure as a reference frame for movements in and on the Earth. *Proceedings of the National Academy of Sciences*, 111(24), 8735-8740.
- Torsvik, T. H., van der Voo, R., Preeden, U., Mac Niocail, C., Steinberger, B., Doubrovine, P. V., et al. (2012). Phanerozoic polar wander, paleogeography and dynamics. *Earth-Science Reviews*, 114(3-4), 325-368.
- Torsvik, T.H. and van der Voo, R., (2002). Refining Gondwana and Pangea paleogeography: estimates of Phanerozoic non-dipole (octupole) fields. *Geophysical Journal International*, 151(3): 771-794.
- Torsvik, T.H., Doubrovine, P.V., Domeier, M. (2014a). Continental drift (paleomagnetism). In: Rink, W., Thompson, J. (eds) *Encyclopedia of Scientific Dating Methods*. Springer, Dordrecht.
- Torsvik, T.H., Doubrovine, P.V., Steinberger, B., Gaina, C., Spakman, W., Domeier, M., 2017. Pacific plate motion change caused the Hawaiian-Emperor Bend. *Nature communications* 8, 15660.
- Tsai, V. C., & Stevenson, D. J. (2007). Theoretical constraints on true polar wander. *Journal of Geophysical Research: Solid Earth*, 112(B5).
- Tsukanov, N., Palechek, T., Soloviev, A., Savelyev, D., 2014. Tectonostratigraphic complexes of the southern Kronotskii paleoarc (Eastern Kamchatka): Structure, age, and composition. *Russian Journal of Pacific Geology* 8, 233-246.
- Tsukanov, N., Saveliev, D., Kovalenko, D., 2018. Magmatic Complexes of the Vetlovaya Marginal Sea Paleobasin (Kamchatka): Composition and Geodynamic Setting. *Oceanology* 58, 92-106.
- Tsukanov, N., Skolotnev, S., Peyve, A., 2009. New data on the composition of ophiolites from the Kumroch-Valagin segment of the Achayvayam-Valagin paleoarc (Eastern Kamchatka), *Doklady Earth Sciences*. Springer, pp. 934-938.
- Tsukanov, N.V., Kramer, W., Skolotnev, S.G., Luchitskaya, M.V., Seifert, W., 2007. Ophiolites of the Eastern Peninsulas zone (Eastern Kamchatka): Age, composition, and geodynamic diversity. *Island Arc* 16, 431-456.
- Tucholke, B.E. and Sibuet, J.-C. (2012). Problematic plate reconstruction. *Nature Geoscience*, 5(10): 676-677.
- Ueda, H., 2016. Hokkaido. *The Geology of Japan*, 201-221.
- Ueda, H., Miyashita, S., 2005. Tectonic accretion of a subducted intraoceanic remnant arc in Cretaceous

- Hokkaido, Japan, and implications for evolution of the Pacific northwest. *Island Arc* 14, 582-598.
- Uzel, B., Langereis, C. G., Kaymakci, N., Sözbilir, H., Özkaymak, Ç., & Özkaptan, M. (2015). Paleomagnetic evidence for an inverse rotation history of Western Anatolia during the exhumation of Menderes core complex. *Earth and Planetary Science Letters*, 414, 108–125. <https://doi.org/10.1016/j.epsl.2015.01.008>
- Uzel, B., Sümer, Ö., Özkaptan, M., Özkaymak, Ç., Kuiper, K., Sözbilir, H., et al. (2017). Paleomagnetic and geochronological evidence for a major middle miocene unconformity in Söke Basin (western Anatolia) and its tectonic implications for the Aegean region. *Journal of the Geological Society*, 174(4), 721–740. <https://doi.org/10.1144/jgs2016-006>
- Vaes, B., (2022). Software for: "On pole position: causes of dispersion of the paleomagnetic poles behind apparent polar wander paths". Zenodo. <https://doi.org/10.5281/zenodo.6366399>
- Vaes, B., Gallo, L. C., & van Hinsbergen, D. J. (2022). On pole position: causes of dispersion of the paleomagnetic poles behind apparent polar wander paths. *Journal of Geophysical Research: Solid Earth*, 127(4), e2022JB023953.
- Vaes, B., Li, S., Langereis, C. G., & van Hinsbergen, D. J. (2021). Reliability of paleomagnetic poles from sedimentary rocks. *Geophysical Journal International*, 225(2), 1281-1303.
- Vaes, B., van Hinsbergen, D. J. J., van de Lagemaat, S.H.A., van der Wiel, E., Lom, N. Advokaat, E. L., . . . and Langereis, C.G. (2023). A global apparent polar wander path for the last 320 Ma calculated from site-level paleomagnetic data. *EarthArXiv*, <https://doi.org/10.31223/X55368>.
- Vaes, B., van Hinsbergen, D. J., & Boschman, L. M. (2019). Reconstruction of subduction and back-arc spreading in the NW Pacific and Aleutian Basin: Clues to causes of Cretaceous and Eocene plate reorganizations. *Tectonics*, 38(4), 1367-1413.
- Valyashko, G., Chernyavsky, G., Seliverstov, N., Ivanenko, A., 1993. Back-arc spreading in the Komandorsky Basin. *Papers of the Russian Academy of Sciences* 338, 212-216.
- van Alstine, D. R., and de Boer, J. (1978). A new technique for constructing apparent polar wander paths and the revised Phanerozoic path for North America. *Geology*, 6(3), 137-139.
- van de Lagemaat, S. H., Kamp, P. J., Boschman, L. M., & van Hinsbergen, D. J. (2023). Reconciling the Cretaceous breakup and demise of the Phoenix Plate with East Gondwana orogenesis in New Zealand. *Earth Science Reviews*, 236, 104276.
- van de Lagemaat, S. H., Swart, M. L., Vaes, B., Kusters, M. E., Boschman, L. M., Burton-Johnson, A., ... and van Hinsbergen, D. J. (2021). Subduction initiation in the Scotia Sea region and opening of the Drake Passage: When and why?. *Earth-Science Reviews*, 215, 103551.
- van de Lagemaat, S. H., van Hinsbergen, D. J., Boschman, L. M., Kamp, P. J., & Spakman, W. (2018). Southwest Pacific absolute plate kinematic reconstruction reveals major Cenozoic Tonga-Kermadec slab dragging. *Tectonics*, 37(8), 2647-2674.
- van der Boon, A., Biggin, A. J., Thallner, D., Hounslow, M. W., Bono, R., Nawrocki, J., ... & Da Silva, A. C. (2022). A persistent non-uniformitarian paleomagnetic field in the Devonian?. *Earth-Science Reviews*, 231, 104073.
- van der Hilst, R., Engdahl, R., Spakman, W., Nolet, G., 1991. Tomographic imaging of subducted lithosphere below northwest Pacific island arcs. *Nature* 353, 37.
- van der Meer, D. G., Spakman, W., van Hinsbergen, D. J., Amaru, M. L., & Torsvik, T. H. (2010). Towards absolute plate motions constrained by lower-mantle slab remnants. *Nature Geoscience*, 3(1), 36-40.
- van der Meer, D. G., van Hinsbergen, D. J., & Spakman, W. (2018). Atlas of the underworld: Slab remnants in the mantle, their sinking history, and a new outlook on lower mantle viscosity. *Tectonophysics*, 723, 309-448.
- van der Meer, D., Torsvik, T., Spakman, W., van Hinsbergen, D., Amaru, M., 2012. Intra-Panthalassa Ocean subduction zones revealed by fossil arcs and mantle structure. *Nature Geoscience* 5, 215.
- van der Voo, R. (1990a). The reliability of paleomagnetic data. *Tectonophysics*, 184(1), 1-9.
- van der Voo, R. (1990b). Phanerozoic paleomagnetic poles from Europe and North America and comparisons with continental reconstructions. *Reviews of Geophysics*, 28(2), 167-206.
- van der Voo, R., and French, R. B. (1974). Apparent polar wandering for the Atlantic-bordering continents: Late Carboniferous to Eocene. *Earth-Science Reviews*, 10(2), 99-119.
- van der Voo, R., van Hinsbergen, D.J.J., Domeier, M., Spakman, W. and Torsvik, T.H., (2015). Latest Jurassic–earliest Cretaceous closure of the Mongol-Okhotsk Ocean: A paleomagnetic and seismological-tomographic analysis, Late Jurassic Margin of Laurasia–A Record of Faulting Accommodating Plate Rotation. *Geological Society of America Special Papers*, pp. 589-606.

- van der Werff, W., 2000. Backarc deformation along the eastern Japan Sea margin, offshore northern Honshu. *Journal of Asian earth sciences* 18, 71-95.
- van Hinsbergen, D. J. J., Dekkers, M. J., Bozkurt, E., & Koopman, M. (2010). Exhumation with a twist: Paleomagnetic constraints on the evolution of the Menderes metamorphic core complex, western Turkey. *Tectonics*, 29(3), 1–33. <https://doi.org/10.1029/2009TC002596>
- van Hinsbergen, D. J. J., Straathof, G. B., Kuiper, K. F., Cunningham, W. D., & Wijbrans, J. (2008). No vertical axis rotations during Neogene transpressional orogeny in the NE Gobi Altai: coinciding Mongolian and Eurasian early Cretaceous apparent polar wander paths. *Geophysical Journal International*, 173(1), 105–126. doi:10.1111/j.1365-246X.2007.03712.x
- van Hinsbergen, D. J., de Groot, L. V., van Schaik, S. J., Spakman, W., Bijl, P. K., Sluijs, A., et al. (2015). A paleolatitude calculator for paleoclimate studies. *PLoS One*, 10(6), e0126946.
- van Hinsbergen, D. J., Dekkers, M. J., & Koc, A., 2010. Testing Miocene remagnetization of Bey Dağları: Timing and amount of Neogene rotations in SW Turkey. *Turk. J. Earth Sci.*, 19(2), 123-156.
- van Hinsbergen, D. J., Lippert, P. C., Dupont-Nivet, G., McQuarrie, N., Doubrovine, P. V., Spakman, W., & Torsvik, T. H., 2012. Greater India Basin hypothesis and a two-stage Cenozoic collision between India and Asia. *Proc. Natl. Acad. Sci. U.S.A.*, 109(20), 7659-7664.
- van Hinsbergen, D. J., Lippert, P. C., Li, S., Huang, W., Advokaat, E. L., & Spakman, W., 2019. Reconstructing Greater India: Paleogeographic, kinematic, and geodynamic perspectives. *Tectonophysics*, 760, 69-94.
- van Hinsbergen, D. J., Spakman, W., Vissers, R. L., and van der Meer, D. G. (2017). Comment on “Assessing Discrepancies Between Previous Plate Kinematic Models of Mesozoic Iberia and Their Constraints” by Barnett-Moore Et Al. *Tectonics*, 36(12), 3277-3285.
- van Hinsbergen, D. J., Straathof, G. B., Kuiper, K. F., Cunningham, W. D., & Wijbrans, J. (2008). No vertical axis rotations during Neogene transpressional orogeny in the NE Gobi Altai: coinciding Mongolian and Eurasian early Cretaceous apparent polar wander paths. *Geophysical Journal International*, 173(1), 105-126.
- van Hinsbergen, D. J., Torsvik, T. H., Schmid, S. M., Mañenco, L. C., Maffione, M., Vissers, R. L., . . . Spakman, W. (2020). Orogenic architecture of the Mediterranean region and kinematic reconstruction of its tectonic evolution since the Triassic. *Gondwana Research*, 81, 79-229.
- van Hinsbergen, D.J., Steinberger, B., Doubrovine, P.V., Gassmöller, R., 2011. Acceleration and deceleration of India-Asia convergence since the Cretaceous: Roles of mantle plumes and continental collision. *Journal of Geophysical Research: Solid Earth* 116.
- van Hinsbergen, D.J.J., Mensink, M., Langereis, C.G., Maffione, M., Spalluto, L., Tropeano, M. and Sabato, L., (2014). Did Adria rotate relative to Africa? *Solid Earth*, 5(2): 611-629.
- van Hinsbergen, D.J.J., Peters, K., Maffione, M., Spakman, W., Guilmette, C., Thieulot, C., Plümper, O., Gürer, D., Brouwer, F.M., Aldanmaz, E., Kaymakçı, N., 2015. Dynamics of intraoceanic subduction initiation: 2. Suprasubduction zone ophiolite formation and metamorphic sole exhumation in context of absolute plate motions. *Geochemistry, Geophysics, Geosystems* 16, 1771-1785.
- van Horne, A., Sato, H., Ishiyama, T., 2017. Evolution of the Sea of Japan back-arc and some unsolved issues. *Tectonophysics* 710-711, 6-20.
- Vandamme, D., 1994. A new method to determine paleosecular variation. *Phys. Earth planet. Inter.*, 85, 131–142.
- Vandamme, D., Courtillot, V., Besse, J., & Montigny, R. (1991). Paleomagnetism and age determinations of the Deccan Traps (India): Results of a Nagpur-Bombay Traverse and review of earlier work. *Reviews of Geophysics*, 29(2), 159-190.
- Veikkolainen, T., & Pesonen, L. J. (2021). Precambrian geomagnetic field—An overview. *Ancient Supercontinents and the Paleogeography of Earth*, 81-108.
- Vine, F. J., & Matthews, D. H. (1963). Magnetic anomalies over oceanic ridges. *Nature*, 199, 947-949.
- Vinogradov, V., Grigorev, V., Leites, A., 1988. Age of metamorphism of Sredinnyi Ridges rocks of Kamchatka *Izvestiya Akademii Nauk SSSR Seriya Geologicheskaya* 30-38.
- Vissers, R. L. M., & Meijer, P. T. (2012). Iberian plate kinematics and Alpine collision in the Pyrenees. *Earth-Science Reviews*, 114(1-2), 61-83.
- Vissers, R. L. M., & Meijer, P. T. (2012). Mesozoic rotation of Iberia: Subduction in the Pyrenees?. *Earth-Science Reviews*, 110(1-4), 93-110.
- Vizán, H. (1998). Paleomagnetism of the Lower Jurassic Lepáand Osta Arena formations, Argentine Patagonia. *Journal of South American Earth Sciences*, 11(4), 333-350.

- Vugteveen, R. W., Barnes, A. E., & Butler, R. F. (1981). Paleomagnetism of the Roskrige and Gringo Gulch Volcanics, southeast Arizona. *Journal of Geophysical Research*, 86(B5). doi:10.1029/JB086iB05p04021
- Wanke, M., Portnyagin, M., Hoernle, K., Werner, R., Hauff, F., van den Bogaard, P., Garbe-Schonberg, D., 2012. Bowers Ridge (Bering Sea): An Oligocene-Early Miocene island arc. *Geology* 40, 687-690.
- Wanke, M., Portnyagin, M., Werner, R., Hauff, F., Hoernle, K., Garbe-Schönberg, D., 2011. Geochemical evidence for subduction related origin of the Bowers and Shirshov Ridges (Bering Sea, NW Pacific), KALMAR - Second Bilateral Workshop on Russian-German Cooperation on Kurile-Kamchatka and Aleutian Marginal Sea-Island Arc Systems. GEOMAR, Trier, Germany.
- Weaver, R., Roberts, A.P., Flecker, R., Macdonald, D.I.M., Fot'yanova, L.M., 2003. Geodynamic implications of paleomagnetic data from Tertiary sediments in Sakhalin, Russia (NW Pacific). *Journal of Geophysical Research: Solid Earth* 108.
- Wegener, A. (1912). Die entstehung der kontinente. *Geologische Rundschau*, 3(4), 276-292.
- Westerweel, J., Roperch, P., Licht, A., Dupont-Nivet, G., Win, Z., Poblete, F., ... & Aung, D. W., 2019. Burma Terrane part of the Trans-Tethyan arc during collision with India according to paleomagnetic data. *Nat. Geosci.*, 12(10), 863-868.
- Whittaker, J. M., Muller, R. D., Leitchenkov, G., Stagg, H., Sdrolias, M., Gaina, C., & Goncharov, A. (2007). Major Australian-Antarctic plate reorganization at Hawaiian-Emperor bend time. *Science*, 318(5847), 83-86.
- Whittaker, J. M., Williams, S. E., & Müller, R. D. (2013). Revised tectonic evolution of the Eastern Indian Ocean. *Geochemistry, Geophysics, Geosystems*, 14(6), 1891-1909.
- Wilkinson, M. D., Dumontier, M., Aalbersberg, Ij. J., Appleton, G., Axton, M., Baak, A., et al. (2016). Comment: The FAIR Guiding Principles for scientific data management and stewardship. *Scientific Data*, 3, 1-9.
- Williams, S. E., Whittaker, J. M., & Müller, R. D. (2011). Full-fit, palinspastic reconstruction of the conjugate Australian-Antarctic margins. *Tectonics*, 30(6).
- Wilson, J. T. (1963). A possible origin of the Hawaiian Islands. *Canadian Journal of Physics*, 41(6), 863-870.
- Woods, M.T., Davies, G.F., 1982. Late Cretaceous genesis of the Kula plate. *Earth and Planetary Science Letters* 58, 161-166.
- Worrall, D.M., 1991. Tectonic history of the Bering Sea and the evolution of Tertiary strike-slip basins of the Bering Shelf. Geological Society of America.
- Worrall, D.M., Kruglyak, V., Kunst, F., Kuznetsov, V., 1996. Tertiary tectonics of the Sea of Okhotsk, Russia: Far-field effects of the India-Eurasia collision. *Tectonics* 15, 813-826.
- Wright, N. M., Müller, R. D., Seton, M., & Williams, S. E. (2015). Revision of Paleogene plate motions in the Pacific and implications for the Hawaiian-Emperor bend. *Geology*, 43(5), 455-458.
- Wright, N. M., Seton, M., Williams, S. E., & Mueller, R. D. (2016). The Late Cretaceous to recent tectonic history of the Pacific Ocean basin. *Earth-Science Reviews*, 154, 138-173.
- Wu, L., Kravchinsky, V. A., & Potter, D. K., 2017. Apparent polar wander paths of the major Chinese blocks since the Late Paleozoic: Toward restoring the amalgamation history of east Eurasia. *Earth-Sci. Rev.*, 171, 492-519.
- Wu, L., Murphy, J. B., Quesada, C., Li, Z. X., Waldron, J. W., Williams, S., ... & Collins, W. J., 2020. The amalgamation of Pangea: Paleomagnetic and geological observations revisited. *Geol. Soc. Am. Bull.*, doi:10.1130/b35633.1.
- Wu, L., Murphy, J. B., Quesada, C., Li, Z. X., Waldron, J. W., Williams, S., et al. (2021). The amalgamation of Pangea: Paleomagnetic and geological observations revisited. *Bulletin*, 133(3-4), 625-646.
- Yamaji, A., Momose, H., & Torii, M. (1999). Paleomagnetic evidence for Miocene transtensional deformations at the eastern margin of the Japan Sea. *Earth, planets and space*, 51(2), 81-92.
- Yang, Y.-T., 2013. An unrecognized major collision of the Okhotomorsk Block with East Asia during the Late Cretaceous, constraints on the plate reorganization of the Northwest Pacific. *Earth-Science Reviews* 126, 96-115.
- Yang, Y.-T., Guo, Z.-X., Song, C.-C., Li, X.-B. and He, S., (2015). A short-lived but significant Mongol-Okhotsk collisional orogeny in latest Jurassic-earliest Cretaceous. *Gondwana Research*, 28(3): 1096-1116.
- Yi, Z., Liu, Y., & Meert, J. G. (2019). A true polar wander trigger for the Great Jurassic East Asian Aridification. *Geology*, 47(12), 1112-1116.
- Yogodzinski, G.M., Rubenstone, J.L., Kay, S.M., Kay, R.W., 1993. Magmatic and tectonic development of

- the western Aleutians: An oceanic arc in a strike-slip setting. *Journal of Geophysical Research: Solid Earth* 98, 11807-11834.
- Yonkee, W.A. and Weil, A.B., (2015). Tectonic evolution of the Sevier and Laramide belts within the North American Cordillera orogenic system. *Earth-Science Reviews*, 150: 531-593.
- Yoon, S.H., Sohn, Y.K., Chough, S.K., 2014. Tectonic, sedimentary, and volcanic evolution of a back-arc basin in the East Sea (Sea of Japan). *Marine Geology* 352, 70-88.
- Yoshida, T., Kimura, J.-I., Yamada, R., Acocella, V., Sato, H., Zhao, D., Nakajima, J., Hasegawa, A., Okada, T., Honda, S., Ishikawa, M., Prima, O.D.A., Kudo, T., Shibazaki, B., Tanaka, A., Imaizumi, T., 2014. Evolution of late Cenozoic magmatism and the crust–mantle structure in the NE Japan Arc. Geological Society, London, Special Publications 385, 335-387.
- Zahirovic, S., Seton, M., Müller, R., 2014. The Cretaceous and Cenozoic tectonic evolution of Southeast Asia. *Solid Earth* 5, 227.
- Zhang, Y., Huang, W., Huang, B., van Hinsbergen, D. J., Yang, T., Dupont-Nivet, G., & Guo, Z., 2018. 53–43 Ma deformation of eastern Tibet revealed by three stages of tectonic rotation in the Gongjue basin. *J. Geophys. Res.*, 123(5), 3320-3338.
- Zhao, P., Alexandrov, I., Jahn, B.m., Ivin, V., 2018. Timing of Okhotsk Sea Plate Collision With Eurasia Plate: Zircon U-Pb Age Constraints From the Sakhalin Island, Russian Far East. *Journal of Geophysical Research: Solid Earth* 123, 8279-8293.
- Zharov, A.E., 2005. South Sakhalin tectonics and geodynamics: A model for the Cretaceous-Paleogene accretion of the East Asian continental margin. *Russian Journal of Earth Sciences* 7, 1-31.
- Zijderveld, J. D. A., 1967. A.C. demagnetization of rocks. In *Methods in Paleomagnetism*, eds D. W. Collinson, K. M. Creer, and S. K. Runcorn (New York, NY: Elsevier), 256–286.
- Zinkevich, V., Kolodyazhny, S.Y., Bragina, L., Konstantinovskaya, Y.A., Fedorov, P., 1994. Tectonics of the eastern edge of Kamchatka's Sredinny metamorphic massif. *Geotectonics* 28, 75.
- Zinkevich, V., Tsukanov, N., 1993. Accretionary tectonics of Kamchatka. *International Geology Review* 35, 953-973.
- Zonenshain, L.P., 1990. *Geology of the USSR: a plate-tectonic synthesis*. Amer. Geophys. Union, Geodynamic Ser. 21, 242.
- Zyabrev, S., 2011. Stratigraphy and structure of the central East Sakhalin accretionary wedge (Eastern Russia). *Russian Journal of Pacific Geology* 5, 313.

Samenvatting in het Nederlands

Paleomagnetisme biedt het enige kwantitatieve instrument om de positie en beweging van tektonische platen en continenten te reconstrueren op geologische tijdschalen. Voor deze reconstructies worden vaak poolpaden gebruikt, die de vroegere positie en beweging van tektonische platen ten opzichte van de rotaties van de aarde beschrijven. Naast het bieden van een paleomagnetisch referentiekader voor het reconstrueren van paleogeografie, worden deze paden gebruikt om relatieve tektonische verplaatsingen ten opzichte van andere lithosferische blokken te kwantificeren. Een bekend probleem hierbij is dat conventionele benaderingen voor het berekenen van poolpaden belangrijke bronnen van onzekerheid in de onderliggende data buiten beschouwing laten, zoals de dispersie van de paleomagnetische data of onzekerheid in de ouderdom van het gemonsterde gesteente. Tot nu toe voorgestelde oplossingen bleven echter grotendeels kwalitatief. Recentelijk is dit probleem urgenter geworden: Rowley (2019) toonde aan dat meer dan 50% van de gegevens die gebruikt zijn voor het berekenen van het meest gebruikte mondiale poolpad statistisch significant verschillen van dat poolpad zelf. Dit suggereert dat de resolutie waarmee een geologisch betekenisvol statistisch verschil tussen een paleomagnetische dataset en een poolpad kan worden bepaald sterk beperkt is, wat de huidige tektonische en paleogeografische toepassingen van paleomagnetisme ondermijnt.

Dit proefschrift heeft als doel de oorzaken van de dispersie van paleomagnetische data achter poolpaden inzichtelijk te maken en een nieuw mondiaal poolpad te berekenen waarin de belangrijkste onzekerheden worden meegenomen, zodat het gebruikt kan worden om geologisch betekenisvolle relatieve verplaatsingen te bepalen. We laten zien dat de onzekerheid van poolpaden die zijn berekend op basis van paleomagnetische polen – de huidige standaard – voornamelijk wordt bepaald door de subjectieve keuzes met betrekking tot het aantal datapunten dat per pool wordt gebruikt. Dit proefschrift presenteert een nieuwe benadering waarbij poolpaden worden berekend op basis van paleomagnetische data op het niveau van individuele spotmetingen in plaats van paleomagnetische polen. Zo wordt er een groter gewicht toegekend aan grotere datasets en worden temporale en ruimtelijke onzekerheden in de paleomagnetische data gepropageerd in het uiteindelijke poolpad. We introduceren hiervoor een reeks betrouwbaarheidscriteria voor het gebruik van paleomagnetische datasets van sedimentair gesteente. We laten zien dat sedimentaire opeenvolgingen waardevolle paleomagnetische data kunnen leveren als ze gecorrigeerd worden voor inklinatievervlakking en als ze adequaat de paleoseculaire variatie van het aardmagnetisch veld weergeven. We tonen aan dat het toepassen van veelgebruikte datafilters niet significant bijdraagt aan de positie of precisie van paleomagnetische polen en dat de meest effectieve manier om de gemiddelde poolpositie door de tijd te bepalen is door zoveel mogelijk onafhankelijke spotmetingen van het aardmagnetische veld te verzamelen. We gebruiken deze criteria vervolgens om een nieuwe mondiale paleomagnetische database samen te stellen, die alleen de ~32% meest betrouwbare gegevens bevat uit eerdere compilaties.

We presenteren een nieuw mondiaal poolpad voor de laatste 320 miljoen jaar met behulp van de nieuwe statistische benadering die in dit proefschrift wordt geïntroduceerd. We constateren dat de eerste-orde geometrie van dit pad vergelijkbaar is met eerdere modellen, maar met kleinere onzekerheden. Bovendien laten we zien dat het corrigeren voor een scheve verdeling van de ouderdommen in de onderliggende paleomagnetische data een verbeterde kwantificering van de snelheid van poolzwerfing mogelijk maakt en dat eerder waargenomen pieken in poolzwerfing waarschijnlijk vertekend werden door deze scheve verdeling. We introduceren vervolgens de open-source webapplicatie *APWP-online.org* die gebruiksvriendelijke tools biedt om poolpaden te berekenen met behulp van onze nieuwe methodologie, evenals voor het berekenen van relatieve paleomagnetische verplaatsingen. Deze website bevat ook de mondiale paleomagnetische referentiedatabase die ten grondslag ligt aan het nieuwe mondiale poolpad. Zo fungeert deze website als een platform voor de wetenschappelijke gemeenschap voor de verbetering van het pad in de toekomst door de toevoeging van nieuwe paleomagnetische data.

Tot slot presenteren we nieuwe kwantitatieve schattingen van werkelijke poolzwerfing tijdens de laatste 320 miljoen jaar door ons nieuwe mondiale poolpad te vergelijken met bestaande referentiekaders voor de beweging van tektonische platen ten opzichte van de aardmantel. De berekende paden van werkelijke poolzwerfing laten zien dat de rotaties van de vaste aarde ten opzichte van de rotatieas als gevolg van werkelijke poolzwerfing voornamelijk plaatsvonden rond twee nagenoeg orthogonale assen in het equatoriale vlak. We bediscussiëren de geodynamische implicaties van deze bevindingen en bespreken toekomstige mogelijkheden voor de identificatie en kwantificering van werkelijke poolzwerfing op geologische tijdschalen.

Acknowledgements

This thesis is the product of many years of research and is the end result of a large chapter of my life here at Utrecht University. Even though there is only one name on the cover of this book, I definitely did not do this alone. Completing this PhD would not have been possible without the great support and guidance from my colleagues, friends and family. I now want to take the opportunity to express my gratitude to some of the many people who supported me along the way to completion of my PhD.

First and foremost, I want to thank my promotor **Douwe** for giving me this opportunity. I could not have wished for a better supervisor, and it has been great to work with you during all these years. It all started in September 2016 when you gave me some dark and forgotten corner of the world (I only knew Kamchatka from the board game Risk) of which I could make a tectonic reconstruction for my master thesis. Since then, your never-ending energy, enthusiasm, creativity, and mind-blowing geological knowledge provided great inspiration and motivation for me during my research. You succeeded very well in challenging me to develop myself in many different areas and I thoroughly enjoyed all the hours we spend together thinking long and hard about how to make paleomagnetism great again. In the end, we did not even start the actual project that I was hired for, but we instead spent >4 years on this side project of ‘just’ updating the paleomagnetic reference frame. Thank you for giving me a ton of opportunities, allowing me to obtain a teaching qualification (and conveniently taking over some of your teaching duties in the process..), to go to a lot of workshops and conferences and to collaborate with many researchers from around the world. I am really thankful for the great team you put together and for the stimulating work environment you created for us. Thank you for being a great person and mentor, I am looking forward to keeping in touch and to continuing our work together.

I am hugely grateful to my two office buddies and paranymphs **Suus** and **Erik**. I am certain that I could not have finished my PhD on time (well, 3 weeks after the end of my contract..) without the support of you guys. You were always there to have long coffee and lunch breaks, to motivate me, listen to my complaints and doubts and to share all kinds of fun experiences with, like fieldwork teaching in Aliaga, conferences and parties. Thanks!

Special thanks to the rest of the TRIGGER team and Mantle Dynamics group - **Abdul, Cedric, Eldert, Goran, Kalijn, Lydian, Nalan, Thomas** and **Wim** - for all the fun, guidance and great conversations over coffee, lunch, beers and dinner. I am still not sure what triggered the plate reorganization, but I guess we will figure it out at some point..

I am indebted to all my collaborators who locked themselves up in a house in Stoutenburg in November 2019 to build a big paleomagnetic database. **Annika, Carl, Pete, Leny, Shihu**, thank you for your help with my project(s). Special thanks to **Cor**, who taught me a lot about the statistics and fundamentals of paleomagnetism, but also about where to find

some of the best UNESCO world heritage sites. I also want to thank **Mathijs** and **Joren** for building some great web applications for paleomagnetism and my master student **Dieke** for organizing a fun field trip together and for writing one of the chapters of this thesis. **Leandro**, thank you for your willingness to collaborate with somebody (in English!) on the other side of the world and for becoming a good friend.

There are many colleagues who made my life as a PhD candidate much easier and much more enjoyable: thank you **Annemijn**, **Rûna**, **Janneke**, **Hen**, **Hanneke**, **Inge Loes**, **Alissa**, **Rosa**, **Liz**, **Frenk**, **Romy**, **Martha**, **Renato**, **Anne**, **Remco**, **Simone**, **Pelle**, **Rob**, **Marius** and **Louise** for having coffee and lunch together, and for having fun at the many borrels and conferences (special shout-out to the NAC parties). Special thanks to **Paul** (Meijer) and **João** for helping me develop myself as a teacher and for being a big inspiration.

Bart, **Esmée**, **Floris**, **Gaston**, **Jos**, **Luuk**, **Miek**, **Noor**, **Sab**, **Sam**, **Rowan**, it has been great to have you in my life for more than 10 years. Many thanks for your friendship, for all the great adventures and for supporting me from our time as bachelor students up to now. I hope our friendship will last the rest of our lives. Special thanks to my roommate Bart, who has been a great friend and who has always been there for me to listen to all my overly detailed stories about everything related to this PhD and to prepare great food when I returned from the office being brain dead after a long day of programming or writing.

Paul and **Floran**, thanks a lot for supporting me and pushing me to become a scientist since 2005 or so. I really enjoyed our trips to places all over Europe and discussions about all sorts of societal problems over beers or Social Deal dinners, and look forward to continuing those. Thanks to everyone from the **Bubs** for your friendship and for not forgetting me when I seem to disappear to some exotic country. I also want to thank **Annerose**, **Chris**, **Wouter**, **Terry Nick** and all my other tennis buddies and teammates for keeping me healthy, both mentally and physically.

I am greatly indebted to my parents, who have supported me all my life and have created a safe and stimulating environment to grow up in. **Mom**, **dad**, I cannot thank you enough. Thanks also to my brother **Tim**, who has always challenged me to be more creative, smarter, and faster in whatever sports, computer or board game we played. A big thanks to my **grandparents**, who greatly stimulated my curiosity and interest in the world around us by taking us to the zoo, museums and many other places. I would like to pay a special tribute to **Opa Ton**, whose enthusiasm and admiration for science and the natural world have always been a great inspiration to me. I know you would have been most proud.

Last but not least, I want to thank my biggest supporter, **Fre**. I am so grateful to have you in my life, you bring me so much joy and love and you have always been there for me in the past 4.5 years. I would not have been able to write a book like this without your support. Thank you so much for listening to my endless stories and incomprehensible ramblings about work and for reminding me sometimes that life is about much more than work. I thoroughly enjoyed travelling and hiking together, going out for a dinner/movie/museum, playing squash or tennis, (sometimes) beating you at a board game, and all the other stuff we did together. Thank you for sharing these years with me, you are the best!

Curriculum vitae

- 13 September 1993 **Born in Eindhoven, The Netherlands**
- 2005 - 2011 **Secondary school (gymnasium)**
Lorentz Casimir Lyceum, Eindhoven
- 2011 - 2014 **BSc Earth Sciences (*cum laude*)**
Utrecht University, The Netherlands
- 2014 - 2017 **MSc Earth Structure & Dynamics (*cum laude*)**
Utrecht University, The Netherlands
- 2015 - 2016 **MSc Geophysics (Swiss-European Mobility Programme)**
ETH Zürich, Switzerland
- 2017 - 2018 **Junior teacher, Department of Earth Sciences**
Utrecht University, The Netherlands
- 2018 - 2019 **Junior researcher, Department of Earth Sciences**
Utrecht University, The Netherlands
- 2019 - 2023 **PhD Candidate, Mantle Dynamics group**
Utrecht University, The Netherlands



Bibliography

Included in this thesis (Chapters 1-6):

1. **Vaes, B.**, van Hinsbergen, D. J. J., & Boschman, L. M. (2019). Reconstruction of subduction and back-arc spreading in the NW Pacific and Aleutian Basin: Clues to causes of Cretaceous and Eocene plate reorganizations. *Tectonics*, 38(4), 1367-1413.
2. **Vaes, B.**, Gallo, L. C., & van Hinsbergen, D. J. J. (2022). On pole position: causes of dispersion of the paleomagnetic poles behind apparent polar wander paths. *Journal of Geophysical Research: Solid Earth*, 127(4), e2022JB023953.
3. **Vaes, B.**, Li, S., Langereis, C. G., & van Hinsbergen, D. J. J. (2021). Reliability of paleomagnetic poles from sedimentary rocks. *Geophysical Journal International*, 225(2), 1281-1303.
4. Gerritsen, D., **Vaes, B.**, & van Hinsbergen, D. J. J. (2022). Influence of data filters on the position and precision of paleomagnetic poles: what is the optimal sampling strategy? *Geochemistry, Geophysics, Geosystems*, 23(4), e2021GC010269.
5. **Vaes, B.**, van Hinsbergen, D. J. J., van de Lagemaat, S. H. A., van der Wiel, E., Lom, N., Advokaat, E. L., Boschman, L. M., Gallo, L. C., Greve, A., Guilmette, C., Li, S., Lippert, P. C., Montheil, L., Qayyum, A. & Langereis, C. G. (in review). A global apparent polar wander path for the last 320 Ma calculated from site-level paleomagnetic data. *Earth-Science Reviews*.
6. **Vaes, B.**, van Hinsbergen, D. J. J., Paridaens, J. (in review). APWP-online.org: a global reference database and open-source tools for calculating apparent polar wander paths and relative paleomagnetic displacements. *Tektonika*.

Not included in this thesis:

7. van de Lagemaat, S. H., Swart, M. L., **Vaes, B.**, Kosters, M. E., Boschman, L. M., Burton-Johnson, A., ... & Van Hinsbergen, D. J. J. (2021). Subduction initiation in the Scotia Sea region and opening of the Drake Passage: When and why? *Earth-Science Reviews*, 215, 103551.
8. Koymans, M. R., van Hinsbergen, D. J. J., Pastor-Galán, D., **Vaes, B.**, & Langereis, C. G. (2020). Towards FAIR paleomagnetic data management through Paleomagnetism.org 2.0. *Geochemistry, Geophysics, Geosystems*, 21(2), e2019GC008838.
9. Gallo, L. C., Domeier, M., Sapienza, F., Swanson-Hysell, N., **Vaes, B.**, Zhang, Y., ... & van der Boon, A. (in press). Embracing uncertainty to resolve polar wander: a case study of Cenozoic North America. *Geophysical Research Letters*.
10. Montheil, L., Philippon, M., Münch, P., Camps, P., **Vaes, B.**, Cornée, J., ... & van Hinsbergen, D. J. J. (in review). Major rotations in the northeastern Caribbean region reveal large-scale intraplate deformation since the Eocene. *Tectonics*.
11. Xu, W., Yan, M., van Hinsbergen, D. J. J., Li, B., Guan, C., Fu, Q., ... & **Vaes, B.** (in review). Paleomagnetic evidence of 50° post-Eocene clockwise rotation of Mangkang and its implications on the tectonic evolution of the southeastern Tibetan Plateau. *Gondwana Research*.

